The Trace Element Composition of Sedimentary Pyrite: Factors Effecting Uptake and Uses of the Data for Determining Paleo-Ocean Conditions

by

Daniel D. Gregory

(BSc. Honours University of British Columbia)

Submitted in fulfillment of the requirements for the

degree of Doctor of Philosophy

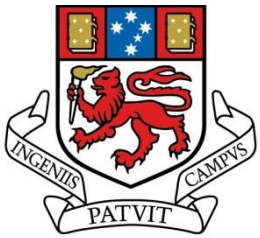

UNIVERSITY
OF TASMANIA

May 2014

Declaration

This thesis does not contain any material that has been accepted for degree or diploma by the University or any other institution, except where it has been duly acknowledged in the thesis. To the best of the author's knowledge it also contains no previously published material written by another person, except where it is acknowledged in the text of the thesis.

Daniel D. Gregory

Date:

Authority of Access

The publishers of the papers comprising Chapters 2 and 3 (Australian Journal of Earth Science and American Mineralogist respectively) hold the copyright for that content, and access to the material should be sought from the respective journals. The remaining non published content of the thesis may be made available for loan and limited copying and communication in accordance with the Copyright Act 1968.

Statement of Co-Authorship

The following people and institutions contributed to the publication of work undertaken as part of this thesis:

Daniel Gregory, University of Tasmania = **Candidate**

Ross Large ,University of Tasmania = **Author 1**

Sebastien Meffre, University of Tasmania = **Author 2**

Jacqueline Halpin, University of Tasmania = **Author 3**

Stuart Bull, University of Tasmania = **Author 4**

Elena Lounejeva, University of Tasmania = **Author 5**

Jeffrey Steadman, University, of Tasmania = **Author 6**

Patrick Sack, Yukon Geological Survey = **Author 7**

Timothy Lyons, University of California Riverside = **Author 8**

Anthony Chappaz, Central Michigan University = **Author 9**

Arthur Hickman, Geological Survey of Western Australia = **Author 10**

Trevor Ireland, Australian National University = **Author 11**

Peter Holden, Australian National University = **Author 12**

Valeriy Maslennikov, Institute of Mineralogy, Russion Academy of Science, Urals Branch = **Author 13**

John Walshe, CSIRO = **Author 14**

Adam Bath, CSIRO = **Author 15**

Author details and their roles:

Paper 1, Mineralogy of metal contaminated estuarine sediments, Derwent estuary, Hobart, Australia: Implications for metal mobility***:***

Located in chapter 2

Candidate was the primary author (90%) and with author 2 contributed to the idea, its formalisation and development (8%).

Author 1 assisted with refinement and presentation (2%).

Paper 2, Comparison of metal enrichment in pyrite framboids from a metal-enriched and metal-poor estuary**:**

Located in chapter 3

Candidate was the primary author (90%) and with author 2 contributed to the idea, its formalisation and development (8%).

Author 1 assisted with refinement and presentation (2%).

Paper 3, Trace Element Content of Unmineralized Sedimentary Pyrite**:**

Located in chapter 4

Candidate was the primary author (54%) and with author 1 (8%) and author 8 (4%) contributed to the idea, its formalisation and development.

Author 3 under took some of the analyses and assisted with refinement and presentation (14%).

Author 4 assisted with refinement and presentation (1%).

Author 5 under took some of the analyses (9%).

Author 7 (2%), 9 (2%), 13 (2%) supplied samples and provided background information on the samples.

Data acquisition was primarily conducted by the primary author (32%), author 3 (24%) and author 5 (41%). The weighting of 54% for the entire paper is due to the primary authors' portion of the data acquisition and the fact that the writing and preparation of the manuscript was completed by the primary author.

Paper 4, The Chemical Conditions of the Late Archean Hamersley Basin Inferred from Whole Rock and Pyrite Geochemistry with $\Delta^{33}S$ and $\delta^{34}S$ Isotope Analyses**:**

Located in chapter 5

Candidate was the primary author (80%) and with author 1 (5%) contributed to the idea, its formalisation and development.

Author 6 (5%) under took some of the analyses.

Author 10 (5%) assisted with refinement and presentation.

Author 11 (2.5%) and 12 (2.5%) provided access to the SHRIMP-SI and aided in the analysis.

Paper 5, Trace element content of pyrite from the Kapai Slate, St. Ives Gold District, Western Australia: Implications for Ocean Chemistry and Ore Deposition**:**

Located in chapter 6

Candidate was the primary author (80%) and author 1 (4%) and 14 (3%) contributed to the idea, its formalisation and development.

Author 6 (4%) under took some of the analyses.

Author 15 (4%) supplied samples and provided background information on the samples and provided early versions of the plan map and cross section using CSIRO's model for the St Ives Gold District.

Author 12 (2.5%) and 13 (2.5%) provided access to the SHRIMP-SI and aided in the analysis.

We the undersigned agree with the above stated "proportion of work undertaken" for each of the above published (or submitted) peer-reviewed manuscripts contributing to this thesis:

Signed: _____ _____

Ross Large	*Jocelyn McPhie*
Supervisor	*Head of School*
CODES, ARC Centre of	*School of Earth Sciences*
Excellence in Ore Deposits	
University of Tasmania	University of Tasmania

Date:_____

Abstract

The trace element content of pyrite has received much research and is important to the fields of environmental geochemistry, ore deposit genesis and paleo-ocean reconstructions. Four aspects of the geochemistry of pyrite are investigated in this thesis: 1) the incorporation of trace elements into pyrite in a modern setting, 2) the variability of trace elements in sedimentary pyrite in ancient marine settings, 3) the use of trace elements in pyrite to interpret palaeo-ocean chemical conditions, and 4) modification of trace elements in sedimentary pyrite associated with later metamorphic and hydrothermal processes. To facilitate these investigations, detailed LA-ICPMS analyses were performed on pyrite from 49 different shale and unconsolidated sediment formations. These include detailed studies of the Derwent and Huon Estuaries that serve as modern high and low metal environments of sedimentary pyrite formation; the Hamersley and Fortescue Basins sediments which provide low metamorphic grade Archean aged examples of sedimentary pyrite; the Kapai Slate which is a high metamorphic grade, hydrothermally overprinted example of Archean aged pyrite and a series of 44 other shale units that are used to create a database of average trace element content of sedimentary pyrite.

The examination of trace element contents of sedimentary pyrite in modern settings is an important component of understanding how trace elements are incorporated into pyrite. Recent studies have provided data on the trace element content of pyrite from modern settings with current oceanic trace element contents. However, as the trace element content of the oceans varies throughout geologic time it is important to examine the incorporation of trace metals in pyrite at higher trace element concentrations than present. The Derwent Estuary provides an ideal site to examine the trace element uptake by pyrite in a high metal environment. Detailed mineralogical and geochemical analyses demonstrated the degree to which trace elements were available to be incorporated into pyrite, and LA-ICPMS analyses show the amount of each element incorporated into the pyrite. The data showed that not only is it important to have significant quantities of trace elements available to be incorporated but also, if the concentrations of certain trace elements available for incorporation are high, they can prevent other trace elements from being incorporated into the pyrite. The data have also shown that even though some trace elements can be incorporated into pyrite in contaminated estuaries, the amount of pyrite formed, and the amount of the trace elements within the pyrite, is not sufficient for pyrite to act as a major sink for the contaminants.

To demonstrate how trace element contents in sedimentary pyrite have varied according to geologic time, depositional setting and pyrite texture, a data base of pyrite chemistry from 45 different shale units was produced using LA-ICPMS. Some trace elements decrease with Earth evolution due to a decrease in Earth degassing and mafic magmatism. However, some elements, such as Mo, increase as a result of enhanced oxygenation that promoted the breakdown of sulfides and contributed additional trace elements to the oceans. Depositional setting of the shales in which the pyrite forms, is also an important control on the trace element content of sedimentary pyrite, with high trace element supply-settings having the highest trace element content. Pyrite texture differs based on diagenetic history and content of Fe and S present at the time of pyrite formation. Generally coarser grained pyrite forms later in digenesis and finer grained pyrite forms earlier (though fine euhedral pyrite is an exception to this). While no systematic differences were noted across the entire dataset with pyrite texture, in individual samples the early formed pyrite had the highest trace element content. The dataset also provides geochemical criteria to characterize sedimentary pyrite and can be used to support inferences made by mineral texture alone. Changes in pyrite from individual basins compared to the averages provided by the dataset can also be used to explain changes in ocean chemistry syn-pyrite deposition, similarly to how traditional analyses of whole rock are compared to average shale chemistry.

The variations in pyrite chemistry, as determined by LA-ICPMS, in the shales from the Hamersley and Fortescue basins, Western Australia, were investigated to provide an alternative method for paleo-ocean reconstructions. Pyrite is a sink for several trace elements in the marine environment and the amount of trace elements captured by sedimentary pyrite is essentially a record of the trace element content of the ocean and/or sediments at the time of deposition. Therefore, the content of trace elements in pyrite can be used to determine the chemical conditions of the ocean basin at the time of deposition of the sediments. In the Hamersley and Fortescue basins, trace elements form cycles that generally increase up-section and then decrease abruptly at the end of each cycle. These cycles are interpreted to be reflective of a series of pulses of atmospheric oxygen which result in the decomposition of continental sulfides and thus an increase of metal flux to the ocean. Periodic drops in trace element content reflect influxes of volcanically sourced S and/or Fe (as suggested by positive $\Delta^{33}S$ shifts) which causes elevated pyrite production and a drawdown of trace elements. Whole rock analyses show similar relationships and support the use of pyrite analyses to determine paleo-oceanic conditions.

One of the main benefits of using LA-ICPMS to determine trace element content of sedimentary pyrite is that it is a selective, in situ technique, unlike traditional bulk sample or sequential extraction techniques. This allows the determination of sedimentary pyrite trace element content in areas that have undergone significant (greenschist facies) metamorphism and/or hydrothermal overprint. The Kapai Slate from the St Ives gold district is an ideal area to demonstrate this capacity. The sedimentary pyrite from the Kapai Slate fit all the geochemical criteria developed for sedimentary pyrite. These analyses were used to determine that the Kapai Slate was deposited in an anoxic to euxinic basin with relatively low iron content and biological productivity. The analyses of the pyrite from the Kapai Slate also showed that it is not likely to be a major source of gold for the St Ives gold district, though the contained pyrite is elevated in gold. Preliminary investigations suggest that ratios of trace elements in pyrite may be a potential tool in mineral exploration, but further research is required for pyrite chemistry to be used as a robust technique with confidence.

By analyzing pyrite from a number of different settings across geologic time this study has greatly increased the understanding of the controls on the trace element contents in pyrite. The analyses of pyrite from the metal enriched Derwent Estuary have demonstrated the effects of high trace element abundance on trace element content in pyrite. The data base of trace element content of pyrite has shown how the trace elements available for incorporation have varied throughout earth's history and how that is reflected in the trace element content of pyrite. A more detailed study of how this element content of pyrite varies within individual basins was provided by the Hamersley and Fortescue basin study which also demonstrated how the pyrite data can be used to determine paleo-oceanic conditions. Finally the Kapai Slate analyses provide an example of how metamorphism and hydrothermal over print effect the trace element content of sedimentary pyrite and how, using LA-ICPMS, the sedimentary pyrite from these basins can still be used to determine paleo-oceanic conditions.

Acknowledgements

This work is part of a larger project under the direction of Ross Large and has been funded by CODES, ARC and CSIRO. Field support and whole rock geochemical analyses for the collection of the St. Ives samples were provided by Goldfields Limited. I would also like to thank the Western Australian core library and Goldfields for access to their core facilities.

I would also like to thank the Society of Economic Geologists who provided funding for me to attend three of their international conferences and several field trips, which greatly expanded my understanding of geology and enhanced my scientific network.

I am deeply indebted to my supervisors Ross Large, Sebastien Meffre and Stuart Bull who were all always happy to entertain my many questions. Without their expertise and patience this thesis would not have been completed. Thank you John Walshe for helping me gain access to the St. Ives drill core and for helping me understand the extensive geology and genetic models for the formation of the St. Ives deposits. Your time and readiness to show your data to me are very much appreciated. Many thanks to Rick Squire who helped me identify the different lithologies present at St Ives. Thank you also to Matt Crawford, Damien Keys, Mary Jane, Ayesha Ahmed and everyone at the St. Ives core facility for helping me find the right drill intervals and for supplying relevant cross sections, geochemical analyses and other drill core data.

I offer my gratitude to Tim Lyons who helped construct an idea of what ultimately became the form in which this thesis would take. Thank you to Bernd Lottermoser and Jacqueline Halpin who provided great critiques of the early versions of some of the chapters. I would also like to thank the reviewers and editors Tony Morrison, Anita Andrew, Martin Reich, Zsolt Berner and Alejandro Fernandez-Martinez of the two chapters that have been accepted for publication. Their comments greatly increased the quality of the chapters in this thesis. Thank you to my co-authors who have contributed comments of the manuscripts, samples for analyses and expertise in the use of the instruments used in my research. I would also like to offer my thanks to Karsten Goemann and Sandrin Feig for their help in the use of the SEM and microprobe and Ashley Townsend, Jay Thompson and Ian Little for conducting the bulk sample analyses used in the study. I must thank Sarah Gilbert, Ian Little, Jay Thompson and Leonid Danyushevsky for their expertise in the use of LA-ICPMS and Stafford McKnight for QXRD analyses in Chapter 2. Thank you to Trevor Ireland and Peter Holden for allowing me to use the SHRIMP-SI and helping me to operate it.

A special thank you is needed for my family, friends and co-workers at CODES who kept me relaxed throughout the completion of my dissertation. I would especially like to thank my wife whose constant support, encouragement and love have motivated me through the difficult times and has greatly helped me to successfully complete this thesis.

Table of Contents

List of Tables

List of Figures

Appendices

Chapter 1:
Introduction

1.1 Preamble

Diagenetic pyrite is an important sink for many different trace elements particularly As, Ni, Pb, Cu, Co, Mo, Sb, Se, Ag, Bi, Te, Cd and Au; listed in decreasing order of abundance. Diagenetic pyrite is generally enriched in these trace elements relative to their abundance in the host sedimentary rocks and in the ocean basin water in which they form. In this study I examine the relationship between the trace element content of the diagenetic pyrite and the geochemical conditions of the host ocean basin. Traditional paleo-ocean basin geochemical studies involve the use of redox sensitive trace elements in the bulk shale (whole rock) to determine paleo redox conditions (Algeo, 2004; Algeo and Lyons, 2006; Algeo and Maynard, 2004; Anbar et al., 2007). An alternate method, utilized here, uses laser ablation ICPMS (LA-ICPMS) to determine the trace metal content of pyrite that forms in the shale. The benefit of using pyrite instead of bulk sample analyses is that trace metals within the crystal structure of pyrite can be shielded from effects of metamorphism and hydrothermal overprint (Large et al., 2007). This could greatly increase the number of basins available that are appropriate to study paleo-oceanic conditions. An additional benefit of the LA-ICPMS technique is that because some trace metals occur in pyrite at much higher concentrations than found in the surrounding sediment it allows examination of elements (e.g. Au, Te, Se, Ag) often below detection limits using traditional analytical techniques. This is currently of particular interest in the field of ore deposit research as some models for the formation of orogenic gold deposits suggest that sedimentary pyrite may be the source for gold in many important deposits (Large et al., 2011; Large et al., 2009; Large et al., 2007; Pitcairn et al., 2006; Steadman et al., 2013; Thomas et al., 2011; Tomkins, 2010). A brief overview of the current understanding of 1) the formation of syngenetic and diagenetic pyrite and its trace metal content, 2) the use of trace metals to determine paleo-oceanic conditions and 3) new ore deposit models that use pyrite-bearing organic rich shale, as a source for major gold deposits, is presented in this chapter. The final section of this introduction includes an overview of the thesis and specific objectives of the individual chapters.

1.2 Formation of Diagenetic Pyrite

Syngenetic and diagenetic pyrite form in euxinic conditions within the water column or, more commonly, within euxinic conditions that develop in organic rich sediments. The mechanisms for the formation of this pyrite have been the focus of much research (Donald and Southam, 1999; Konhauser, 1998; Lennie et al., 1995; Neumann et al., 2005; Rickard and Luther, 1997; Rickard and Luther, 2007; Schoonen and Barnes, 1991; Schoonen, 2004; Wolthers et al., 2003). Most models of pyrite formation begin with the precipitation of iron monosulphides because they are rapidly nucleated, making the direct formation of pyrite effectively prohibited, even though it is more thermodynamically stable (Schoonen and Barnes, 1991). Mackinawite is the most common precursor iron monosulphide used in experimental studies (Lennie et al., 1995; Wolthers et al., 2003). It has been proposed that iron monosulphide is converted into pyrite according to the following reactions (Rickard and Luther, 1997):

$FeS_{am} + H_2S \leftrightarrow FeS_{aq}$

$FeS_{aq} + H_2S \leftrightarrow [FeS\text{-}SH_2]$

$[FeS\text{-}SH_2] \leftrightarrow [FeS_2 \cdot H_2]$

$[FeS_2 \cdot H_2] \leftrightarrow FeS_2(\text{pyrite}) + H_{2g}$

In more recent experiments the role of bacteria in the transformation of iron monosulphides to pyrite has also been examined (Donald and Southam, 1999). Microorganisms facilitate the formation of diagenetic pyrite by binding ferric iron on to anionic sites on their cell walls. The close proximity of these binding sites to one another promotes the growth of a thin FeS film on the cell wall. This film then reacts to form pyrite along a similar reaction pathway to the one outlined above (Schoonen, 2004).

1.3 Trace metal accumulation of diagenetic pyrite

Although the enrichment of trace metals in diagenetic pyrite has been noted in several publications (Huerta-Diaz and Morse, 1990; Huerta-Diaz and Morse, 1992; Large et al., 2011; Large et al., 2009; Large et al., 2007) the methods in which they are accumulated is still not well understood. The pyrite precursor mineral mackinawite (FeS) has been shown to

adsorb and incorporate many trace elements (Morse and Arakaki, 1993). However the importance of this is uncertain as the reaction pathways proposed by Rickard and Luther (1997) require the dissolution of mackinawite, and this dissolution would likely release many of the trace metals.

By analyzing the trace metal content of pyrite with increasing depth Huerta-Diaz and Morse (1992) were able to show that as progressively more reactive iron is converted to pyrite more trace metals are also incorporated into the pyrites structure (excluding Cr). They also showed that some metals (Cd, Zn and Pb) show a less significant increase in concentration than the majority of the other trace metals. This process was found to be limited only by the availability of trace metals to be incorporated into the pyrite and the amount of pyrite produced. Using data accumulated from thousands of analyses Morse and Luther (1999) presented a general pattern of degree of trace metal pyritization where Hg is the element most readily incorporated and other elements decrease in the following order Hg > As = Mo > Cu = Fe > Co > Ni >> Mn > Zn > Cr = Pb > Cd. This order was explained using their thermodynamic and kinetic properties.

The different trace elements that are incorporated into diagenetic pyrite can be split into different groups based on their properties and how the trace elements can be incorporated into pyrite. These include heavy metals (Cu, Ni, Co, Pb, Bi and Tl), oxyanions (As, Mo and Sb), elements held within sphalerite nano-inclusions (Zn and Cd) and elements that are held within organic matter or silicate inclusions (Ga and V) (Berner et al., 2013). Of these, the heavy metals and the oxyanions are of most use in determining the paleo oceanic conditions. They are incorporated into pyrite by either adsorption of outer sphere complexes, adsorption of inner sphere complexes, precipitation of different sulphides onto the pyrite or co-precipitation of different sulfide minerals with pyrite and diffusion of elements into the pyrite lattice (Rosso and Vaughan, 2006). Which of these (or combination of these) processes occurs and the degree to which they occur is dependent on equilibration time, solution pH, concentration of elements available for incorporation, particle size and temperature (Borah and Senapati, 2006).

Arsenic is one of the most common trace elements in pyrite (Huerta-Diaz and Morse, 1992) and it can be found in concentrations up to 6% (Reich and Becker, 2006). The amount of As present in pyrite and the manner in which it is incorporated has been shown to effect the uptake of many other trace elements in pyrite (Deditius et al., 2008). Arsenic can be

incorporated into pyrite in three ways: substituting for S(-II); substituting for Fe(II) (Deditius et al., 2008; Qian et al., 2013) and as nano-scale inclusions of amorphous As-Fe-S (Deditius et al., 2009). Substitution of As for S in the lattice of pyrite enhances the accumulation of elements similar to Fe, such as Co, Ni, Cu and Zn (Deditius et al., 2008). The substitution of As for Fe enhances the incorporation of larger cations such as Au(I), Ag(I) and Pb(II) (Deditius et al., 2008). The relationship between presence of As and its accumulation in pyrite has been especially well studied with regards to gold and it has been shown that the ability of Au to be incorporated into the pyrite lattice is strongly dependent on As content of pyrite (Reich et al., 2005).

Though these studies provide very good background on the accumulation of trace elements in pyrite they do not address how trace metal incorporation may change in higher metal environments or how the incorporation of trace metals into pyrite may have changed throughout geological time due to changes in the physical and chemical conditions. In this thesis I attempt to address these questions by examining the trace metal incorporation of diagenetic pyrite in different environments through geological time.

1.4 Use of trace metals in determining chemical conditions of paleo-oceans

Several authors have made use of trace metal concentrations of bulk rock samples to determine chemical conditions of ancient oceans. This is generally approached by determining whether the shale being studied is relatively enriched or depleted in trace metals relative to a reference shale sample or set of samples, (McLennan, 2001; Taylor and McLennan, 1985; Wedepohl, 1991; Wedepohl, 1995). A complication arises in this process because sediments commonly have different mineralogical compositions due to differences in the sedimentary source, the biological productivity and the types of organisms living in the water column. This leads to trace element variation related to dilution of the sediment by minerals such as quartz, chlorite, calcium carbonate and opal. To correct for this, trace metals within the sediment are often normalized to aluminum content (Lyons et al., 2003; Tribovillard et al., 2006). Some of the most common types of trace metals utilized are redox sensitive elements such as U, V and Mo and to a lesser extent Cr and Co (Algeo and Lyons, 2006; Anbar et al., 2007; Arnold et al., 2004; Lyons et al., 2003; Tribovillard et al., 2006) as these provide information on whether the ocean was oxic, sub-oxic, anoxic or euxinic at the time of sediment deposition. U is used as a redox proxy because it is mobile within oxidizing

conditions ($UO_2(CO_3)_3^{4-}$ but when reduced it forms insoluble compounds in the sediments such as UO_2, U_3O_7 and U_3O_8 (Tribovillard et al., 2006). However, complications do arise in that U also complexes with humic substances (Wood, 1996) and the conditions under which this occurs may vary. Similarly V is mobile within oxic ocean water (HVO_4^{2-} and $H_2VO_4^-$) (Hastings et al., 1996) and under mildly reducing conditions forms both mobile ions (VO^{2-} and $VO(OH)_3^-$) and insoluble compounds ($VO(OH)_2$) (Tribovillard et al., 2006). When V is reduced further it forms solid V_2O_3 or $V(OH)_3$. The two stages of vanadium dissolution allows oxic, anoxic or euxinic conditions to be distinguished (Calvert and Petersen 1993, Algeo and Maynard, 2004). Similarly to U, complexities arise as V too can be immobilized by forming complexes with humic substances (Wood, 1996). Mo differs from the other common redox sensitive elements in that it behaves as a conservative element, showing little affinity for other particles except Mn-oxyhydroxides (Goldberg et al., 1998). Adsorption of Mo onto Mn-oxyhydroxides can explain the transport of Mo to the sediment, however as Mn-oxyhdyroxides dissolve in reducing conditions it does not explain the long term storage of the Mo in reduced sediment. For fixation, the Mo must be converted to thio-molybdates which are reactive particles (Erickson and Helz, 2000) and thus can be scavenged by iron oxides, organic matter and sulphide minerals (Tribovillard et al., 2004). As these reactions take a long time to reach equilibrium, Mo can be used to determine areas of persistently euxinic conditions (Tribovillard et al., 2006). Trace metal concentrations can also be used to approximate biological productivity as metals such as Ni, Cu, Zn and Cd are commonly associated with organic matter and thus their concentration in the sediment can be used as a proxy for original organic matter content (Tribovillard et al., 2006). While these studies are very useful, the techniques are not appropriate for systems that have experienced metamorphism or hydrothermal fluid flow due to the potential for post-diagenesis metal enrichment. Investigating paleo-redox chemical conditions using pyrite chemistry is potentially more robust, as shown by Berner et al. (2013) who used pyrite chemistry to explain differences in depositional conditions in the Toarsian aged shale of the Posidonia Formation. Laser ICPMS mapping of numerous pyrites from ore deposits has shown that early diagenetic pyrite can be shielded from the effects of metamorphism and hydrothermal activity (Large et al., 2007) by later generations of pyrite. In this study the LA-ICPMS technique is used to test its viability for paleo-redox studies. Pyrite from the Hamersley Sedimentary Basin was analyzed and characterized to determine the relationship between pyrite and whole rock chemistry (Chapter 5).

1.5 Model of ore deposits sourcing metal from sediments

Trace metal content of diagenetic pyrite may also play a role in the formation of many sediment-hosted gold deposits (Large et al., 2011; Large et al., 2009; Large et al., 2007; Pitcairn et al., 2006; Thomas et al., 2011). These studies postulate that under anoxic to euxinic conditions a large number of trace metals (Au, As, V, Ni, Se, Ag, Zn, Mo, Cu, U) are concentrated and immobilized in organic rich sediments. During diagenesis trace metals (As, Ni, Se, Te, Ag, Mo, Cu) are released from the organic matter and the iron (hydr)oxides and incorporated into diagenetic pyrite. With a greater degree of burial during late diagenesis and early metamorphism any remaining organic matter is converted to bitumen and pyrite is recrystallized into a coarser grained, trace element poor forms. Further metamorphism (above lower greenschist facies) leads to conversion of pyrite to pyrrhotite. These processes release gold and other trace metals from pyrite into diagenetic-metamorphic fluids which then migrate to favorable depositional sites where they form orogenic or Carlin-type ore deposits (Large et al., 2011).

1.6 Structure of thesis and objectives of each chapter

A study of pyrite forming in the metal rich and metal poor modern estuarine environment is presented in chapters 2 and 3. The objective of this investigation is to determine what factor(s) effect the accumulation of trace elements in pyrite framboids formed in sediments. This also provides important insight into the accumulation of elements less studied in pyrite framboids from modern sedimentary environments such as Ag, Te and Au (though Au especially has received extensive research in hydrothermal systems and laboratory based investigations). This research facilitated the use of these elements in the determination of oceanic conditions in later chapters. Chapter 2 also provides a detailed analysis of the mobility of several metal contaminants in a high metal depositional environment. Chapter 3 utilizes the data presented in Chapter 2 plus laser ablation ICPMS analyses of pyrite, to determine the different trace metal contents of framboidal pyrite, from both the metal rich Derwent Estuary and the background Huon Estuary, to examine the relative ability of different trace metals to be accumulated in diagenetic pyrite and what factors affect their accumulation.

A data base of trace element composition of sedimentary pyrite analyses from several different geological units across geologic time from several different localities around the world are presented in Chapter 4. This data base has been compiled by a team effort under the leadership of Ross Large and includes pyrite analyses by several researchers (Daniel Gregory, Elena Lounejeva and Jacqueline Halpin). The goal of this chapter is to evaluate the pyrite data base and determine 1) chemical criteria for assessing whether pyrite is of diagenetic origin; 2) a baseline average trace element content of sedimentary pyrite so that degree to which pyrite deviates from this can be used to determine changes in ocean chemistry and 3) to determine what, if any, general trends there are in pyrite chemistry with pyrite texture and age, and possible reasons for these changes.

Chapter 5 presents a detailed study of the pyritic, carbonaceous shales of the Hamersley and upper Fortescue Groups, Western Australia. The goal of this chapter is to show that determination of paleo-oceanic conditions by pyrite geochemistry can yield the same results as more traditional whole rock analyses. A secondary goal of this chapter is to use a combination of the whole rock analyses, pyrite analyses and SHRIMP-SI analyses to determine changes in the chemical conditions of the late Archean oceans during the time these shales were deposited. This secondary goal is of interest because this area contains the first known instance of euxinic oceanic conditions (Scott et al., 2011), in the Jeerinah formation of the upper shale unit of the Fortescue Group. This is of particular interest because euxinic conditions represent sulphide dominant and iron limited conditions and should show what trace metals were enriched in the oceans at that time. The sedimentary succession in this area also record an early period of oxygenation in the Mt McRea shale (Anbar et al., 2007). The chemistry of the sequences allows investigation of changes in the amount of chemical erosion of sulphides on land and the amount of trace metals transported to the oceans.

In Chapter 6 analyses of sedimentary pyrite, recrystallized sedimentary pyrite and two different types of ore pyrite from the St Ives gold district are presented. The objective is to determine whether pyrite analyzed in areas that have under-gone high levels of metamorphism (mid green schist) and significant hydrothermal overprint can be used to determine chemical conditions of the ocean basin. Samples from the St Ives gold district were analyzed and compared to similarly aged samples from the Jeerinah formation, Hamersley Basin. There are also two secondary goals for this chapter. The first is to test

whether recrystallized and hydrothermal pyrite can be distinguished from sedimentary pyrite using the chemical criteria determined in Chapter 4. The other secondary objective is to investigate possible sources of gold, for the gold deposits at St Ives, by comparing the gold content and the sulfur isotopic composition of the ores with those from various rock types in the area.

1.7 Statement of authorship

This thesis is organized as a series of five papers that are either published, in press (Chapters 2 and 3) or are in the process of being submitted (Chapter 4, 5 and 6) at the time of completion of the thesis. These make up Chapters 2, 3, 4, 5 and 6. In each of these papers I was the primary author and designed the experiments with the aid of my supervisors Ross Large and Sebastien Meffre. I preformed all analyses myself except for a large portion of the LA-ICPMS analyses in Chapter 4 (in which I performed 32% of the analyses), the other analyses were undertaken by co-authors Halpin (24%), Lounejeva (41%) and Maslennikov (1%) and Dr. Karen Orth (2%). Some of the SHRIMP-SI analyses in chapters 5 and 6 were undertaken by co-author Steadman, although I prepared the samples and selected the areas for the analyses. The whole rock chemical analyses were undertaken by a number of laboratories as discussed in the different chapters. Comments and edits for Chapters 2 were provided by Sebastien Meffre, Bernd Lottermoser, Ashley Townsend, Christine Coughanowr and Jason Whitehead, Tony Morrison and an unnamed reviewer. Aid in detailing the past practices of the zinc smelter were provided by Nick Ramshaw, Todd Milne and James Burke of Nystar Hobart. Comments and edits of Chapter 3 were provided by Sebastien Meffre, Ross Large, Martin Reich, Zsolt Berner, Alejandro Fernandez-Martinez, Leonid Danyushevsky, Sarah Gilbert, Lee Groat, Jacqueline Halpin and Selina Wu. Comments and edits of Chapter 4 and 5 were provided by Ross Large, Jacqueline Halpin and Arthur Hickman. Finally comments and edits for Chapter 6 were provided by Ross Large while ore samples from the East Repulse and Leviathan deposits were provided by Adam Bath.

1.8 Statement of Publication

A version of chapter 2 has been published in the Australian Journal of Earth Science (volume 6 number 5). A version of Chapter 3 is accepted for publication in American Mineralogist and is now in press. Chapters 4,5 and 6 will be submitted for publication in the near future.

1.9 References

Algeo, T.J. (2004) Can marine anoxic events draw down the trace element inventory of seawater? Geology, 32(12), 1057-1060.

Algeo, T.J., and Lyons, T.W. (2006) Mo-total organic carbon covariation in modern anoxic marine environments: Implications for analysis of paleoredox and paleohydrographic conditions. Paleoceanography, 21(1).

Algeo, T.J., and Maynard, J.B. (2004) Trace-element behavior and redox facies in core shales of Upper Pennsylvanian Kansas-type cyclothems. Chemical Geology, 206(3-4), 289-318.

Anbar, A.D., Duan, Y., Lyons, T.W., Arnold, G.L., Kendall, B., Creaser, R.A., Kaufman, A.J., Gordon, G.W., Scott, C., and Garvin, J. (2007) A whiff of oxygen before the great oxidation event? Science, 317(5846), 1903-1906.

Arnold, G.L., Anbar, A.D., Barling, J., and Lyons, T.W. (2004) Molybdenum isotope evidence for widespread anoxia in mid-proterozoic oceans. Science, 304(5667), 87-90.

Berner, Z.A., Puchelt, H., NÖLtner, T., and Kramar, U.T.Z. (2013) Pyrite geochemistry in the Toarcian Posidonia Shale of south-west Germany: Evidence for contrasting trace-element patterns of diagenetic and syngenetic pyrites. Sedimentology, 60(2), 548-573.

Borah, D., and Senapati, K. (2006) Adsorption of Cd(II) from aqueous solution onto pyrite. Fuel, 85(12–13), 1929-1934.

Deditius, A.P., Utsunomiya, S., Ewing, R.C., and Kesler, S.E. (2009) Nanoscale "liquid" inclusions of As-Fe-S in arsenian pyrite. American Mineralogist, 94(2-3), 391-394.

Deditius, A.P., Utsunomiya, S., Renock, D., Ewing, R.C., Ramana, C.V., Becker, U., and Kesler, S.E. (2008) A proposed new type of arsenian pyrite: Composition, nanostructure and geological significance. Geochimica et Cosmochimica Acta, 72(12), 2919-2933.

Donald, R., and Southam, G. (1999) Low temperature anaerobic bacterial diagenesis of ferrous monosulfide to pyrite. Geochimica et Cosmochimica Acta, 63(13), 2019-2023.

Erickson, B.E., and Helz, G.R. (2000) Molybdenum (VI) speciation in sulfidic waters:: Stability and lability of thiomolybdates. Geochimica et Cosmochimica Acta, 64(7), 1149-1158.

Goldberg, S., Su, C., and Forster, H.S. (1998) Sorption of molybdenum on oxides, clay minerals, and soils. Adsorption of Metals by Geomedia. Academic Press, San Diego, 401-426.

Hastings, D.W., Emerson, S.R., and Mix, A.C. (1996) Vanadium in foraminiferal calcite as a tracer for changes in the areal extent of reducing sediments. Paleoceanography, 11(6), 665-678.

Huerta-Diaz, M.A., and Morse, J.W. (1990) A quantitative method for determination of trace metal concentrations in sedimentary pyrite. Marine Chemistry, 29, 119-144.

Huerta-Diaz, M.A., and Morse, J.W. (1992) Pyritization of trace metals in anoxic marine sediments. Geochimica et Cosmochimica Acta, 56(7), 2681-2702.

Konhauser, K.O. (1998) Diversity of bacterial iron mineralization. Earth-Science Reviews, 43(3-4), 91-121.

Large, R.R., Bull, S.W., and Maslennikov, V.V. (2011) A carbonaceous sedimentary source-rock model for Carlin-type and orogenic gold deposits. Economic Geology, 106(3), 331-358.

Large, R.R., Danyushevsky, L., Hollit, C., Maslennikov, V., Meffre, S., Gilbert, S., Bull, S., Scott, R., Emsbo, P., Thomas, H., Singh, B., and Foster, J. (2009) Gold and Trace Element Zonation in Pyrite Using a Laser Imaging Technique: Implications for the Timing of Gold in Orogenic and Carlin-Style Sediment-Hosted Deposits. Economic Geology, 104(5), 635-668.

Large, R.R., Maslennikov, V.V., Robert, F., Danyushevsky, L.V., and Chang, Z.S. (2007) Multistage sedimentary and metamorphic origin of pyrite and gold in the giant Sukhoi Log deposit, Lena gold province, Russia. Economic Geology, 102(7), 1233-1267.

Lennie, A.R., England, K.E., and Vaughan, D.J. (1995) Transformation of synthetic mackinawite to hexagonal pyrrhotite: A kinetic study. American Mineralogist, 80(9), 960-967.

Lyons, T.W., Werne, J.P., Hollander, D.J., and Murray, R.W. (2003) Contrasting sulfur geochemistry and Fe/Al and Mo/Al ratios across the last oxic-to-anoxic transition in the Cariaco Basin, Venezuela. Chemical Geology, 195(1-4), 131-157.

McLennan, S.M. (2001) Relationships between the trace element composition of sedimentary rocks and upper continental crust. Geochemistry, Geophysics, Geosystems, 2(4), Q1021.

Morse, J., and Luther, G. (1999) Chemical influences on trace metal-sulfide interactions in anoxic sediments. Geochimica et Cosmochimica Acta, 63(19), 3373-3378.

Morse, J.W., and Arakaki, T. (1993) Adsorption and coprecipitation of divalent metals with mackinawite (FeS). Geochimica et Cosmochimica Acta, 57(15), 3635-3640.

Neumann, T., Rausch, N., Leipe, T., Dellwig, O., Berner, Z., and Böttcher, M.E. (2005) Intense pyrite formation under low-sulfate conditions in the Achterwasser lagoon, SW Baltic Sea. Geochimica et Cosmochimica Acta, 69(14), 3619-3630.

Pitcairn, I.K., Teagle, D.A., Craw, D., Olivo, G.R., Kerrich, R., and Brewer, T.S. (2006) Sources of metals and fluids in orogenic gold deposits: insights from the Otago and Alpine Schists, New Zealand. Economic Geology, 101(8), 1525-1546.

Qian, G., Brugger, J., Testemale, D., Skinner, W., and Pring, A. (2013) Formation of As(II)-pyrite during experimental replacement of magnetite under hydrothermal conditions. Geochimica et Cosmochimica Acta, 100, 1-10.

Reich, M., and Becker, U. (2006) First-principles calculations of the thermodynamic mixing properties of arsenic incorporation into pyrite and marcasite. Chemical Geology, 225(3), 278-290.

Reich, M., Kesler, S.E., Utsunomiya, S., Palenik, C.S., Chryssoulis, S.L., and Ewing, R.C. (2005) Solubility of gold in arsenian pyrite. Geochimica et Cosmochimica Acta, 69(11), 2781-2796.

Rickard, D., and Luther, G.W. (1997) Kinetics of pyrite formation by the H2S oxidation of iron (II) monosulfide in aqueous solutions between 25 and 125° C: The mechanism. Geochimica et Cosmochimica Acta, 61(1), 135-147.

Rickard, D., and Luther, G.W. (2007) Chemistry of Iron Sulfides. Chemical Reviews, 107(2), 514-562.

Rosso, K.M., and Vaughan, D.J. (2006) Reactivity of sulfide mineral surfaces. Reviews in mineralogy and geochemistry, 61(1), 557-607.

Schoonen, M., and Barnes, H. (1991) Reactions forming pyrite and marcasite from solution: II. Via FeS precursors below 100 C. Geochimica et Cosmochimica Acta, 55(6), 1505-1514.

Schoonen, M.A. (2004) Mechanisms of sedimentary pyrite formation. Special Papers-Geological Society of America, 117-134.

Scott, C.T., Bekker, A., Reinhard, C.T., Schnetger, B., Krapež, B., Rumble, D., and Lyons, T.W. (2011) Late Archean euxinic conditions before the rise of atmospheric oxygen. Geology, 39(2), 119-122.

Steadman, J.A., Large, R.R., Meffre, S., and Bull, S.W. (2013) Age, origin and significance of nodular sulfides in 2680 ma carbonaceous black shale of the eastern goldfields superterrane, yilgarn craton, western australia. Precambrian Research.

Taylor, S.R., and McLennan, S.M. (1985) The continental crust: its composition and evolution.

Thomas, H.V., Large, R.R., Bull, S.W., Maslennikov, V., Berry, R.F., Fraser, R., Froud, S., and Moye, R. (2011) Pyrite and pyrrhotite textures and composition in sediments, laminated quartz veins, and reefs at Bendigo gold mine, Australia: insights for ore genesis. Economic Geology, 106(1), 1-31.

Tomkins, A.G. (2010) Windows of metamorphic sulfur liberation in the crust: Implications for gold deposit genesis. Geochimica et Cosmochimica Acta, 74(11), 3246-3259.

Tribovillard, N., Algeo, T.J., Lyons, T., and Riboulleau, A. (2006) Trace metals as paleoredox and paleoproductivity proxies: An update. Chemical Geology, 232(1), 12-32.

Tribovillard, N., Riboulleau, A., Lyons, T., and Baudin, F. (2004) Enhanced trapping of molybdenum by sulfurized marine organic matter of marine origin in Mesozoic limestones and shales. Chemical Geology, 213(4), 385-401.

Wedepohl, K. (1991) The composition of the upper earth's crust and the natural cycles of selected metals. Metals in natural raw materials. Metals and their compounds in the environment. Occurrence, analysis, and biological relevance. New York, NY: VCH, 3-17.

Wedepohl, K. (1995) The composition of the continental crust. Geochimica et Cosmochimica Acta, 59(7), 1217-1232.

Wolthers, M., Van der Gaast, S.J., and Rickard, D. (2003) The structure of disordered mackinawite. American Mineralogist, 88(11-12), 2007-2015.

Wood, S. (1996) The role of humic substances in the transport and fixation of metals of economic interest (Au, Pt, Pd, U, V). Ore Geology Reviews, 11(1), 1-31.

Chapter 2:

Mineralogy of metal contaminated estuarine sediments, Derwent estuary, Hobart, Australia: Implications for metal mobility

2.1 Abstract

The mobility, bioaccessibility and transfer pathways of metals and metalloids in estuarine sediments have been the focus of much detailed research. However to date, few studies have examined the mineralogical siting of metals and metalloids in such sediments. This is despite the fact the mineralogy of sediments is an important factor that controls which and how much of a particular metal is released to pore waters and overlying water columns. This study reports on the mineralogical siting of metals in contaminated estuarine sediments, Hobart, Australia, and aims to evaluate the mobility of metals in the contaminated substrates. Mineralogical, mineral chemical and chemical analyses demonstrate that the sediments contain very high levels of several metals and metalloids. The contaminated sediments have concentrations of zinc (Zn), lead (Pb), copper (Cu) and cadmium (Cd) ranging from 0.55–4.23 wt%, 0.16–0.70 wt%, 415–951 mg/kg, and 23–300 mg/kg, respectively. Franklinite and lesser sphalerite are the main repositories of Zn, whereas much of the Pb and Cu is hosted by sulfides, organic matter and undetermined iron (Fe) oxides. While the release of contaminant loads from franklinite through dissolution is likely to be insignificant, even small releases of metals from the highly contaminated sediments can still cause the deterioration of local water quality. The contaminated sediments represent long-term sources of metal pollutants, particularly Zn, to local waters. This study demonstrates that mineralogical analyses are vital tool to recognise the potential mobility of trace metals in estuarine environments.

2.2 Introduction

Estuarine sediments act as important sinks for many environmentally significant metals, metalloids and organic contaminants (Bryan & Langston 1992). These contaminants may be released back into the pore water due to changes to pH, eH and salinity, which can then be released into the water column during disruption of the sediments (Bryan & Langston 1992).

The majority of research involving metal and metalloid contamination in rivers and estuaries has focussed on quantifying the degree of contamination and on determining the mobility of

metals. The degree of contamination is determined by calculating enrichment factors in order to determine whether contamination is anthropogenic or naturally occurring and to what degree it is increasing or decreasing with time (for example Feng *et al.* 2004; Santos *et al.* 2005; Zhang *et al.* 2007, 2009; Abrahim & Parker 2008; Beesley *et al.* 2010). Metal mobility and bioavailability of metals is commonly determined using sequential leach extractions (for example Duddridge & Wainwright 1981; Singh *et al.* 2005; Banat *et al.* 2006) to analyse the metals released under different chemical conditions. There are several problems with the use of sequential leaches to directly determine bioavailability and mobility of metals in sediments, such as the specificity of the reagents used and the relation between how leachable an element is and its' bioavailability (Martin *et al.* 1987). However, sequential leach analyses can still be used to determine the load of particulate elements that are available to short term processes and the origin of various metals and metalloids entering the ocean (Martin *et al.* 1987).

The mineral phase that the metals and metalloids are held within has a significant effect on the mobility of the contaminant (Song *et al.* 1999). Therefore it is important to know in what mineral phases the contaminants are held. Studies on mineralogy of the contaminants tend to focus on river systems that drain mining districts and are affected by the weathering of sulfide minerals (Song *et al.* 1999; Hochella *et al.* 2005; Moberly *et al.* 2009). Our study investigates the Derwent estuary, near Hobart, Tasmania, which is strongly contaminated by heavy metals (Birch 2000) mostly originating from a Zn smelter (Whitehead *et al.* 2010) rather than weathering of sulfide material. This estuary provides an ideal site to examine the mineralogy and mobility of smelter-related contamination because the geology of the area creates relatively low background values for most metals and metalloids (Jones *et al.* 2003). To date no study has been completed on the mineralogy of Zn smelter metal contamination in an estuarine environment and how that mineralogy affects the mobility of the contaminants.

The Derwent estuary gives us a unique opportunity to observe how the mineralogy of smelter related contamination has allowed the accumulation of extremely high concentrations of metals and metalloids in the sediments and how this affects the mobility of the elements. By using a variety of analytical techniques we show that the major metal contaminants (Zn, Pb and Cu) are held within different mineral phases and have different mobility both confirming and adding to a previous study (Banks & Ross 2009 in Whitehead *et al.* 2010), which show higher bioavailability of Pb relative to Cu, and Zn. These characteristics have important

implications on potential for release of the metals to the ecosystem and possible future remediation solutions.

2.2 Materials and methods of analysis

2.2.1 Location and setting

The Derwent River and Estuary is located in southeastern Tasmania, Australia, at approximately 42^{o} 52'S 147^{o} 20'E (Figure 1). Some 200,000 people live along the estuary margins (Whitehead *et al*. 2010). The area is underlain by Permian mudstone, Triassic quartz sandstone, Jurassic dolerite, and Cenozoic basalts and sediments (Jones *et al.* 2003; Whitehead *et al.* 2010).

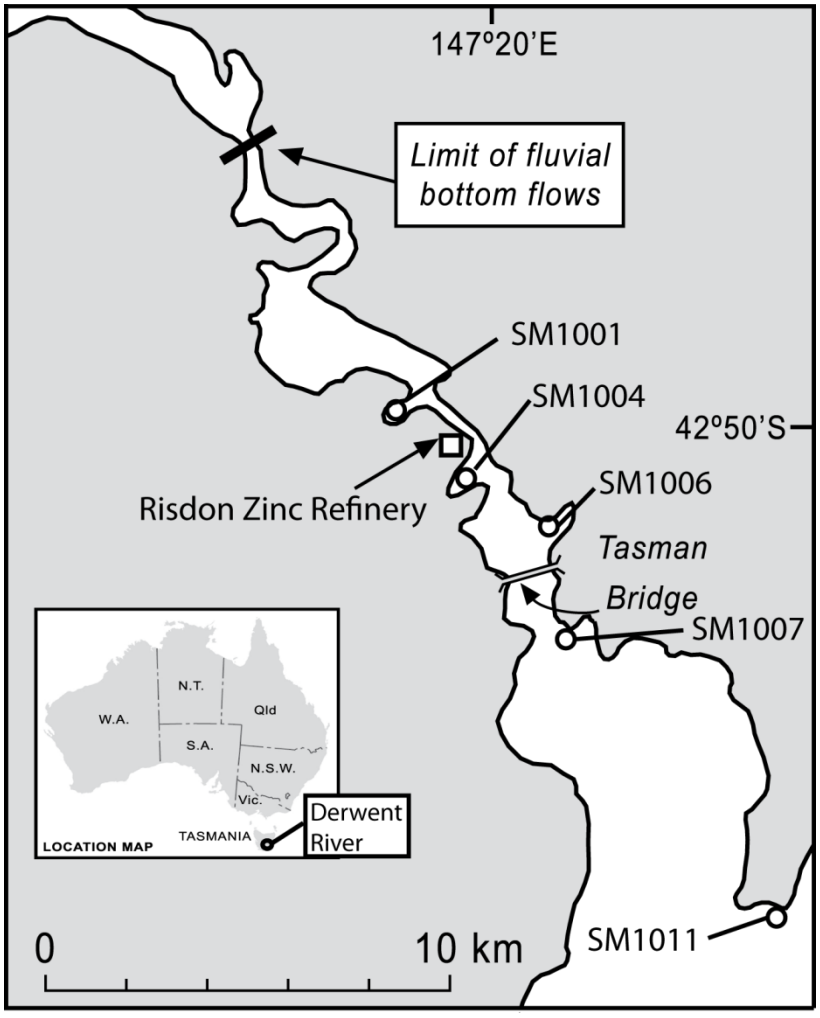

Figure 2.1: Location of core samples taken within the Derwent Estuary.

2.2.2 Anthropogenic contamination sources

A wide variety of anthropogenic contaminants are found within the Derwent Estuary. These include pathogens, nutrients, organic matter, silt and gross solids, wood extractives (such as resin acids), transition metals, metalloids and hydrocarbons (Whitehead *et al.* 2010), for a detailed discussion of these please see Appendix 1. These contaminants enter the estuary at a number of points and have many point and diffuse sources, such as urban runoff, waste disposal sites, sewage treatment plants, current and historical industries (for example Boyer paper mill, textile and dying factory, WW2 munitions complex, small metal foundries), leaded petrol and air pollution (Whitehead *et al.* 2010) (Christine Coughanowr, director Derwent Estuary Program, personal communication, May 2013). The most significant source of Zn, Cd, Pb and Cu is the Zn smelter at Risdon (Figure 1), which has been operating since 1917 (Bloom & Ayling 1977; Jones *et al.* 2003; Townsend & Seen 2012) when environmental precautions for smelting activities were far less rigorous than they are today. Until the 1970s some of the smelter waste was disposed of directly into the estuary and ore stockpiles were left uncovered, allowing particles of ore to be blown into the water. Currently waste water is treated prior to release in the estuary and the main source of contamination is through contaminated ground water draining from the site (Whitehead *et al.* 2010), as determined by observation wells on the smelter site. The changes to environmental management processes at the smelter have led to a considerable reduction of metal content in estuary sediments, which can be observed in core samples. The smelter has steadily been increasing production since operations began and at times has ranked as the second largest producer of Zn in the world. It currently has an annual output of near 280,000 tonnes (Todd Milne, senior environmental officer, Nyrstar Hobart, personal communication, 2013).

The variation in the metal content of surface sediments has been well documented by Jones *et al.* (2003) (from 292–22,600 mg/kg Zn, 142–3900 mg/kg Pb, 14–1200 mg/kg Cu and 8–660 mg/kg As in the mid Derwent estuary and from 24–1200 mg/kg Zn, 4–600 mg/kg Pb, 2–50 mg/kg Cu and 1–20 mg/kg As in Ralphs Bay, with the other parts of the estuary falling between these extremes). Muscle tissue from sand flathead (*Platycephalus bassensis*) within the Derwent estuary have been reported to contain elevated levels of Hg (median of 0.53 ± 0.05 mg/kg wet weight; Verdouw 2008) but low levels of other metals (median values of As 3.91 ± 0.43 mg/kg, Cr 0.01 ± 0.01 mg/kg, Fe 2.57 ± 0.29 mg/kg, Mn 0.05 ± 0.01 mg/kg, Pb 0.06 ± 0.04 mg/kg, Se 0.02 ± 0.02 mg/kg and Zn 5.89 ± 0.26 mg/kg; Verdouw 2008). However, oysters (*Ostrea angasi* and *Crassostrea gigas*) and mussels (*Mytilus edulis*) have

been observed to contain elevated levels of Pb, Zn, Cd and Cu (respective median values of 2.4, 2930, 1.85 and 54 mg/kg for oysters and 9.8, 45, 1.13 and 1 mg/kg for mussels) (Whitehead *et al.* 2010).

Historically the most significant contaminant introduced by the smelter to the Derwent River was through liquid processing waste (Bloom & Ayling 1977). The smelting process is complex and has changed considerably over time. The process can be summarised into three major steps (Alexander 1992):

1. roasting a sphalerite-rich zinc concentrate to make calcine (mostly Zn oxide)
2. leaching in acid to make a Zn solution
3. electrolysis to recover Zn metal.

One of the major waste products from the process was an insoluble iron-rich residue. This residue contained Zn ferrite (franklinite) formed during roasting and hydrated iron hydroxides precipitated during leaching. Prior to 1975 some of this material was discharged directly into the estuary (Nick Ramshaw, senior metallurgist, Nystar Hobart, personal communication, 2013). The main period of discharge was independently constrained to between 1950s and 1980s by (Townsend & Seen 2012) using ^{210}Pb dating of the most contaminated layer in a core sample 3 km upstream from the Zn refinery. However some of the material was also stockpiled on site waiting further processing. The stockpile composed of 66 vol% of zinc ferrite reached six hundred thousand tonnes in the late 1960s (Alexander 1992) and one million tonnes in 1970 (Haigh & Pickering 1970). In 1971 a new plant was commissioned to treat the iron-rich residue from the existing stockpiles and the iron precipitates directly from the plant (Alexander 1992). The process used a higher concentration sulfuric acid to break down the Zn ferrite and addition of ammonium sulfate to form jarosite. Between 1970 and 1973 jarosite was mostly stock piled alongside Newtown Bay, although the pile was kept wet to limit the transfer of dust to the estuary some introduction of jarosite to the estuary was inevitable (personal communication Ashley Townsend 2013). In December 1973 jarosite began to be shipped and dumped off the continental shelf (Alexander 1992). This practice continued until 1997 when the process was changed to eliminate jarosite as a by-product (Waste Management and Environment Magazine 2001).

The smelter has progressively made improvements to reduce contaminants entering the estuary (Whitehead *et al.* 2010). Currently there are four different ways in which transition metals and metalloids enter the estuary from the smelter: treated liquid processing waste, stormwater, groundwater and atmospheric emissions including dust (Whitehead *et al.* 2010). Currently the most significant of these sources is contaminated groundwater draining the site as shown by monitoring wells on the site (Whitehead *et al.* 2010). In 2010 the discharge estimated from the smelter was 99 kg As, 311 kg Cd, 299 kg Cu, 654 kg Pb and 23834 kg Zn (Milne 2012), with the majority of metals and metalloids entering through liquid effluent. Estimates of metal load prior to 1981 are difficult to obtain.

2.2.3 Sample collection and preparation

Eleven 6 cm diameter core samples were taken from the Derwent Estuary in August 2010 using a boat supported Uwitec hammer corer of which five cores were analysed (Figure 1). These were from Prince of Wales Bay (SM10-01, 42°49'33.4"S, 147°18'12.3"E), New Town Bay (SM10-04, 42°50'25.4"S, 147°19'40.8"), Lindisfarne Bay (SM10-06, 42°51'21.0"S, 147°21'2.1"E), Kangaroo Bay (SM10-07, 42°52'42.3"S, 147°21'15.1"E) and the entrance to Ralphs Bay (SM10-11, 42°56'30.2"S, 147°25'40.1"E).

The five cores recovered and examined in detail contained mostly black silt (predominantly 2.5Y 2.5/1 with zones 5Y 2.5/1 on the Munsell colour chart). Average core length was 87 cm varying between 45 and 120 cm. All the cores recovered contained almost no stratification and showed strong evidence of bioturbation by worms and arthropods. Most of the worms were small (>2 cm) and were present in the upper 30 cm of the cores with the exception of the core from Kangaroo Bay (SM10-07) where worms were observed to depths of 80 cm. One core (SM10-11) contained a large (3 cm) burrowing ghost shrimp (species not identified) at about 30 cm depth. Another sample (SM10-06) contained tube worms at the surface (species not identified).

The sediment was extruded by pushing a plunger through the sample tube, with samples taken at 5 cm intervals from all cores with the exception of the first 30 cm of SM10-01, which was sampled at 2.5 cm intervals. One quarter of each sample was retained for heavy mineral separation. Half of each sample was used for geochemical analysis. The remaining quarter was kept in a freezer for future analyses. Heavy minerals were separated from the

matrix materials by mixing the sediment fraction with a mixture of lithium heteropolytungstates in a separatory funnel and leaving for 24 hrs. The dense minerals (> 2.95 specific gravity) then settled to the bottom of the separatory funnel where they were collected by opening the valve at the bottom and draining the bottom third of the lithium heteropolytungstate mixture, along with the dense minerals. The heavy minerals separate was filtered and washed three times with deionised water.

2.2.4 Analytical methods

Samples for geochemical analysis were dried in a 60°C oven for two days. All core samples were analysed as loose dried material in polythene bags using an Innov-X systems X-50 mobile XRF device (at UTas). This method was chosen as a quick, cost effective way to examine levels of contamination. Core SM10-01 was chosen for further analysis on the basis of its long length (1.05 m), high contamination in the upper parts and a relatively uncontaminated basal section. Quality control was assured by analysing aliquots of the geochemical reference material NIST 2781 (domestic sludge) every 5–10 samples. Each of these reference analyses was within 5% of the expected value for abundant elements (Pb, Zn and Mn); with greater deviations for less abundant element (within 20% As and 33% for Cd) (Supplementary Papers). These expected values deviated systematically from certified values for the standard (over estimate by 32% and 35% for Cd and As respectively; under estimate by 18% and 17% for Pb and Zn respectively) (Supplementary Papers). A threshold effect was also identified in comparison of the portable XRF and ICPMS analyses and is probably the reason for the poorer correlation between the measured and expected values for NIST 2781. This effect limits the use of the portable XRF at low metal contents in the sediment core. Error bars in Figure 2 reflect the error of the device based on factory settings.

Samples from SM10-01 were ground to <63 μm using a chromium steel mill, then analysed using LECO, inductively coupled plasma atomic emission spectroscopy (ICPAES) and inductively coupled plasma mass spectrometry (ICPMS) techniques (at ALS Chemex in Brisbane). There the powdered samples were digested by a four acid (HCl, HNO_3, H_2SO_4 and HF) leach prior to being analysed by ICPAES and ICPMS. Total organic carbon (TOC) analyses were performed by treating the sample with a dilute HCl to evolve any carbonate as

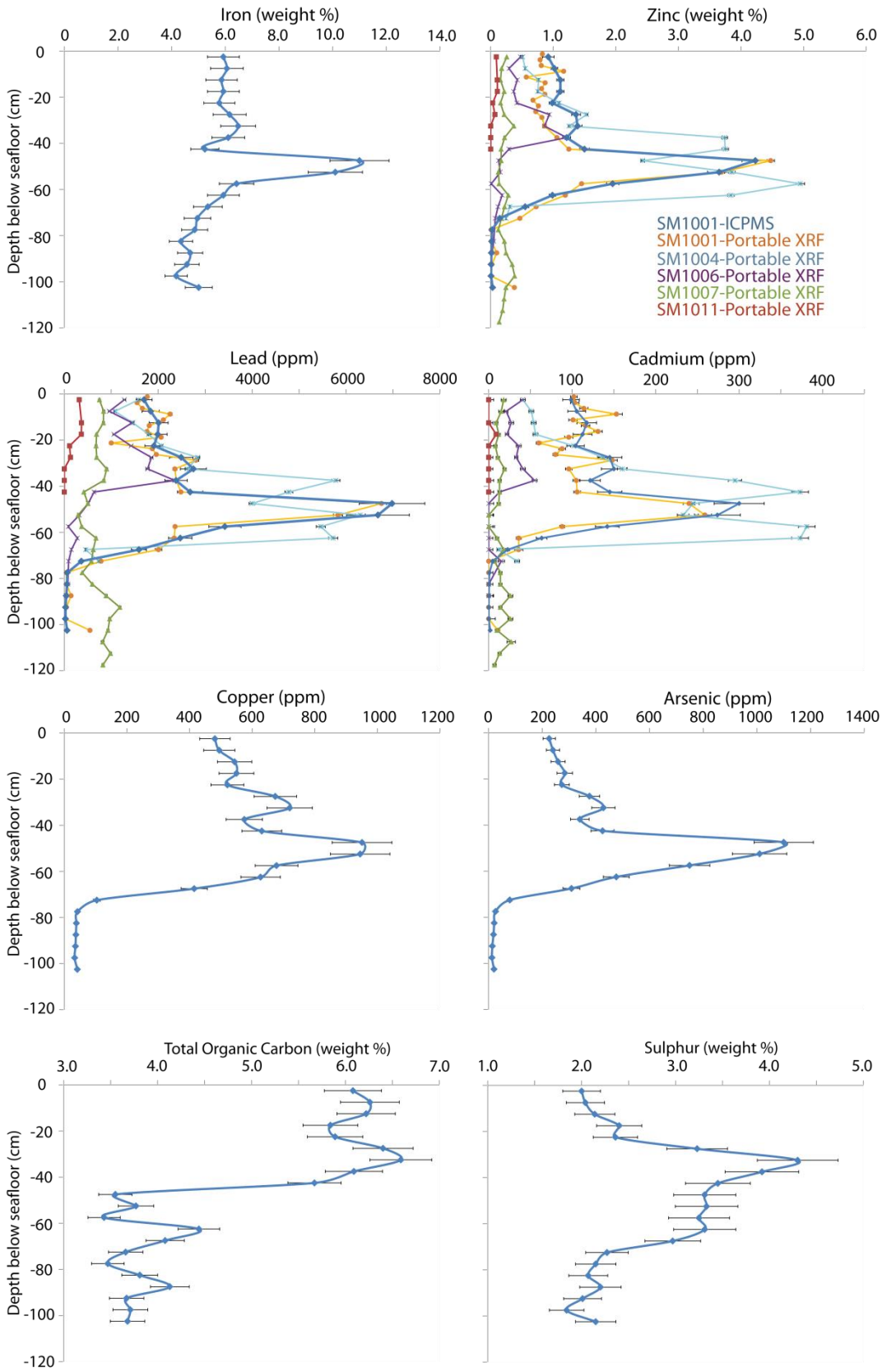

Figure 2.2: Element enrichment with depth for the sediment cores from the Derwent Estuary. Bold black line represents whole rock ICPMS analyses completed on SM10-01. Thin lines represent portable XRF data for SM10-01 (dashed line), SM10-04 (dotted line), SM10-06 (1 dash 2 dot line), SM10-07 (2 dash 1 dot line) and SM10-11 (thin solid black line).

CO_2 before analysing the residue with a Leco carbon (C)/sulfur (S) analyser. Quality control was assured on these analyses by analysing blanks, geochemical reference materials (MRGeo01 and CBM398-1) and sample replicates, all of which were within the criteria for acceptable values (between 10 and 20% for the elements of interest, with higher % variation being permissible for elements that have low accepted values). These data were used to define five different geochemical domains: moderate metal, low S (0 to 25 cm); moderate metal, high S (25 to 45 cm); high metal (45 to 55 cm); high to low metal transition zone (55 to 80 cm) and low metal (80 to 100 cm).

To determine the mobility of the metals and metalloids within four of the identified geochemical domains (omitting the transition zone) sequential leach extractions were performed on four samples based on the method proposed by Zeien & Brümmer (1989) (Table 1). In short the method involves seven extraction steps. The first step targets exchangeable metal ions and water soluble metal salts by reacting the samples with 1 M NH_4NO_3 for 24 hr at 20°C. The second step targets weakly complexed metal ions and metals bound by carbonates by reacting the residue with 1 M NH_4OAc (pH 6) for 24 hr at 20°C. The third step targets metals bound by Mn (hydr)oxides by reacting the residue with 1 M NH_3OHCl + NH_4OAc (pH 6) for 0.5 hr at 20°C. The fourth step targets metals bound by organic matter by reacting the residue with 0.025 M NH_4EDTA (pH 4.6) for 0.5 hr at 20°C. The fifth step targets metals bound by Fe(hydr)oxides of low crystallinity by reacting the residue with 0.2 M NH_4–oxalate (pH 2.6) for 4 hr at 20°C. The sixth step targets metals bound by crystalline Fe(hydr)oxides by reacting the residue with 0.1 M ascorbic acid + 0.2 M NH_4-oxalate (pH 2.6) for 0.5 hr at 97°C. Extracts were analysed using sector field ICPMS at the University of Tasmania's Central Science Laboratory (CSL). Quality control was assured by analysing blank solutions from each on the extraction steps and analysing calibration solutions as unknowns to monitor instrument performance and by analysing a water standard (NIST_RefWater1640a) to verify calibration accuracy. The residues of the sequential leach were digested using a HF-sulfuric acid digestion in the PicoTrace high-pressure digestion system prior to being analysed with an Agilent 7700x ICP-MS. The material in this latter extract includes compounds that would be stable under all but the most aggressively hostile environmental conditions. Quality control was assured by analysing blanks of acid solution used in the digest and four secondary rock standards (GSD-12a, TasBASa, GSR-6aa, and GSR-6ba). Due to analytical problems not all metals were determined by the final analysis of the residue. Where there is no data for the final analysis, estimates (shown in brackets), have

been calculated by subtracting the bulk sample analysis (see Section 3.1) from the sum of the first six steps of the sequential extract.

Table 2.1: Summarized sequential extraction procedure modified from Zeien and Brümmer (1989)

Extraction step	Extracting solution	Extracted species	Reaction time and temperature
1	1 M NH_4NO_3	Exchangeable metal ions, water soluble metal salts	24 hr, 20°C
2	1 M NH_4OAc (pH 6)	Weakly complexed metal ions and metals bound by carbonates	24 hr, 20°C
3	0.1 M NH_3OHCl + NH_4OAc (pH 6)	Metals bound by Mn (hydr)oxides	0.5 hr, 20°C
4	0.025 M NH_4-EDTA (pH 4.6)	Metals bound by organic matter	1.5 hr, 20°C
5	0.2 M NH_4-oxalate (pH 2.6)	Metals bound by Fe(hydr)oxides of low crystallinity	4 hr, 20°C
6	0.1 M ascorbic acid + 0.2 M NH_4-oxalate (pH 2.6)	Metals bound by crystalline Fe(hydr)oxides	0.5 hr, 97°C
7	digested using a HF-Sic acid digestion in the PicoTrace high pressure digestion system	Metals bound by residual fraction	

Table modified from that used by Scheinost et al. (2002)

Representative samples taken throughout the core were analysed by quantitative X-ray diffraction (QXRD) (at the University of Ballarat) with a Siemens D500 diffractometer using Fe-filtered CoK_α radiation. A computer aided search of the ICDD PDF4/Minerals 2010 database was then used to identify the mineral phases present. Additional traces for clay characterisation were obtained from Mg solvated air-dried and glycolated mounts prepared by sedimentation in 1% sodium hexaphosphate aqueous suspensions. SiroQuant™ ver 3.0 and Rietveld refinement of the most suitable structures available in the software package databank were used to obtain quantitative XRD results.

The quantitative XRD (QXRD) and electron microprobe results were used to determine if franklinite (a zinc bearing spinel that was found in high abundance by the QXRD analyses) could be the only host of the metals in the estuary. The calculation used is similar to that used by Day (2011), who used a combination of QXRD and microprobe analyses to determine the concentration of different types of carbonate near Galore Creek, British Columbia. The calculations for the amount of selected metals in the mineral franklinite were determined using the following equation:

$[Me] = \%F * [Me]_{Frank} / 100$

Where [Me] is the calculated concentration of the metal in the sediment, %F is the amount of franklinite in the sediment determined by QXRD, and $[Me]_{Frank}$ is the amount of the metal in franklinite in ppm as determined by microprobe analysis.

SEM analyses and X-ray maps were also carried out using a Hitachi SU-70 field emission scanning electron microscope (FESEM) (at the CSL) to identify additional minerals potentially responsible for metal contamination. Electron microprobe analyses of grains of franklinite were completed using a Cameca SX100 electron microprobe (at the CSL). It was operated at 20 keV, 15nA with a spot size of 2 µm for 20 s per line. The elements were calibrated using forsterite for magnesium (Mg), gahnite for aluminium (Al) and Zn, clinopyroxene for silica, rhodonite for manganese (Mn), hematite for Fe, cobaltite for cobalt, cuprite for Cu, galena for Pb, Cd metal for Cd and rutile for titanium (Ti).

2.3 Results

2.3.1 Geochemical analyses

The sediments analysed in the cores contained large geochemical variation (Table 2; Supplementary Papers) both between different cores and down each of the cores. The results of the geochemical analyses undertaken in this study are presented in Appendix 2.

Background values are considered to be the mean of the concentration of metals found from 90–100 cm in core SM1001. To check that these concentrations of metals are actual background and not a less enriched layer of contaminants deposited from an earlier phase of smelting, we compared our data with that from other core samples collected from the Derwent Estuary. These were analysed by Townsend & Seen (2012), who used Pb isotopes to determine the onset of smelting in the sedimentary record. Our data from 90–100 cm correlated well (r^2 for Cu, Fe, Pb and Zn were all ≥ 0.99 when plotted versus Al to correct for different levels of sand in the samples) with their pre-smelter samples (75–105 cm).

In the late 1970s surface sediments from the Derwent Estuary were among the world's most highly enriched in Cd (1,400 mg/kg), Cu (10,000 mg/kg), Pb (42,000 mg/kg) and Zn (104,000 mg/kg) (Bloom & Ayling 1977). Cores SM10-01, SM10-04 and SM10-06 show a layer(s) of sediment high in Zn, Pb and Cd (45–70 cm, 30–70 cm, 20–40 cm for SM10-01,

SM10-04 and SM10-06, respectively) (Figure 2) with relatively homogenous moderately enriched sediments above, and low levels of metal content below. Although elevated metals do occur in the upper section of SM10-07 and SM10-11 there is no distinct peak. The presence of a peak in metal concentration below the top of the core is consistent with observations from a core sample taken upstream of the smelter by Townsend & Seen (2012).

Table 2.2: Total chemical analysis of a variety of metals in SM1001 and ANZECC/ ARMCANZ interim sedimentary quality guidelines (ISQG)

Element	Ag (mg/kg)	As (mg/kg)	Cd (mg/kg)	Cu (mg/kg)	Pb (mg/kg)	Zn (mg/kg)
ISQG-low	1	20	1.5	65	50	200
ISQG-high	3.7	70	10	270	220	410
0-5 cm	8.7	226	99	481	1700	9220
5-10 cm	9.4	240	106	495	1840	10200
10-15 cm	10.5	259	118	544	2010	11150
15-20 cm	10.3	284	113	550	1990	11150
20-25 cm	9.4	273	104	521	1910	9860
25-30 cm	12.2	376	145	674	2490	13650
30-35 cm	13.7	428	150	720	2750	13900
35-40 cm	11.4	340	122	575	2380	12150
40-45 cm	13.1	425	145	631	2680	15000
45-50 cm	34	1100	300	951	6980	42300
50-55 cm	34.5	1010	274	945	6680	36500
55-60 cm	20.9	749	142	678	3420	19500
60-65 cm	15.7	476	63.5	627	2470	9880
65-70 cm	13.2	309	22.8	415	1590	5540
70-75 cm	3.7	79	4.8	104	363	1470
75-80 cm	0.39	26	1.0	42	64	246
80-85 cm	0.48	21	0.5	39	60	208
85-90 cm	0.26	19	0.4	37	43	142
90-95 cm	0.14	14	0.1	36	28	93
95-100 cm	0.11	13	0.2	33	26	80
100-105 cm	0.35	20	1.9	42	62	333

The small enrichment apparent between 100 and 105 cm is believed to be due to contamination at the bottom of the core tube with the surface sediment during sampling. To check the validity of the data acquired with the portable XRF data from SM1001 from the portable XRF data was compared with data acquired using ICPMS. The data correlated well for As (r^2 0.85), Cd (r^2 0.94), Mn (r^2 0.97), Pb (r^2 0.97) and Zn (r^2 0.94), while Cu (r^2 0.65)

and Fe (r^2 0.57) did not correlate well and will require further investigation into the causes of the poor correlation before the analyses from the portable XRF can be used for these elements.

TOC contents of the core do not correlate any of the elements with $r^2 << 0.1$ for As, Cd, Fe, Pb and Zn, and $r^2 = 0.17$ for Cu. TOC is enriched in the top 45 cm and depleted in the most metal enriched zone (45 to 55 cm) and levels become erratic but moderate from 55 to 105 cm (Figure 2).

2.3.2 Sequential leach analyses

The percentage of the total metals extracted in each leach step are summarised in Table 3. The % difference between the sum of the sequential leach analyses and the bulk sample analysis are generally low with values between: 6 and 14% for Cu; 2 and 10% for Zn; 10 and 21 for Pb; 0 and 3% for Mn and 5 and 9% for As. The % difference in the uncontaminated zone was also low for Pb (22%), Mn (10%) and As (15%). However, for Zn, Cu and Cd there was significantly more variability in the % difference between the two methods (69%, 44% and 169%, respectively; Table 4). Thus any conclusions drawn from the results of the sequential extraction for Zn, Cu and Cd in the uncontaminated sample should be used with caution.

In the enriched sections of the core (samples SM1001-20–25 cm, SM1001-30–35 cm, SM1001-50–55 cm), Zn, Mn and Fe are predominantly leached by step 5 (NH_4–oxalate) (Zn 10.5–13.0 wt%, Mn 9.1–13.9 wt%, Fe 16.8–24.9 wt%), step 6 (ascorbic acid/NH_4–oxalate) (Zn 12.1–28.2 wt%, Mn 24.3–40.1 wt%, Fe 20.8–36.1 wt%) or are held in the residual fractions (Zn 39.6–62.5 wt%, Mn 43.0–54.4 wt%, Fe 32.4–54.5 wt%). Cadmium is almost only found within the residual fraction (73.4–85.4 wt%) (Figure 3). The Zn in the background samples is leached significantly more by step 6 (ascorbic acid/NH_4–oxalate) (49.9 wt%) and less was left in the residue (34.8 wt%). Manganese and Fe were similar in the background sample to the enriched sample but were leached less by step 5 (NH_4-oxalate) (7.5 wt% and 1.5 wt% respectively).

Lead has a very different trend, with the majority of the metal and metalloid enriched samples leached by step 4 (NH_4-EDTA) (60.7–73.1 wt%) and lesser amounts by step 3 (NH_3OHCl/NH_4OAc) (12.5–26.2 wt%) and step 5 (NH_4-oxalate) (6.6–12.5 wt%). In the

background sample (SM1001-95–100 cm) there is more metal relative to the contaminated samples leached by step 6 (ascorbic acid /NH_4-oxalate) (35.0 wt%) and in residual fractions (26.6 wt%), and less metal relative to the contaminated samples leached by step 4 (NH_4-EDTA) (28.7 wt%) (Figure 2.3).

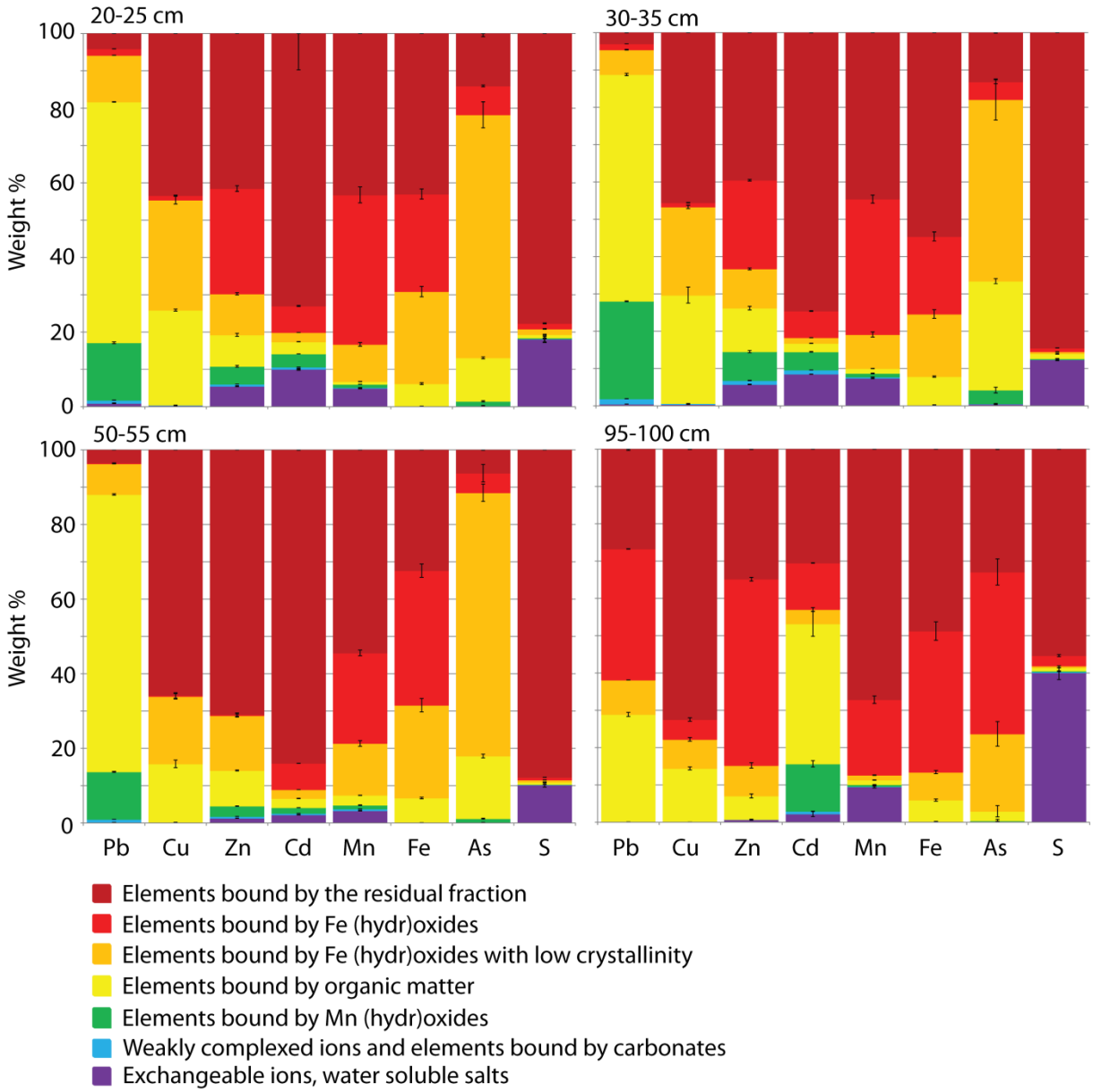

Figure 2.3: Results of sequential leach analyses from 4 samples taken to represent different geochemical domains (20–25 cm: moderate metal enrichment, 30–35 cm: moderate metal enrichment high organic matter enrichment, 50–55 cm: high metal enrichment and 95–100 cm: background in sediment core SM1001).

Table 2.3: Major minerals within silt of from SM1001as determined by QXRD.

Depth (m)	Feldspar	Franklinite	Galena	Gypsum	Smectite	Pyrite	Quartz	Sphalerite
0.10-0.15	17.0	7.7	0.0	3.4	26.8	5.4	39.0	0.6
0.20-0.25	18.4	6.3	0.0	4.3	29.5	5.9	34.5	1.1
0.30-0.35	15.2	5.4	0.0	3.6	25.2	14.9	34.6	1.2
0.40-0.45	9.9	8.2	0.1	8.1	30.3	12.5	29.8	1.1
0.50-0.55	13.8	29.0	0.0	1.4	23.3	4.4	26.5	1.5
0.55-0.60	15.2	11.3	0.0	6.7	24.6	8.1	31.7	2.3
0.60-0.65	17.3	3.9	0.0	2.3	26.9	8.2	40.6	0.8
0.75-0.80	14.5	0.7	0.0	0.7	37.0	7.9	39.2	0.0
0.85-0.90	15.2	0.3	0.0	3.4	35.5	8.6	37.0	0.0
0.95-1.00	16.0	0.0	0.0	8.5	32.8	4.4	38.2	0.0

Copper in the enriched samples is predominantly leached by step 4 (NH_4-EDTA) (15.7–29.1 wt%) and step 5 (NH_4-oxalate) (18.1–29.5 wt%) with a significant amount left in the residual phase (43.3–65.9 wt%). The background sample is similar; however step 6 (ascorbic acid/NH_4-oxalate) leaches more Cu than in the contaminated zone (5.3 wt%) and more is contained in the residual (72.5 wt%) (Figure 3). Arsenic (As) is similar in SM1001-20–25 and SM1001-50–55, where it is dominantly leached by step 5 (NH_4-oxalate) (65.1 wt% and 70.6 wt%, respectively) with less leached by step 4 (NH_4-EDTA) (11.6 wt% and 16.8 wt%, respectively) and step 6 (ascorbic acid/NH_4-oxalate) (7.7 wt% and 5.2 wt%, respectively). A total of 14.1 wt% and 6.2 wt% As in SM1001-20–25 and SM1001-50–55 are respectively retained in the residual fraction. SM1001-30–35 is similar to the other enriched samples; however more is leached by step 4 NH_4-EDTA (29.2 wt%) and less by step 5 NH_4-oxalate (48.7 wt%). The background samples differ from the enriched samples in that much more is leached by step 6 ascorbic acid/NH_4-oxalate (43.4 wt%) and a lower percentage is leached from the step 4 NH_4-EDTA and step 5 NH_4-oxalate phases (2.6 wt% and 20.7 wt%, respectively) (Figure 3).

2.3.3 QXRD analyses

Ten samples were analysed by QXRD to determine the host mineral for the contaminants (Table 5). These analyses determined that the primary mineral responsible for the Zn enrichment is franklinite with a minor contribution from sphalerite. Trace galena was the only Pb containing mineral and no Cu containing minerals were identified. These results for Zn correspond well to the geochemical data and suggest that the majority of Zn is held within

franklinite, while the Pb and Cu appear to be held within phases that have not been identified in this study. Quality control was insured by comparison of the rationalised calculation based on ideal mineral compositions with the full major element analysis. The QXRD computer program uses a least squares chi^2 test to compare the computed trace with the instrumental trace.

Table 2.4: Electron microprobe analyses of franklinite in %.

Description	MgO	Al_2O_3	SiO_2	MnO	Fe_2O_3	CoO	CuO	ZnO	PbO	CdO	TiO_2	Total
Franklinite inhomogeneous sub-rounded	0.09	0.20	3.98	0.31	56.99	0.053	1.41	20.33	0.30	0.06	0.029	83.75
Franklinite rim large round	0.25	1.11	3.72	0.93	59.27	0.062	0.13	23.28	0.09	0.14	0.056	89.05
Franklinite large grain	0.02	0.07	1.14	0.20	66.25	0.040	1.76	23.95	0.25	1.42	0.031	95.13
Franklinite large grain	0.39	1.36	4.12	0.33	59.45	0.027	1.57	24.65	0.27	0.30	0.040	92.51
Franklinite elliptical fine grained	0.11	0.11	1.37	1.36	55.62	0.060	0.12	27.45	0.12	0.20	0.040	86.58
Franklinite small grain	0.41	1.34	3.04	0.15	57.48	0.411	0.91	24.58	0.15	0.95	0.009	89.43
Franklinite small grain	0.19	1.25	6.24	0.39	55.82	0.052	0.02	21.62	0.15	0.06	0.034	85.84
Franklinite small grain oval shaped	0.03	0.18	0.31	1.33	70.98	0.069	0.15	22.91	0.19	0.01	0.012	96.18
Franklinite small angular grain	0.13	0.19	0.14	0.72	66.24	0.052	0.17	28.42	0.03	0.39	0.028	96.52
Franklinite small grain rectangular shaped	0.15	0.26	0.50	0.74	65.68	0.076	0.48	27.50	0.21	0.45	0.031	96.09

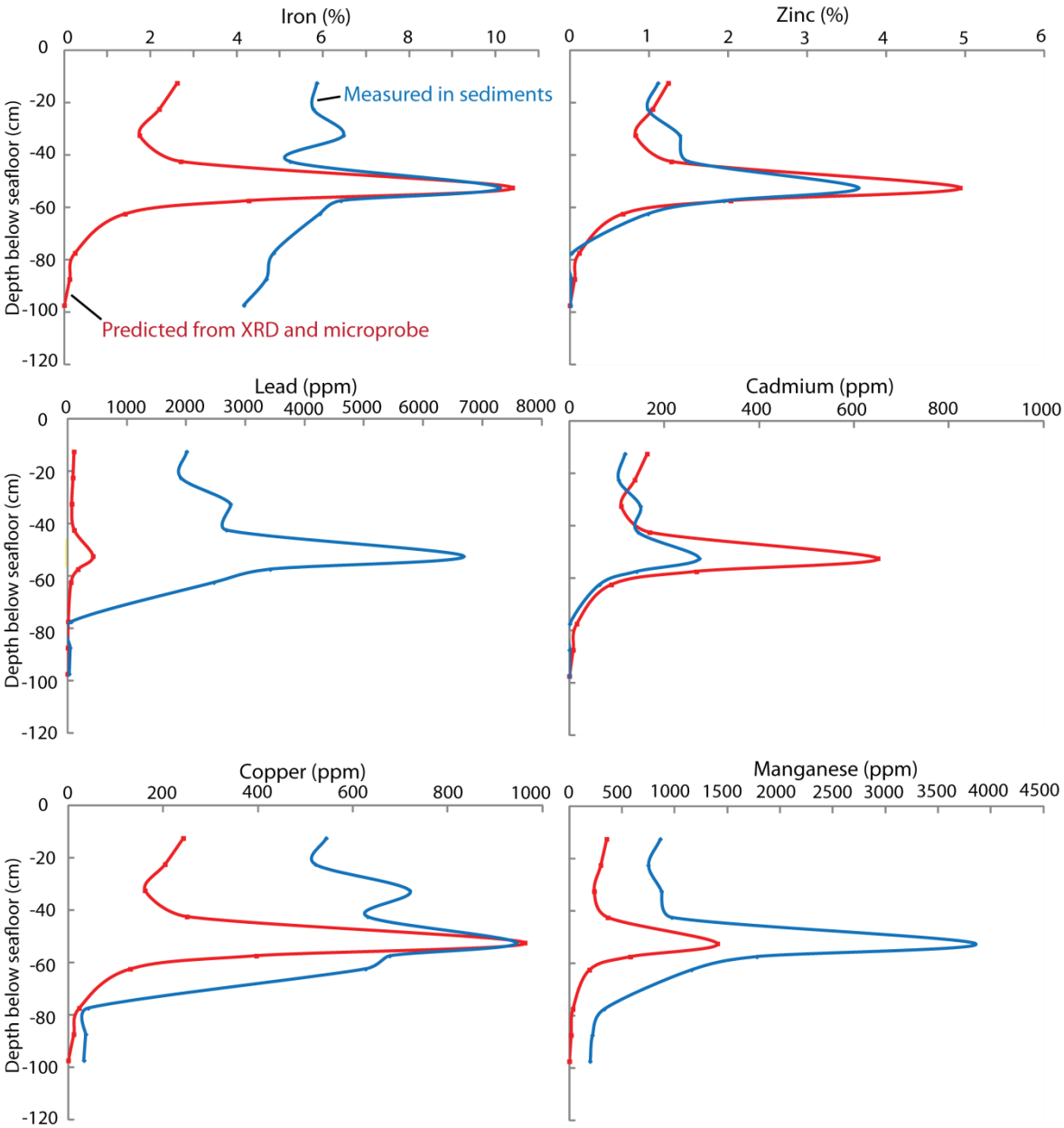

Figure 2.4 ICPMS whole rock data (blue line) and predicted geochemical values contained within franklinite based on QXRD and microprobe data (red line).

2.3.4 Electron microprobe analyses

Electron microprobe analyses were conducted on a series of franklinite crystals from a sample taken at 45–50 cm depth from SM10-01 to determine what metals are contained within the franklinite (Table 4). Analyses show the franklinite is variable in composition with 20–28 wt% ZnO. The wide variation in observed oxide totals is possibly due to different levels of hydration. The medians of franklinite composition from the electron microprobe and amount of franklinite in the samples from the QXRD analyses (Figure 4) was then used to

determine whether franklinite alone could account for the enrichment in the samples as described earlier.

The results show that Fe, Zn and possibly Cd (although degrees of error in the Cd analyses make it difficult to prove whether Cd is largely contained within the franklinite) are predominantly hosted within the franklinite, while Pb and Cu are hosted within at least one other phase, such as adsorbed onto organic matter and/or complexed with Fe or Mn (hydr)oxides, and/or contained within the structure of detrital jarosite sourced from the smelter.

Table 2.5: % yield of different sequential extraction steps from SM1001

Sample	Extraction Step	Pb (%)	Cu (%)	Zn (%)	Cd (%)	Mn (%)	Fe (%)	As (%)	S (%)
20-25	1[a]	0.9	0.3	5.5	10.0	4.9	0.0	0.2	18.1
	2[b]	0.8	0.2	0.6	0.6	0.2	0.0	0.0	0.1
	3[c]	15.4	0.0	4.8	3.5	0.9	0.1	1.1	0.2
	4[d]	64.6	25.4	8.4	3.2	0.8	6.0	11.6	0.9
	5[e]	12.5	29.5	11.0	2.5	10.0	24.7	65.1	1.5
	6[f]	1.7	1.3	28.2	7.1	40.1	26.2	7.7	1.5
	7[g]	4.1	43.3	41.5	73.0	43.0	(43.0)	14.1	(77.7)
30-35	1[a]	0.5	0.4	5.7	8.5	7.4	0.0	0.5	12.4
	2[b]	1.4	0.2	1.1	1.1	0.3	0.0	0.1	0.1
	3[c]	26.2	0.0	7.7	4.9	1.0	0.3	3.7	0.2
	4[d]	60.7	29.1	11.7	2.3	1.3	7.6	29.2	1.4
	5[e]	6.6	23.6	10.5	1.5	9.1	16.8	48.7	0.5
	6[f]	1.6	1.1	23.8	7.1	36.3	20.8	4.8	1.0
	7[g]	3.0	45.6	39.6	74.6	44.6	(54.5)	13.2	(84.5)
50-55	1[a]	0.2	0.1	1.2	2.2	3.3	0.0	0.1	10.2
	2[b]	0.8	0.1	0.4	0.4	0.4	0.0	0.0	0.1
	3[c]	12.5	0.0	2.4	1.5	1.0	0.1	1.0	0.1
	4[d]	73.1	15.7	8.4	2.4	2.6	6.6	16.8	0.6
	5[e]	8.1	18.1	13.0	2.4	13.9	24.9	70.6	0.5
	6[f]	1.8	0.1	12.1	7.0	24.3	36.1	5.2	0.7
	7[g]	3.5	65.9	62.5	84	54.4	(32.4)	6.2	(87.8)
95-100	1[a]	0.0	0.0	0.7	2.2	9.5	0.0	0.2	40.1
	2[b]	0.6	0.0	0.1	0.7	0.1	0.0	0.0	0.2
	3[c]	0.0	0.0	0.0	12.7	0.5	0.2	0.2	0.2
	4[d]	28.7	14.4	6.3	37.5	1.2	5.7	2.6	0.8
	5[e]	9.1	7.8	8.2	3.9	1.3	7.5	20.7	0.5
	6[f]	35.0	5.3	49.9	12.4	20.2	37.8	43.4	2.8
	7[g]	26.6	72.5	34.8	30.5	67.1	(48.7)	32.9	(55.3)

() indicate that the metals were not analysed for and are estimated using the sum of the percentages of the other analyses such that the total equals 100%. [a]1 M NH_4NO_3 [b]1 M NH_4OAc (pH 6) [c]0.1 M NH_3OHCl + NH_4OAc (pH 6) [d]0.025 M NH_4-EDTA (pH 4.6) [e]0.2 M NH_4-oxalate (pH 2.6) [f]0.1 M ascorbic acid + 0.2 M NH_4-oxalate (pH 2.6) [g]digested using a HF-Sulphuric acid digestion in the PicoTrace high pressure digestion system.

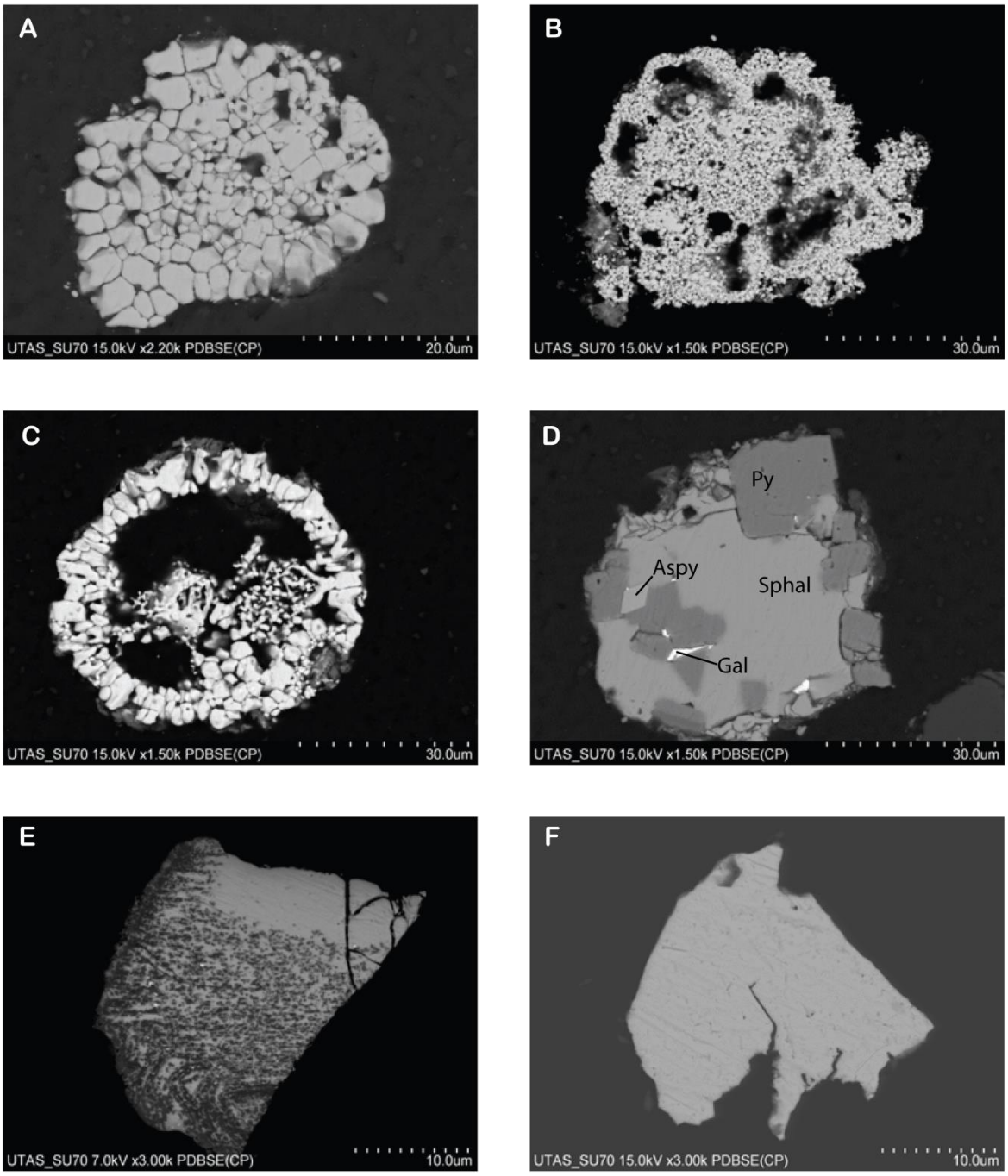

Figure 2.5: SEM images: A) course grained franklinite; B) fine grained franklinite; C) spongy franklinite; D) Mixed sulfide grain with pyrite (py), sphalerite (sphal), arsenopyrite (aspy) and galena (gal); E) unknown Pb silicate mineral, darker patches contain elevated Al and Zn; F) Pb metal.

2.3.5 SEM analyses

Heavy mineral fractions yielded a wide variety of metal-bearing minerals, including (in order of decreasing abundance) franklinite, pyrite, sphalerite, galena, chalcopyrite, arsenopyrite, unidentified Pb silicate, Pb metal and Cu metal (Figure 5). The most commonly identified Zn-bearing mineral was franklinite, which occurs in a wide range of different forms, most commonly as coarse-grained but also as fine-grained and rarely in a rounded form (Figure 5A–C). Sphalerite occurs both as individual sphalerite crystals and in clusters with pyrite, chalcopyrite, galena and arsenopyrite (Figure 5D). Lead is present in minor galena, rare unidentified Pb silicate minerals with varying amounts of Al and Zn (Figure 5E) and very rare pieces of Pb metal (Figure 5F). Although quantitative estimations are difficult due to the small nature of the particles the total amount of Pb in the enriched sediments cannot be explained by the minerals observed. Therefore we infer a significant proportion is held within the organic material or other amorphous materials, as suggested by the sequential leach analyses.

2.4 Discussion

2.4.1 Mineral host of heavy metals

The results of this study show that the majority of the Zn is hosted in franklinite. This can be demonstrated by comparing the observed metal concentrations in the sediments with calculations of the expected metal content, given the percentage of franklinite, and the concentrations of metals measured in the mineral (Figure 4). The Zn in franklinite correlates well with the Zn in the sediments (r^2 0.93) and franklinite is the dominant host mineral within the contaminated zone. Other mineral hosts for Zn include sphalerite (as indicated by SEM and QXRD), pore water solution, organic matter and Mn and/or Fe (hydr)oxides (as indicated by sequential leach extractions). The presence of less-common hosts of Zn are why some of the calculations of total Zn based on franklinite composition and abundance are below the total measured amount of Zn in the samples. Samples where the total metals are over estimated by the totals calculated by franklinite composition and abundance, are due to variability in the amount of Zn in the franklinite acquired by the microprobe. This may reflect that different types of franklinite (coarse, fine and framboidal) may contain different amounts of Zn, and/or that at different times of operation the smelter produced franklinite with different elemental ratios. This prevalence of franklinite in the Derwent Estuary is what

distinguishes it from several other studies that examined contaminated waterways draining mining districts where sulfide minerals were the source of the metal enrichment. They found the Zn to be primarily held within primary sulfides (sphalerite) (Song *et al.* 1999), secondary carbonates (e.g. smithsonite) (Moberly *et al.* 2009), and secondary sulfides, adsorbed onto Fe and Mn oxides or clays (Hochella *et al.* 2005).

The total measured sediment metal content (ICPMS) and calculated content (microprobe and QXRD) for Fe and Mn both correlate well (r^2 0.91 and 0.96, respectively) but the calculated values in the metal enriched zone are off by factors of 0.93 and 4.02 for Fe and 2.63 and 6.51 for Mn. This is due to the presence of Fe and Mn (hydr)oxides (as shown by sequential leach analyses) and pyrite (as shown by QXRD) contributing significant quantities of Fe and/or Mn to the sediments.

Little to no Pb appears to be hosted within the franklinite; however Pb enrichment does occur at the same stratigraphic level as the franklinite contamination. This suggests that although the deposition of Pb was probably at the same time as the deposition of franklinite it is predominantly held within organic matter and Fe and Mn (hydr)oxides (as indicated by the sequential leach analyses) or jarosite (Hage 1999). The slightly ambiguous mineral siting of Pb is expected as synchrotron-based studies have identified a wide variety of Pb minerals (dundasite ($PbAl_2(CO_3)_2(OH)_4*(H_2O)$), coronadite ($PbMn_8O_{16}$), bindheimite ($Pb_2Sb_2O_6(O,OH)$), mattheddleite ($Pb_{20}(SiO_4)_7(SO_4)_4Cl_4$), cerrusite ($PbCO_3$) and anglesite ($PbSO_4$)) (Moberly *et al.* 2009) in other contaminated sites. It is possible that originally a major host of the Pb in the sediment was jarosite as it is known that it was available at the site (Townsend personal communication 2013) and can contain lead in high quantities (Hage 1999). However, no jarosite was identified from XRD and short wavelength IR analyses specifically conducted to target this mineral (Supplementary Papers) and it is possible that the jarosite has broken down in the sediments. Studies by Chu *et al.* (2006) have shown that in organic rich reducing conditions jarosite breaks down in as little as 45 days. As the sediments used in this study are enriched in organic matter (3.4–6.6 wt%) and reduced (framboidal pyrite was observed to form within the sediments at all levels (Gregory, 2013 unpublished data), it is likely that any jarosite present has dissolved and the Pb, and any other metals within it, have been spread out further or have been precipitated as different phases. Copper does not correlate well with the amount expected from franklinite (r^2 0.59) which suggests that either there is another significant source of Cu in the estuary, the Cu content of the

franklinite is highly variable, or the Cu was relatively mobile in the sediments and has moved since deposition. Sequential leach analyses suggest that the Cu is predominantly held within the residual fraction with lesser amounts in Mn and Fe (hydr)oxides with low crystallinity and organic matter. Literature sources discuss Cu as primary sulfides (Song *et al.* 1999) or secondary sulfides (Hochella *et al.* 2005). As no secondary sulfides where identified in SEM analyses we do not expect them to be significant sites of Cu, however high levels of Cu in the residual fraction of the sequential leaches and presence of chalcopyrite in SEM analyses suggest that primary chalcopyrite may be a significant site of Cu in the sediment, although not the only site. Some of the Cu currently bound to organic matter and incorporated with Fe and Mn (hydr)oxides could originate from the breakdown of jarosite.

As defined earlier five different geochemical domains have been defined in core SM1001, of these the upper most three (moderate metal, low S (0 to 25 cm); moderate metal, high S (25 to 45 cm); high metal (45 to 55 cm)) are strongly contaminated. The mobility of different metals varies within the different geochemical domains in the sediment core. The Pb is similar in the three contaminated samples, while the Mn (hydr)oxide-bound component is higher in the organic-rich section between 30 and 35 cm. The least contaminated interval at the base of the core has the majority of the Pb in crystalline Fe (hydr)oxides and the residual fraction. Copper mobility is similar within the moderately contaminated section where approximately 50–55% of the Cu is held within the organic matter and weakly crystalline Fe (hydr)oxide phases. Both the most-contaminated and least-contaminated sections are similar regarding Cu mobility as for both phases 65–70% of the Cu is held within the residual fraction. The As content for the three contaminated samples is similar as all three contain over 70% of the As within the organic matter and weakly crystalline (hydr)oxide phases. Like Pb, As was probably largely held within various mineral phases in the smelter residue, including jarosite, and has been precipitated on/as new phases following the argument outlined above. Over 70% of the As within the uncontaminated interval is held within the crystalline Fe oxide and residual phases. Sulfur is much more enriched in the contaminated intervals than in the uncontaminated interval, which may reflect the presence of sulfides spilled into the river when transporting ore to the smelter or blown into the river from the stockpiles (Figure 3). The S may also have partly originated from sulfide phases formed after the dissolution of jarosite.

2.4.2 Degree of metal enrichment

Much of the research into the mineralogy of high metal contaminated estuaries has looked at drainage systems with a significant mining history in the hinterlands (e.g. Galán *et al.* 2003; Hochella *et al.* 2005). These studies focussed on metal-rich geological sources, such as mines, which discharge metal and acid-rich waters through the oxidation of sulfides, and are deposited downstream when chemical conditions change and allow precipitation. Examples of this are the Rio Tinto and Odeil Rivers, which drain some of the more intensively mined parts of the Iberian pyrite belt. Here the rivers have a pH range of 2–4 and contain more metal contamination than any other major European rivers. The metals As, Pb, Cu and some of the Zn are deposited in poorly crystalline Fe oxides throughout the rivers and estuaries (Galán *et al.* 2003). Moberly *et al.* (2009) used synchrotron-based techniques to determine that heavy metal contamination in the rivers draining the Coeur d'Alene Mining district is hosted by a wide range of minerals that have precipitated out of the river waters. Our study shows that the major source of the Zn, As, Cu, Pb and Cd enrichment in the Derwent Estuary is not derived from sulfides associated with mining but rather as a by-product of smelting. This may explain why samples taken from the Derwent Estuary contain some of the highest Zn concentrations thus far reported from an estuary (Birch 2000; Townsend & Seen 2012). The franklinite is meta-stable in the ambient conditions (Vanaecker *et al.* 2008) found in the river and does not readily dissolve as can be shown by the lack of corrosion on the crystal edges (Figure 5), and that the bulk of the Zn (contained within franklinite) was digested in two of the more chemically aggressive sequential leach steps (steps 5 and 6). This has allowed accumulation of large amounts of Zn in the sediments of the estuary whereas in other sulfide-sourced systems the minerals have oxidised and released their metals. In sulfide-sourced systems the metals are able to flow downstream and precipitate over a larger area (Galán *et al.* 2003; Moberly *et al.* 2009).

2.4.3 Application of the data acquired from SM1001 to the rest of the estuary

In an attempt to determine how trends in the data we acquired in SM1001 apply to the entire Derwent Estuary, data published by Jones *et al.* (2003) was plotted with data obtained from SM1001 (Figure 6). To examine potential sources of the contamination, trend lines of metal ratios from the stockpile at the smelter (Haigh & Pickering 1970) and from franklinite (microprobe data) were added to the plots. The Fe/Zn plot highlights both natural variations

in Fe and franklinite contamination. Less contaminated samples from upriver and downriver have different trends from that near the smelter in the middle of the estuary reflecting change in sediment grainsize (i.e. sandier sediments have less Fe oxides showing Fe increases with increasing mud content). The mid-river data (Jones *et al.* 2003) and core samples (SM10-01 above 80 cm) suggest 4 wt% background Fe content with the remainder of the Fe due to franklinite.

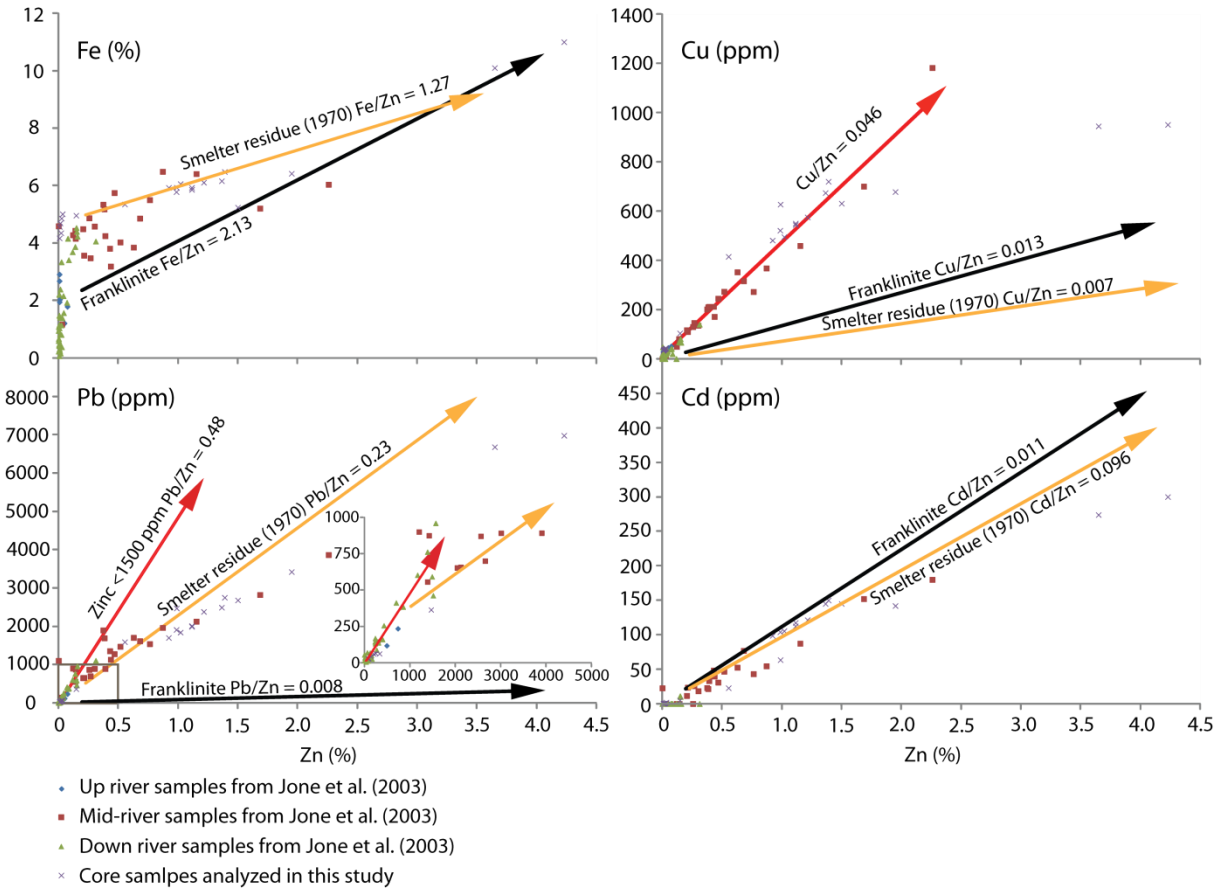

Figure 2.6 Comparison of core data (this study) with surface data (Jones *et al.* 2003). The black line represents the chemical ratios within the franklinite (microprobe data, this study) and the grey line represents the chemical ratios in the stock pile (Haigh & Pickering 1970).

With the exception of the most contaminated layer in SM1001, the mid-river and core data have significantly more Cu and Pb than that expected from the 1970s stockpile trend lines. This probably due to the Cu and Pb being sourced in part from other types of material such as jarosite (post-1970) or from material produced from the early (pre-1960s) part of the smelters history.

2.5 Conclusions

Our research shows that franklinite hosts the majority of the Zn found within the highly enriched Derwent estuary. The lack of corrosion on mineral edges and the chemically aggressive steps used in Zn leaches of franklinite suggest that it is stable within the conditions found. This stability may be what has allowed such high levels of Zn to accumulate in the estuary. The jarosite stockpile may also have been a source for Pb, As, Cu and some of the Cd, however due to its low stability in the reducing, organic-rich sediment much of it has dissolved releasing the metals. Now the Pb is held in a wider range of mineral phases, many of which are more difficult to determine. Similarly Cu is now held within several different phases, only one of which, primary chalcopyrite, was identified. This study shows that mineralogical analysis should be part of future studies investigating contaminated sites as metal mobility greatly affected by mineralogy.

2.6 Acknowledgements

The authors thank the following people: Mark Stalker (Veolia Services) for donation of time and equipment during the sampling of the Derwent sediments; John Gibson and Kerrie Swadling for use of the hammer corer; Ashley Townsend, Ian Little and Jay Thompson for conducting the compositional analyses on the samples and aiding in the composition of the methods section; Sandrin Feig and Karsten Goemann for their aid in the microprobe and SEM analyses and aiding in composition of the methods section; Selina Wu for the SWIR analyses; Anita Parbhakar-Fox and Nathan Fox for XRD analyses targeting jarosite; Stafford McKnight for QXRD analyses; Bernd Lottermoser and Ashley Townsend invaluable comments on early drafts of the manuscript; Nick Ramshaw, Todd Milne and James Burke of Nystar Hobart for their aid in detailing the past practises of the smelter; Christine Coughanowr and Jason Whitehead for their edits of the manuscript. Thank you also to Tony Morrison and an unnamed reviewer whose insightful comments greatly increased the quality of this manuscript. We also thank Karsten Goemann, Bernd Lottermoser and Janina Micko for their translation of the sequential leach method into English.

2.7 References

Abrahim G. M. & Parker R. (2008) Assessment of heavy metal enrichment factors and the degree of contamination in marine sediments from Tamaki Estuary, Auckland, New Zealand. Environmental Monitoring and Assessment, 136, 227–238.

Alexander A. (1992) The Zinc Works – Producing Zinc at Risdon 1916–1991. VIC, Australia: Globe Press.

Banks, J. & Ross J. (2009) From sink to source: how changing oxygen conditions can remobilise heavy metals from contaminated sediments. Report prepared by TAFI for Derwent Estuary Program (Water Quality Improvement Plan).

Banat Howari & Al S. (2006) Stability and Environmental geochemical profile of toxic heavy metals in soils around a crude oil refinery. International Journal of Environment and Pollution, 28, 162–184.

Beesley L., Moreno J. A., Clemente R., Lepp N. & Dickinson N. (2010) Mobility of arsenic, cadmium and zinc in a multi-element contaminated soil profile assessed by in-situ soil pore water sampling, column leaching and sequential extraction. Environmental Pollution, 158, 155–160.

Birch G. (2000) Marine pollution in Australia, with special emphasis on central New South Wales estuaries and adjacent continental margin. International Journal of Environment and Pollution, 13, 573–607.

Bloom H. & Ayling G. M. (1977) Heavy-metals in Derwent estuary. Environmental Geology, 2, 3–22.

Bryan G. W. & Langston W. J. (1992) Bioavailability, accumulation and effects of heavy metals in sediments with special reference to United Kingdom estuaries: a review. Environmental Pollution, 76, 89–131.

Chu C., Lin C., Wu Y., Lu W. & Long J. (2006) Organic matter increases jarosite dissolution in acid sulfate soils under inundation conditions. Soil Research, 44, 11–16.

Day S. (2011) Estimation of Calcium and Magnesium Carbonate Neutralization Potential for Refined Acid-Base Accounting Using Electron Microprobe and X-Ray Diffraction, accessed 01 July, 2013, http://www.inap.com.au/documents/Stephen_Day_B8_T2_Estimation-of-Calcium-and-Magnesium-Carbonate-Neutralization-Potential-for.pdf

Duddridge J. E. & Wainwright M. (1981) Heavy metals in river sediments—calculation of metal adsorption maxima using Langmuir and Freundlich isotherms. Environmental Pollution Series B, Chemical and Physical, 2, 387–397.

Feng H., Han X., Zhang W. & Yu L. (2004) A preliminary study of heavy metal contamination in Yangtze River intertidal zone due to urbanization. Marine Pollution Bulletin, 49, 910–915.

Galán E., Gómez-Ariza J., González I., Fernández-Caliani J., Morales E. & Giráldez I. (2003) Heavy metal partitioning in river sediments severely polluted by acid mine drainage in the Iberian Pyrite Belt. Applied Geochemistry, 18, 409–421.

Hage J. L. T. H. (1999) Autoclave Reduction of Jarosites and Other Metal Sulfates: A New Approach to Major Waste Problems. Geochemistry. Utrecht University.

Haigh C. J. & Pickering R. W. (1970) Treatment of zinc plant residue at the Risdon works of the Electrolytic zinc co. of Australasia ltd.: Paper from world symposium on mining and metallurgy of lead and zinc extractive metallurgy of lead and zin, Aime, New York. 1970, 2, 423–448.

Hochella M. F., Moore J. N., Putnis C. V., Putnis A., Kasama T. & Eberl D. D. (2005) Direct observation of heavy metal–mineral association from the Clark Fork River Superfund Complex: Implications for metal transport and bioavailability. Geochimica et Cosmochimica Acta, 69, 1651–1663.

Jones B., Chenhall B., Debretsion F. & Hutton A. (2003) Geochemical comparisons between estuaries with non-industrialised and industrialised catchments: the Huon and Derwent River estuaries, Tasmania. Australian Journal of Earth Sciences, 50, 653–667.

Martin J., Nirel P. & Thomas A. (1987) Sequential extraction techniques: promises and problems. Marine Chemistry, 22, 313–341.

Milne T. (2012) 2010/2011 report for NYRSTAR HOBART PTY LTD, Nyrstar Hobart Smelter – Lutana, TAS, accessed 10 April, 2013, <http://www.npi.gov.au/npidata/action/load/emission-by-individual-facility-result/criteria/state/TAS/year/2011/jurisdiction-facility/TAS%20120

Moberly J. G., Borch T., Sani R. K., Spycher N. F., Sengoer S., Ginn T. R. & Peyton B. M. (2009) Heavy Metal–Mineral Associations in Coeur d'Alene River Sediments: A Synchrotron-Based Analysis. Water, Air & Soil Pollution, 201, 195–208.

Santos I. R., Silva-Filho E. V., Schaefer C. E. G. R., Albuquerque-Filho M. R. & Campos L. S. (2005) Heavy metal contamination in coastal sediments and soils near the Brazilian Antarctic Station, King George Island. Marine Pollution Bulletin, 50, 185–194.

Scheinost, A. C., Kretzschmar, R., Pfister, S., & Roberts, D.R., (2002) Combining selective sequential extractions, X-ray absorption spectroscopy, and principal component analysis for quantitative zinc speciation in soil. Environmental science & technology, 36, 5021–5028.

Singh K. P., Mohan D., Singh V. K. & Malik A. (2005) Studies on distribution and fractionation of heavy metals in Gomti River sediments; a tributary of the Ganges, India. Journal of Hydrology, 312, 14–27.

Song Y., Wilson M., Moon H.-S., Bacon J. & Bain D. (1999) Chemical and mineralogical forms of lead, zinc and cadmium in particle size fractions of some wastes, sediments and soils in Korea. Applied Geochemistry, 14, 621–633.

Townsend A. T. & Seen A. J. (2012) Historical lead isotope record of a sediment core from the Derwent River (Tasmania, Australia): a multiple source environmen. Science of the Total Environment, 424, 153-161.

Vanaecker M., Vieillard P., Courtin-Nomade A. & Bril H. (2008) KindisP modelisation of the chemical stability of Zn-bearing phases in pyrometallurgical slags. Geochimica et Cosmochimica Acta Supplement, 72, 971.

Verdouw J. J. (2008) Heavy metal contamination in Derwent estuary fish. University of Tasmania Honours Thesis.

Waste Management and Environment Magazine (2001) From wasteland to wetland http://www.wme.com.au/categories/hazard_waste/dec1_01.php

Whitehead J., Coughanowr C., Agius J., Chrispijn J., Taylor U. & Wells F. (2010) State of the Derwent Estuary 2009: a review of pollution sources, loads and Environmental quality data from 2003–2009, Derwent Estuary Program, DPIPWE, Tasmania.

Zeien H. & Brümmer G. W. (1989) Chemische Extraktion zur Bestimmung von Schwermetallbindungsformen in Böden. Mitt. Dtsch. Bodenkundl. Ges, 59, 505–510.

Zhang L., Ye X., Feng H., Jing Y., Ouyang T., Yu X., Liang R., Gao C. & Chen W. (2007) Heavy metal contamination in western Xiamen Bay sediments and its vicinity, China. Marine Pollution Bulletin, 54, 974–982.

Zhang W., Feng H., Chang J., Qu J., Xie H. & Yu L. (2009) Heavy metal contamination in surface sediments of Yangtze River intertidal zone: An assessment from different indexes. Environmental Pollution, 157, 1533–1543.

Chapter 3:

Comparison of metal enrichment in pyrite framboids from a metal-enriched and metal-poor estuary

3.1 Abstract

The accumulation of metals and metalloids in diagenetic pyrite framboids is of interest because framboids can be a sink for heavy metal contaminants, a source of metals in ore deposits, and a tool to interpret paleo-ocean chemistry. In this study we have used laser ablation inductively coupled plasma mass spectrometry (LA-ICPMS) to analyze pyrite framboids from both the contaminated Derwent Estuary and the uncontaminated Huon Estuary in Tasmania, Australia. While the enrichment of many trace metals in the Huon Estuary followed expected trends, the trends in the Derwent were quite different. In addition to the expected high contents of Pb, Zn and Cu in the contaminated interval it was found that a number of elements are incorporated into pyrite less within the contaminated zone. It is suggested that this is due to over competition for adsorption sites on the growing iron sulfides in the contaminated zone resulting in diffusion of several elements down and thus an increase of several elements in pyrite below the zone of major contamination is observed. The LA-ICPMS technique also provided the opportunity to obtain accurate data on gold, silver and tellurium in diagenetic pyrite, something rarely achieved in sequential leach extractions due to the low concentrations of these metals observed in nature.

3.2 Introduction

Metal and metalloid accumulation in sediments has recently become of interest for three main reasons. Firstly, pyrite framboids can be important sinks for metals and metalloids (such as As) in contaminated rivers and estuaries (Lowers et al., 2007). Secondly, trace metal contents of shale can be used to interpret paleo-environmental conditions (Algeo, 2004; Anbar et al., 2007; Berner et al., 2013; Tribovillard et al., 2006) and since diagenetic pyrite is one of the sinks for trace metals in sediments (Dellwig et al., 2002; Huerta-Diaz and Morse, 1992; Neumann et al., 2013), the processes that led to enrichment of trace metals in pyrite are important. Thirdly, recent ore deposit models suggest that diagenetic pyrite is the source for

several significant gold deposits (Large et al., 2007, 2009; Thomas et al., 2011). It is therefore important to gain some understanding of the factors that control the uptake of trace elements in pyrite. Previous studies have used partial digestions (Huerta-Diaz and Morse, 1992) to establish the variations of metal content in diagenetic pyrite according to sediment depth. While this is a useful technique for studying at uncontaminated sediments, there are many potential problems including the specificity of the reagents (Martin et al., 1987). This is of particular concern in contaminated estuaries where there may be other metal bearing sulfides (e.g. sphalerite, chalcopyrite, and galena) which dissolve under similar conditions to pyrite.

This study examines pyrite from a metal-enriched site in the Derwent Estuary in Tasmania and compares them to the pyrite developed in an uncontaminated environment in the Huon Estuary some 45 km to the south to determine relative affinities of different trace metals for incorporation in framboidal pyrite. To avoid problems associated with specificity of reagents in partial digestion chemical analyses we employ LA-ICPMS analyses to directly determine the composition of trace metals in pyrite. To achieve similar results synchrotron µ-XRF has been used to analyze trace element content of pyrite (Berner et al., 2006; Neumann et al., 2013). While synchrotron µ-XRF is preferable due to its superior detection limits and spatial resolution we show in this paper that LA-ICPMS is a useful technique provided that the framboids analysed are large enough to obtain an adequate signal.

3.2.1 Trace element incorporation into diagenetic pyrite

The iron sulfides we examined for this study are pyrite framboids, which are clusters (often spherical) of microcrystalline pyrite rarely over 15µm in diameter (Figure 1). These crystals form throughout the world in sediments under anoxic to euxinic conditions. The mechanism of framboid formation has been the subject of much research and debate (Schoonen, 2004). The process begins with the formation of iron monosulfides, which have a much higher rate of nucleation, effectively prohibiting the direct precipitation of pyrite (Schoonen and Barnes, 1991). However, this nucleation barrier can be overcome by the presence of pyrite seed crystals, allowing pyrite to form in solutions undersaturated with respect to amorphous FeS but oversaturated with respect to pyrite (Schoonen and Barnes, 1991). A common FeS

species used in experimental studies is mackinawite (FeS_m). It forms in solution by the following reaction (Rickard and Luther, 2007):

$Fe^{2+} + H_2S \leftrightarrow FeS_m + 2H^+$

$Fe^{2+} + HS^- \leftrightarrow FeS_m + H^+$

In experimental studies, the early amorphous FeS phase consists of approximately 4 nm crystallites of an iron-rich monosulfide phase called mackinawite (Lennie et al., 1995; Wolthers et al., 2003). Rickard and Luther (1997) suggested that pyrite forms from amorphous FeS by the following reaction series:

$FeS\ (am) + H_2S \leftrightarrow FeS\ (aq)$

$FeS(aq) + H_2S \leftrightarrow [FeS\text{-}SH_2]$

$[FeS\text{-}SH_2] \leftrightarrow [FeS_2 \cdot H_2]$

$[FeS_2 \cdot H_2] \leftrightarrow FeS_2(pyrite) + H_2(g)$

The conversion of FeS to FeS_2 can be enhanced by the presence of sulphur species with oxidation states between SO_4^{2-} and H_2S^{2-} which can be common near the reduced sediment / oxidized water column interface (Neumann et al., 2005).

Donald and Southam (1999) showed that bacteria can play a role in converting organic sulfur compounds to reactants that can take part in pyrite formation. More recent experiments that include sulfur reducing bacteria in an attempt to better simulate natural settings reveal a reaction pathway similar to that outlined above (Schoonen, 2004). Microorganisms can also provide anionic sites on their cell walls that are capable of binding ferric iron (Donald and Southam, 1999; Konhauser, 1998). These ferric iron binding sites promote the growth of a thin FeS film on the outside of the cell wall (Schoonen, 2004), which then can react to form pyrite. However, FeS_m may not be a necessary precursor in many natural systems and is only observed in systems with high Fe concentrations (Rickard and Luther, 2007), though as the system examined in this study has a significant Fe supply (Risdon Zn smelter) FeS_m was probably present at one stage. The presence of organic matter can lower the supersaturation limit of pyrite 3 orders of magnitude (Rickard et al., 2007). This makes the solubility of pyrite and mackinawite close at 25°C and pH 7, which results in the precipitation of both

minerals (Rickard and Luther, 2007). Pyrite precipitation may also be enhanced by presence of an active surface that allows Fe^{2+} to react with S_2(-II) to form pyrite. Other Fe sulfides (such as mackinawite) and/or organic surfaces may also fulfill this role (Rickard and Luther, 2007).

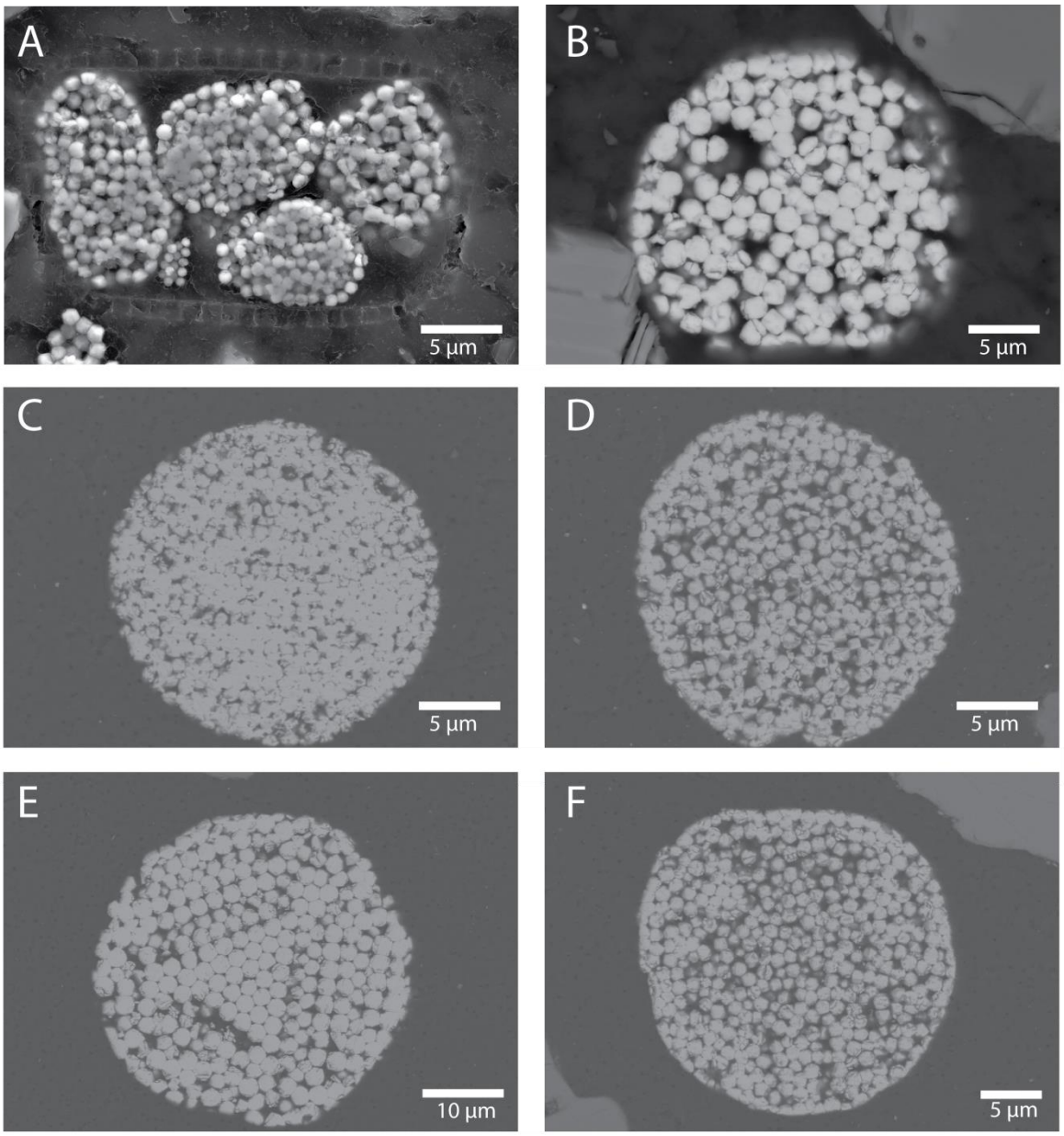

Figure 3.1: Scanning electron microscope images of pyrite framboids from the Derwent Estuary (A and B) and the Huon Estuary (C to F). The framboids are very similar between the relatively uncontaminated Huon Estuary and the contaminated Derwent Estuary.

The mechanisms for the incorporation of trace metals into pyrite framboids are still not fully understood. Work by Morse and Arakaki (1993) showed that many trace metals can be

adsorbed and incorporated into the precursor FeS mineral, mackinawite. They showed that a metal with a sulfide species that has a higher solubility than mackinawite would have a similar surface affinity to mackinawite and a metal with a sulfide species with lower solubility than mackinawite would have a higher surface affinity with decreasing metal sulfide solubility. Renock et al. (2009) showed that the mechanism of arsenic precipitation onto mackinawite differs based on the pH of the solution. Arsenic forms a "realgar like" As sulfide minerals on the surface of mackinawite at pH 5 but at pH 9 it instead forms a coating of arsenic on the surface of the mackinawite, possibly due to adsorption of As oxyanions (Renock et al., 2009). However, mackinawite is not a long lived species and reaction pathways to convert mackinawite to pyrite proposed by (Rickard and Luther, 1997) require dissolution of the mackinawite to produce pyrite, which would likely release some of the trace metals. Work by Huerta-Diaz and Morse (1992) showed that as progressively more mackinawite is converted to pyrite a greater concentration of transition metals (excluding Cr) are incorporated into the structure of pyrite. This process is limited only by the amount of pyrite produced and the amount of trace metals available to be added to the pyrite. They also found that, although metals such as Cr, Zn, Pb and Cd do exhibit increases as more of the reactive iron is converted into pyrite (i.e. with increasing degree of pyritization), the increases are not as significant as with the other transition metals. This may be because these elements are not held within the structure of the pyrite.

Based on their study of the Lower Toarcian Posidonia Shale Berner et al. (2013) separated trace elements in pyrite into four groups: heavy metals (Cu, Ni, Co, Pb, Bi and Tl); oxyanionic elements (As, Mo and Sb); elements that are predominantly in sub-microscopic sphalerite inclusions (Zn and Cd) and elements that occur in micro-inclusions of organic matter or silicates (Ga and V). Berner et al. (2013) and other studies (Dellwig et al., 2002) have shown that heavy metals tend to be incorporated in pyrite predominantly during diagenesis of anoxic sediments. This occurs by a number of different processes: precipitation; co-precipitation; chemical or physical adsorption and redox reactions between dissolved species and the pyrite surface or the surface of pyrites precursors.

The metalloid arsenic is one of the elements that was found to be incorporated most readily into the structure of pyrite (Huerta-Diaz and Morse, 1992). Pyrite can contain up to 6% arsenic, based on first principle calculations, before forming an arsenopyrite and pyrite assemblage (Reich and Becker, 2006). Three ways arsenic is accommodated in the pyrite

lattice have been identified. The first contains As(-I) that substitutes for S(-II) in the pyrite lattice. The second contains As (II) (Qian et al., 2013) or As(III) (Deditius et al., 2008) which substitutes for Fe(II) in the pyrite lattice. The final way arsenic is present in pyrite is as nano-scale micro inclusions of amorphous As-Fe-S that are trapped within the pyrite as melts during pyrite crystallization (Deditius et al., 2009).

The mechanisms in which Arsenic has been found to incorporate into pyrite include: adsorption onto the pyrites surface; co-precipitation with pyrite; substitution with Fe or S in the pyrite lattice and incorporation into FeS_2 phases that depend on interactions of dissolved species with the growth faces (Neumann et al., 2013). However, in reducing environments adsorption is considered to be the most significant of these uptake mechanisms (Neumann et al., 2013). Arsenic incorporation into pyrite has also been linked to the incorporation of several other trace elements (Deditius et al., 2008). Arsenic(-I) arsenian pyrite tends to incorporate equal or more trace elements than As(III) arsenian pyrite, especially those that form divalent cations with similar ionic radia to Fe(II) (i.e. Co, Ni, Cu, Zn) (Deditius et al., 2008). While As(III) arsenian pyrite tends to provide more favourable settings for larger cations such as Au(I), Ag(I) and Pb(II) (Deditius et al., 2008). The most detailed work on the ability of As to enhance the uptake of other trace elements into pyrite has been completed on the incorporation of Au into arsenian pyrite. Reich et al. (2005) showed that when Au/As < 0.02 then gold is structurally bound with the pyrite. They also showed that gold accumulation in arsenian pyrite is strongly dependent on the presence of Au and the presence of lattice defects and/or vacant sites in the pyrite (Reich et al., 2005).

In this study LA-ICPMS was used to analyze individual pyrite framboids and determine their trace metal and metalloid abundance. This is an improvement over sequential extraction techniques of analyzing pyrite as it does not have the problems of selectivity of reactants that were identified by Martin et al. (1987). By avoiding the problem of selectivity of reactants it was possible to examine pyrite framboids that were growing in an area that contains high levels of several trace metals to examine how trace metals are incorporated into diagenetic pyrite. This is the first study to analyze the accumulation of metals in pyrite framboids from a heavily contaminated site and gives insight into the importance of competition for adsorptive sites on the surface of growing pyrite grains for the incorporation of metals within diagenetic pyrite.

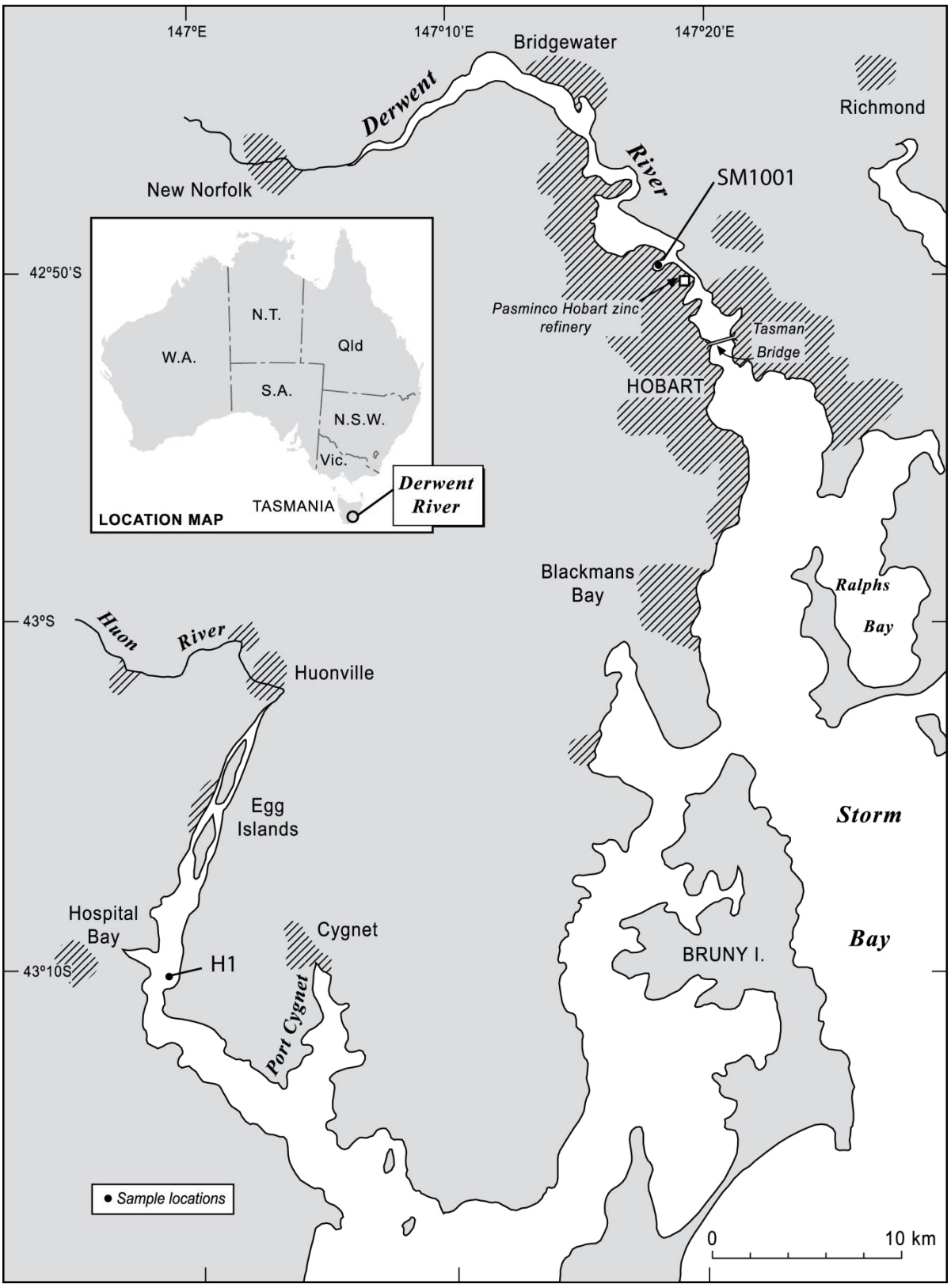

Figure 3.2: Location of samples taken from the Derwent (SM1001) and Huon (H1) Estuaries. Hatched patterns indicate residential areas.

3.3 Material and Methods

3.3.1 Location and setting

Samples were taken from two estuaries in southern Tasmania, Australia. A sediment core from the Derwent Estuary, (Figure 2) (Gregory et al., 2013) was taken from Prince of Wales Bay, adjacent to the Risdon zinc refinery which has been operating since 1917. Prior to the 1970's little environmental precautions were taken; smelter waste was deposited directly into the estuary and ore particles were blown into the water from uncovered stockpiles on the river bank (Gregory et al., 2013). In 2010 the Australian national pollution inventory reported 99 kg As, 311 kg Cd, 299 kg Cu, 654 kg Pb and 23834 kg Zn were deposited into the estuary. For a detailed discussion of the contamination history of the Derwent Estuary please refer to Appendix 1.

The Huon Estuary is located approximately south-southwest of the Derwent Estuary at 43° 14' S and 147° 4' E. The Huon Estuary has similar underlying geology to the Derwent and drains a hinterland of mixed forest and farming areas. In comparison to the Derwent the Huon Estuary is sparsely populated and hosts few major industries on its margins and is therefore a low contamination analogue of the Derwent Estuary (Jones et al., 2003).

3.3.2 Sample collection and preparation

A 1.05 m sediment core taken from Prince of Wales bay (42°49'33"S, 147°18'12"E) in August 2010 and a 0.65 m long sediment core taken from the Huon Estuary (43°10'26"S, 146°59'7"E) in December 2011 were both sampled using an Uwitec hammer corer (Figure 2). The black silt found in both cores (predominantly 2.5Y 2.5/1 with zones of 5Y 2.5/1 on the Munsell colour chart) contained nearly no stratification and exhibited strong evidence of bioturbation by worms and arthropods. The sediment was extruded by pushing a plunger through the tube and samples were taken every 2.5 cm for the first 30 cm of the Derwent sediment core and 5 cm for the remainder of the cores. One half of each sample was dried prior to processing for geochemical analysis; one quarter was removed for heavy mineral separation while the remaining quarter was stored in a freezer for future use. Heavy minerals were separated by either panning or by heavy liquid separation (heavy liquid separation was only used for the Derwent samples). The samples were first panned using a plastic riffled

pan. The concentrate was then transferred to a watch glass which was further panned to produce a concentrated separate of heavy minerals. Individual pyrite framboids were removed from the concentrate using a steel needle. Framboids were then mounted in 2.5 cm diameter epoxy mounts prior to LA-ICPMS analysis. Heavy mineral separates were also made by mixing the sediment sample with lithium heteropolytungstates in a separatory funnel and leaving for 24 hrs. The dense minerals (>2.95 specific gravity) settled to the bottom of the funnel where they were collected by opening the valve and draining the bottom fraction of the lithium heteropolytungstates with the dense minerals. The minerals were filtered out and washed three times with deionized water. This concentrate was mounted in epoxy for LA-ICPMS analysis. The extracted framboids tended to be 10-20 µm in diameter and were usually spherical. However pyrite was also found to replace/fill biological structures and take the shape of that structure, an partially filled example of this is shown in Figure 1A.

3.3.3 Analytical methods

The dried samples were ground to <63 µm using a chromium steel mill. These samples were analyzed for metal concentrations using a combination of ICPAES (Agilent 725 Radial ICPAES) and ICPMS (Perkin Elmer Elan 9000 ICPMS) techniques at ALS Chemex in Brisbane, Australia and separately for gold using the instrumental neutron activation (INAA) technique at the Ecole Polytechnique Montreal in Canada. At ALS Chemex's lab the samples were digested by four acids (HCl, HNO_3, H_2SO_4 and HF) prior to being analyzed by ICPAES and ICPMS. Only ICPAES analysed Al, Ca, Cr Fe, K, Mg, Mn, Na, P, S, V and Zn while only ICPMS analysed Ce, Cs, Ge, Hf, In, Li, Nb, Rb, Re, Sn, Ta, Te, Th and Y. Both methods analysed Ag, As, Ba, Be, Bi, Cd, Co, Cu, Ga, La, Mo, Ni, Pb, Sb, Se, Sr, Ti, Tl, U, W and Zr and the final values were obtained by merging the results from both methods using a complex algorithm. Blanks, geochemical reference materials (MRGeo02 and GBM398-1; prepared by Ore Research & Exploration Pty Ltd and Geostats Pty Ltd respectively) and sample duplicates were used to ensure quality control. These were within the criteria for acceptable values (10-20% of the expected values, with higher variation considered acceptable for elements with low expected values). Details of the Derwent samples have been reported in a companion study (Gregory et al., 2013). At the Ecole Polytechnique the samples were placed into 7 ml irradiation polyethylene vials prior to irradiation in the Slowpoke nuclear reactor, where they were irradiated for 30 min at an average neutron flux

of 5 x 10^{11}/cm^2/s (varying from 4.43 to 5.58 x 10^{11}/cm^2/s as a function of sample position in the irradiation site). They were then allowed to decay between three and five days before the gamma ray spectrum was recorded for three to five hours at a distance of 1.6 mm. The amount of gold was then calculated using EPAA v3.0 (Ecole Polytechnique Activation Analysis) software. Over several years of analyses the reactor neutron flux and detector efficiency has been reproducible to 1% and a quality control standard containing 30 µg gold is routinely analyzed and it was within 5% of the expected value.

Analyses of available metal ions for four of the Derwent samples were conducted as part of the companion study based on the methods proposed by Zeien and Brümmer (1989). This method consisted of seven leach steps designed to release metals that are: easily exchanged, weakly complexed and bound by carbonates, bound by Mn (hydr)oxides, bound by organic matter, bound by Fe (hydr)oxides of low crystallinity, bound by Fe (hydr)oxides of high crystallinity and the residual fraction. Of these the first four leachates have been presented in this study as possibly available for incorporation into pyrite. Though it should be noted that some of the elements held within the Mn (hydr)oxides and organic matter may be unavailable for incorporation into pyrite and some of the elements held within the Fe (hydr)oxides may be available for incorporation into pyrite. The first four leachates were obtained by leaching the samples with: 1 M NH_4NO_3 for 24 hours at 20°C (leach 1); 1 M NH_4OAc (pH 6) for 24 hours at 20°C (leach 2); 0.1 M NH_3OHCl + NH_4OAc (pH 6) for 0.5 hours at 20°C (leach 3) and 0.025 M NH_4-EDTA (pH 4.6) for 1.5 hours at at 20°C (leach 4) (Gregory et al., 2013). The resulting aliquots were analyzed in the Central Science Laboratory at the University of Tasmania using an ELEMENT 2 sector field ICP-MS (Thermo Fisher, Bremen, Germany). Quality control was undertaken by analyzing calibration solutions as 'unknowns' to monitor instrument performance and by analyzing a water standard (NIST_RefWater1640a) to verify calibration accuracy.

The metal and metalloid contents of pyrite framboids were determined using a LA-ICPMS system (a New Wave UP-193SS Nd:YAG Q-switched Laser Ablation System or a New Wave UP-213 Nd:YAG Q-switched Laser Ablation System coupled to an Agilent 7500a Quadrapole ICP-MS) based at the ARC Centre of Excellence in Ore Deposits at the University of Tasmania. Using a 10 µm beam the samples were ablated in an ultra-high purity He atmosphere before being mixed with Ar and flowing into the ICPMS. Laser energy of 1.8 to 2.5 Jcm^{-2} and a repetition rate of 5 Hz were used for all analyses. Data was

collected over 70-90 s intervals, with a 30 s pre-ablation acquisition (background) interval and a 40-60 s acquisition interval. Generally 20 s of the laser on data acquisition was used for data reduction due to the tendency for the laser to completely ablate through the pyrite framboid. However, this was enough time to obtain sufficient signal to produce analyses with adequate detection limits and errors for most elements. Many of these results had relatively high detection limits for Au and Te (>0.1 ppm and >1.0 ppm respectively) and so an additional 97 samples were analyzed for a limited number of elements (Au and Te) in an attempt to lower the detection limits.

The primary standard used to calculate concentrations and correct for instrument drift was STDGL2b-2. The standard is a lithium-borate fused disc of pyrite and sphalerite powder doped with certified element solutions (Danyushevsky et al., 2011). This standard yields an error of less than 15% for most elements. The standards were analyzed twice at the beginning and end of each session, before and after each sample change and every one to two hours of analysis time. A total of 256 analyses were conducted. Iron was used as an internal standard as pyrite rarely varies from its stoichiometric value by more than 5% (Danyushevsky et al., 2011). All results were corrected for linear drift and data reduction was undertaken following the methodology developed by Longerich et al. (1996).

3.4 Results

3.4.1 Geochemistry

Results for the whole sediment analysis are summarized in Figure 3. A more comprehensive analysis of the bulk chemistry of the sediments is presented in a companion paper (Gregory et al., 2013). It is readily apparent that the Derwent samples are much more enriched than the Huon samples above 75 cm depth for all reported elements except Co, Ni, Te and Mo (Figure 3). The increase in S content with depth in the Huon samples may reflect a natural increase in the degree of pyritization in the core (i.e. the amount of reactive Fe that has been precipitated as pyrite) (Figure 3). The Derwent core sample has been divided into 5 different groups based on the geochemical results: moderate metal and low sulfur (0 to 25 cm); moderate metal and high sulfur (25 to 45 cm); high metal (45 to 55 cm); high to low metal transition zone (55 to 80 cm) and low metal (80 to 100 cm). Representative samples from four of these groups were analyzed by sequential analysis to determine what sediment

components the different metals are held within (Gregory et al., 2013). Results for the amount of trace metals that may be available for incorporation into pyrite are summarized in table 1. These are the sum of the easily extractable fraction; carbonate held fraction;

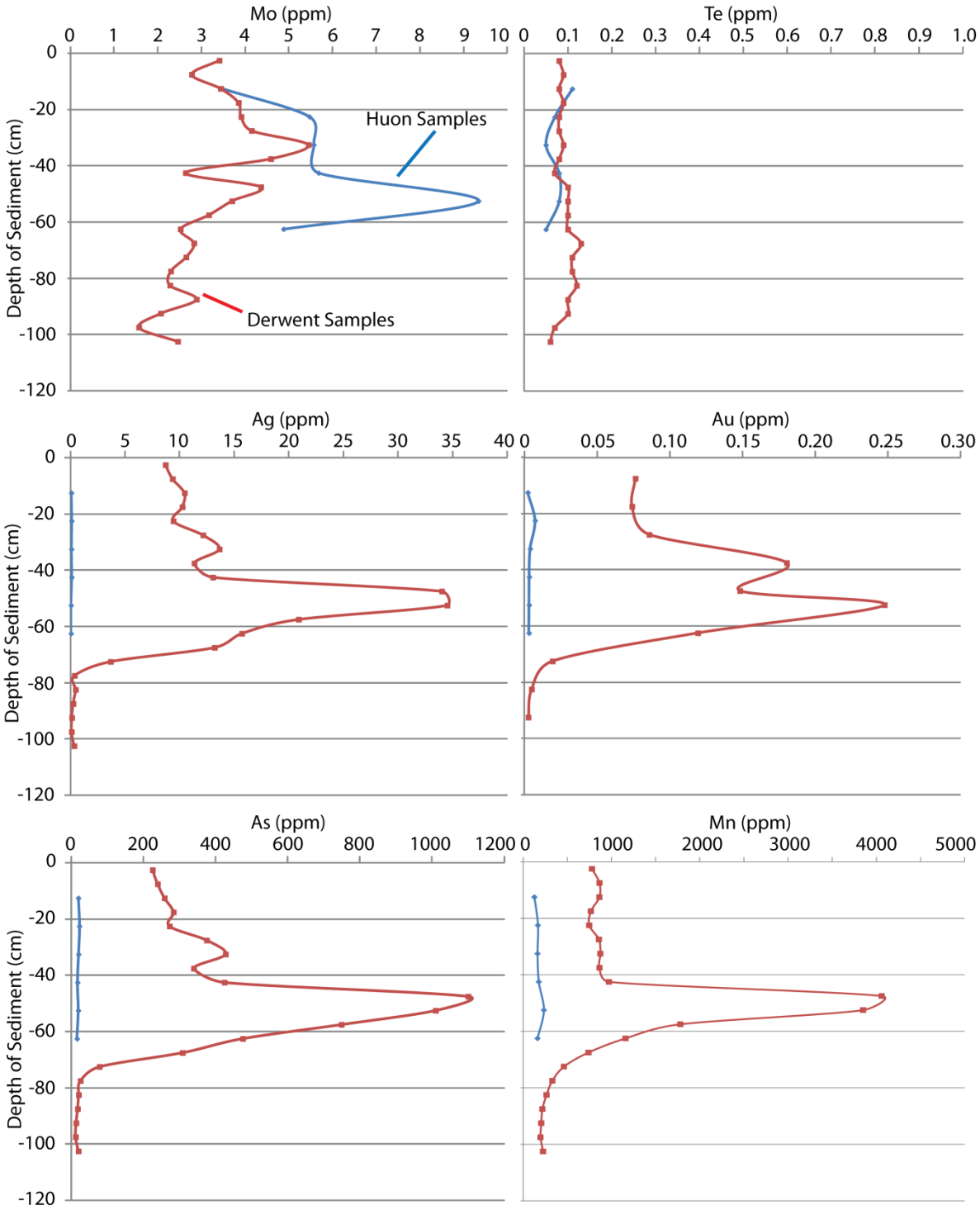

Figure 3.3A: Whole sediment geochemical analyses of sediment cores from the Derwent (red) and Huon (blue) Estuaries for Mo, Te, Ag, Au, As and Mn . The Derwent estuary is enriched in metals and metalloids in the top 45 cm, very enriched from 45-55 cm and tapers down to background values by 75 cm.

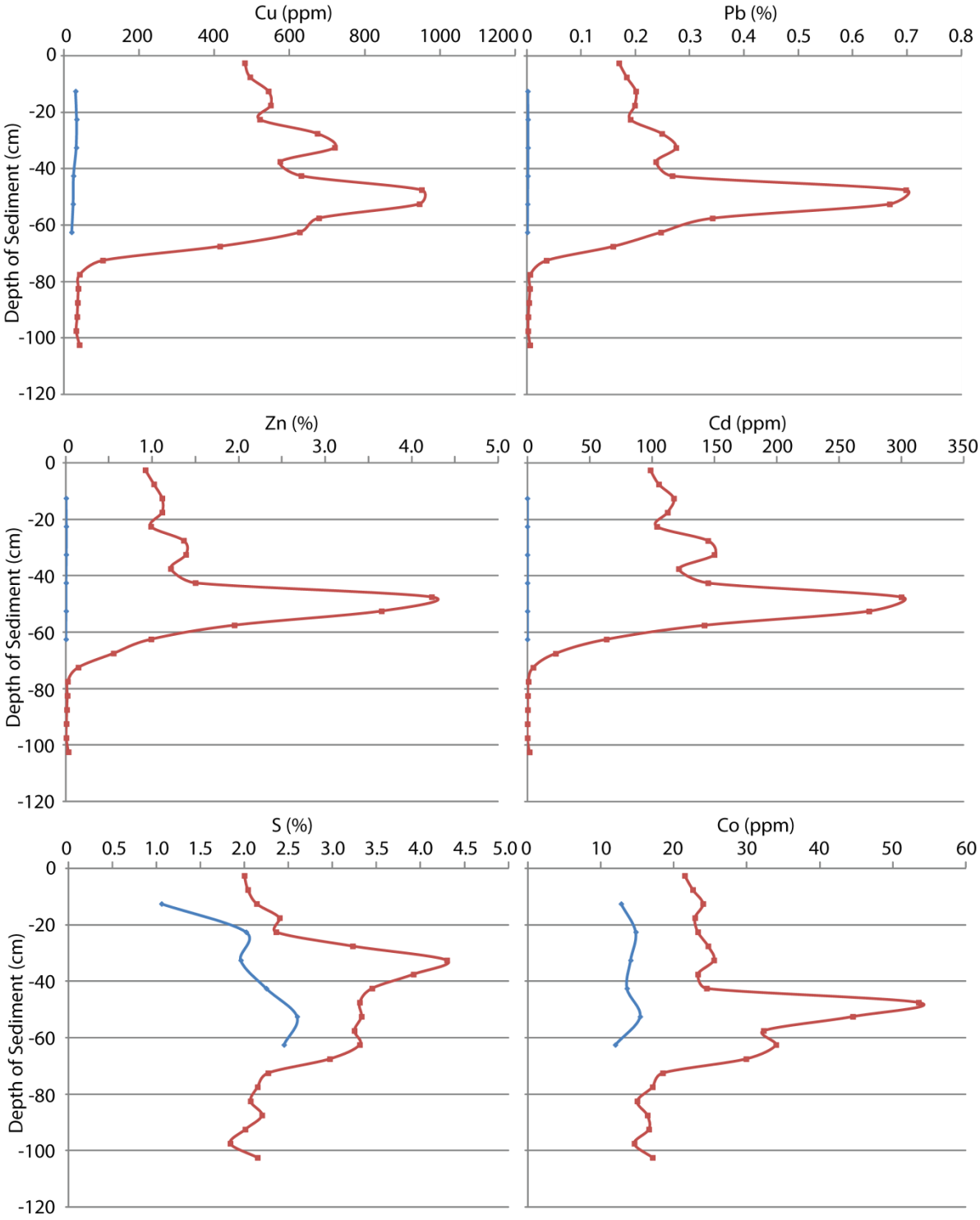

Figure 3.3B: Whole sediment geochemical analyses of sediment cores from the Derwent (red) and Huon (blue) Estuaries for Cu, Pb, Zn, Cd, S and Co. The Derwent estuary is enriched in metals and metalloids in the top 45 cm, very enriched from 45-55 cm and tapers down to background values by 75 cm.

Mn(hydr)oxide fractions and organic held fraction. The poorly crystallized Fe (hydr)oxide and well crystallized Fe (hydr)oxide fractions obtained from the sequential leach extractions were not included because in the Derwent Estuary there is a high concentration of franklinite (zinc ferrite) which dissolves under the conditions used to extract the different Fe (hydr)oxide fractions (Gregory et al., 2013). This franklinite is stable in the sediments as is indicated by SEM analyses that show no alteration on the rims of the grains (Gregory et al., 2013). Thus it was believed that including analyses from these extractions would give concentrations much higher than those actually available for incorporation in the pyrite. Unfortunately degree of pyritization analyses are not possible in the Derwent Estuary due to the presence of significant quantities of Fe (hydr)oxide and sulfide minerals being introduced into the estuary as smelting by products (Gregory et al., 2013). For complete discussion on techniques used to isolate these different fractions please see Gregory et al. (2013).

Table 3.1: Trace metals that are easily exchanged, weakly complexed and bound by carbonates, bound by Mn (hydr)oxides and bound by organic matter from the Derwent Estuary sediments as determined by Gregory et al. (2013).

Depth Interval (cm)	Pb (ppm)	Mn (ppm)	Co (ppm)	Ni (ppm)	Cu (ppm)	Zn (ppm)	As (ppm)	Cd (ppm)	Mo (ppm)
20-25	1415	52	3.0	4.0	143	1935	34	18	0.6
30-35	2007	87	4.0	9.7	225	3459	130	21	1.2
50-55	4750	277	5.0	2.8	172	4645	166	16	0.6
90-95	9.4	25	1.3	4.1	7.5	11.7	0.4	0.62	0.2

During the course of this study 159 pyrite framboids were analyzed for Al, V, Co, Ni, Cu, Zn, As, Mo, Ag, Cd, Te, Au, Pb and Bi and 97 pyrite framboids were analyzed for only Au and Te. Median, maximum and minimum values for Zn, Pb, Cu, Bi, Ni, Co, Mo, As, Au, Ag and Te in pyrite for the Derwent and Huon Estuaries are reported in Table 2 and 3 respectfully.

Median values for pyrite framboids from the Huon Estuary are generally uniform with concentrations of trace metals varying little with depth. Gold, Ag and Te from individual grains are generally below detection limits and medians of Zn (26 – 65 ppm), Pb (0.30 – 2.5 ppm), Bi (0.05 – 12 ppm), Ni (2.77 – 18.8 ppm), Co (0.87 – 25.7 ppm) and As (122 – 590 ppm) show little systematic variation with depth. Whereas the concentration in pyrite of Cu (11 – 82 ppm) and Mo (below 30 cm depth) (5.3 – 40 ppm) show a significant increase with increasing depth (Figure 4).

Table 3.2: Maximum, Minimum and Median element composition of pyrite from the Derwent Estuary

Depth	Zn (ppm)			Pb (ppm)			Cu (ppm)			Bi (ppm)			Ni (ppm)			Co (ppm)		
(cm)	Med	Min	Max	Med	Min	Max	Med	Min	Max	Med	Min	Max	Med	Min	Max	Med	Min	Max
5 - 10	591	453	4370	1400	1320	10600	460	206	704	2.95	1.44	11.23	15.04	1.64	31.7	23.5	4.59	81.3
15 -20	84	24	708	54.5	1.2	1620	17.9	7.55	451	<0.13	<0.09	2.05	2.04	0.79	8.9	18.9	3.06	57.0
20 - 25																		
25 - 30	1180	106	9410	1250	66.8	7290	154	28.2	640	0.36	<0.15	2.38	1.35	<0.5	6.7	12.7	2.09	112
35 - 40	723	92	4540	808	4.9	6130	77.2	16.9	704	0.24	<0.12	4.55	2.84	1.20	80.1	11.7	3.28	146
40 - 45	298	192	2500	635	19.3	3010	102	6.81	273	0.30	<0.06	2.06	0.85	<0.6	5.3	8.9	0.63	56.6
50 - 55	515	34	2460	237	4.3	4970	44.8	2.37	670	0.19	<0.09	2.53	3.61	<0.4	150	9.6	<0.1	667
60 - 65	415	287	1230	211	7.3	1140	130	18.7	351	0.13	<0.04	0.49	6.11	2.77	9.6	32.2	11.9	81.6
70 - 75	326	229	899	184	24.0	1290	79.1	12.0	157	0.09	<0.03	0.25	35.0	5.58	84.2	83.9	2.31	212
80 - 85	82	45	111	55.7	1.4	128	25.2	4.93	56	0.07	<0.03	0.23	4.58	1.22	15.5	2.2	0.29	20.0
90 - 95	94	24	114	29.9	5.9	46	35.0	14.8	209	0.05	<0.02	0.24	9.92	2.20	33.3	1.6	0.72	35.5

	Mo (ppm)			As (ppm)			Au (ppm)			Ag (ppm)			Te (ppm)		
	Med	Min	Max	Med	Min	Max	Med	Min	Max	Med	Min	Max	Med	Min	Max
5 - 10	2.83	2.13	3.4	600	258	2300	0.31	<0.21	0.80	2.90	2.54	3.25	<2.88	<2.5	2.88
15 -20	1.48	0.92	3.7	1730	264	6210	<0.07	<0.03	0.07	<0.17	<0.11	3.32	0.78	0.09	1.17
20 - 25							0.04	<0.19	0.19				1.35	<0.6	2.66
25 - 30	3.84	0.39	14.2	3140	685	4480	0.10	<0.57	0.57	0.82	<0.17	1.60	4.33	0.88	7.07
35 - 40	1.06	<0.4	50.3	758	9	4080	0.03	<1.01	5.98	1.16	<1.15	3.62	2.05	0.59	11.8
40 - 45	0.40	<0.4	32.4	587	193	2520	0.05	<0.49	0.49	0.23	<0.10	1.93	2.16	0.22	12.4
50 - 55	1.93	<0.5	120	795	106	5420	0.08	<0.10	0.45	0.37	<0.24	7.64	3.38	0.58	12.0
60 - 65	2.87	1.33	5.4	1120	680	2020	0.81	<0.16	3.52	4.32	0.58	8.66	1.01	<1.3	6.78
70 - 75	22.1	3.33	73.3	1720	18	6990	0.35	<0.18	0.87	24.0	0.20	90.2	2.49	<1.6	9.60
80 - 85	4.35	0.81	13.6	703	200	1140	0.04	<0.16	0.21	0.63	0.05	26.5	1.51	<1.6	4.39
90 - 95	3.19	1.41	11.0	125	61	624	0.30	<0.14	0.70	0.26	<0.41	38.1	1.72	<1.8	3.75

Table 3.3: Maximum, Minimum and Median element composition of pyrite from the Huon Estuary

Depth	Zn (ppm)			Pb (ppm)			Cu (ppm)			Bi (ppm)			Ni (ppm)			Co (ppm)		
(cm)	Med	Min	Max	Med	Min	Max	Med	Min	Max	Med	Min	Max	Med	Min	Max	Med	Min	Max
10 - 15	36.6	5.35	272	2.00	0.06	27.1	10.7	0.68	45.1	0.07	<0.03	0.38	18.0	0.18	79.6	13.6	<0.05	542
20 - 25	25.7	7.60	103	0.30	0.11	10.2	17.2	3.74	169	0.04	<0.03	0.23	2.77	0.53	67.4	2.51	0.14	152
30 - 35	27.1	14.4	67.0	2.40	0.07	6.83	19.3	1.10	223	0.09	<0.03	0.30	2.89	1.95	87.5	3.59	0.49	153
40 - 45	65.3	5.22	121	0.93	0.04	26.4	30.9	0.75	212	0.05	<0.02	0.33	9.12	0.39	70.0	6.74	0.08	133
50 - 55	59.3	28.4	144	1.31	0.13	18.1	68.0	20.5	510	0.05	<0.02	0.33	3.96	1.07	34.8	0.87	0.15	109
60 - 65	62.1	13.2	168	2.53	0.26	49.1	82.0	3.78	1300	0.12	<0.04	1.11	18.8	2.99	132	25.7	0.74	568
	Mo (ppm)			As (ppm)			Au (ppm)			Ag (ppm)			Te (ppm)					
	Med	Min	Max	Med	Min	Max	Med	Min	Max	Med	Min	Max	Med	Min	Max			
10 - 15	14.4	0.14	200	181	52.8	525	<0.02	<0.01	<0.04	<0.04	<0.03	0.17	0.26	<0.16	0.95			
20 - 25	12.0	4.22	20.8	354	91.1	3450	<0.03	<0.02	0.09	0.07	<0.04	0.62	<0.31	<0.22	0.39			
30 - 35	5.32	0.52	246	590	126	1110	<0.03	<0.02	0.05	<0.05	<0.04	0.13	<0.28	<0.20	1.53			
40 - 45	14.2	1.37	52.4	209	46.1	1920	<0.03	<0.01	<0.05	<0.06	<0.03	0.41	<0.28	<0.20	2.99			
50 - 55	30.2	4.95	202	194	41.0	2210	<0.03	<0.02	0.04	<0.05	<0.03	0.16	<0.26	<0.21	1.23			
60 - 65	40.0	1.32	219	122	36.0	1650	<0.03	<0.02	0.06	0.05	<0.03	0.49	<0.23	<0.15	1.72			

Note: The errors for each laser spot vary but the median values of the errors is as follows: Huon: Ag (0.049), As (5.42), Au (0.026), Cu (4.85), Mo (0.95), Pb (0.33), Te (0.25), Mn (21.98) and Zn (2.24); Derwent: Ag (0.13), As (16.91), Au (0.053), Cu (3.45), Mo (0.31), Pb (4.26), Te (0.26), Mn (21.76) and Zn (6.15).

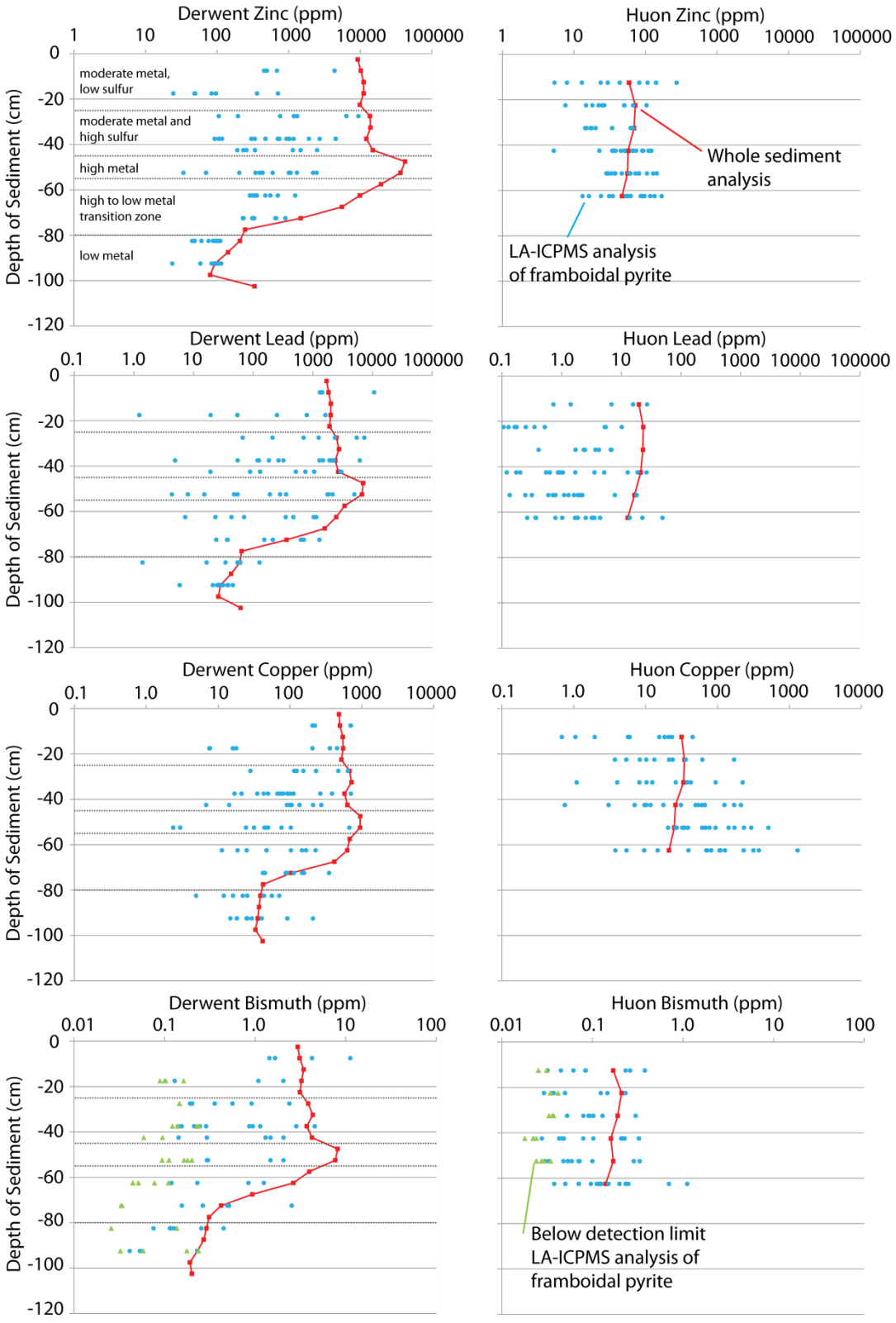

Figure 3.4A: Whole sediment analyses (red squares) and LA-ICPMS analyses (blue circles) of pyrite framboids from the Derwent (left) and Huon (right) Estuaries for Zn, Pb, Cu and Bi. Green refers to the detection limit when analyses are below detection limits.

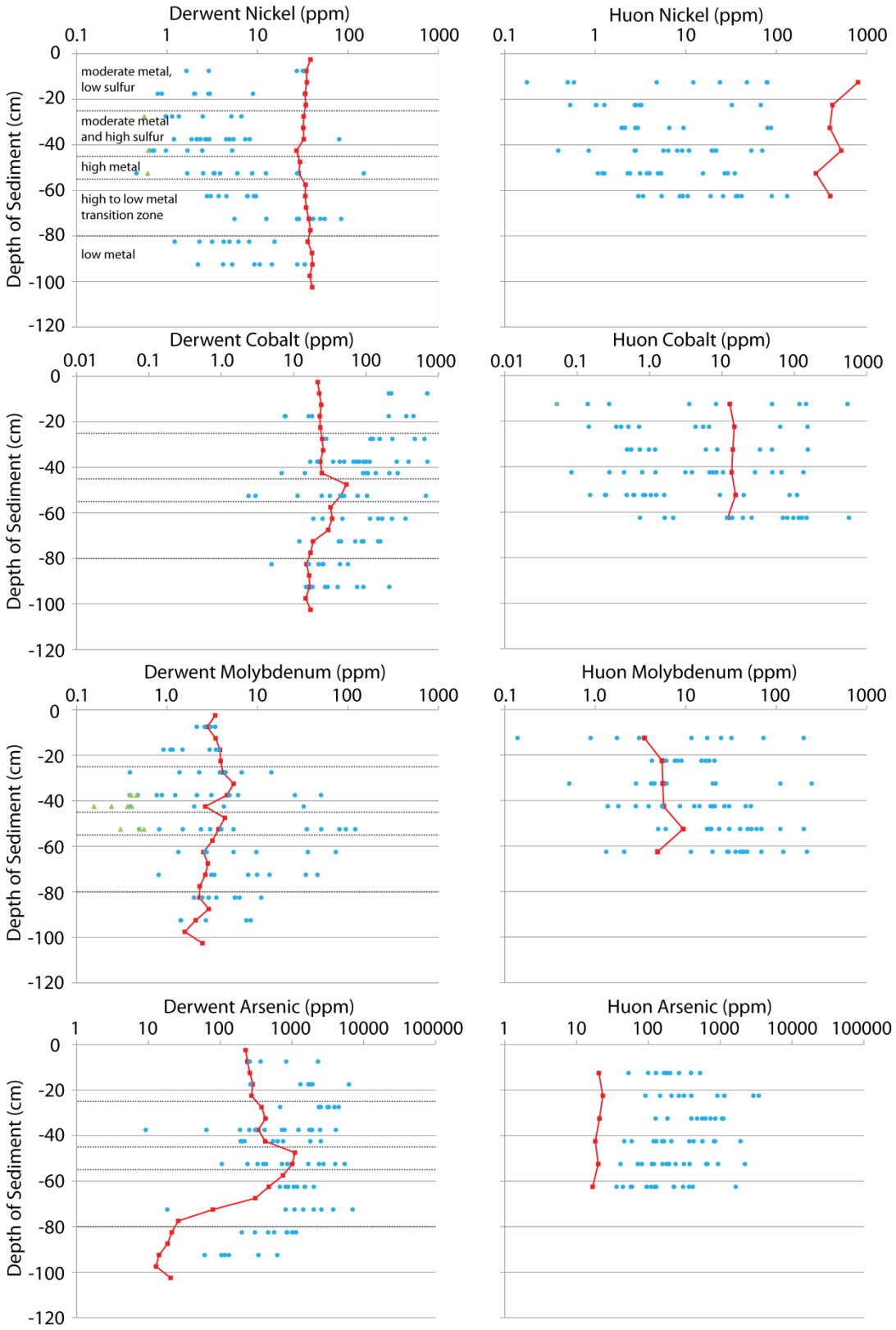

Figure 3.4B: Whole sediment analyses (red) and LA-ICPMS analyses (blue) of pyrite framboids from the Derwent (left) and Huon (right) Estuaries for Ni, Co, Mo and As. Green refers to the detection limit when analyses are below detection limits.

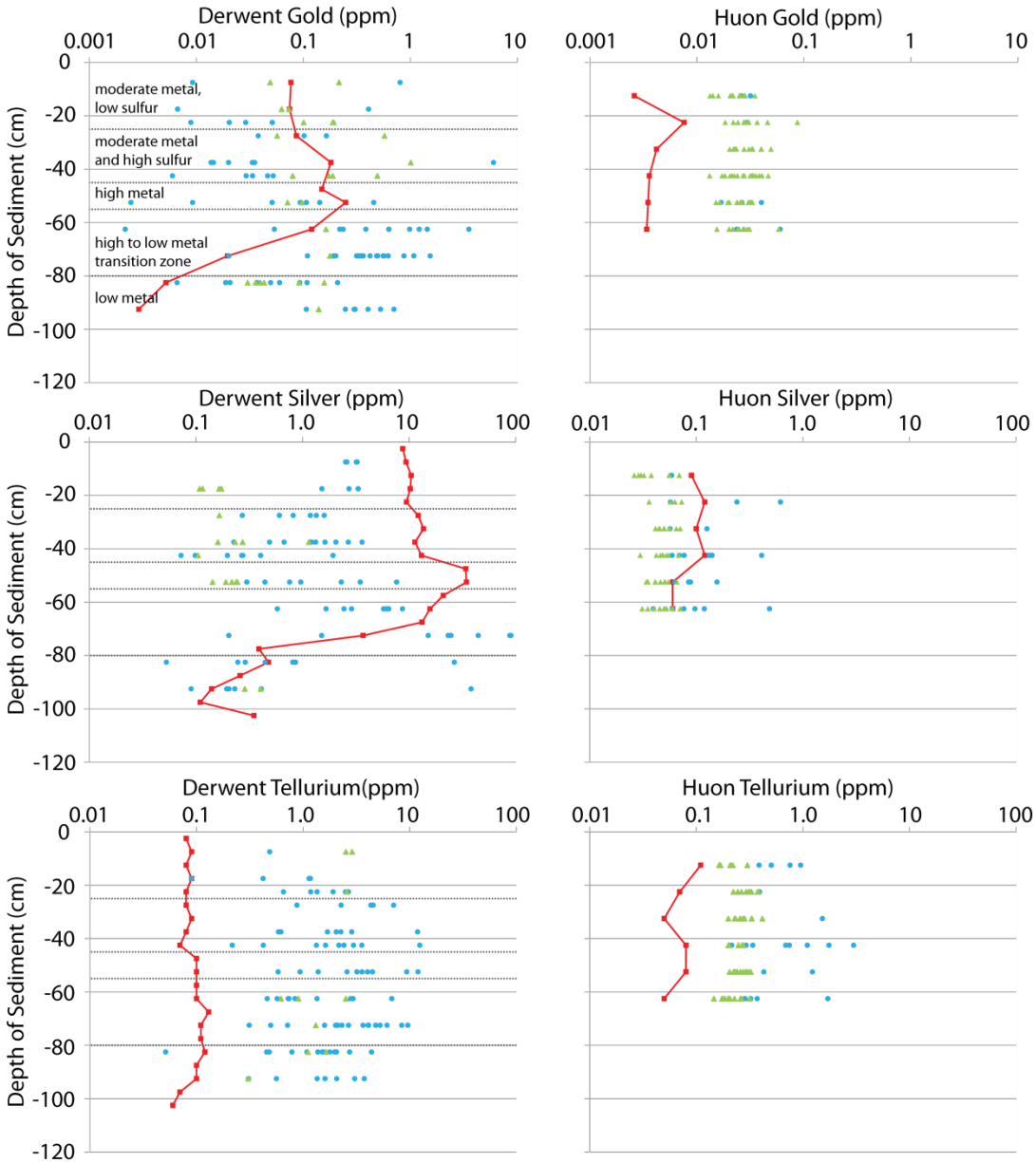

Figure 3.4C: Whole sediment analyses (red) and LA-ICPMS analyses (blue) of pyrite framboids from the Derwent (left) and Huon (right) Estuaries for Au, Ag and Te. Green refers to the detection limit when analyses are below detection limits.

The Zn, Pb, Cu and Bi content in pyrite framboids in the Derwent follow the trend indicated by the whole rock analyses (Figure 4), with the highest amount of metal in the framboids occurring in the most contaminated zone but with much lower content of metal within the pyrite than in the sediment itself. Arsenic in pyrite also follows the whole rock values; however it contains higher As values than the sediment. The concentration of Ag in pyrite is relatively low and uniform throughout the contaminated interval (between <0.11 ppm and 2.90 ppm from 0 to 55 cm) and are highly enriched at 70 to 75 cm (23.96 ppm), with minor

enrichment at 60-65 cm. A similar peak in trace element content of pyrite in the 70 to 75 cm interval is present for Ni, Co and Mo (35.0, 83.8 and 22.1 ppm respectively) despite these elements not being noticeably enriched in any section of the core. Gold behaves similarly, however its interval of major enrichment occurs between 60 and 65 cm below the main zinc enrichment. The Te content of pyrite is not enriched at any level in the core, however it is significantly enriched compared to the Huon core despite both cores having similar bulk Te contents. Both Au and Te are enriched in pyrite compared to the bulk sediment.

The LA-ICPMS data is collected every 0.1-0.5 s as the laser ablates through the framboid and this data can help to distinguish which elements are held within the pyrites structure/micro-inclusions within the pyrite or as larger inclusions within the framboid. Elements that exhibit relatively flat traces throughout the laser ablation are thought to be contained within the structure or micro-inclusions while elements with distinct peaks are thought to exist as larger inclusions (Thomas et al., 2011). Based on this criteria arsenic, manganese and zinc appear to be held within the pyrite structure or as micro-inclusions; tellurium, gold and bismuth are held as inclusions and copper, lead and silver are contained in the framboids as both inclusions and contained within the pyrite structure or microinclusions (Figure 5).

For combined results of all the geochemical analyses undertaken in this study please refer to Appendices 2 and 3.

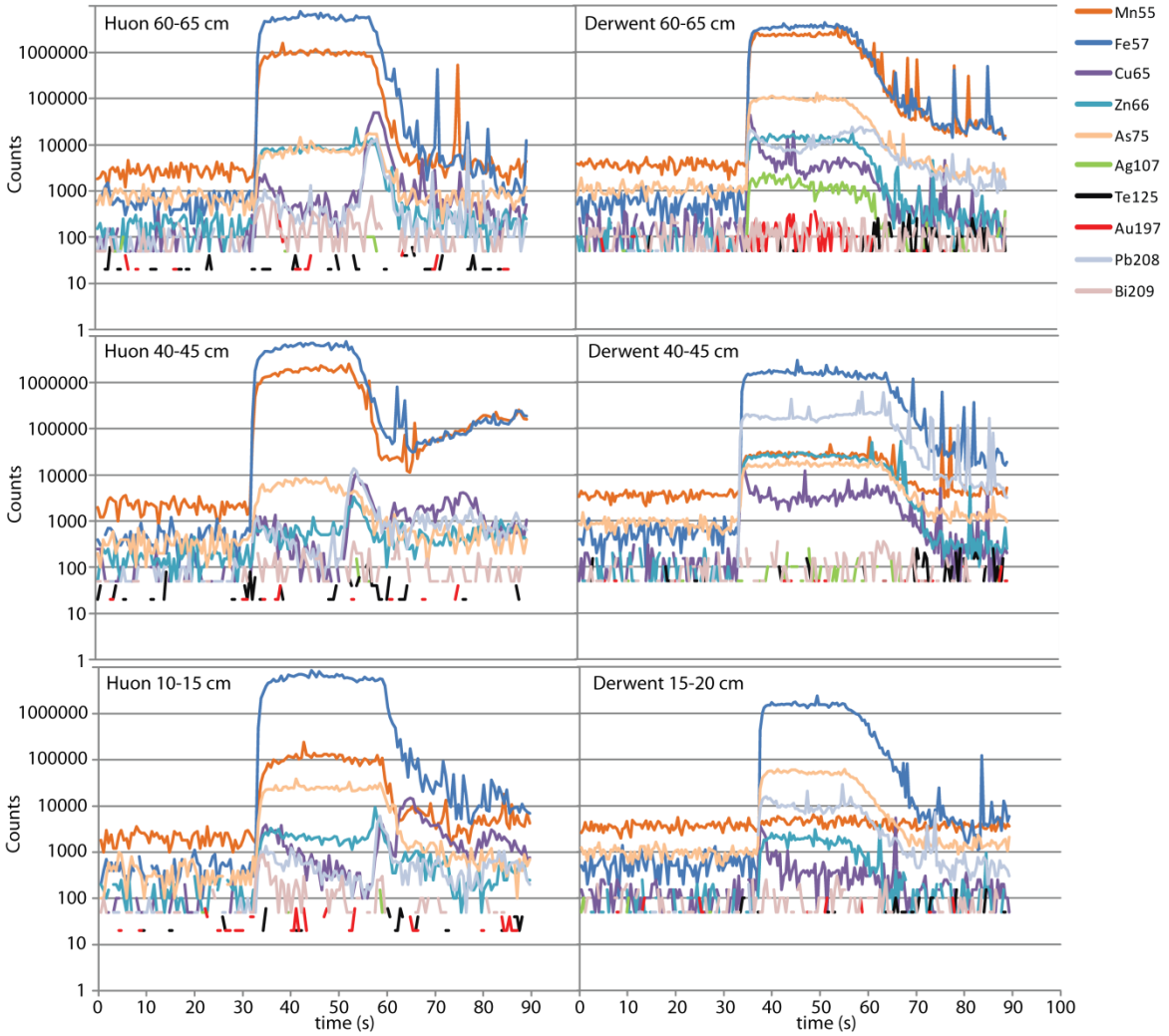

Figure 3.5: Time resolved LA-ICPMS output graphs of pyrite framboid analyses for Derwent and Huon Estuaries. The trace of the iron (when above 1000000 counts) shows where pyrite is being ablated. Spikes in the plots show microinclusions within the pyrite while relatively flat plots indicated the elements are held within the pyrite structure. The framboids are mounted in epoxy then polished down resulting in the laser starting in the centre and ablating to the edge.

3.5 Discussion

Previous enquiries into the accumulation of trace metals within pyrite forming within sediments have shown that mechanisms that incorporate different trace metals into pyrite proceed at different rates. These are, in decreasing order: As = Mo > Cu = Fe > Co > Ni >> Mn > Zn > Cr = Pb > Cd (Morse and Luther, 1999). These were determined using modifications by Huerta-Diaz and Morse (1990) on the pyrite extraction method proposed by Lord (1982) to determine the percentage of different trace metals and metalloids incorporated into pyrite, termed the degree of trace metal pyritization. As this method is not selective for

pyrite, it is only applicable in areas where no other sulfides or minerals with similar chemical properties to sulfides occur. Our study differs in that the LA-ICPMS technique allows us to analyze selected pyrite framboids individually which greatly expands the potential areas of study.

Incorporation of metals and metalloids occurs by uptake of the molecules onto the surface of the growing pyrite, followed by over growth of more pyrite. This occurs in 5 different ways: adsorption of outer-sphere complexes, adsorption of inner-sphere complexes, formation of surface precipitates, co-precipitation of other sulfide minerals with pyrite and diffusion of elements into the pyrite lattice (Rosso and Vaughan, 2006). Which of these, or combination of these, mechanisms occur for the different elements effects how much of them can be incorporated into the individual framboids and the rate of incorporation. These interactions of metals and metalloids with the surface of the growing pyrite are controlled by several factors: equilibration time, solution pH, initial concentration of elements, particle size and temperature (Borah and Senapati, 2006). The temperature is not likely to have changed significantly within the different layers of the sediment core and the size of the pyrite framboids and crystals that make but the framboids do not vary significantly within the core so these are not expected to be major factors effecting the relative accumulation of trace elements in pyrite from the Derwent and Huon Estuaries. The rate of equilibration is also not likely to be significant as the rate of pyrite formation relative to rate of equilibration should be similar throughout the sediment cores. The amount of metals incorporated into pyrite does not change significantly with changes in pH, which suggests that the point of zero change (pzc) is not crossed by the range of the pH values present in the sediments. This is consistent with data produced by Pikaray et al. (2005) which provides results of pzc for pyrite in shale and soil that have an average 7, which is below the pH measured in this study. This suggests that the growing pyrite would have had a slightly negative charge. However, micro-environments with different pH may have formed locally within the sediment. If these local pH values were equal to or lower than the pzc this may have resulted in different amounts of adsorption, resulting in significantly different amounts of trace metal accumulation in pyrite. The existence of differing pH micro-environments may explain the spread that is evident in some of the trace element contents in pyrite. The relative concentrations of elements available for adsorption are thus the most likely factor that controls the amount of trace elements in pyrite framboids in the Derwent and Huon estuaries.

Arsenic is enriched in pyrite by approximately an order of magnitude in both the high metal content Derwent and low metal Huon Estuaries when compared to the whole rock sediment analyses. The only interval where this does not hold is in the most contaminated section of the Derwent core where several framboids have lower arsenic content than that measured in the host sediment. This is due to much of the As being held in other phases (such as arsenopyrite) in this interval and is not available for incorporation into pyrite (Figure 6). This is because As readily substitutes into pyrite at a high rate; which makes incorporation into pyrite the primary mechanism in which As is removed from pore water (Lowers et al., 2007). This is supported by SEM analyses (Gregory et al., 2013) that show the presence of arsenopyrite in the metal enriched sections of the sediment.

Molybdenum behaves differently than expected with several framboids displaying erratic enrichment relative to the host sediment in the contaminated zone and an increase in the molybdenum in pyrite below the contaminated zone at 70-75 cm. Molybdenum exists in the sediment as the molybdate or thoimolybdate anion or one of the intermediates between these two end members (Erickson and Helz, 2000; Helz et al., 1996; Xu et al., 2006). Of these the thoimolybdate anion is likely to be in highest abundance in the sulfide rich conditions of the sediments (Erickson and Helz, 2000). This is also the most efficient form to adsorb onto pyrite, however it is also the most efficient to adsorb onto organic matter (Erickson and Helz, 2000; Helz et al., 1996). In the Derwent samples there is significantly more organic matter above 45 cm depth (Gregory et al., 2013), which is where the Mo content of pyrite is comparatively low. This suggests that competition between pyrite and organic matter for adsorption of Mo may be responsible for the observed lower Mo content of pyrite above 45

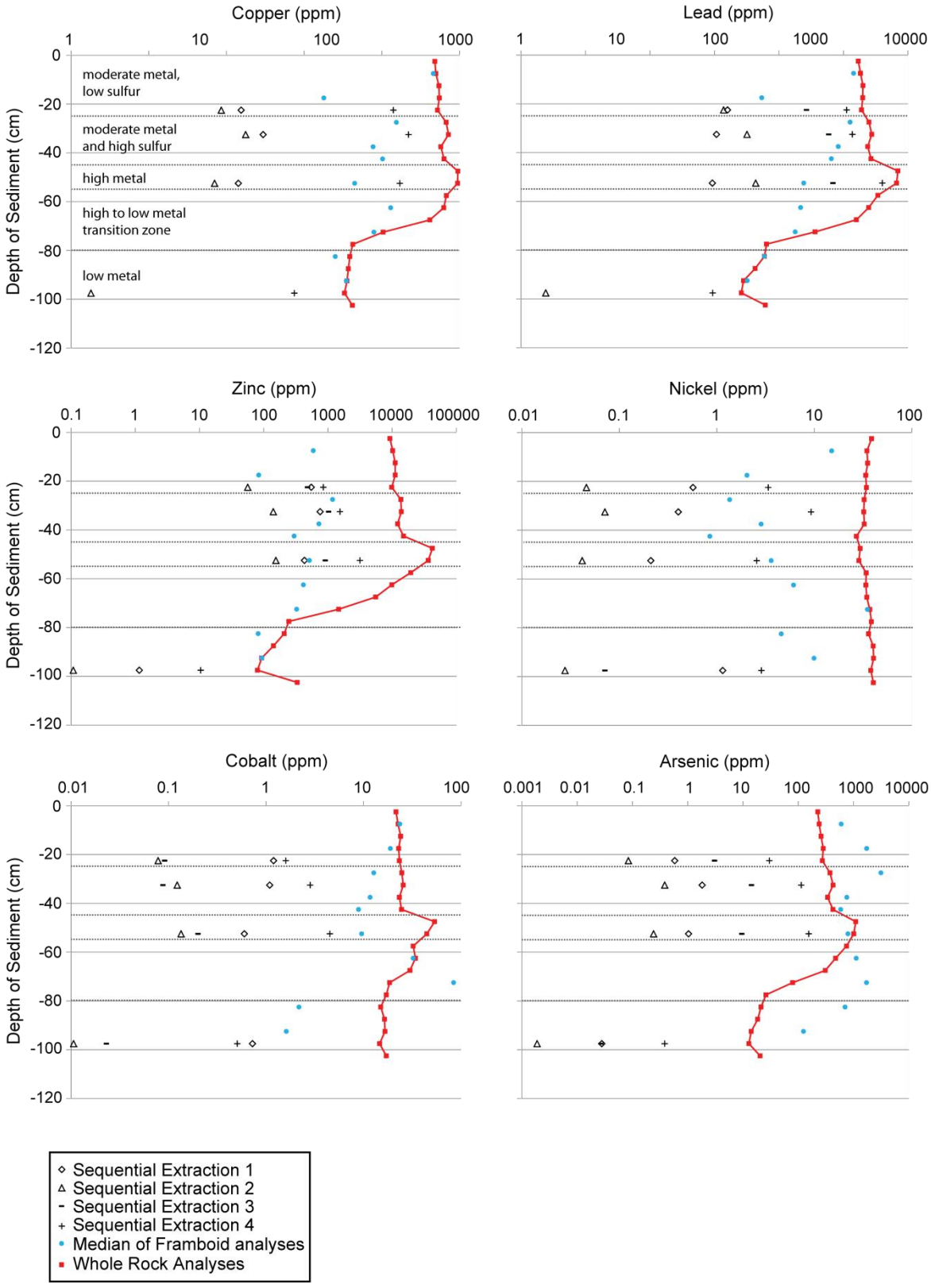

Figure 3.6: Trace metal contents of pyrite, whole sediment and trace metals available to be incorporated into pyrite. Note that both Pb and Zn have very high proportions of metals that can be incorporated into pyrite. This may cause some metals to be unable to adsorb onto the surface of the growing pyrite allowing them to diffuse to lower levels in the sediment and become incorporated into the pyrite there.

cm. In addition to this, competition for the adsorption sites on the surface of the growing iron sulfides due to an abundance of metal ions in the contaminated zones may also have resulted in less Mo in pyrite. This competition for adsorptive sites on the surface of the growing iron sulfide is evident by examining the degree of available metals for pyrite adsorption in the most contaminated zone (Figure 6). Abundances of metals such as lead and zinc available for incorporation into pyrite in the contaminated zone are much higher relative to Mo than in the less contaminated zone (i.e. the Zn/Mo and Pb/Mo ratios are much higher in the contaminated zone). While this may not appear to follow the relative incorporation scheme proposed by Morse and Luther (1999), in which Mo should be one of the first elements to be incorporated in pyrite, the fact that Mo is in relatively low concentration may result in relatively little Mo being incorporated into the pyrite and the additional adsorption sites provided by more organic matter higher in the section resulted in even less Mo available to be incorporated into pyrite. In the uncontaminated Huon Estuary molybdenum holds with the predictions of Morse and Luther (1999) with the medians of the Mo in pyrite above that in the host sediment. The trends with depth also fit with the predictions by Huerta-Diaz and Morse (1992), which predict an increasing trace metal abundance with depth; in the Huon we see this trend below 30 cm of sediment depth (Figure 4).

Water exchange rate kinetics for lead and zinc are faster than that for iron which suggests that lead and zinc sulfides should precipitate earlier than pyrite (Morse and Luther, 1999). The incorporation of these metals in pyrite is also favored under the conditions found in the saline sediments as pH found in the sediments in above the adsorption edge for these metals on pyrite (Jean and Bancroft, 1986). Our data support this in the Huon Estuary where the time resolved LA-ICPMS output graphs show relatively spikey compositions of lead and zinc (Figure 5), suggesting the presence of inclusions of lead and zinc sulfides within the pyrite. The time resolved LA-ICPMS data from the Huon samples also indicates a decrease in the amount of lead and zinc from the center of the framboid to the edge. This is consistent with early rapid crystallization of lead and zinc sulfides, which are associated with the earliest growth of pyrite framboids. Later the low levels of zinc and lead in the pore waters are exhausted and only iron sulfide precipitates, resulting in relatively lead- and zinc-poor rims. In the contaminated sediments of the Derwent Estuary lead and zinc behave somewhat differently with relatively consistent compositions throughout the pyrite framboid (Figure 5). This may be due to the amount of available zinc and lead (from the first four steps of the sequential leach data), which increases from 1935 ppm and 1415 ppm respectively in the 20-

25 cm interval to 4750 ppm and 4645 ppm respectively in the 50-55 ppm interval (Table 1 and Figure 6). This results in the observed increase in Pb and Zn in the framboids. These metals occur most likely as several micro-inclusions that are evenly distributed throughout the framboid. This inclusion hypothesis is supported by work from Deditius et al. (2011) which has shown that a wide range of nano particles are found in pyrite as native metals, sulfides, sulfo-salts and iron bearing nanoparticles. In the course of their study they showed that Pb, Bi, Sb, Au, Ag, Ni, Te and As preferentially distribute into nano particles, with large particles forming by exsolution and small ones forming by direct precipitation. However, they did not investigate Zn, in this study Zn appears to behave similarly to Pb and thus it is suggested that it too preferentially forms nano particles in pyrite.

Zinc tends to be accumulated in pyrite less than Pb and Cu, relative to the total amounts of Zn, Pb and Cu in the system. This may be because the pK_1 for the formation of the $MeOH^{z-1}$ complexes are higher for Zn (8 for Cu, 7.7 for Pb and 9 for Zn) (Baes and Mesmer, 1976), resulting in less efficient Zn adsorption (Müller et al., 2002). A wide degree of variation in the content of lead and copper is found, especially within the most contaminated zones. This may be due to competition for the same adsorption sites, similar to that noted by Müller et al. (2002). Yet changes to element availability in the pore waters in different micro environments within the sediment may also play an important role.

In our experiment Cu behaves very similarly to lead and zinc, as predicted by water exchange reaction kinetics (Morse and Luther, 1999). This is not surprising as Cu adsorption on pyrite has been shown to be rapid and at pH over 5 (Wang et al., 1989). Similar to Pb and Zn, the Cu in framboids from the uncontaminated Huon Estuary sediments has a spiky (inclusion-rich) distribution with an overall decrease in Cu towards the rims of the framboid (Figure 5). In the Derwent Estuary sediments Cu in the framboid is less spikey than in that the Huon River framboids but more spikey than the Derwent Pb and Zn.

Gold content in pyrite was found to be subdued in the most metal enriched part of the Derwent core, with the strongest enrichment present below the major metal enrichment. The Au precipitates from pore waters either by adsorbing onto sulfides or other materials (Jean and G Michael, 1985; Maddox et al., 1998; Mycroft et al., 1995; Renders and Seward, 1989; Schoonen et al., 1992; Widler and Seward, 2002; Woods, 1996) or by precipitation due to bacterial mediated precipitation of gold metal (Gwynne, 2013; Hough et al., 2011; Lengke et al., 2006; Reith et al., 2009). Schoonen et al. (1992) showed that pyrite is a very good

scavenger of gold in natural systems. This is achieved by the adsorption of gold on the surface of the growing crystals with incorporation into the structure of the pyrite by subsequent over growth. However, gold is also adsorbed by organic matter through biologic pathways (Zhang et al., 1997). The top of the sediment section in the Derwent core contains a higher amount of organic matter (Gregory et al., 2013) and in this region pyrite framboids tend to also have lower Au content. This suggests that more of the available Au is adsorbed onto organic matter resulting in less gold accumulation in pyrite. Müller et al. (2002) showed that high concentrations of Cu, Pb and Zn prevented the adsorption onto pyrite of Au in pyrite rich mine tailings. It is possible that this process is occurring in the Derwent core, where additional competition for surface adsorption sites from Pb, Zn and Cu in the contaminated zone has resulted in relatively low Au incorporation into pyrite fraction (Figure 6 and Table 1). This results in diffusion of some of the gold to an area where there are less competing metals so the Au can be adsorbed onto the growing iron sulfides and be incorporated into their structure. The gold most likely diffuses as an $Au(OH)Cl^-$ as the system is chloride rich and has a relatively high pH (Krupp and Weiser, 1992). However, as oxygen fugacity measurements were not taken this cannot be stated with certainty and other gold chlorides, gold thiosulfates, sulfites, polythionates and polysulfides may also be present. Another possibility is that bacterial meditated precipitation of gold is enhanced at this depth. Several studies (Gwynne, 2013; Lengke et al., 2006; Reith et al., 2009) have shown that sulfate-reducing bacteria can precipitate nanoparticle gold in conditions where pyrite can be formed. We consider this mechanism to be plausible in our samples as our data show the small inclusions of gold that are expected from this mechanism and the gold nano-particle fixing bacteria (*Cupiavidus metallidures*) has been identified in Australian field sites (Reith et al., 2006). The question that arises is why is there such an increase in gold below the contaminated zone if the mechanism of gold accumulation in pyrite is bacterial mediated precipitation? It is possible that bacteria may not survive well in the overlying sediments and the over competition for adsorptive sites in the overlying high metal sediments allowed gold to diffuse down to gold precipitating bacteria-rich horizons. However specific studies targeting the possible presence of gold precipitating bacteria will need to be under taken to determine the importance of bacteria in the accumulation of gold in pyrite framboids in the Derwent.

Another factor likely to effect the uptake of Au in pyrite framboids is the presence or lack of As. Several studies have shown that coatings of As on the surface of iron sulphides greatly

enhance the adsorption of Au on pyrite and higher As concentrations are often associated with higher Au concentrations (Deditius et al., 2008; Deditius et al., 2009; Deditius et al., 2011; Hough et al., 2011; Mikhlin et al., 2011; Reich et al., 2005; Reich and Becker, 2006). While the presence of As in pyrite has probably aided in the adsorption and accumulation of Au in pyrite in the Derwent samples As is not significantly enriched in the sections where strong Au enrichment is observed so relative As enrichment in pyrite probably did not result in relative enrichment of Au in pyrite.

Inclusions were found to be an important host of the Ag in diagenetic pyrite. This is consistent with several other studies that have found silver to form Ag metal or Ag sulfide micro particles on or in pyrite (Deditius et al., 2011; Mikhlin et al., 2011; Müller et al., 2002; Pooley and Shrestha, 1996). Previous studies have suggested that these form first as films of Ag_2S that can consolidate into round nanoparticles. Over time these sulphides can decompose to Ag metal (Mikhlin et al., 2011). Similarly to gold the silver in pyrite is at a maximum below the major zone of metal contamination (Figure 4). The pK_1 for the $MeOH^{z-1}$ of Ag is 12 (Baes and Mesmer, 1976), which suggests that the pH conditions of the sediments are not as ideal for Ag adsorption on pyrite as for some other elements (notably Cu, Pb and Zn) (Müller et al., 2002). This coupled with far greater amount of competition for binding sites Cu, Pb and Zn higher in the section resulted in relatively low Ag in pyrite in the more metal enriched part of the sediment and high Ag in pyrite below the major metal enrichment. This is similar to explanations given for low Ag adsorption in zones of high Pb, Cu and Zn adsorption for studies of mine tailings (Müller et al., 2002).

The nickel content of pyrite is generally subdued in most of the Derwent pyrite, despite nickel commonly being enriched in pyrite. This is due to the general low levels of Nickel in the system. The amount of Co in pyrite is similarly subdued, though not to the extent of Ni and probably stems from a similar lack of Cobalt available for adsorption (Figure 6). Competition for adsorption sites on the pyrite may also play a role in the low levels of Ni and Co in the metal enriched sections. This would explain why the highest average Ni and Co enrichment is found in pyrite from the 70 to 75 cm section, coincident with the highest Ag in pyrite. This again is consistent with the explanation for lower adsorption of less abundant trace metals on pyrite when there is significant competition for adsorption sites by Müller et al. (2002).

The reason for the high tellurium measured within the Derwent pyrite framboids compared to the Huon framboids, is not immediately clear, particularly as the total amount of Te (whole sediment) are similar. It may be due to complexing between tellurium and other elements (such as gold) in solution, causing the tellurium to be adsorbed onto the pyrite with the other metals or that Te in the Huon is hosted in an insoluble detrital mineral and is not available for incorporation into pyrite.

As there is no data for the amount of mobile Au, Ag and Te available in the sediments at different depths due to analytical difficulties with measuring these elements in the sequential leaches, we cannot be certain of our competition for adsorption site hypothesis for siting of these elements in diagenetic pyrite. Other explanations for the observations may be that the Au, Ag and Te is entirely held within immobile phases such as franklinite or sulphides in the more contaminated zones and held within more soluble phases, such as organic matter immediately below the contaminated zone. We see this explanation as unlikely because the source of the Au, Ag and Te appears to be the smelter waste and for it to diffuse down to enter the pyrite below the contamination it would have to be mobile and thus would be available for incorporation into the pyrite earlier as well. A second possibility is that trace metal incorporation is at least to some degree controlled by biological processes and the organisms that are needed cannot live in the high metal conditions of the higher sections of the core. Though this is an interesting possibility it is well out of our field of expertise and we are unable to test it at this time.

3.6 Conclusions

The use of LA-ICPMS to analyze framboidal pyrite has allowed us to examine the incorporation of trace metals and metalloids in pyrite in heavily contaminated sediments. We found that the overabundance of metal ions present in the most contaminated layers led to some metals (e.g. Pb, Zn) being incorporated into pyrite at higher rates than normally observed. We also observed migration of some less concentrated elements away from the most contaminated sections of the core to less contaminated sections (e.g. Au, Ag and Te) where they were able be incorporated into pyrite, due to a decrease in competition for surface adsorption sites on the pyrite.

The LA-ICPMS technique also allowed us to examine how metals that are difficult to measure using traditional sequential extraction techniques (e.g. Au, Ag and Te). However, further laboratory based enquiries are needed to substantiate some of the inferences we made regarding silver and tellurium.

3.7 Acknowledgements

The authors thank Viola Services and Mark Stalker for donation of time and equipment during the sampling of the Derwent sediments and John Gibson and Kerrie Swadling for use of the hammer corer. Thanks also to Sandrin Feig and Karsten Goemann for their aid in the SEM analyses and aiding in composition of the methods section and to Leonid Danyushevsky and Sarah Gilbert for their expert advice in the use of LA-ICPMS and for aiding in the composition of the methods section. Thanks also to Lee Groat, Jacqueline Halpin and Selina Wu for invaluable comments on early drafts of the manuscript and Kate Bromfield for help with mineral separations. Michael Roach's help with collection of the Huon cores was greatly appreciated. Thank you also to Martin Reich and Zsolt A. Berner whose insightful comments greatly increased the quality of this manuscript.

3.8 References

Algeo, T.J. (2004) Can marine anoxic events draw down the trace element inventory of seawater? Geology, 32(12), 1057-1060.

Anbar, A.D., Duan, Y., Lyons, T.W., Arnold, G.L., Kendall, B., Creaser, R.A., Kaufman, A.J., Gordon, G.W., Scott, C., and Garvin, J. (2007) A whiff of oxygen before the great oxidation event? Science, 317(5846), 1903-1906.

Baes, C. F., and Mesmer, R. E. (1976) The hydrolysis of cations, Wiley New York.

Berner, Z., Pujol, F., Neumann, T., Kramar, U., Stüben, D., Racki, G., and Simon, R. (2006) Contrasting trace element composition of diagenetic and syngenetic pyrites: implications for the depositional environment, *in* Proceedings Geophysical Research Abstracts 2006, 8, 8281.

Berner, Z. A., Puchelt, H., NÖLtner, T., and Kramar, U. T. Z. (2013) Pyrite geochemistry in the Toarcian Posidonia Shale of south-west Germany: Evidence for contrasting trace-element patterns of diagenetic and syngenetic pyrites: Sedimentology, 60(2), 548-573.

Borah, D., and Senapati, K. (2006) Adsorption of Cd(II) from aqueous solution onto pyrite: Fuel, 85(12–13), 1929-1934.

Danyushevsky, L., Robinson, P., Gilbert, S., Norman, M., Large, R., McGoldrick, P., and Shelley, M. (2011) Routine quantitative multi-element analysis of sulphide minerals by laser ablation ICP-MS: Standard development and consideration of matrix effects. Geochemistry: Exploration, Environment, Analysis, 11(1), 51-60.

Deditius, A. P., Utsunomiya, S., Ewing, R. C., and Kesler, S. E. (2009) Nanoscale "liquid" inclusions of As-Fe-S in arsenian pyrite: American Mineralogist, 94(2-3), 391-394.

Deditius, A. P., Utsunomiya, S., Reich, M., Kesler, S. E., Ewing, R. C., Hough, R., and Walshe, J. (2011) Trace metal nanoparticles in pyrite: Ore Geology Reviews, 42(1), 32-46.

Deditius, A. P., Utsunomiya, S., Renock, D., Ewing, R. C., Ramana, C. V., Becker, U., and Kesler, S. E. (2008) A proposed new type of arsenian pyrite: Composition, nanostructure and geological significance: Geochimica et Cosmochimica Acta, 72(12), 2919-2933.

Dellwig, O., Böttcher, M. E., Lipinski, M., and Brumsack, H.-J. (2002) Trace metals in Holocene coastal peats and their relation to pyrite formation (NW Germany): Chemical Geology, 182(2–4), 423-442.

Donald, R., and Southam, G. (1999) Low temperature anaerobic bacterial diagenesis of ferrous monosulfide to pyrite. Geochimica et Cosmochimica Acta, 63(13), 2019-2023.

Erickson, B. E., and Helz, G. R. (2000) Molybdenum (VI) speciation in sulfidic waters:: Stability and lability of thiomolybdates: Geochimica et Cosmochimica Acta, 64(7), 1149-1158.

Gregory, D., Meffre, S., and Large, R. (2013) Mineralogy of metal contaminated estuarine sediments, Derwent estuary, Hobart, Australia: implications for metal mobility: Australian Journal of Earth Sciences, 60, p. 589-603.

Guillong M, Meier D, Allan M, Heinrich C, Yardley (2008) 'SILLS: a Matlab-based program for the reduction of laser ablation ICP-MS data of homogeneous materials and inclusions', in: 'Laser Ablation ICP-MS in the earth sciences: Current practices and outstanding issues', Paul Sylvester (Ed.), Mineral Association of Canada Short Course Series 40, Vancouver, Canada

Gwynne, P. (2013) Microbiology: There's gold in them there bugs: Nature, 495, S12-S13.

Helz, G., Miller, C., Charnock, J., Mosselmans, J., Pattrick, R., Garner, C., and Vaughan, D. (1996) Mechanism of molybdenum removal from the sea and its concentration in black shales: EXAFS evidence: Geochimica et Cosmochimica Acta, 60, 3631-3642.

Hochella, M.F., Kasama, T., Putnis, A., Putnis, C.V., and Moore, J.N. (2005) Environmentally important, poorly crystalline Fe/Mn hydrous oxides: Ferrihydrite and a possibly new vernadite-like mineral from the Clark Fork River Superfund Complex. American Mineralogist, 90, 718-724.

Hough, R. M., Noble, R. R. P., and Reich, M. (2011) Natural gold nanoparticles: Ore Geology Reviews, 42, 55-61.

Huerta-Diaz, M.A., and Morse, J.W. (1990) A quantitative method for determination of trace metal concentrations in sedimentary pyrite. Marine Chemistry, 29, 119-144.

Huerta-Diaz, M.A., and Morse, J.W. (1992) Pyritization of trace metals in anoxic marine sediments. Geochimica et Cosmochimica Acta, 56, 2681-2702.

Jean, G.E., and G Michael, B. (1985) An XPS and SEM study of gold deposition at low temperatures on sulphide mineral surfaces: Concentration of gold by adsorption/reduction. Geochimica et Cosmochimica Acta, 49, 979-987.

Jean, G. E., and Bancroft, G. M. (1986) Heavy metal adsorption by sulphide mineral surfaces: Geochimica et Cosmochimica Acta, 50, 1455-1463.

Jones, B., Chenhall, B., Debretsion, F., and Hutton, A. (2003) Geochemical comparisons between estuaries with non-industrialised and industrialised catchments: the Huon and Derwent River estuaries, Tasmania. Australian Journal of Earth Sciences, 50, 653-667.

Konhauser, K.O. (1998) Diversity of bacterial iron mineralization. Earth-Science Reviews, 43, 91-121.

Large, R.R., Danyushevsky, L., Hollit, C., Maslennikov, V., Meffre, S., Gilbert, S., Bull, S., Scott, R., Emsbo, P., Thomas, H., Singh, B., and Foster, J. (2009) Gold and Trace Element Zonation in Pyrite Using a Laser Imaging Technique: Implications for the Timing of Gold in Orogenic and Carlin-Style Sediment-Hosted Deposits. Economic Geology, 104, 635-668.

Large, R.R., Maslennikov, V.V., Robert, F., Danyushevsky, L.V., and Chang, Z.S. (2007) Multistage sedimentary and metamorphic origin of pyrite and gold in the giant Sukhoi Log deposit, Lena gold province, Russia. Economic Geology, 102, 1233-1267.

Lengke, M.F., Fleet, M.E., and Southam, G. (2006) Morphology of gold nanoparticles synthesized by filamentous cyanobacteria from gold (I)-thiosulfate and gold (III)-chloride complexes. Langmuir, 22, 2780-2787.

Lennie, A.R., England, K.E., and Vaughan, D.J. (1995) Transformation of synthetic mackinawite to hexagonal pyrrhotite: A kinetic study. American Mineralogist, 80, 960-967.

Longerich, H.P., Jackson, S.E., and Günther, D. (1996) Inter-laboratory note. Laser ablation inductively coupled plasma mass spectrometric transient signal data acquisition and analyte concentration calculation. Journal of Analytical Atomic Spectrometry, 11, 899-904.

Lord, C.J.I. (1982) A Selective and Precise Method for Pyrite Determination in Sedimentary Materials: Research-Method Paper. Journal of Sedimentary Research, 52.

Lowers, H.A., Breit, G.N., Foster, A.L., Whitney, J., Yount, J., Uddin, M.N., and Muneem, A.A. (2007) Arsenic incorporation into authigenic pyrite, Bengal Basin sediment, Bangladesh. Geochimica et Cosmochimica Acta, 71, 2699-2717.

Maddox, L.M., Bancroft, G.M., Scaini, M., and Lorimer, J. (1998) Invisible gold; comparison of Au deposition on pyrite and arsenopyrite. American Mineralogist, 83, 1240-1245.

Martin, J., Nirel, P., and Thomas, A. (1987) Sequential extraction techniques: promises and problems. Marine Chemistry, 22, 313-341.

Mikhlin, Y., Romanchenko, A., Likhatski, M., Karacharov, A., Erenburg, S., and Trubina, S., (2011) Understanding the initial stages of precious metals precipitation: Nanoscale metallic and sulfidic species of gold and silver on pyrite surfaces: Ore Geology Reviews, 42, 47-54.

Milne, T. (2012) 2010/2011 report for Nyrstar Hobart pty. ltd., Nyrstar Hobart Smelter – Lutana, TAS, accessed 10 April, 2013, <http://www.npi.gov.au/npidata/action/load/emission-by-individual-facility-result/criteria/state/TAS/year/2011/jurisdiction-facility/TAS%20120.

Morse, J., and Luther, G. (1999) Chemical influences on trace metal-sulfide interactions in anoxic sediments. Geochimica et Cosmochimica Acta, 63, 3373-3378.

Morse, J.W., and Arakaki, T. (1993) Adsorption and coprecipitation of divalent metals with mackinawite (FeS). Geochimica et Cosmochimica Acta, 57, 3635-3640.

Müller, B., Axelsson, M. D., and Öhlander, B. (2002) Adsorption of trace elements on pyrite surfaces in sulfidic mine tailings from Kristineberg (Sweden) a few years after remediation: Science of the Total Environment, 298, 1-16.

Mycroft, J., Bancroft, G., McIntyre, N., and Lorimer, J. (1995) Spontaneous deposition of gold on pyrite from solutions containing Au (III) and Au (I) chlorides. Part I: A surface study. Geochimica et Cosmochimica Acta, 59, 3351-3365.

Neumann, T., Rausch, N., Leipe, T., Dellwig, O., Berner, Z., and Böttcher, M. E. (2005) Intense pyrite formation under low-sulfate conditions in the Achterwasser lagoon, SW Baltic Sea: Geochimica et Cosmochimica Acta, 69, 3619-3630.

Neumann, T., Scholz, F., Kramar, U., Ostermaier, M., Rausch, N., and Berner, Z. (2013) Arsenic in framboidal pyrite from recent sediments of a shallow water lagoon of the Baltic Sea: Sedimentology, 60, 1389-1404.

Pikaray, S., Banerjee, S., and Mukherji, S., 2005, Sorption of arsenic onto Vindhyan shales: Role of pyrite and organic carbon: Current Science, v. 88, no. 10, p. 1580-1585.

Pooley, F., and Shrestha, G. (1996) The distribution and influence of silver in pyrite bacterial leaching systems: Minerals engineering, 9, 825-836.

Qian, G., Brugger, J., Testemale, D., Skinner, W., and Pring, A. (2013) Formation of As(II)-pyrite during experimental replacement of magnetite under hydrothermal conditions: Geochimica et Cosmochimica Acta, 100, 1-10.

Reich, M., and Becker, U. (2006) First-principles calculations of the thermodynamic mixing properties of arsenic incorporation into pyrite and marcasite: Chemical Geology, 225, 278-290.

Reich, M., Kesler, S. E., Utsunomiya, S., Palenik, C. S., Chryssoulis, S. L., and Ewing, R. C. (2005) Solubility of gold in arsenian pyrite: Geochimica et Cosmochimica Acta, 69, 2781-2796.

Reith, F., Etschmann, B., Grosse, C., Moors, H., Benotmane, M. A., Monsieurs, P., Grass, G., Doonan, C., Vogt, S., and Lai, B. (2009) Mechanisms of gold biomineralization in the bacterium Cupriavidus metallidurans: Proceedings of the National Academy of Sciences, 106, 17757-17762.

Reith, F., Rogers, S. L., McPhail, D., and Webb, D. (2006) Biomineralization of gold: biofilms on bacterioform gold: Science, 313, 233-236.

Renders, P., and Seward, T. (1989) The adsorption of thio gold (I) complexes by amorphous As_2S_3 and Sb_2S_3 at 25 and 90° C. Geochimica et Cosmochimica Acta, 53, 255-267.

Renock, D., Gallegos, T., Utsunomiya, S., Hayes, K., Ewing, R. C., and Becker, U. (2009) Chemical and structural characterization of As immobilization by nanoparticles of mackinawite (FeS_m): Chemical Geology, 268, 116-125.

Rickard, D., and Luther, G.W. (1997) Kinetics of pyrite formation by the H2S oxidation of iron (II) monosulfide in aqueous solutions between 25 and 125° C: The mechanism. Geochimica et Cosmochimica Acta, 61, 135-147.

Rickard, D., Grimes, S., Butler, I., Oldroyd, A., and Davies, K. L. (2007) Botanical constraints on pyrite formation: Chemical Geology, 236, 228-246.

Rickard, D., and Luther, G. W. (2007) Chemistry of Iron Sulfides: Chemical Reviews, 107, 514-562.

Rosso, K. M., and Vaughan, D. J. (2006) Reactivity of sulfide mineral surfaces: Reviews in Mineralogy and Geochemistry, 61, 557-607.

Schoonen, M., and Barnes, H. (1991) Reactions forming pyrite and marcasite from solution: II. Via FeS precursors below 100 C. Geochimica et Cosmochimica Acta, 55, 1505-1514.

Schoonen, M.A. (2004) Mechanisms of sedimentary pyrite formation. Special Papers-Geological Society of Amaerica, 117-134.

Schoonen, M.A., Fisher, N.S., and Wente, M. (1992) Gold sorption onto pyrite and goethite: A radiotracer study. Geochimica et cosmochimica Acta, 56, 1801-1814.

Thomas, H.V., Large, R.R., Bull, S.W., Maslennikov, V., Berry, R.F., Fraser, R., Froud, S., and Moye, R. (2011) Pyrite and pyrrhotite textures and composition in sediments, laminated quartz veins, and reefs at Bendigo gold mine, Australia: insights for ore genesis. Economic Geology, 106, 1-31.

Tribovillard, N., Algeo, T.J., Lyons, T., and Riboulleau, A. (2006) Trace metals as paleoredox and paleoproductivity proxies: An update. Chemical Geology, 232, 12-32.

Wang, X., Forssberg, K., and Bolin, N. (1989) Adsorption of copper (II) by pyrite in acidic to neutral pH media: Scandinavian Journal of Metallurgy, 18, 262-270.

Whitehead, J., Coughanowr, C., Agius, J., Chrispijn, J., Taylor, U., and Wells, F. (2010) State of the Derwent Estuary 2009: a review of pollution sources, loads and environmental quality data from 2003 – 2009. Derwent Estuary Program, DPIPWE, Tasmania.

Widler, A., and Seward, T. (2002) The adsorption of gold (I) hydrosulphide complexes by iron sulphide surfaces. Geochimica et Cosmochimica Acta, 66, 383-402.

Wolthers, M., Van der Gaast, S.J., and Rickard, D. (2003) The structure of disordered mackinawite. American Mineralogist, 88, 2007-2015.

Woods, R. (1996) Chemisorption of Thiols on Metals and Metal Sulfide. Modern Aspects of Electrochemistry, 29, 401-453.

Xu, N., Christodoulatos, C., and Braida, W. (2006) Adsorption of molybdate and tetrathiomolybdate onto pyrite and goethite: Effect of pH and competitive anions: Chemosphere, 62, 1726-1735.

Xia, F., Brugger, J., Chen, G., Ngothai, Y., O'Neill, B., Putnis, A., and Pring, A. (2009) Mechanism and kinetics of pseudomorphic mineral replacement reactions: a case study of the replacement of pentlandite by violarite. Geochimica et Cosmochimica Acta, 73, 1945-1969.

Zeien, H., and Brümmer, G. W., 1989, (in German) Chemische Extraktion zur Bestimmung von Schwermetallbindungsformen in Böden: Mitteilungen der Deutschen Bodenkundlichen Gesellschaft, 59, 505-510.

Zhang, J., Lu, J., Zhai, J., and Yang, F., 1997, Simulating experiments on enrichment of gold by bacteria and their geochemical significance: Chinese Journal of Geochemistry, 16, 369-373.

Chapter 4

Trace Element Content of Unmineralized Sedimentary Pyrite

4.1 Abstract

Analysis of over 1400 sedimentary (diagenetic and syngenetic) pyrites by LA-ICPMS, from 45 carbonaceous shale units ranging in age from Paleoarchean to present day shows a considerable range in trace element composition. Arsenic, Ni, Pb, Cu and Co are commonly the most abundant trace elements, with medians ranging from 100 to 1000 ppm. These are followed by Mo, Sb, Zn and Se with medians ranging from 10 to 100 ppm and finally Ag, Bi, Te, Cd and Au with medians from 0.01 to 10 ppm. Our dataset reveals three main groups that have the trace elements incorporated into the pyrite in different ways. Group 1 (As, Ni, Co, Sb, Se and Mo) is contained uniformly throughout the pyrite and may be held within its crystal structure or as a uniform distribution of nano-inclusions. Group 2 (Ag, Au, Te and Cu) are uniform at low concentrations and may be incorporated into the structure of the pyrite, but are highly variable at high concentrations and may occur as micro-inclusions. While group 3 (Pb, Zn, Cd and Bi) are usually highly variable and are held within micro-inclusions.

We have assessed two factors that may control the trace element composition of sedimentary pyrite: texture and age. Variations in pyrite texture do not show consistent compositional patterns, except for samples metamorphosed above lower greenschist facies, where the pyrite adopts a metamorphic texture and loses certain trace elements. Age has a significant influence on the concentration of trace elements in sedimentary pyrite. Many trace elements associated with mafic extrusions (Ni, Co) are more enriched in older sedimentary pyrite when there was a greater amount of mafic volcanic activity. Similarly some trace elements tend be more enriched in more recent sediments due to increasing levels of atmospheric oxidation.

4.2 Introduction

The trace element contents of black shale, especially Mo, V and U, have been used to determine the chemical conditions of ancient oceans (Algeo, 2004; Algeo and Lyons, 2006; Algeo and Maynard, 2004; Anbar et al., 2007). Sedimentary pyrite has also been recognized as a sink for several trace elements in organic carbon-rich shale (Huerta-Diaz and Morse,

1992; Tribovillard et al., 2006). In a recent study (Large et al., in prep.), the trace element content of sedimentary pyrite has been used to determine temporal variations in trace elements of ancient oceans. In this study data of the trace element composition of sedimentary pyrite from a subset of 45 black shale units investigated by Large et al. (in prep.) ranging in age from Archean to recent are presented and some factors that may affect the uptake of trace elements in sedimentary pyrite are discussed.

It is accepted that trace element contents of fine clastic sedimentary rocks can be used to determine the paleoredox conditions of seawater (Algeo, 2004; Algeo and Maynard, 2004; Anbar et al., 2007; Tribovillard et al., 2006). This is usually done by normalizing the trace element data to aluminum to compensate for differences in rates of sedimentation (Lyons et al., 2003). The sediment rate-corrected trace element compositions are then compared to average sedimentary rock compositions (McLennan, 2001; Taylor and McLennan, 1985; Wedepohl, 1991). However, there is a potential problem with this method when secondary processes have affected the basin under investigation. These processes include late stage diagenesis, metamorphism and hydrothermal activity that can greatly increase or decrease the amount of trace elements present in the black shale. We propose an alternative method to avoid these problems by using the Laser Ablation-Inductively-Coupled Plasma Mass Spectrometry (LA-ICPMS) method to analyze pyrite grains that have been characterized as syngenetic or diagenetic and shown not to be affected by later overprint or recrystallization.

The degree of trace element pyritization has been used to determine the chemical conditions of different depositional environments previously by Huerta-Diaz and Morse (1992). Their technique involved using partial digestions to dissolve pyrite, followed by analysis of the resultant solution to determine the concentration of trace elements in the pyrite. Problems with this technique can arise when applied to ancient rocks because the reactants are not selective for different generations of pyrite. Consequently the resultant analyses give a homogenous average of all pyrite in the sample instead of the trace element signature for only the syngenetic or early diagenetic component that relates to the depositional environment. More recently Berner et al. (2013) has mechanically separated and analysed pyrite from the lower Toarcian Posidonia shale in order to determine relations between trace element content of pyrite and depositional conditions. While this worked well for the unaltered Posidonia shales examined by Berner et al. (2013) it was noted that it is difficult to separate different

textures of pyrite found in the shale. This can be a particular problem in areas of moderate to high metamorphic grade, where post-depositional pyrite related to metamorphism or hydrothermal activity is present. This potential problem was demonstrated by Large et al. (2007) in black shale from Sukhoi Log, Russia, where as many as six different generations of pyrite were identified, four of which were metamorphic and/or hydrothermal with their own distinctive geochemical signature.

Partial digestions have another problem in that the reagents may lack mineral specificity (Martin et al., 1987). The reagents that are used in the sequential leach step to release trace elements from pyrite can also release metals from several other minerals; this can especially be a problem if other sulphides are present (e.g. chalcopyrite, sphalerite, galena) which can lead to erroneous values for several metals. In recent studies of the accumulation of trace elements in pyrite in contaminated estuaries a combination of sequential extractions (Gregory et al., 2013) and LA-ICPMS of selected, diagentic pyrite (Gregory, in press) have been used to determine factors that control trace element content of pyrite from contaminated systems. Similarly, in this study LA-ICPMS is used to avoid the problem of selectivity by analyzing an individual pyrite generation which we have determined to be of sedimentary origin based on textures and relationship to the local sedimentary structures (i.e. soft sediment deformation). One useful observation is that cores of sedimentary pyrite can be preserved in clusters of metamorphic or hydrothermally derived pyrite (Large et al., 2011; Large et al., 2009; Large et al., 2007; Thomas et al., 2011). This allows analyses to be conducted on shale that has experienced metamorphism up to middle greenschist facies and/or has been overprinted by hydrothermal processes. This will greatly increase the number of shale formations that can be investigated because traditional sequential extraction techniques cannot distinguish between sedimentary or hydrothermal/metamorphic pyrites. Also these processes can alter the chemical composition of the host shale making analyses of the matrix minerals of dubious value.

Similarly this *in situ* technique coupled with the narrow (10-40 µm diameter) laser beam allows us to avoid analyzing other sulfides that would result in erroneous trace element values. Another benefit of the LA-ICPMS for the analyses of pyrite is that it can analyze a larger suite of elements than traditional sequential extractions. Elements with low concentration are difficult with sequential extractions due to low amounts contained in the

pyrite, adsorption effects and dilution of the total amount of the element by the solvents. These problems are not present with LA-ICPMS analyses and as such we can measure contents of Au, Ag, Te and Bi with high accuracy and precision to as low as 0.007 ppm. Finally, the use of LA-ICPMS has allowed us to examine not only the trace element content of sedimentary pyrite, but also how the trace elements are held within the pyrite, i.e. whether they are in solid solution or as nano-inclusions within the pyrite or whether they occur as inclusions. This is done by carefully examining the time resolved LA-ICPMS output graphs for the various analyses. Consistent elemental distribution commonly indicates the trace element is contained within the crystal lattice or as nano-inclusions while a highly variable trace element content indicates that the trace element is held within inclusions in the pyrite (Large et al., 2007; Thomas et al., 2011).

In this paper data from sedimentary pyrite from several different sedimentary basins throughout geological time is presented in order to establish a dataset that can be used to determine the range and average trace element chemistry of sedimentary pyrite hosted in black shale. To achieve this pyrite from a number of black shale basins that are well represented in the literature, and also some from less well studied basins, in order to create a comprehensive database incorporating different textures, geological environments/tectonic settings and eras have been analyzed. It was found that different geological eras and epochs have significantly different trace element signatures that can be explained by the different chemical conditions found in the oceans at their times of deposition. Also depositional setting was found to be an important factor in the trace element composition of pyrite with higher metal source areas having systematically more trace element enrichment than relatively metal poor areas, however some metals behaved differently based on their individual chemical behaviors. Finally, while no definitive compositional changes were determined by variation in pyrite texture across the data set, when different textures are found in the same sample the texture interpreted to be formed earlier tends to have higher trace element composition. The one exception to this is small euhedral pyrite crystals which tend to have low trace element compositions.

4.2.1 Sedimentary pyrite formation and incorporated trace elements

Sedimentary pyrite forms within the water column or, more commonly, within sediment pore waters. Trace elements dissolved in the water adsorb on to the surface of the growing iron sulfide and are subsequently incorporated into the structure of the pyrite. Over time trace elements are also released from organic matter and iron (hydr)oxides into the pore water, which can also be incorporated into pyrite (Tribovillard et al., 2006). The exact method by which this occurs is still a matter of debate. Studies by Morse and Arakaki (1993) have shown that the pyrite precursor mineral mackinawite ($FeS_{0.9}$) can adsorb and incorporate several different trace elements (Cd, Co, Cr, Cu, Ni and Zn). The accumulation of these trace elements into the mackinawite structure is controlled by the relative solubility of the metal sulfides and mackinawite. Metal sulphides with higher solubility than mackinawite have similar surface affinities to mackinawite and metal sulphides with lower solubility have higher surface affinities that decrease with increasing metal solubility (Morse and Arakaki, 1993). This seems to explain the incorporation of trace elements into pyrite, however the conversion pathway proposed by Rickard and Luther (1997) of mackinawite to pyrite may involve the dissolution of mackinawite prior to precipitation of pyrite, which would result in the release of the trace elements.

It has been shown that trace elements tend to be incorporated into pyrite during diagenesis of anoxic sediments by one (or more), of four different ways: precipitation; co-precipitation; chemical or physical adsorption and redox reactions between dissolved species and the pyrite surface or the surface of pyrite precursors (Berner et al., 2013; Dellwig et al., 2002). Berner et al. (2013) also showed that different elements tend to be held in pyrite can be grouped as: heavy metals (Cu, Ni, Co, Pb, Bi and Tl); oxyanionic elements (As, Mo and Sb); elements that occur in sub-microscopic sphalerite inclusions (Zn and Cd) and elements that occur as inclusions of slicates or organic matter (Ga and V).

The incorporation of As into pyrite has been particularly well studied. It can be incorporated into pyrite in three different ways: substitution for S(-II) (Reich and Becker, 2006), substitution for Fe(II) (Deditius et al., 2008; Qian et al., 2013) and as nano-scale inclusions of amorphous As-Fe-S that are trapped within the pyrite (Deditius et al., 2008). The presence of As in pyrite is important for the incorporation of other trace elements as well as it enhance their uptake in pyrite (Deditius et al., 2008). The speciation of the As is also important as

favors the uptake of different elements, with As substituted for S increasing the uptake of elements similar to Fe(II) (i.e. Co, Ni, Cu, Zn) and As substituted for Fe enhancing the uptake of larger cations (i.e. Au(I), Ag (I) and Pb (II)) (Deditius et al., 2008). This relationship between the As content of pyrite and the content of other trace metals has been especially well documented for Au which appears to be strongly dependent on the amount of As (Reich et al., 2005).

Though the mechanism of enrichment is still a matter of debate, observations by Morse and Luther (1999) suggest that metals are taken up by sedimentary pyrite as follows: As=Mo > Cu = > Co > Ni >> Mn > Zn > Cr = Pb > Cd. This scheme has since been modified by Gregory et al. (in prep) to include gold and silver as follows: As=Mo > Cu > Co > Ni >> Mn = Au > Ag > Zn > Cr = Pb > Cd.

4.3 Methods

4.3.1 Samples

A total of 114 samples representing 45 pyritic carbonaceous black shale units from a variety of different geological formations, geologic ages and textures were taken to obtain an adequate representation of average trace element abundances of sedimentary pyrite. Formations from which the samples were taken and brief sample descriptions are presented in Appendix 4. Pyrite and matrix was analysed *in situ* via polished laser mounts.

4.3.2 Laser Ablation ICPMS

The trace elements contained within sedimentary pyrite were analyzed at CODES, University of Tasmania using a laser microprobe. Two configurations were used; a 213 nm solid-state laser microprobe (UP213, NewWave Research) that is coupled to an Agilent 7500a quadruple mass-spectrometer, and a 193 nm solid-state laser microprobe (UP193ss, NewWave Research) coupled to Agilent 7700s quadruple mass-spectrometer. The laser microprobes are furnished with ablation cells that have been custom made to ensure constant geometry.

Depending on the size of the pyrite grains analysed the beam size varied from 10 to 40 microns. Ablation was carried out in an atmosphere of pure He that is introduced into the ablation cell at a rate of 0.8 l/min immediately past the ablation point. To improve the efficiency of aerosol transport the He carrier gas is mixed with Ar (0.85 l/min). Ablation was conducted with a laser pulse rate of 5 Hz using beam fluences at the sample of approximately 3.5 J/cm^2 (UP213) and approximately 2 J/cm^2 (UP193ss). Both ICP-MS instruments were adjusted to ensure maximum sensitivity on isotopes between 80 and 240 amu. The production of doubly charged species and production of molecular oxide species were maintained at levels below 0.2%. Each analysis consisted of a 30 s laser off period to measure background and a 60 s laser on period for the analysis.

The reduction of the data was conducted based on the methods proposed by Longerich et al. (1996). Details regarding the selection of the different integration intervals are given in Appendix 5. No correction was applied for the effects of low levels of molecular oxide and doubly charged ion production as they were kept to levels below 0.2%. Also no correction was made for interfering species that were introduced into the analyte signal. Variable amounts of matrix material were ablated with the pyrite due to the porosity of some of the syngenetic and sedimentary pyrite analyzed. To correct for the presence of matrix in some of the analyses all samples were analyzed for all major elements to determine how much matrix was present in each analysis. Matrix near the pyrite was also analyzed to determine the composition of the matrix. With the composition of the matrix known, a standard mass balance approach was used to determine the composition of the pyrite. The same three calibration standards were used for all the analyses: STDGL2b2 (Danyushevsky et al., 2011) for chalcophile and siderophile elements; GSD-1G (Guillong et al., 2005) and for lithophile elements; and pure pyrite for the quantification of sulfur.

4.3.3 Screening method to ensure only syngenetic and diagenetic pyrite was included

The samples and subsequent analyses presented in this study underwent a rigorous screening process by the analyst (analyst for each sample listed in Appendix 6) to ensure only pyrite of syngenetic or diagenetic origin was considered. Detailed microscope examination coupled with nitric acid etching was performed on each pyrite prior to LA-ICPMS analyse. Later

forming varieties of pyrite were only analyzed if the pyrites appeared to be of sedimentary origin (i.e. crystals are aligned with bedding; conform to soft sediment deformation structures etc.). The next phase of the screening process was completed by the analyst during data reduction where each time resolved LA-ICPMS output graph was examined to avoid large inclusions of different minerals that would give extraneous results. After data reduction the amount of matrix was estimated using contents of major elements and comparing them to analyses of the matrix material, samples with greater than 50% matrix were removed from the dataset. The dataset was then examined for metal contents too high to represent the chemistry of pyrite (these represent areas where other minerals were inadvertently ablated with the pyrite) and were removed from the dataset. The final step in the data screening process was to determine different geochemical ratios and ensure they fit within the parameters defined for sedimentary pyrite, for examples Co/Ni < 2 and Ag > Au (Bajwah et al., 1987; Thomas et al., 2011). Samples that only varied from these parameters by a small degree and/or only deviated by the one of the parameters but were well within the sedimentary domain for other parameters were left in the data set.

4.3.4 Justification for geochemical screening of sedimentary pyrite

Co/Ni ratios have long been used to determine the origin of the pyrite (hydrothermal, syngenetic or diagenetic) (Bajwah et al., 1987; Loftus-Hills and Solomon, 1967). Work compiled by Bajwah et al. (1987) (including Botinelly et al., 1985; Campbell and Ethier, 1984; Franklin et al., 1981; Gehrisch et al., 1975; Green et al., 1981; Hawley and Nichol, 1961; Large, 1977; Loftus-Hills and Solomon, 1967; So, 1978; Thole, 1976) show that the majority of pyrite formed from hydrothermal fluids have Co/Ni >2, with only submarine exhalative and magmatic deposits having some pyrite with lower Co/Ni ratios. Less than 3% of our data has Co/Ni >2 and less than 11% has a Co/Ni >1 ratio. Where the Co/Ni ratio exceeds 2 it may reflect the presence of hydrothermal fluids unidentified during sampling, or minor recrystallization that has formed small CoS_x inclusions that have not been identified during data reduction. We can see in the plot of Co vs Ni (Fig. 4) that the data is spread out along and below the 2:1 Co:Ni line. This suggests that the amount of Co accommodated in the pyrite lattice is dependent on the amount of Ni at temperatures encountered during

diagenesis of the ocean floor sediment, with no more than twice as much Co than Ni able to be accommodated in the crystal lattice of pyrite.

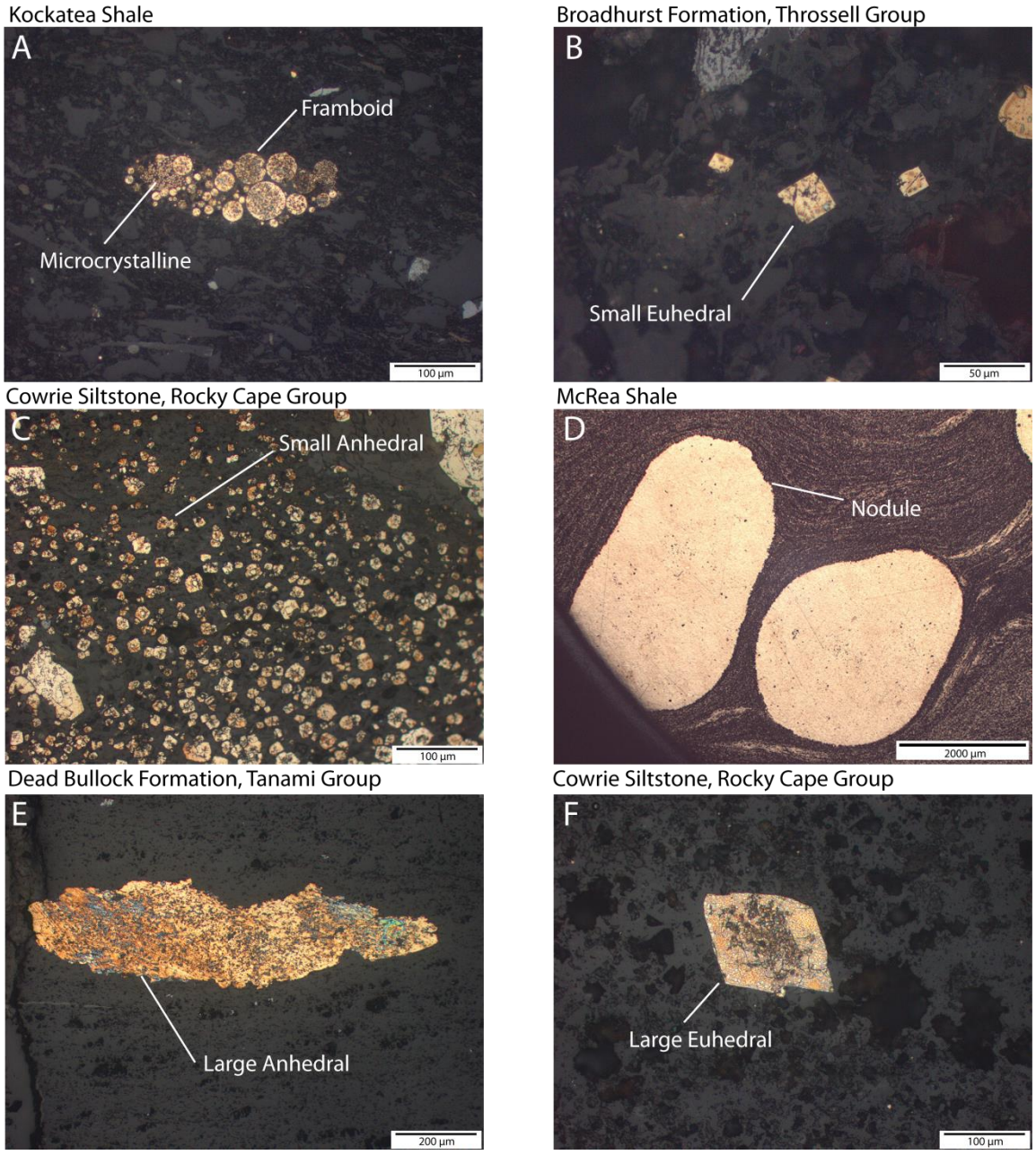

Figure 4.1: Pyrite textures from the samples analyzed in the study. A is microcrystalline and framboidal pyrite from the Kockatea Shale. B is small euhedral pyrite from the Broadhurst Formation. C is small anhedral pyrite from the Cowrie Siltstone. D is nodular pyrite from the McRea shale. E is large anhedral pyrite from the Dead Bullock Formation. F is large euhedral pyrite over growing an earlier pyrite generation from the Rocky Cape Group. All samples except for D have been etched for 30-60 s with nitric acid.

4.4 Results

4.4.1 Textural variation of pyrite and effect of metamorphism

In our samples we have identified seven different major textures of sedimentary pyrite: microcrystalline (<8 µm; Fig. 1a), small anhedral (<15 µm; Fig. 1b), small euhedral (<15 µm; Fig. 1c), framboidal (Fig. 1b, f), nodular (Fig. 1d), large anhedral (>15 µm; Fig. 1f) and large euhedral (>15 µm; Fig. 1e). The microcrystalline, framboidal, small anhedral and small euhedral crystals are interpreted to have formed early during diagenesis, or in the case of framboidal pyrite, possibly within the water column (Large et al., 2007; Raiswell and Plant, 1980; Wilkin et al., 1996). The nodular, large anhedral and large euhedral pyrite forms are interpreted to have formed at greater depths in the unconsolidated sediments where the pore waters are not as supersaturated with respect to pyrite and thus nucleation rate is not as rapid (Butler and Rickard, 2000). The formation of these coarser textures may have involved the recrystallization and migration of iron and sulfur to form the larger pyrite forms. In our discussion we group all forms of pyrite nodule and concretion together as pyrite nodules in order to keep the number of different classifications of texture to a minimum. In future studies we will investigate the changes with the different concretion and nodule classifications used by Selles-Martinez (1996) when more data/analyses are available.

4.4.2 Distribution of trace elements within sedimentary pyrite

Trace elements can be hosted in two ways in sedimentary pyrite, either as inclusions within the pyrite or within the pyrite lattice itself (Large et al., 2009; Rickard, 2012; Thomas et al., 2011). By inspecting the time resolved LA-ICPMS output graphs we can determine which elements are contained within micro inclusions and which are most likely to be within the pyrite crystal lattice or as nano-inclusions. Figure 2 shows a number of time resolved LA-ICPMS output graphs. Count traces that are relatively level or flat (e.g., As in Fig. 2b and 2h and Co and Ni in Fig. 2e and 2g) indicates that the element is contained within the structure of the pyrite, or as very evenly distributed nano-inclusions (Large et al., 2009; Large et al., 2007; Thomas et al., 2011). Zoned pyrites have trace element counts that occur as a series of

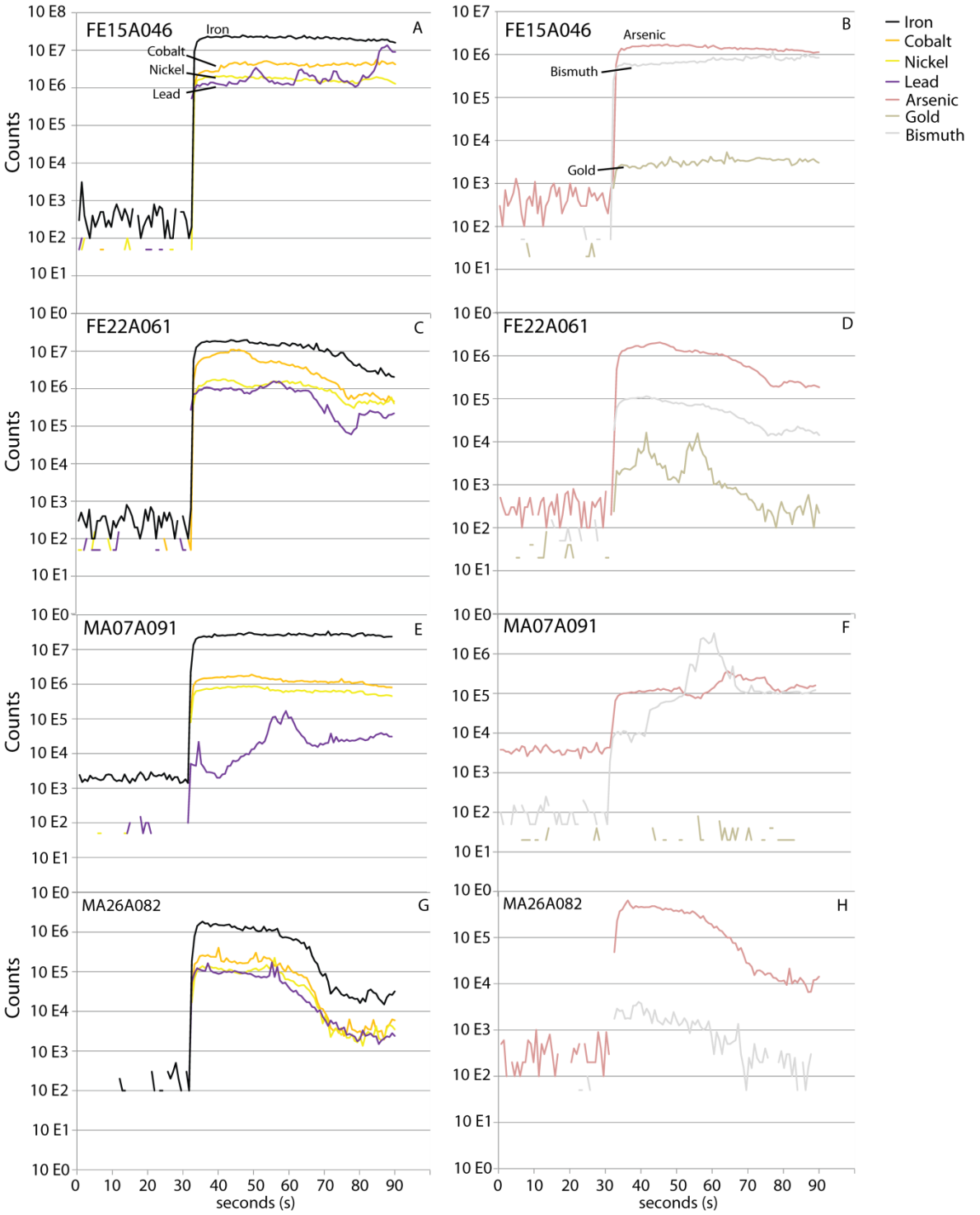

Figure 4.2: Time resolved LA-ICPMS output graphs showing individual analyses for four samples. A, C, E and G show Fe, Co, Ni, Pb, Cu, Mn, Mo and Cd while B, D, F and H show for the respective As, Se, Ag, Sb, Te, Au and Bi contents. A, D, E and F show examples where inclusions that have been ablated through and resulted in peaks of different elements. B, C, G and H show examples of when the elements contain little to no inclusions and the traces of all the elements are relatively flat.

plateaus, being either higher or lower depending on whether there is more or less of the element in the respective zone (e.g. Co and Mn in Fig. 2c). Larger, unevenly distributed inclusions exhibit peaks in the element traces in the time resolved LA-ICPMS output graphs, which is evident for Pb in Fig. 2a and Fig. 2e, Au in Fig. 2d and Bi in Fig. 2f. These patterns indicate primary incorporation of other minerals during pyrite growth and/or recrystallization of the pyrite during metamorphic partitioning of trace elements into their own sulphides phases (Thomas et al., 2011). Care must be taken when interpreting anomalously high trace element contents that may be due to the laser sampling large inclusions of other sulphides.

4.4.3 Content of trace elements in sedimentary pyrite

The common trace element content of sedimentary pyrite can be described as follows based on our data of 1446 analyses: As ≥ Ni > Pb ≥ Cu ≥ Co ≥ Mn > Sb ≥ Zn ≥ Se ≥ Mo > Ag ≥ Bi > Te ≥ Cd > Au (Figure 3). Combined results of the laser analyses are presented in Appendix 6. This differs in several ways from the order proposed by Morse and Luther (1999). The reason for this is their studies dealt with modern environments while ours cover much of geologic time and reflect changes in ocean chemistry, effects of later diagenesis and differences in depositional setting.

Median values of the trace elements in sedimentary pyrite determined from this study are presented in table 4.1. Included here are medians of the entire dataset and sub-sets based on texture, age of deposition and depositional facies. While some of these distinctions are somewhat subjective (difference between large and small anhedral for example), the groupings show interesting results and the use of the median value minimizes the effects of possible ambiguities between the distinctions within different groups.

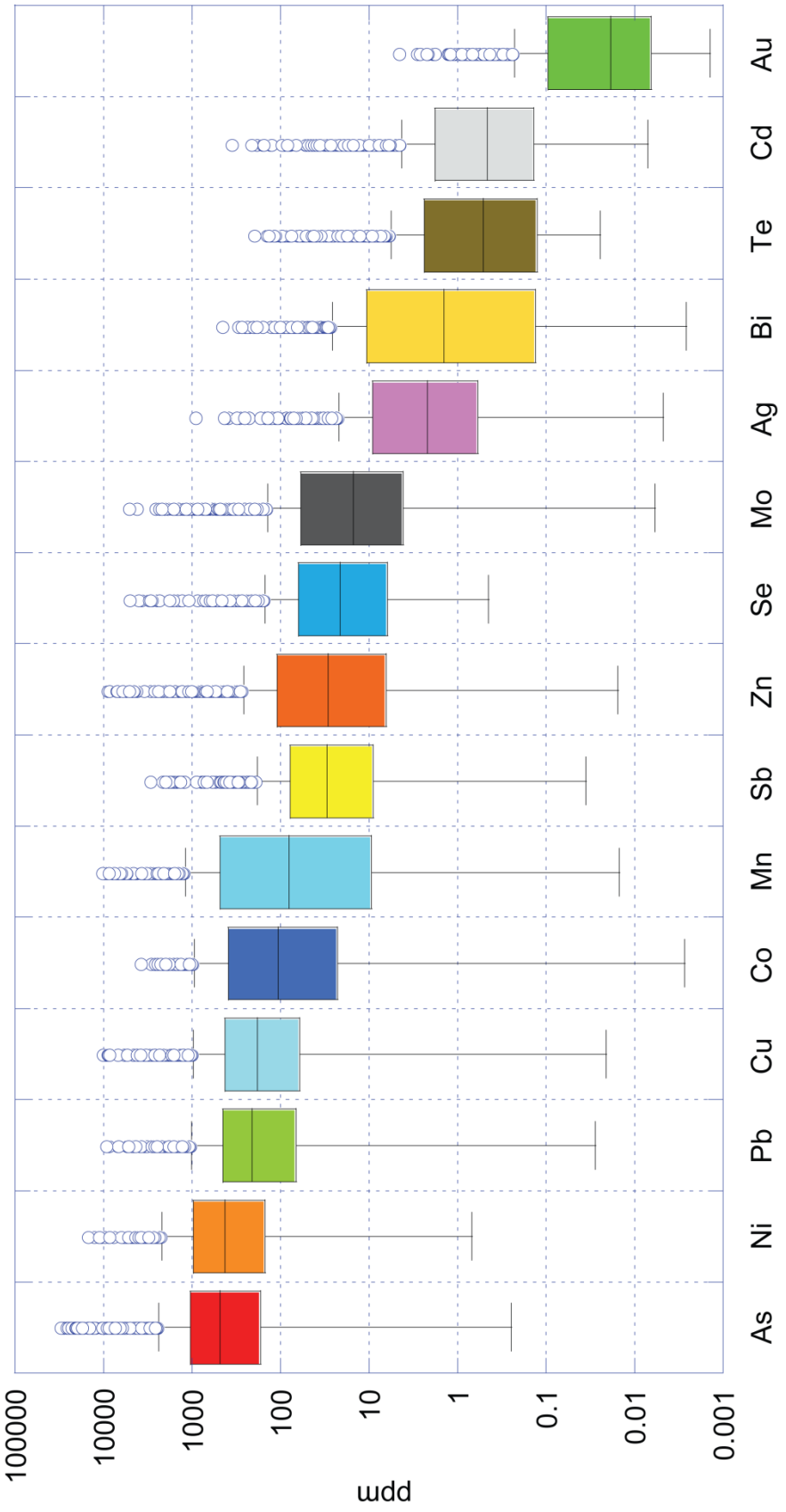

Figure 4.3: Boxplot of trace metal content of pyrite in descending order of elemental abundance I pyrite: As ≥ Ni > Pb ≥ Cu ≥ Co ≥ Mn > Sb ≥ Zn ≥ Se ≥ Mo > Ag ≥ Bi > Te ≥ Cd > Au.

Table 4.1: Median values of data set separated into age, depositional facies and texture. Bracketed numbers indicate instances where the median is below the detection limits, the value given is one half the average detection limits.

Category	Analyses	Mo	Co	Ni	Cu	Se	As	Ag	Te	Au
All data	1446	15.2	107	427	184	21.5	489	2.20	0.52	0.019
Age										
Cenozoic	77	474.3	84	510	329	62.3	289	5.32	(0.13)	(0.0065)
Mesozoic	161	58.7	86	221	55	5.3	489	0.20	(0.13)	(0.0065)
Paleozoic	659	16.9	49	245	134	32.4	245	1.26	0.26	(0.0065)
Proterozoic	341	17.9	167	651	379	22.9	783	5.38	1.10	0.060
Archean	256	1.3	465	912	216	19.4	844	8.02	6.34	0.12
Depositional facies										
Back Arc Basin	12	62.6	72	714	265	168.5	1705	30.78	2.45	1.96
Restricted Basin	153	82.3	67	306	126	7.4	448	0.35	(0.13)	(0.0065)
Rift	536	15.3	59	203	125	28.2	261	1.31	0.30	0.014
Shelf	138	15.4	736	1074	381	16.8	1148	7.37	1.96	0.24
Deep Facies	375	4.6	255	759	256	32.3	649	5.02	1.92	0.068
Texture										
Microcrystalline	58	5.9	51	695	237	44.3	282	16.25	2.71	0.025
Framboid	215	40.7	178	431	186	24.7	427	2.29	0.45	0.024
Small anhedral	252	42.1	161	464	316	23.4	334	3.76	0.65	0.029
Small euhedral	95	9.9	130	773	231	26.7	731	2.78	2.08	0.021
Nodule	466	15.2	72	320	134	18.9	485	1.77	0.30	0.011
Large anhedral	254	11.1	195	611	254	15.5	647	3.06	0.85	0.021
Large euhedral	143	11.2	54	281	131	23.9	428	1.17	0.35	0.015

Nickel is a trace element consistently enriched in most diagenetic pyrite and is often one of the trace elements in greatest abundance in sedimentary pyrite (second only to As). The content of Ni varies between 10 ppm and 10000 ppm with a median value of 427 ppm. Nickel is generally held within the structure of pyrite; this is expected as the metal sulphide phases of Ni form more slowly than iron sulphides and thus a higher proportion of Ni is incorporated into the pyrite lattice (Morse and Luther, 1999). Nickel was chosen as the comparator (in Figure 4) as it is one of the most consistently enriched trace elements in sedimentary pyrite and is not strongly effected by metamorphism or hydrothermal overprint (Large et al., 2007). The trace element content of **cobalt** in pyrite tends to be similar, though of lower magnitude to Ni. The majority of Co is between 1 ppm to 3000 ppm with a median of 107 ppm. Cobalt correlates well with Ni with the majority of sedimentary pyrite having

aCo/Ni ratio between 0.01 and 2 (Fig. 4). As with Ni, Co tends to be incorporated into the structure of pyrite rather than occurring as micro-inclusions. **Copper** has a similar relationship to Ni as Co, with the majority of sedimentary pyrite having Cu/Ni ratios between 0.01 and 10 (Fig. 4). Most Cu ranges between 1 ppm and 10000 ppm and has a median of 184 ppm. At low levels the Cu is held within the structure of the pyrite, however at higher concentrations of Cu the presence of micro inclusions of copper bearing sulphides becomes more common.

Molybdenum is usually present within sedimentary pyrite at values between 0.1 ppm and 1000 ppm with a median content of 15 ppm. The Mo content of pyrite is predominantly held within the structure of pyrite. Correlation between Mo and other trace elements is poor, as is evident in Figure 4 where there is no correlation with Ni. Similar to Mo, **selenium** has little correlation with other trace elements, as can be easily observed in the Se vs Ni plot in Figure 4. Selenium has a median value of 22 ppm and the majority of sedimentary pyrite ranges between 1 ppm and 1000 ppm. The Se within sedimentary pyrite is predominantly accommodated within the pyrites crystal lattice, where Se substitutes for S.

The median for **Arsenic** in sedimentary pyrite is 488 ppm and the majority of analyses range from 10 ppm to 10000 ppm. Most of the arsenic is held within the crystal structure of pyrite, except when it is in very high concentration where some microcrystals of arsenopyrite, or other AsFeS mineral may be present. Arsenic coordinates well with Ni, with the majority of analyses between As/Ni ratios of 0.1 and 10 (Fig. 4).

Plots of Au versus As, Ag, Te, Sb and Bi in sedimentary pyrite are presented in Figure 5. All show weak positive correlations, commonly with >80% of the data within 2 orders of magnitude of the best fit line. Gold content appears to be strongly tied to As content with most analyses falling above an As/Au ratio of 1000 (Fig. 5). The plots show that sedimentary pyrite has the following characteristics; Ag/Au >1, Te/Au >1, Bi/Au >1, Sb/Au >100 and As/Au >200.

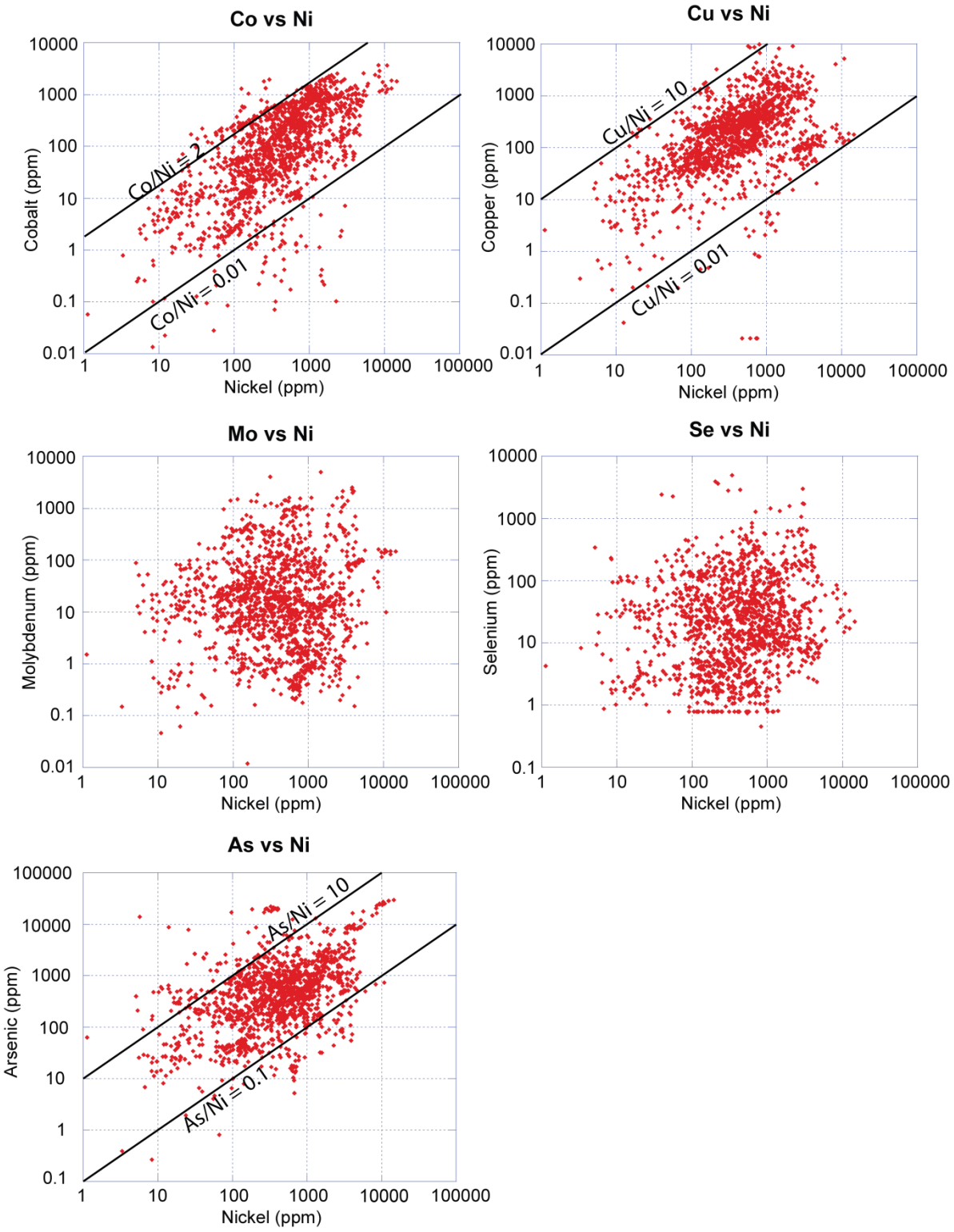

Figure 4.4: Plots of Co, Cu, Mo, Se and As versus Ni. Co, Cu and As correlate well with Ni. The majority of the data has Co/Ni ratios between 2 and 0.01, Cu/Ni ratios between 10 and 0.01 and As/Ni ratios between 10 and 0.1. Mo and Se do not correlate well with Ni.

Gold occurs in sedimentary pyrite with a median concentration of 0.019 ppm and the majority of the data between the detection limit (commonly 0.013 ppm) and 1 ppm. A total of 67% of the gold content is between 10 ppb and 5000 ppb and it has a mean of 160 ppb. Gold occurs either as micro-inclusions or within the structure of pyrite. Similarly **silver** and **tellurium** both occur as micro-inclusions and within the structure of pyrite so careful examination of the time resolved laser ablation output graph is essential when studying these elements. Tellurium correlates well with Au, with the majority of the data having Te/Au ratios between 1 and 1000. Tellurium has a median value of 0.52 ppm and is predominantly between a sub-detection limit value (median of 0.26 ppm) and 100 ppm. The vast majority of sedimentary pyrite has Ag/Au ratios greater than 1. Total silver content ranges between 0.1 ppm and 100 ppm with a median value of 2.20 ppm. **Antimony** correlates well with gold also, with the majority of the data falling between Sb/Au ratios of 100 and 10000. The Sb content of the majority of the pyrite varies from 1 to 1000 ppm. **Bismuth** does not correlate as well with gold and there is much more spread in the data than the other elements discussed, however most of the data does have Bi/Au ratios greater than 1. Total Bi in pyrite varies between 0.1 ppm and 100 ppm for the majority of the pyrite analyzed.

Using these observations we have made some general definitions of the trace element content of sedimentary pyrite (Table 2). 91% of the dataset has $0.01 < Co/Ni < 2$; 98% of the dataset has $0.01 < Co/Ni < 10$ and 83% of the dataset has $0.01 < Zn/Ni < 10$. Similar definitions can be made with data plotted against gold: 100% of the dataset has $As/Au > 200$; 100% of the dataset has $Ag/Au > 2$; 93% of the dataset has $1 < Te/Au < 1000$; 93% of the dataset has $Sb/Au > 100$ and 95% of the dataset has $Bi/Au > 1$). However the Au ratios are less robust than the Ni ratios as the amount of Au is often below detection limits. Though less robust than Ni ratios Au ratios are still useful as in hydrothermal systems Au can be commonly found in pyrite and often has distinctly different high Au/Me ratios (Large et al., 2011; Large et al., 2009; Large et al., 2007; Thomas et al., 2011) and can easily be used to distinguish between hydrothermal and diagenetic pyrite.

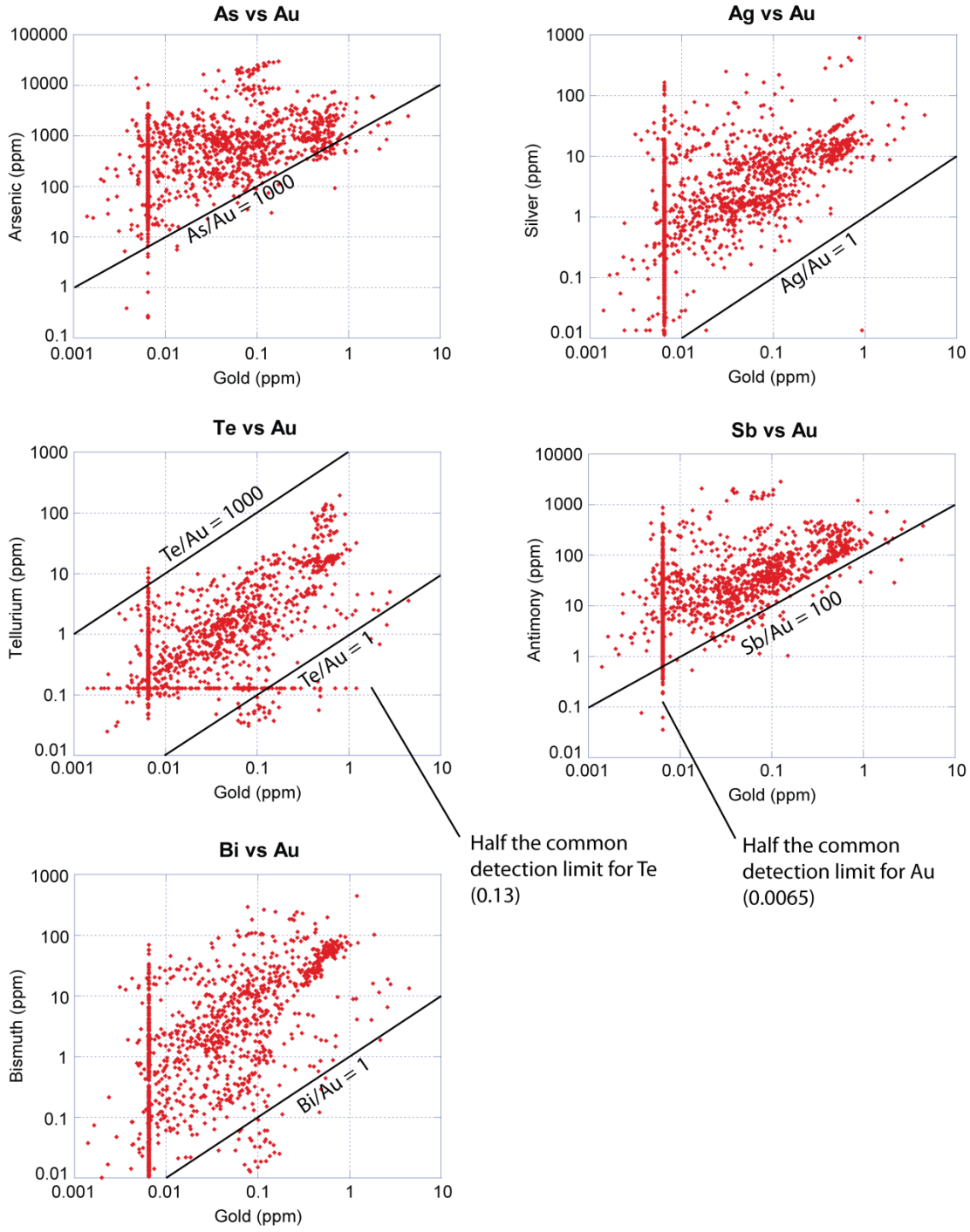

Figure 4.5: Plot of As, Ag, Te, Sb and Bi versus Au. As, Ag, Te and Sb correlate well with Au. The majority of the data has As/Au ratios greater than 1000, Ag/Au ratios greater than 1, Te/Au ratios between 1 and 1000 and Sb/Au ratios greater than 100. Bi does not correlate as well with Au, though most of the data has Bi/Au ratios greater than 1. Several samples are below detection limits for Au and Te. Where this occurs the data is plotted as half the median of the detection limits (0.13 Te and 0.0065 Au). Some of the data is below these values because the detection limits of the procedure depends of several factors and under ideal circumstance can be lower than is possible for all analyses.

Table 4.2: Characteristic ratios of sedimentary pyrite

Ratio	% of data set
0.01 < Co/Ni < 2	91
0.01 < Zn/Ni < 10	83
0.01 < Cu/Ni < 2	89
0.1 < As/Ni < 10	93
1 < Te/Au < 1000	93
As/Au > 200	100
Ag/Au > 2	100
Sb/Au > 100	95
Bi/Au > 1	95

4.5 Discussion

4.5.1 Redox conditions and productivity

Molybdenum is one of the most common elements used to interpret paleo-redox ocean conditions (Algeo and Lyons, 2006; Algeo and Maynard, 2004; Anbar et al., 2007; Lyons and Kashgarian, 2005). While there is significant scatter in the Ni-Mo plot due to differences in texture, tectonic setting and age, as will be discussed in more detail later, some general comments can be made. The higher Mo values (> 50 ppm) probably relate to either areas of abnormally high Mo source values or areas of stratified water column that receives recharge of Mo from the open ocean (Algeo and Lyons, 2006). On the other hand, low Mo samples represent either highly constricted basins where little recharge of Mo is present or oxic/anoxic basins in which the Mo is present in the soluble, oxidized state and little Mo is precipitated in the sediments (Algeo and Lyons, 2006). Other factors, such as changes in provenance of the sediments, i.e. shale basins in which the sediment is sourced from a mafic igneous terrane would have the potential to have more mafic elements (e.g. Ni, Co, Cu) than a sediment basin sourced from a felsic igneous terrane which would provide more felsic elements (e.g., Mo, Bi). Tribovillard et al. (2006) recognized that the elements Ni, Cu, Zn and Cd are associated with rates of organic carbon sinking flux which is frequently associated with productivity. This is because these trace elements adsorb onto organic matter and are incorporated into the sediments, when the organic matter breaks down the trace elements are

left behind, and some are incorporated into pyrite. Another potential complication with the interpretation of the data is the possibility of long term, large scale basin euxinia which may result in draw down and depletion of trace elements in ocean waters (Algeo, 2004).

4.5.2 Relationship between sedimentary pyrite texture and composition.

When pyrite in shale is remobilized (Large et al., 2009; Large et al., 2007) late diagenetic processes can result in the loss of some trace elements. This is due to the dissolution of pyrite and subsequent release of the trace elements, or an increase due to simultaneous release of trace elements from either organic matter or iron (hydr)oxides and subsequent incorporation of the trace elements into pyrite.

Box and whisker plots of our data (Fig. 6) show that for all elements examined there is no obvious enrichment or depletion based on the pyrite texture and therefore the timing of crystallization during diagenesis. Minor trends may be significant; for example Mo is most elevated in framboidal and small anhedral pyrite forms, whereas Ag and Te are most elevated in microcrystalline pyrite. However, even considering these differences the dataset as a whole indicates that the timing and degree of the crystallization of the sedimentary pyrite does not significantly affect the trace element content. This suggests that tectonic environment and chemistry of the oceans at different phases of earth history is more important in determining the trace element content of pyrite. However future studies should continue to collect textural data to monitor the relationship between the texture and timing of sedimentary pyrite growth compared to trace element content.

During metamorphism pyrite is often recrystallized, resulting in large euhedral pyrite formation. This has the effect of forcing many trace elements out of the pyrite and into their own phases (Large et al., 2011; Large et al., 2009; Large et al., 2007; Thomas et al., 2011).

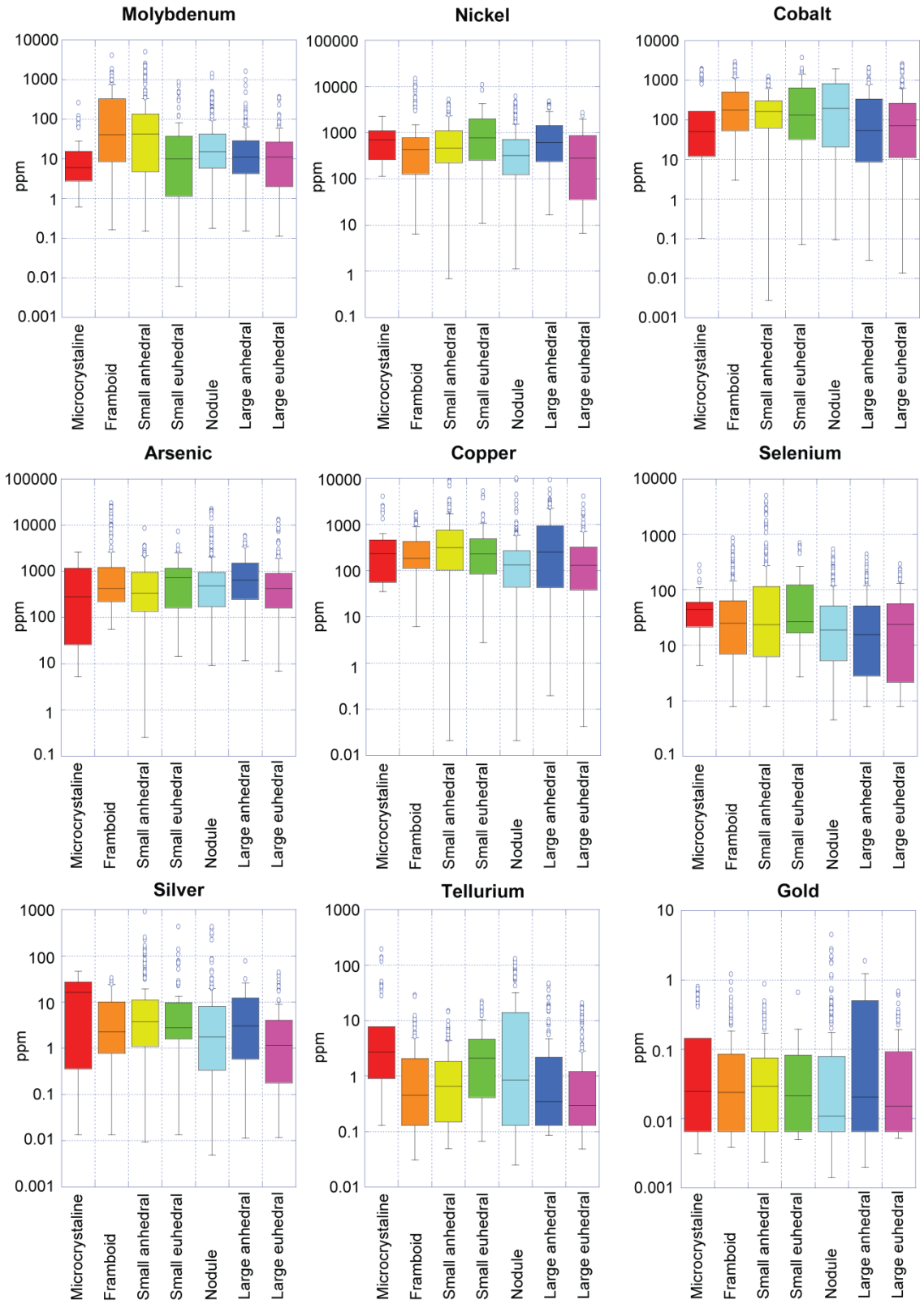

Figure 4.6: Trace metal content of pyrite with groupings based on pyrite texture (microcrystalline, framboidal, small anhedral, small euhedral, nodule, large anhedral, large euhedral) for Mo, Ni, Co, As, Cu, Se, Ag, Te and Au.

Table 4.3: Mean geochemical values for pyrite of different textures but from the same sample

Mount	texture	n	Formation	Co	Ni	Cu	Zn	As	Se	Mo	Ag	Sb	Te	Au	Bi
1	Microcrystalline	6	Jet Rock	75	401	103	122	328	9.3	100.6	1.5	6.7	1.5	0.04	1.3
1	Nodule	22	Jet Rock	48	238	61	51	272	6.6	108.4	0.5	3.2	1.2	0.02	0.6
2	Framboid	5	Que River Shale	297	511	252	128	764	78.7	20.1	16.8	84.5	bdl	0.2	8.8
2	Nodule	5	Que River Shale	100	287	221	46	304	118	0.7	8.3	43.2	0.7	0.1	1.1
3	Microcrystalline	14	McRea Formation	53	125	54	44	1194	21.2	8.3	0.3	18.4	0.9	0.03	1.8
3	Nodule	7	McRea Formation	2	21	212	3	338	3.4	0.8	1.3	21.6	0.7	0.04	1.7
4	Microcrystalline	5	McRea Formation	184	384	233	47	322	13.9	4.7	5.6	57.5	6	0.07	9.4
4	Small anhedral	3	McRea Formation	195	501	328	44	475	14.7	4.4	8.5	74	7.7	0.1	11.3
4	Large euhedral	10	McRea Formation	116	272	264	28	1111	17	3.6	2.6	35.7	4.3	0.05	4.4
5	Small euhedral	12	Alum Shale	137	2888	750	62	2204	204.9	331.5	55.2	122.5	3	0.08	1.3
5	Nodule	5	Alum Shale	88	2170	667	379	5696	405.3	200.3	322.5	228.4	5.8	0.43	0.9
6	Framboid	6	Canol Formation	77	1002	303	153	242	392.6	154.3	2.7	82.9	0.8	0.04	0.5
6	Nodule	8	Canol Formation	2	73	55	22	44	255.5	28.6	0.4	41	0.3	0.01	0.2
7	Small euhedral	6	Warrabarty	416	64	37	13	46	21.7	0.1	0.1	0.6	0.1	0.01	0.2
7	Nodule	10	Warrabarty	300	450	264	58	230	11.3	5.6	0.9	17.7	0.5	0.05	4.8
8	Small anhedral	9	Yul-12005	87	524	206	135	160	41.8	207.8	6.6	19.7	1.9	0.04	13.1
8	Large euhedral	12	Yul-12005	78	295	165	72	156	42.5	76.7	0.4	4.5	0.2	0.01	0.2

While little systematic difference can be determined from pyrites from different units, there are clear trends from pyrites of different texture within a single sample. The means of elements of interest are shown in Table 3. The textures believed to be of early origin (microcrystalline, framboidal, small euhedral and small anhedral) tend to have either the same or higher amounts of trace elements than the pyrite that is interpreted to be of later origin (Nodular, large anhedral and large euhedral). The major exception to this where small euhedral and nodular pyrites are found together (Mounts 5 and 7), in these samples the small euhedral pyrite tends the have significantly less of many trace elements than the nodular pyrite. This may suggest that the small euhedral pyrites are later than the nodules and thus the general trend of less trace elements in older pyrite is maintained. A second possibility is that when the small euhedral pyrite forms much of the trace elements are still adsorbed to other phases, while when the nodules form by remobilizing the sulphides near them (Ono et al., 2003) they scavenge metals from other metal bearing phases as well, increasing the nodules metal content. It is also possible that during this remobilizing phase the small pyrite are recrystallized into the small euhedral forms and some of the trace elements are forced out of the pyrite crystal lattice. To determine which of these hypotheses is correct more detailed work on the effect of recrystallization on the trace element content of pyrite must be conducted. In mount 3 (Cu and Ag) and mount 4 (As) there are also some elements that are significantly higher in the later phases.

4.5.3 Relationship between sedimentary pyrite age and composition

Large et al. (in prep, submitted) have outlined the variation in trace element content of pyrite related to age of sedimentation and argue that these changes reflect global shifts in trace element chemistry of the oceans due largely to the oxygenation of the atmosphere. Here we further document the changes and discuss other potential causes.

The major trace element variations with time intervals are shown in Figure 8. This plot shows that, as outlined by Large et al. (in prep, submitted), many trace elements in sedimentary pyrite have varied through time, some in a very systematic manner. Elements exhibiting a general increase through time are Mo and Se whereas Ni, Co, As, Te and Au show a general decrease through time. However, for many elements the Mesozoic seems to have relatively low values (Ni, Cu, Se, Ag). This may be due to a period of highly stratified

oceans during the Mesozoic which resulted in low trace element inventories in the oceans, similar to the conditions identified in the late Devonian by Algeo (2004).

Mo is significantly depleted in the Archean samples and significantly enriched in the Cenozoic samples with a minor enrichment in the Proterozoic through to the Mesozoic. Strong enrichment in the Cenozoic is likely due to sample bias as most analyses from this time period are from pyrite from the Cariaco Basin. The Cariaco Basin is an euxinic basin that is recharged with some metals by the surrounding ocean waters allowing it to become very enriched in Mo (Lyons et al., 2003). This possible sample bias may also explain the relatively high amounts of Ag, Se, Cu and Mo found in the Ceozoic samples, before conclusive statements can be made about the Cenozoic more sites will have to be examined. The extreme depletion in Mo in the Archean samples is likely due to the unoxygenated state of the atmosphere which would have limited oxidative weathering on land resulting in a lower source of Mo for the entire basin, similar to the results obtained by Scott et al. (2008) using whole rock data. In contrast to molybdenum, Co and Ni show a general decrease with age. This is likely due to the prevalence of komatiite eruptions during the Archean, and to a much lesser extent in the Proterozoic (Konhauser et al. (2009)). Komatiites are well documented as containing anomalously high Ni and Co with contents of >600 ppm (Barley and Bickle, 1982) and >80 ppm (Beswick, 1982) respectively, compared to 149 ppm Ni and

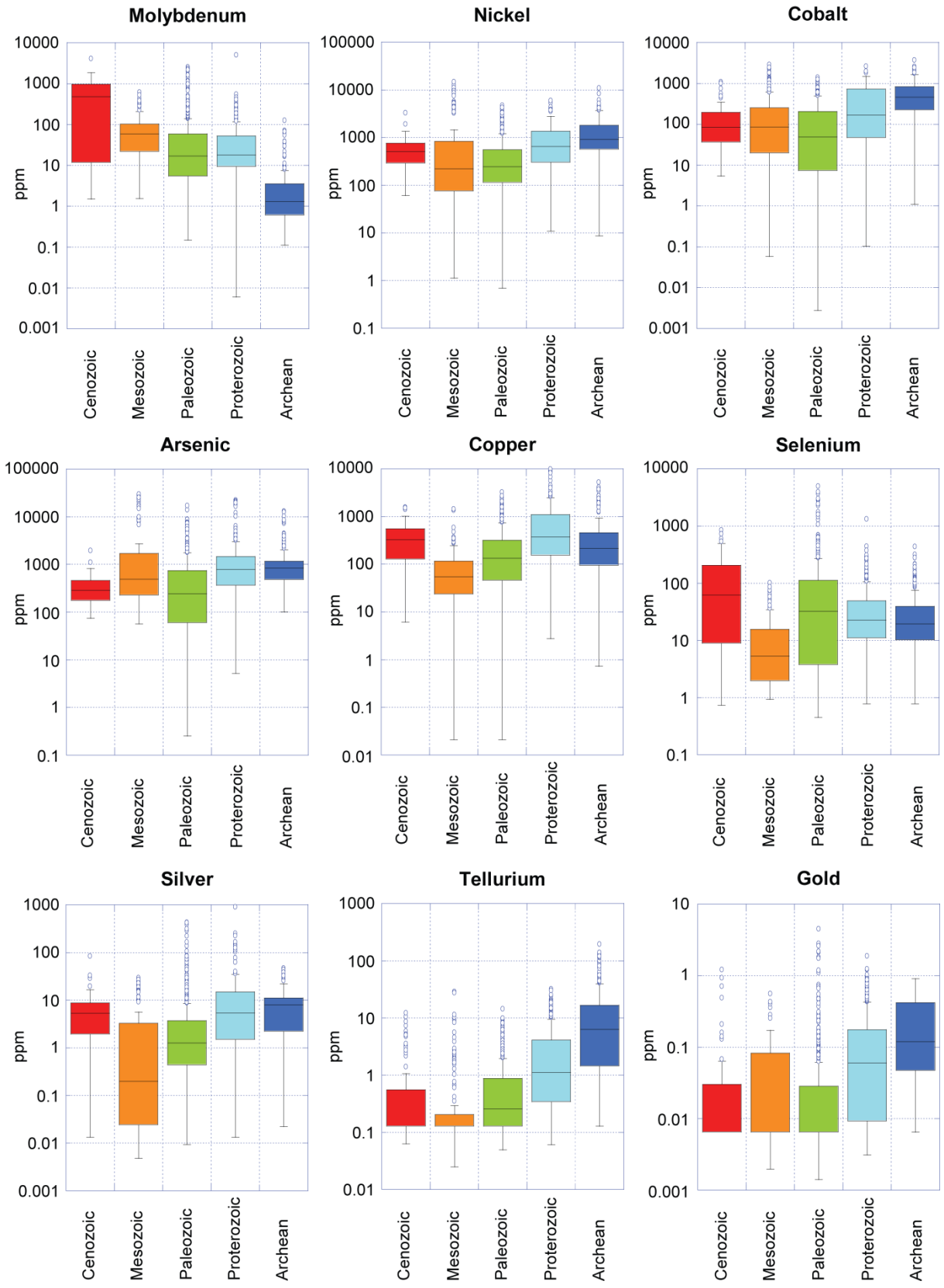

Figure 4.7: Trace metal content of pyrite with groupings based on age (Archean, Proterozoic, Paleozoic, Mesozoic and Cenozoic) for Mo, Ni, Co, As, Cu, Se, Ag, Te and Au.

47 ppm Co for mid ocean ridge basalt (Sun et al., 1979) and 56 ppm Ni and 24 ppm Co for average crustal composition (Wedepohl, 1991). This corresponds well with trends observed for composition of the upper crust across time observed by Condie (1993), who described overall decreases in total Ni and Co from the Archean to the Paleozoic, with much higher contents in the Archean (65-85 ppm Ni, 22-25 ppm Co), compared to Proterozoic (29-31 ppm Ni, 15 ppm Co). Silver, Au and Te have a similar trend to Ni and Co with higher concentrations in the Archean decreasing towards the Paleozoic. This may be due to similar causes to trends observed in Ni and Co, but because there is not as good average crustal abundance data on Ag, Te and Au through time it is difficult to support this hypothesis at this time. It is interesting that Ag is much lower during the Mesozoic while both Au and Te have similar abundances in the Paleozoic and the Mesozoic. This suggests that Te and Au may not be affected by the drawdown of trace elements during periods of anoxia described by (Algeo, 2004), while Ag may be strongly affected by this process.

Arsenic follows a similar trend to Ni and Au with higher concentrations in the Archean, decreasing in the Proterozoic and Paleozoic and then increasing slightly in the Mesozoic. The reason for this is not immediately clear. It may be that late stage mantle degassing resulted in more As released in the Archean and progressively less in the later eras. It is also possible that in the Archean, when the atmosphere was less oxygenated, chemical erosion of sulfides was suppressed in an Fe dominated ocean. This may have resulted in a higher As:S ratio in the oceans causing a greater accumulation of As in pyrite. Similarly in the Proterozoic there was more oxygen in the atmosphere than in the Archean (Farquhar et al., 2000) and less than in the Paleozoic (Holland, 2006) resulting in a As:S ratio midway between that of the Archean and Paleozoic causing an increase in As in pyrite between the Archean and Paleozoic values. This alternative explanation may also account for the increase in Mo in the Mesozoic because all our Mesozoic data comes from the Triassic or Jurassic periods and during these periods atmospheric oxygen was lower than that in the Paleozoic (Berner et al., 2007). Similarly to Mo, the total As:S ratio in the oceans would have lowered resulting in higher As accumulation in pyrite for reasons described above.

The copper content appears to be relatively constant from the Archean to the Paleozoic, with the only deviations occurring in the Mesozoic (major decrease) and the Cenozoic (major increase). The reason for the drastic decrease in the Mesozoic is likely the drawdown of trace

elements as described above. The reason for the major increase in the Cenozoic may reflect sampling bias as the only sample used is from the euxinic Cariaco basin, which reflects relatively unique modern ocean conditions.

Selenium has the opposite trend to all the other trace elements examined except Mo, with contents generally increasing from the Archean to the Cenozoic. This is because one of the main sources of Se is riverine discharge (Mitchell et al., 2012), and like Mo, increased oxygenation of the atmosphere leads to increased amount of mobile selenite species into the ocean for accumulation in black shales and sedimentary pyrite (Large et al., in prep). There is a marked decrease of Se in pyrite in the Mesozoic which is likely due to the drawdown of trace elements in anoxic oceans as mentioned previously.

4.6 Conclusions

A data base of LA-ICPMS analyses of sedimentary and diagenetic pyrite in black shale has been used to characterize sedimentary pyrite trace element compositions and determine controls on the variations in composition.

In general terms sedimentary pyrite is enriched in a suite of trace elements in the following order of abundance: As ≥ Ni > Pb ≥ Cu ≥ Co ≥ Mn > Sb ≥ Zn ≥ Se ≥ Mo > Ag ≥ Bi > Te ≥ Cd > Au. We have defined the characteristic values and composition limits of sedimentary pyrite by; 0.01 < Co/Ni < 2, 0.01 < Cu/Ni < 10, 0.01 < Zn/Ni < 10, 0.1 < As/Ni < 10, Ag/Au > 2, 1 < Te/Au < 1000, Bi/Au > 1, Sb/Au > 100 and As/Au > 200. The gold content of sedimentary pyrite (away from gold productive basins) has a mean of 160 ppb; with over 67% of the data between 10 ppb and 5000 ppm.

Our data shows no significant relationship between textural form of sedimentary pyrite and trace element content exists between basins; provided only sedimentary pyrite in rocks below mid greenschist facies are considered. However, earlier generations of pyrite tend to have equal or higher trace element contents than later pyrite generations within the same sample. In agreement with recent work, this study has emphasized a significant relationship for many trace elements with the age of the pyrite. Some elements increase through time (Mo and Se) where as other elements decrease through time (Ni, Co, As, Te, Ag and Au). This is most

likely controlled by changes to the composition of metal source areas and/or changes in oxygenation of the atmosphere and oceans.

4.7 References

Algeo, T. J. (2004) Can marine anoxic events draw down the trace element inventory of seawater?: Geology, 32(12), 1057-1060.

Algeo, T. J., and Lyons, T. W. (2006) Mo-total organic carbon covariation in modern anoxic marine environments: Implications for analysis of paleoredox and paleohydrographic conditions: Paleoceanography, 21(1).

Algeo, T. J., and Maynard, J. B. (2004) Trace-element behavior and redox facies in core shales of Upper Pennsylvanian Kansas-type cyclothems: Chemical Geology, 206(3-4), 289-318.

Anbar, A. D., Duan, Y., Lyons, T. W., Arnold, G. L., Kendall, B., Creaser, R. A., Kaufman, A. J., Gordon, G. W., Scott, C., and Garvin, J. (2007) A whiff of oxygen before the great oxidation event?: Science, 317(5846), 1903-1906.

Bajwah, Z., Seccombe, P., and Offler, R. (1987) Trace element distribution, Co: Ni ratios and genesis of the big cadia iron-copper deposit, new south wales, australia: Mineralium Deposita, 22(4), 292-300.

Barley, M., and Bickle, M. (1982) Komatiites in the Pilbara Block, Western Australia: Komatiites: London, George Allen and Unwin, 105-115.

Berner, R. A., VandenBrooks, J. M., and Ward, P. D. (2007) Oxygen and evolution: Science, 316(5824), 557-558.

Berner, Z. A., Puchelt, H., NÖLtner, T., and Kramar, U. T. Z. (2013) Pyrite geochemistry in the Toarcian Posidonia Shale of south-west Germany: Evidence for contrasting trace-element patterns of diagenetic and syngenetic pyrites: Sedimentology, 60(2), 548-573.

Beswick, A. (1982) Some geochemical aspects of alteration and genetic relations in komatiitic suites: Ardnt, NT; Nesbitt, EG. Komatiites. London: George Allen and Unwin, 283-308.

Botinelly, T., Siems, D., and Sanzolone, R. (1985) Trace elements in disseminated sulfides, magnetite, and massive sulfides, West Shasta District, California: Economic Geology, 80(8), 2196-2205.

Butler, I. B., and Rickard, D. (2000) Framboidal pyrite formation via the oxidation of iron (II) monosulfide by hydrogen sulphide: Geochimica et Cosmochimica Acta, 64(15), 2665-2672.

Campbell, F. A., and Ethier, V. G. (1984) Nickel and cobalt in pyrrhotite and pyrite from the Faro and Sullivan orebodies: The Canadian Mineralogist, 22(3), 503-506.

Condie, K. C. (1993) Chemical composition and evolution of the upper continental crust: contrasting results from surface samples and shales: Chemical Geology, 104(1), 1-37.

Danyushevsky, L., Robinson, P., Gilbert, S., Norman, M., Large, R., McGoldrick, P., and Shelley, M. (2011) Routine quantitative multi-element analysis of sulphide minerals by laser ablation ICP-MS: Standard development and consideration of matrix effects: Geochemistry: Exploration, Environment, Analysis, 11(1), 51-60.

Deditius, A. P., Utsunomiya, S., Renock, D., Ewing, R. C., Ramana, C. V., Becker, U., and Kesler, S. E. (2008) A proposed new type of arsenian pyrite: Composition, nanostructure and geological significance: Geochimica et Cosmochimica Acta, 72(12), 2919-2933.

Dellwig, O., Böttcher, M. E., Lipinski, M., and Brumsack, H.-J. (2002) Trace metals in Holocene coastal peats and their relation to pyrite formation (NW Germany): Chemical Geology, 182(2–4), 423-442.

Farquhar, J., Bao, H., and Thiemens, M. (2000) Atmospheric influence of Earth's earliest sulfur cycle: Science, 289(5480), 756-758.

Franklin, J., Lydon, J., and Sangster, D. (1981) Volcanic-associated massive sulfide deposits: Economic Geology, 75, 485-627.

Gehrisch, W., Maucher, A., and Nielsen, H. (1975) Sulfur-isotope and trace element analyses from the Sulitjelma ore bodies, northern Norway: Mineralium Deposita, 10(1), 57-69.

Green, G., Solomon, M., and Walshe, J. (1981) The formation of the volcanic-hosted massive sulfide ore deposit at Rosebery, Tasmania: Economic Geology, 76(2), 304-338.

Gregory, D., Meffre, S., and Large, R. (2013) Mineralogy of metal contaminated estuarine sediments, Derwent estuary, Hobart, Australia: implications for metal mobility: Australian Journal of Earth Sciences, 60, p. 589-603.

Guillong, M., Hametner, K., Reusser, E., Wilson, S. A., and Günther, D. (2005) Preliminary Characterisation of New Glass Reference Materials (GSA-1G, GSC-1G, GSD-1G and GSE-1G) by Laser Ablation-Inductively Coupled Plasma-Mass Spectrometry Using 193 nm, 213 nm and 266 nm Wavelengths: Geostandards and Geoanalytical Research, 29(3), 315-331.

Hawley, J., and Nichol, I. (1961) Trace elements in pyrite, pyrrhotite and chalcopyrite of different ores: Economic Geology, 56(3), 467-487.

Holland, H. D. (2006) The oxygenation of the atmosphere and oceans: Philosophical Transactions of the Royal Society B: Biological Sciences, 361(1470), 903-915.

Huerta-Diaz, M. A., and Morse, J. W. (1992) Pyritization of trace metals in anoxic marine sediments: Geochimica et Cosmochimica Acta, 56(7), 2681-2702.

Konhauser, K. O., Pecoits, E., Lalonde, S. V., Papineau, D., Nisbet, E. G., Barley, M. E., Arndt, N. T., Zahnle, K., and Kamber, B. S. (2009) Oceanic nickel depletion and a methanogen famine before the Great Oxidation Event: Nature, 458(7239), 750-753.

Large, R. R. (1977) Chemical evolution and zonation of massive sulfide deposits in volcanic terrains: Economic Geology, 72(4), 549-572.

Large, R. R., Bull, S. W., and Maslennikov, V. V. (2011) A carbonaceous sedimentary source-rock model for Carlin-type and orogenic gold deposits: Economic Geology, 106(3), 331-358.

Large, R. R., Danyushevsky, L., Hollit, C., Maslennikov, V., Meffre, S., Gilbert, S., Bull, S., Scott, R., Emsbo, P., Thomas, H., Singh, B., and Foster, J. (2009) Gold and Trace Element Zonation in Pyrite Using a Laser Imaging Technique: Implications for the Timing of Gold in Orogenic and Carlin-Style Sediment-Hosted Deposits: Economic Geology, 104(5), 635-668.

Large, R. R., Maslennikov, V. V., Robert, F., Danyushevsky, L. V., and Chang, Z. S. (2007) Multistage sedimentary and metamorphic origin of pyrite and gold in the giant Sukhoi Log deposit, Lena gold province, Russia: Economic Geology, 102(7), 1233-1267.

Loftus-Hills, G., and Solomon, M. (1967) Cobalt, nickel and selenium in sulphides as indicators of ore genesis: Mineralium Deposita, 2(3), 228-242.

Longerich, H. P., Jackson, S. E., and Günther, D. (1996) Inter-laboratory note. Laser ablation inductively coupled plasma mass spectrometric transient signal data acquisition and analyte concentration calculation: Journal of Analytical Atomic Spectrometry, 11(9), 899-904.

Lyons, T. W., and Kashgarian, M. (2005) Paradigm lost, paradigm found; the Black Sea shale connection as viewed from the anoxic basin margin: Oceanography, 18(2), 86-99.

Lyons, T. W., Werne, J. P., Hollander, D. J., and Murray, R. W. (2003) Contrasting sulfur geochemistry and Fe/Al and Mo/Al ratios across the last oxic-to-anoxic transition in the Cariaco Basin, Venezuela: Chemical Geology, 195(1-4), 131-157.

Martin, J., Nirel, P., and Thomas, A. (1987) Sequential extraction techniques: promises and problems: Marine Chemistry, 22(2), 313-341.

McLennan, S. M. (2001) Relationships between the trace element composition of sedimentary rocks and upper continental crust: Geochemistry, Geophysics, Geosystems, 2(4).

Mitchell, K., Mason, P. R., Cappellen, P. V., Johnson, T. M., Gill, B. C., Owens, J. D., Diaz, J., Ingall, E. D., Reichart, G.-J., and Lyons, T. W. (2012) Selenium as paleo-oceanographic proxy: A first assessment: Geochimica et Cosmochimica Acta.

Morse, J., and Luther, G. (1999) Chemical influences on trace metal-sulfide interactions in anoxic sediments: Geochimica et Cosmochimica Acta, 63(19), 3373-3378.

Morse, J. W., and Arakaki, T. (1993) Adsorption and coprecipitation of divalent metals with mackinawite (FeS): Geochimica et Cosmochimica Acta, 57(15), 3635-3640.

Ono, S., Eigenbrode, J. L., Pavlov, A. A., Kharecha, P., Rumble, D., Kasting, J. F., and Freeman, K. H. (2003) New insights into Archean sulfur cycle from mass-independent sulfur isotope records from the Hamersley Basin, Australia: Earth and Planetary Science Letters, 213(1), 15-30.

Qian, G., Brugger, J., Testemale, D., Skinner, W., and Pring, A. (2013) Formation of As(II)-pyrite during experimental replacement of magnetite under hydrothermal conditions: Geochimica et Cosmochimica Acta, 100, 1-10.

Raiswell, R., and Plant, J. (1980) The incorporation of trace elements into pyrite during diagenesis of black shales, Yorkshire, England: Economic geology, 75(5), 684-699.

Reich, M., and Becker, U. (2006) First-principles calculations of the thermodynamic mixing properties of arsenic incorporation into pyrite and marcasite: Chemical Geology, 225(3), 278-290.

Reich, M., Kesler, S. E., Utsunomiya, S., Palenik, C. S., Chryssoulis, S. L., and Ewing, R. C. (2005) Solubility of gold in arsenian pyrite: Geochimica et Cosmochimica Acta, 69(11), 2781-2796.

Rickard, D. (2012) Sulfidic Sediments and Sedimentary Rocks, Elsevier.

Rickard, D., and Luther, G. W. (1997) Kinetics of pyrite formation by the H2S oxidation of iron (II) monosulfide in aqueous solutions between 25 and 125° C: The mechanism: Geochimica et Cosmochimica Acta, 61(1), 135-147.

Scott, C., Lyons, T., Bekker, A., Shen, Y., Poulton, S., Chu, X., and Anbar, A. (2008) Tracing the stepwise oxygenation of the Proterozoic ocean: Nature, 452(7186), 456-459.

Selles-Martinez, J. (1996) Concretion morphology, classification and genesis: Earth-Science Reviews, 41(3), 177-210.

So, C.-S. (1978) Geochemistry and origin of amphibolite and magnetite from the Yangyang iron deposit in the Gyeonggi metamorphic complex, Republic of Korea: Mineralium Deposita, 13(1), 105-117.

Taylor, S. R., and McLennan, S. M. (1985) The continental crust: its composition and evolution.

Thole, R. (1976) The geology of the Shamrocke Mine, Rhodesia; a stratiform copper deposit: Economic Geology, 71(1), 202-228.

Thomas, H. V., Large, R. R., Bull, S. W., Maslennikov, V., Berry, R. F., Fraser, R., Froud, S., and Moye, R. (2011) Pyrite and pyrrhotite textures and composition in sediments,

laminated quartz veins, and reefs at Bendigo gold mine, Australia: insights for ore genesis: Economic Geology, 106(1), 1-31.

Tribovillard, N., Algeo, T. J., Lyons, T., and Riboulleau, A. (2006) Trace metals as paleoredox and paleoproductivity proxies: An update: Chemical Geology, 232(1), 12-32.

Wedepohl, K. (1991) The composition of the upper earth's crust and the natural cycles of selected metals. Metals in natural raw materials: Metals and their compounds in the environment. Occurrence, analysis, and biological relevance. New York, NY: VCH, 3-17.

Wilkin, R., Barnes, H., and Brantley, S. (1996) The size distribution of framboidal pyrite in modern sediments: An indicator of redox conditions: Geochimica et Cosmochimica Acta, 60(20), 3897-3912.

5.0 The Chemical Conditions of the Late Archean Hamersley Basin Inferred from Whole Rock and Pyrite Geochemistry with $\Delta^{33}S$ and $\delta^{34}S$ Isotope Analyses

5.1 Abstract

The well-preserved late Archean sedimentary rocks of the Fortescue and Hamersley basins, Western Australia offer fascinating insight into early Earth ocean chemistry prior to the GOE. Here we use a combination of whole rock geochemistry, LA-ICPMS trace element analysis of sedimentary pyrite and SHRIMP-SI sulfur isotope analyses to elucidate the chemical changes in these sedimentary rocks. These proxies are used to examine chemical conditions of the ocean during the late Archaean. Three periods of oxygen enrichment prior to deposition of banded iron formations are evident. Two stages of general increases in whole rock enrichment factors and trace elements in pyrite are observed with younging direction in the Jeerinah Formation, Fortescue Basin and in the Paraburdoo Member and Bee Gorge Members of the Wittenoom Formation, Hamersley Basin. Some of these trace elements indicate organic matter burial flux (Ni, Cr, Zn, Co and Cu) which suggests an increase in biological productivity. If the increased biological activity reflects an increase in cyanobacteria activity then an associated increase in oxygen is also to be expected. An increase in oxygen would result in the weathering of sulfide and other minerals, increasing the trace element content of the water column via erosion and avoiding excessive depletion of trace elements due to drawdown in seawater. Since some of these trace elements may also be limiting nutrients (such as Mo and Se) for the cyanobacteria, the degree of biological productivity may have increased due to an increasing amount of trace elements introduced by oxygenation in a positive feedback loop. These periods of increased productivity and oxygen formation stop prior to the onset of banded iron formation (BIF) deposition in the Hamersley Basin. This may be due to the ocean reaching an oxidation threshold, allowing for the precipitation of BIF. Compared to the other units examined (except the BIF), the top of the Mt. McRae Shale exhibits a much higher whole rock trace element content (Mo, Co, Cr, Ni, Cu and Zn) accompanied by a lower trace element content in pyrite. This may be due to greater amounts of oxygen being produced than during deposition of Mt McRae Shale. This increased the oxidation of sulfides and resulted in more sulfur released into the oceans. This resulted in greater pyrite precipitation in deeper water and/or below the sediment sea water interface where the reducing conditions necessary for pyrite precipitation were still present. There were not enough trace elements released to yield trace metal rich pyrite equivalent to the whole rock enrichment. An increase in volcanism at the same time may also have

contributed to the increased amount of sulphur. The $\Delta^{33}S$ and $\delta^{34}S$ isotope analyses suggest that the source of sulfur was largely seawater sulfate with varying degrees of elemental sulfur contributed by volcanic eruptions. Intervals containing high proportions of volcanically derived sulfur have corresponding low levels of trace elements in pyrite due to an increase in sulfur availability in the ocean forming excess pyrite that scavenges trace metals from the water column.

5.2 Introduction

Neoarchean shales within the Fortescue and Hamersley basins of northwest Australia preserve evidence of two important events in ocean chemistry. Sulfidic shale of the 2690−2629 Ma Jeerinah Formation records the oldest known period of euxinia in earth's history (Scott et al., 2011). By contrast, the c.2500 Ma Mt. McRae Shale records a slight increase of oxygen before the Great Oxygenation Event (GOE) between 2220 and 2450 Ma (Anbar et al., 2007). Recent studies have used trace element contents of sedimentary pyrite to determine chemical conditions during deposition of the host sediments (Berner et al., 2013)(Chapter 4). The purpose of this study is to examine the trends in the trace metal chemistry of syngenetic and diagenetic pyrite deposited during and between 2690 and 2500 Ma. We have examined two drill holes: DD86WRL1 that passes through the Jeerinah Formation (Fortescue Group) and ABDP9 that passes through the Mt. McRae Shale, and the Bee Gorge and Paraburdoo members of the Wittenoom Formation (Hamersley Group). We employed a combination of whole rock geochemistry, Laser Ablation-ICPMS (LA-ICPMS) analyses of pyrite and SHRIMP-SI (Sensitive High Resolution Ion MicroProbe, Stable Isotopes) sulfur isotope analyses of pyrite to enable a robust and comprehensive assessment of the ocean and atmosphere chemistry for the Neoarchean. We significantly expanded the number of trace metals investigated in shales of both the Jeerinah Formation and Mt McRae Shale relative to previous studies (Anbar et al., 2007; Raiswell et al., 2011; Scott et al., 2008), and we extended geochemical and isotopic investigations into the intervening strata to include the Bee Gorge and Paraburdoo members of the Wittenoom Formation. Our data show that trace metal content of the ocean has changed significantly between 2690 Ma and 2500 Ma. This key period includes the first known euxinic events and some of the earliest reported oxygenation events to have occurred on Earth.

5.2.1 Previous work

Previous investigations of the Jeerinah Formation have been based on detailed iron speciation, S isotope, C and Mo whole rock analyses. Scott et al. (2011) showed that the top of the Jeerinah Formation is enriched in organic matter. This enrichment is coincident with an increase in both reactive iron (Fe_{HR})/total iron (Fe_T) and pyrite iron (Fe_{PY})/Fe_{HR} ratios. As a $Fe_{HR}/Fe_T > 0.38$ is indicative of anoxic conditions (Raiswell and Canfield, 1998) and a $Fe_{PY}/Fe_{HR} < 0.8$ (Scott et al., 2011) are indicative of euxinic conditions they concluded that the upper part of the Jeerinah Formation was deposited under euxinic conditions. They also reported low Mo levels in the top of the Jeerinah formation; which was interpreted to be due to a lack of oxidative weathering of sulfides to provide the source for Mo. ^{34}S and ^{33}S isotope analyses were also reported in their study, these analyses suggested that the pyrite was of sedimentary origin.

The Mt. McRae Shale has been the focus of extensive research including detailed trace metal geochemical (Anbar et al., 2007), C and S isotope (Kakegawa et al., 1998; Kaufman et al., 2007) and iron speciation analyses (Raiswell et al., 2011). Many of these studies have been used to argue that a significant period of oxygen production occurred during the deposition of the Mt. McRae Shale, prior to the GOE. Anbar et al. (2007) showed that there was a coincident and substantial increase in organic carbon, Mo and Re content near the top of the Mt. McRae Shale. The increase in these elements is indicative of the presence of oxygen in the atmosphere, because in sedimentary rocks their primary source is the weathering of sulfides, which requires the presence of oxygen to proceed. In a companion study, Kaufman et al. (2007) reported negative $\delta^{34}S$ values coincident with the high organic C, Mo and Re, reported by Anbar et al. (2007). This negative $\delta^{34}S$ suggests bacterial reduction of sulfate, which may be related to cyanobacteria creating O_2. These results correlate with similar data from contemporaneous African shales (Gamohaan and Kuruman formations) suggesting that O_2 production may have been global in scale (Kaufman et al., 2007). Iron speciation analyses of the same samples were then used to show that there has been a dynamic history of Fe input into the Mt. McRae Shale due to changes in the amount of Fe supplied by hydrothermal sources into the ocean. The lower part of the Mt. McRae Shale was found to be dominated by iron-rich conditions, while the upper Mt. McRae shale was found to be dominated by S-rich conditions (Raiswell et al., 2011).

5.2.2 The incorporation of trace elements into pyrite

Sedimentary pyrite is incorporated into diagenetic pyrite by precipitation; co-precipitation; chemical or physical adsorption and redox reactions at the pyrites surface (Berner et al., 2013; Dellwig et al., 2002). By combining sequential extractions, detailed mineralogy (Gregory et al., 2013) and LA-ICPMS (Gregory, in press) it was shown that in high element environments adsorption, and competition between different elements for adsorption sites on pyrite, is the most significant factor.

Factor analyses of trace elements in pyrite from the Posidonia shale have shown that the trace-element in pyrite can be subdivided into 4 groups based on their method of occurrence, these are: heavy metals (Cu, Ni, Co, Pb, Bi and Tl); oxyanionic elements (As, Mo and Sb); elements partitioned into sub-microspic sphalerite (Zn and Cd) and elements related to organic or silicate impurities (Ga and V). Arsenic in particular has been well investigated and its speciation in pyrite has been linked to the type and amount of other trace elements that can be incorporated into pyrite (Deditius et al., 2008). The uptake of trace elements similar to Fe (II) (i.e. Co, Ni, Cu, Zn) is enhanced by the substitution of As for S. However, the substitution of As for Fe enhances the uptake of larger cations (i.e. Au(I), Ag(I) and Pb(II)) (Deditius et al., 2008). Gold in pyrite has been found to be particular strongly dependant on the amount of As with in pyrite (Reich et al., 2005).

5.2.3 Geology of the Hamersley Basin

The Fortescue and Hamersley basins comprise a 2775−2450 Ma sequence of supracrustal rocks that unconformably overlie the southern two thirds of the 3530−2830 Ma Pilbara Craton in the northern part of Western Australia. Compared to other rocks of this age, the volcanic and sedimentary rocks of these Neoarchean−Paleoproterozoic basins have been relatively unaffected by regional metamorphism, with grades ranging from prehnite-pumpellyite facies in the north to lower greenschist facies in the south (Trendall, 1990). This makes these basins ideal places to study late Archean and early Proterozoic ocean chemistry.

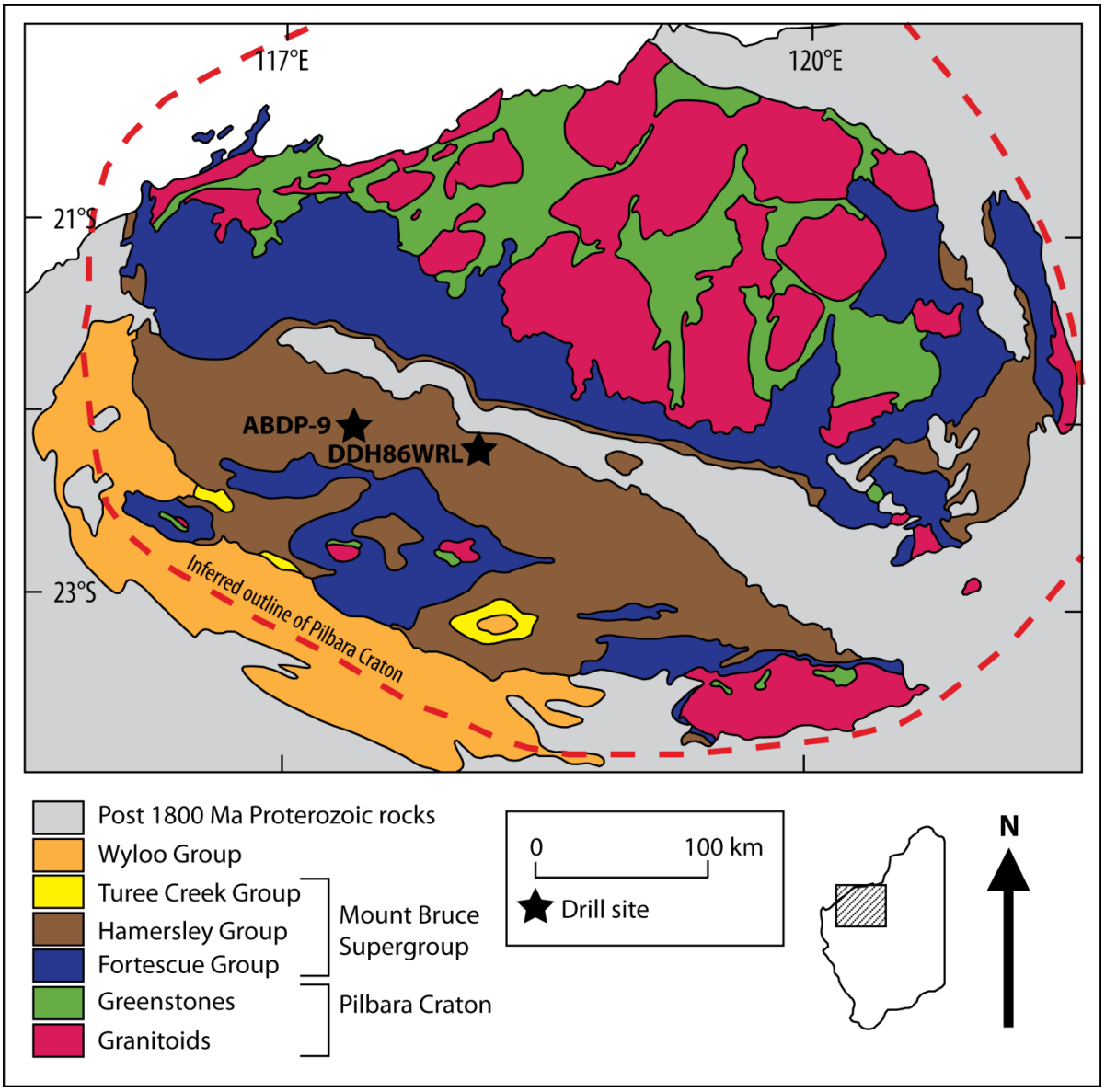

Figure 5.1: Regional Geology of the Pilbara Craton and location of ABDP9 and DDH86WRL1 modified after Hickman and Van Kranendonk (2012).

For this study we focus on sedimentary rocks from the top of the Fortescue Group and the lower and central sections of the Hamersley Group (Figures 5.1 and 5.2). The Jeerinah Formation forms the top of the Fortescue Group and its base is defined by the Maddina Formation. The Jeerinah Formation includes carbonaceous shale with trace to percent-range pyrite, occurring as bands, nodules and disseminations along bedding. The grain size is generally silt sized, however some beds are up to sand size. The shales are overlain by the Marra Mamba Iron Formation, a mixed sequence of BIF, dolomite and minor shales at the base of the Hamersley Group (Trendall, 1990). The Hamersley Group is made up of a sequence of BIF, shale, and sedimentary carbonate rocks.

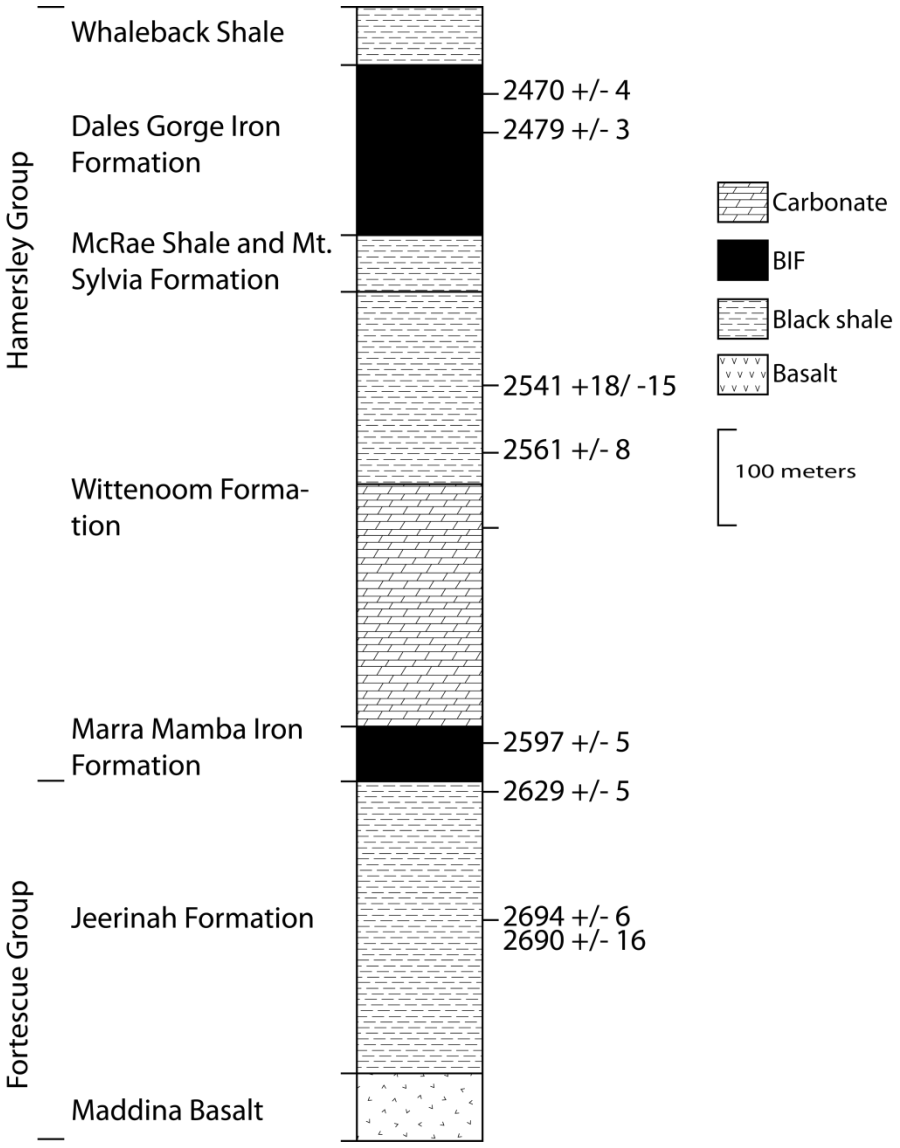

Figure 5.2: Stratigraphic section of the sedimentary rocks from the Hamersley Group and the top of the Fortescue Group, modified after (Hassler et al., 2011).

The 2597−2565 Ma Paraburdoo Member of the Wittenoom Formation is the lowest sequence in the Hamersley Group that was investigated in this study. It consists predominantly of carbonate rocks but includes thin units of sandstone and shale. Medium-grey, fine-grained dolomitic sandstone is interbedded with 80% fine-grained carbonaceous layers at the bottom of the member, decreasing to 20% fine-grained black to dark grey carbonaceous shale interbedded with medium grey dolomitic sandstone present at the top of the member. Pyrite is rare, occurring in bands at the contacts between the carbonaceous and sandy layers. The Paraburdoo Member is overlain by the Bee Gorge Member, which includes interbedded fine-grained black to dark grey siltstone, medium to light grey fine sandstone and carbonate. The sandy intervals decrease in frequency and thickness up section, from approximately 50% at the base of the interval to 20% of the unit at the top. The Bee Gorge Member contains approximately 1% pyrite which occurs as thin beds and small (1-2 mm) concretions. In the top half of the interval, there are two 10 m thick zones of silicification that have bands of pyrite at the margins. Overlying the Bee Gorge Member is the Mt Silvia Formation, which is

predominantly carbonaceous shale interspersed with minor BIF. The shale beds are predominantly black to dark grey, fine-grained with 10% lighter coloured fine sandy layers. Near the BIF these sandy beds are variably silicified. The shale intervals contain 1 to 5% pyrite occurring predominantly as thin bands and small (2-3 mm) concretions that tend to increase in abundance towards the base of the interval. Due to the close association between the pyritic shale and BIF only one sample (Brunos Band) from the top of the Mt. Silvia Formation was analysed. This is because the focus of the study was to determine the chemistry of the ocean during deposition of the carbonaceous sediments. A detailed discussion of ocean chemistry during deposition of the BIF units of the Hamersley Group is beyond the scope of this study and will be examined in future work.

The uppermost unit examined is the Mt. McRae Shale. It is made up of well laminated carbonaceous sedimentary rocks accumulated well below wave base (Anbar et al., 2007). The unit is generally fine-grained with minor fine sandy beds increasing from 5 to 40% towards its top. These sand-rich beds are lighter in colour than the more organic-rich fine grained intervals. Pyrite is found as nodules, layers, and fine disseminations throughout the unit, although its abundance tends to increase progressively up section. For a more detailed description of the geology of the Mount Bruce Supergroup please see Appendix 7 and references therein.

5.3 Methods

5.3.1 Drill Holes

Two drill holes were examined in the course of this study. The first was DDH86WRL1 (Figure 5.3), which intersected the Jeerinah Formation and was collared at 118°12.6'E and 22°11'S. The purpose of the hole was exploration for Au/U paleoplacer deposits where the sedimentary rocks have an unconformable contact with the underlying granite/greenstone sequences, though no mineralisation was discovered. The second drill hole examined was ABDP9 (Figure 5.4), which intersected the Mt. McRae Shale, Bee Gorge Member and Paraburdoo Member, it was collared at 21°59.5'S and 117°25.2'E (Anbar et al., 2007). The drill hole was completed as part of the Archean Biosphere Drilling Program (ABDP) and was one of ten holes drilled to obtain core free of modern contamination and weathering effects to

determine the nature of Archean life and its environment. Logs of the drill holes examined in this study are contained within Appendix 8.

5.3.2 Analytical Methods

Approximately 10-20 cm long quarter core samples were selected from representative horizons within the drill holes (rational for the selection of sample intervals is contained within Appendix 9). The quarter core was cut again to provide two eighth cores, with one milled using a chromium steel mill for bulk sample geochemical analysis while the remaining eighth was used to prepare polished laser mounts for LA-ICPMS and SHRIMP analyses. Laser mounts were created from a 2.5 cm diameter piece of core that is mounted in epoxy resin and polished to 1 µm diamond polishing compound.

5.3.3 Whole rock analyses

Trace and major element compositions were determined using a combination of ICP-MS and XRF. All analyses were conducted at the School of Earth Sciences, University of Tasmania. Trace metal analyses were conducted by first digesting a fraction of the rock powder in a PicoTrace high pressure digestion system prior to being analysed with an Agilent 7700x ICP-MS. Four secondary rock standards (GSD-12a, TasASa, GSR-6aa, GSR-6ba) and blanks of acid solutions were analysed along with the unknowns to insure quality control. Major elements were analysed using a PANalytical Axios Advanced X-Ray Spectrometer. A mixture of 0.500 g of sample, 4.500 g 12-22 flux (lithium teraborate-metaborate mix) and 0.0606g $LiNO_3$ were heated at 1100°C in a 5%Au/5%Pt crucible to form 32 mm fusion discs. The discs were then analysed using a 4 kW maximum x-ray tube with an Rh anode window. PANalytical super-Q software with classic calibration model and alpha coefficients were used to correct for mass absorption. Calibration of the system was done using pure element oxide mixes in pure silica as well as a variety of international and Tasmanian reference rocks. Quality control was maintained by analysing TASBAS, TASDIOR, TASMONZ, GXR4, GSP-2 and TASGRAN reference rocks as unknowns.

5.3.4 Laser Ablation-ICPMS pyrite analysis

Recent studies have used the results of LA-ICPMS trace element analyses of sedimentary pyrite to infer the chemical conditions of ancient oceans (Large, in prep; Chapter 4). This technique has significant advantages; many elements can be analysed at lower detection limits by LA-ICPMS (Chapter 3), different pyrite generations can be analysed separately allowing for chemical analyses of diagenetic pyrite to be analysed from deposits that have undergone significant degrees of metamorphism (up to mid-greenschist facies) (Large et al., 2011; Large et al., 2007; Thomas et al., 2011) and very fine scale differences in trace metal composition between different stratigraphic layers or parts of nodules can be determined. Here we have presented both whole rock and LA-ICPMS pyrite analyses and endeavour to show that both methods can produce similar and complimentary conclusions.

The trace element content of diagenetic pyrite was analysed by laser microprobe at CODES, University of Tasmania. A 213 nm solid-state laser microprobe (UP213, NewWave Research) coupled to an Agilent 7500a quadruple mass-spectrometer and a 193 nm solid-state laser microprobe (UP193ss, NewWave Research) coupled to an Argilent 7700s quadruple mass-spectrometer were used. Beam sizes of 10 - 35 µm were employed, depending on pyrite size. The ablation used a pulse rate of 5 Hz and beam fluences of approximately 3.5 J/cm^2 for UP213 and 2 J/cm^2 for UP193ss. The pyrite was ablated in a pure He atmosphere that was introduced into the ablation cell at 0.8 l/min immediately past the ablation point. The He carrier gas was mixed with Ar (0.85 l/min) to improve the efficiency of aerosol transport. A 30 second laser-off period to measure background and a 60s laser-on period for the analyses were implemented for each analysis. The production of doubly charged species and of molecular oxide species were maintained at levels below 0.2%. Data was reduced based on the methods proposed by Longerich et al. (1996). Corrections were not applied for the effects of low levels of molecular oxide, doubly charges ions or interfering species that were introduced into the analytes signal as none of these were at significantly high levels. Due to porosity of some of the pyrite analysed variable amounts of matrix material was also ablated. To correct for the presence of some matrix contamination all major elements were analysed to approximate the amount of matrix ablated. Several matrix spots were also analysed near the pyrite. These data were then used to determine the composition of the pyrite using a standard mass balance calculation. The same three calibration standards were used for all analyses: STDGL2b2 (Danyushevsky et al., 2011) for chalcophile and siderophile

elements; GSD-1G (Guillong et al., 2005) for lithophile elements; and pure pyrite for the quantification of sulfur.

5.3.5 S isotope analyses

Pyrite samples chosen to be representative of their respective stratigraphic positions were analysed for $^{32}S^-$, $^{33}S^-$ and $^{34}S^-$ using a SHRIMP-SI at the Australian National University (ANU). Prior to analysis, pyrite samples of interest were removed from earlier mounts that had been analysed with LA-ICPMS and combined into a new 25 mm diameter epoxy mount. These mounts were coated in 0.01 µm of gold to dissipate charge build up during analysis and to carry -10 kV so that the ions coming off the surface have the correct potential. The mounts were then placed in a vacuum (10^{-6} Pa). A primary 10 keV Cs^+ beam was focussed to 25 µm on the target pyrite. The impacting Cs^+ ions are accelerated to +5 kV in the primary column while the sample surface is held at -10 kV, making the impact energy 15 kV. The area surrounding the analysis spot was then pre-ablated, and sputtered for 120 s to ensure no contamination prior to data acquisition. The analysis consists of 10 cycles of 10 s data acquisition intervals. The isotopes $^{32}S^-$, $^{33}S^-$ and $^{34}S^-$ were analysed with respective count rates of 630 MHz, 5 MHz and 28 MHz. The different S isotopes were detected and measured using Faraday cups (Ireland et al., 2008). Approximately 2 analyses of the standard (Ruttan pyrite (Whitehouse, 2013)) were conducted for every 7 analyses.

5.4 Results

5.4.1 Whole Rock Geochemistry

Enrichment factors for whole rock geochemical data (V, U, Mo, Co, Cr, Ni, Cu, Zn, Cd) from DDH86WRL1 and ABDP9 are presented in Figures 5.3 and 5.4, and the Fe/Al ratios are presented in Figure 5.5. Enrichment factors are calculated to reduce the element variations due to differing sedimentary facies. This is done by normalising the data to Al and then dividing the result by the metal-aluminium (Me/Al) ratio for average upper crust (Tribovillard et al., 2006). This can be expressed using the following equation: $EF_{Me} = (Me_x/Al_x)/ (Me_{ave}/Al_{ave})$; where EF_{Me} is the enrichment factor for the metal of interest; Me_x is the amount of the metal of interest in the unknown sample; Al_x is the amount of Al in the unknown sample; Me_{ave} is the amount of metal in average upper crust and Al_{ave} is the amount

of Al in average upper crust. In this study, two sources for average upper crust values are used. Condie (1993) is used for U, V, Cr, Co and Ni because these data are of juvenile crust from 3.5-2.5 Ga, which corresponds to the age of the sedimentary rock used in this study. Composition of the upper crust from Wedepohl (1995) was used for Mo, Cu, Zn and Cd because these data were not available in Condie (1993). A summary of the whole rock analyses is provided in Appendix 10.

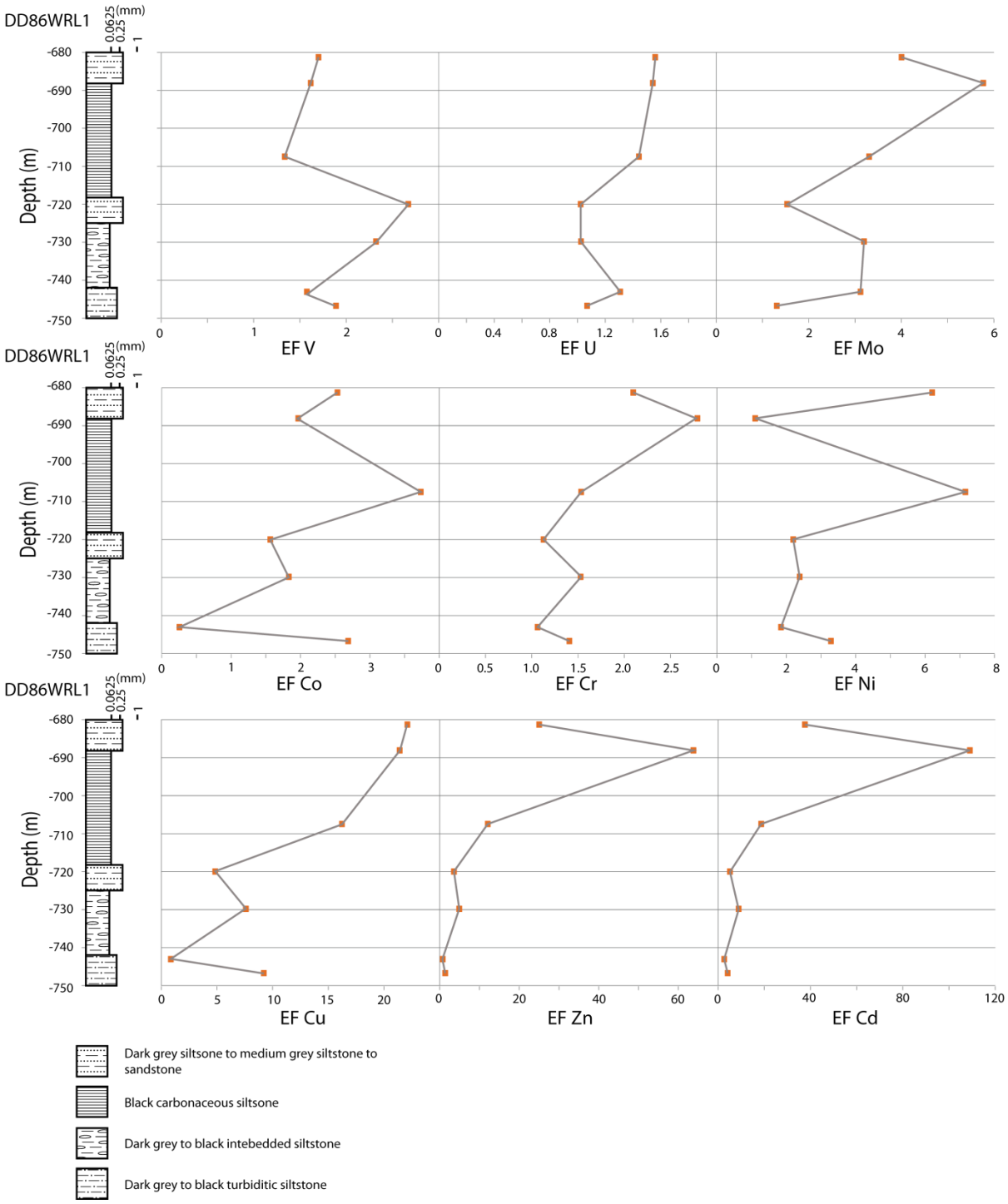

Figure 5.3: Enrichment factors of V, U, Mo, Co, Cr, Ni, Cu, Zn and Cd varying with depth in drill hole DDH86WRL1. Simplified stratigraphic sections are presented on the left side of the figure, for detailed stratigraphy please see Appendix 8.

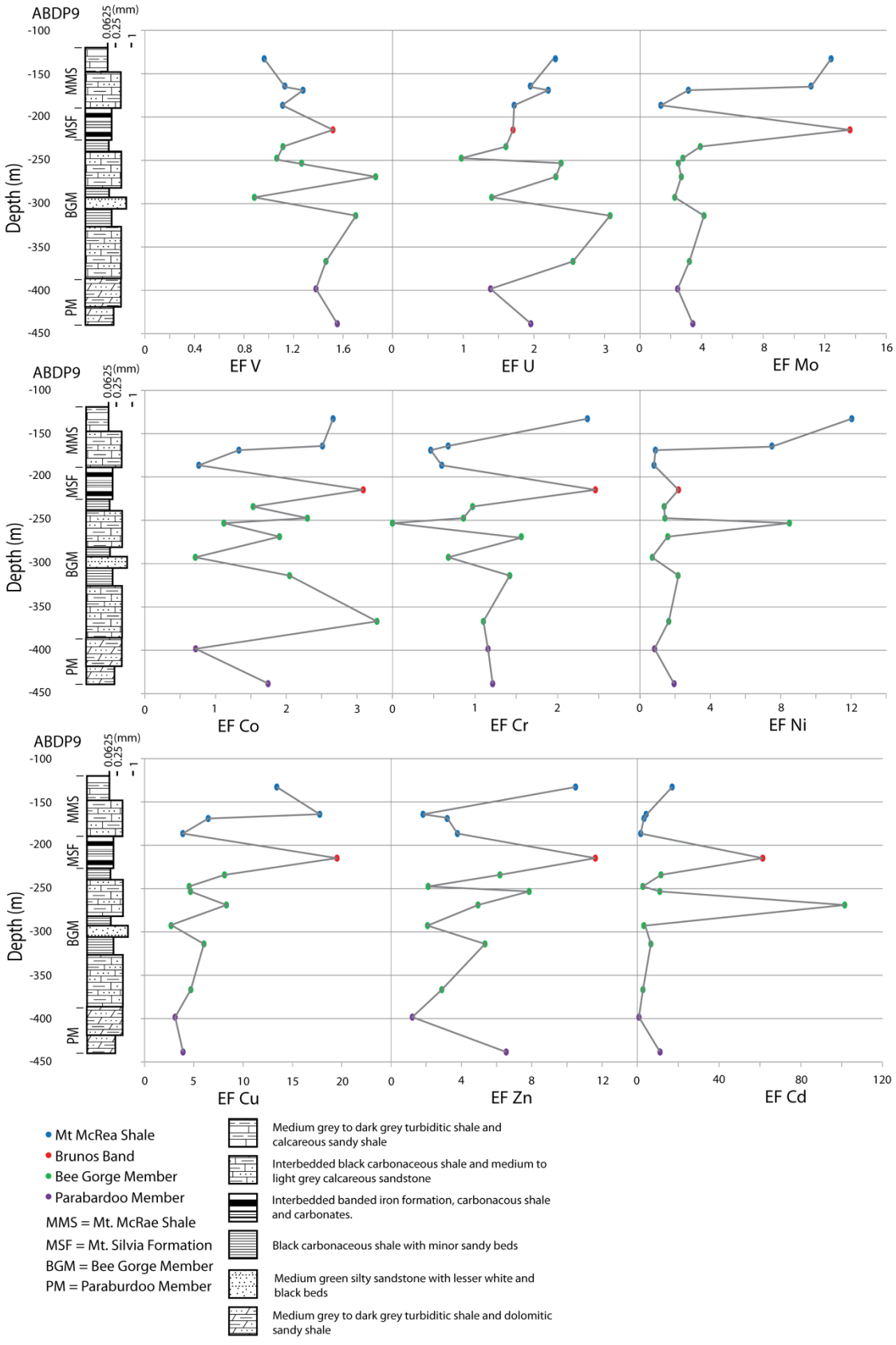

Figure 5.4: Enrichment factors of V, U, Mo, Co, Cr, Ni, Cu, Zn and Cd varying with depth in drill hole ABDP9. Member boundaries, carbonate variety and content are modified from Buick, unpublished data. Simplified stratigraphic sections are presented on the left side of the figure, for detailed stratigraphy please see Appendix 8.

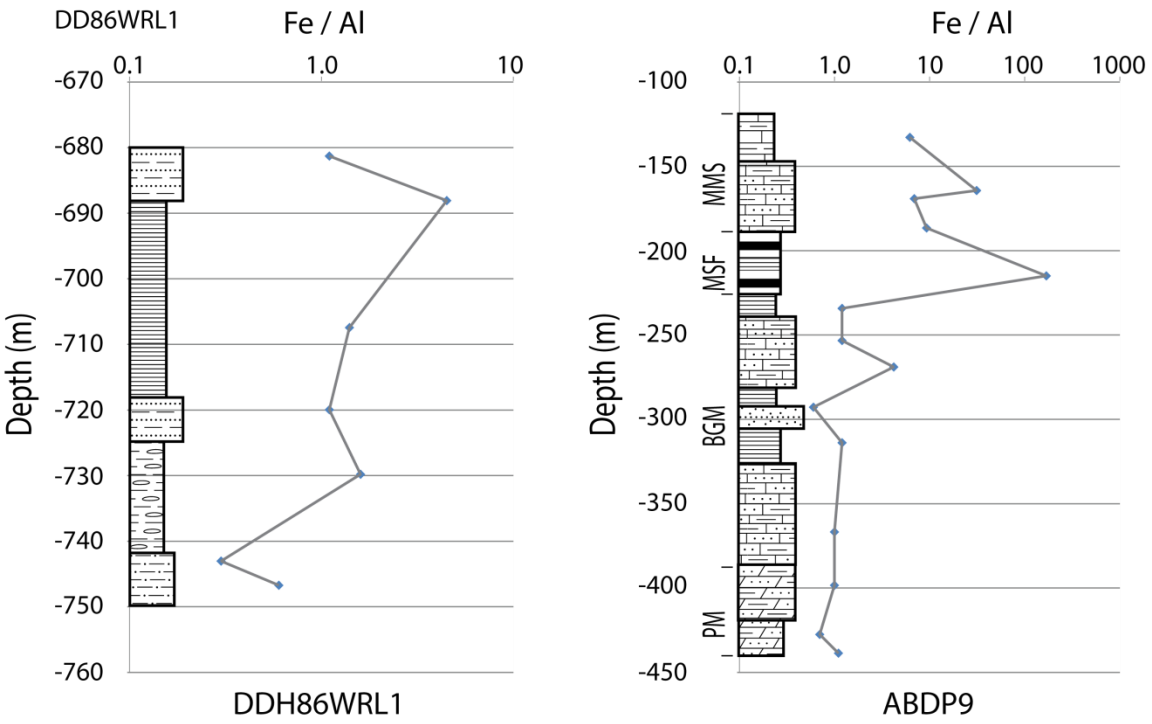

Figure 5.5: Fe/Al ratios varying with depth of DDH86WRL1 and ABDP9. Member boundaries, carbonate variety and content are modified from Buick, unpublished data. Simplified stratigraphic sections are presented on the left side of the figure, for detailed stratigraphy please see Appendix 8.

5.4.1.1 Drill hole DD86WRL1

The enrichment factors for DD86WRL1 are plotted down hole in Figure 5.3. Except for V and Co, all of the trace metals examined show a general increase up section through the central and upper parts of the Jeerinah Formation in this drill hole. The U enrichment factor (EF_U) displays average shale contents (1.02-1.31) in the lower part of the section and progressively increases slowly up section to a maximum of 1.65. Mo enrichment factors (EF_{Mo}) are consistently between 1.31 and 3.31 throughout the drill hole, except at the top of the Jeerinah Formation where two samples have elevated Mo (EF_{Mo} of 5.77 and 4.01).

Cr and Cu have similar enrichment factor (EF_{Cr} and EF_{Cu}) trends, with a general increase in younging direction (EF_{Cr} from 1.06 to 2.79 and EF_{Cu} from 0.87 to 22.11). The enrichment factors for Ni and Co (EF_{Ni} and EF_{Co}) are quite erratic varying from 0.26 to 1.11 and 3.73 to 11.67 respectively. However, there is a general increase in Ni and Co towards the top of the

section. The enrichment factors for Zn and Cd start close to average continental crust levels and increase to maximums of 63.81 and 109.09 for EF_{Zn} and EF_{Cd} respectively near the top of the Jeerinah Formation. Two different domains are evident in the V enrichment factor (EF_V) in the Jeerinah Formation. The lower Jeerinah Formation shows a generally increasing trend up to a maximum EF_V of 2.67, before dropping to mild enrichments (1.34 to 1.75). The Fe/Al ratios in the Jeerinah Formation are generally near crustal abundance and increase slowly up section (Figure 5.5).

5.4.1.2 Drill hole ABDP9

Enrichment factors for the upper part of ABDP9 are plotted down hole in Figure 5.4. Similar to the Jeerinah Formation samples, there is a tendency for trace elements of interest (except V) to exhibit a general increase up section through the Paraburdoo Member to the middle of the Bee Gorge Member. A similar pattern of increase in trace element enrichment factors with younging direction is present in the overlying Mt. McRae Shale, though the enrichments tend to be much greater. These patterns are exhibited in U as three loosely defined domains at 450-300 m, 300-250 m and 250-100 m. In the lower section (450-300 m), EF_U increases to a maximum of 3.08 before dropping above 300 m to 1.40 and increasing again to 2.38 (250 m). In the Mt. McRae Shale (200 m) the EF_U drops again to 0.98 and increases steadily to 2.31. The EF_{Mo} exhibit a similar rise, drop and rise again pattern from the base of the sequence to the BIF, while the Mt. McRae Shale shows a marked increase in EF_{Mo} (11.11 - 12.41).

In the Paraburdoo and Bee Gorge members both EF_{Co} and EF_{Cr} behave erratically, ranging from 0.72 to 3.28 and 0 to 2.36 respectively. Within the Mt. McRae Shale there is an increase of trace element content with younging to a maximum of 2.66 (EF_{Co}) and 2.36 (EF_{Cr}) respectively at the top of the section. Generally EF_{Ni} is consistent for most of the section ranging from 0.71 to 1.94 until the upper part of the Mt. McRae Shale where the EF_{Ni} rapidly increases to a max of 12.04. The Cu enrichment factor (EF_{Cu}) increases slightly with younging before dropping rapidly at the BIF and rapidly increasing at the top of the Mt. McRae Shale (maximum EF_{Cu} of 17.78). EF_{Cd} varies in a similar manner and reaches a maximum of 17.07 at the top of the Mt. McRae Shale, except for a very anomalous sample (EF_{Cd} 101.54) at 269 m. The Zn enrichment factor (EF_{Zn}) varies erratically throughout the drill hole from 1.22 to 10.49. Vanadium enrichment factors (EF_V) differ somewhat from

other elements and tend to fall within two domains. EF_V within the Paraburdoo Member and mid- to lower part of the Bee Gorge Member exhibits a general increase from lower in the sequence to a maximum (1.86) at 267 m depth, similar to many of the other elements. However, at the top section of the Bee Gorge Member and the Mt. McRae Shale, the EF_V is erratic and approximates average crustal abundance (EF_V ranges from 0.96 to 1.28). In the Paraburdoo Member through the Bee Gorge Member the Fe/Al ratios are low near 1, with a general increase up section. As expected the BIF sample is very high in Fe/Al ratio due to its high concentration of Fe oxide minerals. The McRae Shale is also elevated relative to the lower shale sequences with Fe/Al ratios near 10.

5.4.2 LA-ICPMS pyrite chemistry

5.4.2.1 DD86WRL1

Laser Ablation-ICPMS data for samples from drill hole DD86WRL1 are presented and summarised in Table 5.1, Figure 5 and Appendix 10. 6 (Mo, Ni, Co, As, Cu, Zn, Ag, Te and Au). The whole rock geochemical data, and the whole rock data normalised to total S for the 10 -20 cm interval from which the laser mount was taken, are also presented in this figure and/or table in order to compare the two techniques. Sulfur normalised values are provided because when high degrees of pyritization are present, many trace metals become scarce due to an insufficient supply relative to the amount of pyrite formed, yielding lower trace metal contents in pyrite than otherwise expected. This is due to pyrite being removed from the water column by the higher amounts of pyrite formed there and/or excess pyrite forming in the sediment causing a higher pyrite to trace element available for incorporation ratio resulting in relatively low trace element contents in pyrite.

The samples from the Jeerinah Formation can be split into 3 different domains: an oldest domain containing 2 samples from 743.05-746.74 m; a middle domain containing 3 samples from 707.46-729.82 m; and a youngest domain containing 2 samples from 681.29-688.09 m. The samples from the oldest domain have distinctly different trace element concentrations from the rest of the formation. The oldest domain is strongly elevated in Mo, Ni, Co, As, Zn, Ag, Te and Au while the middle domain is depleted in many of these same elements. In the middle domain, Mo, As and Cu start at a moderate level, drop to a low, before increasing to a maximum at 707.46 m. The contrary is observed for Ni, Co, Zn, Ag and Au, where most of

the these elements are at a minimum at 729.82 m before increasing and then dropping again at 707.46 m. Only Te shows an increasing trend across this interval. The youngest domain exhibits an increase in trace element content from a low at 688.09 m to a high at 681.29 m in every trace element of interest except Zn. Zinc has significant overlap in the box plot (Figure 5.6), making it difficult to determine with certainty whether there is a general increase up section as well.

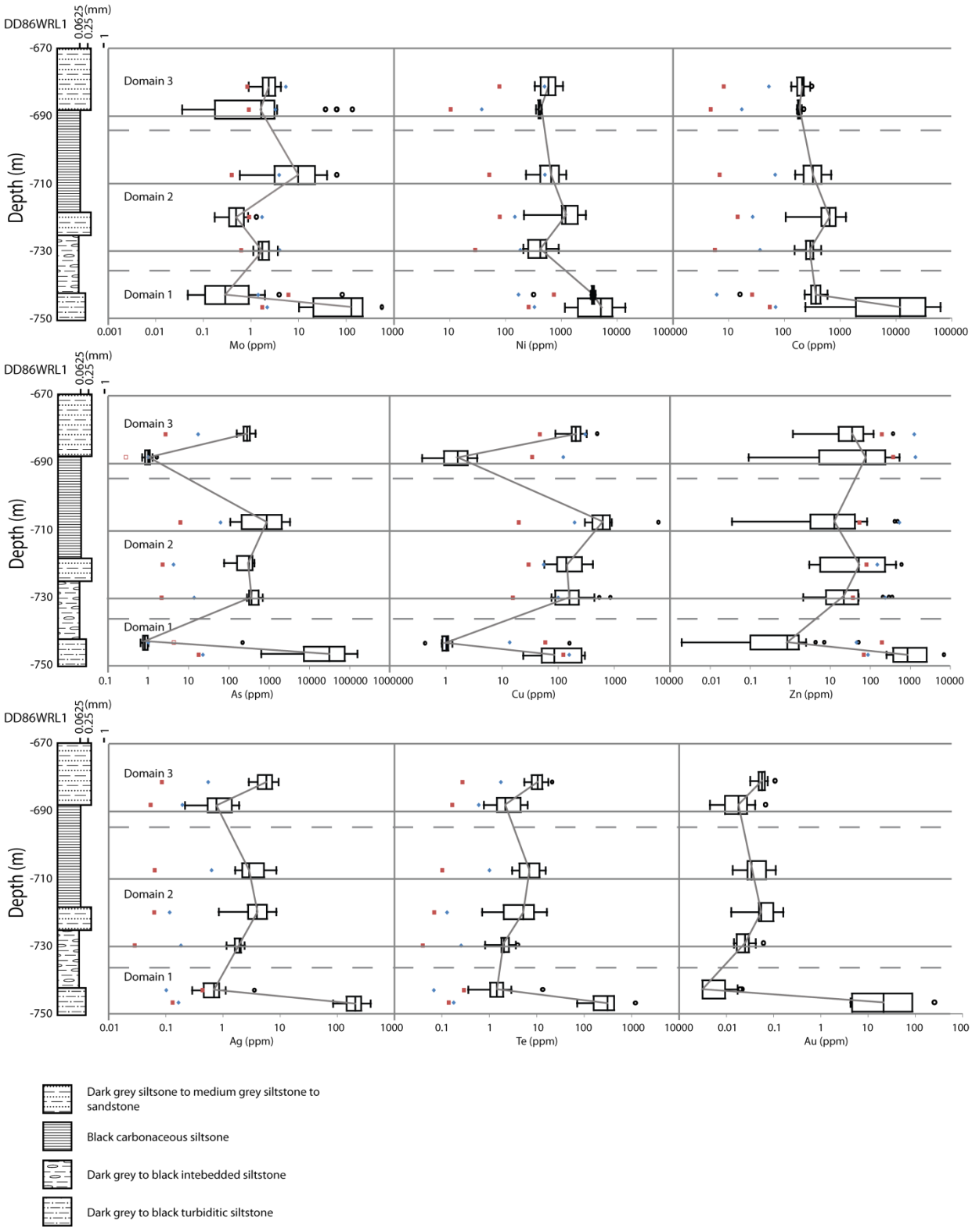

Figure 5.6: Changes in the content of Mo, Ni, Co, As, Cu, Zn, Ag, Te and Au in pyrite with depth in drill hole DDH86WRL1. The total whole rock content and total whole rock content normalised to S are represented as blue diamonds and red squares respectively. Simplified stratigraphic sections are presented on the left side of the figure, for detailed stratigraphy please see Appendix 8.

Table 5.1: Medians of LA-ICPMS data for Drill hole DD86WRL1

Depth of sample (m)	Mo (ppm)	Ni (ppm)	Co (ppm)	As (ppm)	Cu (ppm)	Zn (ppm)	Ag (ppm)	Te (ppm)	Au (ppm)
-681.29	2.3	623	229	276	203	35.8	5.88	10.98	0.058
-688.09	1.6	427	185	1.06	1.60	78.5	0.78	2.13	0.019
-707.46	9.7	687	336	893	617	12.7	2.97	6.83	0.035
-719.98	0.5	1251	674	304	137	53.0	4.02	5.12	0.056
-729.82	1.7	444	303	355	155	22.2	1.98	2.11	0.026
-743.05	0.3	3884	380	0.82	1.01	0.85	0.71	1.51	(0.003)
-746.74[Y]	126.7	5416	12396	29268	84	863	216.88	303.94	22.18

*Note bracketed number reflects where the median is below the detection limits, the value given is 50% of the average detection limit for that sample.
[Y] indicates the pyrite is most likely of hydrothermal origin

5.4.2.2 Drill hole ABDP9

Laser Ablation-ICPMS data for samples from drill hole ABDP9 are presented in Figure 5.7 (Mo, Ni, Co, As, Cu and Zn) and Figure 5.8 (Ag, Te and Au) and medians of these data are shown in Table 5.2. A summary of all the laser data for ABDP9 is in Appendix 10. There are two phases of a general increase in the trace element content in pyrite up section in ABDP9. The first of these phases occurs from 427.56 m to 313.92 and the increases are apparent in Ni, Co, As, Cu, Ag, Te and Au; however, some elements drop after 366.74 m. The increase is less noticeable in the second phase between 292.82 m and 234.24 m, and is only apparent in Ni and Ag while the other elements are relatively equal. This general trend does not hold for the oldest sample which is enriched in Ni, Co, Ag, Te and Au. Also the sample at 313.92 m does not fit the general trend in the data as it is lower in (Co, Cu, Ag, Te and Au) than expected by the general trend. The Zn content of pyrite follows a similar trend, generally increasing up section before decreasing above the BIF. However, there is a wide range of values in Zn content and it is difficult to say with confidence what the trend is across the section.

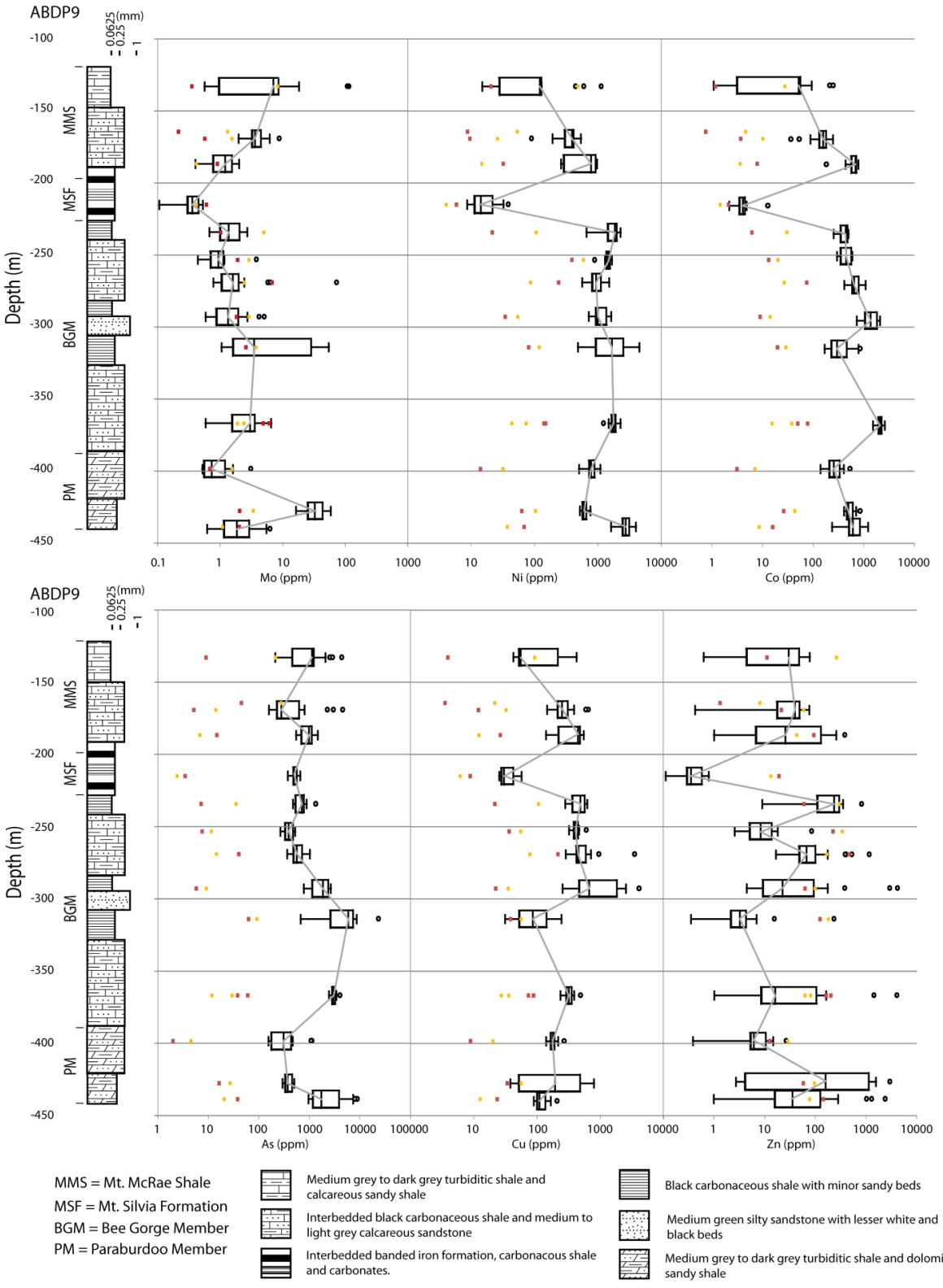

Figure 5.7: Changes in the content of Mo, Ni, Co, As, Cu and Zn in pyrite with depth in drill hole ABDP9. The total whole rock content and total whole rock normalized to S are represent as blue diamonds and red squares respectively. Member boundaries carbonate variety and content are modified from Buick, unpublished data. Simplified stratigraphic sections are presented on the left side of the figure, for detailed stratigraphy please see Appendix 8.

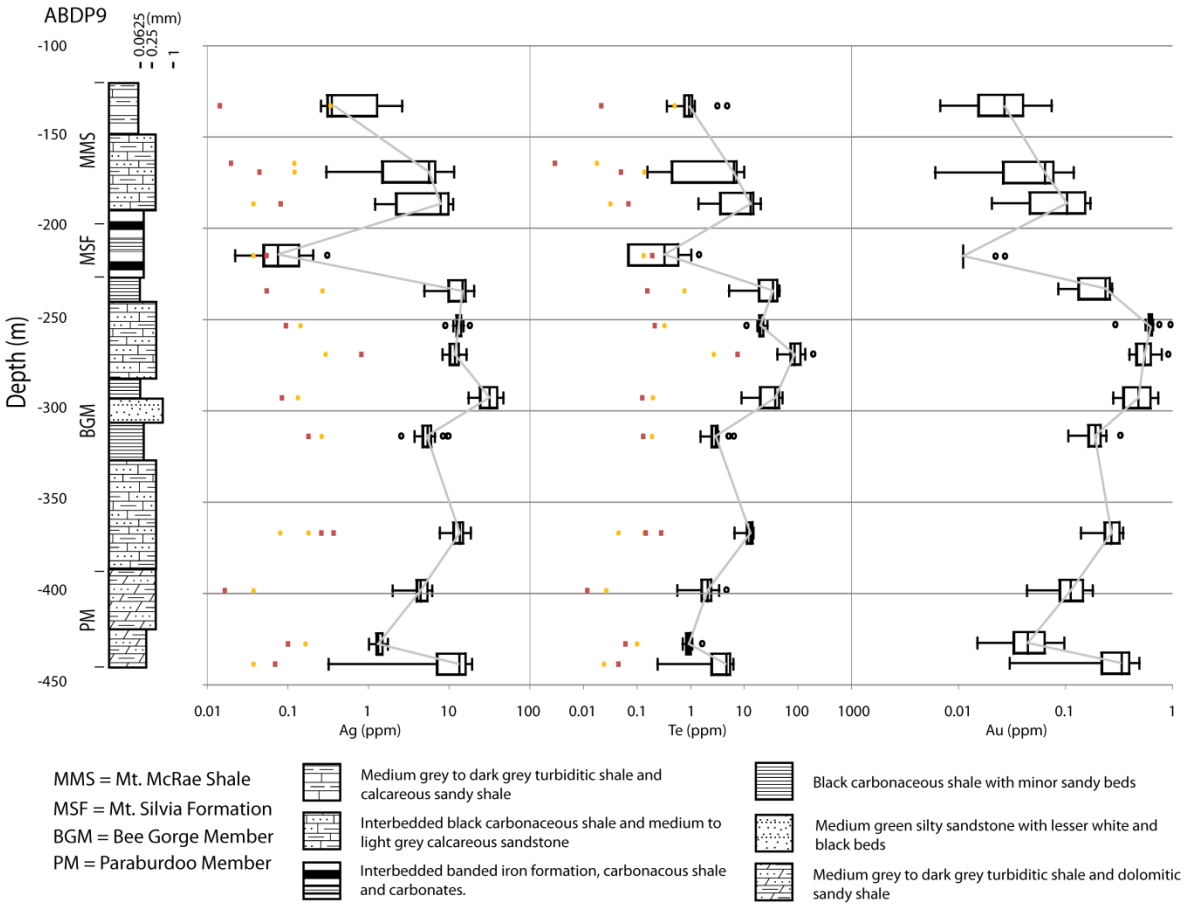

Figure 5.8: Changes in the content of Ag, Te and Au in pyrite with depth in drill hole ABDP9. The total whole rock content and total whole rock normalized to S are represent as blue diamonds and red squares respectively, with the exception of Au which wasn't analysed in whole rock. Member boundaries carbonate variety and content are modified from Buick, unpublished data. Simplified stratigraphic sections are presented on the left side of the figure, for detailed stratigraphy please see Appendix 8.

5.4.3 Sulfur Isotopes

A total of 111 SHRIMP-SI analyses of $\Delta^{33}S$ and $\delta^{34}S$ were undertaken of sedimentary pyrite within the Mt. McRae Shale, Bee Gorge Member, Paraburdoo Member and Jeerinah Formation. These data are presented in Figure 5.9 and Appendix 10 and data through the cores are plotted in Figures 5.10 and 5.11.

Table 5.2: Median values of LA-ICPMS analyses of trace metals in pyrite from ABDP9.

Depth of sample (m)	Mo (ppm)	Ni (ppm)	Co (ppm)	As (ppm)	Cu (ppm)	Zn (ppm)	Ag (ppm)	Te (ppm)	Au (ppm)
-132.87	7.0	123	52	1111	55	29.5	0.35	0.91	0.027
-169.16	3.6	381	157	275	239	39.3	5.48	6.06	0.062
-186.56	1.5	836	698	885	463	22.0	7.82	14.32	0.126
-214.96	0.4	14	4	485	30	0.35	0.08	0.32	(0.011)
-234.24	1.3	1908	435	697	512	234	14.39	33.57	0.237
-253.32	0.9	1520	440	384	401	8.25	12.99	20.17	0.624
-269.01	1.6	964	634	517	449	66.8	11.59	87.56	0.548
-292.82	1.4	1027	1343	1824	662	22.3	31.23	36.90	0.479
-313.92	3.7	1705	294	5778	85	3.20	5.32	2.99	0.191
-366.74	3.0	1827	2098	2908	315	16.1	13.34	12.74	0.269
-398.39	0.7	798	252	304	177	6.08	4.34	2.04	0.112
-427.56	33.7	605	489	369	191	158	1.29	0.95	0.044
-438.62	1.9	2873	600	1697	111	35.0	13.17	4.52	0.334

Most of the Jeerinah Formation varies from -3 to +4 $\Delta^{33}S$ and -2 to +5 $\delta^{34}S$. The majority of the Paraburdoo Member samples range from -2 to 0 $\Delta^{33}S$ and 5 to 15 $\delta^{34}S$, except for 5 analyses which have $\Delta^{33}S$ between 0 and 4 and $\delta^{34}S$ between 7 and 16. The data for the Bee Gorge Member are consistent, with the majority of the data belonging to one group with $\Delta^{33}S$ ranging between -1 and 2 and $\delta^{34}S$ ranging between -10 and 10. The data obtained from the Mt. McRae Shale shows two distinct populations. One set has high, positive $\Delta^{33}S$ shifts (7 to 12) and relatively high $\delta^{34}S$ (ranging from 9 to 14). The second population has a very different signature that is similar to that of the Paraburdoo Member, with the majority of the data falling between 0 and -3 for $\Delta^{33}S$ and 0 and 21 for $\delta^{34}S$.

The wide range in $\delta^{34}S$ in some of the Mt. McRae Shale samples is due to variations in isotope concentration across pyrite nodules, with higher $\delta^{34}S$ in rims and lower $\delta^{34}S$ in cores (Figure 5.12A). This relationship is not observed in the underlying Jeerinah Formation (Figure 5.12B). The $\Delta^{33}S$ isotopes do not vary systematically across the pyrite nodules.

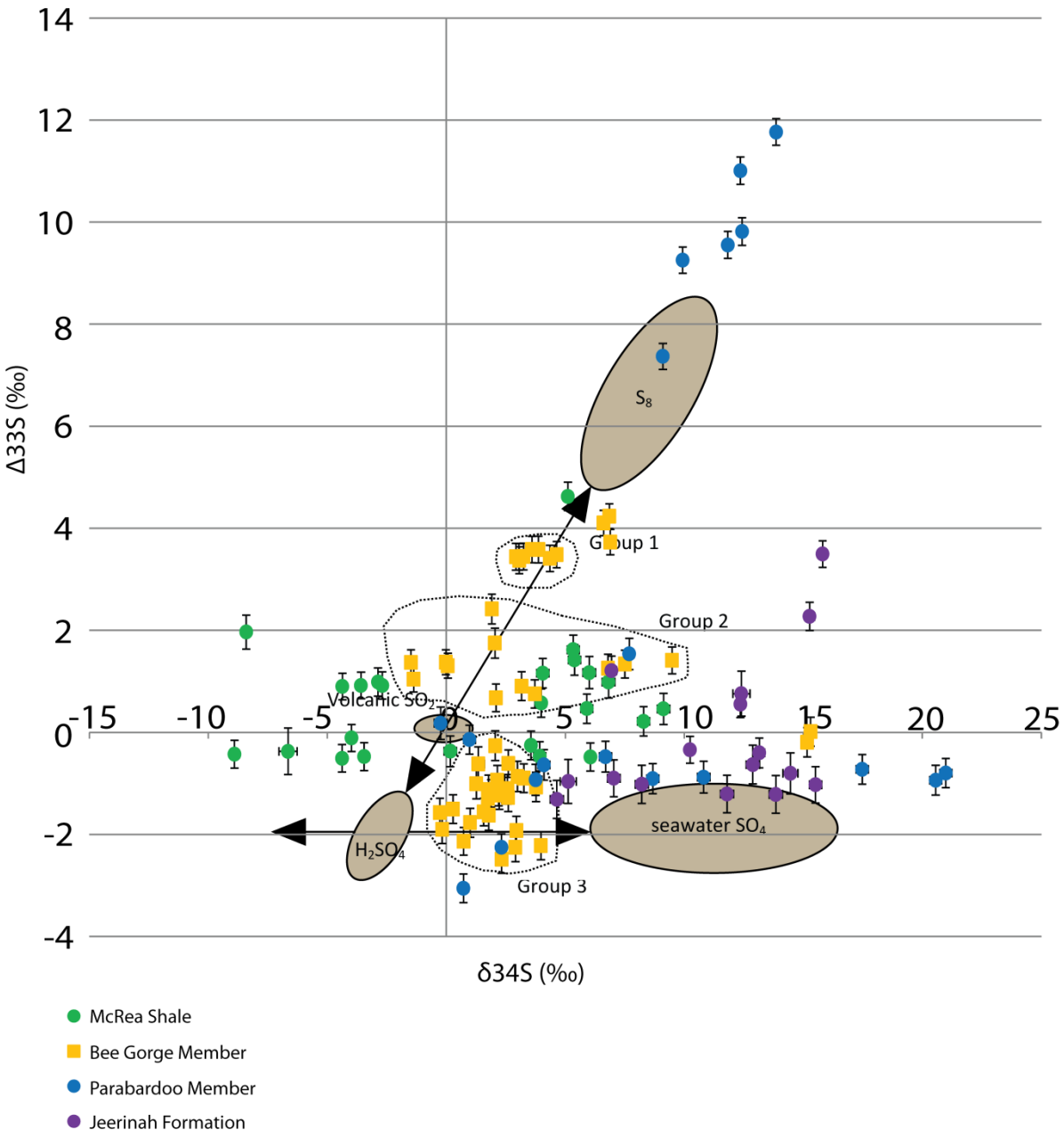

Figure 5.9: Sulfur isotope systematics for the McRae Shale, Bee Gorge Member, Paraburdoo Member and Jeerinah Formation. Fields for S_8, SO_2, $H_2SO_4$and seawater SO_4 are from Ono et al.,(2003).

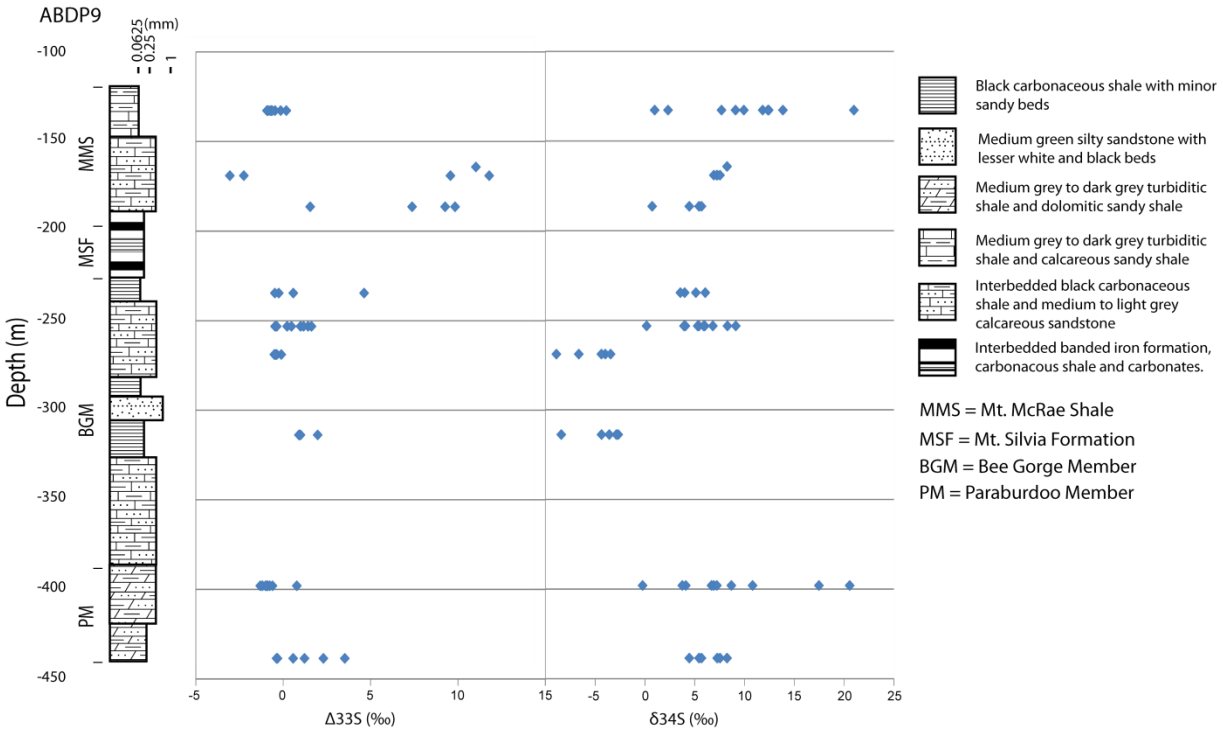

Figure 5.10: Variation of sulfur isotopes with depth in ABDP9 (McRae Shale, Bee Gorge Member, Paraburdoo Member). Simplified stratigraphic sections are presented on the left side of the figure, for detailed stratigraphy please see Appendix 8.

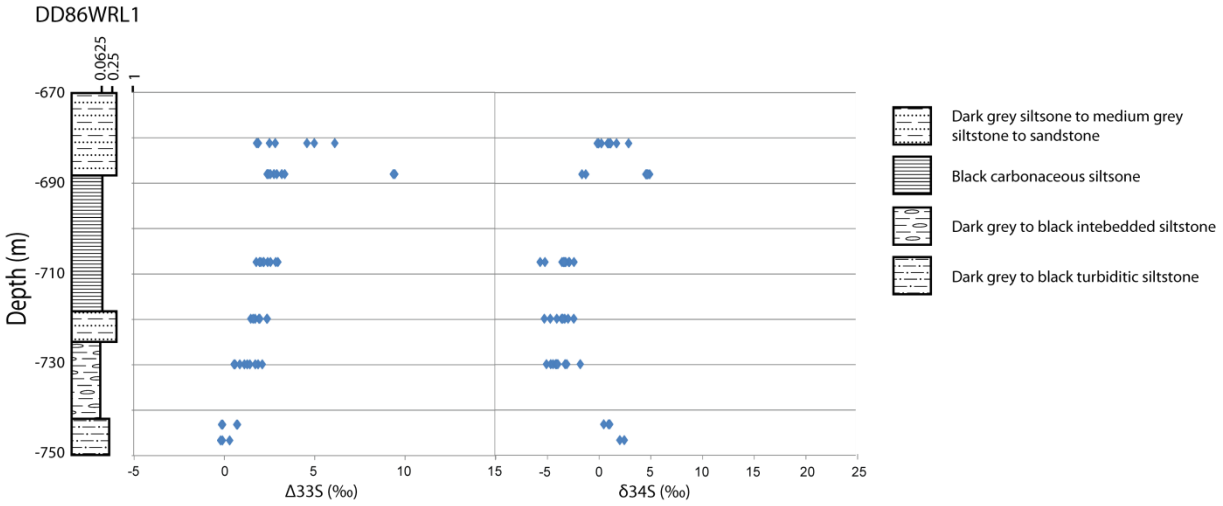

Figure 5.11: Variation of sulfur isotopes with depth in DDH86WRL1 (Jeerinah Formation). Member boundaries carbonate variety and content are modified from Buick, unpublished data. Simplified stratigraphic sections are presented on the left side of the figure, for detailed stratigraphy please see Appendix 8.

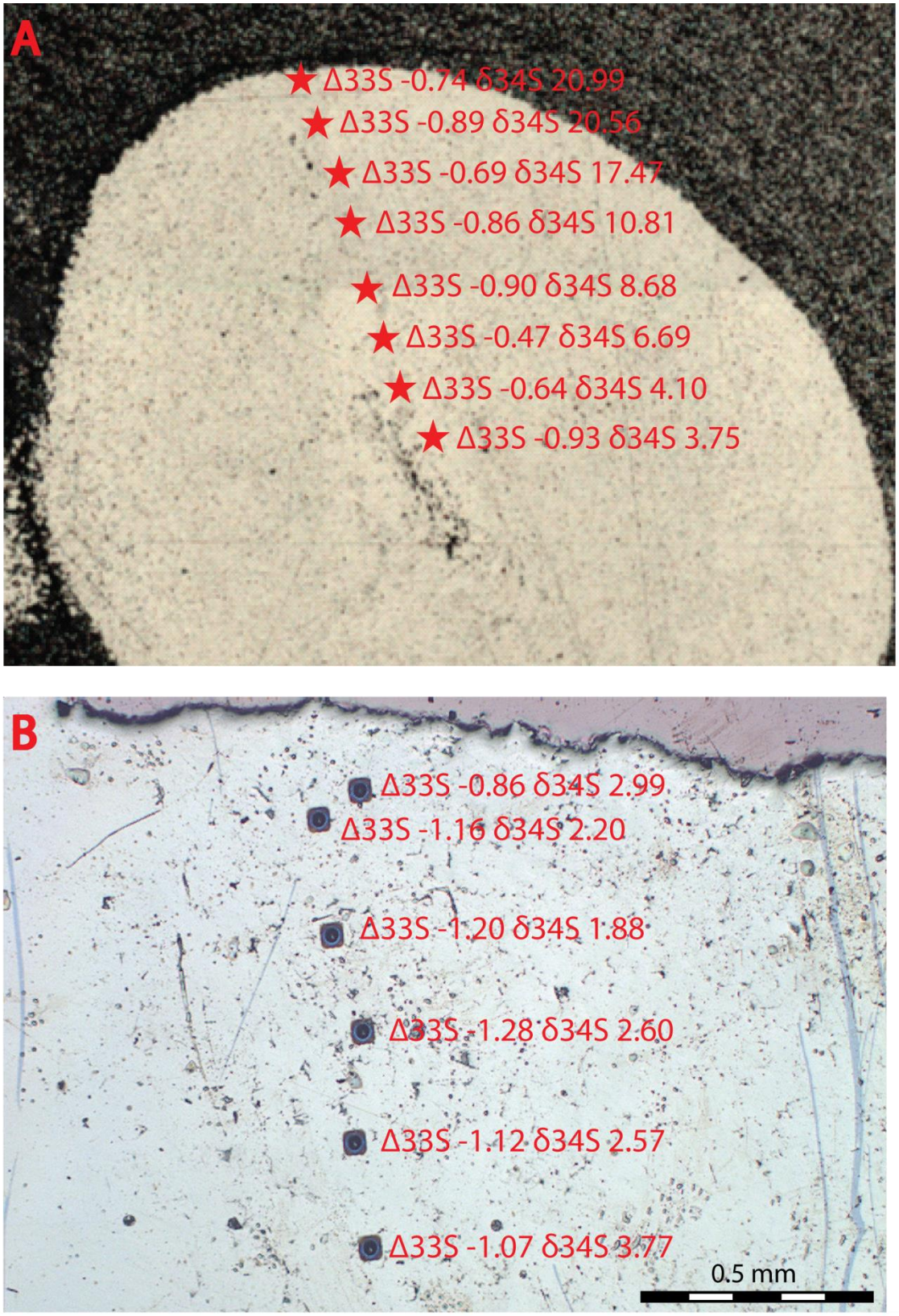

Figure 5.12: Reflected light images with SHRIMP S isotope analyses across selected representative pyrite nodules. The Mt McRae Shale nodule (a) shows variance of $\delta^{34}S$ across the nodule while Jeerinah Formation sample (b) shows little variance across the nodule.

5.5 Discussion

5.5.1 Iron enrichment and depletion during in the late Archean

During the deposition of the Mt. McRae Shale, the availability of Fe may have changed due to changes in the flux of hydrothermal Fe into the oceans (Raiswell et al., 2011), though it should be noted that a similar increase in Fe flux from a sedimentary source is also a possibility. Such changes in Fe flux are suggested by comparing the ratio of Fe to Al in some ancient shales (Scott et al., 2011). All but one of the Fe/Al ratios from the Jeerinah Formation are between 0.3 and 1.6 (Figure 5.5 and Table 5.3), which reflect a water column with limited iron content. Some of the low Fe/Al ratio horizons may be correlated with the Jeerinah Formation shale analysed by Scott et al. (2011), the upper part of which is believed to have been deposited under euxinic conditions. However, correlations are difficult due to the distance (approximately 130 km) between the drill holes used in the two studies and the presence of major lateral and facies changes observed by Thorne and Trendall (2001) in the Jeerinah Formation. The Bee Gorge Member and Paraburdoo Formation have similar Fe/Al ratios (all but one sample between 0.6 and 1.2) that reflect a relatively low iron supply at the time (Scott et al., 2011). The samples analysed from the Mt. McRae Shale are significantly different with Fe/Al ratios > 6.0, consistent with the > 3.0 results obtained by Reinhard et al. (2009) for the intervals within which these samples were taken, though this sampling was done with closer spacing and smaller sample size compared with ABDP9. This reflects the presence of a relatively high Fe^{2+} supply to the ocean (Scott et al., 2011) during Mt Silvia and McRae Shale deposition. However, there have been units with low Fe/Al identified (Reinhard et al., 2009) in the McRae Shale but these intervals were not sampled in this study.

5.5.2 Source of Sulfur

The isotopic composition of pyrite in the Archean can be used to determine the source of sulfur for the pyrite (Farquhar et al., 2000; Kaufman et al., 2007; Ono et al., 2003). Prior to the GOE (2220 to 2450 Ma) sulfur released into the atmosphere was able to undergo photochemical reactions that produced Mass Independent Fractionation (MIF) of S^{33} (Farquhar et al., 2000). These data are presented as $\Delta^{33}S$, which express the difference between the measured values of $\delta^{33}S$ and the expected value calculated from $\delta^{34}S$, calculated using the following equation:

$\Delta^{33}S = 1000*\ln(1+\delta^{33}S/1000) - 0.515*1000*\ln(1+\delta^{34}S/1000)$ (Ono et al., 2003).

Modelling by Ono et al. (2003) indicate that volcanically derived sulfur released as elemental sulfur (S_8) has a positive $\Delta^{33}S$ and $\delta^{34}S$ signatures, whereas sulfur released as SO_2 has $\Delta^{33}S$ and $\delta^{34}S$ near the origin (i.e. zero values). On the other hand a negative $\Delta^{33}S$ and $\delta^{34}S$ signature suggests that the S was released as sulfuric acid (H_2SO_4), and a positive $\delta^{34}S$ but a negative $\Delta^{33}S$ signature suggests a seawater sulfate source in Archean times (Ono et al., 2003). As shown in Figure 5.9 much of our data fall out of the idealised fields of isotopic composition based on sources proposed by Ono et al. (2003); however we believe that the observed $\Delta^{33}S$ and $\delta^{34}S$ are due to mixing of different S sources and secondary bacterial reduction that has shifted the $\delta^{34}S$ to lower values as it is the only way to achieve the observed $\Delta^{33}S$ and $\delta^{34}S$ ratios using the criteria defined by Ono et al., (2003).

The $\Delta^{33}S$ and $\delta^{34}S$ can be split into three groups in the Jeerinah Formation, the first group has $\Delta^{33}S$ and $\delta^{34}S$ values on trend with the S_8 field (Figure 5.9). It probably represents a predominantly S_8 source with minor mixing of volcanic SO_2 and/or seawater sulfate with bacterial reduction. The second group is similar to the Bee Gorge Member and likely reflects seawater sulfate mixing with S_8 (slightly more S_8 than the Bee Gorge Member as this group has a higher $\Delta^{33}S$ signature) followed by bacterial reduction of the sulfate to form pyrite indicated by a negative shift in $\delta^{34}S$. The final Jeerinah Formation group has little to no positive $\Delta^{33}S$ shift and a minor negative shift of $\delta^{34}S$. This suggests a significant contribution from biogenic reduction of seawater sulfate in the pyrite. The same inference was made for similar data obtained in the upper part of the Mt. McRae Shale (not sampled in this study) by Kaufman et al. (2007).

The Paraburdoo Member has a S isotope signature closest to that of sea water sulfate. The lack of a major shift in $\delta^{34}S$ towards more negative values suggests that relatively little biogenic sulfate reduction has taken place. There is one small subset of analyses that has a positive $\Delta^{33}S$ shift. We interpret this to be due to minor introduction of some S_8 that has been incorporated into the pyrite. The $\Delta^{33}S$ in the Bee Gorge Member is slightly enriched from the seawater sulfate average. This indicates a small degree of mixing with S_8 and seawater sulfate. However, $\delta^{34}S$ in some of the Bee Gorge Member pyrite has a negative shift indicating a greater degree of bacterial reduction. Of the two S isotope domains defined for the Mt. McRae Shale, one has a clear positive shift in $\Delta^{33}S$ and $\delta^{34}S$. This shift is higher than that shown by Ono et al. (2003) but it is along the same trend. We consider it to be part of

the same group that Ono et al. (2003) defined, and thus this pyrite group is primarily of S_8 origin. The second domain defined by the Mt. McRae Shale S isotope signature is predominantly within the seawater sulfate zone or slightly higher in $\Delta^{33}S$ with slightly lower $\delta^{34}S$. This suggests minor mixing with S_8 and a degree of bacterial reduction to shift the $\delta^{34}S$ towards lower values.

The pattern of increasing $\delta^{34}S$ values from core to rim of pyrite nodules in the Mt. McRae Shale may indicate that the nodules formed in a closed system (presumably by sulfur reducing bacteria (Kaufman et al., 2007)). This spatial variation is not present in the older Jeerinah Formation bands and nodules, and may reflect either less bacterial sulfate reduction or a more open system during formation.

Table 5.3: Fe/Al ratios of whole rock from drill hole ABDP9 and drill hole DDH86WRL1

Top of sample interval (m)	Bottom of sample interval (m)	Average depth of sample interval (m)	Unit	Fe/Al
132.77	132.97	132.87	Mt. McRae Shale	6.2
164.24	164.40	164.32	Mt. McRae Shale	31.2
169.07	169.25	169.16	Mt. McRae Shale	6.9
186.42	186.69	186.56	Mt. McRae Shale	9.3
214.87	215.04	214.96	Bruno's Band BIF	168.7
234.16	234.31	234.24	Bee Gorge Member	1.2
253.24	253.39	253.32	Bee Gorge Member	1.2
268.93	269.08	269.01	Bee Gorge Member	4.2
292.74	292.90	292.82	Bee Gorge Member	0.6
313.82	314.02	313.92	Bee Gorge Member	1.2
366.61	366.87	366.74	Bee Gorge Member	1.0
398.3	398.47	398.39	Bee Gorge Member	1.0
427.48	427.64	427.56	Paraburdoo Member	0.7
438.51	438.73	438.62	Paraburdoo Member	1.1
681.20	681.38	681.29	Jeerinah Formation	1.1
688.00	688.18	688.09	Jeerinah Formation	4.5
707.37	707.55	707.46	Jeerinah Formation	1.4
719.87	720.09	719.98	Jeerinah Formation	1.1
729.72	729.91	729.82	Jeerinah Formation	1.6
742.92	743.18	743.05	Jeerinah Formation	0.3
746.66	746.81	746.74	Jeerinah Formation	0.6

Table 5.4: Sulfur isotope data for drill hole ABDP9 and drill hole DDH86WRL1

Average depth of sample interval (m)	Unit	Mean $\delta^{34}S$	Mean $\Delta^{33}S$	Standard deviation $\delta^{34}S$	Standard deviation $\Delta^{33}S$
132.77	Mt. McRae Shale	9.4	-0.6	7.9	0.4
164.24	Mt. McRae Shale	12.4	11.0		
169.07	Mt. McRae Shale	7.2	4.0	6.6	7.8
186.42	Mt. McRae Shale	9.8	7.0	2.0	3.8
234.60	Bee Gorge Member	4.7	1.1	1.1	2.4
253.24	Bee Gorge Member	5.5	0.7	2.5	0.7
268.93	Bee Gorge Member	-5.5	-0.4	2.3	0.2
313.82	Bee Gorge Member	-4.4	1.1	2.3	0.5
398.00	Bee Gorge Member	10.6	-0.8	4.0	0.6
438.51	Paraburdoo Member	12.3	1.2	3.3	1.5
681.20	Jeerinah Formation	4.6	1.3	2.9	0.6
688.00	Jeerinah Formation	5.9	2.8	4.9	1.5
707.37	Jeerinah Formation	2.8	-1.3	0.7	0.6
719.87	Jeerinah Formation	2.1	-1.4	0.6	0.5
729.91	Jeerinah Formation	1.0	-1.4	1.0	0.6
743.05	Jeerinah Formation	-0.7	1.3	0.8	0.2
746.66	Jeerinah Formation	-1.2	2.0	0.5	0.1

5.5.3 Trace element composition of the late Archean ocean, possible causes and sources

There is a general increase in whole rock enrichment factors of trace elements (U, Mo, Cr, Cu, Zn and Cd) with younging direction in the Jeerinah Formation, with an exception of the sample at 688.09 m where the amount of many trace elements were significantly lower. The trend in EF_{Ni}, EF_{Co} and EF_{V} is similar though the data are more erratic and in the case of V and it may indicate two periods of enrichment. These trends can be explained in two ways.

The increase in EF_{Ni}, EF_{Cr}, EF_{Zn}, EF_{Co} and EF_{Cu} reflect an increase in productivity (Tribovillard et al., 2004) within the basin with sufficient recharge in these elements so as to avoid depletion. At the same time general increases in EF_{V}, EF_{U}, and EF_{Mo} indicate a transition to more reducing conditions. Alternatively, the data may indicate an increase in the supply of these metals to the basin. This may be caused by a greater degree of localised oxygen production which would result in the oxidation of sulfides and release of metals. However, a combination of both of these processes may best explain the observations. An increase in productivity caused by cyanobacteria, which were likely present in the ocean at the time of Jeerinah Formation deposition (Scott et al., 2011), would produce oxygen. The additional oxygen would then increase the weathering of sulfides and other minerals, releasing trace metals. These trace metals could then be adsorbed onto organic matter and be incorporated into the sediment. The increase in trace metals in the water column may also have increased the biological activity as several studies (Anbar and Knoll, 2002; Large et al., in prep.) have suggested that ocean biological productivity is limited by availability of some trace metals (Mo and Se). Thus, as trace metal availability increases so will organic matter and oxygen production in a positive feedback loop until the maximum carrying capacity of the water mass is reached. While this model suggests an increase in O_2 production, the O_2 was not of sufficient concentration to overwhelm the MIF signal.

The trace element content of pyrite supports this model. From 746.74 m to 729.82 m in the Jeerinah Formation there is a marked increase in the amount of Mo, As, Cu, Zn, Ag, Au and Te in pyrite before stabilising and then dropping at 688.09 m. This corresponds with the general trend of increasing whole rock enrichment factors. The increase of these trace elements in pyrite suggests an increase of supply of trace elements to the ocean. While it is possible that this increase in trace elements is from a hydrothermal source, it seems unlikely as all the samples (except those taken from 688.09 and 743.05 m) have trace element ratios within the ranges for sedimentary pyrite (Table 5.5) (Chapter 4). This supports the hypothesis that the trace elements came from a sedimentary source, such as weathered sulfide minerals. The increase in the trace metal enrichment factors in whole rock and trace metals in pyrite correspond to a switch from positive $\Delta^{33}S$ in the 743.05 m sample to a negative $\Delta^{33}S$ in the overlying samples. This means that at the onset of higher trace metals accumulation, there is a coincident greater contribution of bacterial reduced sulfur to the pyrite forming in the sediments. This is what is predicted by the positive feedback loop hypothesis discussed earlier. The increase in oxygen and productivity is terminated by the onset of Banded Iron

Formation deposition. This may reflect a crossing of the threshold oxygen levels required for the deposition of iron oxides. The onset of BIF deposition is preceded by a positive $\Delta^{33}S$ signature which suggests it is the onset of magmatism that provides elemental S. This magmatism may also provide hydrothermal iron to the ocean that is deposited as Banded Iron Formations. A schematic of the increases and decreases in productivity and oxygenation is shown in Figure 5.13.

The samples from 688.09 and 743.05 m have very low concentrations of several trace metals in pyrite. This is coincident with a positive $\Delta^{33}S$ signature, which likely reflects increased S_8 producing volcanism. The addition of volcanically sourced S to the basin would have resulted in more pyrite formation and drawdown of trace elements, resulting in the low trace element content in pyrite that is observed. Ni and Co do not show depletion in pyrite in these intervals. The volcanism producing the S_8 may be mafic, and thus would have enriched the ocean in Ni and Co as observed by Large et al. (in prep.) for major Large Igneous Province (LIP) eruptive events.

Table 5.5: Median trace elements ratios for pyrite from Jeerinah Formation.

Depth of sample (m)	Co/Ni	Cu/Ni	As/Ni	Ag/Au	Te/Au	As/Au
Average sedimentary pyrite	0.01 < Co/Ni < 2	0.01 < Cu/Ni < 10	0.1 < As/Ni < 10	Ag/Au > 1	Te/Au > 1	As/Au > 200
-681.29	0.37	0.33	0.44	101.38	189.31	4759
-688.09	0.43	0	0	41.05	112.11	56
-707.46	0.49	0.9	1.3	84.86	195.14	25514
-719.98	0.54	0.11	0.24	71.79	91.43	5429
-729.82	0.68	0.35	0.8	76.15	81.15	13654
-743.05	0.1	0	0	236.67	503.33	273
-746.74	2.29	0.02	5.4	9.78	13.7	1320

So far we have not discussed the sample from 746.74 m, which has especially high amounts of Ag, Te, Au, As and Mo. While metal ratios are not outside those expected for diagenetic pyrite (Chapter 4) the magnitude of these elements are anomalous compared to other pyrite in the Jeerinah Formation. The analyses may reflect an influence of hydrothermal fluids effecting the composition of the pyrite. Due to this uncertainty, we did not include the sample in our discussion of trace element chemistry of the Jeerinah Formation.

Similar to the Jeerinah Formation, there is a general increase in EF_V, EF_{Cu}, EF_{Zn}, EF_{Cd}, and to a lesser extent EF_{Ni}, from the top of the Paraburdoo Member through to the middle of the Bee Gorge Member (269.01 m) (Figure 5.4). This is coincident with a negative shift in $\delta^{34}S$ values, which suggests increases in bacterial sulfate reduction. Because Cu, Zn, Cd and Ni are good proxies for organic carbon sinking flux (productivity) and the sulfur isotope analyses support the presence of bacterial reduction we believe that this period marks a time of relatively high productivity in the basin.

The trace element content of pyrite (Mo, Ni, Co and Cu) in the Paraburdoo Member and Bee Gorge Member correlate well with the whole rock data (Figure 5.7). Similarly, within the Bee Gorge Member there is a general increase in Au, Te and Ag in pyrite up stratigraphy. This may be due to an increase in biological activity as the incorporation of gold into pyrite has been suggested to be linked to cyanobacteria in modern systems (Lengke et al., 2006). Because Te and Ag have been shown to be associated with gold in diagenetic pyrite (Chapters 3 and 4) they may be incorporated into pyrite by the same mechanism. However, an alternative explanation for the increased incorporation of these trace elements into pyrite is that the supply of these metals to the basin increased over time.

These data suggest similar chemical conditions to those defined for the Jeerinah Formation (Figure 5.13). Increased biologic activity is suggested by negatively shifted $\delta^{34}S$ and possibly by an increase in Au, Te and Ag. If this biological activity included cyanobacteria it would have increased O_2 production, which would have resulted in weathering of sulfides and increased the amount of trace metals in the water column. This would have increased the content of trace metals in the sediment and pyrite, as is observed. Also the increase of trace metals in the water column may have promoted biological activity (Anbar and Knoll, 2002; Large et al., in prep.). Similarly to the Jeerinah Formation, these periods of increased productivity and oxygen production are ended by the onset of Banded Iron Formation deposition. We believe that this is due to the oceans reaching a critical oxygenation level to precipitate the iron oxides found in BIFs.

Arsenic differs from most other elements in that it is enriched in pyrite in the lower part of the Bee Gorge Member and decreases up stratigraphy. This may be due to an increase in bacterial sulfate reduction over this time period. With less S present there would be less competition for As binding sites in the growing pyrite but with more S from bacterial sulfate reduction there would be more competition for the binding sites and less As could be

incorporated into the pyrite structure. Interestingly As is not depleted in the Mt. McRae Shale pyrite when there were very high amounts of pyrite produced which depleted many of the other trace elements. This must be due to a similar relative increase in the As to S ratio in the seawater at the time.

Strong enrichments in Mo, Co, Cr, Cu and Zn are coupled with weaker enrichments in Cd and U in whole rock analyses from one or both of the top 2 samples of ABDP9 (132.87 m and 169.16 m). These enrichments in the upper Mt. McRae Shale match the top part of the oxygenation event identified by Anbar et al. (2007), while the lower enriched sample (169.16 m) corresponds to a zone enriched in Mn and S identified by Anbar et al. (2007). These strong enrichments are likely due to increases in atmospheric oxygen (Anbar et al., 2007). This is because the presence of atmospheric oxygen would have resulted in the oxidation and destruction of sulfides on land which would have released trace elements into the ocean waters where they could be incorporated into the sediments.

In general, the opposite trend in pyrite Ni, Co, Cu, Te, Au and Ag to that of the equivalent whole rock enrichment factor is observed in the Mt. McRae Shale (Figure 5.7). That is, there is a decrease in trace metals contained within pyrite up-section. This is because the area sampled in the Mt. McRae Shale records a change between iron-limited ocean waters at the base to iron-enriched ocean waters at the top. Thus as high amounts of sulfur were introduced into the system (possibly due to oxidative weathering as suggested by Anbar et al. (2007)), the supply of trace metals was not sufficient to maintain a balance between trace metals in pyrite and trace metals in the whole rock. However, by normalizing anomalously pyrite-rich samples to sulfur the amount of trace metals in the S normalized pyrite rich (>10% pyrite) samples correlates well with the amount of trace metals in pyrite (Figure 5.7). The enrichment factors for several elements (Mo, Ni, Co, Cr and Cd) in the upper part of the Mt. McRae Shale are much higher than in other sequences. This may represent a more intense instance of atmospheric oxygen weathering sulfides on land.

5.5.4 Mineral exploration potential

Recent models for the deposition of orogenic gold deposits have suggested that pyritic, carbonaceous shale may be an important source of gold (Large et al., 2011; Large et al., 2009; Large et al., 2007; Pitcairn et al., 2006; Steadman et al., 2013; Thomas et al., 2011;

Tomkins, 2010). Pyrite from the top of the Bee Gorge Member contains high contents (>0.2 ppm) of gold, making it a good potential source rock for gold deposits. Further studies should test whether gold deposits hosted in these units are sourced from these sedimentary units.

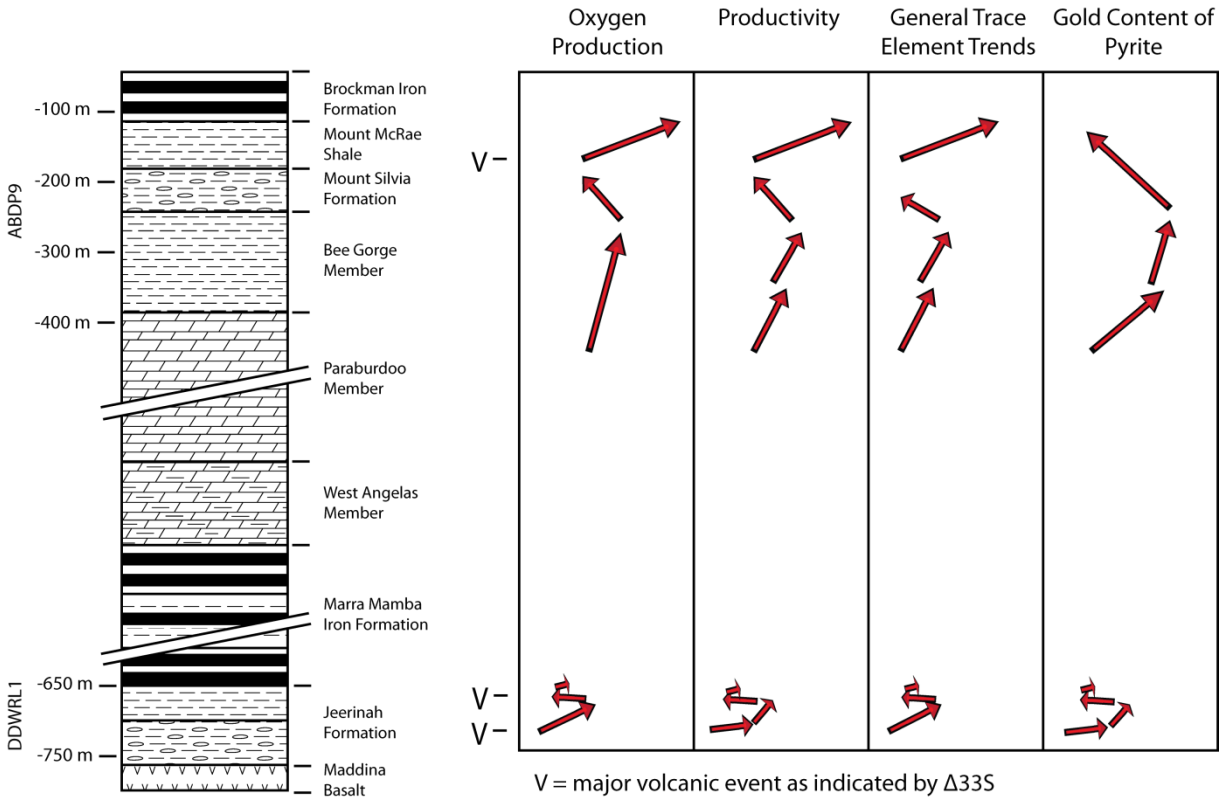

Figure 5.13: Schematic diagram of general trends of oxygenation, productivity, trace element content and gold in pyrite for the sedimentary rocks of the Jeerinah Formation, Paraburdoo Member, Bee Gorge Member and Mt. McRae Shale.

Table 5.6: Median trace element ratios for pyrite from ABDP9.

Depth of sample (m)	Co/Ni	Cu/Ni	As/Ni	Ag/Au	Te/Au	As/Au
Average sedimentary pyrite	0.01 < Co/Ni < 2	0.01 < Cu/Ni < 10	0.1 < As/Ni < 10	Ag/Au > 1	Te/Au > 1	As/Au > 200
-132.87	0.42	0.45	9.03	12.96	33.7	41148
-169.16	0.41	0.63	0.72	88.39	97.74	4435
-186.56	0.83	0.55	1.06	62.06	113.65	7024
-214.96	0.29	2.14	34.64	7.27	29.09	44091
-234.24	0.23	0.27	0.37	60.72	141.65	2941
-253.32	0.29	0.26	0.25	20.82	32.32	615
-269.01	0.66	0.47	0.54	21.15	159.78	943
-292.82	1.31	0.64	1.78	65.2	77.04	3808
-313.92	0.17	0.05	3.39	27.85	15.65	30251
-366.74	1.15	0.17	1.59	49.59	47.36	10810
-398.39	0.32	0.22	0.38	38.75	18.21	2714
-427.56	0.81	0.32	0.61	29.32	21.59	8386
-438.62	0.21	0.04	0.59	39.43	13.53	5081

5.6 Conclusions

A combination of whole rock geochemistry, sedimentary pyrite geochemistry and S isotope analyses have been used to determine paleo-oceanic conditions in the late Archean (2660-2500 Ma).

In the Jeerinah Formation, the increase in trace metals in whole rock and pyrite, combined with a negative shift of $\delta^{34}S$ isotopes, suggest that there is a general increase in productivity. This may also reflect an increase in oxygen production by cyanobacteria. As trace elements are often limiting factors for biologic productivity, a trace element increase will increase biological production in a positive feedback loop. A similar increase in productivity, based on the whole rock and pyrite geochemistry and S isotopes, is also observed in the Paraburdoo Member to the middle of the Bee Gorge Member, before dropping prior to the deposition of the overlying Banded Iron Formation. These periods of high productivity and oxygen production tend to end prior to the onset of deposition of Banded Iron Formations, presumably due to the ocean reaching the critical level of oxygenation to allow the precipitation of the iron oxides found in Banded Iron Formations. The $\Delta^{33}S$ and $\delta^{34}S$ isotopes reflect several different S sources within the units examined, predominantly elemental S (from volcanic eruptions) and oceanic sulfate. The $\delta^{34}S$ isotope signature of these S sources

was affected by bacterial reduction. Periods of increased S_8 production appear to have resulted in draw down of many trace metals, resulting in low trace metal content of pyrite when $\Delta^{33}S$ shifts are present. The data obtained from whole rock and pyrite analyses supports the conclusions of Anbar et al. (2007) that a greater amount of oxygen was present in the atmosphere during the deposition of the Mt. McRae Shale.

Correlation between the trace metal content in pyrite and the trace metal content of whole rock was found to be generally good, except when the ocean conditions produce a high amount of pyrite (>10%). Under these circumstances the whole rock normalized to S correlates better to the trace metal content of pyrite. An exception to this is Mo, which in all cases correlates well to the whole rock analyses. This demonstrates that as long as care is taken in choosing which environments are sampled (i.e. moderate to low pyrite production) pyrite geochemistry can be used to determine paleo-oceanic conditions. Our work has also shown that a combination of pyrite trace element geochemistry with $\delta^{34}S$ and $\Delta^{33}S$ isotopes provides a powerful mechanism for interpreting paleo-oceanic conditions.

5.7 Reference

Anbar, A. D., Duan, Y., Lyons, T. W., Arnold, G. L., Kendall, B., Creaser, R. A., Kaufman, A. J., Gordon, G. W., Scott, C., and Garvin, J. (2007) A whiff of oxygen before the great oxidation event?: Science, 317(5846), 1903-1906.

Anbar, A. D., and Knoll, A. (2002) Proterozoic ocean chemistry and evolution: a bioinorganic bridge?: Science, 297(5584), 1137-1142.

Berner, Z. A., Puchelt, H., NÖLtner, T., and Kramar, U. T. Z. (2013) Pyrite geochemistry in the Toarcian Posidonia Shale of south-west Germany: Evidence for contrasting trace-element patterns of diagenetic and syngenetic pyrites: Sedimentology, 60(2), 548-573.

Condie, K. C. (1993) Chemical composition and evolution of the upper continental crust: contrasting results from surface samples and shales: Chemical Geology, 104(1), 1-37.

Danyushevsky, L., Robinson, P., Gilbert, S., Norman, M., Large, R., McGoldrick, P., and Shelley, M. (2011) Routine quantitative multi-element analysis of sulphide minerals by laser ablation ICP-MS: Standard development and consideration of matrix effects: Geochemistry: Exploration, Environment, Analysis, 11(1), 51-60.

Deditius, A. P., Utsunomiya, S., Renock, D., Ewing, R. C., Ramana, C. V., Becker, U., and Kesler, S. E. (2008) A proposed new type of arsenian pyrite: Composition, nanostructure and geological significance: Geochimica et Cosmochimica Acta, 72(12), 2919-2933.

Dellwig, O., Böttcher, M. E., Lipinski, M., and Brumsack, H.-J. (2002) Trace metals in Holocene coastal peats and their relation to pyrite formation (NW Germany): Chemical Geology, 182(2–4), 423-442.

Farquhar, J., Bao, H., and Thiemens, M. (2000) Atmospheric influence of Earth's earliest sulfur cycle: Science, 289(5480), 756-758.

Gregory, D., Meffre, S., and Large, R. (2013) Mineralogy of metal contaminated estuarine sediments, Derwent estuary, Hobart, Australia: implications for metal mobility: Australian Journal of Earth Sciences, no. ahead-of-print, p. 1-15.

Guillong, M., Hametner, K., Reusser, E., Wilson, S. A., and Günther, D. (2005) Preliminary Characterisation of New Glass Reference Materials (GSA-1G, GSC-1G, GSD-1G and GSE-1G) by Laser Ablation-Inductively Coupled Plasma-Mass Spectrometry Using 193 nm, 213 nm and 266 nm Wavelengths: Geostandards and Geoanalytical Research, 29(3), 315-331.

Hassler, S. W., Simonson, B. M., Sumner, D. Y., and Bodin, L. (2011) Paraburdoo spherule layer (Hamersley Basin, Western Australia): Distal ejecta from a fourth large impact near the Archean-Proterozoic boundary: Geology, 39(4), 307-310.

Hickman, A. H., and Van Kranendonk, M. J. (2012) Early Earth evolution: evidence from the 3.5-1.8 Ga geological history of the Pilbara region of Western Australia: Episodes, 35, (1), 283.

Ireland, T., Clement, S., Compston, W., Foster, J., Holden, P., Jenkins, B., Lanc, P., Schram, N., and Williams, I. (2008) Development of SHRIMP: Australian Journal of Earth Sciences, 55(6-7), 937-954.

Kakegawa, T., Kawai, H., and Ohmoto, H. (1998) Origins of pyrites in the~ 2.5 Ga Mt. McRae Shale, the Hamersley District, Western Australia: Geochimica et Cosmochimica Acta, 62(19), 3205-3220.

Kaufman, A. J., Johnston, D. T., Farquhar, J., Masterson, A. L., Lyons, T. W., Bates, S., Anbar, A. D., Arnold, G. L., Garvin, J., and Buick, R. (2007) Late Archean biospheric oxygenation and atmospheric evolution: Science, 317(5846), 1900-1903.

Large, R. R., Bull, S. W., and Maslennikov, V. V. (2011) A carbonaceous sedimentary source-rock model for Carlin-type and orogenic gold deposits: Economic Geology, 106(3), 331-358.

Large, R. R., Danyushevsky, L., Hollit, C., Maslennikov, V., Meffre, S., Gilbert, S., Bull, S., Scott, R., Emsbo, P., Thomas, H., Singh, B., and Foster, J. (2009) Gold and Trace Element Zonation in Pyrite Using a Laser Imaging Technique: Implications for the Timing of Gold in Orogenic and Carlin-Style Sediment-Hosted Deposits: Economic Geology, 104(5), 635-668.

Large, R. R., Maslennikov, V. V., Robert, F., Danyushevsky, L. V., and Chang, Z. S. (2007) Multistage sedimentary and metamorphic origin of pyrite and gold in the giant Sukhoi Log deposit, Lena gold province, Russia: Economic Geology, 102(7), 1233-1267.

Lengke, M. F., Fleet, M. E., and Southam, G. (2006) Morphology of gold nanoparticles synthesized by filamentous cyanobacteria from gold (I)-thiosulfate and gold (III)-chloride complexes: Langmuir, 22(6), 2780-2787.

Longerich, H. P., Jackson, S. E., and Günther, D. (1996) Inter-laboratory note. Laser ablation inductively coupled plasma mass spectrometric transient signal data acquisition and analyte concentration calculation: Journal of Analytical Atomic Spectrometry, 11(9), 899-904.

Ono, S., Eigenbrode, J. L., Pavlov, A. A., Kharecha, P., Rumble, D., Kasting, J. F., and Freeman, K. H. (2003) New insights into Archean sulfur cycle from mass-independent sulfur isotope records from the Hamersley Basin, Australia: Earth and Planetary Science Letters, 213(1), 15-30.

Pitcairn, I. K., Teagle, D. A., Craw, D., Olivo, G. R., Kerrich, R., and Brewer, T. S. (2006) Sources of metals and fluids in orogenic gold deposits: insights from the Otago and Alpine Schists, New Zealand: Economic Geology, 101(8), 1525-1546.

Raiswell, R., and Canfield, D. E. (1998) Sources of iron for pyrite formation in marine sediments: American Journal of Science, (298)(3), 219-245.

Raiswell, R., Reinhard, C. T., Derkowski, A., Owens, J., Bottrell, S. H., Anbar, A. D., and Lyons, T. W. (2011) Formation of syngenetic and early diagenetic iron minerals in the late Archean Mt. McRae Shale, Hamersley Basin, Australia: New insights on the patterns, controls and paleoenvironmental implications of authigenic mineral formation: Geochimica et Cosmochimica Acta, 75(4), 1072-1087.

Reich, M., Kesler, S. E., Utsunomiya, S., Palenik, C. S., Chryssoulis, S. L., and Ewing, R. C. (2005) Solubility of gold in arsenian pyrite: Geochimica et Cosmochimica Acta, 69(11), 2781-2796.

Reinhard, C. T., Raiswell, R., Scott, C., Anbar, A. D., and Lyons, T. W. (2009) A late Archean sulfidic sea stimulated by early oxidative weathering of the continents: Science, 326(5953), 713-716.

Scott, C., Lyons, T., Bekker, A., Shen, Y., Poulton, S., Chu, X., and Anbar, A. (2008) Tracing the stepwise oxygenation of the Proterozoic ocean: Nature, 452(7186), 456-459.

Scott, C. T., Bekker, A., Reinhard, C. T., Schnetger, B., Krapež, B., Rumble, D., and Lyons, T. W. (2011) Late Archean euxinic conditions before the rise of atmospheric oxygen: Geology, 39(2), 119-122.

Steadman, J. A., Large, R. R., Meffre, S., and Bull, S. W. (2013) Age, origin and significance of nodular sulfides in 2680 ma carbonaceous black shale of the eastern goldfields superterrane, yilgarn craton, western australia: Precambrian Research, 230, 227-247.

Thomas, H. V., Large, R. R., Bull, S. W., Maslennikov, V., Berry, R. F., Fraser, R., Froud, S., and Moye, R. (2011) Pyrite and pyrrhotite textures and composition in sediments,

laminated quartz veins, and reefs at Bendigo gold mine, Australia: insights for ore genesis: Economic Geology, 106(1), 1-31.

Tomkins, A. G. (2010) Windows of metamorphic sulfur liberation in the crust: Implications for gold deposit genesis: Geochimica et Cosmochimica Acta, 74(11), 3246-3259.

Trendall, A. (1990) Hamersley Basin, in Geology and mineral resources of Western Australia: Western Australia Geological Survey, Memoir 3, p. 77-119., in Geology and mineral resources of Western Australia: Western Australia Geological Survey, Memoir 3, 3, 163-191.

Trendall, A., Compston, W., Nelson, D., De Laeter, J., and Bennett, V. (2004) SHRIMP zircon ages constraining the depositional chronology of the Hamersley Group, Western Australia*: Australian Journal of Earth Sciences, 51(5), 621-644.

Tribovillard, N., Algeo, T. J., Lyons, T., and Riboulleau, A. (2006) Trace metals as paleoredox and paleoproductivity proxies: An update: Chemical Geology, 232(1), 12-32.

Tribovillard, N., Riboulleau, A., Lyons, T., and Baudin, F. (2004) Enhanced trapping of molybdenum by sulfurized marine organic matter of marine origin in Mesozoic limestones and shales: Chemical Geology, 213(4), 385-401.

Wedepohl, K. (1995) The composition of the continental crust: Geochimica et Cosmochimica Acta, 59(7), 1217-1232.

Whitehouse, M. J. (2013) Multiple Sulfur Isotope Determination by SIMS: Evaluation of Reference Sulfides for Δ33S with Observations and a Case Study on the Determination of Δ36S: Geostandards and Geoanalytical Research.

Table of Contents

6.0 Trace element content of pyrite from the Kapai Slate, St. Ives Gold District, Western Australia: Implications for Ocean Chemistry and Ore Deposition

6.1 Abstract

A combination of LA-ICPMS and SHRIMP SI has been used to examine pyrite from the St. Ives gold district, Western Australia. The study includes sedimentary pyrite from the Kapai Slate distal to mineralization, recrystallized Kapai Slate pyrite, magnetite altered Kapai slate, and pyrite from the Repulse and Leviathan ore deposits. The $\Delta^{33}S$ and $\delta^{34}S$ signature of the sedimentary pyrite suggest two different sources of S in the system. Weakly positive $\delta^{34}S$ and negative $\Delta^{33}S$ signatures indicate bacterial reduction of SO_4^{2-} from seawater, while positive $\delta^{34}S$ and negative $\Delta^{33}S$ signatures indicate elemental S_8 from volcanic eruptions. These data provide evidence for early enrichment of trace elements in sedimentary pyrite in the Kapai Slate (median values of 180 ppm Ni, 311 ppm Co, 83 ppm Cu, 741 ppm As, 1.67 ppm Mo, 13 ppm Se, 0.28 ppm Au, 7.66 ppm Te and 3.61 ppm Ag). Concentration of Ni, Co and Cu are low, relative to other late Archean sedimentary pyrite (194 ppm, 401 ppm and 898 ppm respectively). Molybdenum levels are near that of the euxinic shales of the Jeerinah Formation, of the same age in the Hammersly Basin. and no major depletion in trace metals is observed. This suggests that the pyrite formed in an anoxic to euxinic basin with low dissolved iron and relatively low biological production.

Weakly positive $\Delta^{33}S$ analyses suggest that there is a contribution of sedimentary S to the ore forming fluids, which could also suggest that Au is contributed from a sedimentary source as well. Approximations of destruction of sedimentary pyrite in the pyrrhotite/pyrite dominated zones and pyrrhotite/magnetite/pyrite zones of the northern part of the district were used to calculate the amount of gold released from the pyrite. This resulted in 734,000 ounces, which is approximately 10% of the gold found in the study area. On this basis the Kapai Slate cannot have been a major source of gold for the deposits. Thus, while elevated gold was found in the sedimentary pyrite of the Kapai Slate, the gold concentrations and the volume of the rock are not sufficient to contribute significant quantities of gold to the ore deposits. However this does not preclude the possibility that other sedimentary or mafic units of the host sequence could be the source of gold in the deposit.

6.2 Introduction

The Kapai Slate is a continuous shale unit within the Kambalda Sequence of the Yilgarn Craton, Western Australia. It is important for two reasons: it represents a period of quiescence during deposition of the Kambalda Sequence, which could potentially be used to determine ocean chemistry at the time of deposition, and it is a host unit of gold mineralisation in the St. Ives gold district. In this study we use a combination of reflected light microscopy, laser ablation inductively coupled plasma mass spectrometer (LA-ICPMS) analyses and sensitive high resolution ion microprobe (SHRIMP SI) analyses to examine pyrite in the Kapai Slate, mafic units and ore samples from the St. Ives gold district. The trace metal content of pyrite is used to make inferences of the chemical conditions of the oceans when the sedimentary pyrite was deposited. These data are also used to test whether new orogenic gold deposit models that suggest carbonaceous, pyritic shales are important contributors of gold and other elements to the formation of sediment hosted gold deposits (Large et al., 2011) can be applied to greenstone hosted gold deposits such as those in the St. Ives District, Yilgarn Province. A brief overview of the possible uses of pyrite geochemistry in ore deposit exploration is also discussed.

6.2.1 The use of pyrite chemistry to determine chemical conditions of ancient ocean basins

Traditional methods used to determine the chemical conditions of ancient oceans involve the analysis of whole rock samples of fine grained sedimentary rocks that are usually normalized to aluminium to account for differences in sedimentation rates (Lyons et al., 2003). Trace elements such as Mo, V, U, Cr and Co (for redox conditions); Ni, Cu, Zn and Cd (for organic matter sinking flux); and Ba and P (for paleo-productivity) are then used to determine the chemical conditions of ancient oceans (Tribovillard et al., 2004). To undertake this type of research the sediments must not be significantly altered by metamorphism or overprinted by hydrothermal fluids as both these processes could remobilise some or all of the trace metals of interest. This requirement limits the number of areas where the chemical conditions of ancient oceans can be studied.

Studies have shown that early syngenetic/diagenetic pyrite can be preserved in areas that have been overprinted by hydrothermal fluids and/or metamorphosed up to greenschist facies (Large et al., 2011; Large et al., 2009; Large et al., 2007; Thomas et al., 2011). As pyrite is a

major sink for several trace elements (Huerta-Diaz and Morse, 1992; Tribovillard et al., 2006) the trace element content of pyrite can reflect the trace element content of the sedimentary depositional environment. Based on this hypothesis trace metal content of pyrite has been used to determine temporal variations in ocean chemistry (Berner et al., 2013) (Large et. al., in prep, Chapter 2). This approach was continued in chapter 4 where the results of the pyrite analyses were compared with traditional whole rock analyses. In this paper we will use the trace element content of pyrite from the Kapai Slate in the St. Ives gold district to investigate the chemical conditions of the Archean ocean at the time of sedimentation.

6.2.2 Current gold deposition models

The orogenic gold deposits in the Yilgarn Craton have been extensively researched and several models have been proposed. A metamorphic devolatilization model for formation of orogenic gold deposits has been investigated for some time (Phillips and Powell, 2010; Phillips et al., 1987; Phillips and Powell, 1993; Phillips and Powell, 2009; Powell et al., 1991); here we present a summary of the model described by Phillips and Powell (2010). In this model it is proposed that the source of the ore fluids are hydrated and carbonated greenschist facies metamorphic rocks, with metabasic rocks considered to be the most fertile. When these source rocks are metamorphosed past greenschist facies to amphibolite facies devolatilization reactions proceed and release H_2O, CO_2, S and Au (Phillips and Powell, 2010). Gold rich ore fluids are produced by H_2CO_3 buffering the solution close to the optimal pH for maximum gold solubility and the Au is transported in sulfide complexes. These fluids then travel up shear zones and/or hydraulic fracture zones to suitable depositional sites (Phillips and Powell, 2010). Gold is deposited by the breakdown of the gold sulfide complexes; due to reactions between the ore fluids and reduced carbonaceous rocks and/or production of Fe sulfides by sulfidation of wall rocks. The best units for these reactions to occur are: black slate, carbon seams, banded iron formation, tholeiitic basalt, magnetite bearing diorite and differentiated tholeitic sills (Phillips and Powell, 2010). As the major gold deposits can be correlated with rock types, despite much of the ore being vein hosted, it is probable that the deposition system is rock, not fluid, dominated (Phillips and Powell, 2010). Therefore this model suggests that fluid mixing, temperature decrease, boiling and/or fluid decrease are unlikely to by major factors in gold deposition in orogenic gold deposits (Phillips and Powell, 2010). Weaknesses with this model include: an inability

to predict the presence of amphibolite and granulite facies rocks; ore related potassic alteration and Pb and Sr isotopes reported for the ore and gangue minerals (Witt and Vanderhor, 1998); and the lack of a source for As, which is common in all orogenic gold deposits.

Groves (1993) described a crustal continuum model for the formation of orogenic gold deposits. In brief this model suggests that Archean lode gold deposits form in different areas of a crustal scale hydrothermal system. Groves (1993) noted that the majority of Archean lode gold deposits were deposited at the same time and from similar fluids, which were argued to be derived from the lower crust and/or mantle and were equilibrated with older felsic rocks (as implicated by Pb and Sr isotope data from ore minerals). Deposits described in this model form in a wide range of crustal regimes ranging from 180°C and < 1 kb to 700°C and 5 kb. This represents at least a 15 km crustal profile. Distinct changes were noted in the structural style of the different deposits ranging from brittle structures (sub-greenschist facies), through brittle-ductile structures (green schist facies) to ductile structures (amphibolite facies). Similarly the vein styles vary with plumose, comb, cockade and vugh filling textures in the brittle structures, massive or laminated quartz in the brittle-ductile structures and coarse grained, granoblastic veins in the ductile structures (Groves, 1993). Groves argued that this evidence of gold deposition in several different conditions with similar isotopic signature and time deposition is best explained by the gold deposits forming from deep fluids along major structures that extend from the lower crust to near surface. However, there are problems with this model too. It is difficult to explain how a deep source of fluids was able to pass through high pressure-temperature space in the lower crust without initiating partial melting and then not be absorbed by the resultant melt (Witt and Vanderhor, 1998).

A third model (termed the mixing model), involving the mixing of two fluids, has recently been proposed for the St. Ives gold district (Neumayr et al., 2008). In this study Neumayr et al., (2008) made use of extensive S and C isotope analyses covering much of the St. Ives area. Further studies have provided detailed mineral mapping to support the model (Bath et al., 2013). This demonstrates the possibility of an oxidized and a reduced fluid related to the gold mineralisation. They propose that a central oxidizing domain is present and is defined by negative $\delta^{34}S$ and $\delta^{13}C$ values. This is flanked to the east and the west by reduced fluid domains that are indicated by positive $\delta^{34}S$ and positive $\delta^{13}C$ values. It is argued that the

oxidized fluids are sourced from a deep, magmatic or mantle source because the negative $\delta^{34}S$ values indicate sulphide forming in the presence of aqueous sulphate. They took the source of sulphate to be a magmatic intrusion indicated by seismic surveys across the district (Neumayr et al., 2008), however it should be noted that seawater is another viable source of sulphate. The origin of the reduced fluids is less clear and Neumayr et al. (2008) favoured a deep source for the reducing fluids also, because they could not identify any sedimentary or lithological sources of positive $\delta^{34}S$ in the late Archean. However several studies (Kakegawa et al., 1998; Kaufman et al., 2007; Ono et al., 2003; Partridge et al., 2008; Xue et al., 2013, chapter 5) have reported positive $\delta^{34}S$ values within Archean sediments from other sedimentary basins. This study and Xue et al. (2013) have found positive $\delta^{34}S$ from the sedimentary rocks of the Kapai Slate. Similarly to the crustal continuum model, it is difficult to explain how the deeply sourced fluids in this model were able to pass through the high pressure-temperature space of the lower crust without causing partial melting and being absorbed by the melt (Witt and Vanderhor, 1998). An additional problem with this model is that the established correlation between host rocks and gold deposits suggests that the depositional mechanism involves low fluid rock reactions (Phillips and Powell, 2010) rather than the high fluid rock reactions described by the mixing model.

A further recent model for orogenic gold deposits has suggested that pyritic black shale may be the principal source of gold and other elements associated with the deposits. In these models it is proposed that during metamorphism metal-rich diagenetic pyrite is recrystallized, replaced by pyrrhotite and/or dissolved which releases the trace metals held within its structure. These trace metals, including gold, are then transported by the metamorphic fluids to favourable structural sites where they are precipitated to form the gold deposit (Large et al., 2011; Large et al., 2007; Pitcairn et al., 2006; Thomas et al., 2011; Tomkins, 2010). This depositional model has been applied to the Randalls deposit in the Yilgarn Craton, near the St. Ives gold district (Steadman et al., 2013). In this study we test whether some of the gold in the St Ives gold district may have been sourced from the Kapai Slate.

6.2.3 St. Ives Gold District

The St. Ives gold district is located 60 to 80 km south of Kalgoorlie, Western Australia. It occurs within the Eastern Goldfields Superterrane of the Yilgarn Craton. The gold district is approximately 40 by 10 km and trends north-northwest, extending from the Red Hill deposit

in the North to the Junction Deposit in the south (Roberts and Elias, 1990b). The camp is centred at approximately 121°45'N and 31° 20'E (Figure 6.1). There have been over 12 million ounces produced in the district to date (Miller et al., 2010). Details of the mining history of the St. Ives district are provided in Appendix 11 and references therein.

`

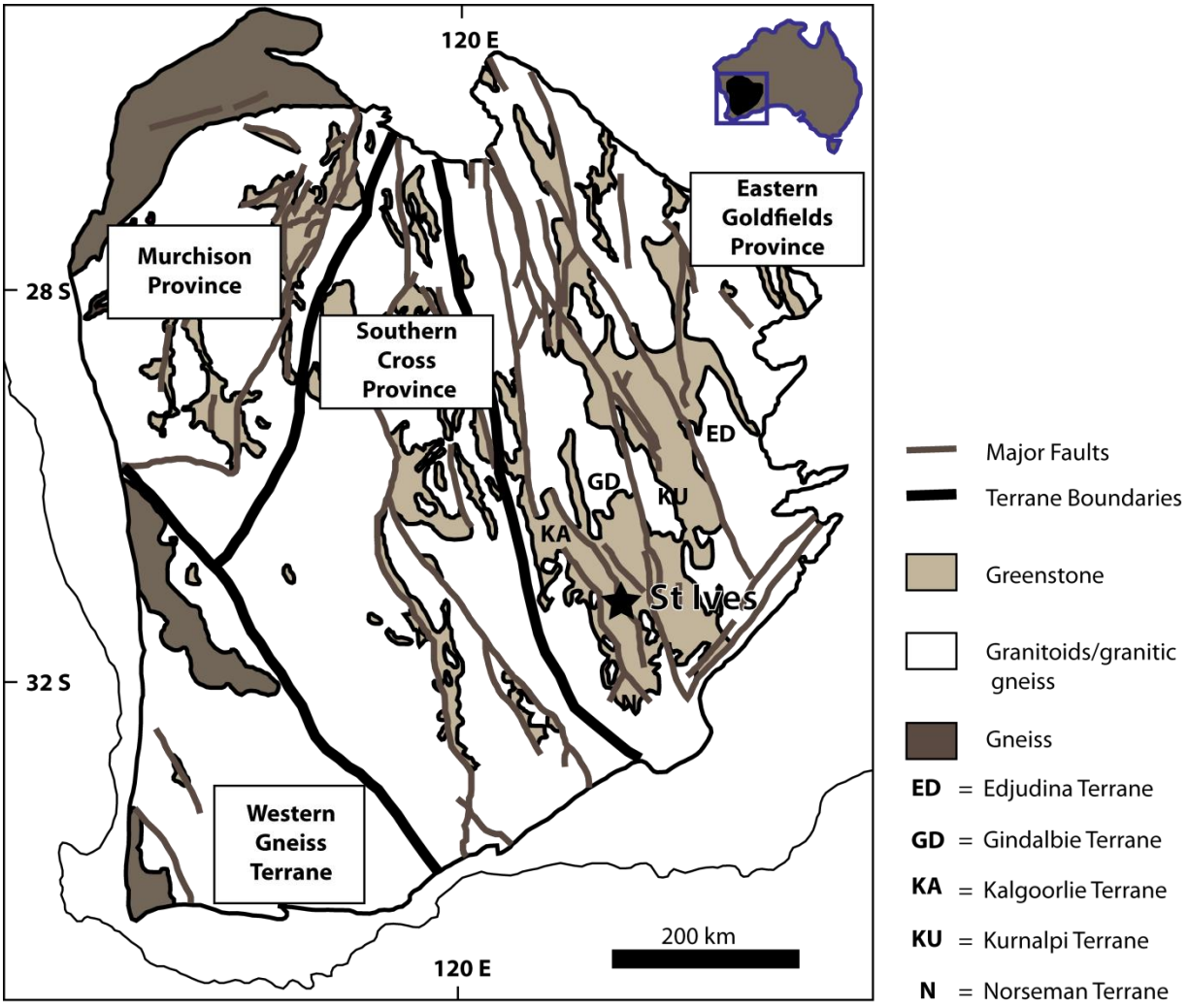

Figure 6.1: Regional Geology of the Yilgarn Craton and location of the St. Ives gold district.

6.2.4 Local Geology

The St. Ives district lies within the volcano-stratigraphic sequences that make up the Eastern Goldfields Super Terrane in the Yilgarn craton, Western Australia. These rocks were deposited during a period of regional extension between 2700 and 2660 Ma (Barley and Groves, 1990). The gold deposits are hosted by the Kambalda Sequence which consists of the Lunnon Basalt (>2000 m thick), the Kambalda Komatiite (50 to 200 mm thick), the

Devon Consuls Basalt (DCB) (60 to 100 m thick), the Kapai Slate (1 to 10 m thick), the Paringa Basalt (> 500 m thick), the Black Flag Group (>1000 m thick) and the Merougill Formation (2000 m thick). These units are intruded by dolerite, high Ca granitoids and syenitic intrusions (Champion and Cassidy, 2007) (Figures 6.2 and 6.3). For detailed descriptions of the lithologic units of the Kambalda sequence other than the Kapai Slate please refer to the Appendix 11. The Kapai Slate and the syngenetic/diagenetic pyrite held within it, are the focus of this study. The unit is a persistent, 1-10 m thick shale that is found between the Devon Consuls Basalt and Paringa Basalt throughout the St. Ives district. It has been divided into five facies: laminated siliceous magnetite-bearing slate to phyllite, siliceous pyrrhotite-bearing slate to phyllite, magnetite-bearing chert to phyllite and carbonaceous pyrite-bearing slate to phyllite and sulphide-bearing chert (Conners et al., 2005).

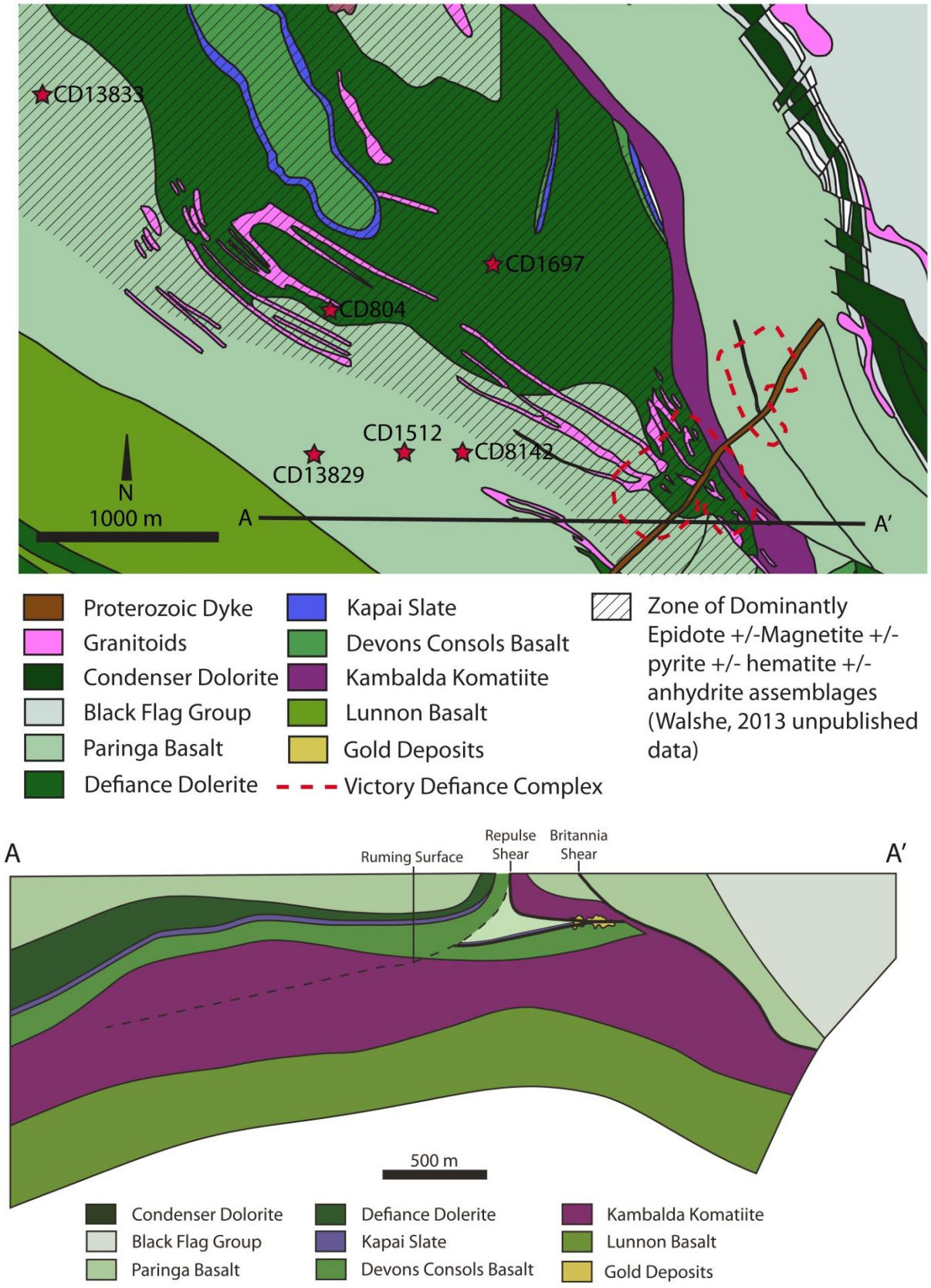

Figure 6.2: Local geology of the St. Ives gold district and location of drill holes used in this study. Both map and section are constructed using the models built by CSIRO.

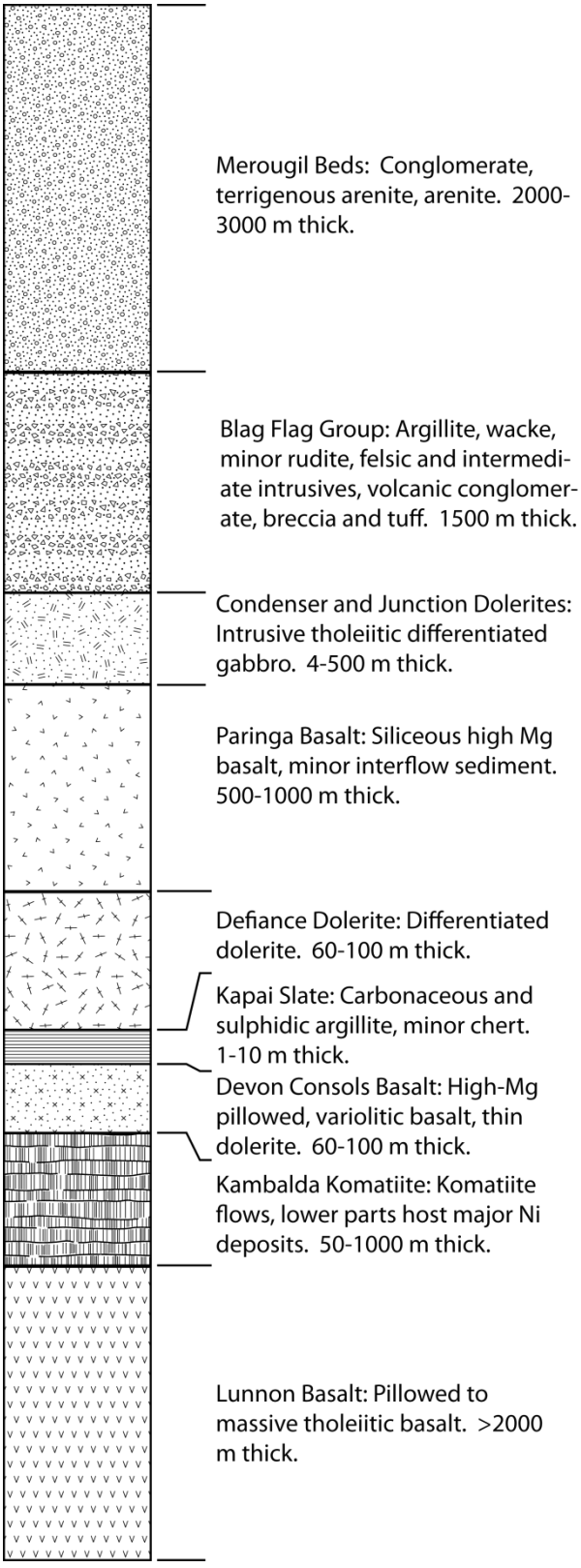

Figure 6.3: Stratigraphic section of St. Ives gold district.

Pyrite within the Kapai Slate shows six different texture types. Py_1 is comprised of fine (~10 µm diameter) euhedral pyrite crystals accumulated into bands with a black shale matrix (Figure 6.4a, 6.4b and 6.4c). The second pyrite texture (py_2) is in the form of nodules which appear to be an agglomeration of several smaller grained pyrite crystals with minor recrystallization (Figure 6.4a, 6.4b and 6.4c). The third texture (py_3) is pyrite bands/veins which are coarse grained, near massive and related to variable amounts of pyrrhotite and up to 5% sphalerite and trace chalcopyrite. These bands both cut and are parallel to bedding (figure 6.4a, 6.4d and 6.4e). The fourth pyrite (py_4) texture is very coarse grained, often inclusion-poor and occurs as thick bands crosscutting pre-existing sulphides (Figure 6.4f, 6.4g, 6.4h and 6.4i). The fifth texture (py_5) is found only in the magnetite bearing Kapai Slate and is subhedral and very inclusion-rich (Figure 6.4f). The last texture is subhedral to euhedral pyrite grains found within the mafic units of the Kambalda Sequence (Figure 6.4j, 6.4k, and 6.4l).

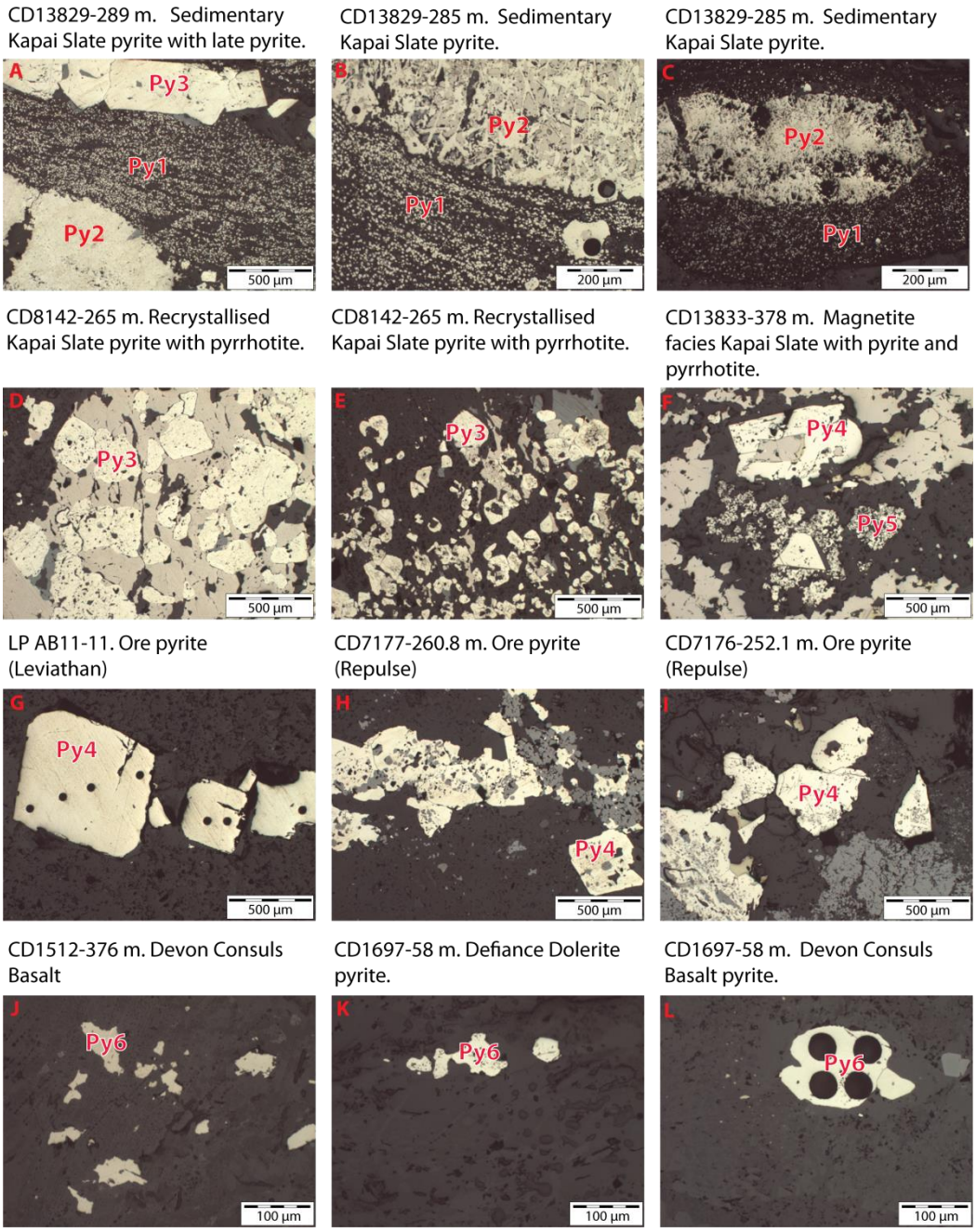

Figure 6.4: Reflected light microscope images showing textures of sulphides found in the St. Ives gold district. A) shows a diagenetic pyrite nodule and diagenetic fine grained euhedral pyrite. Near the top of the image large euhedral metamorphic or hydrothermal pyrite is also present. B) and C) show diagenetic pyrite nodules with variable degrees of pyrrhotisation and diagenetic fine grained euhedral pyrite. D) and E) show recrystallised diagenetic pyrite, it is inclusion rich and euhedral, with pyrrhotite +/- sphalerite +/- chalcopyrite. F) shows inclusion poor euhedral pyrite and suhedral very inclusion rich pyrite and pyrrhotite found in the magnetite altered Kapai Slate. G) shows the euhedral inclusion poor pyrite from the Leviathan deposit ore stage pyrite. H) and I) show the inclusion rich euhedral to subhedral pyrite from the ore stage pyrite from Repulse. J), K) and L) show the anhedral pyrite from the mafic units of the St. Ives gold district.

The second and third texture types contain variable pyrrhotite alteration ranging from 20% to 90%. The coarse, euhedral pyrite appears to overprint the pyrrhotite, but overprinting relationships are difficult to determine. The other sulphides (such as chalcopyrite and sphalerite) tend to be associated more with pyrrhotite than pyrite.

6.2.5 Metamorphism and Alteration

The metamorphic history and alteration of the St. Ives district have been summarised by Roberts and Elias (1990b). The district has been regionally metamorphosed to upper greenschist from lower amphibolites facies (Swager, 1997). The metamorphic assemblage contains hornblende-actinolite-plagioclase-chlorite-epidote-quartz-sphene-ilmenite and the original igneous textures are preserved by the metamorphism. Prior to the formation of the major gold deposits the central corridor of the St. Ives gold district experienced strong magnetite alteration (Neumayr et al., 2008). No sedimentary pyrite was preserved in these magnetite altered units in the drill holes examined in this study, thus we are assuming the magnetite series Kapai slate to contain no sedimentary pyrite. However, there are likely transition zones on the margin of the magnetite rich domain.

The gold deposits display distinct alteration zoning within the mafic host rocks. The regional metamorphism is overprinted by a 10 to 30 m chlorite zone that extends outwards from the centre of the mineralized shear zones (Nguyen et al., 1998a). With increasing proximity to the shear zones chlorite is replaced by biotite, carbonate, pyrite, magnetite and minor albite. The inner most zone is the albite zone that contains the highest gold grades which are associated with euhedral pyrite (Roberts and Elias, 1990a). The mineral assemblage that defines the albite zone is albite-ankerite/dolomite-quartz-pyrite with minor chlorite, biotite, muscovite and calcite. Geochemically this alteration zone is depleted in SiO_2, CaO, K_2O and Al_2O_3 and enriched in Na_2O relative to the outer alteration zones (Roberts and Elias, 1990a). The biotite alteration zone marks a change in the bulk rock composition with an increase in K_2O and a decrease in MgO, CaO and FeO represented by a mineral assemblage of albite-biotite-quartz-calcite/dolomite-magnetite-muscovite (Roberts and Elias, 1990a).

6.2.6 Structural Geology

The structural history of the St. Ives District has been discussed in detail by Blewett et al. (2010) and Miller (2010). There are six major phases of deformation recognised in the St. Ives area: D_1 (thrusting), D_{1e} (extension), D_2 (NE-SW compression), D_3 (NE-SW extension), D_4 (NW-SE compression) and D_5 (NE-SW shortening). For a more rigorous discussion of the structural history of the St. Ives gold field please see Appendix 11 and references therein.

The majority of the gold mineralisation in the St. Ives District formed during the D_4 compressional event (Blewett and Czarnota, 2007). Movement along the Playa Fault is believed to have created permeability in the footwall and hanging wall units that acted as an important fluid conduit. The flanks of the Kambalda antiform and areas along some of the major intrusive bodies (Neumayr et al., 2008) are also important pathways for the mineralising fluids. Nguyen et al. (1998b) showed the role that transpressional and contractional faults played in the deposition of gold. During gold deposition the SW-NE trending faults formed domain boundaries for the north trending fault segments. The mineralisation along these faults is interpreted to be due to fluid flow allowed by failure during periodic seismicity (Cox and Ruming, 2004).

6.3 Methods

6.3.1 Sample Preparation

Representative pyrite from different geochemical facies and geological units (with a focus on the Kapai Slate) were selected from across the St. Ives gold district, the sample locations are given in Figure 6.2 and drill logs for these holes is provided in Appendix 12. These samples were set into 25 mm epoxy mounts and were finished with a 1 µm diamond polishing paste. After detailed optical microscope observation and LA-ICPMS analyses, selected pyrite types were cut out of the mounts using a diamond saw. These pyrites were then mounted into a 25 mm epoxy mount and again polished with 1 µm diamond paste. These mounts were used for the SHRIMP SI analyses.

6.3.2 LA-ICPMS

The total trace element content of the pyrite sampled from the St. Ives gold district was analysed at the University of Tasmania using a laser microprobe and ICPMS. A 193 nm solid-state laser microprobe (UP193ss, NewWave Research) coupled to an Argilent 7700s quadruple mass-spectrometer and a 213 nm solid-state laser microprobe (UP213, NewWave Research) coupled to an Agilent 7500a quadruple mass-spectrometer were used to conduct the analyses.

Due to variations in size of the pyrite, beam sizes ranging from 10 to 35 µm were utilised in the analyses. Background was measured for 30 s prior to a 60 s period of laser ablation for each analysis. Beam fluences of approximately 2 J/cm^2 and 3.5 J/cm^2 were used for UP193ss and UP213, respectively and a pulse rate of 5 Hz was used for both lasers. The analyses were carried out in an atmosphere of pure He which was introduced into the cell at a rate of 0.8 l/min. To improve the aerosol transport, 0.85 l/min of Ar was mixed with the He carrier gas. Double charged species and molecular oxide species were kept at levels below 0.2%. Because these species were maintained at such low levels no correction was applied to account for associated interferences. Calibration standard STDGL2b2 (Danyushevsky et al., 2011) was analysed twice between every 15-25 unknown analyses and at the beginning and end of each sample change. The methods proposed by Longerich et al. (1996) were used for data reduction.

6.3.3 Sulphur isotope analysis by SHRIMP SI

Pyrite chosen to be representative of many different lithologic units within the St. Ives gold district were analysed by SHRIMP SI at the Australian National University (ANU). Prior to analysis the sample mounts were coated with 0.01 µm of gold to dissipate the charge produced on the surface of the sample during analysis and to carry the -10 kV charge so that the ions coming off the surface had the correct potential. The samples were then placed into an ultrahigh vacuum (10^{-6} Pa) where a primary beam of 5 kV Cs^+ was focussed to 25 µm on the target pyrite. As the sample surface was held at -10 kV and the impacting Cs^+ ions are accelerated to 5 kV the impact energy is 15 kV. The beam pre-ablated the surface of the area to be analysed and then the analysis spot was sputtered for 120 s to ensure no contamination. This was followed by 10 cycles of 10 s data acquisition intervals in which count rates of 630

MHz, 5 MHz and 28 MHz were utilised for $^{32}S^-$, $^{33}S^-$ and $^{34}S^-$ respectively. Faraday cups were used to detect and measure the $^{32}S^-$, $^{33}S^-$ and $^{34}S^-$ isotopes (Ireland et al., 2008). Well characterised Ruttan pyrite (Whitehouse, 2013) was used as a standard and two analyses of the standard were conducted approximately every 7 analyses.

6.4 Results

6.4.1 Pyrite Textures

Sedimentary pyrite from the Kapai Slate occurs in two different types of small (> 10 µm diameter) euhedral crystal clusters (py1) and centimetre scale nodules or bands (py2). The nodular pyrite exhibits variable degrees of pyrrhotization. When pyrite has been extensively altered to pyrrhotite, associated sphalerite and chalcopyrite are also present (Figure 6.4a, 6.4b and 6.4c). In some areas the pyrite facies Kapai Slate pyrite has been recrystallised to a subhedral texture ranging from 20 µm to 1 mm scale crystals (py3). This pyrite is associated with pyrrhotite, lesser sphalerite, chalcopyrite and minor gold (Figure 6.4d and 6.4e). These recrystallised textures are most commonly associated with fault and/or vein structures.

The magnetite bearing Kapai Slate contains significant magnetite and early, diagenetic pyrite has not been identified in this study. In these samples pyrrhotite is often the dominant sulfide and where pyrite is present there are two textures observed (Figure 6.4f). One is inclusion-poor and ranges from subhedral to euhedral (py4). The second texture is inclusion-rich, anhedral and sometimes occurs as clusters of smaller pyrite crystals (py5). Pyrite associated with the gold mineralisation are large (>300 µm), euhedral in shape, range from inclusion-poor to moderately inclusion-rich (25% inclusions) and can be associated with other sulphide species (Figure 6.4g, 6.4h and 6.4i). Pyrite is also present in the mafic units of the Kambalda Sequence. They tend to be small (<100 µm) anhedral crystals with minor inclusions (Figure 6.4j, 6.4k and 6.4l).

6.4.2 LA-ICPMS analyses

The Sedimentary pyrite from the Kapai Slate that is distal to the ore zones has a relatively tight distribution of the elements of interest that are presented in Figures 6.5, 6.6 and 6.7, table 6.1 and Appendix 13. The majority of the sedimentary pyrite data varies between 80-

1000 ppm for Ni and Co, 50-1500 ppm for Cu, 100-1500 ppm for As, 1-10 ppm for Mo and 2-50 ppm for Se. This data plots within or adjacent to the field for Archean pyrite defined in chapter 4. The recrystallised sedimentary pyrite from the Kapai Slate differs from the uncrystallised sedimentary pyrite by showing a broad scatter in the data points, especially for Ni, Co and Mo. The pyrite from the magnetite bearing Kapai Slate forms a distinct field separate from the sedimentary pyrite. This is enriched in Co and Se but depleted in Cu, As and Mo compared to the unaltered sedimentary pyrite.

Two different ore related pyrites were analysed in this study, one from the Repulse deposit and one from the Leviathan deposit. The ore related pyrite tends to be enriched in Ni but depleted in Cu, As and Mo, similar to the pyrite in the magnetite bearing Kapai Slate. Pyrite from the basalt is similarly depleted in Cu, As and Mo but is also depleted in Se. The basalt pyrite trace element content differs from the other depleted units in that it is very enriched (over an order of magnitude) in Ni.

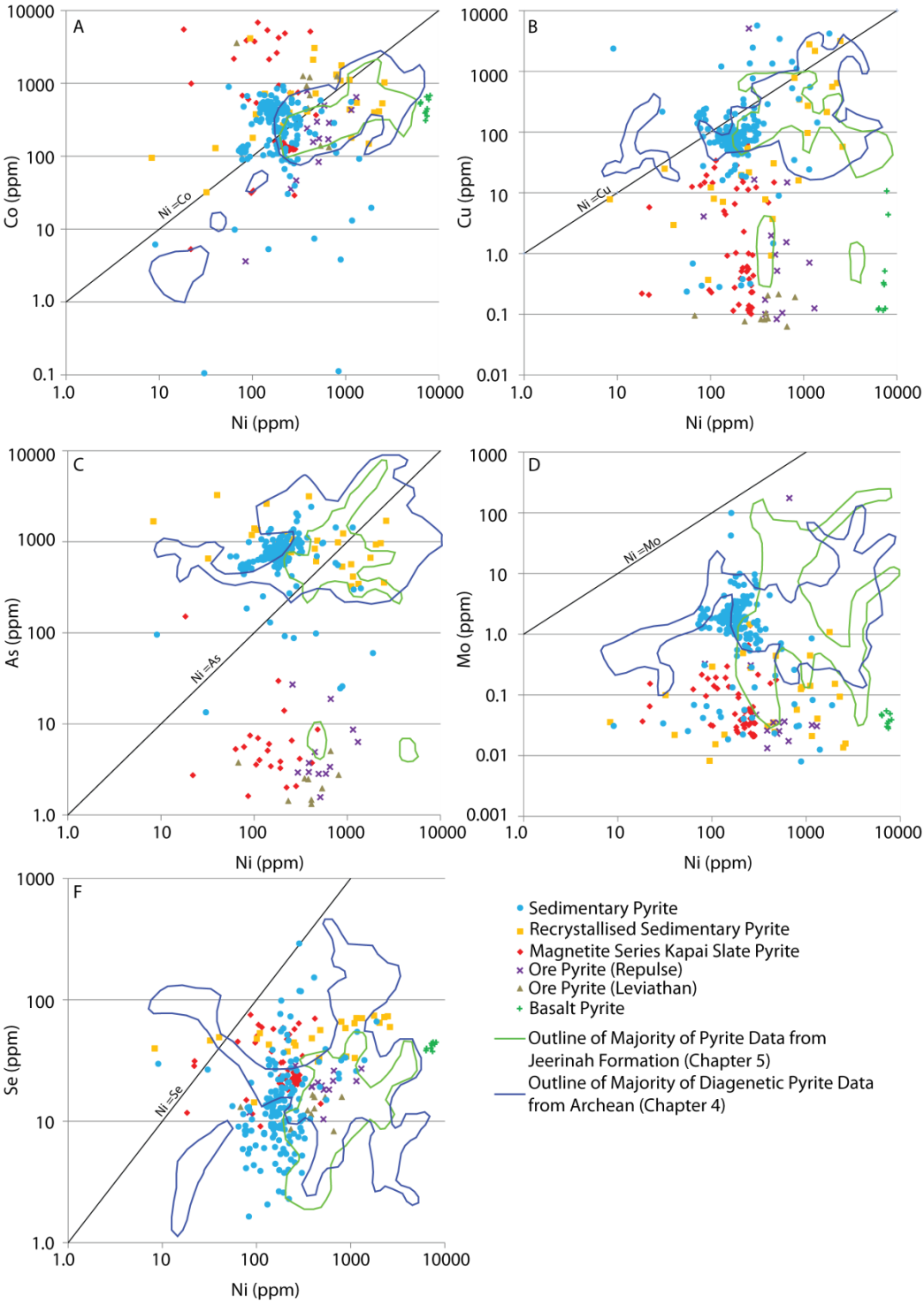

Figure 6.5: Scatter plots of Co, Cu, As, Mo and Se in pyrite against Ni in pyrite. Outlines of these elements against Ni for the Jeerinah Formation and Archean pyrite from Chapters 4 and 5 show how the different types of pyrite from the St. Ives gold district compare with other trace element pyrite from the Archean.

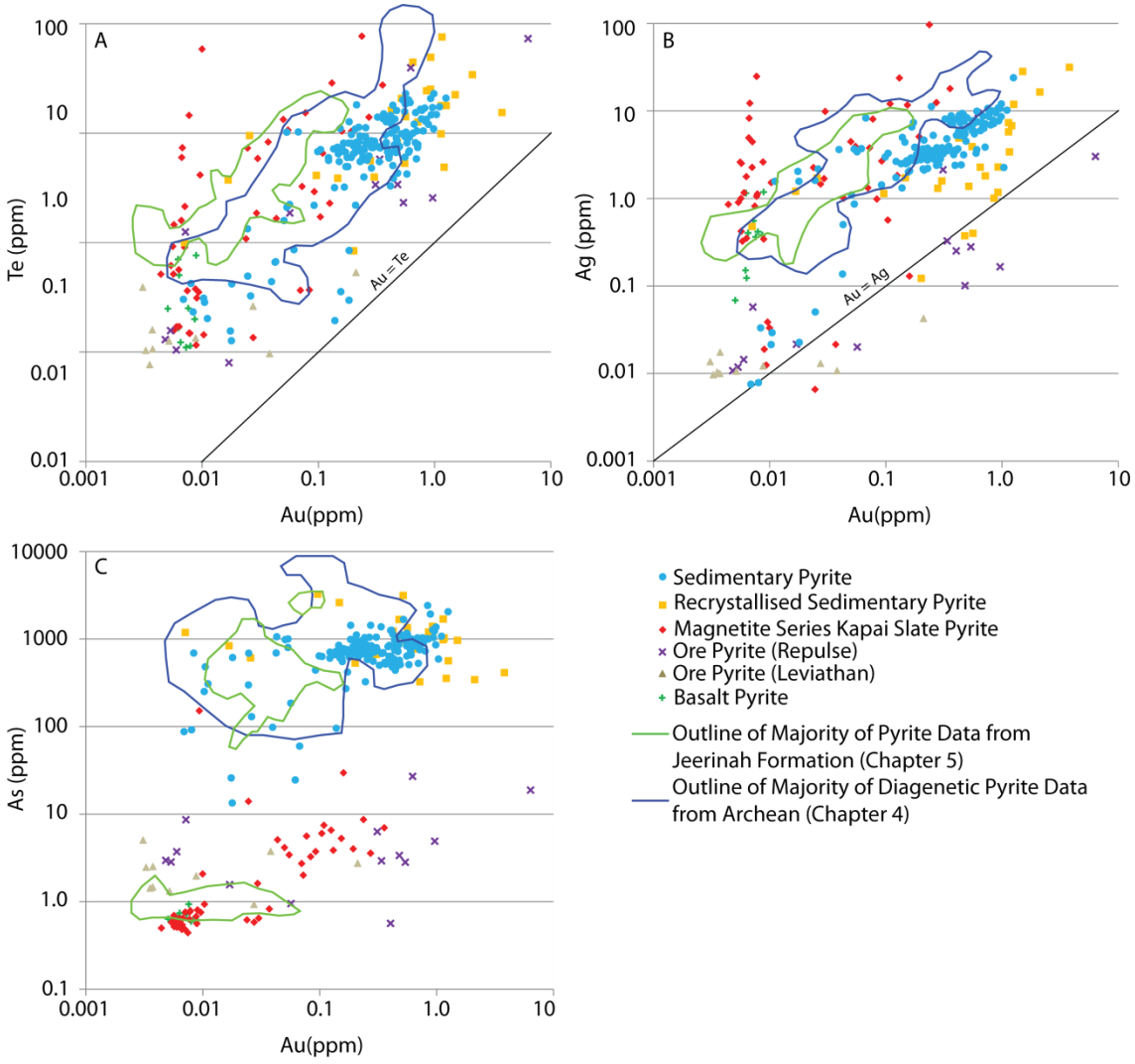

Figure 6.6: Scatter plots of Te, Ag and As in pyrite against Au in pyrite. Outlines of these elements against Au for the Jeerinah Formation and Archean pyrite from Gregory et al., (papers 3 and 4) show how the different types of pyrite from the St. Ives gold district compare with other trace element pyrite from the Archean.

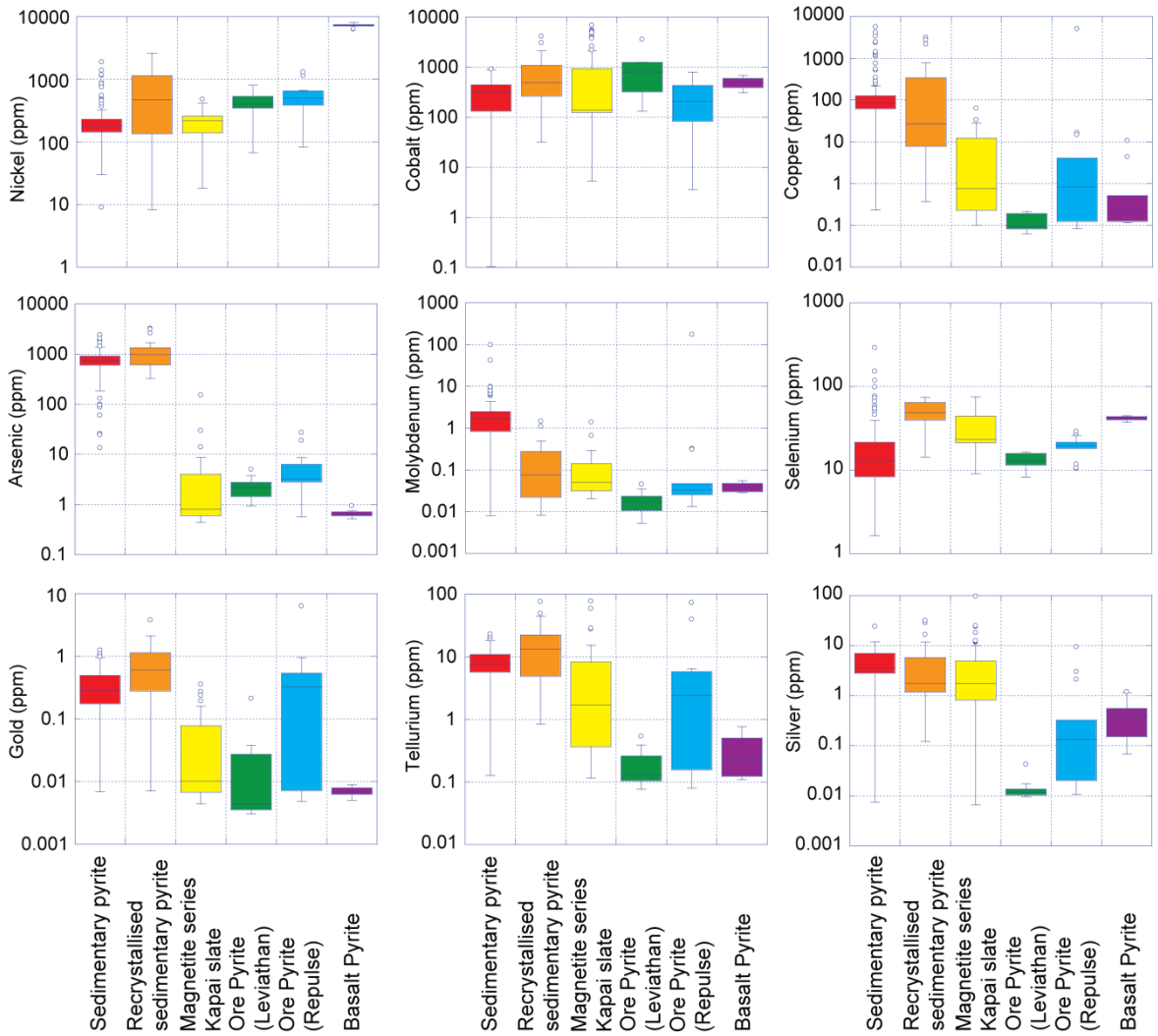

Figure 6.7: Box plots of Ni, Co, Cu, As, Mo, Se, Au, Te and Ag in pyrite from the St. Ives gold district. The horizontal line represents the median while the box represents the 25th to 75th percentile of the data. Whiskers are drawn to the last data point that is 1.5 times the length for the box from the maximum of minimum. Open circles are outliers.

A similar tight cluster of data in the sedimentary pyrite from the Kapai Slate is present for Au, Te and Ag (Figure 6.7). These data range from 0.1-1 ppm for Au, 1- 20 ppm for Te and 1-10 for Ag and plot in or adjacent to the fields for sedimentary pyrite defined in chapter 4. Similar to other elements the recrystallised pyrite has a wide range of values for these elements, ranging over two to three orders of magnitude. The pyrite from the magnetite series Kapai Slate is depleted in these elements. The ore stage pyrites differ from each other. The pyrite from Leviathan deposit is depleted in Au, Ag and Te while the Repulse pyrite is similar to sedimentary pyrite in Au content but depleted in Te and Ag. However, it should be noted that during data reduction inclusions, including gold inclusions, are avoided to try and

determine the element content of the pyrite. The Leviathan pyrite had large Au large gold inclusions that were easily avoided. Thus it may be that the differences in gold content in the two ore stage pyrites may be due to a difference in size of inclusions rather than an actual difference in amount of gold in the pyrite structure. The basalt pyrite is low in Au, Ag and Te.

Table 6.1: Median values of trace elements in pyrite from St. Ives gold district

Unit	n	Ni (ppm)	Co (ppm)	Cu (ppm)	As (ppm)	Mo (ppm)	Se (ppm)	Au (ppm)	Te (ppm)	Ag (ppm)
Sedimentary pyrite	164	180	311	83	741	1.67	13	0.28	7.66	3.61
Recrystallized Kapai Slate	26	470	485	27.6	972	0.08	49	0.61	13.37	1.76
Ore pyrite (Leviathan)	10	403	804	BD	2	BD	13	BD	BD	BD
Ore pyrite (Repulse)	14	503	208	0.8	3	BD	20	0.32	2.44	0.13
Magnetite bearing Kapai Slate	50	219	138	0.8	BD	BD	23	BD	1.69	1.73
Basalt pyrite	10	7353	485	BD	BD	BD	43	BD	BD	0.39

6.4.3 Sulphur isotopes

The sedimentary Kapai Slate pyrite typically has weak positive $\delta^{34}S$ (generally ranging from 2.3 – 7.4) as can be seen it Figure 6.8 and Appendix 13. Two different $\Delta^{33}S$ signatures are evident for this pyrite. One of these has a positive MIF signature, with a range of $\Delta^{33}S$ from 0.7 to 2.4. The second group has a negative shift with $\Delta^{33}S$ ranging from -0.9 to 0.1. Recrystallised Kapai Slate pyrite has a similar $\delta^{34}S$ and $\Delta^{33}S$ signature to the first of these groups. The $\delta^{34}S$ for these pyrites ranges from 1.1 to 5.2 and $\Delta^{33}S$ ranges from 1.0 to 1.3. The magnetite containing (magnetite series) Kapai Slate have similar $\delta^{34}S$ values to the sedimentary Kapai Slate pyrite with values from 1.6 to 7.1, however the $\Delta^{33}S$ are different and contain no to minor MIF signal ($\Delta^{33}S$ values between -0.05 to 0.23). The ore stage pyrite (from Repulse) has a different $\delta^{34}S$ signature, which ranges from -7.7 to -8.5. While the $\Delta^{33}S$ signature is similar to the magnetite series Kapai slate pyrite, ranging from -0.13 to 0.24.

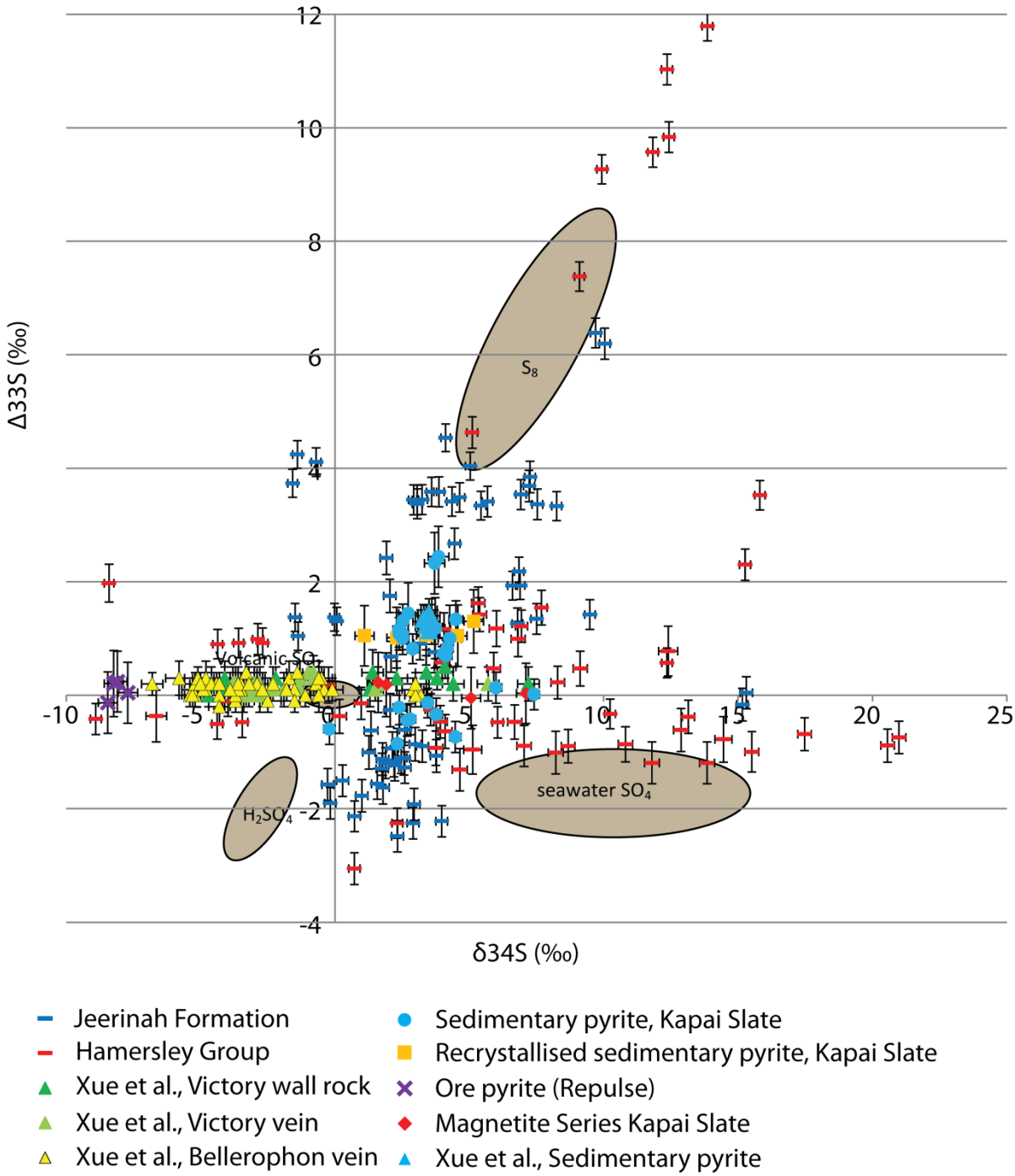

Figure 6.8: $\Delta^{33}S$ versus $\delta^{34}S$ for SHRIMP SI analyses of pyrite for the St. Ives gold district, Hamersley Group and Jeerinah Formation. The diagenetic Kapai Slate samples and recrystallised Kapai Slate pyrite correlate well with some of the Archean sedimentary pyrite analyses from the Jeerinah Formation and Hamersley Group. While the ore phase Leviathan and Repulse pyrite and the magnetite altered Kapai Slate correlate well with the ore phase pyrite analyses of Xue et al. (2013). Fields for S_8, SO_2, H_2SO_4 and SO_4 are from Ono et al., (2003).

6.5 Discussion

6.5.1 Geochemical evidence supporting textural classification of sedimentary pyrite

In an area that has undergone significant regional metamorphism and hydrothermal alteration the preservation of sedimentary pyrite is sometimes debated. However, syngenetic/diagenetic pyrite has distinctive geochemical characteristics that can be summarised in the following trace element ratios: $0.01 < Co/Ni < 2$, $0.01 < Cu/Ni < 10$, $0.1 < As/Ni < 10$, $Ag/Au > 1$, $Te/Au > 1$ and $As/Au > 200$ (chapter 4). Data for these elemental ratios are presented in table 6.2. When examining the median of these ratios, only the Co/Ni ratio is satisfied for all of the lithologies examined in the St. Ives district (Table 6.2). As expected for the ore pyrite (Leviathan), magnetite facies Kapai Slate and the basalt pyrite, one or several of the other elements are below detection limits or the ratios are below those defined for diagenetic pyrite. Similarly the ore pyrite (Repulse) also does not meet the criteria for diagenetic pyrite in regards to Cu/Ni and As/Ni ratios, which are much lower than expected for diagenetic pyrite. The recrystallised sedimentary pyrite and sedimentary pyrite both have trace metal ratios expected for diagentic pyrite. However, the recrystallised sedimentary pyrite has significantly lower Cu/Ni, As/Ni, Ag/Au and As/Au due to loss of these trace metals during recrystallization. Overall, the pyrite within the Kapai Slate that was determined to be of sedimentary origin based on texture is consistent with the trace metal content expected for sedimentary pyrite, while the ore pyrite, magnetite bearing Kapai Slate and basalt pyrite show significantly different trace element content ratios.

Table 6.2: Medians of elemental ratios for pyrite from St. Ives.

Unit	n	Co/Ni	Cu/Ni	As/Ni	Ag/Au	Te/Au	As/Au
Sedimentary pyrite (KSSP)	164	1.51	0.46	4.58	12.92	24.83	2475
Non-ore mineralized structure (KS-RMS)	26	1.38	0.11	1.62	5.40	22.52	1595
Leviathan pit ore (LP-OP)	10	1.60	0.0003	0.005	BD	BD	BD
Altered porphyry (APR-OP)	14	0.36	0.001	0.007	1.12	16.57	19
Magnetite altered Kapai Slate (KS-OMS)	50	0.68	0.005	0.006	BD	BD	BD
Basalt pyrite (BP)	10	0.07	0.00003	0.00009	BD	BD	BD

6.5.2 Sulphur Sources

Modelling by Ono et al. (2003) has shown that a combination of $\Delta^{33}S$ and $\delta^{34}S$ groups can be used to determine the source of sulphur in pyrite prior to the great oxygenation event (GOE). They showed that a positive $\Delta^{33}S$ and $\delta^{34}S$ signature reflects a conversion of volcanically soured sulfur to S_8 via atmospheric reactions, a near zero $\Delta^{33}S$ and $\delta^{34}S$ signature reflects a volcanic SO_2 source, a negative $\Delta^{33}S$ and $\delta^{34}S$ signature reflects a H_2SO_4 source and a negative $\Delta^{33}S$ and positive $\delta^{34}S$ signature reflects a sea water sulphate source. The $\delta^{34}S$ of the sedimentary pyrite is lower than expected for Archean seawater sulphate (Ono et al., 2003). Bacterial reduction of seawater sulphate can create this negative shift and this $\delta^{34}S$ signature is consistent with sedimentary pyrite in the Archean (chapter 5, Ono et al., 2003; Partridge et al., 2008). The pyrite from the magnetite bearing Kapai Slate has a positive $\delta^{34}S$ and a $\Delta^{33}S$ that is slightly positive but with no major MIF signal. This data is consistent with homogenised sedimentary source of pyrite where $\delta^{34}S$ is consistent with bacterial reduced sea water sulphate sourced pyrite and the $\Delta^{33}S$ could reflect homogenisation of the positive and negative $\Delta^{33}S$ signatures found in sedimentary pyrite in the Kapai Slate. These S isotope results are also consistent with the results by Neumayr et al. (2008), who interpreted them to represent the presence of the reduced fluid component of their fluid mixing model. Ore stage pyrite from our study has negative $\delta^{34}S$ isotope results that overlap with those of other studies (Neumayr et al., 2008; Xue et al., 2013). Neumayr et al. (2008) used these results, and associated magnetite in the ore zones, to argue for the presence of oxidising fluids in the ore zones. The $\Delta^{33}S$ for the ore pyrite (Repulse) and magnetite series Kapai Slate pyrite have a minor to no MIF signal. Models for the formation of the gold deposits have suggested two possible sources of the gold and sulphur found at St. Ives: metamorphic devolatilization and a deep magmatic or mantle source. These data can be used to support both models. Sulphur derived from metamorphism of the mafic rocks of the Kambalda Sequence (Phillips and Powell, 2010) would not be expected to have a MIF signal as the sulfur found would not have been exposed to the atmosphere and thus would not have been exposed to the necessary radiation to gain a MIF signature (Farquhar et al., 2000). The Kapai Slate contains both positive and negative shifted $\Delta^{33}S$ signatures, with a positive signature being more common in our analyses, though only a small number of core samples contain persevered sedimentary pyrite, so it is difficult to be certain that these samples are representative of the entire area. Homogenisation of these two signatures would result in the slightly positive $\Delta^{33}S$ signal observed in the magnetite series Kapai Slate and the ore stage pyrite. A second interpretation

is that the lack of an obvious MIF signal suggests that the sulphur is from a source not related to the sedimentary or mafic rocks of the basin (Xue et al., 2013). A combination of both hypotheses is also possible. If the sulphur source was a magmatic or mantle sourced fluid it would be expected to have a $\Delta^{33}S$ signature of zero (Farquhar and Wing, 2003). Thus, a 15% contribution of the positive MIF Kapai Slate (mean $\Delta^{33}S$ =1.3) is needed to achieve the mean $\Delta^{33}S$ (0.2) for the analyses from the magnetite series Kapai Slate and the ore pyrite (Repulse) analyses presented in this study. Similar proportions would be required to explain the analyses of pyrite from Bellerophon, Victory vein and Victory "host rock" from Xue et al. (2013).

The two different $\Delta^{33}S$ groups identified for the sedimentary pyrite are similar to two of the three groups identified in chapter 5 for the 2662 Ma Jeerinah Formation of the same age in the Hamersley Basin. In chapter 5 it was considered that these groups are from pyrite formed in the Archean ocean, with the positive MIF signal group being from a mixed elemental sulphur (from volcanic eruptions) and bacterially reduced seawater sulphate source based on the sulphur source signatures defined by Ono et al. (2003). The negative MIF signal represents a seawater sulphate source with the $\delta^{34}S$ decreased by bacterial reduction of the sulphate (Ono et al., 2003). The positive shift in the $\Delta^{33}S$ is expected, as much of the clastic sediments that make up the Kapai Slate are interpreted to be from pyroclastic material (Squire et al., 2010), and it is reasonable that volcanic-derived S was included with the material, and later formed pyrite. The recrystallised Kapai Slate pyrite has a similar $\Delta^{33}S$ and $\delta^{34}S$ signature to the sedimentary pyrite. This supports the identification of the pyrite being recrystallised and/or remobilised from the Kapai Slate.

6.5.3 Chemical conditions of the ocean basin at the time of Kapai Slate deposition

Molybdenum is one of the most common elements used to determine paleo-redox conditions as it is mobile in the oxidised MoO_4^{2-} form and immobile in its reduced form (Tribovillard et al., 2004). There was a lack of Mo in Archean oceans due to a lack of atmospheric oxygen, which limits the source of Mo from weathered sulphides (Scott et al., 2008; Scott et al., 2011). This decreases the usefulness of Mo as an indicator of redox conditions in the Archean. However, our results from the sedimentary pyrite from the Kapai Slate (median Mo of 1.7 ppm) are still within the range of Mo content of pyrite from the anoxic to euxinic Jeerinah Formation (0.3-9.7 ppm medians), making the Mo content of the Kapai Slate pyrite

consistent with pyrite from the earliest known euxinic interval identified in the 2662 Ma Jeerinah Formation (Scott et al., 2011).

Nickel and copper are both indicators of organic carbon sinking flux (productivity) (Tribovillard et al., 2004). The pyrite from the Kapai Slate has less Cu, Co and Ni (medians of 83 ppm, 311 ppm and 180 ppm respectively) compared to the overall median for the Jeerinah Formation and Hamersley Basin (overall median of 194 ppm, 401 ppm and 898 ppm respectfully) (chapter 5). This is despite the Kapai Slate being hosted in a predominantly mafic sequence which may be expected to result in elevated Cu and Ni in pyrite (Large et al., in press). This suggests that productivity in the depositional setting of the Kapai Slate was lower than that of the Jeerinah Formation. In chapter 4 it was shown that the Au and Co contents in pyrite are higher in shallower facies. A lack of trace metals was evident in the pyrite from the iron-dominated part of the McRea Shale (chapter 5). No similar lack of trace elements was observed in the Kapai Slate, suggesting that at the time of deposition the ocean was iron limited. These data suggest that the Kapai Slate was deposited in an anoxic to euxinic iron limited basin with relatively low biologic activity.

6.5.4 Possible alternate source of S and Au for Archean Lode Gold Deposits

Xue et al. (2013) used the presence on only minor MIF signals to support the hypothesis that the sulphur (and therefore the gold) is from a magmatic or mantle source. However, as there is a minor positive shift in $\Delta^{33}S$ signature in some of the ore related pyrite and the sedimentary rocks in the Kambalda Sequence have both positive and negative MIF signals the possibility cannot be discounted that there was a significant contribution of sulphur (and therefore gold) from the mafic and sedimentary units of the Kambalda Sequence. Also the metamorphic model for the gold deposit cannot be discounted based on this data because the $\Delta^{33}S$ signature of the mafic sequences is not known and as much of the S within the mafic units would not have been exposed to the atmosphere thus it is expected that it would not have acquired a significant MIF signature.

It has been shown by several authors (Large et al., 2011; Large et al., 2009; Large et al., 2007; Thomas et al., 2011) and in chapters 3, 4 and 5 that gold, arsenic and several other trace metals can accumulate in diagenetic pyrite. This enrichment of gold and arsenic in diagenetic pyrite is also present in the Kapai Slate distal from mineralization. Prior to the

major gold deposition the central corridor of the St. Ives gold district experienced extensive magnetite alteration (Neumayr et al., 2008). Based on our observation of drill core that intersected the magnetite bearing Kapai slate, there does not appear to be any residual sedimentary pyrite left. However, our survey of drill core of the magnetite bearing Kapai Slate was by no means exhaustive and some residual pyrite may be found in other cores.

Following the models for a sedimentary source of gold for orogenic gold deposits (Large et al., 2011; Large et al., 2009; Large et al., 2007; Steadman et al., 2013; Thomas et al., 2011; Tomkins, 2010) we tested the possibility that some of the gold in the St. Ives gold district maybe sourced from the Kapai Slate. To do this we used the following equations:

1) $M_{Au\ oxidised} = V_{KS\ oxidised} * \%Py_{KS} * KS_{med\ Au} * \%Py_{destroyed} / Py_{density}$

Where $M_{Au\ oxidised}$ is the mass of gold released from the magnetite series Kapai Slate; $V_{KS\ oxidised}$ is the volume of magnetite bearing Kapai Slate, $KS_{med\ Au}$ is the median gold content of sedimentary pyrite in the Kapai Slate and $\%Py_{destroyed}$ is the percent of diagenetic pyrite recrystallised or dissolved. A similar equation can be written for the sedimentary pyrite replaced by pyrrhotite on the eastern side of the gold district as pyrrhotite retains little of the trace metals contained within diagenetic pyrite (Large et al., 2007).

2) $M_{Au\ reduced} = V_{KS\ reduced} * \%Py_{KS} * KS_{med\ Au} * \%Po / Py_{density}$

Where $M_{Au\ reduced}$ is the mass of gold released from the pyrrhotite bearing Kapai Slate between the magnetite bearing Kapai Slate and major NNW trending faults to the east; $V_{KS\ reduced}$ is the volume of Kapai Slate between the oxidised series and major NNW trending faults to the east; $KS_{med\ Au}$ is the median gold content of sedimentary pyrite in the Kapai Slate and %Po is the average degree of pyrrhotization. Volumes were calculated based on the boundaries on oxidized (average of 11.7 km by 2.5 km) and reduced facies (average of 11.5 km by 1.7 km) in Neumayr et al. (2008) and a 7 m average thickness for the Kapai Slate. Average precent diagenetic pyrite in the Kapai Slate was taken to be 6%, though it should be noted that this is difficult to determine exactly due to the amount of subsequent alteration and variation in pyrite content within the unit. In the case of the reduced facies Kapai Slate, %Po was taken to be 33%, but the degree of pyrrhotization also varies significantly. Finally, median gold content of pyrite was 0.28 ppm, as determined by LA-ICPMS analyses in this study. The substitution of these values into equations 1 and 2 yields a total of 150,000 oz Au released by alteration of pyrite in the Kapai Slate. This is far less than the 6,250,000 oz of

gold held in the deposits discovered thus far in the northern part of the St. Ives gold district (predominantly in the Victory-Defiance complex (3,000,000 oz) and Revenge complex (3,000,000 oz)) (Watchorn, 1998). Thus even if 50% of the gold released during this alteration event precipitated in the ore zones only 5% of the total gold could have been released from pyrite in the Kapai Slate. Therefore we conclude that even though some locally significant gold mineralisation could be sourced from the Kapai Slate, it is not likely to be a significant source for gold in the St. Ives gold district. However, this does not discount the possibility of other sedimentary (e.g. Black Flag Beds) or mafic units above or below the Kapai slate being a source for the gold.

6.5.5 Exploration Implications

One important application of trace element content of pyrite is its use as a vectoring tool in finding new ore deposits. As demonstrated above the trace element chemistry differs significant within the country rocks and in the lodes themselves. In Figure 6.9 we plot the ratios of Ni/Cu, Ni/Te and Se/Cu as these are elements that commonly change with proximity to ore deposits. It is readily apparent that there is a significant increase in all these ratios in the ore related pyrite. Similarly there is a moderate increase in the Ni/Cu ratio for the magnetite facies pyrite, which also reflects an increasing proximity to ore. The Se/Cu ratios are not significant for the magnetite series and ore series pyrite; however the recrystallised sedimentary pyrite is elevated compared to the sedimentary pyrite. Thus, the Se/Cu ratio might be used to determine proximity to ore in a regional context. However, in terms of direct application to exploration these results must be viewed as preliminary and further research into changes in trace element content of pyrite with increasing distance from gold lodes on a deposit scale must be completed before these methods could be used for exploration of ore deposits.

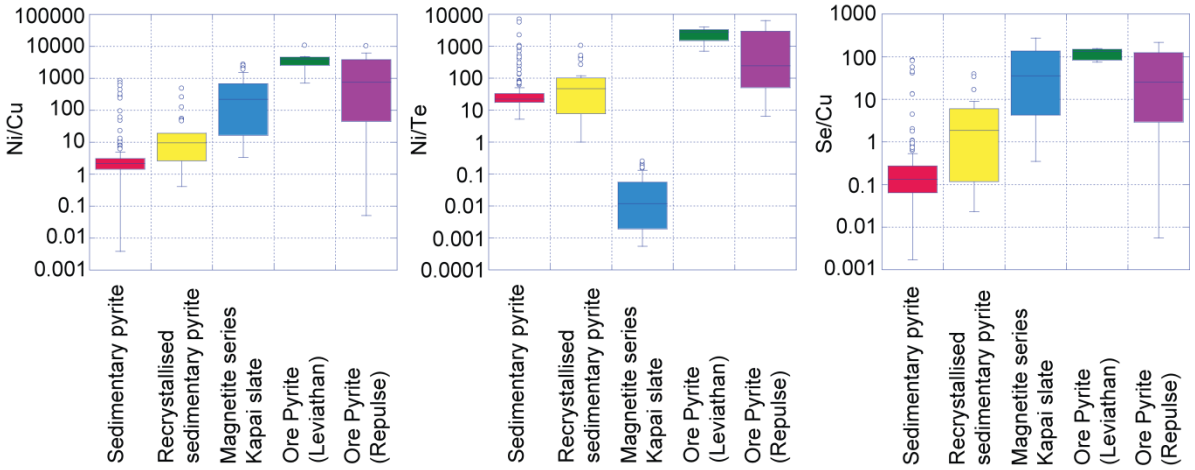

Figure 6.9: Ni/Cu; Ni/Te and Se/Cu ratios for sedimentary pyrite, recrystallized sedimentary pyrite, magnetite series pyrite and ore pyrite from St Ives. These are possible vectors to ore and it can be observed that these ratios are significantly higher for the ore stage pyrite.

6.6 Conclusions

Due to the introduction of hydrothermal fluids and remobilisation of trace metals related to metamorphism, analyses of preserved diagenetic pyrite is one of the only ways to approximate chemical conditions present during deposition of sedimentary rocks in many localities. In this study we have examined one such locality, the St Ives gold district. A combination of Mo, Cu, Ni and Co content of pyrite and a comparison with other similarly aged units has allowed us to determine that the Kapai Slate was deposited in a iron limited, anoxic to euxinic environment with low biological productivity. Proximal volcanic activity was indicated by a predominantly positive $\Delta^{33}S$ signature as suggested by previous studies. However the presence of negative $\Delta^{33}S$ signatures does indicate there were also periods of quiescence.

Pyrite geochemistry and sulfur isotope analyses were also used to determine whether the Kapai Slate may have been an important source of gold in the St Ives district. We determined that while it is a fertile source there is not a significant quantity of shale to provide the necessary gold and sulfur to form the deposits in the St. Ives district. However, this conclusion neither supports nor refutes any of the models proposed for gold deposition in the area. Preliminary investigations of the exploration uses of pyrite geochemistry suggest that it may be of use, however further studies must be completed before it can be applied in an exploration program.

6.7 References

Barley, M., and Groves, D. (1990) Deciphering the tectonic evolution of Archaean greenstone belts: the importance of contrasting histories to the distribution of mineralization in the Yilgarn Craton, Western Australia: Precambrian Research, 46(1), 3-20.

Bath, A. B., Walshe, J. L., Cloutier, J., Verrall, M., Cleverley, J. S., Pownceby, M. I., Macrae, C. M., Wilson, N. C., Tunjic, J., and Nortje, G. S. (2013) Biotite and Apatite as Tools for Tracking Pathways of Oxidized Fluids in the Archean East Repulse Gold Deposit, Australia: Economic Geology, 108(4), 667-690.

Berner, Z. A., Puchelt, H., Noltner, T., and Kramar, U. T. Z. (2013) Pyrite geochemistry in the Toarcian Posidonia Shale of south-west Germany: Evidence for contrasting trace-element patterns of diagenetic and syngenetic pyrites: Sedimentology, 60(2), 548-573.

Blewett, R., and Czarnota, K. (2007) A new integrated tectonic framework of the Eastern Goldfields Superterrane: Proceedings of Geoconference (WA) Inc Kalgoorlie, 7.

Champion, D. C., and Cassidy, K. F. (2007) An overview of the Yilgarn Craton and its crustal evolution: Record - Geoscience Australia, 8-13.

Conners, K., Donaldson, J. S., Morrison, R. S., Davy's, C., and Neumayr, P. (2005) The Stratigraphy of the Kambalda-St Ives District: Workshop Notes.

Cox, S. F., and Ruming, K. (2004) The St Ives mesothermal gold system, Western Australia - a case of golden aftershocks?: Journal of Structural Geology, 26(6-7), 1109-1125.

Danyushevsky, L., Robinson, P., Gilbert, S., Norman, M., Large, R., McGoldrick, P., and Shelley, M. (2011) Routine quantitative multi-element analysis of sulphide minerals by laser ablation ICP-MS: Standard development and consideration of matrix effects: Geochemistry: Exploration, Environment, Analysis, 11(1), 51-60.

Farquhar, J., Bao, H., and Thiemens, M. (2000) Atmospheric influence of Earth's earliest sulfur cycle: Science, 289(5480), 756-758.

Farquhar, J., and Wing, B. A. (2003) Multiple sulfur isotopes and the evolution of the atmosphere: Earth and Planetary Science Letters, 213(1), 1-13.

Groves, D. (1993) The crustal continuum model for late-Archaean lode-gold deposits of the Yilgarn Block, Western Australia: Mineralium Deposita, 28(6), 366-374.

Huerta-Diaz, M. A., and Morse, J. W. (1992) Pyritization of trace metals in anoxic marine sediments: Geochimica et Cosmochimica Acta, 56(7), 2681-2702.

Ireland, T., Clement, S., Compston, W., Foster, J., Holden, P., Jenkins, B., Lanc, P., Schram, N., and Williams, I. (2008) Development of SHRIMP: Australian Journal of Earth Sciences, 55(6-7), 937-954.

Kakegawa, T., Kawai, H., and Ohmoto, H. (1998) Origins of pyrites in the∼ 2.5 Ga Mt. McRae Shale, the Hamersley District, Western Australia: Geochimica et Cosmochimica Acta, 62(19), 3205-3220.

Kaufman, A. J., Johnston, D. T., Farquhar, J., Masterson, A. L., Lyons, T. W., Bates, S., Anbar, A. D., Arnold, G. L., Garvin, J., and Buick, R. (2007) Late Archean biospheric oxygenation and atmospheric evolution: Science, 317(5846), 1900-1903.

Large, R. R., Bull, S. W., and Maslennikov, V. V. (2011) A carbonaceous sedimentary source-rock model for Carlin-type and orogenic gold deposits: Economic Geology, 106(3), 331-358.

Large, R. R., Danyushevsky, L., Hollit, C., Maslennikov, V., Meffre, S., Gilbert, S., Bull, S., Scott, R., Emsbo, P., Thomas, H., Singh, B., and Foster, J. (2009) Gold and Trace Element Zonation in Pyrite Using a Laser Imaging Technique: Implications for the Timing of Gold in Orogenic and Carlin-Style Sediment-Hosted Deposits: Economic Geology, 104(5), 635-668.

Large, R. R., Maslennikov, V. V., Robert, F., Danyushevsky, L. V., and Chang, Z. S. (2007) Multistage sedimentary and metamorphic origin of pyrite and gold in the giant Sukhoi Log deposit, Lena gold province, Russia: Economic Geology, 102(7), 1233-1267.

Longerich, H. P., Jackson, S. E., and Günther, D. (1996) Inter-laboratory note. Laser ablation inductively coupled plasma mass spectrometric transient signal data acquisition and analyte concentration calculation: Journal of Analytical Atomic Spectrometry, 11(9), 899-904.

Lyons, T. W., Werne, J. P., Hollander, D. J., and Murray, R. W. (2003) Contrasting sulfur geochemistry and Fe/Al and Mo/Al ratios across the last oxic-to-anoxic transition in the Cariaco Basin, Venezuela: Chemical Geology, 195(1-4), 131-157.

Miller, J., Blewett, R., Tunjic, J., and Connors, K. (2010) The role of early formed structures on the development of the world class St Ives Goldfield, Yilgarn, WA: Precambrian Research, 183(2), 292-315.

Neumayr, P., Walshe, J., Hagemann, S., Petersen, K., Roache, A., Frikken, P., Horn, L., and Halley, S. (2008) Oxidized and reduced mineral assemblages in greenstone belt rocks of the St. Ives gold camp, Western Australia: vectors to high-grade ore bodies in Archaean gold deposits?: Mineralium Deposita, 43(3), 363-371.

Nguyen, P., Donaldson, J., and Ellery, S. (1998a), Revenge gold deposit, Kambalda: Geology of Australian and Papua New Guinean Mineral Deposits, 233-238.

Nguyen, P. T., Cox, S. F., Harris, L. B., and Powell, C. M., (1998b), Fault-valve behaviour in optimally oriented shear zones; an example at the Revenge gold mine, Kambalda, Western Australia: Journal of Structural Geology, 20(12), 1625-1640.

Ono, S., Eigenbrode, J. L., Pavlov, A. A., Kharecha, P., Rumble, D., Kasting, J. F., and Freeman, K. H. (2003) New insights into Archean sulfur cycle from mass-independent sulfur isotope records from the Hamersley Basin, Australia: Earth and Planetary Science Letters, 213(1), 15-30.

Partridge, M. A., Golding, S. D., Baublys, K. A., and Young, E. (2008) Pyrite paragenesis and multiple sulfur isotope distribution in late Archean and early Paleoproterozoic Hamersley Basin sediments: Earth and Planetary Science Letters, 272(1–2), 41-49.

Phillips, G., and Powell, R. (2010) Formation of gold deposits: a metamorphic devolatilization model: Journal of Metamorphic Geology, 28(6), 689-718.

Phillips, G. N., Groves, D. I., and Brown, I. J. (1987) Source requirements for the Golden Mile, Kalgoorlie: significance to the metamorphic replacement model for Archean gold deposits: Canadian Journal of Earth Sciences, 24(8), 1643-1651.

Phillips, G. N., and Powell, R. (1993) Link between gold provinces: Economic Geology, 88(5), 1084-1098.

Phillips, G. N., and Powell, R. (2009) Formation of gold deposits: Review and evaluation of the continuum model: Earth-Science Reviews, 94(1), 1-21.

Pitcairn, I. K., Teagle, D. A., Craw, D., Olivo, G. R., Kerrich, R., and Brewer, T. S. (2006) Sources of metals and fluids in orogenic gold deposits: insights from the Otago and Alpine Schists, New Zealand: Economic Geology, 101(8), 1525-1546.

Powell, R., Will, T., and Phillips, G. (1991) Metamorphism in Archaean greenstone belts: Calculated fluid compositions and implications for gold mineralization: Journal of Metamorphic Geology, 9(2), 141-150.

Roberts, D., and Elias, M. (1990a) Gold deposits of the Kambalda-St Ives region: Geology of the mineral deposits of Australia and Papua New Guinea. Australasian Institute of Mining and Metallurgy Monograph, 14, 479-491.

Roberts, D. E., and Elias, M. (1990b) Gold deposits of the Kambalda-St Ives region: Monograph Series - Australasian Institute of Mining and Metallurgy, 14, 479-491.

Scott, C., Lyons, T., Bekker, A., Shen, Y., Poulton, S., Chu, X., and Anbar, A. (2008) Tracing the stepwise oxygenation of the Proterozoic ocean: Nature, 452(7186), 456-459.

Scott, C. T., Bekker, A., Reinhard, C. T., Schnetger, B., Krapež, B., Rumble, D., and Lyons, T. W. (2011) Late Archean euxinic conditions before the rise of atmospheric oxygen: Geology, 39(2), 119-122.

Squire, R. J., Allen, C. M., Cas, R. A., Campbell, I. H., Blewett, R. S., and Nemchin, A. A. (2010) Two cycles of voluminous pyroclastic volcanism and sedimentation related to episodic granite emplacement during the late Archean: Eastern Yilgarn Craton, Western Australia: Precambrian Research, 183(2), 251-274.

Steadman, J. A., Large, R. R., Meffre, S., and Bull, S. W. (2013) Age, origin and significance of nodular sulfides in 2680 ma carbonaceous black shale of the eastern goldfields superterrane, yilgarn craton, western australia: Precambrian Research, 230, 227-247.

Swager, C. P. (1997), Tectono-stratigraphy of late Archaean greenstone terranes in the southern Eastern Goldfields, Western Australia: Precambrian Research, 83(1-3), 11-42.

Thomas, H. V., Large, R. R., Bull, S. W., Maslennikov, V., Berry, R. F., Fraser, R., Froud, S., and Moye, R. (2011) Pyrite and pyrrhotite textures and composition in sediments, laminated quartz veins, and reefs at Bendigo gold mine, Australia: insights for ore genesis: Economic Geology, 106(1), 1-31.

Tomkins, A. G. (2010) Windows of metamorphic sulfur liberation in the crust: Implications for gold deposit genesis: Geochimica et Cosmochimica Acta, 74(11), 3246-3259.

Tribovillard, N., Algeo, T. J., Lyons, T., and Riboulleau, A. (2006) Trace metals as paleoredox and paleoproductivity proxies: An update: Chemical Geology, 232(1), 12-32.

Tribovillard, N., Riboulleau, A., Lyons, T., and Baudin, F. (2004) Enhanced trapping of molybdenum by sulfurized marine organic matter of marine origin in Mesozoic limestones and shales: Chemical Geology, 213(4), 385-401.

Watchorn, R. B. (1998) Kambalda-St. Ives gold deposits: Monograph Series - Australasian Institute of Mining and Metallurgy, 22, 243-254.

Whitehouse, M. J. (2013) Multiple Sulfur Isotope Determination by SIMS: Evaluation of Reference Sulfides for Δ33S with Observations and a Case Study on the Determination of Δ36S: Geostandards and Geoanalytical Research.

Witt, W., and Vanderhor, F. (1998) Diversity within a unified model for Archaean gold mineralization in the Yilgarn Craton of Western Australia: an overview of the late-orogenic, structurally-controlled gold deposits: Ore Geology Reviews, 13(1), 29-64.

Xue, Y., Campbell, I., Ireland, T. R., Holden, P., and Armstrong, R. (2013) No mass-independent sulfur isotope fractionation in auriferous fluids supports a magmatic origin for Archean gold deposits: Geology, 41(7), 791-794.

7.0 Conclusions

7.1 Key results and contribution to knowledge

7.1.1 The Incorporation of trace elements into diagenetic pyrite).

Detailed mineralogical and geochemical analyses of bottom sediments in the Derwent estuary (Chapter 2) show the availability of many trace metals that maybe accumulated into the diagenetic pyrite. LA-ICPMS analyses of the trace element content of pyrite (Chapter 3) have been used to develop new insights into the mechanisms by which trace elements are incorporated into pyrite framboids. In the high metal environment of the Derwent Estuary competition for different adsorption sites on the surface of the growing pyrite was found to be particularly important. This study differed from previous studies in several ways. In particular, it utilized LA-ICPMS for the first time (to our knowledge) to analyze individual framboids while most previous studies have utilized sequential extractions techniques (Huerta-Diaz and Morse, 1990; Huerta-Diaz and Morse, 1992; Morse and Luther, 1999; Morse, 1994). LA-ICPMS is preferable because it does not have the problems of specificity of reagents that are common with sequential extraction techniques (Martin et al., 1987). Also the LA-ICPMS allowed analysis of several elements (Au, Ag, Te) that cannot be analysed by traditional sequential extractions due to low abundance of the element present, adsorption effects and dilution effects present in wet chemistry analytical procedures.

This data was used to show that competition for different adsorption sites between different trace elements is an important factor controlling which trace elements are incorporated into pyrite and how far different elements may diffuse before they are incorporated into pyrite. This study compliments laboratory based studies and studies focusing on a lower number of elements (Deditius et al., 2011; Hough et al., 2011; Mitchell et al., 2012; Qian et al., 2013; Reich and Becker, 2006; Reich et al., 2005) by giving a natural example of the incorporation of several elements into pyrite forming in a high metal, low temperature, environment. This study also showed how the results from a combination of bulk chemistry, sequential leach extractions, mineral abundance analyses and LA-ICPMS analyses of pyrite can be used to explain why different trace elements observed in pyrite occur in different parts of the sediment core.

7.1.2 Environmental Implications of Derwent Estuary Study.

As this was the first study to examine the accumulation of trace elements in pyrite in a heavy metal contaminated estuary it was possible to determine to what extent heavy metals can be contained within diagenetic pyrite and thus made unavailable to the biosphere. This is of interest because pyrite is recognized as a sink for many trace elements (Dellwig et al., 2002; Huerta-Diaz and Morse, 1992; Lowers et al., 2007; Neumann et al., 2013) and if enough of these trace metals are incorporated into pyrite there may be implications on possible future remediation of the site. However, although we found that the elevated elements (Cu, Pb, Zn, As amongst others) were present in the diagenetic pyrite in the contaminated sections of the sediments they were not in sufficient quantities for pyrite to be considered a major host of the enriched elements.

In the process of determining the availability of the different trace metals to be incorporated into pyrite, a number of mineralogical and chemical analyses were performed on the sediments of the contaminated Derwent Estuary. In addition to providing data on the ability of the different elements to be incorporated into pyrite, the study showed that Zn is held predominantly within the mineral franklinite while Pb and Cu are held within a series of different phase such as organic matter, iron oxides or other unknown minerals. This data shows that the major contaminants in the Derwent Estuary are held within different phases which may have important implications for future remediation efforts.

7.1.3 Data base of average trace element concentrations of sedimentary pyrite.

One of the main goals of this study was the evaluation of the data base of trace element content of sedimentary pyrite presented in Chapter 4 in terms of quantifying the compositional range of diagenetic pyrite. The establishment and interpretation of this data base will be of great use in the field of paleo-oceanic chemical conditions research because it will allow researchers to compare trace elements found in their pyrites with the means and ranges given by the data base, in a manner similar to how current researchers compare whole rock analyses of trace metals with data bases of average whole rock composition (McLennan, 2001; Taylor and McLennan, 1985; Wedepohl, 1991; Wedepohl, 1995). The data base provided in Chapter 4 shows that trace elements are generally enriched in pyrite in the following order of abundance: As ≥ Ni > Pb ≥ Cu ≥ Co ≥ Mn > Sb ≥ Zn ≥ Se ≥ Mo > Ag ≥ Bi

> Te ≥ Cd > Au. A geochemical classification system for sedimentary pyrite was also developed in the course of study. This shows that sedimentary pyrite commonly has a composition that satisfies the following criteria: 0.01 < Co/Ni < 2, 0.01 < Cu/Ni < 10, 0.01 < Zn/Ni < 10, 0.1 < As/Ni < 10, Ag/Au > 2, 1 < Te/Au < 1000, Bi/Au > 1, Sb/Au > 100 and As/Au > 200. These criteria will allow researchers to evaluate whether pyrite interpreted to be of sedimentary origin based on texture also satisfies the criteria for sedimentary origin based on composition. It will also allow researchers investigating pyrite from highly metamorphosed areas (up to upper green-schist facies) or hydrothermally overprinted areas to test whether the sedimentary pyrite has gained or lost trace elements.

The data set was also subdivided by pyrite texture and geological age to determine to what extent the average trace element content of pyrite varies based on these factors. Over the entire data set the trace element content of pyrite was not found to vary significantly with texture. However, when different pyrite textures were found within the same sample the textures interpreted to have formed earliest (except for fine euhedral texture) were determined to have the highest trace element content, while pyrite formed later, during late diagenesis and metamorphism, had lower trace element content. These observations will be important to consider when determining why different pyrite types deviate from the mean trace element content of pyrite.

The average contents of several trace elements in pyrite were found to vary significantly with geological era/epoch of deposition. Elements such as Mo and Se were found to increase with time, probably due to increasing levels of atmospheric oxygen causing increased oxidative weathering, allowing more of these elements to be released into the oceans. This explanation is coherent with similar results obtained by Scott et al. (2008) using whole rock data. The opposite trend was obtained for Ni, Co, As, Te and Au which show a general decrease in composition with increasing age. The decrease in Ni and Co with time is interpreted to be due to a decrease in the eruption of Ni and Co rich komatiitic magmas with decreasing age (Konhauser et al., 2009; Large et al., 2013).

7.1.4 Correspondence of laser data with whole rock data.

In Chapter 4 a combination of pyrite chemistry and traditional whole rock chemistry analyses were used to determine trends in ocean chemistry from the late Archean Hamersley Group

and Jeerinah Formation. This is significant for two reasons. First it shows that both pyrite chemistry and whole rock chemistry can be used to reach the same conclusions on paleo-ocean chemistry. This is important because it shows that LA-ICPMS analyses can be an alternate tool for researchers interested in the chemical conditions of ancient oceans. Traditional studies involve the use of bulk sample geochemistry and/or sequential extraction technique to determine trace metal geochemistry or Fe speciation and then those results are used to interpret chemistry of the oceans at the time of deposition (Algeo and Lyons, 2006; Anbar et al., 2007; Kakegawa et al., 1998; Kaufman et al., 2007; Lyons and Severmann, 2006; Lyons et al., 2003; Mitchell et al., 2012; Raiswell and Canfield, 1998; Raiswell and Plant, 1980; Raiswell et al., 2011; Reinhard et al., 2009; Scott et al., 2011; Tribovillard et al., 2006; Tribovillard et al., 2004). A similar methodology was under taken in this study in addition to the pyrite analyses. Both of these studies returned similar results, showing that pyrite chemistry is a viable tool that can be used to determine paleo-oceanic conditions.

The sedimentary rocks used in this comparative study are also of broad scientific interest in their own right. The Jeerinah formation include one of the first recorded periods of euxinia in earth's history (Scott et al., 2011) while the Mt. McRae Shale records a pulse of oxygen prior to the GOE (Anbar et al., 2007). In this study a broad time period was examined including these two time periods and shale units between them. It was found that there is a general trend of increasing trace elements in whole rock and in pyrite, interrupted and reset by periods of volcanic activity and/or periods of banded iron formation deposition. The periods of trace element increase are interpreted to be due to increases of biological activity and oxygenation. These results agree with others (e.g. Anbar et al., (2007)) who proposed the existence of early increases in oxygen within the late Archean ocean.

7.1.5 The use of pyrite geochemistry to determine ocean conditions in shale of high metamorphic grade that have been over printed by hydrothermal processes.

Sedimentary pyrite from the St Ives gold district was used to determine whether inferences could be made about the geochemistry of paleo-oceans based on LA-ICPMS analyses of early pyrite in areas that have been highly metamorphosed and have experienced hydrothermal overprint (s). Traditional bulk rock analyses cannot be used in these areas because metamorphic and hydrothermal fluids can both remove and add trace elements to the rock. However, because trace element content of the oceans can be preserved in the

sedimentary pyrite (Large et al., 2011; Large et al., 2007; Thomas et al., 2011) it is possible to determine their chemistry using LA-ICPMS. In this way the chemistry of the ocean in which the sedimentary pyrite formed can be determined. This has wide implications in the field of paleo-ocean chemistry as it greatly increases the number of shale units that can be studied.

Sedimentary pyrite from the metamorphosed Kapai Slate was found to be relatively low in elements that indicate organic matter sinking flux (Ni, Cu) (Tribovillard et al., 2006) relative to the similarly aged but less metamorphosed Jeerinah formation. Also, as evidenced by the upper part of the Mt McRae Shale, iron dominated oceans tend to have low total trace metal contents. As this lack of trace elements was not observed in the Kapai Slate the pyrite was probably deposited in iron limited conditions. Finally as Mo, a common redox indicator (Tribovillard et al., 2006), is in the same concentration in pyrite from the Kapai Slate as in pyrite from the euxinic Jeerinah formation (Scott et al., 2011) the Kapai Slate is interpreted to have been deposited under anoxic to euxinic conditions. Thus, using the chemistry of diagenetic pyrite the Kapai Slate was likely to have been deposited in an anoxic to euxinic basin that was iron limited with relatively low biological productivity.

Analyses of sedimentary pyrite from the Kapai Slate, as well as hydrothermal pyrites from the surrounding deposits and lithologies, provided a test for the classification of sedimentary pyrite based on geochemistry of pyrite developed in Chapter 4. The results of this test were encouraging as the majority of Kapai Slate sedimentary pyrite fit the scheme ($0.01 < Co/Ni < 2$, $0.01 < Cu/Ni < 10$, $0.1 < As/Ni < 10$, $Ag/Au > 1$, $Te/Au > 1$ and $As/Au > 200$) while the other pyrite varieties (recrystallised pyrite, basalt pyrite, ore pyrite and magnetite series pyrite) did not. The only pyrite variety that was near to satisfying all the criteria for sedimentary pyrite was the recrystallised pyrite, this is most likely because the recrystallized pyrite was originally sedimentary pyrite and must have inherited the trace metal signature from its previous form.

7.1.6 Gold deposition models for the St Ives gold district.

A secondary goal of the examination of pyrite in the St. Ives gold district was to determine whether new sedimentary source models for the formation of orogenic gold deposits (Large et al., 2011; Large et al., 2009; Thomas et al., 2011) could be applied to the formation of the

deposits found at St Ives. Average pyrite contents, Au content in pyrite and volume of sedimentary rock that potentially could have provided gold to the formation of the deposits were used to calculate the maximum amount of gold that could have been sourced from the Kapai Slate. As this was less than 10% of the known resources and reserves of the deposits in the study area the study suggests that the Kapai Slate was not the major gold source at St Ives.

In the course of the study SHRIMP-SI analyses were also conducted on different pyrite from the St Ives gold district. Generally the results were similar to a study conducted by Xue et al. (2013) (except a population of negative $\Delta^{33}S$ values from sedimentary pyrite), however they interpreted the data to support a deep source for gold in the St Ives district while our interpretation is compatible with both the deep gold source model (Bath et al., 2013; Groves, 1993; Neumayr et al., 2008) and the metamorphic model (Phillips and Powell, 2010; Phillips et al., 1987; Phillips and Powell, 1993; Phillips and Powell, 2009; Powell et al., 1991).

7.2 Future Research

7.2.1 Analyses of pyrite forming in modern sedimentary basins.

The methodology developed in Chapters 2 and 3 should be applied to a number of different sedimentary basins with different sediment sources, redox conditions and rates of sedimentation. This would provide a data base that would show how trace metal content of pyrite from different environments changes within the modern ocean. These observations could then be used to determine how these factors change in the modern setting, enabling a more rigorous examination of changes of trace element content in pyrite with depositional setting in the rock record. An attempt was made to do this in the current study, however most of the samples received from the ocean drilling program (ODP) contained no preserved pyrite framboids so this line of inquiry was not continued. Future studies must involve targeting of potentially pyritic sediments by ocean drilling cruises coupled with early extraction and preservation of the pyrite.

7.2.2 Continued development of the trace element content of diagenetic pyrite data base.

Future studies into the trace element content of diagenetic pyrite should continue to add to the data base available to this study. Additional analyses will continue to make the data base more robust. As the number of samples that fit into the different sub-classes examined in Chapter 4 increases these sub classes should be separated to try and limit the number of variables that affect the chemistry of the pyrite examined. This would be similar to some current average shale compositions being subdivided on the basis of age (e.g. Wedepohl (1991)).

7.2.3 Continued use of whole rock and pyrite chemistry to determine paleo-ocean conditions.

Future studies to determine the chemical conditions of the paleo-oceans should continue to use a combination of traditional whole rock analysis and LA-ICPMS pyrite analysis, similar to the methods used in Chapter 5. This will continue to validate the method of using LA-ICPMS analyses of pyrite to determine paleo-ocean conditions, as has been shown in Chapter 5. It will also result in a more robust interpretation of the paleo-ocean conditions present when the shale under investigation was deposited. A good location for one of these studies is sedimentary rocks from Kapval craton, southern Africa which have similar age to the Kapai Slate and Jeerinah formation (Nelson et al., 1999) and would also help to determine whether the trends observed in this study are global in extent.

7.2.4 Continued use of LA-ICPMS to determine chemical conditions of deposition of shales that have been metamorphosed and/or overprinted by hydrothermal fluids.

Future studies of the oceanic conditions during deposition of shales from metamorphosed or hydrothermally overprinted areas should utilize LA-ICPMS to determine trace element content of preserved, sedimentary pyrite, similar to the method outlined in Chapter 6. Ideally these studies should also include a combination of whole rock and LA-ICPMS analyses from a correlatable unit that has not been subjected to the same degree of metamorphism or hydrothermal overprint. This would continue to test the validity of using relict sedimentary pyrite found in metamorphically or hydrothermally overprinted areas to determine paleo-oceanic conditions. One prospective study site is the Selwyn Basin, Yukon Territory, Canada, because it is a large basin with abundant pyritic shales that are host to several different deposit types from orogenic gold (Brewery Creek), Carlin Style gold (Osiris),

SEDEX (Anvil) and VHMS (Tom, Jason, Kudz Ze Kayah, Wolverine). A study of this type would allow researchers to determine whether 1) hydrothermal overprint affects trace element content of preserved pyrite and 2) different deposit types give rise to different overprint signatures.

7.3 References

Algeo, T.J., and Lyons, T.W. (2006) Mo-total organic carbon covariation in modern anoxic marine environments: Implications for analysis of paleoredox and paleohydrographic conditions. Paleoceanography, 21(1).

Anbar, A.D., Duan, Y., Lyons, T.W., Arnold, G.L., Kendall, B., Creaser, R.A., Kaufman, A.J., Gordon, G.W., Scott, C., and Garvin, J. (2007) A whiff of oxygen before the great oxidation event? Science, 317(5846), 1903-1906.

Bath, A.B., Walshe, J.L., Cloutier, J., Verrall, M., Cleverley, J.S., Pownceby, M.I., Macrae, C.M., Wilson, N.C., Tunjic, J., and Nortje, G.S. (2013) Biotite and Apatite as Tools for Tracking Pathways of Oxidized Fluids in the Archean East Repulse Gold Deposit, Australia. Economic Geology, 108(4), 667-690.

Deditius, A.P., Utsunomiya, S., Reich, M., Kesler, S.E., Ewing, R.C., Hough, R., and Walshe, J. (2011) Trace metal nanoparticles in pyrite. Ore Geology Reviews, 42(1), 32-46.

Dellwig, O., Böttcher, M.E., Lipinski, M., and Brumsack, H.-J. (2002) Trace metals in Holocene coastal peats and their relation to pyrite formation (NW Germany). Chemical Geology, 182(2–4), 423-442.

Groves, D. (1993) The crustal continuum model for late-Archaean lode-gold deposits of the Yilgarn Block, Western Australia. Mineralium Deposita, 28(6), 366-374.

Hough, R.M., Noble, R.R.P., and Reich, M. (2011) Natural gold nanoparticles. Ore Geology Reviews, 42(1), 55-61.

Huerta-Diaz, M.A., and Morse, J.W. (1990) A quantitative method for determination of trace metal concentrations in sedimentary pyrite. Marine Chemistry, 29, 119-144.

Huerta-Diaz, M.A., and Morse, J.W. (1992) Pyritization of trace metals in anoxic marine sediments. Geochimica et Cosmochimica Acta, 56(7), 2681-2702.

Kakegawa, T., Kawai, H., and Ohmoto, H. (1998) Origins of pyrites in the∼ 2.5 Ga Mt. McRae Shale, the Hamersley District, Western Australia. Geochimica et Cosmochimica Acta, 62(19), 3205-3220.

Kaufman, A.J., Johnston, D.T., Farquhar, J., Masterson, A.L., Lyons, T.W., Bates, S., Anbar, A.D., Arnold, G.L., Garvin, J., and Buick, R. (2007) Late Archean biospheric oxygenation and atmospheric evolution. Science, 317(5846), 1900-1903.

Konhauser, K.O., Pecoits, E., Lalonde, S.V., Papineau, D., Nisbet, E.G., Barley, M.E., Arndt, N.T., Zahnle, K., and Kamber, B.S. (2009) Oceanic nickel depletion and a methanogen famine before the Great Oxidation Event. Nature, 458(7239), 750-753.

Large, R.R., Gregory, D., Halpin, J., Danyushevsky, L., Lounejeva, E., Steadman, J., Maslennikov, V., Lyons, T., Sack, P., Guy, B., Hickman, A., Calver, C. (2013) Trace Elements in Sedimentary Pyrite Through Time; Apllication to Understanding Temporal Changes in Ocean Oxygenation and Ore Deposit Cycles in Marine Basins. Conference Abstract: Mineral Deposit Research in a High-Tech World, 12th SGA Biennial Meeting 2013, Upsalla, Sweden.

Large, R.R., Bull, S.W., and Maslennikov, V.V. (2011) A carbonaceous sedimentary source-rock model for Carlin-type and orogenic gold deposits. Economic Geology, 106(3), 331-358.

Large, R.R., Danyushevsky, L., Hollit, C., Maslennikov, V., Meffre, S., Gilbert, S., Bull, S., Scott, R., Emsbo, P., Thomas, H., Singh, B., and Foster, J. (2009) Gold and Trace Element Zonation in Pyrite Using a Laser Imaging Technique: Implications for the Timing of Gold in Orogenic and Carlin-Style Sediment-Hosted Deposits. Economic Geology, 104(5), 635-668.

Large, R.R., Maslennikov, V.V., Robert, F., Danyushevsky, L.V., and Chang, Z.S. (2007) Multistage sedimentary and metamorphic origin of pyrite and gold in the giant Sukhoi Log deposit, Lena gold province, Russia. Economic Geology, 102(7), 1233-1267.

Lowers, H.A., Breit, G.N., Foster, A.L., Whitney, J., Yount, J., Uddin, M.N., and Muneem, A.A. (2007) Arsenic incorporation into authigenic pyrite, Bengal Basin sediment, Bangladesh. Geochimica et cosmochimica acta, 71(11), 2699-2717.

Lyons, T.W., and Severmann, S. (2006) A critical look at iron paleoredox proxies: New insights from modern euxinic marine basins. Geochimica et Cosmochimica Acta, 70(23), 5698-5722.

Lyons, T.W., Werne, J.P., Hollander, D.J., and Murray, R.W. (2003) Contrasting sulfur geochemistry and Fe/Al and Mo/Al ratios across the last oxic-to-anoxic transition in the Cariaco Basin, Venezuela. Chemical Geology, 195(1-4), 131-157.

Martin, J., Nirel, P., and Thomas, A. (1987) Sequential extraction techniques: promises and problems. Marine Chemistry, 22(2), 313-341.

McLennan, S.M. (2001) Relationships between the trace element composition of sedimentary rocks and upper continental crust. Geochemistry, Geophysics, Geosystems, 2(4), Q1021.

Mitchell, K., Mason, P.R., Cappellen, P.V., Johnson, T.M., Gill, B.C., Owens, J.D., Diaz, J., Ingall, E.D., Reichart, G.-J., and Lyons, T.W. (2012) Selenium as paleo-oceanographic proxy: A first assessment. Geochimica et Cosmochimica Acta.

Morse, J., and Luther, G. (1999) Chemical influences on trace metal-sulfide interactions in anoxic sediments. Geochimica et Cosmochimica Acta, 63(19), 3373-3378.

Morse, J.W. (1994) Interactions of trace metals with authigenic sulfide minerals: implications for their bioavailability. Marine chemistry, 46(1), 1-6.

Nelson, D., Trendall, A., and Altermann, W. (1999) Chronological correlations between the Pilbara and Kaapvaal cratons. Precambrian Research, 97(3), 165-189.

Neumann, T., Scholz, F., Kramar, U., Ostermaier, M., Rausch, N., and Berner, Z. (2013) Arsenic in framboidal pyrite from recent sediments of a shallow water lagoon of the Baltic Sea. Sedimentology.

Neumayr, P., Walshe, J., Hagemann, S., Petersen, K., Roache, A., Frikken, P., Horn, L., and Halley, S. (2008) Oxidized and reduced mineral assemblages in greenstone belt rocks of the St. Ives gold camp, Western Australia: vectors to high-grade ore bodies in Archaean gold deposits? Mineralium Deposita, 43(3), 363-371.

Phillips, G., and Powell, R. (2010) Formation of gold deposits: a metamorphic devolatilization model. Journal of Metamorphic Geology, 28(6), 689-718.

Phillips, G.N., Groves, D.I., and Brown, I.J. (1987) Source requirements for the Golden Mile, Kalgoorlie: significance to the metamorphic replacement model for Archean gold deposits. Canadian Journal of Earth Sciences, 24(8), 1643-1651.

Phillips, G.N., and Powell, R. (1993) Link between gold provinces. Economic Geology, 88(5), 1084-1098.

Phillips, G.N., and Powell, R. (2009) Formation of gold deposits: Review and evaluation of the continuum model. Earth-Science Reviews, 94(1), 1-21.

Powell, R., Will, T., and Phillips, G. (1991) Metamorphism in Archaean greenstone belts: Calculated fluid compositions and implications for gold mineralization. Journal of Metamorphic Geology, 9(2), 141-150.

Qian, G., Brugger, J., Testemale, D., Skinner, W., and Pring, A. (2013) Formation of As(II)-pyrite during experimental replacement of magnetite under hydrothermal conditions. Geochimica et Cosmochimica Acta, 100(0), 1-10.

Raiswell, R., and Canfield, D.E. (1998) Sources of iron for pyrite formation in marine sediments. American Journal of Science, 298(3), 219-245.

Raiswell, R., and Plant, J. (1980) The incorporation of trace elements into pyrite during diagenesis of black shales, Yorkshire, England. Economic geology, 75(5), 684-699.

Raiswell, R., Reinhard, C.T., Derkowski, A., Owens, J., Bottrell, S.H., Anbar, A.D., and Lyons, T.W. (2011) Formation of syngenetic and early diagenetic iron minerals in the late Archean Mt. McRae Shale, Hamersley Basin, Australia: New insights on the patterns, controls and paleoenvironmental implications of authigenic mineral formation. Geochimica et Cosmochimica Acta, 75(4), 1072-1087.

Reich, M., and Becker, U. (2006) First-principles calculations of the thermodynamic mixing properties of arsenic incorporation into pyrite and marcasite. Chemical Geology, 225(3), 278-290.

Reich, M., Kesler, S.E., Utsunomiya, S., Palenik, C.S., Chryssoulis, S.L., and Ewing, R.C. (2005) Solubility of gold in arsenian pyrite. Geochimica et Cosmochimica Acta, 69(11), 2781-2796.

Reinhard, C.T., Raiswell, R., Scott, C., Anbar, A.D., and Lyons, T.W. (2009) A late Archean sulfidic sea stimulated by early oxidative weathering of the continents. Science, 326(5953), 713-716.

Scott, C., Lyons, T., Bekker, A., Shen, Y., Poulton, S., Chu, X., and Anbar, A. (2008) Tracing the stepwise oxygenation of the Proterozoic ocean. Nature, 452(7186), 456-459.

Scott, C.T., Bekker, A., Reinhard, C.T., Schnetger, B., Krapež, B., Rumble, D., and Lyons, T.W. (2011) Late Archean euxinic conditions before the rise of atmospheric oxygen. Geology, 39(2), 119-122.

Steadman, J.A., Large, R.R., Meffre, S., and Bull, S.W. (2013) Age, origin and significance of nodular sulfides in 2680 ma carbonaceous black shale of the eastern goldfields superterrane, yilgarn craton, western australia. Precambrian Research.

Taylor, S.R., and McLennan, S.M. (1985) The continental crust: its composition and evolution.

Thomas, H.V., Large, R.R., Bull, S.W., Maslennikov, V., Berry, R.F., Fraser, R., Froud, S., and Moye, R. (2011) Pyrite and pyrrhotite textures and composition in sediments, laminated quartz veins, and reefs at Bendigo gold mine, Australia: insights for ore genesis. Economic Geology, 106(1), 1-31.

Tribovillard, N., Algeo, T.J., Lyons, T., and Riboulleau, A. (2006) Trace metals as paleoredox and paleoproductivity proxies: An update. Chemical Geology, 232(1), 12-32.

Tribovillard, N., Riboulleau, A., Lyons, T., and Baudin, F. (2004) Enhanced trapping of molybdenum by sulfurized marine organic matter of marine origin in Mesozoic limestones and shales. Chemical Geology, 213(4), 385-401.

Wedepohl, K. (1991) The composition of the upper earth's crust and the natural cycles of selected metals. Metals in natural raw materials. Metals and their compounds in the environment. Occurrence, analysis, and biological relevance. New York, NY: VCH, 3-17.

Wedepohl, K. (1995) The composition of the continental crust. Geochimica et Cosmochimica Acta, 59(7), 1217-1232.

Xue, Y., Campbell, I., Ireland, T.R., Holden, P., and Armstrong, R. (2013) No mass-independent sulfur isotope fractionation in auriferous fluids supports a magmatic origin for Archean gold deposits. Geology.

Appendix 1:

Location and contamination history of the Derwent Estuary

A1.1 Geology of the Derwent Estuary

The Derwent Estuary is largely underlain by Jurassic dolerite and Cambrian basalts with sedimentary deposits of Triassic and Recent age (Department of Mines, 1976). The presence of tertiary volcanic centres is indicated by seismic reflection profiles (Roach and Gibbons, 2001). Current geomorphological features along the foreshore include sea cliffs, steep bluffs, platforms, rocky and sandy beaches and sandy or muddy intertidal flats (Sharples, 2006).

A1.2 Water Circulation of the Derwent Estuary

The circulation in the Derwent Estuary has been described by most researchers as wind- and tidal-driven. It is partially to well-mixed in the middle to lower reaches of the estuary and highly stratified in the middle to upper reaches with a distinct saltwater wedge in the upper reaches (Whitehead et al., 2010). The Derwent River has relatively weak tidal velocities of approximately 0.1 to 0.2 m/s (Thomson and Godfrey, 1985; Davies and Kalish, 1994). Models proposed by CSIRO suggest surface velocities in the estuary tend to flow southwards at velocities of 0.1 to 0.2 m/s while bottom currents flow northwards at velocities of 0.02 to 0.05 m/s (Whitehead et al., 2010).

A1.3 Anthropogenic Contamination Sources

A wide variety of anthropogenic contaminants are found within the Derwent Estuary. These include pathogens, nutrients, organic matter, silt and gross solids, wood extractives, such as resin acids and a range of toxicants including heavy metals and hydrocarbons (Whitehead et al., 2010). These contaminants enter the estuary at a number of points and have many point and diffuse sources, such as urban runoff, waste disposal sites, sewage treatment plants, current and historical industries (for example Boyer paper mill, textile and dying factory, WW2 munitions complex, small metal foundries), leaded petrol and air pollution (Whitehead et al., 2010; Christine Coughanowr, director of Derwent Estuary Program, personal communication, May 2013). The Nyrstar Hobart zinc smelter and Norske Skog paper mill

are the most significant point sources; however, the ten sewage treatment plants are also important point sources of pollution. Diffuse sources include urban stormwater runoff, rubbish tips and contaminated sites, farming and other run-offs from the Derwent and Jordan Rivers catchments, wastes associated with shipping, port facilities, marinas, and atmospheric contributions (Whitehead et al., 2010).

The Nyrstar Hobart zinc smelter has been operating since 1917 and is the closest pollution source to the sample site and likely the most significant source of anthropogenic metal contamination in the Derwent Estuary. Historically the most significant contaminant introduced by the smelter to the Derwent River was through liquid processing waste (Bloom and Ayling, 1977). The smelting process is complex and has changed considerably over time. The process can be summarised into three major steps (Alexander 1992):

1) roasting a sphalerite-rich zinc concentrate to make calcine (mostly Zn oxide)
2) leaching in acid to make a Zn solution
3) electrolysis to recover Zn metal.

One of the major waste products from the process was the insoluble iron-rich residue. These residues contained Zn ferrite (franklinite) formed during roasting and hydrated iron hydroxides precipitated during leaching. Prior to 1975 some of this material was discharged directly into the estuary (Nick Ramshaw, senior metallurgist, Nystar Hobart, personal communication, 2013). The main period of discharge was independently constrained to between 1950s-1980s by (Townsend and Seen, 2012) using ^{210}Pb dating of the most contaminated layer in a core sample 3 km upstream for the Zn refinery. However some of the material was also stockpiled on site waiting further processing. The stockpile composed 66% of zinc ferrite reached 600,000 tonnes in the late 1960s (Alexander 1992) and 1,000,000 tonne in 1970 (Haigh and Pickering, 1970). In 1971 a new plant was commissioned to treat the iron-rich residue from the existing stockpiles and the iron precipitates directly from the plant (Alexander 1992). The process used a higher concentration sulphuric acid to break down the Zn ferrite and addition of ammonium sulphate to form jarosite. Between 1970 and 1973 jarosite was mostly stock piled alongside Newtown bay. Although the pile was kept wet to limit the transfer of dust to the estuary, some introduction of jarosite to the estuary was inevitable (Ashley Townsend, personal communication, 2013). In December 1973 jarosite began to be shipped and dumped off the continental shelf (Alexander, 1992). This practice continued until 1997 when the process was changed to eliminate jarosite as a by-product (Waste management and environment magazine, 2001).

There are four different ways in which the pollution enters the estuary from the smelter: liquid processing wastes, stormwater, groundwater and atmospheric emissions including dust. Prior to 1981, liquid emissions that contain dissolved Zn, Pb, Cd, Cu, Fe, Hg, As, F, Se, sulphate, ammonia and suspended solids were disposed directly into the estuary (Coughanowr, 1997). Since then the smelter has progressively made significant improvements to reduce the point source contaminants entering the estuary (Whitehead et al., 2010); however, estimates of metal load prior to these improvements over the long history of the smelter are difficult to obtain (Whitehead et al., 2010). Approximately 3.3kL/day of treated waste water was used in the smelting process and 80,000 to 100,000 kL/day of saltwater was pumped through a scrubber system to remove SO_2 from tail gas exiting the acid plants. Both of these water sources are mixed prior to being released into the estuary. It is difficult to measure the amount of contaminants released to the estuary as all, except Zn and Hg, are below detection limits after being mixed with the large volume of water used for the SO_2scrubbing system. It is estimated that annual mass emissions of Zn range from 4.0 to 14.7 tonnes/year and in 2008-2009 there were 31 kg of mercury released (Whitehead et al., 2010).

The majority of stormwater at the site is contained and treated at the effluent treatment plant and released via the diffuser. However, in extreme rainfall events, stormwater is released directly into the river but overflows are controlled so that only the least contaminated waters are released directly into the estuary. There has been zero to three stormwater overflows per year between 2003 and 2008. It is estimated that annual zinc loads associated with stormwater is below one tonne (Whitehead et al., 2010).

Heavy metal load from the Nystar stacks is considered to be relatively low. However 190 tonnes/year of SO_2 and 140 tonnes/year of NO_x are released into the air from the site and it is unknown how much of this has entered the estuary (Whitehead et al., 2010).

The most significant source of metals currently released from the Nystar site is through groundwater draining the site. The local aquifer below the Nystar site is considered to be relatively shallow with flow rates in the order of 30 to 150 m/year. This flow is controlled by a geological contact or fault running through the site (GHD, 2006) and an unknown amount of zinc is released into the estuary through the groundwater system. Since 1999, Nystar has been recovering metal from the groundwater at areas of high contamination. Since 2003, over 250 tonnes of zinc and two tonnes of cadmium has been recovered (Whitehead et al.,

2010). It is estimated that 50-75% of the groundwater is captured at these sites (Whitehead et al., 2010) and therefore there is potential for the groundwater to have discharged 125-250 tonnes of zinc since 2003.

A1.4 Climate

The Derwent Estuary experiences a mean maximum temperature of 22°C in February and a mean minimum temperature of 12°C in July (Whitehead et al., 2010). The predominant winds are katabolic and blow from the northwest due to topographic features and the northwest orientation of the Derwent River valley. During the summer months there is also a southerly sea breeze that is common in the afternoon.

In years of drought there is often low estuarine mixing which results in low dissolved oxygen in the upper estuary. Higher than normal rainfall leads to higher surface runoff and elevated amounts of litter, silt, faecal bacteria and other pollutants.

A1.5 References

Alexander, A., 1992, The Zn Works - Producing Zn at Risdon 1916-1991., VIC, Australia: Globe Press.

Coughanowr, C., 1997, State of the Derwent Estuary: a review of environmental quality data to 1997. Supervising scientist report 129, Supervising scientist, Canberra.

Davies, P. and Kalish, S., (1994) Influence of river hydrology on the dynamics and water quality of the upper Derwent Estuary, Tasmania. Aust. J. Mar. Freshwater Res. 45, 109-130.

Department of Mines, 1976, Geological Map of Tasmania 1-500,000, Hobart.

GHD, 2006, Groundwater Management Plan prepared by GHD for Nyrstar Hobart smelter site.

Haigh, C. J., and Pickering, R. W., 1970, Treatment of Zn plant residue at the Risdon works of the Electrolytic Zn co. of Australasia ltd.: Paper from world symposium on mining and metallurgy of Pb and Zn extractive metallurgy of Pb and Zn, Aime, New York. 1970, 2, 423-448.

Roach, M., and Gibbons, D., 2001, The Geology and Sedimentary history of the Derwent Estuary, School of Earth Sciences, University of Tasmania.

Sharples, C., 2006, Indicative Mapping of Tasmanian Coastal Vulnerability to Climate Change and Sea-Level Rise: Explanatory Report (Second Edition); Consultant Report to Department of Primary Industries and Water, Tasmania, p. 173.

Thompson, J. and Godfrey, J., 1985, Circulation dynamics in the Derwent estuary: Australian Journal of Marine and Freshwater Research 36, 765-772.

Townsend, A. T., and Seen, A. J., 2012, Historical Pb isotope record of a sediment core from the Derwent River (Tasmania, Australia): a multiple source environment: Science of the Total Environment.

Waste Management and Environment Magazine, 2001, From wasteland to wetland http://www.wme.com.au/categories/hazard_waste/dec1_01.php

Whitehead, J., Coughanowr, C., Agius, J., Chrispijn, J., Taylor, U., and Wells, F., 2010, State of the Derwent Estuary 2009: a review of pollution sources, loads and environmental quality data from 2003 – 2009, Derwent Estuary Program, DPIPWE, Tasmania.

Appendix 2:

Geochemical data presented in Chapter 1

Table A2.1: Bulk Sample XRF analyses of SM1001										
Sample	**MgO (%)**	**CaO (%)**	**Na2O (%)**	**K2O (%)**	**P2O5 (%)**	**CuO (%)**	**PbO (%)**	**ZnO (%)**	**BaO (%)**	**S (%)**
SM1001(0-5)	2.07	1.50	5.74	1.20	0.30	0.05	0.18	1.16	0.01	1.78
SM1001(5-10)	2.05	1.63	5.50	1.23	0.29	0.06	0.20	1.28	0.01	1.79
SM1001(10-15)	2.05	1.40	5.47	1.26	0.27	0.06	0.22	1.43	0.02	1.93
SM1001(15-20)	1.96	1.26	5.31	1.22	0.25	0.06	0.21	1.34	0.02	2.12
SM1001(20-25)	1.95	1.28	5.18	1.18	0.25	0.06	0.21	1.27	0.02	2.08
SM1001(25-30)	2.12	1.46	5.71	1.20	0.23	0.08	0.27	1.71	0.02	2.76
SM1001(30-35)	2.23	1.52	6.18	1.17	0.22	0.08	0.29	1.77	0.02	3.68
SM1001(35-40)	2.21	1.51	6.24	1.14	0.21	0.07	0.26	1.53	0.02	3.50
SM1001(40-45)	1.99	1.35	5.45	1.05	0.20	0.07	0.30	1.91	0.01	3.32
SM1001-(45-50)	1.92	0.96	4.82	1.22	0.17	0.11	0.74	5.12	0.02	2.85
SM1001-(50-55)	2.06	1.26	5.04	1.18	0.17	0.11	0.70	4.74	0.02	2.89
SM1001-(55-60)	1.88	1.43	4.14	1.18	0.15	0.07	0.37	2.44	0.02	3.13
SM1001-(65-70)	2.02	2.57	4.05	1.50	0.14	0.05	0.18	0.66	0.02	2.64
SM1001(60-65)	2.12	1.81	4.60	1.39	0.15	0.08	0.27	1.19	0.02	2.92
SM1001(70-75)	1.99	1.82	4.10	1.59	0.13	0.01	0.05	0.17	0.02	2.09
SM1001(75-80)	1.97	1.34	4.04	1.62	0.13	0.00	0.02	0.03	0.02	2.03
SM1001(80-85)	1.89	5.02	4.07	1.38	0.15	0.00	0.02	0.02	0.02	1.93

Table A2.1: Bulk Sample XRF analyses of SM1001

Sample	SiO2 (%)	TiO2 (%)	Al2O3 (%)	Fe2O3 (%)	MnO (%)
SM1001(0-5)	38.10	0.54	11.21	7.96	0.09
SM1001(5-10)	38.81	0.56	11.43	8.11	0.10
SM1001(10-15)	39.49	0.57	11.65	8.08	0.10
SM1001(15-20)	39.05	0.55	11.52	7.95	0.09
SM1001(20-25)	38.51	0.55	11.49	7.91	0.09
SM1001(25-30)	37.29	0.55	11.24	8.31	0.10
SM1001(30-35)	35.64	0.52	10.79	8.65	0.10
SM1001(35-40)	35.05	0.51	10.50	8.37	0.10
SM1001(40-45)	30.71	0.45	9.33	7.79	0.13
SM1001-(45-50)	34.80	0.48	11.02	15.06	0.50
SM1001-(50-55)	35.82	0.50	10.38	13.87	0.48
SM1001-(55-60)	36.59	0.52	10.27	9.31	0.23
SM1001-(65-70)	45.99	0.69	12.91	7.46	0.09
SM1001(60-65)	43.22	0.63	12.05	8.09	0.14
SM1001(70-75)	47.76	0.70	13.82	6.86	0.06
SM1001(75-80)	47.57	0.69	14.37	6.85	0.04
SM1001(80-85)	43.36	0.60	12.72	6.19	0.03

Table A2.1: Bulk Sample XRF analyses of SM1001

Sample	MgO (%)	CaO (%)	Na2O (%)	K2O (%)	P2O5 (%)	CuO (%)	PbO (%)	ZnO (%)	BaO (%)	S (%)
SM1001(85-90)	1.96	1.45	4.11	1.47	0.14	0.00	0.02	0.02	0.02	2.16
SM1001(90-95)	1.90	1.55	3.68	1.47	0.14	0.00	0.01	0.01	0.02	1.93
SM1001(95-100)	1.76	1.53	3.31	1.38	0.13	0.01	0.01	0.01	0.02	1.91
SM1001-(100-105)	1.96	1.20	3.73	1.62	0.14	0.01	0.01	0.05	0.02	2.09

Table A2.1: Bulk Sample XRF analyses of SM1001

Sample	SiO2 (%)	TiO2 (%)	Al2O3 (%)	Fe2O3 (%)	MnO (%)
SM1001(0-5)	46.10	0.65	13.81	6.79	0.03
SM1001(5-10)	45.63	0.64	13.67	6.59	0.03
SM1001(10-15)	43.03	0.62	12.74	6.33	0.03
SM1001(15-20)	47.78	0.72	15.29	7.36	0.03

Table A2.2: Bulk Sample ICPMS analyses of SM1001										
Sample	Ag (ppm)	Al (%)	As (ppm)	Ba (ppm)	Be (ppm)	Bi (ppm)	Ca (%)	Cd (ppm)	Ce (ppm)	Co (ppm)
SM1001-0-5	8.71	6.3	226	200	1	2.95	1.15	98.7	46.6	21.5
SM1001-5-10	9.36	6.47	240	210	0.97	3.1	1.23	105.5	47.2	22.6
SM1001-10-15	10.45	6.32	259	210	1	3.43	1.05	117.5	46.9	24
SM1001-15-20	10.25	6.45	284	210	1.07	3.24	0.97	112.5	46.7	22.9
SM1001-20-25	9.43	6.25	273	210	0.96	3.12	0.98	104	47	23.3
SM1001-25-30	12.15	6.23	376	210	0.95	3.85	1.11	145	44.9	24.7
SM1001-30-35	13.65	6.14	428	210	1.01	4.33	1.17	150	44.6	25.5
SM1001-35-40	11.35	5.76	340	190	0.86	3.71	1.14	121.5	40.8	23.3
SM1001-40-45	13.05	4.68	425	170	0.83	4.24	0.94	145	36.6	24.5
SM1001-45-50	34	6.17	1100	200	0.86	8.15	0.73	300	46.7	53.5
SM1001-50-55	34.5	5.8	1010	190	0.89	7.66	0.95	274	46.9	44.5
SM1001-55-60	20.9	5.36	749	170	0.86	3.96	1.03	142	41	32.3
SM1001-60-65	15.7	6.63	476	210	1.1	2.64	1.34	63.5	48.1	34
SM1001-65-70	13.2	7.09	309	220	1.18	0.93	1.86	22.8	50.9	29.9
SM1001-70-75	3.69	7.47	79.2	230	1.2	0.42	1.32	4.78	53.9	18.5
SM1001-75-80	0.39	7.57	26.1	230	1.18	0.31	0.98	0.97	54	17.1
SM1001-80-85	0.48	6.85	21.2	190	1.01	0.29	3.54	0.52	46.8	15

Table A2.2: Bulk Sample ICPMS analyses of SM1001										
Sample	Cr (ppm)	Cs (ppm)	Cu (ppm)	Fe (%)	Ga (ppm)	Ge (ppm)	Hf (ppm)	In (ppm)	K (%)	La (ppm)
SM1001-0-5	177	3.78	481	5.93	15.65	0.19	2.8	7.2	1.03	21.8
SM1001-5-10	188	3.88	495	6.06	16.2	0.19	2.8	7.5	1.06	22.2
SM1001-10-15	198	3.8	544	5.86	16.9	0.2	2.8	8.07	1.03	21.6
SM1001-15-20	217	3.77	550	5.93	15.45	0.18	2.8	7.44	1.04	21.7
SM1001-20-25	205	3.9	521	5.78	16.35	0.18	2.8	7.12	1.03	21.8
SM1001-25-30	192	3.7	674	6.16	16.05	0.18	2.7	8.58	1.05	21.3
SM1001-30-35	183	3.76	720	6.48	16.2	0.2	2.7	9.61	1.05	20.9
SM1001-35-40	263	3.53	575	6.11	15.2	0.18	2.5	7.7	0.93	19.3
SM1001-40-45	126	3.24	631	5.24	14	0.17	2.1	9.01	0.81	17.1
SM1001-45-50	132	3.95	951	11	24.9	0.29	2.6	18.45	1.02	22
SM1001-50-55	115	3.65	945	10.1	24.9	0.27	2.6	20.8	0.99	21.9
SM1001-55-60	173	3.51	678	6.42	20.5	0.19	2.4	14.05	0.93	19
SM1001-60-65	138	4.15	627	5.93	20.3	0.2	2.9	10.5	1.15	22.3
SM1001-65-70	137	4.42	415	5.35	18.35	0.19	3.1	3.55	1.25	23.6
SM1001-70-75	133	4.74	104	4.96	18.5	0.19	3.3	0.407	1.31	25.4
SM1001-75-80	121	4.96	42.3	4.86	18.85	0.2	3.2	0.149	1.24	25.3
SM1001-80-85	137	4.1	38.7	4.35	16.25	0.19	2.8	0.099	1.15	21.6

Table A2.2: Bulk Sample ICPMS analyses of SM1001										
Sample	Li (ppm)	Mg (%)	Mn (ppm)	Mo (ppm)	Na (%)	Nb (ppm)	Ni (ppm)	P (ppm)	Pb (ppm)	Rb (ppm)
SM1001-0-5	31.7	1.11	780	3.41	4.13	8.2	38.6	1360	1700	61.7
SM1001-5-10	34.6	1.12	864	2.78	3.97	8	34.6	1320	1840	61.6
SM1001-10-15	34.6	1.08	863	3.44	3.79	8.3	35.2	1190	2010	63.1
SM1001-15-20	34.7	1.06	767	3.85	3.8	8.2	33.6	1150	1990	61.1
SM1001-20-25	34.1	1.05	749	3.91	3.66	7.9	34.2	1140	1910	59.4
SM1001-25-30	32	1.16	858	4.15	4.15	7.8	32.4	1060	2490	61
SM1001-30-35	33.2	1.24	874	5.45	4.54	7.9	32.1	1000	2750	60.2
SM1001-35-40	31.1	1.18	864	4.59	4.42	7.6	32.5	930	2380	55.4
SM1001-40-45	26.8	0.99	972	2.64	3.6	6.1	27	810	2680	46.8
SM1001-45-50	30.5	1.01	4060	4.36	3.42	7.2	29.5	740	6980	60.1
SM1001-50-55	28.1	1.08	3850	3.7	3.56	7.5	28.6	750	6680	57.6
SM1001-55-60	29.1	0.96	1780	3.17	2.83	7.2	34	630	3420	57
SM1001-60-65	35.4	1.13	1160	2.52	3.22	9	33.7	680	2470	71.6
SM1001-65-70	38.6	1.07	740	2.83	2.88	9.5	34.5	620	1590	77.8
SM1001-70-75	42.6	1.05	462	2.65	2.88	9.9	37	570	363	85.4
SM1001-75-80	43.9	1.03	331	2.3	2.8	9.5	38.5	570	64.2	86.2
SM1001-80-85	37.4	0.98	265	2.28	2.85	8.4	35.9	640	59.6	71.3

Table A2.2: Bulk Sample ICPMS analyses of SM1001										
Sample	Re (ppm)	S (%)	Sb (ppm)	Sc (ppm)	Se (ppm)	Sn (ppm)	Sr (ppm)	Ta (ppm)	Te (ppm)	Th (ppm)
SM1001-0-5	0.006	2	21.9	17.4	3	7.8	139.5	0.61	0.08	6.6
SM1001-5-10	0.005	2.04	24.7	17.6	3	7.5	139	0.6	0.09	6.6
SM1001-10-15	0.006	2.14	26.7	17.6	3	8.1	127.5	0.59	0.08	6.7
SM1001-15-20	0.006	2.4	23.2	17.6	3	8.1	123	0.58	0.09	6.7
SM1001-20-25	0.006	2.36	22.6	17.6	3	7.9	123	0.56	0.08	6.5
SM1001-25-30	0.006	3.23	27.3	16.6	4	9.5	137	0.54	0.08	6.6
SM1001-30-35	0.008	4.3	31.8	16.4	4	9.3	144	0.56	0.09	6.6
SM1001-35-40	0.005	3.92	25.9	15.1	4	7.9	137.5	0.51	0.08	6
SM1001-40-45	0.005	3.45	31.9	13.4	3	7.8	119.5	0.45	0.07	5.3
SM1001-45-50	0.004	3.31	146.5	15.5	5	10.3	97.4	0.55	0.1	6.9
SM1001-50-55	0.005	3.33	134.5	14.8	5	9.9	115.5	0.56	0.1	6.9
SM1001-55-60	0.003	3.25	65.7	15.7	3	7.6	111	0.5	0.1	5.8
SM1001-60-65	0.004	3.31	52.6	18.6	3	6.9	135	0.61	0.1	6.7
SM1001-65-70	0.005	2.97	34.8	19.9	3	5.7	149	0.68	0.13	7.1
SM1001-70-75	0.005	2.27	8.31	21.8	2	4.4	141	0.71	0.11	7.7
SM1001-75-80	0.004	2.15	1.33	22.6	2	4.1	121.5	0.7	0.11	7.4
SM1001-80-85	0.005	2.07	1.02	20.1	2	4	262	0.6	0.12	6.3

Table A2.2: Bulk Sample ICPMS analyses of SM1001

Sample	Ti (ppm)	Tl (ppm)	U (ppm)	V (ppm)	W (ppm)	Y (ppm)	Zn (ppm)	Zr (ppm)
SM1001-0-5	0.35	0.6	2.6	104	2.5	21.9	9220	95.3
SM1001-5-10	0.358	0.6	3	106	2.6	21.4	10200	93.6
SM1001-10-15	0.352	0.62	3.2	108	2.6	22.7	11150	96.6
SM1001-15-20	0.361	0.65	3.3	109	2.7	22	11150	93.7
SM1001-20-25	0.35	0.61	3.2	108	2.6	21.6	9860	92.8
SM1001-25-30	0.353	0.73	3.8	106	2	22.3	13650	93.1
SM1001-30-35	0.34	0.73	3.4	106	2	22.5	13900	92.9
SM1001-35-40	0.305	0.65	2.7	95	2.6	20.5	12150	84.5
SM1001-40-45	0.258	0.66	2.5	83	2.1	17	15000	71
SM1001-45-50	0.307	0.68	3	126	3.4	19.6	42300	86
SM1001-50-55	0.315	0.84	2.8	118	3.3	20.1	36500	87.8
SM1001-55-60	0.306	0.58	2.3	101	2.4	18.8	19500	82
SM1001-60-65	0.395	0.45	2.3	115	1.9	21.8	9880	103
SM1001-65-70	0.428	0.4	2.5	113	1.8	22.3	5540	106.5
SM1001-70-75	0.435	0.41	2.5	116	1.6	23.2	1470	112.5
SM1001-75-80	0.4	0.42	2.3	111	1.5	22	246	108
SM1001-80-85	0.384	0.34	2.2	105	1.4	20.2	208	97.2

Table A2.2: Bulk Sample ICPMS analyses of SM1001

Sample	Ag (ppm)	Al (%)	As (ppm)	Ba (ppm)	Be (ppm)	Bi (ppm)	Ca (%)	Cd (ppm)	Ce (ppm)	Co (ppm)
SM1001-85-90	0.26	7.08	18.5	190	1.13	0.27	1.04	0.37	44.1	16.4
SM1001-90-95	0.14	7.07	14.1	190	1.18	0.23	1.09	0.14	48.2	16.6
SM1001-95-100	0.11	6.36	12.8	180	1.16	0.19	1.04	0.17	47.4	14.6
SM1001-100-105	0.35	7.91	20.4	210	1.33	0.2	0.86	1.86	53.7	17.1

Table A2.2: Bulk Sample ICPMS analyses of SM1001

Sample	Cr (ppm)	Cs (ppm)	Cu (ppm)	Fe (%)	Ga (ppm)	Ge (ppm)	Hf (ppm)	In (ppm)	K (%)	La (ppm)
SM1001-85-90	144	4.1	37.1	4.69	16.2	0.18	2.8	0.091	1.15	21.1
SM1001-90-95	143	4.38	35.6	4.57	17.75	0.19	2.9	0.065	1.21	22.6
SM1001-95-100	149	4.3	33.1	4.17	16.1	0.19	2.9	0.063	1.06	22.2
SM1001-100-105	109	5.1	41.8	5.01	19.65	0.21	3.3	0.204	1.29	25.2

Table A2.2: Bulk Sample ICPMS analyses of SM1001

Sample	Li (ppm)	Mg (%)	Mn (ppm)	Mo (ppm)	Na (%)	Nb (ppm)	Ni (ppm)	P (ppm)	Pb (ppm)	Rb (ppm)
SM1001-85-90	43	0.99	218	2.89	2.73	8.4	40.1	590	42.7	71.2
SM1001-90-95	42.9	0.97	205	2.07	2.46	8.7	40.5	580	28.2	75.9
SM1001-95-100	40.3	0.88	197	1.57	2.19	8.6	37.9	520	26.1	74
SM1001-100-105	48.5	1.03	226	2.46	2.53	9.4	40.3	600	61.5	87.8

Table A2.2: Bulk Sample ICPMS analyses of SM1001

Sample	Re (ppm)	S (%)	Sb (ppm)	Sc (ppm)	Se (ppm)	Sn (ppm)	Sr (ppm)	Ta (ppm)	Te (ppm)	Th (ppm)
SM1001-85-90	0.005	2.2	0.72	22	2	3.5	116.5	0.58	0.1	6.6
SM1001-90-95	0.004	2.01	0.48	22.4	2	3.6	120	0.61	0.1	6.7
SM1001-95-100	0.004	1.84	0.42	21.2	2	3.3	117.5	0.59	0.07	6.6
SM1001-100-105	0.005	2.15	1.21	24.5	2	3.3	114	0.67	0.06	7.6

Table A2.2: Bulk Sample ICPMS analyses of SM1001

Sample	Ti (ppm)	Tl (ppm)	U (ppm)	V (ppm)	W (ppm)	Y (ppm)	Zn (ppm)	Zr (ppm)
SM1001-85-90	0.392	0.35	2.2	111	1.4	19.8	142	98.6
SM1001-90-95	0.408	0.35	2.1	114	1.5	20.6	93	102
SM1001-95-100	0.358	0.34	2.1	95	1.5	20.3	80	100.5
SM1001-100-105	0.42	0.42	2.5	118	1.3	23.4	333	111.5

Table A2.3: Organic Carbon analyses by LECO of SM1001

Sample	Organic Carbon
SM1001-0-5	6.08
SM1001-5-10	6.26
SM1001-10-15	6.22
SM1001-15-20	5.84
SM1001-20-25	5.89
SM1001-25-30	6.4
SM1001-30-35	6.59
SM1001-35-40	6.09
SM1001-40-45	5.67
SM1001-45-50	3.55
SM1001-50-55	3.77
SM1001-55-60	3.43
SM1001-60-65	4.44
SM1001-65-70	4.08
SM1001-70-75	3.66
SM1001-75-80	3.47
SM1001-80-85	3.81
SM1001-85-90	4.13
SM1001-90-95	3.67
SM1001-95-100	3.71
SM1001-100-105	3.68

Table A2.4: Portable XRF analyses of SM1001

Sample	Mn	Mn +/-	Fe	Fe +/-	Co	Co +/-	Ni	Ni +/-
sm1001-0-2.5	606	25	60883	676	1106	120	0	57
sm1001-2.5-5	640	25	60974	692	1111	122	0	57
sm1001-5-7.5	801	29	61280	748	1032	131	0	60
sm1001-7.5-10	829	24	42889	532	1264	144	0	69
sm1001-10-12.5	344	14	32998	444	675	98	0	50
sm1001-12.5-15	610	18	30263	383	646	116	0	58
sm1001-15-17.5	555	22	45448	534	974	106	0	52
sm1001-17.5-20	534	17	33770	427	928	125	0	61
sm1001-20-22.5	520	17	33851	357	1128	107	0	50
sm1001-22.5-25	447	15	25803	314	1087	105	0	54
sm1001-25-27.5	312	10	18055	231	855	88	0	46
sm1001-27.5-30	220	9	12923	232	718	98	0	57
sm1001-30-35	567	18	31657	417	1154	128	0	63
sm1001-35-40	531	14	25127	335	1074	113	0	56
sm1001-40-45	856	29	52754	581	1000	109	0	53
sm1001-45-50	3670	78	78453	1046	2649	223	0	106
sm1001-50-55	3151	67	65192	879	1911	200	0	97

Table A2.4: Portable XRF analyses of SM1001

Sample	Cu	Cu +/-	Zn	Zn +/-	As	As +/-	Pb	Pb +/-
sm1001-0-2.5	258	16	8279	103	227	24	1767	31
sm1001-2.5-5	396	19	7921	102	167	23	1550	29
sm1001-5-7.5	237	17	8102	111	189	26	1664	33
sm1001-7.5-10	228	17	11676	159	318	31	2255	43
sm1001-10-12.5	136	14	5704	85	233	29	2111	38
sm1001-12.5-15	265	17	8722	122	195	26	1809	36
sm1001-15-17.5	178	14	8137	103	321	25	1761	32
sm1001-17.5-20	352	20	8677	124	247	29	2063	40
sm1001-20-22.5	249	14	6775	85	224	18	1001	22
sm1001-22.5-25	270	17	7653	104	136	25	1875	35
sm1001-25-27.5	207	15	7229	98	175	25	1960	35
sm1001-27.5-30	194	19	8208	141	158	38	2803	58
sm1001-30-35	164	16	8624	127	219	31	2356	45
sm1001-35-40	128	14	10594	147	218	31	2385	44
sm1001-40-45	436	19	12503	141	363	28	2483	38
sm1001-45-50	480	29	44746	593	961	59	6755	108
sm1001-50-55	410	27	36898	494	579	53	5828	96

Table A2.4: Portable XRF analyses of SM1001								
Sample	Mn	Mn +/-	Fe	Fe +/-	Co	Co +/-	Ni	Ni +/-
sm1001-55-60	1512	32	35370	374	1067	110	0	54
sm1001-60-65	1041	26	35105	405	808	117	0	59
sm1001-65-70	644	22	38914	845	760	223	0	119
sm1001-70-75	613	17	23185	255	987	89	0	43
sm1001-75-80	101	6	11080	143	828	65	0	35
sm1001-80-85	80	6	14625	193	486	55	0	29
sm1001-85-90	240	13	31495	364	761	82	0	41
sm1001-90-95	46	6	12227	174	739	56	0	30
sm1001-95-100	175	9	24743	325	1032	110	0	54
sm1001-100-105	366	10	15817	201	1005	82	0	41

Table A2.4: Portable XRF analyses of SM1001								
Sample	Cu	Cu +/-	Zn	Zn +/-	As	As +/-	Pb	Pb +/-
sm1001-55-60	222	15	14534	159	404	26	2359	37
sm1001-60-65	336	18	11941	147	299	28	2342	40
sm1001-65-70	430	37	7292	187	346	49	2006	68
sm1001-70-75	95	10	4679	64	191	16	783	19
sm1001-75-80	0	18	109	9	21	7	45	6
sm1001-80-85	19	6	119	8	0	20	49	5
sm1001-85-90	26	7	996	23	65	9	145	8
sm1001-90-95	0	18	206	10	0	20	46	5
sm1001-95-100	0	22	79	9	26	8	21	7
sm1001-100-105	56	9	3804	59	108	14	547	16

Table A2.5: Portable XRF analyses of SM1004								
Sample	Mn	Mn +/-	Fe	Fe +/-	Co	Co +/-	Ni	Ni +/-
sm1004-0-5	537	22	51444	556	939	105	<LOD	51
sm1004-5-10	446	20	51742	570	1025	108	<LOD	49
sm1004-10-15	480	16	34536	359	1147	107	<LOD	52
sm1004-15-20	397	14	24079	277	872	94	<LOD	47
sm1004-20-25	693	26	58813	650	1425	119	<LOD	56
sm1004-25-30	1033	35	71289	808	1294	135	<LOD	66
sm1004-30-35	922	31	60909	734	959	129	<LOD	60
sm1004-35-40	2833	85	136573	1726	1962	215	<LOD	102
sm1004-40-45	3058	89	120345	1683	2137	224	<LOD	102
sm1004-45-50	2078	49	60103	725	1557	170	<LOD	79
sm1004-50-55	3389	80	89195	1215	2472	240	<LOD	110
sm1004-55-60	4750	108	93250	1303	2369	251	<LOD	118
sm1004-60-65	2595	56	63550	879	2775	209	<LOD	102
sm1004-65-70	1169	27	37927	401	932	113	<LOD	54
sm1004-70-75	1617	31	35590	412	1105	120	<LOD	53

Table A2.5: Portable XRF analyses of SM1004								
Sample	Cu	Cu +/-	Zn	Zn +/-	As	As +/-	Pb	Pb +/-
sm1004-0-5	251	14	5116	68	65	21	1584	28
sm1004-5-10	270	15	5528	73	59	18	1076	22
sm1004-10-15	305	15	7664	93	95	20	1460	27
sm1004-15-20	269	15	7552	96	0	67	1800	32
sm1004-20-25	418	19	10926	128	147	26	2067	34
sm1004-25-30	623	24	15348	180	419	32	2841	44
sm1004-30-35	618	25	12561	158	622	34	2619	44
sm1004-35-40	1674	47	37373	473	2039	62	5783	89
sm1004-40-45	1083	42	37479	520	1877	62	4781	84
sm1004-45-50	616	27	24295	300	1641	48	4000	64
sm1004-50-55	896	38	38553	531	1925	66	6302	105
sm1004-55-60	860	39	49463	690	1475	61	5462	96
sm1004-60-65	746	35	38391	525	1982	64	5725	97
sm1004-65-70	88	10	3066	50	1889	30	456	15
sm1004-70-75	78	10	2473	47	1792	32	734	20

Table A2.6: Portable XRF analyses of SM1006

Sample	Mn	Mn +/-	Fe	Fe +/-	Co	Co +/-	Ni	Ni +/-
sm1006-0-5	479	20	55489	651	923	118	<LOD	56
sm1006-5-10	349	16	39074	439	865	92	<LOD	43
sm1006-10-15	344	13	30616	451	1174	140	<LOD	68
sm1006-15-20	442	19	46471	521	679	100	<LOD	50
sm1006-20-25	328	14	33904	461	407	97	<LOD	47
sm1006-25-30	914	25	39414	400	1122	112	<LOD	54
sm1006-30-35	982	36	79547	912	1484	145	<LOD	63
sm1006-35-40	1078	28	44309	495	1492	134	<LOD	62
sm1006-40-45	400	17	40246	402	753	83	<LOD	40
sm1006-45-50	117	6	12868	171	515	70	<LOD	37
sm1006-50-55	120	7	16209	220	677	85	<LOD	46
sm1006-55-60	63	5	11870	147	891	66	<LOD	33
sm1006-60-65	249	11	20820	240	721	85	<LOD	43
sm1006-65-70	257	15	38581	400	679	83	<LOD	38
sm1006-70-75	241	11	34709	490	957	142	<LOD	65
sm1006-80-85	125	7	15005	184	782	74	<LOD	39
sm1006-85-90	160	9	22396	258	824	89	<LOD	44

Table A2.6: Portable XRF analyses of SM1006								
Sample	Cu	Cu +/-	Zn	Zn +/-	As	As +/-	Pb	Pb +/-
sm1006-0-5	238	15	4787	71	139	22	1280	27
sm1006-5-10	164	12	2948	46	0	51	959	20
sm1006-10-15	134	16	4280	84	0	81	1443	37
sm1006-15-20	186	13	3681	55	0	55	1058	22
sm1006-20-25	188	15	4199	69	0	72	1424	30
sm1006-25-30	122	11	9396	108	179	22	1856	31
sm1006-30-35	275	17	8611	113	158	26	1774	33
sm1006-35-40	218	16	12165	148	140	27	2353	40
sm1006-40-45	95	9	2937	41	137	14	634	14
sm1006-45-50	49	9	1279	30	61	14	509	16
sm1006-50-55	42	9	1564	36	0	37	321	14
sm1006-55-60	28	7	123	9	0	22	86	7
sm1006-60-65	58	9	1860	36	0	32	277	12
sm1006-65-70	33	7	1200	24	28	8	152	8
sm1006-70-75	43	11	746	29	33	11	91	10
sm1006-80-85	40	8	511	18	31	8	77	7
sm1006-85-90	27	7	234	12	23	7	39	6

Table A2.7: Portable XRF analyses of SM1007

Sample	Mn	Mn +/-	Fe	Fe +/-	Co	Co +/-	Ni	Ni +/-
sm1007-0-5	328	17	47251	548	689	105	<LOD	50
sm1007-5-10	161	8	12697	185	674	78	<LOD	42
sm1007-10-15	119	6	9437	140	883	68	<LOD	37
sm1007-15-20	286	15	36261	423	804	91	<LOD	44
sm1007-20-25	175	11	21544	327	410	81	<LOD	44
sm1007-25-30	205	11	26241	349	621	83	<LOD	43
sm1007-30-35	431	19	42103	470	878	96	<LOD	47
sm1007-35-40	171	7	11533	150	437	63	<LOD	34
sm1007-40-45	249	12	30870	366	719	83	<LOD	44
sm1007-45-50	294	15	37876	459	659	96	<LOD	48
sm1007-50-55	215	9	20914	245	716	86	<LOD	45
sm1007-55-60	218	11	20475	292	725	103	<LOD	45
sm1007-60-65	385	15	31570	339	1022	103	<LOD	54
sm1007-65-70	285	15	39366	419	727	87	<LOD	43
sm1007-70-75	261	14	34265	362	601	78	<LOD	38
sm1007-75-80	164	10	21870	213	468	53	<LOD	27
sm1007-80-85	259	12	32544	391	707	87	<LOD	43

Table A2.7: Portable XRF analyses of SM1007								
Sample	Mn	Mn +/-	Fe	Fe +/-	Co	Co +/-	Ni	Ni +/-
sm1007-85-90	211	12	30347	421	798	97	<LOD	48
sm1007-90-95	320	13	26573	296	1072	98	<LOD	49
sm1007-95-100	333	13	31044	360	1092	111	<LOD	53
sm1007-100-105	197	9	17672	208	813	79	<LOD	42
sm1007-105-110	195	10	19143	332	745	120	<LOD	62
sm1007-110-115	161	7	11681	165	814	74	<LOD	35
sm1007-115-120	71	5	6905	121	454	60	<LOD	37

Table A2.7: Portable XRF analyses of SM1007

Sample	Cu	Cu +/-	Zn	Zn +/-	As	As +/-	Pb	Pb +/-
sm1007-0-5	104	11	2592	45	54	16	749	19
sm1007-5-10	61	10	1767	40	0	53	838	23
sm1007-10-15	56	9	1590	35	0	50	833	21
sm1007-15-20	87	10	2188	39	50	15	687	17
sm1007-20-25	47	10	1593	37	0	53	677	20
sm1007-25-30	73	10	2170	41	0	48	690	19
sm1007-30-35	107	10	3714	54	84	17	902	20
sm1007-35-40	70	9	2242	40	0	46	840	20
sm1007-40-45	85	10	1690	33	0	37	417	13
sm1007-45-50	99	11	1697	35	0	42	503	16
sm1007-50-55	57	9	1248	29	36	11	295	12
sm1007-55-60	55	10	1377	37	0	43	371	16
sm1007-60-65	124	11	2845	47	53	15	676	18
sm1007-65-70	86	9	2233	36	54	14	617	15
sm1007-70-75	76	8	1738	30	0	38	578	14
sm1007-75-80	60	6	1245	21	0	27	382	10
sm1007-80-85	90	10	2207	39	0	43	598	16

Table A2.7: Portable XRF analyses of SM1007								
Sample	Cu	Cu +/-	Zn	Zn +/-	As	As +/-	Pb	Pb +/-
sm1007-85-90	94	12	2474	48	69	20	891	23
sm1007-90-95	115	11	3452	54	61	18	1181	24
sm1007-95-100	149	13	3843	62	89	18	967	23
sm1007-100-105	98	10	2448	42	0	49	930	21
sm1007-105-110	73	14	2156	58	79	23	816	29
sm1007-110-115	58	9	1924	40	74	18	984	23
sm1007-115-120	60	10	1380	35	0	54	823	23

Table A2.8: Portable XRF analyses of SM1011								
Sample	Mn	Mn +/-	Fe	Fe +/-	Co	Co +/-	Ni	Ni +/-
sm10-11-0-5	143	11	30987	349	526	78	<LOD	37
sm10-11-15-20	199	12	34451	376	658	81	<LOD	40
sm10-11-20-25	179	10	31575	355	571	79	<LOD	40
sm10-11-25-30	128	8	23738	280	504	68	<LOD	36
sm1011-30-35	182	9	18423	195	658	72	<LOD	35
sm10-11-35-40	101	7	19841	236	373	60	<LOD	31
sm10-11-40-50	77	7	14502	218	335	60	<LOD	33
sm1011-50-55	105	6	11128	150	338	63	<LOD	33

Table A2.8: Portable XRF analyses of SM1011

Sample	Cu	Cu +/-	Zn	Zn +/-	As	As +/-	Pb	Pb +/-
sm10-11-0-5	57	8	916	22	0	32	318	11
sm10-11-15-20	40	7	1077	23	0	33	367	12
sm10-11-20-25	47	8	1096	24	0	33	363	12
sm10-11-25-30	29	7	348	13	0	23	114	7
sm1011-30-35	35	7	704	19	0	23	132	8
sm10-11-35-40	0	17	29	5	22	6	0	12
sm10-11-40-50	0	17	25	5	20	7	0	14
sm1011-50-55	0	18	32	6	0	20	0	15

Table A2.9: Sequential Leach Extractions of SM1001

Sample	Reagent	Cd (ppm)	Pb (ppm)	S (ppm)	Mn (ppm)	Fe (ppm)	Cu (ppm)	Zn (ppm)	As (ppm)
SM1001-20-25	1 M NH4NO3	10.28	15.94	4268.36	37.74	1.32	1.55	550.64	0.58
SM1001-20-25	1 M NH4OAc (pH 6)	0.61	13.86	25.58	1.45	0.16	0.86	56.28	0.08
SM1001-20-25	0.1 M NH3OHCl + NH4OAc (pH 6)	3.61	267.10	51.83	6.57	75.63	0	480.89	3.06
SM1001-20-25	0.025 M NH4-EDTA (pH 4.6)	3.33	1118.58	217.52	5.76	3491.53	140.65	847.98	30.07
SM1001-20-25	0.2 M NH4-oxalate (pH 2.6)	2.53	216.33	353.62	76.00	14255.67	162.86	1107.09	168.26
SM1001-20-25	0.1 M ascorbic acid + 0.2 M NH4-oxalate (pH 2.6)	7.31	29.59	349.84	305.75	15117.76	6.99	2837.75	20.02
SM1001-20-25	digested using a HF-Sic acid digestion in the PicoTrace high pressure digestion system	0.36	71.50	NA	146.70	NA	239.93	4181.27	4.91

Table A2.9: Sequential Leach Extractions of SM1001									
Sample	Reagent	Cd (ppm)	Pb (ppm)	S (ppm)	Mn (ppm)	Fe (ppm)	Cu (ppm)	Zn (ppm)	As (ppm)
SM1001-20-25	1 M NH4NO3	10.71	10.73	5317.55	64.81	0.27	2.97	756.01	1.83
SM1001-20-25	1 M NH4OAc (pH 6)	1.38	31.94	21.74	2.89	0.34	1.77	140.78	0.38
SM1001-20-25	0.1 M NH3OHCl + NH4OAc (pH 6)	6.13	591.06	88.92	8.51	172.31	0	1022.46	14.27
SM1001-20-25	0.025 M NH4-EDTA (pH 4.6)	2.87	1373.46	585.83	11.24	4901.55	220.39	1540.01	113.57
SM1001-20-25	0.2 M NH4-oxalate (pH 2.6)	1.90	149.98	220.62	79.84	10862.14	179.21	1387.15	189.51
SM1001-20-25	0.1 M ascorbic acid + 0.2 M NH4-oxalate (pH 2.6)	8.98	36.15	434.42	317.45	13474.98	8.61	3138.05	18.51
SM1001-20-25	digested using a HF-Sic acid digestion in the PicoTrace high pressure digestion system	74.84	67.32	NA	330.06	NA	345.56	5223.59	36.31

Table A2.9: Sequential Leach Extractions of SM1001									
Sample	Reagent	Cd (ppm)	Pb (ppm)	S (ppm)	Mn (ppm)	Fe (ppm)	Cu (ppm)	Zn (ppm)	As (ppm)
SM1001-50-55	1 M NH4NO3	5.53	9.27	3390.36	123.25	-0.17	1.42	430.31	1.04
SM1001-50-55	1 M NH4OAc (pH 6)	0.99	43.59	26.68	16.36	0.05	0.70	154.34	0.24
SM1001-50-55	0.1 M NH3OHCl + NH4OAc (pH 6)	3.77	686.77	28.80	38.69	61.34	0	909.03	9.53
SM1001-50-55	0.025 M NH4-EDTA (pH 4.6)	6.11	4009.89	207.32	98.26	6709.89	170.19	3151.80	154.88
SM1001-50-55	0.2 M NH4-oxalate (pH 2.6)	5.91	443.41	182.47	516.05	25126.39	196.87	4849.82	651.05
SM1001-50-55	0.1 M ascorbic acid + 0.2 M NH4-oxalate (pH 2.6)	17.57	100.57	234.72	902.37	36418.11	1.19	4536.87	48.39
SM1001-50-55	digested using a HF-Sic acid digestion in the PicoTrace high pressure digestion system	93.89	190.08	NA	390.44	NA	716.00	23378.01	51.23

Table A2.9: Sequential Leach Extractions of SM1001									
Sample	Reagent	Cd (ppm)	Pb (ppm)	S (ppm)	Mn (ppm)	Fe (ppm)	Cu (ppm)	Zn (ppm)	As (ppm)
SM1001-95-100	1 M NH4NO3	0.03	0	7373.97	20.78	5.46	0	1.16	0.03
SM1001-95-100	1 M NH4OAc (pH 6)	0.01	0.02	44.93	0.25	0.08	0.02	0.11	0.00
SM1001-95-100	0.1 M NH3OHCl + NH4OAc (pH 6)	0.15	0	45.72	1.03	93.75	0	-0.77	0.03
SM1001-95-100	0.025 M NH4-EDTA (pH 4.6)	0.44	9.37	153.20	2.70	2382.60	7.48	10.43	0.38
SM1001-95-100	0.2 M NH4-oxalate (pH 2.6)	0.05	3.00	90.23	2.88	3124.61	4.02	13.44	3.09
SM1001-95-100	0.1 M ascorbic acid + 0.2 M NH4-oxalate (pH 2.6)	0.15	11.40	510.49	44.17	15769.59	2.75	82.33	6.47
SM1001-95-100	digested using a HF-Sic acid digestion in the PicoTrace high pressure digestion system	209.57	8.69	NA	2023.70	NA	37.59	57.47	57.63

Table A2.10: Franklinite Analyses by Ion Microprobe												
Sample	Mg	Al	Si	Mn	Fe	Co	Cu	Zn	Pb	Cd	Ti	O
Franklinite inhomogeneous sub rounded	0.05	0.10	1.86	0.24	39.86	0.04	1.12	16.34	0.28	0.05	0.02	18.07
Franklinite rim	0.15	0.59	1.74	0.72	41.46	0.05	0.10	18.70	0.09	0.12	0.03	19.36
Franklinite large grain	0.01	0.04	0.53	0.16	46.33	0.03	1.40	19.24	0.23	1.24	0.02	19.25
Franklinite large grain	0.24	0.72	1.93	0.25	41.58	0.02	1.25	19.80	0.25	0.26	0.02	20.22
Franklinite framboid ellipse	0.07	0.06	0.64	1.05	38.90	0.05	0.10	22.06	0.12	0.18	0.02	17.77
Franklinite small iron rich	0.25	0.71	1.42	0.11	40.20	0.32	0.73	19.75	0.14	0.83	0.01	19.20
Franklinite small	0.12	0.67	2.92	0.30	39.04	0.04	0.02	17.37	0.14	0.05	0.02	19.56
Franklinite small	0.02	0.10	0.15	1.03	49.65	0.05	0.12	18.41	0.17	0.01	0.01	19.36
Franklinite small	0.08	0.10	0.07	0.56	46.33	0.04	0.14	22.83	0.03	0.34	0.02	19.35
Franklinite small	0.09	0.14	0.23	0.58	45.94	0.06	0.39	22.09	0.19	0.40	0.02	19.38

Appendix 3:

Geochemical Data presented in Chapter 3

Table A3.1: Bulk Sample ICPMS analyses of H1										
SAMPLE	Ag (ppm)	Al (%)	As (ppm)	Ba (ppm)	Be (ppm)	Bi (ppm)	Ca (%)	Cd (ppm)	Ce (ppm)	Co (ppm)
H1-10-15	0.09	4.37	20.4	150	0.9	0.17	0.8	0.08	41	12.8
H1-20-25	0.12	4.96	23.2	170	1.1	0.21	0.94	0.1	45.7	14.8
H1-30-35	0.1	4.65	20.8	160	1.11	0.19	0.89	0.11	43.8	14.1
H1-40-45	0.12	4.26	18.2	150	0.97	0.16	0.76	0.13	42.3	13.6
H1-50-55	0.06	4.74	20	170	1.1	0.17	0.93	0.13	47.5	15.4
H1-60-65	0.06	4.23	16.7	150	0.95	0.14	0.96	0.12	42.8	12

Table A3.1: Bulk Sample ICPMS analyses of H1

SAMPLE	Cr (ppm)	Cs (ppm)	Cu (ppm)	Fe (%)	Ga (ppm)	Ge (ppm)	Hf (ppm)	In (ppm)	K (%)	La (ppm)
H1-10-15	220	3.61	31.6	3.18	10.35	0.42	2.6	0.035	1.02	18.6
H1-20-25	170	4.06	34.6	3.58	11.6	0.39	2.8	0.046	1.19	20.4
H1-30-35	156	3.95	33.6	3.58	11.5	0.25	2.7	0.046	1.15	19.6
H1-40-45	170	3.8	26	3.23	10.5	0.24	2.6	0.038	1.04	19.2
H1-50-55	128	4.22	25	3.47	11.8	0.26	2.9	0.042	1.16	21.6
H1-60-65	143	3.83	21.1	3.12	10.25	0.2	2.5	0.031	1.04	19.7

Table A3.1: Bulk Sample ICPMS analyses of H1										
SAMPLE	Li (ppm)	Mg (%)	Mn (ppm)	Mo (ppm)	Na (%)	Nb (ppm)	Ni (ppm)	P (ppm)	Pb (ppm)	Rb (ppm)
H1-10-15	44.4	0.92	128	3.48	2.59	7.4	800	610	19.7	57.9
H1-20-25	53.5	1.13	168	5.47	3.34	8.4	418	540	23.3	63.7
H1-30-35	52.3	1.07	163	5.57	3.09	8	391	530	23	61.2
H1-40-45	46.2	0.93	177	5.68	2.43	7.7	523	410	21.1	57.9
H1-50-55	52.3	1	235	9.34	2.54	8.5	274	480	16.6	65.1
H1-60-65	45.7	0.92	163	4.88	2.39	7.6	395	450	12.8	57.9

Table A3.1: Bulk Sample ICPMS analyses of H1										
SAMPLE	Re (ppm)	S (%)	Sb (ppm)	Sc (ppm)	Se (ppm)	Sn (ppm)	Sr (ppm)	Ta (ppm)	Te (ppm)	Th (ppm)
H1-10-15	0.008	1.06	0.59	13.6	11	2	98.8	0.5	0.11	5.7
H1-20-25	0.009	2.02	0.59	15.7	2	2.3	116.5	0.57	0.07	6.3
H1-30-35	0.008	1.96	0.58	15.2	5	2.1	112.5	0.57	0.05	6
H1-40-45	0.007	2.25	0.54	13.4	3	2	97.6	0.52	0.08	5.6
H1-50-55	0.009	2.6	0.57	14.8	2	1.8	111.5	0.57	0.08	6.2
H1-60-65	0.006	2.45	0.46	13	2	1.5	107	0.51	0.05	5.7

Table A3.1: Bulk Sample ICPMS analyses of H1

SAMPLE	Ti (%)	Tl (ppm)	U (ppm)	V (ppm)	W (ppm)	Y (ppm)	Zn (ppm)	Zr (ppm)
H1-10-15	0.267	0.32	4	88	1.3	14.6	59	89.1
H1-20-25	0.295	0.37	4.2	93	1.4	15.8	72	98.6
H1-30-35	0.289	0.35	4	94	1.3	14.7	69	94.9
H1-40-45	0.278	0.32	3.3	82	1.2	14	57	90.4
H1-50-55	0.302	0.39	4.2	90	1.2	16.2	56	100
H1-60-65	0.267	0.34	2.8	79	1.1	14.4	47	89.6

Table A3.2: LA-ICPMS Analyses of Pyrite from H1

Sample	Mg24	Al27	Ca43	Ti49	V51	Cr53	Mn55	Fe57	Co59	Ni60	Cu65	Zn66	As75
H160-65-01	145.64	31.88	249.35	4.69	0.15	<1.07	1548.16	465500.00	1.61	8.59	3.78	92.34	56.73
H160-65-02	13.38	4.03	<248.57	<2.60	0.12	<1.36	7.15	465500.00	114.36	25.86	9.53	13.19	93.95
H160-65-03	157.51	308.91	478.89	39.34	1.36	<2.06	1080.38	465500.00	13.82	37.09	315.47	133.88	1646.44
H160-65-04	179.75	49.62	393.99	6.12	0.40	<1.85	1914.76	465500.00	127.02	89.19	71.69	116.17	303.76
H160-65-05	76.87	31.17	376.82	7.36	1.20	<2.29	1165.38	465500.00	147.47	35.90	82.00	96.61	224.74
H160-65-06	86.16	38.60	<172.71	16.72	0.11	<1.30	1241.86	465500.00	1.62	3.38	14.70	31.08	44.12
H160-65-07	41.37	28.36	<312.92	4.46	1.18	<1.75	2464.81	465500.00	79.78	41.33	375.70	85.86	128.79
H160-65-08	141.67	32.41	314.39	4.74	1.17	<2.11	1154.02	465500.00	96.87	37.41	39.35	88.48	109.81
H160-65-09	342.60	246.82	1793.39	67.84	30.86	<3.46	1775.36	465500.00	567.89	131.78	1303.09	168.07	368.65
H160-65-10	48.26	124.25	<235.09	13.01	0.28	<1.63	1106.94	465500.00	0.74	3.00	106.29	34.83	122.44
H160-65-11	91.40	41.75	<251.01	5.70	0.19	<1.66	1340.20	465500.00	2.12	2.99	69.84	16.19	59.25
H160-65-12	206.07	869.53	<276.05	26.48	0.60	<2.35	958.70	465500.00	69.28	5.42	231.26	56.59	227.62
H160-65-13	132.26	64.27	627.88	42.47	32.24	<3.21	501.02	465500.00	19.43	18.79	127.02	62.13	415.09
H160-65-14	78.62	38.82	<242.66	8.04	0.14	<2.52	911.34	465500.00	25.70	10.50	109.38	53.56	36.04
H160-65-15	109.95	31.22	230.64	4.02	2.34	<2.66	123.49	465500.00	11.77	9.24	5.41	23.88	95.46
H150-55-1	20.33	20.20	<264.24	5.29	1.44	<4.89	1658.81	465500.00	0.25	1.20	27.06	37.19	80.88
H150-55-2	25.09	11.09	<323.48	4.23	2.65	<3.72	1412.77	465500.00	0.61	5.25	26.19	33.09	179.33

Table A3.2: LA-ICPMS Analyses of Pyrite from H1

Sample	Se77	Mo95	Ag107	Cd111	Sb121	Te125	Gd157	Hf178	Ta181	Au197	Tl205	Pb208	Bi209
H160-65-01	<4.78	218.63	<0.06	0.51	2.22	<0.21	<0.10	<0.04	<0.01	0.06	<0.02	0.37	0.12
H160-65-02	<4.91	1.32	<0.05	<0.22	0.28	<0.20	0.07	<0.05	<0.01	<0.02	0.04	0.26	0.07
H160-65-03	12.33	40.02	<0.07	0.90	4.49	0.32	0.14	<0.05	0.05	<0.03	0.18	3.50	0.70
H160-65-04	12.01	119.62	0.08	1.04	3.54	0.29	<0.08	<0.04	<0.02	<0.03	0.27	22.51	0.20
H160-65-05	8.76	35.57	0.12	0.72	1.71	<0.32	<0.12	<0.03	<0.01	<0.03	2.90	4.40	0.07
H160-65-06	<3.69	2.09	<0.03	<0.01	0.25	<0.23	<0.14	<0.03	<0.02	<0.02	0.01	0.79	0.15
H160-65-07	<4.44	47.73	<0.05	0.29	1.72	0.37	<0.17	<0.03	<0.02	<0.02	0.45	3.21	0.12
H160-65-08	<5.87	19.73	<0.05	0.29	2.16	<0.26	<0.24	<0.05	<0.03	<0.02	0.12	1.86	0.10
H160-65-09	13.51	68.60	0.49	0.89	5.23	1.72	0.78	<0.05	<0.02	<0.06	3.03	49.07	1.11
H160-65-10	<3.64	41.42	0.06	<0.12	0.58	<0.15	<0.09	<0.02	0.01	<0.02	0.02	1.67	0.11
H160-65-11	3.73	40.40	<0.05	<0.11	0.86	<0.18	<0.06	<0.03	<0.01	<0.02	0.07	1.02	0.05
H160-65-12	<3.89	28.75	0.10	<0.19	2.14	<0.27	0.15	<0.04	<0.02	<0.03	<0.02	2.53	0.25
H160-65-13	6.03	29.76	<0.04	0.40	3.97	<0.21	0.11	0.02	<0.02	<0.03	0.72	3.54	0.12
H160-65-14	<3.60	11.39	0.04	0.33	0.15	<0.17	<0.16	<0.05	<0.02	0.02	1.03	13.86	0.23
H160-65-15	<3.68	43.57	<0.04	<0.23	0.30	<0.19	<0.14	<0.02	<0.02	<0.02	0.05	0.36	0.04
H150-55-1	<6.00	19.18	<0.05	<0.19	0.39	<0.24	<0.01	<0.04	<0.02	<0.03	<0.02	1.31	0.07
H150-55-2	<5.68	30.16	<0.04	<0.23	0.59	<0.21	<0.14	<0.03	<0.02	0.03	<0.03	1.88	0.10

Table A3.2: LA-ICPMS Analyses of Pyrite from H1													
Sample	Mg24	Al27	Ca43	Ti49	V51	Cr53	Mn55	Fe57	Co59	Ni60	Cu65	Zn66	As75
H150-55-3	32.48	42.64	<301.91	3.11	2.77	<3.68	5804.61	465500.00	0.15	1.26	38.72	61.76	40.98
H150-55-4	110.88	43.18	403.59	12.23	5.22	<4.22	9154.26	465500.00	1.24	3.73	294.44	127.83	193.63
H150-55-5	192.45	345.27	420.63	28.46	1.41	<3.86	1681.81	465500.00	19.97	15.49	233.17	80.67	71.28
H150-55-6	39.97	35.59	<249.19	<2.24	0.57	<2.86	490.33	465500.00	1.59	3.12	171.72	30.04	931.74
H150-55-7	91.62	141.01	490.27	3.80	3.83	<3.44	5095.58	465500.00	0.60	4.92	142.41	81.42	239.47
H150-55-8	113.47	26.17	<300.07	3.49	0.41	<2.77	314.00	465500.00	108.75	34.83	20.53	33.22	112.02
H150-55-9	75.43	44.42	290.41	68.03	4.29	<2.94	7208.83	465500.00	0.48	3.96	510.31	104.82	311.69
H150-55-10	37.27	7.05	<293.14	<1.89	0.23	<2.88	346.78	465500.00	0.82	2.42	61.19	28.44	2205.81
H150-55-11	99.01	50.59	303.97	38.58	22.45	<3.94	1306.15	465500.00	1.04	5.33	77.30	46.72	374.67
H150-55-12	39.42	24.46	<254.24	4.92	0.10	<2.63	1245.17	465500.00	0.87	2.28	32.39	37.80	639.34
H150-55-13	52.47	62.29	<240.83	5.14	4.82	<2.99	39.39	465500.00	85.90	29.15	34.87	144.38	156.80
H150-55-14	173.03	47.69	490.89	34.19	18.24	<3.21	843.70	465500.00	9.36	26.91	68.03	72.37	665.62
H150-55-15	101.54	87.50	585.97	36.37	27.11	<2.59	3424.75	465500.00	0.24	1.07	93.84	59.29	119.28
H150-55-16								465500.00					
H150-55-17								465500.00					
H150-55-18								465500.00					
H150-55-19								465500.00					

Table A3.2: LA-ICPMS Analyses of Pyrite from H1

Sample	Se77	Mo95	Ag107	Cd111	Sb121	Te125	Gd157	Hf178	Ta181	Au197	Tl205	Pb208	Bi209
H150-55-3	6.08	6.00	<0.04	<0.26	0.23	<0.32	0.03	<0.05	<0.03	<0.03	<0.03	0.13	<0.03
H150-55-4	8.74	19.15	<0.05	<0.24	1.23	<0.23	0.12	<0.03	<0.02	0.04	<0.02	0.71	0.03
H150-55-5	<6.50	68.64	0.09	0.26	2.25	<0.23	<0.10	<0.02	0.02	<0.03	0.17	7.80	0.29
H150-55-6	<4.69	23.43	<0.04	<0.20	1.08	<0.27	<0.17	<0.04	<0.01	<0.02	<0.02	0.25	<0.03
H150-55-7	10.91	53.25	<0.07	0.60	4.59	<0.31	<0.15	<0.07	<0.04	<0.03	<0.02	0.32	<0.03
H150-55-8	<4.36	201.51	<0.03	0.25	0.79	<0.22	<0.10	<0.08	<0.03	<0.03	0.06	1.61	0.05
H150-55-9	<5.14	60.77	<0.05	0.27	10.74	<0.26	<0.09	<0.04	0.03	<0.03	0.02	2.22	<0.03
H150-55-10	<5.11	17.18	0.08	<0.30	0.93	<0.29	<0.18	<0.05	<0.02	<0.02	0.03	1.88	0.07
H150-55-11	<5.83	48.23	0.06	0.35	1.84	<0.29	0.30	<0.04	<0.03	<0.03	<0.04	2.00	0.05
H150-55-12	<5.10	18.28	<0.03	<0.34	0.70	<0.24	<0.01	<0.04	<0.01	<0.02	0.02	1.10	0.03
H150-55-13	<4.74	4.95	0.16	<0.21	0.46	1.23	<0.09	<0.04	<0.03	<0.03	0.23	18.08	0.33
H150-55-14	10.81	110.86	<0.05	0.76	7.94	0.43	0.11	<0.03	<0.02	<0.03	0.08	0.79	0.06
H150-55-15	5.51	39.87	<0.03	<0.27	1.68	<0.24	0.30	0.03	<0.01	<0.03	<0.02	0.60	<0.02
H150-55-16										<0.02			
H150-55-17										<0.02			
H150-55-18										<0.02			
H150-55-19										<0.02			

Table A3.2: LA-ICPMS Analyses of Pyrite from H1													
Sample	Mg24	Al27	Ca43	Ti49	V51	Cr53	Mn55	Fe57	Co59	Ni60	Cu65	Zn66	As75
H150-55-20								465500.00					
H140-45-1								465500.00					
H140-45-2								465500.00					
H140-45-3								465500.00					
H140-45-4								465500.00					
H140-45-5								465500.00					
H140-45-6	61.14	10.35	<197.86	3.03	0.05	<1.85	2741.43	465500.00	0.79	0.85	3.05	5.22	46.12
H140-45-7	34.82	43.90	<293.81	4.42	1.42	<2.42	95.72	465500.00	28.51	10.89	10.19	35.84	129.19
H140-45-8	76.43	124.27	355.18	7.95	3.93	<2.88	2269.36	465500.00	3.84	8.04	124.46	92.96	209.06
H140-45-9	54.27	137.61	<375.63	3.46	4.05	<3.31	2003.26	465500.00	10.36	21.68	17.62	50.97	817.58
H140-45-10	128.65	170.87	<383.06	7.04	5.48	<4.06	3408.20	465500.00	132.88	53.04	30.94	65.26	155.60
H140-45-11	323.55	104.58	1039.03	64.59	20.90	<3.77	112.28	465500.00	7.51	19.95	170.16	90.17	565.27
H140-45-12	102.09	232.86	<401.61	<4.18	5.89	<3.62	1344.53	465500.00	8.39	10.84	66.62	67.50	847.50
H140-45-13	22.87	49.01	<284.51	3.25	1.08	<2.69	3172.57	465500.00	0.08	0.39	7.03	38.26	425.64
H140-45-14	68.18	7.15	330.18	<1.55	0.08	<3.27	275.73	465500.00	3.13	6.41	0.75	66.27	58.39
H140-45-15	145.54	360.69	<382.40	29.09	19.86	<3.60	72.44	465500.00	49.55	19.39	60.65	74.05	1919.31
H140-45-16	17.83	5.98	<295.08	3.73	0.26	<2.65	508.33	465500.00	6.74	9.12	9.61	110.31	563.16

Table A3.2: LA-ICPMS Analyses of Pyrite from H1

Sample	Se77	Mo95	Ag107	Cd111	Sb121	Te125	Gd157	Hf178	Ta181	Au197	Tl205	Pb208	Bi209
H150-55-20										0.02			
H140-45-1										<0.02			
H140-45-2										<0.02			
H140-45-3										<0.04			
H140-45-4										<0.02			
H140-45-5										<0.01			
H140-45-6	<4.02	1.37	<0.05	<0.20	0.36	<0.20	0.02	<0.03	<0.01	<0.02	<0.02	0.87	0.04
H140-45-7	<4.02	1.80	0.06	<0.23	0.62	<0.27	<0.08	<0.04	<0.01	<0.02	0.08	1.69	0.10
H140-45-8	5.19	26.75	0.41	<0.33	2.68	0.34	<0.02	<0.04	<0.02	<0.03	<0.02	5.17	0.21
H140-45-9	9.19	14.19	<0.07	0.27	1.83	<0.28	<0.11	<0.03	<0.02	<0.05	<0.02	0.20	0.05
H140-45-10	8.64	12.39	0.13	0.44	1.10	0.75	<0.17	<0.08	<0.02	<0.04	0.65	26.39	0.33
H140-45-11	10.85	45.92	0.14	1.25	9.10	1.76	0.73	<0.05	<0.01	<0.04	0.10	3.56	0.23
H140-45-12	<7.20	30.21	<0.05	<0.36	4.71	0.69	<0.17	0.05	<0.01	<0.03	<0.02	0.63	0.05
H140-45-13	<5.33	2.81	<0.05	<0.23	<0.09	<0.20	0.02	<0.04	<0.01	<0.03	<0.02	<0.04	<0.02
H140-45-14	<3.95	18.78	<0.03	0.10	<0.09	<0.27	0.14	<0.04	<0.02	<0.02	<0.02	0.17	<0.02
H140-45-15	9.94	20.86	0.07	<0.25	3.14	1.10	<0.24	<0.03	<0.02	<0.03	0.23	18.75	0.22
H140-45-16	<4.34	5.48	<0.05	<0.18	0.36	<0.20	<0.01	<0.04	<0.02	<0.03	<0.01	1.05	<0.02

Table A3.2: LA-ICPMS Analyses of Pyrite from H1													
Sample	Mg24	Al27	Ca43	Ti49	V51	Cr53	Mn55	Fe57	Co59	Ni60	Cu65	Zn66	As75
H140-45-17	81.90	116.34	<224.59	2.51	0.43	<3.58	605.42	465500.00	1.21	5.68	211.92	45.18	372.38
H140-45-18	67.08	17.30	<287.45	3.24	0.26	<4.36	470.95	465500.00	0.44	2.73	53.95	34.29	118.22
H140-45-19	23.64	11.32	<203.93	<3.91	0.16	<3.76	165.27	465500.00	0.28	2.79	11.72	22.64	208.49
H140-45-20	99.48	228.64	<321.01	4.56	4.52	<3.94	1139.85	465500.00	66.62	69.96	49.47	120.63	164.78
H130-35-1	171.53	114.20	658.01	6.64	3.37	<3.36	288.71	465500.00	33.49	80.03	42.49	67.00	731.23
H130-35-2	40.93	16.69	<334.90	4.39	<0.05	<3.41	226.05	465500.00	0.49	2.76	4.03	34.05	559.30
H130-35-3	12.35	2.58	<257.37	<2.36	0.09	<3.07	119.46	465500.00	0.98	2.13	1.10	17.10	475.06
H130-35-4	91.16	22.93	<318.94	<2.15	1.45	<3.87	294.83	465500.00	153.44	87.48	12.39	34.15	126.10
H130-35-5	48.69	13.76	<286.37	4.45	0.13	<3.84	1819.73	465500.00	8.60	9.45	10.32	61.97	1057.01
H130-35-6	15.44	3.85	<261.71	2.53	0.17	<2.99	820.54	465500.00	1.19	2.95	8.17	34.24	395.69
H130-35-7	50.48	7.43	<296.17	2.59	0.25	<4.35	142.86	465500.00	5.99	2.82	94.21	17.68	620.75
H130-35-8	44.28	23.68	<311.96	<1.77	0.63	<4.44	216.38	465500.00	0.73	2.07	26.23	14.38	851.55
H130-35-9	138.18	33.92	<457.33	12.75	0.68	<5.72	14.33	465500.00	0.56	1.95	223.41	20.15	1109.93
H130-35-10	93.03	78.99	<293.33	<2.52	3.33	<4.82	819.07	465500.00	49.02	6.57	38.12	14.95	184.24
H110-15-1	109.99	285.49	<338.93	15.76	0.85	4.86	1139.18	465500.00	8.28	23.80	45.14	272.17	179.48
H110-15-2	91.05	25.75	441.74	4.43	0.74	<3.49	1795.48	465500.00	144.80	78.53	23.26	140.42	524.56
H110-15-3	118.34	76.60	317.87	3.53	0.39	<3.55	256.46	465500.00	3.52	4.76	18.34	29.68	127.31

Table A3.2: LA-ICPMS Analyses of Pyrite from H1

Sample	Se77	Mo95	Ag107	Cd111	Sb121	Te125	Gd157	Hf178	Ta181	Au197	Tl205	Pb208	Bi209
H140-45-17	<3.87	20.21	0.08	0.26	3.47	0.29	<0.19	<0.04	<0.02	<0.03	0.02	0.55	0.03
H140-45-18	9.23	3.89	<0.05	<0.19	1.17	<0.25	<0.01	<0.03	<0.02	<0.03	<0.02	0.12	<0.02
H140-45-19	<3.92	8.62	<0.04	<0.21	1.29	0.21	0.06	<0.03	<0.02	<0.03	<0.02	0.93	0.08
H140-45-20	7.81	52.42	0.13	0.18	2.43	2.99	0.09	<0.02	<0.02	<0.04	0.80	12.81	0.33
H130-35-1	23.71	246.20	0.13	1.14	8.63	1.53	<0.13	<0.03	<0.02	<0.04	0.85	3.68	0.30
H130-35-2	10.61	4.35	<0.05	<0.31	1.27	<0.28	<0.09	<0.02	0.02	<0.03	<0.02	0.41	0.09
H130-35-3	13.56	4.14	<0.05	<0.26	<0.11	<0.27	<0.08	<0.03	<0.02	<0.02	<0.02	0.07	<0.03
H130-35-4	<5.77	111.07	<0.05	<0.35	2.31	<0.33	<0.11	<0.05	0.02	<0.03	0.59	6.83	0.05
H130-35-5	<6.59	19.87	<0.07	<0.14	0.72	<0.20	<0.13	<0.06	<0.03	<0.02	0.14	2.35	0.10
H130-35-6	<3.98	21.33	<0.04	<0.20	0.95	<0.23	<0.01	<0.04	<0.02	<0.02	<0.02	1.71	<0.04
H130-35-7	<4.88	2.82	<0.06	<0.26	0.42	<0.26	<0.13	<0.05	<0.02	<0.02	0.04	6.66	0.08
H130-35-8	6.43	6.13	<0.07	<0.39	0.88	<0.33	<0.24	<0.06	0.03	<0.02	0.07	2.45	<0.04
H130-35-9	<7.70	4.51	0.06	<0.39	0.51	<0.42	<0.16	<0.09	<0.02	<0.04	<0.03	2.35	0.09
H130-35-10	<4.96	0.52	<0.04	<0.29	0.60	<0.23	<0.12	<0.05	<0.02	<0.03	0.29	4.21	0.13
H110-15-1	<5.10	72.24	0.17	0.48	11.29	0.39	0.06	<0.01	<0.03	<0.03	0.17	15.73	0.23
H110-15-2	9.48	200.31	<0.06	0.29	6.93	0.76	<0.09	<0.06	<0.01	<0.03	0.45	6.85	0.26
H110-15-3	<4.35	31.92	<0.03	<0.17	0.58	<0.16	0.04	<0.04	<0.02	<0.02	0.05	1.42	0.04

Table A3.2: LA-ICPMS Analyses of Pyrite from H1													
Sample	Mg24	Al27	Ca43	Ti49	V51	Cr53	Mn55	Fe57	Co59	Ni60	Cu65	Zn66	As75
H110-15-4	104.44	78.88	<276.12	6.37	1.42	<4.46	12.28	465500.00	541.77	79.64	20.99	106.97	99.01
H110-15-5	25.92	16.46	<169.06	2.34	0.11	<2.43	159.50	465500.00	0.28	0.49	5.67	23.69	182.28
H110-15-6	32.90	12.66	<322.23	<2.06	0.52	<3.64	2.76	465500.00	0.14	0.58	6.00	7.98	391.77
H110-15-7	27.14	<0.81	<193.23	2.30	0.03	<2.89	2.82	465500.00	<0.05	0.18	1.05	5.35	164.74
H110-15-8	104.56	23.09	<312.06	3.50	0.88	<4.62	4783.69	465500.00	117.52	47.30	15.47	81.90	200.96
H110-15-9	31.54	32.64	<292.80	<1.70	0.51	<3.16	36.85	465500.00	49.15	23.88	1.95	43.60	52.76
H110-15-10	77.08	112.99	<257.76	6.39	0.70	<3.15	30.91	465500.00	18.82	12.12	0.68	12.93	266.60
H120-25-1	21.92	13.24	<275.29	4.83	0.35	<3.95	90.24	465500.00	0.72	1.03	5.39	22.06	2902.28
H120-25-2	51.56	68.70	<263.57	3.46	1.94	<3.54	321.54	465500.00	0.51	2.73	3.74	24.88	1141.69
H120-25-3	71.73	125.38	<412.01	4.81	5.04	<5.96	3943.53	465500.00	0.40	2.82	61.54	67.18	209.45
H120-25-4	40.27	23.53	334.30	<2.90	0.98	<4.57	359.11	465500.00	0.14	1.02	8.28	18.09	313.07
H120-25-5	40.12	56.04	226.82	1.79	2.19	<3.14	135.36	465500.00	152.15	67.39	36.17	103.40	91.12
H120-25-6	166.60	209.75	420.25	25.32	54.40	<3.51	3796.26	465500.00	6.63	1.26	13.19	50.80	395.44
H120-25-7	34.21	49.43	315.03	1.99	1.88	<3.55	79.58	465500.00	4.31	3.12	10.18	26.51	3449.95
H120-25-8	33.66	53.53	257.10	6.15	0.06	<3.32	11.75	465500.00	0.35	0.53	21.18	7.60	145.38
H120-25-9	276.92	304.38	673.11	12.60	45.15	<4.56	229.22	465500.00	5.50	3.23	169.43	50.16	265.31
H120-25-10	55.58	38.65	260.84	2.96	0.80	<3.61	1218.01	465500.00	63.69	32.28	23.69	14.77	913.91

Table A3.2: LA-ICPMS Analyses of Pyrite from H1

Sample	Se77	Mo95	Ag107	Cd111	Sb121	Te125	Gd157	Hf178	Ta181	Au197	Tl205	Pb208	Bi209
H110-15-4	<4.36	0.89	0.08	<0.31	0.90	0.95	<0.12	<0.04	0.02	<0.03	0.53	27.10	0.38
H110-15-5	<2.65	1.73	<0.03	0.12	<0.06	<0.17	<0.06	<0.03	<0.02	<0.02	0.07	0.73	0.06
H110-15-6	<6.01	24.53	0.02	<0.18	0.21	<0.30	<0.01	<0.05	<0.01	<0.02	<0.02	<0.06	<0.03
H110-15-7	<4.03	3.05	<0.04	<0.23	<0.06	<0.21	<0.12	<0.03	<0.02	<0.01	<0.02	0.07	<0.03
H110-15-8	<7.46	11.56	<0.07	<0.25	2.62	0.51	<0.11	<0.04	<0.02	<0.03	0.17	2.58	0.08
H110-15-9	4.84	0.14	<0.03	<0.17	0.94	<0.22	<0.10	<0.05	<0.02	<0.02	0.32	4.10	0.08
H110-15-10	<4.09	17.23	<0.03	<0.01	0.49	<0.21	<0.11	<0.05	<0.02	<0.01	0.04	0.61	0.03
H120-25-1	13.73	8.12	0.05	<0.30	0.83	<0.24	<0.18	<0.04	<0.03	<0.02	0.04	0.35	0.03
H120-25-2	7.14	7.58	<0.04	<0.36	2.59	<0.32	<0.17	<0.04	<0.03	<0.03	<0.03	0.13	<0.03
H120-25-3	<7.21	20.69	0.08	<0.49	4.58	<0.33	<0.26	<0.04	<0.03	0.09	<0.03	0.11	<0.04
H120-25-4	11.52	14.96	<0.06	<0.31	1.68	<0.38	0.05	<0.05	<0.02	<0.04	<0.02	0.16	0.04
H120-25-5	6.99	18.12	0.24	0.21	0.94	0.39	<0.12	<0.04	<0.02	<0.03	0.21	10.16	0.23
H120-25-6	<7.40	8.95	0.07	<0.31	1.61	<0.27	<0.11	<0.05	<0.03	<0.03	<0.03	0.52	<0.03
H120-25-7	<5.37	20.80	<0.06	<0.18	1.85	<0.29	<0.12	<0.08	<0.02	<0.03	0.06	0.18	0.04
H120-25-8	6.20	6.09	<0.07	<0.27	<0.07	<0.22	<0.09	<0.06	0.01	<0.03	<0.02	0.25	0.05
H120-25-9	<6.99	4.22	0.62	<0.24	1.30	<0.31	<0.15	<0.05	<0.02	<0.05	0.13	5.47	0.15
H120-25-10	8.41	16.60	0.06	0.35	0.61	<0.38	0.12	<0.04	<0.01	<0.03	0.22	5.25	0.12

Table A3.2: LA-ICPMS Analyses of Pyrite from H1													
Sample	Mg24	Al27	Ca43	Ti49	V51	Cr53	Mn55	Fe57	Co59	Ni60	Cu65	Zn66	As75
H130-35-11								465500.00					
H130-35-12								465500.00					
H130-35-13								465500.00					
H130-35-14								465500.00					
H130-35-15								465500.00					
H130-35-16								465500.00					
H110-15-11								465500.00					
H110-15-12								465500.00					
H110-15-13								465500.00					
H110-15-14								465500.00					
H110-15-15								465500.00					
H120-25-11								465500.00					
H120-25-12								465500.00					
H120-25-13								465500.00					
H120-25-14								465500.00					
H120-25-15								465500.00					

Table A3.2: LA-ICPMS Analyses of Pyrite from H1													
Sample	Se77	Mo95	Ag107	Cd111	Sb121	Te125	Gd157	Hf178	Ta181	Au197	Tl205	Pb208	Bi209
H130-35-11										<0.03			
H130-35-12										0.02			
H130-35-13										0.05			
H130-35-14										<0.03			
H130-35-15										<0.03			
H130-35-16										<0.02			
H110-15-11										<0.03			
H110-15-12										<0.02			
H110-15-13										<0.02			
H110-15-14										<0.03			
H110-15-15										<0.02			
H120-25-11										<0.02			
H120-25-12										<0.03			
H120-25-13										<0.03			
H120-25-14										<0.03			
H120-25-15										<0.02			

Table A3.3: LA-ICPMS Analyses of Pyrite from SM1001

Sample	Al27	V51	Mn55	Fe57	Co59	Ni60	Cu65	Zn66	As75	Mo95	Ag107	Cd111
SM1001 5-10_1	61.52	21.21	636.59	465500	4.81	1.95	215.83	502.02	261.19	2.66	2.96	2.85
SM1001 5-10_2	1836.00	30.24	28.45	465500	81.38	30.84	747.56	552.46	364.02	2.86	3.68	28.17
SM1001 5-10_3	1968.99	176.26	212.71	465500	34.97	28.51	692.63	4673.79	2264.06	3.17	3.57	21.21
SM1001 15-20_1	1666.75	58.44	4388.69	465500	13.74	9.14	451.60	386.29	266.18	1.59	2.68	7.15
SM1001 15-20_2	8.56	2.20	25.00	465500	20.36	2.32	11.59	51.42	1713.38	3.03	<0.11	1.01
SM1001 15-20_3	156.17	18.11	7.06	465500	18.74	1.07	205.52	93.14	1308.48	1.13	1.60	10.73
SM1001 15-20_4	44.31	17.45	6.70	465500	59.24	3.19	9.13	86.35	1866.86	0.77	<0.16	7.39
SM1001 15-20_5	19.77	0.25	8.64	465500	4.97	0.80	10.31	24.12	1683.08	1.11	<0.12	<0.65
SM1001 15-20_6	20.13	6.60	9.48	465500	25.08	1.86	5.66	48.83	1936.54	3.36	<0.16	2.40
SM1001 25-30_1	1435.72	14.92	18.18	465500	3.71	3.56	177.41	1435.37	3181.20	1.49	4.39	17.13
SM1001 25-30_2	376.61	142.18	214.45	465500	18.99	5.00	640.63	9147.19	3216.81	13.96	1.30	21.69
SM1001 25-30_3	204.66	145.85	1156.45	465500	13.05	2.64	483.21	6454.04	3973.98	6.93	1.23	17.47
SM1001 25-30_4	466.19	18.97	994.52	465500	112.13	7.09	226.75	1292.59	693.18	3.82	0.80	6.04
SM1001 25-30_5	141.24	4.70	153.53	465500	2.28	1.26	137.53	208.57	2421.10	4.70	0.71	1.27
SM1001 25-30_6	151.21	1.73	272.44	465500	15.74	<0.54	23.07	97.60	2539.90	0.47	<0.17	7.62
SM1001 25-30_7	2431.82	24.66	101.21	465500	6.43	1.52	154.45	1214.94	4401.28	2.35	0.29	11.44

Table A3.3: LA-ICPMS Analyses of Pyrite from SM1001

Sample	Te125	Au197	Pb204	Pb206	Pb207	Pb208	Bi209
SM1001 5-10_1	0.41	<0.06	1371.88	1401.78	1363.60	1371.60	1.45
SM1001 5-10_2	<2.96	0.34	1270.10	1378.09	1269.30	1293.38	4.06
SM1001 5-10_3	<2.32	<0.24	10077.84	10316.05	10161.73	10338.36	11.53
SM1001 15-20_1	<1.35	<0.20	775.55	815.26	767.88	778.12	2.17
SM1001 15-20_2	<1.21	<0.29	60.10	62.02	60.09	60.67	0.10
SM1001 15-20_3	<2.64	<0.23	260.06	250.10	252.80	245.96	<0.17
SM1001 15-20_4	<1.44	<0.18	66.25	57.15	54.86	53.72	0.12
SM1001 15-20_5	<1.42	<0.17	9.19	1.51	1.17	1.09	<0.10
SM1001 15-20_6	<1.13	<0.15	21.49	16.59	15.44	18.67	<0.10
SM1001 25-30_1	<0.14	0.04	775.99	815.74	765.49	771.66	0.44
SM1001 25-30_2	<0.90	<0.10	7217.98	7291.32	7079.68	7185.58	0.93
SM1001 25-30_3	1.57	<0.05	5428.96	5600.55	5496.38	5506.35	0.19
SM1001 25-30_4	<0.37	<0.05	1227.55	1256.32	1212.38	1232.73	0.55
SM1001 25-30_5	<0.30	<0.04	239.60	245.84	237.97	238.48	0.22
SM1001 25-30_6	<1.99	<0.18	60.16	66.98	65.55	63.55	<0.15
SM1001 25-30_7	0.67	<0.03	2332.25	2408.40	2290.24	2346.96	2.38

Table A3.3: LA-ICPMS Analyses of Pyrite from SM1001												
Sample	Al27	V51	Mn55	Fe57	Co59	Ni60	Cu65	Zn66	As75	Mo95	Ag107	Cd111
SM1001 40-45_1	181.77	1.69	352.16	465500	6.96	0.68	13.75	337.56	605.32	0.41	0.36	5.45
SM1001 40-45_1	181.77	1.69	352.16	465500	6.96	0.68	13.75	337.56	605.32	0.41	0.36	5.45
SM1001 40-45_2	155.77	41.06	12466.30	465500	31.30	5.09	185.41	2457.25	1794.63	4.31	1.93	13.39
SM1001 40-45_3	8.77	0.30	181.69	465500	0.75	0.98	12.45	166.83	202.01	<0.43	<0.11	0.76
SM1001 40-45_4	16.56	24.78	134.10	465500	6.19	0.66	81.76	1120.70	540.24	<0.25	0.39	2.81
SM1001 40-45_5	55.91	42.71	285.49	465500	10.61	1.70	263.65	1455.21	733.68	<0.37	0.29	5.34
SM1001 40-45_6	341.93	2.40	2796.28	465500	21.36	2.56	101.59	233.02	192.65	1.97	0.21	6.35
SM1001 40-45_7	77.27	9.83	235.27	465500	53.45	0.75	103.83	271.23	2433.16	<0.15	0.10	1.39
SM1001 40-45_8	43.60	12.31	169.20	465500	2.19	0.65	95.83	331.27	215.67	31.00	0.07	1.93
SM1001 60-65_1	118.99	0.73	10584.21	465500	15.62	4.99	26.73	342.21	663.95	2.78	2.95	0.37
SM1001 60-65_2	87.83	4.91	9209.67	465500	68.55	9.40	174.17	322.15	2069.71	2.73	6.27	1.98
SM1001 60-65_3	53.87	1.62	6313.43	465500	36.79	8.37	50.22	287.66	1515.72	2.73	5.98	0.95
SM1001 60-65_4	91.15	8.34	6188.83	465500	57.81	3.03	145.69	643.89	1494.62	1.30	0.60	4.17
SM1001 60-65_5	126.65	13.14	11529.48	465500	13.02	3.15	344.09	1267.73	1074.95	2.66	5.75	3.97
SM1001 60-65_6	1902.57	2.35	21685.65	465500	30.08	9.58	112.66	473.92	1177.04	5.38	8.56	17.76
SM1001 70-75_1	57.75	42.07	2349.84	465500	67.43	48.49	51.15	322.56	3757.95	45.74	25.69	5.03
SM1001 70-75_2	46.96	9.84	537.89	465500	112.69	89.86	15.63	240.23	2044.05	8.38	0.25	3.71

Table A3.3: LA-ICPMS Analyses of Pyrite from SM1001

Sample	Te125	Au197	Pb204	Pb206	Pb207	Pb208	Bi209
SM1001 40-45_1	<0.84	<0.10	94.55	95.96	88.23	91.51	0.09
SM1001 40-45_1	<0.78	0.63	2920.70	3026.31	2914.44	2967.97	1.33
SM1001 40-45_2	<1.37	<0.18	39.10	23.52	17.76	15.96	<0.10
SM1001 40-45_3	<1.57	<0.14	931.70	982.28	941.64	1008.53	0.11
SM1001 40-45_4	<1.30	<0.19	2800.11	2853.88	2750.47	2894.39	2.05
SM1001 40-45_5	<1.49	<0.22	140.32	145.83	135.32	132.36	0.28
SM1001 40-45_6	<0.47	<0.05	545.17	558.25	534.94	541.14	1.55
SM1001 40-45_7	0.12	<0.01	732.28	755.00	724.20	741.12	0.33
SM1001 40-45_8	0.43	1.32	9.36	7.57	7.28	7.71	<0.04
SM1001 60-65_1	0.88	0.44	379.75	385.95	368.61	374.89	0.16
SM1001 60-65_2	<0.61	0.59	27.97	27.77	28.19	27.84	<0.07
SM1001 60-65_3	<1.30	<0.16	499.31	483.16	462.98	473.21	0.49
SM1001 60-65_4	0.44	1.53	1214.47	1232.34	1195.28	1221.17	0.51
SM1001 60-65_5	<1.11	1.08	83.40	75.22	71.95	72.12	<0.11
SM1001 60-65_6	2.34	0.43	51.58	46.32	48.01	48.56	<0.03
SM1001 70-75_1	0.36	0.03	45.51	45.06	42.18	43.98	0.14

Table A3.3: LA-ICPMS Analyses of Pyrite from SM1001												
Sample	Al27	V51	Mn55	Fe57	Co59	Ni60	Cu65	Zn66	As75	Mo95	Ag107	Cd111
SM1001 70-75_3	40.53	10.78	1990.34	465500	87.48	5.65	66.79	239.57	806.13	8.72	13.39	2.50
SM1001 70-75_4	28.95	9.08	2658.83	465500	2.74	12.45	97.56	338.91	1086.50	33.92	22.71	2.20
SM1001 70-75_5	46.69	10.27	703.26	465500	108.34	29.78	101.25	348.26	1422.75	9.39	43.42	2.66
SM1001 70-75_6	23.96	77.66	4090.96	465500	10.37	28.20	48.40	660.64	2608.30	74.50	93.18	10.44
SM1001 70-75_7	327.13	78.92	1291.64	465500	92.26	57.27	169.71	693.95	7045.02	33.40	87.62	2.87
SM1001 70-75_8	5595.28	591.17	14135.08	465500	211.67	40.85	151.90	923.35	20.39	3.22	1.98	<0.98
SM1001 80-85_1	11.51	202.20	467.66	465500	3.18	2.98	24.51	59.94	571.93	2.75	0.89	1.77
SM1001 80-85_2	6.67	34.72	517.75	465500	2.41	2.48	57.69	79.92	844.52	0.96	0.31	0.18
SM1001 80-85_3	8.26	45.29	864.13	465500	2.08	4.69	44.58	86.46	199.79	13.91	0.80	0.91
SM1001 80-85_4	1.58	0.72	227.73	465500	0.30	1.28	4.20	45.82	1186.80	2.52	0.06	0.25
SM1001 80-85_5	5.75	69.57	53.75	465500	1.46	8.34	19.56	49.15	850.55	5.76	26.68	3.31
SM1001 80-85_6	11.01	77.07	968.10	465500	1.32	5.03	13.92	98.85	452.45	5.96	0.44	6.17
SM1001 80-85_7	13.85	151.94	1779.88	465500	3.05	5.90	26.09	102.28	303.01	5.89	0.84	36.54
SM1001 80-85_8	30.38	67.74	810.73	465500	18.93	14.80	24.24	112.31	976.57	2.09	0.24	3.99
SM1001 90-95_1	62.12	87.62	1280.51	465500	1.61	5.83	20.88	121.51	108.12	3.67	0.39	2.12
SM1001 90-95_2	217.81	47.51	1949.34	465500	5.73	12.11	38.80	89.42	73.90	3.69	45.22	4.79
SM1001 70-75_3	40.53	10.78	1990.34	465500	87.48	5.65	66.79	239.57	806.13	8.72	13.39	2.50

Table A3.3: LA-ICPMS Analyses of Pyrite from SM1001

Sample	Te125	Au197	Pb204	Pb206	Pb207	Pb208	Bi209
SM1001 70-75_3	0.66	0.17	665.72	637.15	647.38	666.49	0.15
SM1001 70-75_4	1.36	0.21	702.82	649.12	668.56	651.90	0.12
SM1001 70-75_5	0.52	0.11	240.94	232.54	238.40	239.73	<0.03
SM1001 70-75_6	4.81	0.58	29.20	29.05	28.84	28.36	<0.03
SM1001 70-75_7	2.12	0.37	1361.32	1290.08	1307.37	1298.89	0.07
SM1001 70-75_8	<1.64	<0.20	168.32	160.84	165.93	164.88	0.25
SM1001 80-85_1	1.61	0.06	16.12	14.41	13.66	13.81	0.04
SM1001 80-85_2	0.48	<0.044	68.79	69.59	63.85	66.68	0.07
SM1001 80-85_3	1.48	<0.054	119.88	125.97	116.37	121.50	0.24
SM1001 80-85_4	<0.34	<0.05	2.22	1.47	1.36	1.40	<0.03
SM1001 80-85_5	1.65	0.06	35.29	35.73	32.85	34.72	0.05
SM1001 80-85_6	1.55	<0.11	69.06	67.08	57.55	61.15	0.09
SM1001 80-85_7	2.52	0.13	57.91	55.84	51.58	52.77	0.11
SM1001 80-85_8	<1.71	0.27	54.94	57.75	57.51	54.00	<0.13
SM1001 90-95_1	<0.40	0.04	18.67	19.59	18.20	18.96	0.03
SM1001 90-95_2	0.63	0.23	30.87	30.87	28.19	29.57	0.06

Table A3.3: LA-ICPMS Analyses of Pyrite from SM1001												
Sample	Al27	V51	Mn55	Fe57	Co59	Ni60	Cu65	Zn66	As75	Mo95	Ag107	Cd111
SM1001 90-95_3	13.40	65.32	3083.49	465500	0.74	9.35	194.49	113.30	132.36	7.56	0.20	8.82
SM1001 90-95_4	4.31	45.91	745.90	465500	1.26	2.20	10.65	56.94	119.48	1.44	0.09	2.42
SM1001 90-95_5	451.95	10.28	7.47	465500	35.68	27.86	27.03	33.91	644.85	1.25	0.15	4.65
SM1001 90-95_6	17.36	42.59	1021.15	465500	1.46	4.37	75.48	105.48	107.88	2.70	0.24	2.72

Table A3.3: LA-ICPMS Analyses of Pyrite from SM1001

Sample	Te125	Au197	Pb204	Pb206	Pb207	Pb208	Bi209
SM1001 90-95_3	<1.00	0.22	44.80	40.68	36.65	38.25	<0.06
SM1001 90-95_4	<0.37	<0.04	6.16	5.87	5.95	5.76	0.03
SM1001 90-95_5	<0.80	<0.08	37.61	40.03	37.05	36.45	0.23
SM1001 90-95_6	<0.62	<0.07	30.53	31.88	29.25	29.74	<0.03

Table A3.4: Gold Analyses of SM1001 by Neutron Activation Analysis

Sample	Au (ppm)
SM1001-5-10	0.077
SM1001-15-20	0.074
SM1001-25-30	0.086
SM1001-35-40	0.181
SM1001-45-50	0.149
SM1001-50-55	0.248
SM1001-60-65	0.120
SM1001-70-75	0.020
SM1001-80-85	0.005*
SM1001-90-95	0.003*
Uncertainty = +/-5% * Uncertainty = +/-10%	

Table A3.5: Gold Analyses of H1 by Neutron Activation Analysis

Sample	Au (ppm)
H1-10-15	<0.0026
H1-20-25	<0.0076
H1-30-35	<0.0042
H1-40-45	<0.0036
H1-50-55	<0.0035
H1-60-65	<0.0034
Uncertainty = +/-5%	

Appendix 4:

Sample location, sedimentary unit and description for samples used Chapter 4

Table A4.1: Sample location, sedimentary unit and description for samples used Chapter 4

Sample No.	Member, Formation or Group	Location	Age (Ma)	Analyses	Description
CB5_1	Unconsolidated sediment, Cariaco Basin	Cariaco Basin, Venezuela	0.1	AP13A007-AP13A026	unconsolidated black organic-rich sediment with 3% framboidal pyrite
CB7_1	Unconsolidated sediment, Cariaco Basin	Cariaco Basin, Venezuela	0.1	AP13A091-AP13A105	unconsolidated black organic-rich sediment with 3% framboidal pyrite
CB8_1	Unconsolidated sediment, Cariaco Basin	Cariaco Basin, Venezuela	0.1	AP13A036-AP13A041; AP13A043-AP13A049	unconsolidated black organic-rich sediment with 3% framboidal pyrite
CR-1A	Muderong Shale, Winning Group	Canarvon Basin, WA, Australia	125	JL31D07; JL31D10; JL31D12; JL31D14-JL31D16; JL31D18-JL31D26; JL31D28-JL31D30	black/grey carbonaceous mudstone; <1% pyrite
TM-12-21-A	J3, Oxford	Volga River, Kazan, Russia	169	MY09A066-MY09A078	pyritised belemnite
TM-12-25	J3, Oxford	Volga River, Kazan, Russia	169	MA22A044-MA22A053; MA22A055-MA22A063	pyritised belemnite
DO-PS-25	Posidonia	Dotternhausen, Germany	180	MA21B007-MA21B011; MA21B015-MA21B020; MA21B023-MA21B031	black shale with 6% pyrite
PM-BS-280	Jet Rock, Whitby Mudstone	Yorkshire, UK	180	MA21B142; MA21B147; MA21B149; MA21B152-MA21B158; MA21B161; MA21B164-MA21B165; MY21A033-MY21A047	Black carbonaceous shale with minor 0.5 mm x 3 mm pyrite blebs
KURE-10-27	Shales over lying Kure VHMS deposits	Kure, Turkey	190	MA22A007-MA22A009; MA22A011-MA22A017; MA22A020-MA22A029	5mm pyrite nodules in black shale

Sample No.	Member, Formation or Group	Location	Age (Ma)	Analyses	Description
WI-2C	Woody Island Siltstone, Lower Parmeener Group	Woody Island, Tas, Australia	297	MA08A164-MA08A174	black pyritic siltstone with 2-10cm nodules of pyrite
WI-2R	Woody Island Siltstone, Lower Parmeener Group	Woody Island, Tas, Australia	297	MA08A146-MA08A156	black pyritic siltstone with 2-10cm nodules of pyrite
RMC JB 13A	Linton Formation, Huchpuckney	Missouri, USA	305	JL18B008-JL18B009; JL18B013; JL18B017-JL18B022; JL18B024; JL18B026-JL18B028	laminated organic-rich black shale; pyrite <1%
RMC (MECCA) G9	Linton Formation, Mecca Quarry Shale	Kentucky, USA	310	JL05A009-JL05A010; JL05A012-JL05A013; JL05A022-JL05A023; JL05A061; JL05A065-JL05A066; JL05A071	laminated organic-rich black shale; pyrite <1%
RMC JB	Linton Formation, Anna Shale	Illinois, USA	310	JL05A095-JL05A098; JL05A101-JL05A102; JL05A104-JL05A105; JL05A108; JL05A111-JL05A112; JL05A114; JL05A116-JL05A117; JL05A121	laminated organic-rich black shale; pyrite <1%
YuI 12006	Yulleroo Formation, Canning Basin	Canning Basin, WA, Australia	355	JN19A030-JN19A045; JN19A047-JN19A052; JN19A056-JN19A057	Laminated black mudstone with very fine disseminated pyrite (1-2%)
YuI 12009	Yulleroo Formation, Canning Basin	Canning Basin, WA, Australia	355	JN19A067-JN19A069; JN19A071-JN19A072; JN19A074-JN19A080; JN19A082-JN19A088; JN19A090-JN19A092; JN19A095-JN19A100	Laminated black mudstone with very fine disseminated pyrite (1-2%)
YuI-12005	Yulleroo Formation, Canning Basin	Canning Basin, WA, Australia	355	MY24A008-MY24A016; MY24A018-MY24A020; MY24A023-MY24A027; MY24A029-MY24A030; MY24A033-MY24A034	Laminated black mudstone with very fine disseminated pyrite (1-2%)
P4-6	Upper D unit, Brigadier Formation	NW Shelf, WA, Australia	202	MA28A165-MA28A179	black to dark grey shale with 1-2% pyrite

Sample No.	Member, Formation or Group	Location	Age (Ma)	Analyses	Description
Yul 12587	Yulleroo Formation, Canning Basin	Canning Basin, WA, Australia	359	JN18A047-JN18A054; JN18A057-JN18A061; JN18A063	thinly bedded dark grey mudstone with very fine disseminated pyrite (1-2%)
Yul-12590	Yulleroo Formation, Canning Basin	Canning Basin, WA, Australia	359	MY24B007-MY24B018; MY24B020-MY24B024	thinly bedded dark grey mudstone with very fine disseminated pyrite (1-2%)
Yul 12660	Yulleroo Formation, Canning Basin	Yullerool	360	JL31D75-JL31D76; JL31D79; JL31D81; JL31D83-JL31D84; JL31D87-JL31D88	dark grey mudstone with 1-2% framboidal pyrite
Yul 14382	Clanmeyer Formation, Canning Basin	Yullerool	365	JL31D91-JL31D94; JL31D96-JL31D97; JL31D106; JL31D108; JL31D110-JL31D113	Laminated black mudstone with very fine disseminated pyrite (1-2%)
Yul-13309	Clanmeyer Formation, Canning Basin	Canning Basin, WA, Australia	365	MY24B032-MY24B034; MY24B036; MY24B038; MY24B040-MY24B041; MY24B046-MY24B048; MY24B050-MY24B051	Laminated black mudstone with very fine disseminated pyrite (1-2%)
SUB-2	Orlovsky Horizon	SW Urals, Russia	367	AP17A013-AP17A015; AP17A017-AP17A023; AP17A026-AP17A029; AP17A032-AP17A033	black shale and sandstone with pyrite nodule
SUB-3	Orlovsky Horizon	SW Urals, Russia	367	MY09A081-MY09A093	black shale and sandstone with pyrite nodule
Yul 14733	Clanmeyer Formation, Canning Basin	Canning Basin, WA, Australia	370	MY28A023-MY28A025; MY28A036; MY28A039; MY28A041; MY28A048-MY28A052; MY28A056-MY28A058	black mudstone with coral fragments and fine-grained pyrite
Yul 14738	Clanmeyer Formation, Canning Basin	Yullerool	370	JL31D115-JL31D119; JL31D121-JL31D123; JL31D127	black mudstone with coral fragments and fine-grained pyrite

Sample No.	Member, Formation or Group	Location	Age (Ma)	Analyses	Description
ED20 102.4	Gogo Formation, Canning Basin	Canning Basin, WA, Australia	383	JN18A007-JN18A030	Laminated grey-brown calcareous siltstone with very fine disseminated pyrite (1-2%)
ED20 129.9	Gogo Formation, Canning Basin	Canning Basin, WA, Australia	383	MY28A007; MY28A011-MY28A013; MY28A015-MY28A017; MY28A019	Laminated grey-brown calcareous siltstone with very fine disseminated pyrite (1-2%)
ED20 186.2	Gogo Formation, Canning Basin	Canning Basin, WA, Australia	384	JN12A009; JN12A014; JN12A017-JN12A019; JN12A021-JN12A025; JN12A035-JN12A040; JN12A042-JN12A046	Laminated grey-brown calcareous siltstone with very fine disseminated pyrite (1-2%)
RI07-38.3A_01	Canol Formation	Yukon, Canada	384	JL30A085-JL30A098; JL30A101-JL30A105; JL30A108; JL30A111	black shale with minor thin calcareous laminations
RI07-50.7B_01	Canol Formation	Yukon, Canada	384	JL30A147-JL30A149; JL30A152-JL30A165	black shale with minor thin calcareous laminations
RI07-63.4B_01	Canol Formation	Yukon, Canada	385	JL30A119-JL30A124; JL30A128-JL30A138	black shale with very fine pyrite
RI07-78.1A_01	Canol Formation	Yukon, Canada	385	JL30A181-JL30A187; JL30A191-JL30A199	black shale with very fine pyrite
RI07-91mA	Canol Formation	Yukon, Canada	386	JL30A274-JL30A276; JL30A281-JL30A287; JL30A292-JL30A293	black organic-rich mudstone and siltstone wth very fine grained disseminated pyrite (~6%)
RI07-102.4A_01	Canol Formation	Yukon, Canada	386.5	JL30A210-JL30A216; JL30A220-JL30A227	black shale with bedding parallel pyrite framboids

Sample No.	Member, Formation or Group	Location	Age (Ma)	Analyses	Description
RI07-114.8A_02	Canol Formation	Yukon, Canada	386.5	JL30A301-JL30A307; JL30A311-JL30A320; JL30A323-JL30A324	black shale with bedding parallel pyrite framboids
R107-147.2A_011	Canol Formation	Yukon, Canada	387	AU03A098-AU03A104; AU03A108-AU03A121	black shale with bedding parallel pyrite framboids
RI07-127.6A_01	Canol Formation	Yukon, Canada	387	JL30A236-JL30A243; JL30A247-JL30A250; JL30A252-JL30A253	black shale with bedding parallel pyrite framboids
RI07-140A_01	Canol Formation	Yukon, Canada	387	JL30A325-JL30A330; JL30A332	black shale with bedding parallel pyrite framboids
R107-166.5A_001	Road River Group	Yukon, Canada	388	AU03A131-AU03A146	black shale with pyrite nodules and framboids
R107-170.5A_001	Road River Group	Yukon, Canada	388	AU03A157-AU03A167	black shale with pyrite nodules and framboids
Saf-10-21'	Safyanovka Horizon	Central Urals	388	MA23A007-MA23A009; MA23A012-MA23A018; MA23A021-MA23A022	black shale with pyrite nodule
157348	Benjamin Limestone, Gordon Group	Florentine Valley, Tas, Australia	450	FE23A082-FE23A083; FE23A091; FE23A095; FE23A097-FE23A100; FE23A108-FE23A111	black limestone with very fine trace framboidal pyrite
AS-4-8/2/31C	Alum Shale	Kallsedet, Western Sweden	490	MY03A082-MY03A098; MY03A107-MY03A117	foliated, deformed pyritic black shale with white quartz bands (2-7% pyrite)

Sample No.	Member, Formation or Group	Location	Age (Ma)	Analyses	Description
79989	Que River Shale, Mt Charter Group	Bulgobac River, Tas, Australia	505	FE10B007; FE10B010; FE10B016-FE10B022	black shale with 1cm pyrite nodule and trace fine framboids
79990	Que River Shale, Mt Charter Group	Bulgobac River, Tas, Australia	505	FE10A034-FE10A038	black shale with 3cm pyrite nodule
157414	Salmon River Siltsone, Togari Group	Arthur River, Tas, Australia	540	MA26A031-MA26A046	chocolate brown to dark grey, thin-bedded siltstone; rare horizons of pyrite microcrystals with porous cores (1-2%)
HN-15	Miaohe Member, Doushantou Formation	Guizhou Province, China	550	MA21B075-MA21B076; MA21B080-MA21B086; MA21B088-MA21B090; MA21B094-MA21B098	fossiliferous shale with 3% fine anhedral pyrite
FOREST-1@287.2m	Lower Keppel Creek, Togari Group	Smithton, Tas, Australia	630	JL24A007; JL24A010-JL24A023;	laminated black shale with ~5% framboidal pyrite
FOREST-1@321.3m	Lower Keppel Creek, Togari Group	Smithton, Tas, Australia	630	JL24A031-JL24A038; JL24A040-JL24A047	laminated black shale with ~5% framboidal pyrite
WALLARA-1@1173m	Aralka Formation	Armadeus Basin, NT, Australia	630	JL24A088-JL24A092; JL24A095-JL24A098; JL24A100-JL24A101; JL24A103	laminated black shale with ~2% framboidal pyrite
FOREST-1@828.5m	Black River Dolomite, Togari Group	Smithton, Tas, Australia	640	JL24A055-JL24A059; JL24A061-JL24A065; JL24A067-JL24A070; JL24A072-JL24A075	laminated black shale with ~2% framboidal pyrite
WALLARA-1@1305.1m	Aralka Formation	Armadeus Basin, NT, Australia	657	JL24A111-JL24A122; JL24A130-JL24A137; JL24A139-JL24A143	laminated black shale with ~2% framboidal pyrite

Sample No.	Member, Formation or Group	Location	Age (Ma)	Analyses	Description
WarYen 9/3_3-4	Broadhurst (upper) Formation, Throssell Group	Yeneena Basin, WA, Australia	860	MY09A008-MY09A017	grey to black shale with disseminated pyrite (~10% pyrite)
WarYen_16/3_15	Broadhurst (upper) Formation, Throssell Group	Yeneena Basin, WA, Australia	860	MY09A048-MY09A050; MY09A053; MY09A055; MY09A058	black shale with bedded disseminated pyrite (3-5% pyrite)
MD1	Meidang Formation, Kunyang Group	SE Yunnan, China	980	MA08A013-MA08A027; MA08A035-MA08A048	Black calcareous mudstone with bedding parallel disseminated pyrite (10-12%)
MD2	Meidang Formation, Kunyang Group	SE Yunnan, China	980	MA08A056-MA08A069; MA08A077-MA08A086	black shale with bedded disseminated pyrite (~3%)
157395	Cowrie Siltstone, Rocky Cape Group	Arthur River, Tas, Australia	1290	FE23A133; FE23A135-FE23A136; FE23A138-FE23A139; FE23A141-FE23A147; FE23A149	weakly bedded dark grey shale/siltstone with 1-2% framboidal pyrite
157402	Cowrie Siltstone, Rocky Cape Group	Irishtown, Tas, Australia	1290	MA26A054; MA26A056-MA26A057; MA26A060-MA26A061; MA26A063; MA26A076-MA26A078; MA26A082; MA26A084; MA26A087	bedded dark grey shale/siltstone with trace framboidal/euhedral microcystals of pyrite
DUCK BAY-1@244m	Cowrie Siltstone, Rocky Cape Group	Smithton, Tas, Australia	1290	MA07A032-MA07A033; MA07A035	bedded dark grey shale/siltstone with <1cm pyrite noldule and pyritic layers
V3-65.1	Valkykerri Formation, Roper River	McArthur Basin, NT, Australia	1360	MA08A131-MA08A144	pyrite nodule in carbonaceous shale
KRUP-2-07-7-4	Satka Formation, Burzyun Group	Satka, South Urals, Russia	1550	AP17A066-AP17A081; AP17A083-AP17A088; MA23A388-MA23A393; MA23A395-MA23A396	pyrite nodules in dolomitic black shale

Sample No.	Member, Formation or Group	Location	Age (Ma)	Analyses	Description
BMR2-261'10"	Barney Creek Formation	McArthur Basin, NT, Australia	1640	MA26A097-MA26A112	black dolomitic siltstone with <2% pyrite
BEN1078@224.1m		Curnamona, NSW, Australia	1690	MY07A081-MY07A091; MY07A093-MY07A097	Black carbonaceous shale with minor 1 mm x 3 mm pyrite blebs
MUL221@226.6m(A)		Curnamona, NSW, Australia	1690	MY07A029-MY07A036; MY07A038-MY07A044; MY07A061-MY07A067	Black carbonaceous shale with minor 5 mm x 15 mm zoned pyrite nodules.
437-166.9m	Upper Callie Member, Dead Bullock Formation, Tanami Group	Tanami, NT, Australia	1840	MY28A177; MY28A179-MY28A180; MY28A183-MY28A184	dark grey/black shale with ~1% very fine framboidal pyrite
437-178.56m	Upper Callie Member, Dead Bullock Formation, Tanami Group	Tanami, NT, Australia	1840	MY28A124-MY28A138	laminated black shale with ~5% framboids/porous nodules
437-197.7m	Upper Callie Member, Dead Bullock Formation, Tanami Group	Tanami, NT, Australia	1840	MY28A109-MY28A110; MY28A113-MY28A115	laminated black shale with ~5% very fine framboid-rich horizons and <5mm porous nodules
IIC-2011-1a	IV sedimentary unit, PR1 Oroziriy Zhdanovskaya suite	Pechenga, Russia	2000	AP27A015-AP27A021	crystalline nodules in black shale
IIC-2011-1b	IV sedimentary unit, PR1 Oroziriy Zhdanovskaya suite	Pechenga, Russia	2000	MA26A013; MA26A015; MA26A021; MA26A023	crystalline nodules in black shale
M-1-13'	PR1, Oroziriy Zhdanovskaya suite	Pechenga, Russia	2000	MA23A219; MA23A227; MA23A231; MA23A233	crystalline nodules in black shale

Sample No.	Member, Formation or Group	Location	Age (Ma)	Analyses	Description
TDH01-162.7-162.8	Johnson Cairn Formation, Yerrida Group	N Yilgarn, WA, Australia	2170	AU010010-AU010016; AU010020-AU010029	laminated black shale with layers of bedded pyrite (~5% pyrite)
ADBP9-132.77	Mount Bruce Suppergroup, Hamersley Group, Mount McRae Shale	Hammersly Basin, WA, Australia	2504	MA26A007-MA26A017; MA26A020-MA26A022; MA26A026-MA26A032	Medium grey turbidites as before with 3-5 mm spherical blebs, erratic. Broad (1-3 cm) bands of ~50% fine pyrite siltstone mix.~10% total pyrite: 5% in diffuse bands; 4% in pyrite nodules and 1% in coarse bands.
ADBP9-169.07	Mount Bruce Suppergroup, Hamersley Group, Mount McRae Shale	Hammersly Basin, WA, Australia	2504	MA26A070-MA26A077; MA26A081-MA26A091	Interbands of medium grey fine grained siltstone (50%) with 15-20% fine grained pyrite and medium to light grey bands of fine calcareous sandstone finely interbedded with black siltstone.
ADBP9-186.42	Mount Bruce Suppergroup, Hamersley Group, Mount McRae Shale	Hammersly Basin, WA, Australia	2504	MA26A106-MA26A112; MA26A115-MA26A121	Interbeds of (50%) fine grained black pyritic siltstone and (50%) medium grey fine grained sandstone, ~3% thin pyrite bands with lesser fine grained pyrite
GKF-442.48	Transval supergroup, Upper Nauga Formation, N2	Kaapvaal Craton, South Africa	2521	MA21B112; MA21B116; MA21B119-MA21B120; MA21B122; MA21B124-MA21B125; MA21B128; MA21B130-MA21B134	2.4% pyrite - laminated black to dark grey shale
ADBP9-214.87	Mount Bruce Suppergroup, Hamersley Group, Mt Sylvia Formation	Hammersly Basin, WA, Australia	2530	MA26A137-MA26A140; MA26A144-MA26A145; MA26A151; MA26A153-MA26A158	Banded iron formation with ~5% pyrite beds and blebs most common in magnetite rich intervals.
ABDP9-268.93-269.08	Mount Bruce Suppergroup, Hamersley Group, Bee Gorge Member	Hammersly Basin, WA, Australia	2561	FE27A007-FE27A019; FE27A032-FE27A041; FE27A043-FE27A050	Interbeds of (50%) fine grained black pyritic siltstone and (50%) medium grey fine grained sandstone. Beds generally 3-5 cm wide but occasionally much thicker. ~10% pyrite in elongated pyrite nodules.
ADBP9-292.74	Mount Bruce Suppergroup, Hamersley Group, Bee Gorge Member	Hammersly Basin, WA, Australia	2561	MA26A204-MA26A213; MA26A217-MA26A226	black shale, 50% silicified, with pyrite bands associated with silicified zones, ~3% pyrite blebs with minor fine grained pyrite
ADBP9-366.61-366.67	Mount Bruce Suppergroup, Hamersley Group, Bee Gorge Member	Hammersly Basin, WA, Australia	2561	FE27A122-FE27A130; FE27A132-FE27A136	interbedded (65%) medium to light grey fine sandstone and (35%) carbonaceous black shale. <1% pyrite predominantly in rare nodules

Sample No.	Member, Formation or Group	Location	Age (Ma)	Analyses	Description
GKF01-637.72	Transval supergroup, Upper Nauga Formation, N2	Kaapvaal Craton, South Africa	2563	MA21B044; MA21B047; MA21B049; MA21B056-MA21B058; MA21B061-MA21B064; MA21B066-MA21B067	2.4% pyrite - laminated black to dark grey shale
ADBP9-398.30-398.47	Mount Bruce Suppergroup, Hamersley Group, Paraburdoo Member	Hammersly Basin, WA, Australia	2575	FE27A064-FE27A069; FE27A070-FE27A076	interbedded (65%) medium to light grey fine sandstone and (35%) carbonaceous black shale. <1% pyrite predominantly in blebs and beds associated with carbonaceous layers
ADBP9-438.5-438.71	Mount Bruce Suppergroup, Hamersley Group, Paraburdoo Member	Hammersly Basin, WA, Australia	2575	FE27A159-FE27A166; FE27A174-FE27A190	Medium to dark grey turbidites, anhedral pyrite band 2 mm thick (~5% pyrite)
LBRC022D-1	Black Flag Group	Kalgoolie, WA, Australia	2680	AP27A035-AP27A049	dark grey/black shale with ~1-2 % disseminated pyrite and 1 large pyrite nodule; weakly bedded
LBRC019D-2	Black Flag Group	Kalgoolie, WA, Australia	2680	AP27A079-AP27A086	dark grey/black shale, thin bedded, contains disseminated pyrite, a zone of nodules (~cm-thick) and folded quartz-pyrite layers (0.5-1 cm) (total pyrite ~30%)
LBRC022D-16	Black Flag Group	Kalgoolie, WA, Australia	2680	AP27A057-AP27A071	dark grey/black shale with ~3 % disseminated pyrite and 1 large pyrite nodule; thin silt interbeds
PDP2C2	Warrawoona	Pilbara WA	3470	JL23A053-JL23A056; JL23A060-JL23A063; JL23A067-JL23A080	laminated black pyritic chert
ABD8-7	Conical Formation	Pilbara, WA, Australia	3515	MY02A090-MY02A097	laminated black pyritic chert
RB2-1	Kockatea Shale	Perth Basin, WA, Australia	252	JN28a007; JN28a010; JN28a012; JN28a020-JN28a021; JN28a023; JN28a071-JN28a073; JN28a077-JN28a083	Fine grained black shale with ~10% 0.5 x 1 cm pyrite nodules

Sample No.	Member, Formation or Group	Location	Age (Ma)	Analyses	Description
RB2-2	Kockatea Shale	Perth Basin, WA, Australia	252	MA28A114-MA28A131	Fine grained black shale with ~10% 0.8 x 1.5 cm pyrite nodules
RB2-3A	Kockatea Shale	Perth Basin, WA, Australia	252	MA28A099-MA28A111	Fine grained black shale with minor diffuse microscopic pyrite
AS-3-8/2/15	Alum Shale	Kallsedet, Western Sweden	490	MY03A048-MY03A058; MY03A067-MY03A079	Fine grained very carbonaceous black shale with ~5% 2 mm x 4 mm pyrite blebs and ~5% milky quartz blebs.

Appendix 5:

Selection of intervals for data reduction

Most pyrite analyses are similar to Figures A5.1 and A5.2. They have relatively levelled elemental counts across the pyrite. In each case, an interval is selected for the background signal (blue section) and the unknown signal (pink section). Some analyses have obvious large inclusions. When these are present the interval for data reduction is shortened to avoid the inclusions as in Figure A5.3. However, sometimes it is not clear whether peaks and/or changes in counts of an element are due to inclusions or elemental zoning in the pyrite. When this cannot be determined multiple reductions are made on the same analysis and the results are used to determine the most appropriate interval to use, or if zoning is evident, both pyrite types are used. Examples of this case are shown in Figures A5.4, A5.5 and A5.6.

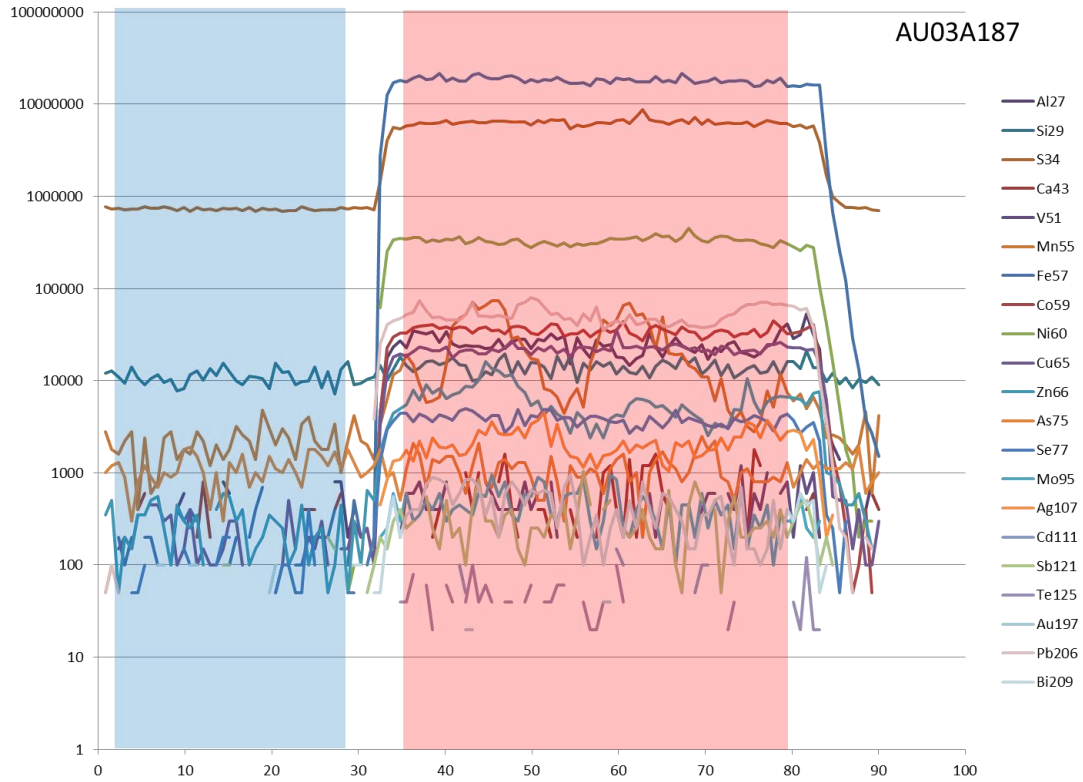

Figure A5.1: Average pyrite analysis. Blue represents the signal of the background and pink represents signal of the sample used in the data reduction.

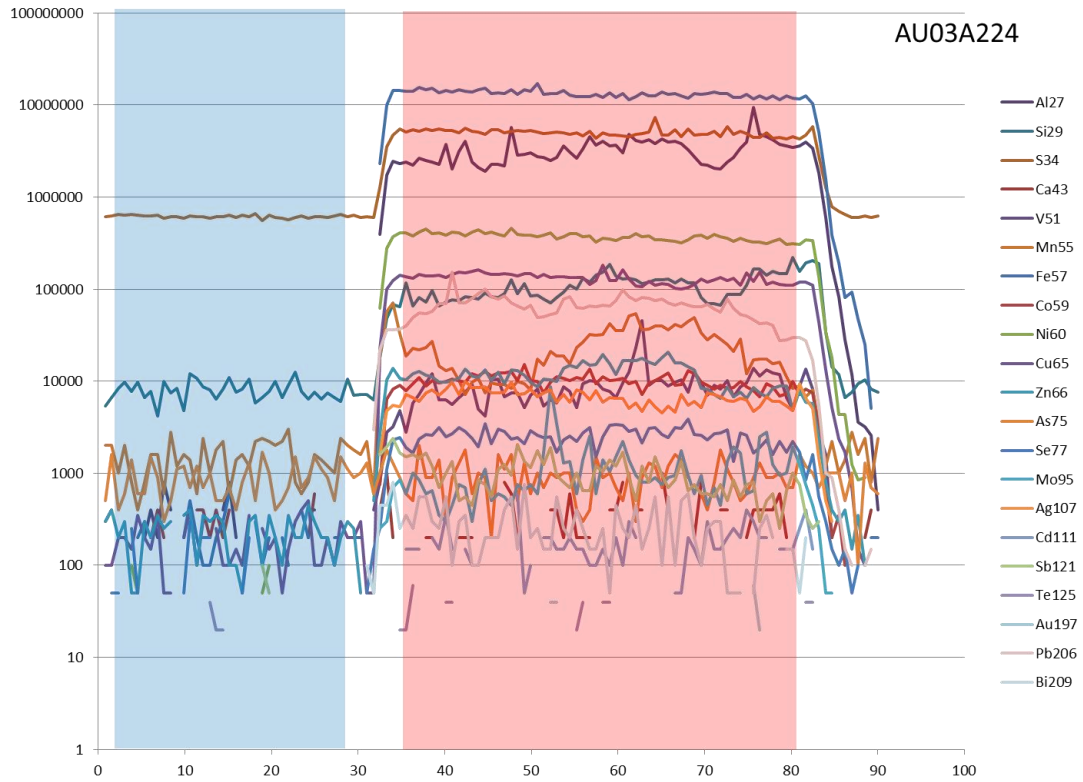

Figure A5.2: Average pyrite analysis. Blue represents the signal of the background and pink represents signal of the sample used in the data reduction.

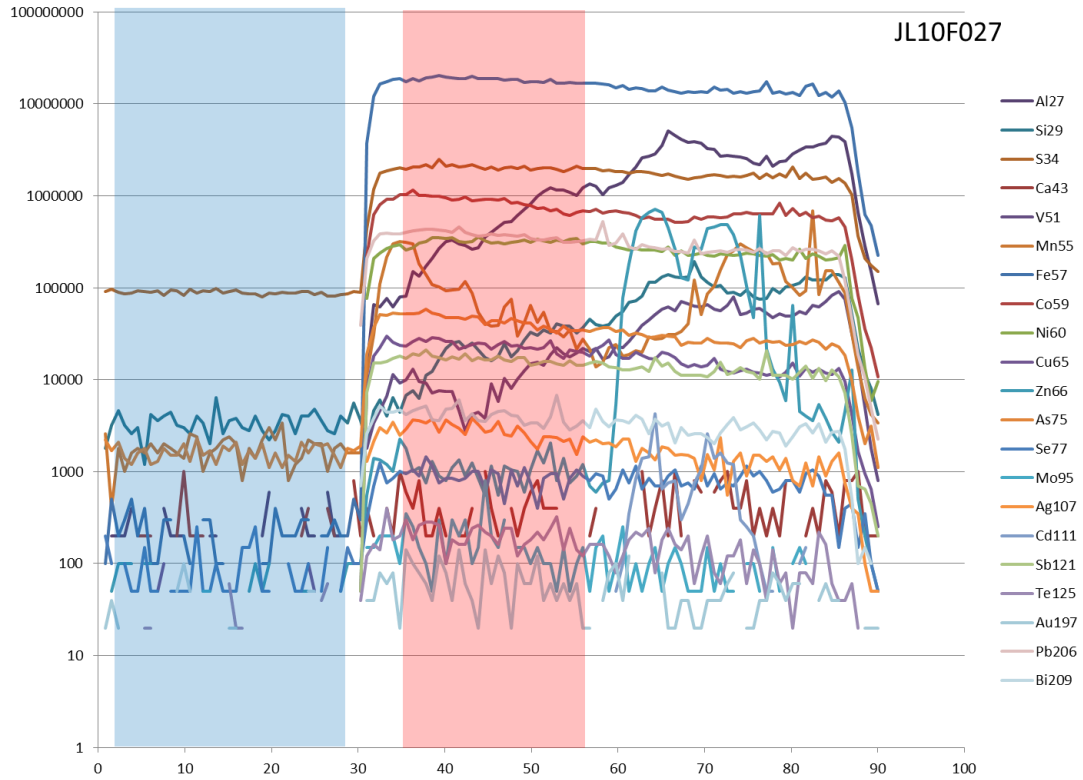

Figure A5.3: Pyrite with micro-inclusions analysis. High Zn inclusions are avoided by not using the entire unknown interval. Blue represents the signal of the background signal and pink represents the signal of the sample used in the data reduction.

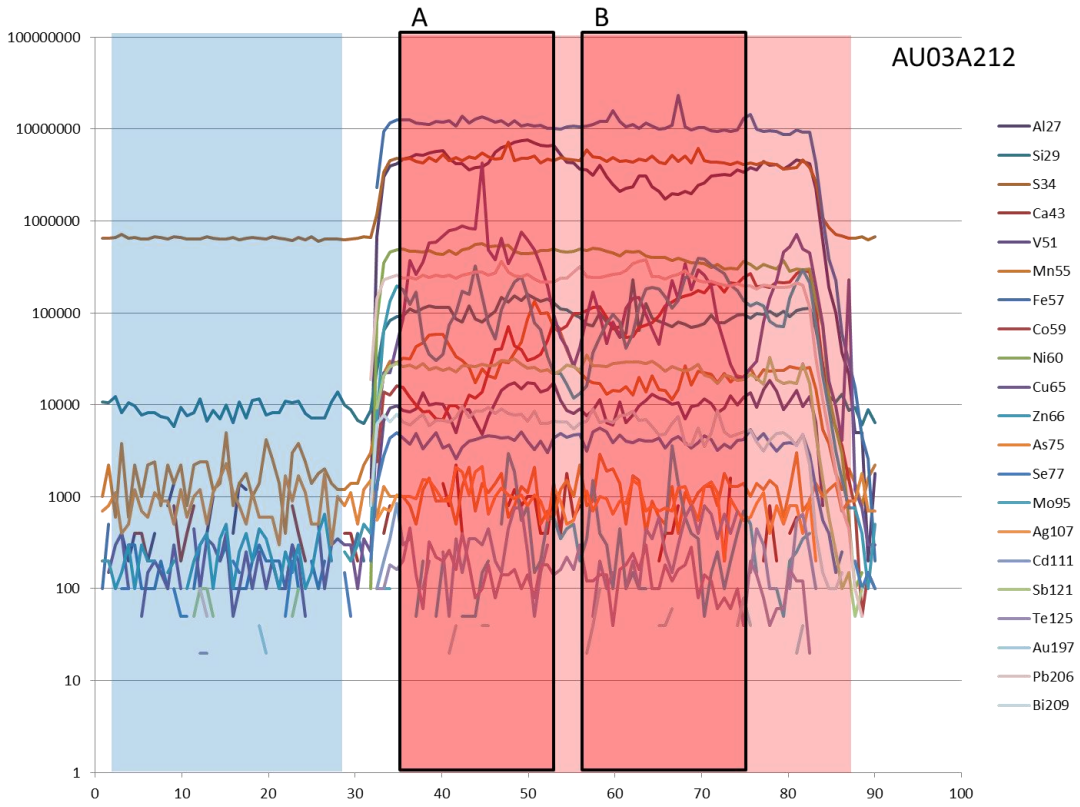

Figure A5.4: Zoned pyrite or pyrite with micro-inclusions analysis. Alternative intervals are also reduced separately to determine if differences in Cu are due to micro-inclusions or zoning in the pyrite. Blue represents the signal of the background and pink represents signal of the unknown used in the data reduction.

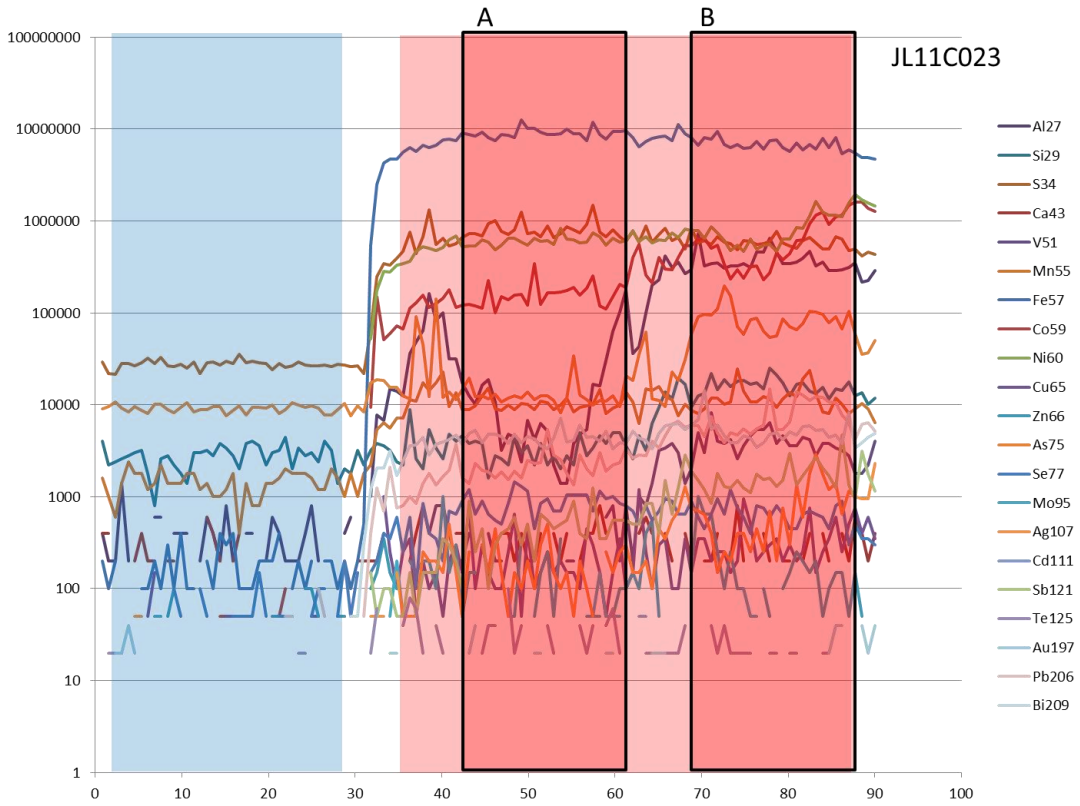

Figure A5.5: Zoned pyrite or pyrite with micro-inclusions analysis. Alternative intervals are also reduced separately to determine if differences in Cu are due to micro-inclusions or zoning in the pyrite. Blue represents the signal of the background and pink represents the signal of the unknown used in the data reduction.

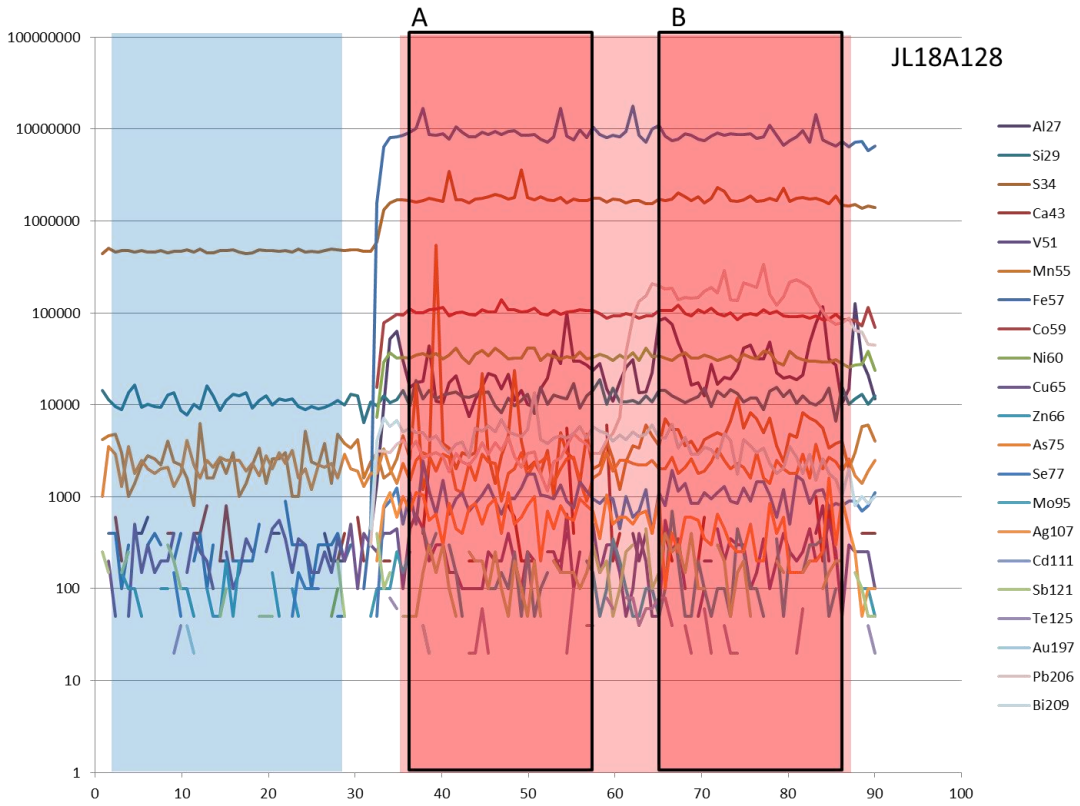

Figure A5.6: Zoned pyrite or pyrite with micro-inclusions analysis. Alternative intervals are also reduced separately to determine if differences in Pb are due to micro-inclusions or zoning in the pyrite. Blue represents the signal of the background and pink represents the signal of the unknown used in the data reduction.

Appendix 6:

Geochemical Data presented in Chapter 4

Table A6.1: LA-ICPMS Analyses of Pyrite from Chapter 4

File	Analyst	Age (Ma)	Pyrite type	Setting	Mn (ppm)	Fe (ppm)	Co (ppm)	Ni (ppm)	Cu (ppm)	Zn(ppm)
AP13A037	D Gregory	0.1	framboid	Restricted Basin	1867.41	465500.00	265.83	515.93	589.82	540.45
AP13A044	D Gregory	0.1	framboid	Restricted Basin	1406.41	465500.00	132.22	247.07	357.70	548.71
AP13A017	D Gregory	0.1	framboid	Restricted Basin	1963.66	465500.00	39.17	142.83	76.80	982.26
AP13A038	D Gregory	0.1	framboid	Restricted Basin	2075.97	465500.00	35.01	169.12	98.18	1066.34
AP13A011	D Gregory	0.1	framboid	Restricted Basin	707.75	465500.00	96.08	433.43	265.67	295.22
AP13A099	D Gregory	0.1	framboid	Restricted Basin	2975.28	465500.00	263.15	672.59	643.43	469.99
AP13A023	D Gregory	0.1	framboid	Restricted Basin	2558.00	465500.00	33.83	151.02	427.57	581.92
AP13A039	D Gregory	0.1	framboid	Restricted Basin	3176.61	465500.00	90.52	526.90	408.64	132.17
AP13A049	D Gregory	0.1	framboid	Restricted Basin	1315.10	465500.00	286.06	625.27	396.03	722.92
AP13A026	D Gregory	0.1	framboid	Restricted Basin	720.64	465500.00	125.89	289.42	153.89	453.17
AP13A008	D Gregory	0.1	framboid	Restricted Basin	4119.94	465500.00	58.34	443.66	383.69	780.15
AP13A016	D Gregory	0.1	framboid	Restricted Basin	3687.37	465500.00	5.80	92.29	344.73	734.02
AP13A013	D Gregory	0.1	framboid	Restricted Basin	2817.31	465500.00	23.21	447.93	231.75	1060.67
AP13A048	D Gregory	0.1	framboid	Restricted Basin	1079.57	465500.00	37.85	450.83	123.91	527.10
AP13A093	D Gregory	0.1	framboid	Restricted Basin	2425.88	465500.00	53.51	618.30	360.56	549.12
AP13A098	D Gregory	0.1	framboid	Restricted Basin	116.14	465500.00	5.39	157.90	406.38	189.93
AP13A020	D Gregory	0.1	framboid	Restricted Basin	3540.71	465500.00	6.65	114.72	293.95	712.05
AP13A019	D Gregory	0.1	framboid	Restricted Basin	3361.55	465500.00	8.21	210.50	848.04	1099.03
AP13A094	D Gregory	0.1	framboid	Restricted Basin	3211.01	465500.00	48.13	482.23	883.65	506.49
AP13A010	D Gregory	0.1	framboid	Restricted Basin	1187.28	465500.00	39.72	559.68	437.52	391.63
AP13A097	D Gregory	0.1	framboid	Restricted Basin	3429.91	465500.00	36.90	632.01	216.85	452.88
AP13A018	D Gregory	0.1	framboid	Restricted Basin	1252.83	465500.00	35.70	477.93	292.21	431.20
AP13A015	D Gregory	0.1	framboid	Restricted Basin	729.75	465500.00	80.81	465.81	264.79	371.82

Table A6.1: LA-ICPMS Analyses of Pyrite from Chapter 4

File	As(ppm)	Se(ppm)	Mo(ppm)	Ag(ppm)	Cd(ppm)	Sb(ppm)	Te(ppm)	Au(ppm)	Pb(ppm)	Bi(ppm)
AP13A037	459.88	536.95	954.71	<0.01	19.05	29.88	<0.13	0.93	<7.2	<0.01
AP13A044	245.63	495.58	447.23	4.28	18.83	12.18	12.16	<0.01	17.27	<0.01
AP13A017	95.14	276.96	417.84	2.61	8.13	15.19	<0.13	<0.01	23.07	<0.01
AP13A038	93.07	200.00	365.78	<0.01	<0.066	<11.60	<0.13	<0.01	25.74	<0.01
AP13A011	491.90	389.03	507.35	5.91	24.82	85.65	<0.13	<0.01	28.05	<0.01
AP13A099	181.26	368.41	823.74	12.24	<0.066	25.00	<0.13	<0.01	52.65	<0.01
AP13A023	154.78	125.00	737.54	<0.01	<0.066	53.87	<0.13	<0.01	59.89	<0.01
AP13A039	828.78	490.40	467.37	8.33	35.89	28.20	<0.13	<0.01	76.63	<0.01
AP13A049	277.18	846.76	1025.03	<0.01	<0.066	30.01	<0.13	<0.01	84.88	<0.01
AP13A026	336.31	277.03	364.89	3.06	14.14	25.91	10.47	<0.01	37.74	0.24
AP13A008	317.39	152.49	1200.61	3.01	39.57	129.75	<0.13	<0.01	<7.2	0.66
AP13A016	534.96	77.70	1412.46	10.76	50.80	172.94	4.98	<0.01	34.54	0.92
AP13A013	147.99	237.62	649.29	2.49	<0.066	51.44	<0.13	<0.01	20.11	1.02
AP13A048	135.14	52.62	305.59	<0.01	28.55	24.59	4.81	<0.01	55.18	1.12
AP13A093	74.25	81.50	751.91	4.73	<0.066	5.36	<0.13	0.13	130.44	1.25
AP13A098	1954.27	108.90	387.68	12.67	11.68	22.66	<0.13	<0.01	19.56	1.28
AP13A020	207.74	34.00	1490.73	5.48	<0.066	44.26	<0.13	<0.01	31.01	1.40
AP13A019	538.80	162.15	1841.48	13.62	37.30	186.36	4.73	<0.01	41.80	1.45
AP13A094	99.35	219.94	1425.47	8.11	29.09	21.60	<0.13	<0.01	156.11	1.69
AP13A010	466.03	255.12	924.83	7.12	31.54	96.10	<0.13	<0.01	30.82	1.79
AP13A097	289.21	9.00	457.06	2.84	7.57	68.02	<0.13	<0.01	49.22	1.82
AP13A018	362.93	21.00	742.83	6.16	17.50	93.05	<0.13	0.49	24.10	1.87
AP13A015	541.39	309.57	655.90	5.55	10.90	63.07	5.84	<0.01	126.11	1.91

Table A6.1: LA-ICPMS Analyses of Pyrite from Chapter 4

File	Analyst	Age (Ma)	Pyrite type	Setting	Mn (ppm)	Fe (ppm)	Co (ppm)	Ni (ppm)	Cu (ppm)	Zn (ppm)
AP13A014	D Gregory	0.1	framboid	Restricted Basin	5261.47	465500.00	7.09	75.32	479.03	551.48
AP13A091	D Gregory	0.1	framboid	Restricted Basin	1992.00	465500.00	36.47	685.31	328.91	649.66
AP13A043	D Gregory	0.1	framboid	Restricted Basin	3622.21	465500.00	6.68	204.49	472.08	705.98
AP13A022	D Gregory	0.1	framboid	Restricted Basin	4181.42	465500.00	21.88	172.90	583.94	1054.90
AP13A045	D Gregory	0.1	framboid	Restricted Basin	1520.96	465500.00	123.15	730.43	514.68	1000.47
AP13A036	D Gregory	0.1	framboid	Restricted Basin	1686.35	465500.00	194.44	763.34	477.74	718.41
AP13A025	D Gregory	0.1	framboid	Restricted Basin	3545.94	465500.00	14.16	383.93	573.70	852.59
AP13A021	D Gregory	0.1	framboid	Restricted Basin	3595.59	465500.00	36.93	547.46	495.27	866.28
AP13A046	D Gregory	0.1	framboid	Restricted Basin	1965.94	465500.00	177.64	699.45	316.52	857.38
AP13A104	D Gregory	0.1	framboid	Restricted Basin	1237.96	465500.00	118.84	661.37	1411.90	319.79
AP13A102	D Gregory	0.1	framboid	Restricted Basin	1881.94	465500.00	290.52	1020.55	602.22	486.70
AP13A100	D Gregory	0.1	framboid	Restricted Basin	2107.53	465500.00	37.50	509.75	840.58	551.01
AP13A012	D Gregory	0.1	framboid	Restricted Basin	1639.18	465500.00	93.13	976.32	565.79	1070.62
AP13A101	D Gregory	0.1	framboid	Restricted Basin	2132.99	465500.00	43.65	875.80	560.92	790.17
AP13A009	D Gregory	0.1	framboid	Restricted Basin	3131.44	465500.00	12.59	318.10	744.91	761.77
AP13A041	D Gregory	0.1	framboid	Restricted Basin	4256.56	465500.00	28.01	488.81	451.12	721.68
AP13A092	D Gregory	0.1	framboid	Restricted Basin	1524.60	465500.00	67.10	1131.93	689.34	821.47
AP13A096	D Gregory	0.1	framboid	Restricted Basin	1791.45	465500.00	84.44	792.14	803.70	818.19
AP13A040	D Gregory	0.1	framboid	Restricted Basin	1702.74	465500.00	109.93	782.22	620.06	720.37
AP13A024	D Gregory	0.1	framboid	Restricted Basin	878.97	465500.00	233.78	627.22	637.64	403.33
AP13A095	D Gregory	0.1	framboid	Restricted Basin	2069.90	465500.00	52.82	946.66	1014.16	711.18
AP13A007	D Gregory	0.1	framboid	Restricted Basin	1591.08	465500.00	195.73	627.93	503.17	367.56
AP13A103	D Gregory	0.1	framboid	Restricted Basin	2946.52	465500.00	23.01	312.41	1513.73	523.55

Table	Table A6.1: LA-ICPMS Analyses of Pyrite from Chapter 4										
Zn (ppm)	File	As(ppm)	Se(ppm)	Mo(ppm)	Ag(ppm)	Cd(ppm)	Sb(ppm)	Te(ppm)	Au(ppm)	Pb(ppm)	Bi(ppm)
505.15	AP13A014	**289**	**49**	960.292	**14.42**	**40.05**	**123.63**	**<0.13**	**<0.01**	**15.17**	**2.00**
1555.58	AP13A091	141.9	95.9	678.76	6.17	3.92	9.39	<0.13	<0.01	36.88	2.06
1.90	AP13A043	125.0	62.3	1340.58	7.93	8.73	22.34	<0.13	<0.01	27.91	2.21
1.43	AP13A022	93.1	51.0	679.68	7.72	<0.066	57.72	<0.13	0.71	109.13	2.22
1.98	AP13A045	497.5	436.8	1038.91	6.51	<0.066	34.84	<0.13	<0.01	62.20	2.26
12.88	AP13A036	320.6	355.4	1106.52	6.51	<0.066	49.90	<0.13	<0.01	76.31	2.33
1.58	AP13A025	289.0	135.1	1112.01	11.27	35.32	113.50	5.15	<0.01	56.03	2.38
11.55	AP13A021	559.3	70.7	1358.84	8.55	35.71	169.81	8.59	<0.01	72.04	2.63
3.06	AP13A046	363.7	345.5	1024.85	7.14	18.63	32.89	<0.13	<0.01	114.61	2.73
0.08	AP13A104	226.7	330.0	1082.56	29.69	29.94	31.92	<0.13	<0.01	70.95	2.76
5.42	AP13A102	387.9	191.4	508.27	2.07	12.20	92.85	<0.13	<0.01	134.09	2.83
6.14	AP13A100	175.1	116.1	717.82	10.21	6.40	10.79	2.46	<0.01	125.53	2.84
9.50	AP13A012	189.2	43.0	740.22	6.80	31.61	61.66	<0.13	<0.01	98.86	2.85
111.99	AP13A101	220.2	32.0	980.64	7.55	13.59	21.04	1.06	<0.01	116.84	2.88
83.43	AP13A009	375.9	205.8	1243.50	16.62	25.13	114.58	3.54	<0.01	41.28	2.98
17.27	AP13A041	122.2	141.8	935.33	9.11	50.36	31.14	<0.13	<0.01	80.54	3.10
12.61	AP13A092	215.8	144.4	958.53	13.23	7.44	22.29	<0.13	<0.01	212.64	3.57
40.08	AP13A096	212.7	42.0	474.28	2.77	8.89	14.49	4.82	<0.01	117.24	3.78
42.94	AP13A040	503.5	352.9	1551.96	8.75	22.02	46.41	<0.13	1.21	71.89	4.12
200.75	AP13A024	518.7	600.0	869.25	11.70	24.77	97.24	2.16	<0.01	88.92	4.18
169.04	AP13A095	102.9	161.2	1074.90	28.55	15.64	29.47	<0.13	<0.01	160.46	4.22
30.24	AP13A007	417.7	721.7	574.09	8.31	41.52	62.69	<0.13	<0.01	56.33	4.31
14.55	AP13A103	191.1	198.7	4064.19	19.50	9.82	36.04	2.71	0.14	200.39	4.73

File	Analyst	Age (Ma)	Pyrite type	Setting	Mn (ppm)	Fe (ppm)	Co (ppm)	Ni (ppm)	Cu (ppm)
AP13A105	D Gregory	0.1	framboid	Restricted Basin	2720.96	465500.00	10.74	502.84	1573.70
AP13A047	D Gregory	0.1	framboid	Restricted Basin	3114.08	465500.00	62.90	272.38	501.20
OC11B012		91.0	nodule		0.81	465379.50	192.78	423.27	78.45
OC11B013		91.0	nodule		0.44	465355.95	60.48	541.14	132.01
OC11A016		91.0	nodule		1.08	465516.14	1000.45	1342.95	183.47
OC11A024		91.0	nodule		14.92	465454.86	198.62	1021.34	259.26
OC11B014		91.0	nodule		1.88	465436.76	317.31	795.91	184.10
OC11A023		91.0	nodule		13.23	465482.48	165.40	1053.98	274.72
OC11A015		91.0	nodule		2.52	465516.20	330.01	500.81	117.45
OC11A014		91.0	nodule		0.40	465505.92	1073.64	1251.01	121.67
OC11A017		91.0	nodule		13.50	465478.28	556.94	768.88	154.36
OC11A013		91.0	nodule		3.89	465456.09	343.96	642.86	131.74
OC11B009		91.0	small anhedral		29.63	465408.82	94.89	235.49	77.91
OC11B011		91.0	small anhedral		540.66	465493.08	217.81	465.04	118.72
OC11A020		91.0	small anhedral		167.07	465257.47	735.74	689.93	125.72
OC11B007		91.0	small anhedral		37.31	465453.30	111.31	240.64	121.59
OC11B010		91.0	small anhedral		36.41	465402.80	27.44	114.78	22.10
OC11A009		91.0	framboid		95.63	465455.44	45.11	61.00	6.14
OC11A025		91.0	nodule		36.17	465457.72	298.72	852.45	192.71
OC11A010		91.0	framboid		107.33	465497.73	63.00	62.04	19.59
OC11A021		91.0	small anhedral		261.66	465514.87	47.61	418.25	154.17
OC11A018		91.0	framboid		4.26	465339.07	54.42	96.47	101.53
OC11B008		91.0	small anhedral		43.19	465452.28	241.97	714.51	129.40

Table A6.1: LA-ICPMS Analyses of Pyrite from Chapter 4

File	As(ppm)	Se(ppm)	Mo(ppm)	Ag(ppm)	Cd(ppm)	Sb(ppm)	Te(ppm)	Au(ppm)	Pb(ppm)	Bi(ppm)
AP13A105	313.6	88.0	1429.34	32.81	<0.066	33.36	7.28	<0.01	152.83	6.16
AP13A047	592.2	170.0	168.97	<0.01	<0.066	11.60	<0.13	<0.01	55.90	33.56
OC11B012	650.9	1.3	12.85	0.79	0.04	33.95	<0.13	0.01	70.72	0.01
OC11B013	739.1	0.7	13.19	1.44	0.08	39.15	<0.13	<0.01	112.29	0.02
OC11A016	139.0	11.0	7.71	2.24	<0.066	6.22	<0.13	0.04	308.27	0.03
OC11A024	368.6	14.0	11.71	4.67	0.17	41.71	0.07	0.06	690.36	0.04
OC11B014	436.4	2.0	9.60	1.45	0.05	20.93	<0.13	<0.01	345.88	0.05
OC11A023	265.1	8.9	8.04	5.32	0.18	33.19	<0.13	0.06	644.55	0.06
OC11A015	138.7	5.8	8.50	1.06	0.05	5.99	<0.13	0.02	273.52	0.06
OC11A014	177.3	12.0	12.81	1.76	<0.066	6.92	<0.13	0.05	297.76	0.10
OC11A017	280.8	10.2	16.02	1.16	<0.066	12.02	<0.13	0.03	693.25	0.17
OC11A013	364.0	11.3	9.93	3.58	0.12	5.31	0.19	0.05	582.79	0.17
OC11B009	541.1	2.3	10.67	1.12	0.05	8.76	<0.13	0.01	202.52	0.35
OC11B011	225.4	2.2	8.06	1.76	0.10	11.40	<0.13	<0.01	235.97	0.72
OC11A020	1108.1	30.5	15.74	2.10	0.36	79.11	0.49	0.03	315.63	0.80
OC11B007	374.4	3.5	7.07	0.84	0.06	13.48	0.28	0.01	221.65	0.89
OC11B010	563.6	<0.78	1.49	1.59	<0.066	0.69	<0.13	<0.01	71.58	1.08
OC11A009	366.4	4.2	6.75	0.22	<0.066	1.29	0.28	<0.01	46.57	1.32
OC11A025	357.8	11.7	13.65	2.05	0.15	28.94	0.15	0.03	667.86	1.37
OC11A010	208.0	3.9	4.56	0.18	0.09	1.24	0.23	<0.01	44.38	1.47
OC11A021	143.7	<0.78	3.36	13.25	<0.066	2.01	<0.13	0.03	245.60	2.02
OC11A018	802.4	21.5	5.26	1.94	0.05	36.81	0.38	0.03	206.11	2.17
OC11B008	378.2	5.0	10.00	4.11	<0.066	20.99	0.56	0.07	374.03	2.65

Table A6.1: LA-ICPMS Analyses of Pyrite from Chapter 4

File	Analyst	Age (Ma)	Pyrite type	Setting	Mn (ppm)	Fe (ppm)	Co (ppm)	Ni (ppm)	Cu (ppm)	Zn (ppm)
OC11A022		91.0	small anhedral		24.15	465420.21	174.67	3295.39	896.09	17.36
OC11B033		92.0	nodule		1.35	465529.54	71.28	220.40	69.49	2.23
OC11B032		92.0	nodule		1.17	465530.59	180.80	333.55	111.14	2.50
OC11B034		92.0	nodule		3.58	465483.14	164.47	362.00	63.83	1.88
OC11B031		92.0	nodule		2.89	465500.07	550.35	942.20	121.16	3.58
OC11B025		92.0	small anhedral		72.96	465527.97	180.50	971.13	108.04	72.39
OC11B026		92.0	small anhedral		2451.33	465480.01	477.08	1167.44	231.66	39.78
OC11B027		92.0	small anhedral		83.65	465477.75	443.56	1907.90	449.32	26.47
JL31D18	E Lounejeva	125.0	framboid		101.20	465529.26	3.01	6.34	50.03	53.47
JL31D23	E Lounejeva	125.0	framboid		4763.91	465359.01	15.02	110.16	1355.39	262.33
JL31D28	E Lounejeva	125.0	framboid		11.68	465226.25	74.05	62.34	78.07	76.82
JL31D29	E Lounejeva	125.0	framboid		12.13	465219.89	91.04	60.92	74.73	82.90
JL31D30	E Lounejeva	125.0	framboid		9.41	465214.02	117.52	50.85	72.66	73.27
JL31D12	E Lounejeva	125.0	framboid		670.85	465529.05	12.36	21.87	223.35	64.83
JL31D15	E Lounejeva	125.0	framboid		5348.54	465170.43	24.10	168.15	1436.82	167.18
JL31D14	E Lounejeva	125.0	framboid		1234.57	465492.14	9.46	81.26	134.26	386.69
JL31D10	E Lounejeva	125.0	framboid		726.46	465532.10	17.81	62.98	476.91	89.32
JL31D19	E Lounejeva	125.0	framboid		1900.61	465525.43	39.09	54.49	118.93	154.59
JL31D24	E Lounejeva	125.0	framboid		1392.38	465419.09	56.44	128.18	581.84	237.76
JL31D25	E Lounejeva	125.0	framboid		204.73	465434.48	49.88	78.25	327.20	171.07
JL31D22	E Lounejeva	125.0	framboid		699.56	465459.24	37.15	73.56	339.38	190.16
JL31D07	E Lounejeva	125.0	framboid		437.27	465494.27	29.75	35.49	180.01	153.73
JL31D26	E Lounejeva	125.0	framboid		464.22	465429.90	56.45	89.31	366.68	201.28

Table A6.1: LA-ICPMS Analyses of Pyrite from Chapter 4

File	As(ppm)	Se(ppm)	Mo(ppm)	Ag(ppm)	Cd(ppm)	Sb(ppm)	Te(ppm)	Au(ppm)	Pb(ppm)	Bi(ppm)
OC11A022	498	12.3	7.3	82.66	0.11	15.53	1.39	0.16	748.90	4.33
OC11B033	89	0.8	3.9	1.30	<0.066	11.00	0.06	<0.01	69.93	0.01
OC11B032	85	2.0	8.0	2.21	0.06	14.00	<0.13	<0.01	118.05	0.01
OC11B034	263	1.8	12.6	2.81	0.04	24.96	<0.13	0.02	183.55	0.02
OC11B031	199	3.5	13.5	3.68	0.11	30.09	<0.13	0.03	284.15	0.06
OC11B025	95	3.8	6.6	5.82	<0.066	26.67	0.58	0.03	305.91	1.18
OC11B026	274	6.8	11.8	9.04	0.10	40.66	3.01	0.13	760.21	3.71
OC11B027	283	6.0	16.2	15.27	0.03	34.92	3.26	0.21	1474.27	8.27
JL31D18	90	2.3	32.9	0.23	<0.066	10.52	<0.13	<0.01	23.96	0.52
JL31D23	728	57.9	378.0	9.12	0.33	39.79	11.36	0.56	668.32	1.82
JL31D28	1225	2.7	19.9	0.19	0.05	5.60	0.13	0.01	64.65	1.86
JL31D29	1249	2.7	21.4	0.19	0.04	4.82	0.14	0.00	68.14	1.90
JL31D30	1271	2.6	19.0	0.21	0.04	3.64	0.15	<0.01	64.98	1.92
JL31D12	91	32.7	15.6	0.47	<0.066	5.13	<0.13	0.02	248.35	1.99
JL31D15	1434	85.4	517.1	11.60	0.79	146.80	27.31	0.43	434.65	2.12
JL31D14	229	19.3	430.9	0.41	0.11	34.23	0.29	0.04	105.41	3.39
JL31D10	79	75.0	24.1	1.72	0.23	6.88	0.35	0.02	216.16	3.72
JL31D19	104	40.6	92.5	1.03	<0.066	7.98	0.76	0.04	168.15	4.48
JL31D24	503	34.6	346.0	5.67	0.06	24.31	4.54	0.40	971.39	4.72
JL31D25	445	26.7	272.1	3.39	<0.066	20.30	1.92	0.12	960.98	4.79
JL31D22	352	27.2	283.4	3.22	<0.066	18.99	2.70	0.35	978.64	4.92
JL31D07	221	40.6	205.3	1.79	0.20	65.13	0.67	<0.01	287.24	5.06
JL31D26	462	26.0	297.2	5.15	0.11	16.14	2.25	0.28	1109.75	5.13

Table A6.1: LA-ICPMS Analyses of Pyrite from Chapter 4

File	Analyst	Age (Ma)	Pyrite type	Setting	Mn (ppm)	Fe (ppm)	Co (ppm)	Ni (ppm)	Cu (ppm)	Zn (ppm)
JL31D16	E Lounejeva	125.0	framboid		3586.68	465217.79	27.12	132.52	1349.55	218.92
JL31D20	E Lounejeva	125.0	framboid		329.52	465439.23	59.86	76.27	290.38	234.55
JL31D21	E Lounejeva	125.0	framboid		70.89	465374.23	75.94	95.69	281.13	267.58
MA22A061	E Lounejeva	169.0	nodule	Restricted Basin	144.88	465433.77	62.09	608.55	<0.02	3.15
MA22A049	E Lounejeva	169.0	nodule	Restricted Basin	3.05	465406.39	75.77	807.99	0.79	3.09
MA22A052	E Lounejeva	169.0	nodule	Restricted Basin	2.76	465415.12	67.19	585.67	1.95	1.84
MA22A047	E Lounejeva	169.0	nodule	Restricted Basin	1.48	465437.64	48.01	695.79	0.89	2.20
MA22A056	E Lounejeva	169.0	nodule	Restricted Basin	8.51	465423.22	82.04	778.58	0.81	1.75
MA22A051	E Lounejeva	169.0	nodule	Restricted Basin	0.14	465380.93	85.74	963.55	2.07	3.14
MA22A059	E Lounejeva	169.0	nodule	Restricted Basin	125.34	465400.15	66.52	758.81	<0.02	1.54
MA22A045	E Lounejeva	169.0	nodule	Restricted Basin	668.14	465401.05	66.21	851.59	5.42	2.66
MA22A048	E Lounejeva	169.0	nodule	Restricted Basin	0.03	465357.28	114.89	1324.54	2.49	3.60
MA22A055	E Lounejeva	169.0	nodule	Restricted Basin	5.16	465417.34	103.21	997.82	3.65	1.95
MA22A044	E Lounejeva	169.0	nodule	Restricted Basin	331.52	465341.81	94.88	1071.29	5.69	2.35
MA22A060	E Lounejeva	169.0	nodule	Restricted Basin	22.93	465387.98	113.34	1453.26	13.50	2.47
MA22A050	E Lounejeva	169.0	nodule	Restricted Basin	2.77	465384.02	110.89	1175.13	14.30	3.23
MA22A057	E Lounejeva	169.0	nodule	Restricted Basin	2.97	465415.72	106.19	1018.65	4.56	2.55
MA22A058	E Lounejeva	169.0	nodule	Restricted Basin	0.97	465390.49	95.94	1098.86	5.18	2.21
MA22A062	E Lounejeva	169.0	nodule	Restricted Basin	1115.12	465429.96	73.86	731.50	<0.02	0.84
MY09A066	E Lounejeva	169.0	nodule	Restricted Basin	19.06	464841.91	104.32	31.41	5.20	12.27
MY09A073	E Lounejeva	169.0	nodule	Restricted Basin	14.41	465004.84	215.36	127.39	3.72	6.48
MY09A077	E Lounejeva	169.0	nodule	Restricted Basin	10.51	464870.42	214.57	80.56	6.29	11.73
MY09A075	E Lounejeva	169.0	nodule	Restricted Basin	14.09	464957.57	324.22	268.13	6.79	5.73

Table A6.1: LA-ICPMS Analyses of Pyrite from Chapter 4

File	As(ppm)	Se(ppm)	Mo(ppm)	Ag(ppm)	Cd(ppm)	Sb(ppm)	Te(ppm)	Au(ppm)	Pb(ppm)	Bi(ppm)
JL31D16	1256.8	101.2	614.16	14.83	1.32	150.66	28.59	0.25	929.47	5.13
JL31D20	427.1	31.8	206.85	1.22	<0.066	6.98	1.02	<0.01	455.32	6.67
JL31D21	670.6	31.8	292.98	1.56	0.64	14.32	1.75	0.05	742.20	7.55
MA22A061	447.6	1.4	5.96	<0.01	10.13	50.33	<0.13	<0.01	28.77	<0.01
MA22A049	550.2	1.0	7.59	0.00	6.07	57.61	<0.13	<0.01	53.63	<0.01
MA22A052	517.5	1.1	5.93	0.01	6.50	50.23	<0.13	<0.01	66.61	<0.01
MA22A047	433.1	1.4	8.83	<0.01	1.71	41.63	<0.13	<0.01	73.46	<0.01
MA22A056	487.1	1.4	5.72	0.01	5.27	55.01	<0.13	<0.01	81.62	<0.01
MA22A051	645.6	1.4	10.03	0.01	5.45	63.48	<0.13	<0.01	92.77	<0.01
MA22A059	573.5	1.6	8.35	0.01	4.76	55.89	<0.13	<0.01	107.84	<0.01
MA22A045	570.2	2.3	10.40	0.02	2.66	52.51	0.05	<0.01	157.60	<0.01
MA22A048	734.1	1.9	12.32	0.01	4.41	63.68	<0.13	<0.01	174.61	<0.01
MA22A055	509.1	1.9	6.57	0.01	5.07	54.87	<0.13	<0.01	202.08	<0.01
MA22A044	792.1	3.4	14.33	0.04	2.66	70.39	<0.13	<0.01	212.73	<0.01
MA22A060	619.1	2.3	9.02	0.04	3.71	64.71	<0.13	<0.01	331.93	<0.01
MA22A050	634.0	3.0	14.45	0.05	3.59	64.82	<0.13	0.01	234.38	0.01
MA22A057	515.2	1.4	6.61	0.03	8.20	61.62	<0.13	<0.01	159.17	0.01
MA22A058	609.7	1.8	8.64	0.02	6.08	63.16	<0.13	<0.01	126.79	0.01
MA22A062	461.8	1.6	7.29	<0.01	9.07	50.31	<0.13	<0.01	75.06	0.02
MY09A066	2665.0	2.8	26.59	0.02	0.61	4.32	0.11	<0.01	1.94	0.03
MY09A073	2054.6	2.9	18.56	0.02	1.22	6.81	0.08	0.00	10.06	0.04
MY09A077	2558.1	2.7	17.77	<0.01	1.68	10.05	0.07	0.01	11.97	0.04
MY09A075	2231.7	4.2	19.29	0.03	1.65	10.24	0.11	0.01	12.15	0.04

Table A6.1: LA-ICPMS Analyses of Pyrite from Chapter 4

File	Analyst	Age (Ma)	Pyrite type	Setting	Mn (ppm)	Fe (ppm)	Co (ppm)	Ni (ppm)	Cu (ppm)	Zn (ppm)
MY09A072	E Lounejeva	169.0	nodule	Restricted Basin	9.10	465100.65	205.06	63.22	6.54	3.69
MY09A070	E Lounejeva	169.0	nodule	Restricted Basin	9.42	465085.53	224.07	68.33	7.13	3.66
MY09A074	E Lounejeva	169.0	nodule	Restricted Basin	10.75	465114.92	240.30	172.62	10.15	11.06
MY09A071	E Lounejeva	169.0	nodule	Restricted Basin	19.81	465098.43	40.93	24.57	3.98	4.80
MY09A068	E Lounejeva	169.0	nodule	Restricted Basin	14.25	464839.03	95.80	31.15	5.37	5.42
MY09A076	E Lounejeva	169.0	nodule	Restricted Basin	32.64	464948.53	52.62	40.80	16.35	8.42
MY09A078	E Lounejeva	169.0	nodule	Restricted Basin	288.12	465097.68	160.70	69.42	11.28	14.54
MY09A067	E Lounejeva	169.0	nodule	Restricted Basin	9.44	464978.12	156.58	41.62	9.84	4.13
MY09A069	E Lounejeva	169.0	nodule	Restricted Basin	13.84	464836.32	123.10	44.78	27.63	4.70
MY21A034	E Lounejeva	180.0	nodule	Restricted Basin	<0.02	465497.22	0.29	5.37	20.95	1.06
MY21A046	E Lounejeva	180.0	nodule	Restricted Basin	<0.02	465536.40	130.90	407.70	44.28	6.42
MY21A043	E Lounejeva	180.0	nodule	Restricted Basin	<0.02	465536.49	0.06	1.13	2.57	0.36
MA21B026	D Gregory	180.0	large anhedral	Restricted Basin	22.49	465500.14	7.81	31.53	1.89	3.41
MA21B019	D Gregory	180.0	large anhedral	Restricted Basin	29.38	465475.57	4.80	17.54	17.87	0.73
MA21B017	D Gregory	180.0	large anhedral	Restricted Basin	4.31	465415.00	7.74	20.21	30.05	1.96
MA21B020	D Gregory	180.0	large anhedral	Restricted Basin	15.34	465476.29	5.25	19.94	21.34	1.99
MA21B028	D Gregory	180.0	large anhedral	Restricted Basin	47.06	465503.15	9.41	33.12	21.45	4.20
MA21B024	D Gregory	180.0	large anhedral	Restricted Basin	7.72	465496.68	10.54	38.29	2.40	3.71
MA21B031	D Gregory	180.0	large anhedral	Restricted Basin	8.25	465505.31	10.90	35.13	5.70	4.14
MA21B023	D Gregory	180.0	large anhedral	Restricted Basin	11.93	465435.36	13.75	82.68	54.94	1.33
MA21B007	D Gregory	180.0	large anhedral	Restricted Basin	6.06	465475.51	5.22	19.78	29.56	2.37
MY21A044	E Lounejeva	180.0	nodule	Restricted Basin	<0.02	465489.92	5.19	45.88	23.83	1.43
MA21B157	D Gregory	180.0	microcrystalline clusters	Restricted Basin	<0.02	465516.13	72.64	258.34	35.30	4.09

Table A6.1: LA-ICPMS Analyses of Pyrite from Chapter 4

File	As(ppm)	Se(ppm)	Mo(ppm)	Ag(ppm)	Cd(ppm)	Sb(ppm)	Te(ppm)	Au(ppm)	Pb(ppm)	Bi(ppm)
JL31D16	1696	2.5	15.3	0.02	1.46	9.07	<0.13	0.01	5.75	0.05
JL31D20	1752	3.1	16.8	0.03	1.39	9.23	0.11	0.01	6.76	0.06
JL31D21	1642	3.2	16.2	0.03	1.34	9.43	0.10	0.01	14.00	0.07
MA22A061	1704	1.0	33.1	0.02	0.22	2.34	<0.13	<0.01	4.16	0.07
MA22A049	2676	2.4	28.3	0.03	0.69	4.92	0.10	<0.01	7.28	0.08
MA22A052	2266	3.5	35.3	<0.01	0.53	4.86	0.09	0.01	12.53	0.08
MA22A047	1707	1.7	19.0	0.02	0.85	14.08	0.13	0.01	35.22	0.10
MA22A056	2155	3.4	16.2	0.02	1.53	7.77	<0.13	<0.01	7.30	0.10
MA22A051	2686	3.1	30.1	0.05	1.42	8.11	0.19	0.01	13.59	0.14
MA22A059	210	9.3	13.0	<0.01	0.01	0.35	<0.13	<0.01	10.94	0.00
MA22A045	63	5.7	130.5	0.03	0.42	2.35	<0.13	0.00	35.20	0.00
MA22A048	63	4.3	1.5	<0.01	<0.066	11.60	<0.13	<0.01	1.60	<0.01
MA22A055	199	8.6	44.3	0.05	0.71	1.48	<0.13	<0.01	11.36	<0.01
MA22A044	291	17.5	82.3	0.07	0.64	2.12	<0.13	<0.01	12.22	<0.01
MA22A060	518	23.4	64.8	0.06	0.65	2.00	0.18	<0.01	13.60	<0.01
MA22A050	288	17.6	67.6	0.11	0.54	2.37	<0.13	<0.01	14.10	<0.01
MA22A057	188	11.7	61.5	0.11	0.51	1.96	<0.13	<0.01	14.12	<0.01
MA22A058	212	15.2	50.7	0.12	0.88	1.80	0.20	<0.01	14.14	<0.01
MA22A062	180	10.2	43.9	0.16	0.32	1.99	<0.13	<0.01	14.35	<0.01
MY09A066	442	29.6	92.8	0.08	0.67	2.27	<0.13	<0.01	15.21	<0.01
MY09A073	291	30.6	81.0	0.15	0.97	2.62	0.26	0.03	18.50	<0.01
MY09A077	237	11.4	32.0	<0.01	0.13	1.09	<0.13	<0.01	20.64	<0.01
MY09A075	139	4.3	119.1	<0.01	0.21	2.46	<0.13	<0.01	21.23	<0.01

Table 6.1: LA-ICPMS Analyses of Pyrite from Chapter 4

File	Analyst	Age (Ma)	Pyrite type	Setting	Mn (ppm)	Fe (ppm)	Co (ppm)	Ni (ppm)	Cu (ppm)	Zn (ppm)
MA21B158	D Gregory	180.0	microcrystalline clusters	Restricted Basin	<0.02	465538.06	125.52	351.89	43.55	7.06
MA21B153	D Gregory	180.0	nodule	Restricted Basin	<0.02	465534.09	125.27	424.12	48.41	5.27
MY21A042	E Lounejeva	180.0	nodule	Restricted Basin	0.78	465537.68	106.49	339.96	44.46	4.59
MY21A037	E Lounejeva	180.0	nodule	Restricted Basin	<0.02	465536.42	139.18	410.63	44.88	4.81
MY21A040	E Lounejeva	180.0	nodule	Restricted Basin	<0.02	465518.58	93.14	308.69	40.82	5.13
MY21A047	E Lounejeva	180.0	nodule	Restricted Basin	<0.02	465455.52	13.11	125.26	68.69	3.27
MA21B152	D Gregory	180.0	small euhedral	Restricted Basin	<0.02	465525.98	82.27	296.37	41.09	4.22
MY21A045	E Lounejeva	180.0	nodule	Restricted Basin	0.64	465484.17	23.33	150.76	56.43	1.60
MY21A038	E Lounejeva	180.0	nodule	Restricted Basin	<0.02	465459.90	10.62	123.59	55.20	0.95
MY21A035	E Lounejeva	180.0	nodule	Restricted Basin	<0.02	465484.35	21.95	156.75	45.85	3.22
MA21B156	D Gregory	180.0	small euhedral	Restricted Basin	<0.02	465454.97	10.76	132.17	75.96	2.80
MA21B165	D Gregory	180.0	nodule	Restricted Basin	36.04	465506.32	88.70	290.41	106.58	4.68
MY21A039	E Lounejeva	180.0	nodule	Restricted Basin	<0.02	465442.92	11.92	121.15	71.20	2.66
MY21A041	E Lounejeva	180.0	nodule	Restricted Basin	<0.02	465452.25	9.68	114.74	40.43	2.26
MA21B164	D Gregory	180.0	nodule	Restricted Basin	4.89	465502.27	105.16	352.07	126.16	2.35
MA21B154	D Gregory	180.0	nodule	Restricted Basin	0.25	465392.59	11.25	159.78	47.53	0.23
MY21A036	E Lounejeva	180.0	nodule	Restricted Basin	2.63	465430.20	9.91	122.16	52.55	9.68
MA21B155	D Gregory	180.0	nodule	Restricted Basin	0.85	465429.85	7.53	74.90	37.90	0.42
MA21B015	D Gregory	180.0	large anhedral	Restricted Basin	31.38	465476.30	19.79	94.63	47.63	2.70
MA21B009	D Gregory	180.0	large anhedral	Restricted Basin	11.70	465490.84	7.45	23.51	25.30	5.24
MA21B018	D Gregory	180.0	large anhedral	Restricted Basin	14.27	465422.74	10.23	46.95	44.76	3.03
MA21B025	D Gregory	180.0	large anhedral	Restricted Basin	29.48	465502.11	12.06	38.08	23.25	2.48
MA21B008	D Gregory	180.0	large anhedral	Restricted Basin	17.36	465489.20	8.84	27.00	33.17	4.70

Table A6.1: LA-ICPMS Analyses of Pyrite from Chapter 4

File	As(ppm)	Se(ppm)	Mo(ppm)	Ag(ppm)	Cd(ppm)	Sb(ppm)	Te(ppm)	Au(ppm)	Pb(ppm)	Bi(ppm)
MA21B158	56.9	4.9	101.05	<0.01	0.46	2.13	<0.13	<0.01	27.11	<0.01
MA21B153	71.7	7.4	120.75	<0.01	0.47	2.42	<0.13	<0.01	30.29	<0.01
MY21A042	58.3	5.3	114.26	<0.01	0.46	2.21	<0.13	<0.01	31.06	<0.01
MY21A037	63.0	5.6	120.67	0.02	0.54	2.48	<0.13	0.01	32.46	<0.01
MY21A040	129.8	4.7	132.04	<0.01	0.45	2.46	<0.13	<0.01	33.30	<0.01
MY21A047	366.1	4.1	92.07	<0.01	<0.066	2.21	<0.13	<0.01	36.81	<0.01
MA21B152	102.1	6.6	119.76	<0.01	0.49	2.28	<0.13	<0.01	37.43	<0.01
MY21A045	258.8	3.1	86.98	<0.01	0.30	2.00	<0.13	0.00	41.75	<0.01
MY21A038	349.7	4.9	93.70	<0.01	0.24	2.33	<0.13	<0.01	45.28	<0.01
MY21A035	258.1	4.2	144.32	<0.01	0.17	1.94	<0.13	<0.01	45.51	<0.01
MA21B156	368.2	7.2	79.92	<0.01	0.10	2.39	<0.13	<0.01	46.09	<0.01
MA21B165	175.8	5.8	223.50	0.04	0.37	2.32	<0.13	<0.01	49.00	<0.01
MY21A039	413.3	5.3	94.67	<0.01	0.20	2.53	<0.13	<0.01	52.97	<0.01
MY21A041	378.4	4.9	103.90	<0.01	0.14	2.86	<0.13	0.00	57.32	<0.01
MA21B164	190.9	6.8	318.98	0.05	0.56	2.97	<0.13	<0.01	61.83	<0.01
MA21B154	601.9	10.3	120.43	<0.01	0.15	4.25	<0.13	<0.01	71.46	<0.01
MY21A036	460.9	6.6	103.39	<0.01	0.17	3.09	<0.13	<0.01	55.42	0.01
MA21B155	462.3	4.7	106.16	<0.01	0.15	3.17	<0.13	<0.01	41.67	0.02
MA21B015	288.3	19.5	67.94	0.07	0.50	1.62	<0.13	<0.01	11.42	0.05
MA21B009	233.8	24.5	69.33	0.12	0.73	2.45	<0.13	<0.01	19.01	0.06
MA21B018	488.9	36.6	84.07	0.14	0.70	3.16	0.22	<0.01	18.95	0.06
MA21B025	191.5	12.5	53.76	0.25	0.95	2.62	<0.13	<0.01	19.38	0.06
MA21B008	239.9	24.6	71.07	0.20	1.04	2.65	<0.13	<0.01	18.59	0.07

Table A6.1: LA-ICPMS Analyses of Pyrite from Chapter 4

File	Analyst	Age (Ma)	Pyrite type	Setting	Mn (ppm)	Fe (ppm)	Co (ppm)	Ni (ppm)	Cu (ppm)	Zn (ppm)
MA28A130	E Lounejeva	252.0	framboid	Rift Basin	2.11	463729.62	488.74	3246.13	91.95	4.13
MA28A118	E Lounejeva	252.0	framboid	Rift Basin	17.88	463160.65	530.83	4030.69	117.82	3.48
MA28A122	E Lounejeva	252.0	framboid	Rift Basin	4.02	463403.54	513.70	3438.74	113.97	3.90
MA28A121	E Lounejeva	252.0	framboid	Rift Basin	13.63	462975.91	497.79	4191.32	124.21	3.81
MA28A117	E Lounejeva	252.0	framboid	Rift Basin	6.99	463339.79	404.37	3868.22	104.17	3.94
MA28A129	E Lounejeva	252.0	framboid	Rift Basin	105.28	463363.80	613.50	4747.81	111.10	4.49
MA28A116	E Lounejeva	252.0	framboid	Rift Basin	87.92	463415.98	663.90	4328.12	120.18	4.13
MA28A126	E Lounejeva	252.0	framboid	Rift Basin	10.47	463293.58	606.54	4874.06	112.06	3.69
MA28A114	E Lounejeva	252.0	framboid	Rift Basin	222.57	463333.90	760.19	4410.80	122.44	7.11
MA28A124	E Lounejeva	252.0	framboid	Rift Basin	4.72	463131.87	548.31	3513.27	98.61	3.35
MA28A104	E Lounejeva	252.0	framboid	Rift Basin	0.74	460125.56	2221.97	8449.20	229.58	3.05
MA28A119	E Lounejeva	252.0	framboid	Rift Basin	3.45	463402.57	611.65	4728.08	148.61	3.54
MA28A125	E Lounejeva	252.0	framboid	Rift Basin	169.87	463368.37	783.93	4808.27	109.67	3.77
MA28A115	E Lounejeva	252.0	framboid	Rift Basin	241.76	463735.20	631.66	3456.99	109.45	7.83
MA28A120	E Lounejeva	252.0	framboid	Rift Basin	3.35	463168.28	752.06	5095.08	162.62	4.36
MA28A101	E Lounejeva	252.0	framboid	Rift Basin	1.18	457893.64	1320.32	12447.74	141.03	6.77
MA28A103	E Lounejeva	252.0	framboid	Rift Basin	2.08	457653.27	1793.79	14594.62	179.84	7.16
MA28A109	E Lounejeva	252.0	framboid	Rift Basin	1.80	458038.85	1869.48	12426.93	188.36	6.40
MA28A127	E Lounejeva	252.0	framboid	Rift Basin	24.56	463044.28	719.88	3726.04	112.99	2.92
MA28A128	E Lounejeva	252.0	framboid	Rift Basin	264.71	462929.99	816.53	4257.98	114.31	6.02
MA28A123	E Lounejeva	252.0	framboid	Rift Basin	27.77	463201.10	1173.78	5364.21	171.60	4.55
MA28A131	E Lounejeva	252.0	framboid	Rift Basin	172.46	463275.55	985.04	5212.44	134.68	4.67
MA28A100	E Lounejeva	252.0	framboid	Rift Basin	1.65	458260.44	1104.38	10508.54	124.23	6.76

Table A6.1: LA-ICPMS Analyses of Pyrite from Chapter 4

File	As(ppm)	Se(ppm)	Mo(ppm)	Ag(ppm)	Cd(ppm)	Sb(ppm)	Te(ppm)	Au(ppm)	Pb(ppm)	Bi(ppm)
MA28A130	6832	5.0	78.7	21.65	0.03	16.15	0.03	0.07	44.92	0.00
MA28A118	8964	5.9	87.7	22.12	0.06	23.25	0.03	0.08	74.73	<0.01
MA28A122	8054	6.8	89.9	18.46	0.03	19.76	<0.13	0.09	121.77	<0.01
MA28A121	9656	5.5	89.8	26.68	0.04	24.78	0.04	0.06	45.47	0.01
MA28A117	8293	4.7	85.1	17.28	<0.066	21.88	0.05	0.04	31.83	0.01
MA28A129	8203	5.8	96.4	20.94	0.05	33.94	0.03	0.08	82.07	0.01
MA28A116	8007	6.8	89.1	20.66	0.08	29.74	<0.13	0.08	97.77	0.01
MA28A126	8466	6.8	93.6	22.76	0.05	32.53	0.05	0.09	76.48	0.01
MA28A114	8315	6.9	91.0	18.56	0.08	33.73	<0.13	0.08	152.03	0.01
MA28A124	9072	6.0	80.1	19.38	0.05	19.96	0.05	0.08	82.17	0.01
MA28A104	20335	51.6	60.0	11.81	0.26	135.10	0.09	0.10	548.85	0.02
MA28A119	8057	6.9	103.3	26.32	0.05	29.45	0.04	0.07	76.14	0.02
MA28A125	8186	8.1	92.4	20.79	0.10	30.47	0.06	0.11	133.38	0.02
MA28A115	6811	9.7	83.0	15.57	0.07	23.92	0.05	0.09	198.63	0.02
MA28A120	8935	9.0	103.6	29.21	0.07	38.05	0.04	0.12	150.54	0.02
MA28A101	28697	17.0	149.2	22.93	0.11	98.85	0.05	0.13	181.67	0.02
MA28A103	29597	21.9	146.6	24.65	0.12	106.24	0.06	0.17	258.10	0.03
MA28A109	28152	32.9	129.5	21.45	0.21	112.67	0.04	0.15	353.86	0.03
MA28A127	9400	11.5	62.7	17.93	0.11	35.71	0.04	0.11	203.49	0.03
MA28A128	9828	13.3	77.2	15.24	0.08	44.54	0.05	0.09	243.60	0.03
MA28A123	8812	15.6	96.9	21.40	0.16	47.26	0.08	0.15	379.60	0.04
MA28A131	8533	9.3	102.5	22.57	0.13	45.44	0.05	0.14	217.75	0.04
MA28A100	27322	14.9	158.1	20.94	0.12	90.86	0.05	0.12	161.27	0.04

Table A6.1: LA-ICPMS Analyses of Pyrite from Chapter 4

File	Analyst	Age (Ma)	Pyrite type	Setting	Mn (ppm)	Fe (ppm)	Co (ppm)	Ni (ppm)	Cu (ppm)	Zn (ppm)
MA28A110	E Lounejeva	252.0	framboid	Rift Basin	32.55	461153.26	2858.80	8577.44	280.29	5.66
MA28A106	E Lounejeva	252.0	framboid	Rift Basin	10.55	458787.87	1222.30	9421.85	155.19	6.12
MA28A111	E Lounejeva	252.0	framboid	Rift Basin	79.72	461626.02	2408.80	7510.92	248.32	5.65
MA28A108	E Lounejeva	252.0	framboid	Rift Basin	1.59	459407.82	1148.55	8623.13	132.84	6.21
MA28A107	E Lounejeva	252.0	framboid	Rift Basin	1.30	459059.70	1745.74	9491.44	186.73	5.34
MA28A105	E Lounejeva	252.0	framboid	Rift Basin	1.05	459181.22	1479.20	10291.67	157.29	6.11
MA28A102	E Lounejeva	252.0	framboid	Rift Basin	1.34	460788.87	961.55	5657.83	106.94	5.41
MA28A099	E Lounejeva	252.0	framboid	Rift Basin	2.66	458770.28	1276.23	10988.04	135.29	6.46
JN28a077	E Lounejeva	254.0	framboid	Rift Basin	9.51	465495.79	178.37	384.53	130.51	<0.02
JN28a081	E Lounejeva	254.0	framboid	Rift Basin	70.95	465481.60	210.88	397.34	105.58	18.08
JN28a080	E Lounejeva	254.0	framboid	Rift Basin	31.61	465472.50	205.21	403.27	102.70	<0.02
JN28a082	E Lounejeva	254.0	framboid	Rift Basin	65.26	465487.79	205.30	406.07	76.97	12.60
JN28a083	E Lounejeva	254.0	framboid	Rift Basin	59.34	465476.78	224.25	453.63	111.82	11.89
JN28a078	E Lounejeva	254.0	framboid	Rift Basin	55.20	465495.85	200.26	403.05	80.67	19.72
JN28a079	E Lounejeva	254.0	framboid	Rift Basin	59.82	465482.76	242.61	480.08	104.42	25.97
JN28a072	E Lounejeva	254.0	framboid	Rift Basin	14.43	463977.75	313.43	600.88	289.82	2.68
JN28a071	E Lounejeva	254.0	framboid	Rift Basin	<0.02	464099.29	321.93	630.23	294.01	<0.02
JN28a073	E Lounejeva	254.0	framboid	Rift Basin	28.13	464035.62	427.22	837.51	360.79	<0.02
JN28a021	E Lounejeva	254.0	framboid	Rift Basin	55.68	464804.72	294.49	535.83	257.84	44.34
JN28a007	E Lounejeva	254.0	framboid	Rift Basin	77.80	464676.36	385.50	771.43	418.86	62.26
JN28a012	E Lounejeva	254.0	framboid	Rift Basin	38.46	464892.40	342.87	543.78	192.47	68.06
JN28a020	E Lounejeva	254.0	framboid	Rift Basin	54.54	464104.73	391.02	779.07	446.11	34.35
JN28a023	E Lounejeva	254.0	framboid	Rift Basin	57.44	464889.79	366.78	656.20	274.49	54.88

Table A6.1: LA-ICPMS Analyses of Pyrite from Chapter 4

File	As(ppm)	Se(ppm)	Mo(ppm)	Ag(ppm)	Cd(ppm)	Sb(ppm)	Te(ppm)	Au(ppm)	Pb(ppm)	Bi(ppm)
MA28A110	16484.4	72.9	30.28	9.47	0.52	151.15	0.18	0.09	821.08	0.04
MA28A106	25346.3	25.5	142.56	17.46	0.12	93.96	<0.13	0.12	359.89	0.04
MA28A111	14713.2	63.8	45.22	9.41	0.44	133.82	0.15	0.08	808.68	0.05
MA28A108	23023.7	21.5	161.29	17.27	0.11	87.44	0.06	0.10	253.57	0.05
MA28A107	24327.9	34.2	115.90	19.83	0.19	110.50	0.28	0.13	378.44	0.06
MA28A105	23872.6	27.8	137.21	16.80	0.16	92.38	0.06	0.12	346.17	0.06
MA28A102	17849.6	17.2	155.02	10.01	0.16	69.11	0.05	0.07	226.96	0.06
MA28A099	25412.2	17.9	146.89	19.20	0.16	87.26	0.07	0.10	187.53	0.09
JN28a077	215.2	31.1	3.47	2.21	0.12	6.62	4.38	0.02	524.11	1.53
JN28a081	268.4	32.7	3.90	1.19	0.10	5.50	4.63	0.02	396.73	1.55
JN28a080	302.5	39.9	4.84	1.24	0.16	7.98	5.28	0.03	491.49	1.86
JN28a082	245.2	28.7	4.18	0.95	0.10	6.66	4.73	0.01	415.34	1.95
JN28a083	286.4	32.0	8.38	1.48	0.13	6.49	5.35	0.02	446.52	2.04
JN28a078	215.0	27.7	4.81	0.84	0.11	6.49	4.33	0.01	423.83	2.07
JN28a079	264.1	31.1	7.16	1.44	0.08	9.77	5.86	0.02	516.55	2.29
JN28a072	5902.5	47.1	10.97	3.23	0.20	6.92	5.55	0.05	763.99	3.97
JN28a071	5447.2	50.5	11.02	2.92	0.43	7.93	6.17	0.04	855.71	4.58
JN28a073	5685.7	60.0	15.25	2.68	0.31	7.95	7.18	0.03	917.99	6.32
JN28a021	2804.3	45.0	17.27	1.47	0.39	5.61	5.10	0.02	736.57	7.77
JN28a007	3285.2	60.1	24.55	1.54	0.55	5.97	5.36	0.02	880.61	7.87
JN28a012	2475.8	45.2	8.11	2.86	0.25	8.49	9.19	0.04	674.37	10.34
JN28a020	5426.8	61.9	17.12	4.33	0.51	9.01	7.94	0.08	1232.75	12.22
JN28a023	2485.6	62.7	19.25	2.29	0.22	11.84	9.84	0.02	963.57	15.69

Table A6.1: LA-ICPMS Analyses of Pyrite from Chapter 4

File	Analyst	Age (Ma)	Pyrite type	Setting	Mn (ppm)	Fe (ppm)	Co (ppm)	Ni (ppm)	Cu (ppm)	Zn (ppm)
JN28a010	E Lounejeva	254.0	framboid	Rift Basin	87.65	464848.52	335.88	739.43	279.08	80.26
oc12a015		285.0	small anhedral		18.68	465529.07	94.79	132.25	0.46	2.20
oc12a019		285.0	small anhedral		2.28	465545.51	0.26	6.43	0.47	3.02
oc12a017		285.0	small anhedral		39.82	465513.15	532.32	533.38	2.75	5.73
oc12a011		285.0	large anhedral		11.43	465536.54	6.60	16.72	0.20	0.71
oc12a007		285.0	large anhedral		7.67	465510.91	40.78	66.68	0.20	1.16
oc12a010		285.0	large anhedral		7.12	465488.31	44.39	169.54	0.48	1.74
oc12a009		285.0	large anhedral		10.67	465525.88	27.38	26.40	0.21	1.64
oc12a013		285.0	small anhedral		24.13	465498.22	333.24	500.04	12.95	7.81
oc12a014		285.0	small anhedral		26.57	465453.28	1019.61	1197.17	3.54	12.89
oc12a008		285.0	large anhedral		9.30	465525.10	70.80	20.71	0.46	1.05
oc12a012		285.0	large anhedral		26.52	465451.38	1070.93	1133.68	3.29	14.02
oc12a018		285.0	small anhedral		19.16	465463.13	1144.55	1418.84	5.37	7.92
oc12a016	E Lounejeva	285.0	small anhedral		25.87	465507.26	528.14	676.59	2.46	5.22
MA08A164	E Lounejeva	297.0	nodule	Rift Basin	2.84	461808.73	2.11	5.72	0.67	3.85
MA08A165	E Lounejeva	297.0	nodule	Rift Basin	4.64	463203.69	3.53	13.99	0.77	3.73
MA08A172	E Lounejeva	297.0	nodule	Rift Basin	11.73	461034.28	80.79	96.94	4.47	5.53
MA08A168	E Lounejeva	297.0	nodule	Rift Basin	24.36	463689.33	169.05	163.50	9.12	12.04
MA08A169	E Lounejeva	297.0	nodule	Rift Basin	16.95	464923.02	420.72	355.62	10.42	9.01
MA08A174	E Lounejeva	297.0	nodule	Rift Basin	13.10	463223.52	254.41	207.38	8.39	11.18
MA08A167	E Lounejeva	297.0	nodule	Rift Basin	5.49	463463.92	18.16	25.65	22.77	61.35
MA08A170	E Lounejeva	297.0	nodule	Rift Basin	36.25	463876.74	530.66	477.95	22.16	16.73
MA08A173	E Lounejeva	297.0	nodule	Rift Basin	16.41	465154.96	348.21	282.00	10.30	20.42

Table A6.1: LA-ICPMS Analyses of Pyrite from Chapter 4

File	As(ppm)	Se(ppm)	Mo(ppm)	Ag(ppm)	Cd(ppm)	Sb(ppm)	Te(ppm)	Au(ppm)	Pb(ppm)	Bi(ppm)
JN28a010	2640	63.6	28.3	2.87	0.48	7.23	7.89	0.03	741.62	15.81
oc12a015	91	14.2	16.7	<0.01	0.18	4.92	0.54	<0.01	10.76	<0.01
oc12a019	29	6.6	16.3	<0.01	0.22	2.97	0.19	<0.01	11.63	<0.01
oc12a017	150	33.6	38.1	0.04	0.87	21.26	0.53	<0.01	51.88	<0.01
oc12a011	63	1.5	8.0	<0.01	<0.066	0.19	0.26	<0.01	2.36	0.01
oc12a007	159	2.7	10.0	<0.01	0.06	1.27	0.33	<0.01	8.93	0.01
oc12a010	243	4.3	13.2	<0.01	0.09	2.48	0.37	<0.01	17.37	0.01
oc12a009	102	2.4	9.8	<0.01	0.02	0.41	0.39	<0.01	4.72	0.01
oc12a013	206	41.8	38.9	<0.01	0.66	23.65	0.45	<0.01	24.20	0.02
oc12a014	374	59.7	78.7	<0.01	1.45	33.52	<0.13	0.02	84.29	0.02
oc12a008	105	3.3	11.2	0.01	0.04	0.55	0.44	<0.01	5.90	0.02
oc12a012	382	51.2	79.0	<0.01	1.82	35.49	0.86	<0.01	66.73	0.03
oc12a018	338	80.6	53.2	<0.01	1.11	27.44	0.47	<0.01	91.93	0.03
oc12a016	172	31.1	36.0	<0.01	0.67	20.10	0.44	<0.01	10.86	0.04
MA08A164	14029	14.6	9.4	0.02	0.09	431.54	<0.13	0.00	98.55	0.01
MA08A165	8803	7.9	6.1	0.37	0.08	257.02	<0.13	0.01	34.10	0.03
MA08A172	16930	48.7	8.4	5.02	<0.066	344.64	<0.13	0.09	448.04	0.13
MA08A168	6983	23.0	6.1	8.71	0.07	163.75	<0.13	0.11	337.58	0.29
MA08A169	2361	16.2	5.4	29.08	0.18	107.28	0.09	0.49	508.01	0.29
MA08A174	8728	28.5	5.7	12.14	0.13	186.24	0.11	0.17	462.08	0.34
MA08A167	7828	15.5	7.3	1.66	0.42	252.62	<0.13	0.03	76.66	0.34
MA08A170	6281	26.6	5.0	19.60	0.08	163.15	0.17	0.46	943.19	0.57
MA08A173	1492	12.2	2.2	19.40	0.15	71.58	<0.13	0.26	347.01	0.61

Table A6.1: LA-ICPMS Analyses of Pyrite from Chapter 4

File	Analyst	Age (Ma)	Pyrite type	Setting	Mn (ppm)	Fe (ppm)	Co (ppm)	Ni (ppm)	Cu (ppm)	Zn (ppm)
MA08A171	E Lounejeva	297.0	nodule	Rift Basin	15.89	465095.94	597.38	449.30	10.89	8.01
MA08A166	E Lounejeva	297.0	nodule	Rift Basin	22.31	463541.54	459.49	681.05	50.30	19.49
JL18B028	E Lounejeva	305.0	small anhedral		390.33	465532.16	51.37	1797.25	30.49	6981.21
JL18B017	E Lounejeva	305.0	small anhedral		566.41	465533.99	55.84	2411.42	59.79	2436.57
JL18B027	E Lounejeva	305.0	small anhedral		335.26	465485.06	61.76	3031.80	178.80	4819.43
JL18B026	E Lounejeva	305.0	small anhedral		366.12	465538.65	64.04	3890.34	98.36	4461.37
JL18B022	E Lounejeva	305.0	small anhedral		363.64	465529.63	53.74	2836.16	92.40	1713.11
JL18B013	E Lounejeva	305.0	small anhedral		636.26	465467.26	42.66	2109.77	236.91	5955.46
JL18B008	E Lounejeva	305.0	small anhedral		708.81	465506.98	65.81	2887.45	196.07	2109.71
JL18B009	E Lounejeva	305.0	small anhedral		240.92	465505.71	55.54	3833.11	398.62	8303.38
JL18B024	E Lounejeva	305.0	small anhedral		446.78	465534.01	72.42	4034.87	144.18	6829.74
JL18B020	E Lounejeva	305.0	small anhedral		545.44	465524.30	78.30	3829.14	73.23	13.32
JL18B019	E Lounejeva	305.0	small anhedral		355.32	465486.76	73.10	3879.97	329.63	5365.09
JL05A009	E Lounejeva	310.0	small anhedral	Shelf Facies	363.27	465347.08	301.12	475.56	<0.02	<0.02
JL05A071	E Lounejeva	310.0	small anhedral	Shelf Facies	722.46	465450.56	205.93	1871.07	262.31	4402.13
JL05A010	E Lounejeva	310.0	small anhedral	Shelf Facies	548.91	465433.32	312.86	2827.16	147.34	1832.15
JL05A061	E Lounejeva	310.0	small anhedral	Shelf Facies	553.33	465464.98	1222.18	3355.05	349.43	8771.87
JL05A065	E Lounejeva	310.0	small anhedral	Shelf Facies	520.00	465451.78	85.82	1103.78	383.36	4166.60
JL05A096	E Lounejeva	310.0	small anhedral		0.26	464873.66	5.46	220.39	552.84	6.02
JL05A116	E Lounejeva	310.0	small anhedral		267.15	465551.75	2.18	39.24	18.70	220.92
JL05A095	E Lounejeva	310.0	small anhedral		17.98	464942.23	5.79	203.60	471.64	63.66
JL05A111	E Lounejeva	310.0	small anhedral		139.53	465464.09	13.92	435.95	493.15	128.95
JL05A117	E Lounejeva	310.0	small anhedral		219.34	465552.16	2.65	55.56	33.33	319.49

Table A6.1: LA-ICPMS Analyses of Pyrite from Chapter 4

File	As(ppm)	Se(ppm)	Mo(ppm)	Ag(ppm)	Cd(ppm)	Sb(ppm)	Te(ppm)	Au(ppm)	Pb(ppm)	Bi(ppm)
MA08A171	1713.2	21.1	2.29	31.12	0.16	93.11	0.12	0.48	499.10	0.85
MA08A166	7536.8	46.8	11.02	16.90	<0.066	149.66	0.34	0.27	818.22	3.21
JL18B028	79.0	140.1	502.00	10.67	93.93	63.02	<0.13	<0.01	122.53	0.76
JL18B017	72.1	172.4	1579.50	13.17	40.21	92.40	0.88	<0.01	147.96	0.89
JL18B027	255.4	285.0	1194.19	19.03	91.60	98.49	1.15	<0.01	176.61	1.05
JL18B026	54.6	197.9	1992.48	13.17	89.46	112.65	<0.13	<0.01	158.83	1.08
JL18B022	88.4	189.4	1634.81	12.95	65.40	90.35	<0.13	<0.01	177.49	1.16
JL18B013	322.1	617.6	1135.54	164.53	82.51	165.34	1.24	0.08	303.28	1.18
JL18B008	173.3	365.8	2155.67	32.36	38.13	157.78	<0.13	<0.01	302.83	1.49
JL18B009	178.0	336.4	2521.63	66.48	154.78	213.91	3.14	<0.01	361.31	1.61
JL18B024	72.0	234.1	2152.50	17.56	150.21	159.26	<0.13	<0.01	216.47	1.77
JL18B020	108.4	264.7	2297.23	19.12	22.08	165.91	1.68	<0.01	259.94	1.85
JL18B019	249.0	368.6	2266.45	31.04	207.42	225.81	2.63	<0.01	332.79	3.00
JL05A009	772.4	458.1	878.15	3.95	64.85	30.79	0.50	0.05	47.78	0.69
JL05A071	384.7	627.6	747.11	6.81	123.39	58.08	0.63	0.10	71.45	1.23
JL05A010	449.3	543.7	1054.74	9.10	126.78	81.80	0.97	0.06	120.76	1.48
JL05A061	330.6	636.0	1394.33	34.19	343.98	100.29	1.35	0.04	123.81	3.84
JL05A065	380.1	1448.7	1608.33	14.80	181.46	124.97	2.07	0.03	160.54	4.91
JL05A096	2546.0	3637.1	98.73	53.38	2.47	358.46	<0.13	0.01	223.88	0.06
JL05A116	5.6	2413.4	20.40	2.32	7.22	4.69	<0.13	0.01	12.60	0.07
JL05A095	2289.1	3914.7	110.60	41.53	3.71	394.02	<0.13	<0.01	143.56	0.08
JL05A111	334.0	2886.6	307.41	69.85	6.70	170.39	<0.13	0.02	632.20	0.11
JL05A117	4.0	2262.0	31.43	1.94	9.51	4.39	<0.13	<0.01	34.13	0.13

Table A6.1: LA-ICPMS Analyses of Pyrite from Chapter 4

File	Analyst	Age (Ma)	Pyrite type	Setting	Mn (ppm)	Fe (ppm)	Co (ppm)	Ni (ppm)	Cu (ppm)	Zn (ppm)
JL05A097	E Lounejeva	310.0	small anhedral		100.83	465054.86	8.57	302.01	476.36	77.04
JL05A098	E Lounejeva	310.0	small anhedral		67.24	464978.15	9.44	340.71	650.05	43.03
JL05A102	E Lounejeva	310.0	small anhedral		251.96	465547.28	20.33	700.20	138.12	233.72
JL05A101	E Lounejeva	310.0	small anhedral		302.74	465546.39	17.23	443.81	44.33	384.31
JL05A105	E Lounejeva	310.0	small anhedral		809.73	465529.34	60.75	1973.41	735.29	1300.68
JL05A114	E Lounejeva	310.0	small anhedral		577.76	465531.63	81.87	2977.51	1132.90	681.33
JL05A104	E Lounejeva	310.0	small anhedral		768.03	465528.49	79.81	2961.14	1131.74	1798.95
JL05A121	E Lounejeva	310.0	small anhedral		583.45	465530.92	82.36	2839.51	1014.63	935.34
JL05A108	E Lounejeva	310.0	small anhedral		541.69	465536.20	72.16	3098.19	1211.52	1539.79
JN19A034	E Lounejeva	355.0	nodule	Rift Basin	1.87	465523.35	65.01	246.62	230.49	<0.02
MY24A015	E Lounejeva	355.0	large euhedral	Rift Basin	1.28	465530.91	45.36	169.10	139.23	1.65
MY24A020	E Lounejeva	355.0	large euhedral	Rift Basin	31.84	465540.74	2.69	12.96	25.46	8.55
JN19A083	E Lounejeva	355.0	nodule	Rift Basin	2.15	465312.22	24.94	101.83	142.05	0.90
JN19A030	E Lounejeva	355.0	nodule	Rift Basin	18.14	465318.23	20.10	99.26	144.94	6.90
JN19A047	E Lounejeva	355.0	large anhedral	Rift Basin	16.81	465520.67	231.73	345.75	148.84	34.73
JN19A095	E Lounejeva	355.0	nodule	Rift Basin	19.57	465360.29	32.43	123.91	199.58	9.52
JN19A057	E Lounejeva	355.0	large anhedral	Rift Basin	121.19	465518.74	131.97	294.23	120.49	28.79
JN19A085	E Lounejeva	355.0	nodule	Rift Basin	3.71	465321.74	23.48	96.62	150.77	2.38
MY24A009	E Lounejeva	355.0	large euhedral	Rift Basin	0.49	465502.64	45.14	245.20	245.18	0.35
JN19A084	E Lounejeva	355.0	nodule	Rift Basin	6.80	465322.43	27.26	95.40	148.57	1.18
MY24A018	E Lounejeva	355.0	large euhedral	Rift Basin	35.76	465535.43	25.16	168.43	77.78	11.93
JN19A056	E Lounejeva	355.0	large anhedral	Rift Basin	79.20	465509.67	195.69	322.54	201.84	30.29
MY24A012	E Lounejeva	355.0	large euhedral	Rift Basin	25.30	465509.28	111.80	333.40	191.42	3.17

Table A6.1: LA-ICPMS Analyses of Pyrite from Chapter 4

File	As(ppm)	Se(ppm)	Mo(ppm)	Ag(ppm)	Cd(ppm)	Sb(ppm)	Te(ppm)	Au(ppm)	Pb(ppm)	Bi(ppm)
JL05A097	1867	2784.9	86.5	47.15	2.46	296.58	0.18	0.01	227.41	0.19
JL05A098	2155	4948.2	96.9	78.26	2.65	419.19	0.09	0.01	198.54	0.30
JL05A102	22	1272.8	128.7	15.21	2.49	12.77	<0.13	<0.01	180.74	0.92
JL05A101	26	682.2	84.8	12.47	2.62	12.81	<0.13	<0.01	175.92	1.57
JL05A105	90	1591.4	312.2	47.88	12.51	58.40	<0.13	0.10	151.73	2.30
JL05A114	81	1751.3	345.7	67.45	5.82	67.74	1.68	0.07	174.65	3.96
JL05A104	93	2980.2	376.5	60.99	12.29	90.14	1.63	0.09	218.15	4.14
JL05A121	84	1064.7	419.4	43.70	5.25	42.02	1.64	0.07	130.87	4.15
JL05A108	64	1708.3	382.4	55.42	35.08	76.10	<0.13	<0.01	177.04	4.30
JN19A034	112	71.6	58.7	0.35	0.56	5.35	0.11	0.01	229.73	<0.01
MY24A015	84	28.0	11.2	0.40	0.44	1.88	<0.13	<0.01	128.58	0.01
MY24A020	47	34.6	22.5	0.05	0.27	0.46	<0.13	<0.01	27.15	0.02
JN19A083	903	26.6	360.7	0.43	1.60	31.17	<0.13	<0.01	408.29	0.02
JN19A030	880	42.0	355.9	0.34	1.13	55.19	0.10	0.01	239.56	0.03
JN19A047	122	65.1	86.9	0.16	0.76	3.83	<0.13	0.06	145.21	0.03
JN19A095	723	19.1	391.5	0.49	1.90	27.85	0.12	<0.01	343.50	0.04
JN19A057	129	75.0	64.7	0.31	0.71	3.02	<0.13	0.01	102.32	0.04
JN19A085	867	23.4	400.6	0.38	1.53	29.85	0.07	<0.01	366.95	0.05
MY24A009	190	35.6	32.7	0.35	0.79	3.18	0.11	<0.01	195.53	0.05
JN19A084	865	24.1	403.3	0.42	1.55	29.78	<0.13	<0.01	350.58	0.05
MY24A018	67	31.0	40.7	0.19	0.41	1.74	<0.13	<0.01	99.78	0.05
JN19A056	163	57.3	140.2	0.39	0.92	7.00	<0.13	<0.01	211.74	0.05
MY24A012	165	41.9	41.1	0.36	0.65	2.78	<0.13	0.01	180.99	0.08

Table A6.1: LA-ICPMS Analyses of Pyrite from Chapter 4

File	Analyst	Age (Ma)	Pyrite type	Setting	Mn (ppm)	Fe (ppm)	Co (ppm)	Ni (ppm)	Cu (ppm)	Zn (ppm)
MY24A019	E Lounejeva	355.0	large euhedral	Rift Basin	46.87	465540.09	5.87	26.17	67.82	9.55
JN19A036	E Lounejeva	355.0	nodule	Rift Basin	321.07	465448.55	5.06	95.97	128.90	10.20
JN19A043	E Lounejeva	355.0	nodule	Rift Basin	54.54	465412.85	16.76	173.97	249.35	7.88
JN19A037	E Lounejeva	355.0	nodule	Rift Basin	112.97	465377.65	27.38	166.87	193.45	11.53
JN19A045	E Lounejeva	355.0	nodule	Rift Basin	364.85	465371.88	10.88	156.29	208.90	12.80
JN19A086	E Lounejeva	355.0	nodule	Rift Basin	53.53	465345.05	63.76	153.51	204.43	35.35
MY24A010	E Lounejeva	355.0	large euhedral	Rift Basin	8.95	465506.24	92.85	298.39	188.26	7.70
JN19A039	E Lounejeva	355.0	nodule	Rift Basin	94.98	465329.51	32.50	138.84	176.70	28.13
JN19A032	E Lounejeva	355.0	nodule	Rift Basin	374.70	465381.06	24.11	183.23	203.91	11.78
MY24A008	E Lounejeva	355.0	large euhedral	Rift Basin	93.19	465530.97	38.83	132.35	81.46	14.13
MY24A014	E Lounejeva	355.0	large euhedral	Rift Basin	65.38	465510.56	143.49	481.02	115.56	25.94
JN19A090	E Lounejeva	355.0	nodule	Rift Basin	306.79	465343.40	52.44	152.05	295.50	112.76
JN19A044	E Lounejeva	355.0	nodule	Rift Basin	417.07	465392.11	14.12	133.71	234.88	10.61
JN19A038	E Lounejeva	355.0	nodule	Rift Basin	763.62	465380.81	14.03	153.99	197.76	19.48
JN19A041	E Lounejeva	355.0	nodule	Rift Basin	744.96	465371.94	11.90	159.51	250.24	14.22
JN19A035	E Lounejeva	355.0	nodule	Rift Basin	93.75	465390.93	7.85	116.68	191.21	9.83
JN19A082	E Lounejeva	355.0	small anhedral	Rift Basin	159.67	465291.31	115.76	245.63	222.32	145.44
JN19A097	E Lounejeva	355.0	nodule	Rift Basin	288.81	465355.31	58.93	174.48	286.35	41.88
JN19A042	E Lounejeva	355.0	nodule	Rift Basin	519.14	465399.66	13.99	174.17	294.40	17.67
JN19A049	E Lounejeva	355.0	large anhedral	Rift Basin	15.77	465526.65	95.73	98.67	34.26	24.27
JN19A031	E Lounejeva	355.0	nodule	Rift Basin	930.68	465428.35	20.29	179.54	242.99	24.83
MY24A013	E Lounejeva	355.0	large euhedral	Rift Basin	115.93	465476.03	97.90	456.41	291.71	20.63
JN19A098	E Lounejeva	355.0	nodule	Rift Basin	316.04	465355.63	68.68	186.84	323.87	40.22

Table A6.1: LA-ICPMS Analyses of Pyrite from Chapter 4

File	As(ppm)	Se(ppm)	Mo(ppm)	Ag(ppm)	Cd(ppm)	Sb(ppm)	Te(ppm)	Au(ppm)	Pb(ppm)	Bi(ppm)
MY24A019	49.2	24.1	82.58	0.15	0.39	1.51	0.13	<0.01	76.92	0.09
JN19A036	392.2	35.8	143.52	0.60	0.66	19.23	0.14	0.01	95.56	0.09
JN19A043	526.0	48.5	1388.06	0.77	1.46	33.74	0.10	0.01	317.62	0.10
JN19A037	657.8	30.7	260.16	0.49	1.34	34.30	0.10	0.01	250.77	0.10
JN19A045	679.5	38.9	480.57	0.70	1.27	37.78	0.18	0.01	196.71	0.11
JN19A086	780.0	25.7	400.18	0.57	1.89	26.67	0.09	<0.01	472.31	0.12
MY24A010	176.1	38.7	50.56	0.46	0.77	2.78	<0.13	<0.01	181.27	0.12
JN19A039	838.2	21.8	372.12	0.48	1.18	40.66	0.14	0.01	229.82	0.15
JN19A032	645.1	45.9	458.93	0.96	1.52	39.12	0.20	0.02	300.91	0.15
MY24A008	83.4	31.9	19.91	0.27	0.36	1.36	0.13	<0.01	75.42	0.16
MY24A014	159.9	46.5	23.69	0.11	0.54	1.42	0.19	<0.01	89.99	0.18
JN19A090	786.1	37.0	457.91	1.29	3.38	35.84	<0.13	0.01	507.16	0.19
JN19A044	603.7	41.1	346.42	0.73	1.29	33.53	0.24	0.01	216.42	0.20
JN19A038	646.0	26.6	256.60	1.09	1.34	34.50	0.16	0.02	181.31	0.21
JN19A041	679.2	32.9	279.87	1.79	1.64	37.68	0.17	0.03	199.14	0.22
JN19A035	608.1	21.5	241.71	0.56	1.08	32.83	0.13	<0.01	162.62	0.22
JN19A082	981.3	75.5	347.99	1.00	3.21	45.16	0.26	0.01	981.26	0.28
JN19A097	741.5	36.2	345.83	1.20	2.71	35.35	0.15	0.01	509.52	0.29
JN19A042	575.4	26.3	211.70	1.25	1.81	29.11	0.27	0.02	238.10	0.29
JN19A049	99.6	32.8	58.39	0.08	0.17	1.10	0.21	<0.01	43.75	0.30
JN19A031	467.9	53.0	264.39	1.49	1.71	28.69	0.24	0.03	278.42	0.31
MY24A013	289.3	50.0	128.56	0.69	1.37	12.06	0.15	0.01	343.34	0.32
JN19A098	740.3	24.4	465.53	1.37	3.22	30.51	0.28	0.01	406.07	0.35

Table A6.1: LA-ICPMS Analyses of Pyrite from Chapter 4

File	Analyst	Age (Ma)	Pyrite type	Setting	Mn (ppm)	Fe (ppm)	Co (ppm)	Ni (ppm)	Cu (ppm)	Zn (ppm)
MY24A016	E Lounejeva	355.0	large euhedral	Rift Basin	154.36	465421.03	295.02	1062.62	488.27	666.94
JN19A092	E Lounejeva	355.0	nodule	Rift Basin	28.33	465374.05	88.16	261.68	253.98	17.47
JN19A040	E Lounejeva	355.0	nodule	Rift Basin	1495.45	465372.17	12.83	165.54	302.55	24.34
JN19A076	E Lounejeva	355.0	small anhedral	Rift Basin	279.10	465248.59	94.94	270.39	294.37	131.28
JN19A087	E Lounejeva	355.0	nodule	Rift Basin	252.49	465370.37	82.53	195.45	321.91	135.71
JN19A088	E Lounejeva	355.0	nodule	Rift Basin	115.75	465343.23	56.33	152.85	235.19	75.73
JN19A077	E Lounejeva	355.0	small anhedral	Rift Basin	103.96	465247.43	154.86	405.64	240.35	197.25
JN19A050	E Lounejeva	355.0	large anhedral	Rift Basin	1514.43	465504.75	220.92	488.33	408.21	275.94
JN19A091	E Lounejeva	355.0	nodule	Rift Basin	491.11	465330.20	57.88	197.97	358.38	109.44
JN19A048	E Lounejeva	355.0	large anhedral	Rift Basin	2776.90	465462.80	85.42	233.25	526.08	108.89
MY24A011	E Lounejeva	355.0	large euhedral	Rift Basin	411.76	465534.25	34.08	155.42	65.15	91.70
JN19A033	E Lounejeva	355.0	nodule	Rift Basin	1470.03	465354.53	23.66	266.02	429.48	21.77
JN19A099	E Lounejeva	355.0	nodule	Rift Basin	1426.04	465341.72	108.86	341.12	626.22	308.02
JN19A052	E Lounejeva	355.0	large anhedral	Rift Basin	5632.23	465460.33	179.53	784.59	729.92	545.34
JN19A080	E Lounejeva	355.0	small anhedral	Rift Basin	678.97	465272.18	91.11	303.36	422.61	261.92
JN19A078	E Lounejeva	355.0	small anhedral	Rift Basin	866.82	465334.43	134.81	339.86	445.83	378.60
JN19A079	E Lounejeva	355.0	small anhedral	Rift Basin	1179.12	465267.26	113.16	333.33	707.73	362.49
JN19A051	E Lounejeva	355.0	large anhedral	Rift Basin	9941.06	465419.19	116.99	555.89	1051.98	366.13
JN19A096	E Lounejeva	355.0	nodule	Rift Basin	5589.62	465362.18	59.59	329.74	1014.72	174.50
JN19A100	E Lounejeva	355.0	nodule	Rift Basin	2304.57	465414.87	81.24	259.20	622.89	474.70
JN19A075	E Lounejeva	355.0	small anhedral	Rift Basin	3211.68	465303.34	146.63	410.71	1218.22	332.31
MY24A026	E Lounejeva	355.0	small anhedral	Rift Basin	2914.80	465506.98	92.42	565.12	1555.87	959.81
MY24A027	E Lounejeva	355.0	small anhedral	Rift Basin	4517.04	465512.24	65.55	401.88	2044.31	532.56

Table A6.1: LA-ICPMS Analyses of Pyrite from Chapter 4

File	As(ppm)	Se(ppm)	Mo(ppm)	Ag(ppm)	Cd(ppm)	Sb(ppm)	Te(ppm)	Au(ppm)	Pb(ppm)	Bi(ppm)
MY24A016	495	92.1	347.2	1.48	9.88	22.05	0.35	0.02	701.15	0.40
JN19A092	671	32.6	315.3	0.87	1.81	26.94	<0.13	0.01	466.98	0.43
JN19A040	678	34.7	269.2	2.90	1.79	40.13	0.31	0.05	170.95	0.43
JN19A076	1141	108.5	315.2	2.05	3.11	61.64	0.20	0.02	1087.46	0.44
JN19A087	685	31.3	457.4	1.94	4.15	26.16	0.27	0.01	485.43	0.45
JN19A088	787	25.5	452.2	1.40	2.82	31.00	0.19	0.01	417.52	0.48
JN19A077	1146	121.6	328.8	1.93	4.61	64.29	0.23	0.02	1183.81	0.53
JN19A050	182	105.6	694.6	1.87	3.43	13.93	0.41	0.04	306.89	0.59
JN19A091	836	35.6	411.4	1.74	4.57	33.85	0.33	0.01	476.03	0.64
JN19A048	339	58.3	470.1	4.47	3.94	21.89	0.81	0.05	332.10	0.84
MY24A011	71	56.1	119.2	0.62	1.24	2.95	0.38	<0.01	118.83	0.86
JN19A033	744	66.1	1116.6	2.51	2.95	46.21	0.60	0.04	466.66	1.05
JN19A099	792	54.6	421.9	4.18	10.78	41.99	1.14	0.01	765.73	1.18
JN19A052	348	140.3	958.3	6.39	7.27	34.47	0.82	0.14	505.04	1.19
JN19A080	1053	95.3	297.9	3.72	5.02	53.48	0.40	0.03	911.26	1.23
JN19A078	820	102.0	306.4	6.07	6.65	44.29	0.79	0.05	870.58	1.59
JN19A079	1071	104.2	347.4	5.25	6.41	60.82	0.65	0.04	1038.56	1.74
JN19A051	502	156.3	1603.2	15.41	10.40	56.63	2.37	0.23	509.46	2.35
JN19A096	716	74.6	338.9	20.41	12.56	39.36	1.95	0.13	465.49	2.47
JN19A100	518	54.1	353.7	7.82	11.99	31.16	1.52	0.04	574.80	2.98
JN19A075	936	138.8	342.5	14.56	14.53	60.71	2.06	0.05	1172.89	3.30
MY24A026	173	45.6	181.9	7.53	10.62	17.55	1.44	0.03	911.59	8.02
MY24A027	154	27.6	194.7	7.66	5.52	17.82	1.29	0.05	1007.09	9.74

Table A6.1: LA-ICPMS Analyses of Pyrite from Chapter 4

File	Analyst	Age (Ma)	Pyrite type	Setting	Mn (ppm)	Fe (ppm)	Co (ppm)	Ni (ppm)	Cu (ppm)	Zn (ppm)
MY24A024	E Lounejeva	355.0	small anhedral	Rift Basin	3283.84	465517.09	67.83	391.54	1520.14	1280.02
MY24A030	E Lounejeva	355.0	small anhedral	Rift Basin	6167.37	465528.86	57.99	329.82	1291.69	661.47
MY24A029	E Lounejeva	355.0	small anhedral	Rift Basin	5440.92	465508.87	100.98	633.36	2068.89	1064.78
MY24A025	E Lounejeva	355.0	small anhedral	Rift Basin	6310.30	465474.75	134.25	916.99	3237.15	986.89
MY24A023	E Lounejeva	355.0	small anhedral	Rift Basin	5354.88	465521.01	79.92	428.00	1980.00	1927.90
MY24A034	E Lounejeva	355.0	small anhedral	Rift Basin	7444.73	465513.27	89.26	516.44	2592.82	2588.07
MY24A033	E Lounejeva	355.0	small anhedral	Rift Basin	8517.27	465512.15	91.40	533.25	2299.11	2191.86
MY24B009	E Lounejeva	359.0	small anhedral	Rift Basin	100.43	465539.44	213.56	121.50	74.60	215.80
MY24B011	E Lounejeva	359.0	small anhedral	Rift Basin	180.10	465534.10	347.77	191.39	185.85	223.35
MY24B020	E Lounejeva	359.0	small anhedral	Rift Basin	1095.81	465541.48	204.02	101.00	62.56	126.50
MY24B024	E Lounejeva	359.0	small anhedral	Rift Basin	40.65	465540.41	227.98	114.92	57.14	180.82
MY24B008	E Lounejeva	359.0	small anhedral	Rift Basin	122.03	465535.61	272.29	163.39	88.60	219.19
MY24B007	E Lounejeva	359.0	small anhedral	Rift Basin	228.42	465522.63	485.35	257.90	313.89	209.90
MY24B021	E Lounejeva	359.0	small anhedral	Rift Basin	59.14	465539.79	238.63	125.76	80.50	196.58
MY24B017	E Lounejeva	359.0	small anhedral	Rift Basin	83.39	465537.42	255.03	133.34	72.44	174.67
MY24B023	E Lounejeva	359.0	small anhedral	Rift Basin	256.06	465537.60	290.68	146.16	76.99	206.32
MY24B018	E Lounejeva	359.0	small anhedral	Rift Basin	61.48	465539.34	263.77	130.72	54.16	166.79
MY24B022	E Lounejeva	359.0	small anhedral	Rift Basin	72.52	465538.44	261.20	131.59	74.04	174.49
MY24B014	E Lounejeva	359.0	small anhedral	Rift Basin	78.82	465538.14	266.68	136.79	72.46	221.28
MY24B010	E Lounejeva	359.0	small anhedral	Rift Basin	296.86	465534.78	340.12	177.40	93.89	251.96
MY24B015	E Lounejeva	359.0	small anhedral	Rift Basin	106.76	465535.95	290.10	167.76	96.04	161.33
MY24B016	E Lounejeva	359.0	small anhedral	Rift Basin	80.14	465539.47	279.08	117.15	59.49	214.08
JN18A054	E Lounejeva	359.0	framboid	Rift Basin	96.20	465529.03	265.44	193.86	63.08	192.29

Table A6.1: LA-ICPMS Analyses of Pyrite from Chapter 4

File	As(ppm)	Se(ppm)	Mo(ppm)	Ag(ppm)	Cd(ppm)	Sb(ppm)	Te(ppm)	Au(ppm)	Pb(ppm)	Bi(ppm)
MY24A024	135.4	38.6	137.52	5.95	11.19	15.34	1.79	0.04	814.21	9.87
MY24A030	91.3	23.2	193.37	4.47	5.99	14.44	1.44	0.03	631.96	10.05
MY24A029	166.2	42.2	230.75	6.82	9.58	20.91	1.60	0.04	1074.77	10.74
MY24A025	294.1	63.2	259.63	11.52	9.90	30.64	1.86	0.08	1710.56	13.85
MY24A023	120.7	44.3	201.30	5.11	15.73	17.72	2.27	0.03	875.31	14.82
MY24A034	149.7	45.8	220.60	5.20	21.02	21.09	2.81	0.04	1079.97	19.15
MY24A033	153.9	46.1	250.85	4.90	18.63	22.20	2.59	0.05	1060.76	21.79
MY24B009	51.7	4.0	0.49	0.72	<0.066	3.42	0.39	<0.01	210.50	19.93
MY24B011	71.7	3.7	0.75	0.76	0.49	5.62	0.54	<0.01	265.94	20.28
MY24B020	44.0	1.7	1.62	0.45	0.04	5.50	0.28	0.01	153.32	20.46
MY24B024	48.0	3.0	0.39	0.52	0.04	6.51	0.25	<0.01	248.46	23.14
MY24B008	66.0	3.1	0.36	0.85	0.12	6.74	0.39	0.02	310.14	23.45
MY24B007	114.7	4.5	0.72	1.11	<0.066	6.96	0.53	<0.01	455.96	24.14
MY24B021	50.4	2.4	0.72	0.58	<0.066	6.57	0.37	0.01	191.45	26.15
MY24B017	59.3	2.6	0.82	0.54	0.10	5.69	0.35	<0.01	226.97	26.99
MY24B023	58.6	1.7	1.24	0.61	0.09	6.94	0.43	0.01	237.22	27.50
MY24B018	52.0	1.5	1.03	0.43	<0.066	5.00	0.44	0.01	246.86	28.19
MY24B022	55.4	2.6	1.26	0.52	0.12	5.76	0.35	0.01	279.11	29.12
MY24B014	56.6	1.6	0.80	0.61	0.09	7.38	0.28	<0.01	283.72	29.33
MY24B010	69.1	2.9	0.56	1.00	0.25	5.72	0.49	0.02	314.59	29.91
MY24B015	64.8	2.9	1.28	0.69	0.07	6.50	0.43	0.01	302.13	30.85
MY24B016	51.6	1.1	0.41	0.62	0.04	6.46	0.43	<0.01	200.38	31.19
JN18A054	90.7	5.3	0.16	1.10	0.05	8.12	0.74	<0.01	337.64	33.81

Table A6.1: LA-ICPMS Analyses of Pyrite from Chapter 4

File	Analyst	Age (Ma)	Pyrite type	Setting	Mn (ppm)	Fe (ppm)	Co (ppm)	Ni (ppm)	Cu (ppm)	Zn (ppm)
MY24B012	E Lounejeva	359.0	small anhedral	Rift Basin	415.40	465536.54	266.70	174.94	47.30	295.61
MY24B013	E Lounejeva	359.0	small anhedral	Rift Basin	306.50	465534.16	327.01	158.01	86.87	210.78
JN18A063	E Lounejeva	359.0	framboid	Rift Basin	332.81	465504.86	666.92	431.33	191.08	177.14
JN18A047	E Lounejeva	359.0	framboid	Rift Basin	155.56	465470.48	625.42	458.23	307.34	254.79
JN18A049	E Lounejeva	359.0	framboid	Rift Basin	162.31	465473.02	598.99	430.05	282.66	226.39
JN18A048	E Lounejeva	359.0	framboid	Rift Basin	154.88	465458.98	680.29	498.06	334.83	296.62
JN18A050	E Lounejeva	359.0	framboid	Rift Basin	351.72	465439.85	541.07	408.03	172.40	239.86
JN18A057	E Lounejeva	359.0	framboid	Rift Basin	283.47	465501.05	590.57	401.14	186.23	239.70
JN18A051	E Lounejeva	359.0	framboid	Rift Basin	349.93	465459.36	776.97	945.54	985.15	229.64
JN18A052	E Lounejeva	359.0	framboid	Rift Basin	294.90	465456.22	844.27	898.83	858.46	234.84
JN18A053	E Lounejeva	359.0	framboid	Rift Basin	315.07	465452.51	788.09	889.07	880.65	242.19
JN18A058	E Lounejeva	359.0	framboid	Rift Basin	557.83	465458.49	1087.16	1078.72	1128.79	215.47
JN18A060	E Lounejeva	359.0	framboid	Rift Basin	613.45	465441.78	1227.81	1470.67	1781.72	186.58
JN18A059	E Lounejeva	359.0	framboid	Rift Basin	607.11	465449.91	1197.87	1223.54	1339.55	193.74
JN18A061	E Lounejeva	359.0	framboid	Rift Basin	558.62	465434.41	1391.63	901.37	640.70	271.26
JL31D75	E Lounejeva	360.0	small anhedral	Rift Basin	115.62	465526.63	222.95	176.80	151.53	38.91
JL31D81	E Lounejeva	360.0	small anhedral	Rift Basin	900.36	465517.03	84.47	295.22	279.32	67.83
JL31D83	E Lounejeva	360.0	small anhedral	Rift Basin	1024.71	465537.89	69.26	333.10	273.68	122.58
JL31D79	E Lounejeva	360.0	small anhedral	Rift Basin	1183.66	465508.28	103.29	433.93	360.07	178.83
JL31D84	E Lounejeva	360.0	small anhedral	Rift Basin	3082.01	465420.65	274.33	987.39	707.30	182.18
JL31D88	E Lounejeva	360.0	small anhedral	Rift Basin	2769.22	465461.35	301.07	1064.50	1341.68	523.39
JL31D76	E Lounejeva	360.0	small anhedral	Rift Basin	1948.29	465488.90	216.08	818.82	726.99	215.08
JL31D87	E Lounejeva	360.0	small anhedral	Rift Basin	2330.95	465491.45	374.25	1302.72	1623.17	393.21

Table A6.1: LA-ICPMS Analyses of Pyrite from Chapter 4

File	As(ppm)	Se(ppm)	Mo(ppm)	Ag(ppm)	Cd(ppm)	Sb(ppm)	Te(ppm)	Au(ppm)	Pb(ppm)	Bi(ppm)
MY24B012	63	4.3	1.1	0.78	0.15	10.00	0.47	0.02	271.84	41.03
MY24B013	71	2.4	0.8	0.87	0.14	10.32	0.46	0.01	290.44	45.34
JN18A063	181	5.1	0.3	5.46	0.11	27.38	2.03	0.11	759.83	103.78
JN18A047	310	7.4	1.0	3.77	0.12	18.26	1.89	0.11	943.41	103.85
JN18A049	301	5.2	2.0	3.93	0.11	17.74	1.90	0.11	885.20	106.44
JN18A048	353	8.1	0.5	4.06	0.09	18.66	2.22	0.09	918.34	108.63
JN18A050	425	8.7	1.2	3.54	0.20	18.69	2.78	0.09	824.31	109.94
JN18A057	196	5.4	0.5	2.48	0.14	22.36	1.45	0.06	565.39	118.24
JN18A051	352	9.5	0.7	11.77	0.31	35.43	3.01	0.25	2675.99	177.53
JN18A052	363	9.2	0.9	10.41	0.37	39.18	3.59	0.22	2516.80	184.84
JN18A053	377	8.6	0.7	10.56	0.30	37.53	3.38	0.24	2586.13	185.02
JN18A058	355	9.5	0.9	13.03	0.33	47.28	3.87	0.25	3375.43	215.88
JN18A060	418	12.1	1.5	17.41	0.41	53.11	4.24	0.31	5041.68	229.54
JN18A059	387	10.4	0.8	14.61	0.35	49.99	4.13	0.27	3790.90	242.22
JN18A061	445	8.1	0.7	7.92	0.16	48.02	3.74	0.16	1785.43	245.00
JL31D75	100	6.0	17.7	0.40	1.55	7.10	0.78	0.02	187.32	1.43
JL31D81	136	14.1	25.3	2.68	0.89	8.66	4.32	0.04	189.77	2.76
JL31D83	57	8.0	8.7	0.19	0.48	3.57	1.94	<0.01	212.86	3.48
JL31D79	168	13.2	18.1	1.96	1.34	8.83	3.59	0.04	269.19	4.57
JL31D84	497	44.0	66.2	9.00	2.87	27.83	14.35	0.15	492.64	7.20
JL31D88	344	23.2	41.5	4.64	5.23	24.45	8.12	0.08	837.87	15.01
JL31D76	241	14.9	21.3	1.95	2.45	15.18	3.47	<0.01	730.42	15.49
JL31D87	231	16.2	29.1	2.06	3.98	21.84	5.56	0.03	1017.66	19.32

Table A6.1: LA-ICPMS Analyses of Pyrite from Chapter 4

File	Analyst	Age (Ma)	Pyrite type	Setting	Mn (ppm)	Fe (ppm)	Co (ppm)	Ni (ppm)	Cu (ppm)	Zn (ppm)
MY24B033	E Lounejeva	365.0	framboid	Rift Basin	1241.16	465391.88	68.09	162.03	130.50	77.14
MY24B032	E Lounejeva	365.0	framboid	Rift Basin	1020.91	465382.72	83.64	166.07	139.55	84.79
MY24B034	E Lounejeva	365.0	framboid	Rift Basin	1116.40	465373.23	65.46	194.61	138.00	87.84
MY24B051	E Lounejeva	365.0	framboid	Rift Basin	1443.28	465331.38	104.41	167.29	182.10	71.83
MY24B041	E Lounejeva	365.0	framboid	Rift Basin	1851.36	465354.34	122.21	116.18	236.59	167.45
MY24B047	E Lounejeva	365.0	framboid	Rift Basin	1918.03	465373.79	115.04	123.70	130.19	174.17
MY24B050	E Lounejeva	365.0	framboid	Rift Basin	1672.04	465306.32	155.48	177.22	239.58	77.74
MY24B048	E Lounejeva	365.0	framboid	Rift Basin	1619.61	465412.05	129.40	132.52	161.31	267.19
MY24B036	E Lounejeva	365.0	framboid	Rift Basin	1289.96	465455.30	156.17	153.42	168.88	231.98
MY24B038	E Lounejeva	365.0	framboid	Rift Basin	653.85	465451.22	340.22	374.79	233.89	131.98
JL31D110	E Lounejeva	365.0	framboid	Rift Basin	2158.65	465509.07	177.17	57.45	69.96	173.03
JL31D106	E Lounejeva	365.0	framboid	Rift Basin	80.79	465508.54	185.11	57.21	46.38	109.65
MY24B040	E Lounejeva	365.0	framboid	Rift Basin	1936.36	465328.36	615.00	560.58	458.68	205.27
MY24B046	E Lounejeva	365.0	framboid	Rift Basin	3105.29	465258.34	604.79	783.46	1072.36	161.20
JL31D94	E Lounejeva	365.0	framboid	Rift Basin	1107.75	465522.04	166.21	58.09	53.32	87.10
JL31D92	E Lounejeva	365.0	framboid	Rift Basin	409.93	465511.28	263.61	98.85	80.40	169.85
JL31D93	E Lounejeva	365.0	framboid	Rift Basin	254.16	465510.98	253.18	98.05	74.01	201.30
JL31D91	E Lounejeva	365.0	framboid	Rift Basin	492.15	465511.81	288.98	115.02	80.92	194.79
JL31D108	E Lounejeva	365.0	framboid	Rift Basin	213.84	465515.37	231.07	90.87	56.87	152.69
JL31D96	E Lounejeva	365.0	framboid	Rift Basin	137.58	465487.37	370.87	108.49	79.35	196.49
JL31D97	E Lounejeva	365.0	framboid	Rift Basin	255.19	465504.25	487.46	121.63	90.07	214.11
JL31D112	E Lounejeva	365.0	framboid	Rift Basin	1161.17	465497.04	594.36	128.77	112.66	93.19
JL31D113	E Lounejeva	365.0	framboid	Rift Basin	1985.89	465506.63	562.55	131.07	111.22	106.66

Table A6.1: LA-ICPMS Analyses of Pyrite from Chapter 4

File	As(ppm)	Se(ppm)	Mo(ppm)	Ag(ppm)	Cd(ppm)	Sb(ppm)	Te(ppm)	Au(ppm)	Pb(ppm)	Bi(ppm)
MY24B033	604.5	7.2	26.93	0.83	0.22	4.20	0.98	0.03	229.21	1.68
MY24B032	638.8	7.1	28.29	0.84	0.18	5.08	0.74	0.04	247.66	2.07
MY24B034	674.4	7.1	29.71	1.01	0.29	4.74	1.17	0.04	301.49	2.22
MY24B051	831.2	2.4	39.13	0.79	0.31	7.58	1.13	0.02	338.95	3.23
MY24B041	745.2	15.9	40.69	0.59	0.46	5.95	0.63	0.07	196.79	3.33
MY24B047	672.3	2.7	31.75	0.60	0.23	4.62	0.27	0.02	230.03	4.34
MY24B050	925.1	2.4	57.22	0.90	0.42	11.40	1.56	0.03	421.00	4.67
MY24B048	529.0	4.3	53.58	0.40	0.31	6.39	0.42	0.12	260.63	5.78
MY24B036	366.9	3.0	23.55	0.62	0.81	5.49	0.91	0.03	251.34	6.82
MY24B038	382.2	4.4	30.74	0.84	0.11	12.01	1.10	<0.01	440.69	12.76
JL31D110	165.5	3.1	1.30	0.49	<0.066	1.70	0.71	<0.01	102.10	16.02
JL31D106	167.5	4.2	0.76	0.41	<0.066	1.36	1.04	0.02	75.05	19.21
MY24B040	842.5	11.2	82.88	2.10	0.63	26.30	2.12	0.05	947.58	20.65
MY24B046	1104.8	16.4	270.80	2.64	1.31	43.00	5.65	0.16	1083.32	24.83
JL31D94	116.9	1.5	1.37	0.32	0.10	3.69	1.24	0.02	93.41	27.69
JL31D92	157.2	2.8	2.05	0.74	0.11	2.18	1.82	0.04	157.94	30.93
JL31D93	158.3	3.2	1.89	0.58	0.17	2.07	1.50	0.02	140.02	30.96
JL31D91	155.2	4.8	2.37	0.86	0.19	2.41	1.89	0.02	163.23	33.51
JL31D108	141.9	<0.78	1.32	0.47	<0.066	1.67	1.34	<0.01	166.08	49.01
JL31D96	246.8	2.9	0.66	0.80	0.26	7.12	2.82	0.06	262.92	68.93
JL31D97	183.5	4.8	0.69	0.87	<0.066	9.63	3.53	0.04	333.79	90.70
JL31D112	210.5	3.0	0.80	1.08	0.25	15.10	4.10	0.06	253.18	95.21
JL31D113	174.6	4.0	0.92	0.91	0.18	12.33	3.39	0.07	248.20	98.30

Table A6.1: LA-ICPMS Analyses of Pyrite from Chapter 4

File	Analyst	Age (Ma)	Pyrite type	Setting	Mn (ppm)	Fe (ppm)	Co (ppm)	Ni (ppm)	Cu (ppm)	Zn (ppm)
JL31D111	E Lounejeva	365.0	framboid	Rift Basin	2316.93	465508.26	573.30	137.66	122.67	115.39
AP17A019	E Lounejeva	367.0	nodule		807.34	465485.75	87.12	367.45	239.80	29.98
AP17A018	E Lounejeva	367.0	nodule		1061.01	465484.40	272.32	540.96	260.48	40.81
AP17A023	E Lounejeva	367.0	nodule		697.41	465487.66	314.50	711.22	346.25	47.35
MY09A093	E Lounejeva	367.0	nodule		191.42	465446.51	614.89	1274.73	44.96	623.64
MY09A090	E Lounejeva	367.0	nodule		103.16	465447.42	624.64	528.11	305.69	121.99
MY09A081	E Lounejeva	367.0	nodule		12.08	465430.05	394.79	443.69	259.79	2.05
AP17A013	E Lounejeva	367.0	nodule		1312.00	465469.83	381.55	584.11	299.42	36.46
AP17A015	E Lounejeva	367.0	nodule		1057.09	465466.31	345.31	569.69	297.30	28.12
AP17A014	E Lounejeva	367.0	nodule		1895.42	465465.53	382.41	625.22	309.81	31.92
AP17A020	E Lounejeva	367.0	nodule		1262.45	465466.24	450.12	658.81	347.64	48.59
AP17A022	E Lounejeva	367.0	nodule		1521.56	465459.06	491.42	716.83	368.37	39.98
MY09A089	E Lounejeva	367.0	nodule		131.10	465428.09	690.14	578.45	355.59	141.65
AP17A021	E Lounejeva	367.0	nodule		76.66	465460.45	385.86	789.00	389.28	42.46
MY09A082	E Lounejeva	367.0	nodule		3.00	465415.24	609.00	555.45	374.35	22.40
AP17A017	E Lounejeva	367.0	nodule		1583.42	465454.41	514.84	717.91	359.35	44.06
AP17A026	E Lounejeva	367.0	nodule		130.25	465504.14	281.24	986.99	359.38	59.25
AP17A029	E Lounejeva	367.0	nodule		190.97	465490.41	240.39	1387.52	354.83	74.39
MY09A087	E Lounejeva	367.0	nodule		104.32	465424.06	709.79	567.51	347.67	133.83
AP17A028	E Lounejeva	367.0	nodule		158.82	465488.08	222.27	825.61	371.75	76.08
MY09A083	E Lounejeva	367.0	nodule		124.36	465429.78	680.97	563.51	401.88	110.95
MY09A091	E Lounejeva	367.0	nodule		154.87	465427.75	728.74	672.95	453.89	147.07
MY09A084	E Lounejeva	367.0	nodule		100.03	465401.28	572.01	590.12	418.83	95.68

Table A6.1: LA-ICPMS Analyses of Pyrite from Chapter 4

File	As(ppm)	Se(ppm)	Mo(ppm)	Ag(ppm)	Cd(ppm)	Sb(ppm)	Te(ppm)	Au(ppm)	Pb(ppm)	Bi(ppm)
JL31D111	169	3.8	1.0	1.09	0.25	11.33	3.94	0.08	283.88	107.11
AP17A019	253	1.1	1.0	1.14	1.06	12.51	0.17	<0.01	145.25	0.48
AP17A018	258	2.9	1.6	2.04	1.09	14.15	0.14	<0.01	335.91	0.52
AP17A023	246	1.7	2.3	2.66	0.82	14.29	0.37	<0.01	282.82	0.56
MY09A093	400	7.6	2.3	0.67	0.46	102.96	0.47	<0.01	445.29	0.57
MY09A090	396	2.4	6.8	2.87	1.12	36.88	0.31	<0.01	511.48	0.59
MY09A081	462	1.9	10.4	3.09	1.79	27.01	0.50	<0.01	415.41	0.69
AP17A013	312	3.1	3.6	2.52	1.02	17.43	0.17	<0.01	413.20	0.69
AP17A015	326	2.3	1.6	2.20	1.19	17.79	0.26	<0.01	461.71	0.70
AP17A014	329	2.3	1.8	2.51	0.88	16.82	0.21	<0.01	404.70	0.70
AP17A020	326	1.6	2.0	2.44	0.89	17.66	0.28	<0.01	343.04	0.73
AP17A022	353	2.2	2.6	2.63	1.06	18.15	0.26	<0.01	413.58	0.80
MY09A089	469	2.3	8.1	3.29	1.24	48.58	0.55	<0.01	735.30	0.88
AP17A021	348	1.4	1.5	2.89	0.98	16.98	0.25	<0.01	315.78	0.89
MY09A082	517	3.0	23.7	4.60	1.55	39.74	0.62	<0.01	547.35	0.92
AP17A017	370	1.9	1.7	2.52	1.17	20.75	0.30	<0.01	434.32	0.98
AP17A026	184	0.9	1.2	4.02	0.40	5.38	0.15	<0.01	194.28	1.00
AP17A029	235	0.8	1.6	3.73	0.93	12.75	0.22	<0.01	282.77	1.08
MY09A087	484	2.2	13.0	3.35	1.39	52.25	0.59	<0.01	624.72	1.12
AP17A028	244	0.5	1.6	3.37	0.42	9.57	0.19	<0.01	161.65	1.17
MY09A083	463	2.1	9.1	3.63	1.16	49.43	0.65	<0.01	592.94	1.31
MY09A091	470	2.4	8.2	3.63	1.39	52.93	0.86	<0.01	644.29	1.53
MY09A084	569	2.2	9.8	4.11	1.29	48.72	0.95	<0.01	698.81	1.57

Table A6.1: LA-ICPMS Analyses of Pyrite from Chapter 4

File	Analyst	Age (Ma)	Pyrite type	Setting	Mn (ppm)	Fe (ppm)	Co (ppm)	Ni (ppm)	Cu (ppm)	Zn (ppm)
MY09A092	E Lounejeva	367.0	nodule		160.29	465423.88	719.15	688.97	413.49	137.38
MY09A086	E Lounejeva	367.0	nodule		136.27	465421.10	779.07	611.20	411.48	207.26
AP17A027	E Lounejeva	367.0	nodule		183.28	465476.12	249.21	904.30	346.61	78.08
MY09A085	E Lounejeva	367.0	nodule		119.21	465439.39	656.61	574.54	405.64	166.23
AP17A032	E Lounejeva	367.0	nodule		160.33	465478.87	160.80	997.77	134.37	138.27
MY09A088	E Lounejeva	367.0	nodule		118.78	465407.88	971.58	1015.99	455.38	118.05
AP17A033	E Lounejeva	367.0	nodule		1905.11	465460.19	395.50	692.52	305.32	79.72
JL31D121	E Lounejeva	370.0	framboid	Rift Basin	518.65	465537.12	172.45	26.67	59.19	19.82
JL31D122	E Lounejeva	370.0	framboid	Rift Basin	476.79	465536.82	141.14	32.28	59.56	32.63
JL31D123	E Lounejeva	370.0	framboid	Rift Basin	345.99	465532.37	221.08	37.84	50.75	57.56
JL31D115	E Lounejeva	370.0	framboid	Rift Basin	1043.35	465491.27	196.27	67.65	32.44	180.71
JL31D119	E Lounejeva	370.0	framboid	Rift Basin	477.23	465428.55	136.19	69.10	41.10	271.24
JL31D118	E Lounejeva	370.0	framboid	Rift Basin	344.91	465431.68	151.22	69.35	35.01	191.70
JL31D117	E Lounejeva	370.0	framboid	Rift Basin	3528.12	465524.21	202.47	97.54	48.80	52.35
MY28A023	E Lounejeva	370.0	small anhedral	Rift Basin	279.50	465126.84	233.16	116.61	67.35	51.48
MY28A039	E Lounejeva	370.0	small anhedral	Rift Basin	1220.13	464890.21	506.22	274.91	385.72	165.48
MY28A041	E Lounejeva	370.0	small anhedral	Rift Basin	1502.82	464956.68	460.45	228.05	400.13	120.11
MY28A025	E Lounejeva	370.0	small anhedral	Rift Basin	282.41	465114.59	276.52	122.86	111.55	62.31
MY28A056	E Lounejeva	370.0	small anhedral	Rift Basin	1045.62	465147.93	378.69	203.42	119.55	105.92
MY28A024	E Lounejeva	370.0	small anhedral	Rift Basin	245.02	465128.69	242.43	115.77	100.57	54.92
MY28A051	E Lounejeva	370.0	small anhedral	Rift Basin	1435.78	465042.87	397.31	305.54	390.30	2348.13
MY28A048	E Lounejeva	370.0	small anhedral	Rift Basin	1581.62	465085.09	517.38	367.32	301.82	1754.99
MY28A049	E Lounejeva	370.0	small anhedral	Rift Basin	1102.95	464973.79	586.67	384.00	422.71	5036.76

Table A6.1: LA-ICPMS Analyses of Pyrite from Chapter 4

File	As(ppm)	Se(ppm)	Mo(ppm)	Ag(ppm)	Cd(ppm)	Sb(ppm)	Te(ppm)	Au(ppm)	Pb(ppm)	Bi(ppm)
MY09A092	484.6	2.3	8.51	4.04	1.44	55.12	0.75	<0.01	665.20	1.59
MY09A086	495.1	2.5	8.86	3.42	1.35	69.56	0.86	<0.01	712.21	1.59
AP17A027	288.9	1.0	1.78	3.41	0.59	12.15	0.26	<0.01	213.61	1.60
MY09A085	426.5	1.4	9.78	3.11	1.33	54.57	0.82	<0.01	636.37	1.79
AP17A032	278.6	1.2	11.81	1.87	1.71	13.79	0.71	<0.01	900.38	2.19
MY09A088	544.6	<0.78	5.84	7.92	1.77	57.50	1.11	<0.01	899.95	3.26
AP17A033	348.6	1.1	4.22	3.35	1.38	26.39	0.93	<0.01	625.84	4.32
JL31D121	60.4	2.3	25.04	0.12	0.09	2.94	0.21	<0.01	232.25	3.68
JL31D122	61.5	2.1	9.92	0.16	0.11	2.90	0.18	<0.01	181.55	3.99
JL31D123	78.2	2.5	24.21	0.25	0.18	2.99	0.23	0.01	203.38	5.37
JL31D115	232.1	3.8	5.17	0.21	0.30	3.58	0.43	<0.01	103.43	8.77
JL31D119	467.1	52.6	8.31	0.40	<0.066	1.03	0.47	0.15	58.03	10.62
JL31D118	455.4	66.0	8.25	0.32	<0.066	1.13	0.52	0.07	68.74	11.43
JL31D117	108.8	5.6	9.32	0.46	<0.066	3.79	0.83	<0.01	152.91	13.29
MY28A023	1597.5	1.9	1.21	0.52	0.13	5.93	0.62	0.02	184.00	17.13
MY28A039	2484.0	8.1	218.13	1.38	1.31	12.16	2.00	0.04	270.76	17.77
MY28A041	2235.0	7.4	182.70	1.41	1.02	12.14	2.70	0.08	283.50	17.91
MY28A025	1643.4	2.3	5.22	0.59	0.15	7.36	1.05	0.03	219.59	18.49
MY28A056	1518.5	2.0	5.67	0.71	<0.066	7.50	1.61	0.13	221.99	18.51
MY28A024	1590.5	1.5	2.82	0.57	0.12	7.29	1.12	0.02	214.11	18.94
MY28A051	1912.1	4.5	154.06	1.56	6.47	17.49	1.80	0.08	373.39	28.13
MY28A048	1753.9	12.5	114.30	1.38	5.97	17.70	2.79	0.09	420.35	30.21
MY28A049	2170.9	8.4	143.38	1.61	12.12	18.12	2.16	0.05	457.72	30.82

Table A6.1: LA-ICPMS Analyses of Pyrite from Chapter 4

File	Analyst	Age (Ma)	Pyrite type	Setting	Mn (ppm)	Fe (ppm)	Co (ppm)	Ni (ppm)	Cu (ppm)	Zn (ppm)
JL31D127	E Lounejeva	370.0	framboid	Rift Basin	824.98	465412.64	356.19	186.14	86.27	313.67
MY28A057	E Lounejeva	370.0	small anhedral	Rift Basin	0.42	465253.61	555.78	276.58	215.10	48.19
JL31D116	E Lounejeva	370.0	framboid	Rift Basin	770.89	465421.90	611.25	351.56	161.00	203.71
MY28A058	E Lounejeva	370.0	small anhedral	Rift Basin	656.58	465263.04	627.91	667.09	522.56	1.05
JN18A025	E Lounejeva	383.0	large euhedral	Rift Basin	5.42	465542.65	12.26	18.36	2.80	5.45
JN18A012	E Lounejeva	383.0	large euhedral	Rift Basin	2.53	465550.26	2.25	8.92	0.18	3.88
JN18A008	E Lounejeva	383.0	large euhedral	Rift Basin	1.28	465546.09	8.15	11.61	2.55	3.71
JN18A021	E Lounejeva	383.0	large euhedral	Rift Basin	11.06	465540.73	12.21	17.63	5.16	4.66
JN18A010	E Lounejeva	383.0	large euhedral	Rift Basin	2.26	465541.43	16.73	19.33	4.12	3.80
JN18A029	E Lounejeva	383.0	large euhedral	Rift Basin	8.00	465547.49	3.76	9.70	3.02	5.46
JN18A014	E Lounejeva	383.0	large euhedral	Rift Basin	40.42	465534.04	20.31	22.22	1.35	6.35
JN18A015	E Lounejeva	383.0	large euhedral	Rift Basin	5.96	465539.81	17.13	18.91	2.27	4.87
JN18A019	E Lounejeva	383.0	large euhedral	Rift Basin	38.52	465534.56	34.23	20.23	3.33	1.78
JN18A009	E Lounejeva	383.0	large euhedral	Rift Basin	0.89	465533.91	5.92	10.40	3.41	3.40
JN18A022	E Lounejeva	383.0	large euhedral	Rift Basin	20.54	465547.79	3.70	8.34	3.79	6.91
JN18A017	E Lounejeva	383.0	large euhedral	Rift Basin	33.33	465530.39	43.91	24.40	3.07	0.33
JN18A023	E Lounejeva	383.0	large euhedral	Rift Basin	16.68	465547.21	18.27	19.62	2.84	7.58
JN18A030	E Lounejeva	383.0	large euhedral	Rift Basin	0.04	465545.90	5.67	12.58	0.04	2.91
JN18A018	E Lounejeva	383.0	large euhedral	Rift Basin	36.64	465549.58	14.10	15.05	0.61	0.12
JN18A028	E Lounejeva	383.0	large euhedral	Rift Basin	19.14	465533.95	17.21	22.00	9.95	4.22
JN18A020	E Lounejeva	383.0	large euhedral	Rift Basin	24.13	465549.63	10.63	9.58	3.16	1.86
JN18A016	E Lounejeva	383.0	large euhedral	Rift Basin	4.06	465546.47	5.03	8.58	2.87	5.81
JN18A024	E Lounejeva	383.0	large euhedral	Rift Basin	39.37	465550.21	6.34	12.87	6.07	8.96

Table A6.1: LA-ICPMS Analyses of Pyrite from Chapter 4

File	As(ppm)	Se(ppm)	Mo(ppm)	Ag(ppm)	Cd(ppm)	Sb(ppm)	Te(ppm)	Au(ppm)	Pb(ppm)	Bi(ppm)
JL31D127	527	<0.78	3.7	1.71	0.65	18.65	1.44	0.04	358.76	38.39
MY28A057	1123	3.3	1.2	1.65	0.16	23.86	2.40	0.03	549.62	62.69
JL31D116	492	6.3	9.5	1.44	0.26	12.34	3.31	0.11	339.32	73.60
MY28A058	1087	3.4	6.6	1.43	0.24	27.48	6.32	0.03	835.50	73.95
JN18A025	40	1.8	8.8	0.02	0.42	0.94	0.12	<0.01	8.86	0.00
JN18A012	11	2.4	4.3	<0.01	0.22	0.69	0.12	<0.01	1.31	<0.01
JN18A008	27	2.3	10.6	0.02	0.37	0.75	0.14	<0.01	10.21	<0.01
JN18A021	47	2.5	11.7	0.05	0.60	1.13	0.09	<0.01	16.51	<0.01
JN18A010	44	2.7	16.6	0.03	0.29	1.03	0.14	<0.01	17.22	<0.01
JN18A029	22	1.0	9.8	0.02	0.36	0.85	0.16	<0.01	6.86	0.01
JN18A014	72	3.2	12.4	0.04	0.17	0.86	0.15	<0.01	9.16	0.01
JN18A015	50	1.8	10.8	0.01	0.26	0.90	0.09	<0.01	10.11	0.01
JN18A019	70	3.0	12.1	0.02	0.41	0.64	0.10	<0.01	10.60	0.01
JN18A009	72	2.8	15.7	0.05	0.36	1.00	0.10	<0.01	22.39	0.01
JN18A022	20	1.8	11.6	0.02	0.53	1.06	0.15	<0.01	10.16	0.01
JN18A017	86	3.2	20.7	0.02	0.31	0.64	0.17	<0.01	14.40	0.01
JN18A023	23	1.8	13.1	0.02	0.29	0.97	0.17	<0.01	12.82	0.01
JN18A030	27	1.7	4.2	0.05	0.13	0.66	0.22	<0.01	6.82	0.02
JN18A018	14	2.0	8.0	0.01	0.35	0.99	0.10	<0.01	5.61	0.02
JN18A028	72	1.5	67.0	0.04	0.49	3.36	0.15	<0.01	69.36	0.02
JN18A020	14	1.8	21.6	0.01	0.71	1.38	0.15	<0.01	15.32	0.02
JN18A016	25	1.6	7.6	0.02	0.23	0.71	0.13	<0.01	6.73	0.02
JN18A024	11	1.8	7.1	0.02	0.58	5.85	0.16	0.01	10.11	0.02

Table A6.1: LA-ICPMS Analyses of Pyrite from Chapter 4

File	Analyst	Age (Ma)	Pyrite type	Setting	Mn (ppm)	Fe (ppm)	Co (ppm)	Ni (ppm)	Cu (ppm)	Zn (ppm)
JN18A007	E Lounejeva	383.0	large euhedral	Rift Basin	11.11	465543.70	9.48	17.03	4.23	3.75
JN18A013	E Lounejeva	383.0	large euhedral	Rift Basin	118.75	465548.14	13.01	16.89	6.47	7.42
JN18A027	E Lounejeva	383.0	large euhedral	Rift Basin	24.55	465551.42	1.65	6.70	3.86	6.11
JN18A011	E Lounejeva	383.0	large euhedral	Rift Basin	57.74	465538.08	33.03	25.24	10.00	3.86
MY28A019	E Lounejeva	383.0	small anhedral	Rift Basin	6.57	465538.91	239.08	121.11	37.69	4.46
MY28A017	E Lounejeva	383.0	small anhedral	Rift Basin	82.70	465536.02	337.19	191.53	65.66	5.26
MY28A013	E Lounejeva	383.0	small anhedral	Rift Basin	368.85	465543.89	305.91	227.62	61.42	3.58
MY28A007	E Lounejeva	383.0	small anhedral	Rift Basin	2542.85	465503.83	281.67	131.63	584.97	6.15
MY28A015	E Lounejeva	383.0	small anhedral	Rift Basin	569.10	465536.49	348.03	220.51	69.43	1.78
MY28A012	E Lounejeva	383.0	small anhedral	Rift Basin	113.66	465540.62	392.19	264.55	69.68	4.52
MY28A016	E Lounejeva	383.0	small anhedral	Rift Basin	106.43	465528.83	532.13	275.85	83.90	6.32
MY28A011	E Lounejeva	383.0	small anhedral	Rift Basin	117.75	465525.10	557.50	334.64	94.14	5.98
JL30A104	D Gregory	384.0	nodule	Rift Basin	67.27	465509.20	0.51	8.48	9.82	25.13
JL30A094	D Gregory	384.0	nodule	Rift Basin	364.49	465446.86	0.25	5.13	16.28	68.26
JL30A092	D Gregory	384.0	nodule	Rift Basin	17.20	465482.45	1.26	26.03	17.89	18.99
JL30A149	D Gregory	384.0	small anhedral	Rift Basin	136.52	465545.58	238.20	429.84	12.66	49.22
JL30A165	D Gregory	384.0	nodule	Rift Basin	<0.02	465542.59	11.78	126.18	34.04	<0.02
JL30A089	D Gregory	384.0	nodule	Rift Basin	119.50	465504.87	1.70	36.37	37.42	25.67
JL30A088	D Gregory	384.0	nodule	Rift Basin	107.37	465512.83	0.96	25.70	31.15	24.29
JL30A105	D Gregory	384.0	nodule	Rift Basin	91.89	465515.77	0.63	8.35	11.36	26.18
JL30A095	D Gregory	384.0	nodule	Rift Basin	103.22	465541.75	0.89	15.00	18.99	22.55
JN12A037	E Lounejeva	384.0	small anhedral	Rift Basin	274.88	465482.64	44.22	105.20	222.26	5.46
JN12A038	E Lounejeva	384.0	small anhedral	Rift Basin	590.59	465430.27	217.42	237.24	157.75	4.32

Table A6.1: LA-ICPMS Analyses of Pyrite from Chapter 4

File	As(ppm)	Se(ppm)	Mo(ppm)	Ag(ppm)	Cd(ppm)	Sb(ppm)	Te(ppm)	Au(ppm)	Pb(ppm)	Bi(ppm)
JN18A007	35.7	2.1	19.57	0.04	0.53	1.22	0.10	<0.01	18.26	0.02
JN18A013	19.1	2.2	25.63	0.04	0.49	1.28	0.14	<0.01	18.65	0.03
JN18A027	6.8	0.9	4.11	<0.01	0.21	0.51	0.10	<0.01	1.85	0.03
JN18A011	56.8	3.1	16.02	0.04	0.79	0.93	0.18	<0.01	17.32	0.04
MY28A019	53.7	3.0	0.80	0.44	0.02	2.92	0.46	0.02	60.45	7.28
MY28A017	64.5	5.5	0.99	1.04	0.02	3.88	<0.13	0.06	99.23	10.42
MY28A013	35.0	2.8	0.68	1.68	0.02	4.13	<0.13	0.08	119.70	10.68
MY28A007	185.1	3.7	1.55	0.77	<0.066	6.93	5.75	0.07	287.94	11.95
MY28A015	62.7	5.0	0.96	1.48	0.03	4.56	<0.13	0.06	133.73	12.78
MY28A012	47.3	7.1	0.55	1.30	<0.066	5.09	0.15	0.06	127.96	13.41
MY28A016	91.4	6.7	1.20	1.57	<0.066	5.85	0.19	0.08	129.43	14.49
MY28A011	105.4	7.3	1.20	1.41	<0.066	6.70	0.30	0.08	144.09	16.00
JL30A104	165.0	220.6	17.32	0.12	0.57	7.82	0.09	0.01	2.63	<0.01
JL30A094	398.5	341.9	89.04	0.44	1.04	21.30	0.26	0.01	4.84	<0.01
JL30A092	265.2	82.2	20.58	0.14	1.21	12.21	0.14	<0.01	7.27	<0.01
JL30A149	28.7	90.7	13.19	<0.01	0.65	7.18	<0.13	0.00	7.53	<0.01
JL30A165	39.9	114.2	13.68	<0.01	1.12	14.72	<0.13	<0.01	12.41	<0.01
JL30A089	181.2	115.5	71.71	0.52	1.67	12.47	0.42	<0.01	16.89	<0.01
JL30A088	151.4	106.8	43.10	0.60	1.46	8.90	0.32	0.01	18.10	<0.01
JL30A105	140.4	231.4	21.61	0.17	0.60	7.59	0.15	0.01	3.29	0.01
JL30A095	43.0	33.6	13.44	0.23	0.84	3.52	0.14	<0.01	6.10	0.01
JN12A037	264.5	3.0	6.07	10.10	0.13	11.52	0.14	<0.01	51.16	0.01
JN12A038	460.7	4.7	28.33	1.57	1.14	11.64	<0.13	<0.01	161.65	0.01

Table A6.1: LA-ICPMS Analyses of Pyrite from Chapter 4

File	Analyst	Age (Ma)	Pyrite type	Setting	Mn (ppm)	Fe (ppm)	Co (ppm)	Ni (ppm)	Cu (ppm)	Zn (ppm)
JN12A039	E Lounejeva	384.0	small anhedral	Rift Basin	188.97	465466.40	219.78	213.67	271.67	49.83
JL30A085	D Gregory	384.0	nodule	Rift Basin	116.19	465495.37	1.62	33.57	27.01	34.93
JL30A093	D Gregory	384.0	nodule	Rift Basin	30.88	465477.46	2.07	40.68	22.91	14.54
JL30A102	D Gregory	384.0	nodule	Rift Basin	31.40	465540.86	0.02	12.01	9.31	10.35
JL30A101	D Gregory	384.0	nodule	Rift Basin	6.16	465549.50	0.01	8.27	3.66	0.51
JN12A036	E Lounejeva	384.0	small anhedral	Rift Basin	181.04	465504.11	54.11	144.33	210.52	5.70
JL30A103	D Gregory	384.0	nodule	Rift Basin	31.03	465535.15	0.13	31.77	15.09	13.73
JN12A042	E Lounejeva	384.0	small anhedral	Rift Basin	434.88	465463.98	256.48	328.30	343.93	4.85
JN12A035	E Lounejeva	384.0	small anhedral	Rift Basin	192.25	465500.24	34.50	102.41	268.89	6.40
JN12A040	E Lounejeva	384.0	small anhedral	Rift Basin	281.95	465375.46	275.99	180.34	226.41	3.88
JL30A098	D Gregory	384.0	nodule	Rift Basin	177.32	465496.17	1.85	46.40	39.01	32.70
JN12A043	E Lounejeva	384.0	small anhedral	Rift Basin	102.53	465504.28	99.91	288.32	352.58	6.55
JL30A091	D Gregory	384.0	nodule	Rift Basin	447.76	465511.58	3.47	56.79	97.74	18.36
JL30A096	D Gregory	384.0	nodule	Rift Basin	533.70	465498.88	4.99	70.34	93.84	20.01
JN12A045	E Lounejeva	384.0	small anhedral	Rift Basin	52.22	465500.30	165.37	362.67	372.24	6.68
JL30A090	D Gregory	384.0	nodule	Rift Basin	567.74	465503.43	2.64	46.77	109.59	17.48
JL30A147	D Gregory	384.0	small anhedral	Rift Basin	23.88	465301.66	21.63	101.95	17.61	15.48
JL30A097	D Gregory	384.0	nodule	Rift Basin	435.06	465498.18	3.40	75.90	97.86	17.89
JL30A086	D Gregory	384.0	nodule	Rift Basin	369.88	465507.66	5.63	86.67	90.23	22.95
JL30A087	D Gregory	384.0	nodule	Rift Basin	372.31	465498.05	5.91	135.11	102.63	21.06
JL30A152	D Gregory	384.0	nodule	Rift Basin	1.08	465543.83	9.61	77.69	30.70	2.86
JL30A164	D Gregory	384.0	nodule	Rift Basin	7.26	465544.42	10.10	131.31	32.76	2.62
JL30A161	D Gregory	384.0	nodule	Rift Basin	4.00	465542.28	8.07	93.74	34.88	3.67

Table A6.1: LA-ICPMS Analyses of Pyrite from Chapter 4

File	As(ppm)	Se(ppm)	Mo(ppm)	Ag(ppm)	Cd(ppm)	Sb(ppm)	Te(ppm)	Au(ppm)	Pb(ppm)	Bi(ppm)
JN12A039	325	4.9	37.7	4.37	0.13	14.28	0.10	<0.01	244.58	0.01
JL30A085	217	202.8	47.8	0.33	1.27	10.73	0.34	0.00	9.86	0.01
JL30A093	284	95.2	33.4	0.28	1.16	13.77	0.13	<0.01	11.08	0.02
JL30A102	46	49.0	2.9	0.10	0.41	2.07	0.12	<0.01	2.74	0.02
JL30A101	14	26.2	1.1	0.08	0.34	1.17	0.10	<0.01	2.17	0.02
JN12A036	184	3.7	5.3	9.18	0.08	12.07	0.14	<0.01	48.62	0.02
JL30A103	68	70.1	3.7	0.15	0.62	3.73	0.17	<0.01	4.71	0.02
JN12A042	334	7.2	18.4	7.67	0.10	18.33	0.16	<0.01	200.46	0.03
JN12A035	199	4.6	5.4	16.16	0.10	13.50	0.11	<0.01	21.51	0.03
JN12A040	666	6.2	42.6	1.26	0.09	20.77	0.13	<0.01	251.52	0.03
JL30A098	214	213.3	68.7	0.62	1.67	12.81	0.59	<0.01	18.50	0.04
JN12A043	183	6.4	5.5	11.33	0.16	14.10	0.18	0.00	148.92	0.04
JL30A091	156	64.5	170.4	1.83	5.29	21.75	1.18	0.02	59.18	0.05
JL30A096	204	61.9	170.1	1.79	4.73	21.65	1.05	0.02	56.13	0.05
JN12A045	198	6.3	5.6	12.76	0.17	15.46	0.16	<0.01	153.08	0.05
JL30A090	187	60.0	166.8	2.37	6.44	25.01	1.32	0.01	73.63	0.06
JL30A147	943	368.0	64.0	0.61	1.01	38.21	0.43	<0.01	18.59	0.07
JL30A097	206	51.4	194.9	2.06	5.66	23.15	1.29	0.02	62.32	0.07
JL30A086	171	58.4	137.5	1.95	5.43	19.50	1.21	0.03	50.25	0.08
JL30A087	207	58.5	186.2	2.09	6.10	23.45	1.16	0.03	63.51	0.11
JL30A152	35	130.6	12.0	0.50	1.00	13.77	0.14	<0.01	10.27	0.12
JL30A164	33	145.3	16.6	0.65	0.71	12.30	0.14	<0.01	10.90	0.13
JL30A161	41	119.1	13.5	0.74	1.00	16.02	0.25	<0.01	12.44	0.13

Table A6.1: LA-ICPMS Analyses of Pyrite from Chapter 4

File	Analyst	Age (Ma)	Pyrite type	Setting	Mn (ppm)	Fe (ppm)	Co (ppm)	Ni (ppm)	Cu (ppm)	Zn (ppm)
JL30A162	D Gregory	384.0	nodule	Rift Basin	10.76	465544.59	8.47	89.36	27.90	1.80
JN12A044	E Lounejeva	384.0	small anhedral	Rift Basin	536.81	465467.19	264.01	385.73	345.94	5.83
JL30A156	D Gregory	384.0	nodule	Rift Basin	3.83	465541.48	18.81	102.33	36.25	1.79
JL30A153	D Gregory	384.0	nodule	Rift Basin	5.79	465538.58	14.22	150.51	43.83	6.85
JL30A158	D Gregory	384.0	nodule	Rift Basin	10.16	465540.87	12.91	126.79	39.92	3.82
JL30A157	D Gregory	384.0	nodule	Rift Basin	6.57	465542.12	14.15	159.15	39.28	9.83
JL30A159	D Gregory	384.0	nodule	Rift Basin	4.35	465539.93	13.14	140.89	46.12	3.95
JL30A163	D Gregory	384.0	nodule	Rift Basin	4.87	465542.66	11.85	120.10	37.02	4.42
JL30A160	D Gregory	384.0	nodule	Rift Basin	9.67	465542.28	13.94	151.75	40.54	13.15
JL30A154	D Gregory	384.0	nodule	Rift Basin	7.53	465540.44	12.39	148.13	41.64	3.49
JL30A155	D Gregory	384.0	nodule	Rift Basin	5.13	465541.15	12.31	130.74	41.68	5.79
JN12A046	E Lounejeva	384.0	small anhedral	Rift Basin	2576.21	465477.11	275.72	341.73	241.42	6.42
JL30A148	D Gregory	384.0	small anhedral	Rift Basin	193.47	465412.75	40.03	113.42	66.96	35.07
JN12A025	E Lounejeva	384.0	small anhedral	Rift Basin	15.74	465387.57	173.86	148.98	173.27	5.04
JL30A111	D Gregory	384.0	nodule	Rift Basin	707.13	465391.49	42.63	922.46	500.32	311.56
JL30A108	D Gregory	384.0	nodule	Rift Basin	58.87	465481.42	120.01	663.51	218.30	313.83
JN12A024	E Lounejeva	384.0	small anhedral	Rift Basin	401.66	465495.55	776.35	613.58	310.43	12.59
JN12A018	E Lounejeva	384.0	small anhedral	Rift Basin	576.58	465513.98	171.28	438.08	266.78	6.21
JN12A019	E Lounejeva	384.0	small anhedral	Rift Basin	442.11	465506.28	239.17	570.61	343.38	9.18
JN12A014	E Lounejeva	384.0	small anhedral	Rift Basin	539.85	465516.05	262.42	463.33	324.32	8.27
JN12A017	E Lounejeva	384.0	small anhedral	Rift Basin	532.22	465502.52	319.30	613.12	348.37	6.65
JN12A009	E Lounejeva	384.0	small anhedral	Rift Basin	493.31	465515.40	301.29	512.01	355.09	6.26
JN12A021	E Lounejeva	384.0	small anhedral	Rift Basin	358.60	465425.03	364.30	195.35	266.91	3.90

Table A6.1: LA-ICPMS Analyses of Pyrite from Chapter 4

File	As(ppm)	Se(ppm)	Mo(ppm)	Ag(ppm)	Cd(ppm)	Sb(ppm)	Te(ppm)	Au(ppm)	Pb(ppm)	Bi(ppm)
JL30A162	32.4	135.3	15.61	0.48	0.66	9.80	0.21	<0.01	9.89	0.14
JN12A044	322.4	8.3	17.76	7.81	0.20	19.91	0.19	<0.01	216.19	0.16
JL30A156	44.0	124.9	17.36	0.81	0.91	16.26	0.24	<0.01	17.92	0.18
JL30A153	54.9	126.2	17.94	0.79	1.18	17.11	0.22	0.00	17.58	0.21
JL30A158	46.3	129.9	19.95	0.84	1.17	16.78	0.14	<0.01	14.84	0.22
JL30A157	41.6	131.8	18.56	0.89	0.95	13.68	0.28	<0.01	13.11	0.22
JL30A159	49.8	122.6	22.05	0.90	1.24	21.47	0.22	<0.01	17.35	0.23
JL30A163	39.6	103.2	16.09	1.02	1.23	18.18	0.18	<0.01	16.70	0.23
JL30A160	41.0	126.3	20.27	0.99	1.25	15.85	0.24	<0.01	17.04	0.23
JL30A154	47.9	126.6	17.69	1.02	1.02	18.18	0.29	<0.01	15.91	0.25
JL30A155	45.3	114.3	17.93	1.08	1.33	19.92	0.25	<0.01	17.10	0.26
JN12A046	285.2	9.3	12.51	4.24	1.04	15.83	<0.13	<0.01	228.04	0.26
JL30A148	526.3	492.9	74.60	1.09	3.46	97.99	1.14	<0.01	34.19	0.28
JN12A025	620.7	4.9	46.19	0.54	0.12	29.44	0.15	<0.01	318.09	0.81
JL30A111	606.0	60.9	162.98	7.39	28.52	70.90	2.81	0.13	217.04	0.83
JL30A108	269.0	102.2	101.70	2.64	9.24	20.41	1.00	<0.01	64.77	0.85
JN12A024	216.1	16.8	2.66	7.81	0.28	23.36	0.22	0.04	657.11	1.70
JN12A018	147.1	11.6	3.55	8.15	0.17	17.79	<0.13	0.04	474.40	1.83
JN12A019	175.9	12.9	4.61	10.06	0.55	21.27	0.23	0.05	620.35	2.50
JN12A014	139.3	10.4	3.47	7.80	0.24	18.90	0.26	0.03	661.87	2.63
JN12A017	190.0	16.7	3.94	8.51	0.28	22.27	<0.13	0.03	585.22	3.11
JN12A009	141.8	14.2	3.19	7.06	0.11	17.44	0.13	0.06	738.02	3.84
JN12A021	480.3	7.9	59.66	1.09	0.13	29.27	<0.13	<0.01	306.49	6.14

Table A6.1: LA-ICPMS Analyses of Pyrite from Chapter 4

File	Analyst	Age (Ma)	Pyrite type	Setting	Mn (ppm)	Fe (ppm)	Co (ppm)	Ni (ppm)	Cu (ppm)	Zn (ppm)
JN12A022	E Lounejeva	384.0	small anhedral	Rift Basin	188.86	465395.58	421.07	242.39	332.33	4.53
JN12A023	E Lounejeva	384.0	small anhedral	Rift Basin	165.69	465394.57	396.87	317.30	323.32	5.51
JL30A134	D Gregory	385.0	nodule	Rift Basin	0.78	465546.00	12.01	32.35	0.82	0.28
JL30A131	D Gregory	385.0	nodule	Rift Basin	5.49	465546.41	2.55	5.58	10.41	1.79
JL30A129	D Gregory	385.0	nodule	Rift Basin	2.96	465547.14	4.98	15.20	9.73	1.45
JL30A121	D Gregory	385.0	nodule	Rift Basin	5.19	465546.18	5.62	12.77	13.01	2.64
JL30A133	D Gregory	385.0	nodule	Rift Basin	6.13	465546.01	12.36	20.08	17.72	2.80
JL30A136	D Gregory	385.0	nodule	Rift Basin	5.88	465546.86	13.40	23.23	6.10	2.79
JL30A122	D Gregory	385.0	nodule	Rift Basin	2.92	465547.51	4.48	9.80	9.02	3.90
JL30A130	D Gregory	385.0	nodule	Rift Basin	5.32	465546.74	9.43	17.49	13.46	12.05
JL30A138	D Gregory	385.0	nodule	Rift Basin	5.09	465546.17	19.11	36.62	11.70	5.81
JL30A124	D Gregory	385.0	nodule	Rift Basin	4.67	465550.78	36.92	72.62	7.88	7.45
JL30A123	D Gregory	385.0	nodule	Rift Basin	4.44	465546.61	5.17	17.11	10.14	0.52
JL30A199	D Gregory	385.0	nodule	Rift Basin	0.75	465546.88	2.43	88.81	22.78	11.60
JL30A196	D Gregory	385.0	nodule	Rift Basin	0.46	465546.89	1.21	22.92	25.68	28.20
JL30A120	D Gregory	385.0	nodule	Rift Basin	17.34	465546.18	5.39	15.59	10.78	2.05
JL30A197	D Gregory	385.0	nodule	Rift Basin	1.50	465545.90	1.93	68.69	26.07	38.20
JL30A128	D Gregory	385.0	nodule	Rift Basin	8.35	465548.56	68.30	147.15	12.68	10.93
JL30A183	D Gregory	385.0	nodule	Rift Basin	7.78	465544.19	1.09	29.79	34.35	9.48
JL30A137	D Gregory	385.0	nodule	Rift Basin	2.88	465545.84	6.41	7.31	7.70	0.92
JL30A119	D Gregory	385.0	nodule	Rift Basin	5.60	465547.96	10.71	26.29	10.04	<0.02
JL30A193	D Gregory	385.0	nodule	Rift Basin	85.59	465541.20	1.09	35.97	37.70	6.77
JL30A135	D Gregory	385.0	nodule	Rift Basin	3.98	465546.38	9.75	20.42	10.82	2.34

Table A6.1: LA-ICPMS Analyses of Pyrite from Chapter 4

File	As(ppm)	Se(ppm)	Mo(ppm)	Ag(ppm)	Cd(ppm)	Sb(ppm)	Te(ppm)	Au(ppm)	Pb(ppm)	Bi(ppm)
JN12A022	591	9.3	65.6	1.41	0.13	33.33	0.14	0.01	366.58	6.60
JN12A023	594	10.1	47.0	1.48	0.17	44.06	0.10	0.01	361.29	8.60
JL30A134	27	38.3	21.9	<0.01	0.37	0.88	<0.13	<0.01	3.11	0.04
JL30A131	26	28.4	51.5	0.03	0.34	0.62	<0.13	0.00	4.11	0.04
JL30A129	23	42.1	38.1	0.05	0.51	0.84	<0.13	<0.01	3.78	0.04
JL30A121	26	39.8	38.6	0.13	0.58	0.84	<0.13	<0.01	4.89	0.05
JL30A133	27	39.6	47.3	0.03	0.41	0.71	<0.13	<0.01	3.41	0.05
JL30A136	24	26.0	15.4	0.06	0.53	0.91	<0.13	<0.01	3.70	0.06
JL30A122	21	32.4	6.8	0.03	0.63	1.19	0.06	<0.01	4.39	0.06
JL30A130	24	30.9	13.8	0.07	0.55	0.93	0.13	<0.01	4.13	0.06
JL30A138	26	32.3	26.0	0.09	0.48	1.17	0.11	<0.01	4.63	0.07
JL30A124	9	37.9	5.0	0.07	0.53	0.86	<0.13	<0.01	3.24	0.07
JL30A123	25	39.4	30.5	0.10	0.49	0.98	<0.13	<0.01	4.08	0.07
JL30A199	24	40.9	5.2	0.06	0.90	2.04	0.15	<0.01	9.56	0.07
JL30A196	24	30.6	7.4	0.11	0.94	2.45	<0.13	0.00	12.25	0.07
JL30A120	26	45.7	22.6	0.04	0.59	1.16	<0.13	<0.01	4.02	0.08
JL30A197	27	38.6	11.5	0.09	1.03	2.70	0.12	<0.01	11.04	0.08
JL30A128	18	42.6	7.8	0.09	0.66	1.28	0.16	0.00	4.93	0.08
JL30A183	34	29.2	13.1	0.14	1.04	3.55	0.21	0.00	14.23	0.08
JL30A137	28	29.5	53.1	0.09	0.46	0.95	<0.13	0.01	4.59	0.09
JL30A119	20	41.8	6.8	0.06	0.64	1.47	<0.13	<0.01	5.14	0.09
JL30A193	45	20.2	9.6	0.07	1.22	2.63	0.19	<0.01	14.49	0.10
JL30A135	26	31.8	21.8	0.13	0.52	1.02	0.07	<0.01	5.40	0.11

Table A6.1: LA-ICPMS Analyses of Pyrite from Chapter 4

File	Analyst	Age (Ma)	Pyrite type	Setting	Mn (ppm)	Fe (ppm)	Co (ppm)	Ni (ppm)	Cu (ppm)	Zn (ppm)
JL30A187	D Gregory	385.0	nodule	Rift Basin	3.51	465544.28	11.14	253.87	35.06	3.73
JL30A181	D Gregory	385.0	nodule	Rift Basin	2.94	465541.03	1.64	39.60	40.76	3.09
JL30A195	D Gregory	385.0	nodule	Rift Basin	3.04	465542.86	1.94	84.71	36.59	51.81
JL30A198	D Gregory	385.0	nodule	Rift Basin	1.44	465547.41	2.54	59.34	26.24	74.83
JL30A182	D Gregory	385.0	nodule	Rift Basin	7.36	465544.21	2.44	62.58	36.72	34.13
JL30A185	D Gregory	385.0	nodule	Rift Basin	5.13	465545.75	1.25	36.98	31.69	23.84
JL30A186	D Gregory	385.0	nodule	Rift Basin	8.46	465544.42	1.79	60.68	37.30	0.77
JL30A132	D Gregory	385.0	nodule	Rift Basin	6.68	465547.55	50.38	73.44	12.97	6.43
JL30A194	D Gregory	385.0	nodule	Rift Basin	6.63	465539.32	1.26	61.71	44.36	12.01
JL30A192	D Gregory	385.0	nodule	Rift Basin	5.04	465542.95	2.43	121.44	54.17	45.51
JL30A184	D Gregory	385.0	nodule	Rift Basin	4.77	465544.99	3.05	83.06	43.68	39.53
JL30A191	D Gregory	385.0	nodule	Rift Basin	213.09	465528.04	32.15	171.75	65.92	69.38
JL30A275	D Gregory	386.0	small anhedral	Rift Basin	<0.02	465553.17	0.00	0.77	0.15	<0.02
JL30A274	D Gregory	386.0	small anhedral	Rift Basin	<0.02	465553.17	0.10	8.36	0.57	0.33
JL30A276	D Gregory	386.0	small anhedral	Rift Basin	<0.02	465553.16	0.01	0.70	0.35	0.37
JL30A292	D Gregory	386.0	small anhedral	Rift Basin	<0.02	465553.13	0.79	3.32	0.30	<0.02
JL30A287	D Gregory	386.0	small anhedral	Rift Basin	0.52	465552.00	8.63	57.77	5.83	0.23
JL30A293	D Gregory	386.0	small anhedral	Rift Basin	0.27	465551.51	8.57	98.11	6.79	1.71
JL30A285	D Gregory	386.0	small anhedral	Rift Basin	8.82	465551.11	18.83	142.20	5.54	5.62
JL30A281	D Gregory	386.0	small anhedral	Rift Basin	1.07	465552.73	3.08	23.70	4.99	2.19
JL30A283	D Gregory	386.0	small anhedral	Rift Basin	<0.02	465553.02	21.27	66.77	2.90	0.52
JL30A284	D Gregory	386.0	small anhedral	Rift Basin	1.43	465550.58	6.80	102.01	7.73	1.75
JL30A286	D Gregory	386.0	small anhedral	Rift Basin	17.61	465551.48	0.78	35.63	9.63	1.69

Table A6.1: LA-ICPMS Analyses of Pyrite from Chapter 4

File	As(ppm)	Se(ppm)	Mo(ppm)	Ag(ppm)	Cd(ppm)	Sb(ppm)	Te(ppm)	Au(ppm)	Pb(ppm)	Bi(ppm)
JL30A187	33.6	50.2	5.80	0.10	1.02	3.95	0.20	<0.01	13.72	0.11
JL30A181	45.7	34.5	11.78	0.14	1.21	4.76	0.18	<0.01	17.45	0.12
JL30A195	38.9	38.9	9.60	0.08	1.75	3.39	0.16	<0.01	21.84	0.13
JL30A198	21.8	39.4	8.84	0.12	1.46	2.47	<0.13	<0.01	11.54	0.13
JL30A182	33.8	29.2	11.05	0.14	1.11	3.96	0.18	<0.01	16.65	0.13
JL30A185	28.1	27.5	8.94	0.15	1.03	3.32	0.14	<0.01	13.16	0.13
JL30A186	33.0	61.2	13.10	0.22	1.47	3.10	0.25	<0.01	15.68	0.14
JL30A132	21.3	32.4	9.39	0.16	0.67	1.53	<0.13	<0.01	7.03	0.17
JL30A194	52.1	47.0	8.11	0.16	3.57	4.34	0.24	<0.01	19.66	0.17
JL30A192	38.5	48.7	7.56	0.16	1.90	3.05	0.17	<0.01	19.28	0.17
JL30A184	30.9	25.7	32.09	0.32	0.86	2.82	0.23	<0.01	14.98	0.26
JL30A191	94.4	33.2	58.96	0.88	1.05	6.81	0.30	<0.01	22.82	0.27
JL30A275	0.3	5.1	0.25	<0.01	0.01	11.60	<0.13	<0.01	0.03	<0.01
JL30A274	0.3	5.3	1.11	<0.01	<0.066	0.04	0.07	<0.01	0.03	<0.01
JL30A276	0.3	9.2	0.21	<0.01	<0.066	11.60	<0.13	<0.01	0.03	<0.01
JL30A292	0.4	8.3	0.15	0.01	<0.066	0.08	0.08	0.00	0.06	<0.01
JL30A287	4.6	14.1	2.49	<0.01	0.02	0.38	0.05	<0.01	0.59	<0.01
JL30A293	6.5	12.6	0.70	<0.01	0.03	0.35	0.11	<0.01	0.67	<0.01
JL30A285	8.0	12.0	1.51	0.02	0.08	0.37	<0.13	<0.01	0.79	<0.01
JL30A281	1.9	7.2	23.86	0.03	0.04	0.06	<0.13	<0.01	0.39	0.01
JL30A283	0.8	4.2	23.02	0.02	0.03	11.60	<0.13	<0.01	0.33	0.02
JL30A284	10.0	15.3	1.33	0.02	0.08	0.43	<0.13	<0.01	1.25	0.02
JL30A286	6.6	17.1	3.47	0.06	<0.066	0.54	0.11	0.01	1.31	0.02

Table A6.1: LA-ICPMS Analyses of Pyrite from Chapter 4

File	Analyst	Age (Ma)	Pyrite type	Setting	Mn (ppm)	Fe (ppm)	Co (ppm)	Ni (ppm)	Cu (ppm)	Zn (ppm)
JL30A282	D Gregory	386.0	small anhedral	Rift Basin	3.45	465551.07	0.12	11.90	27.53	1.08
JL30A320	D Gregory	386.5	nodule	Rift Basin	6.88	465542.41	4.92	136.44	53.03	17.80
JL30A211	D Gregory	386.5	nodule	Rift Basin	28.90	465547.84	2.68	115.17	68.66	6.74
JL30A315	D Gregory	386.5	nodule	Rift Basin	2.94	465546.64	1.82	77.81	43.37	6.34
JL30A213	D Gregory	386.5	nodule	Rift Basin	4.21	465548.34	2.60	75.33	37.87	14.13
JL30A306	D Gregory	386.5	nodule	Rift Basin	1.97	465542.65	1.54	71.89	65.76	19.75
JL30A304	D Gregory	386.5	nodule	Rift Basin	4.41	465544.15	2.21	93.91	66.72	20.32
JL30A312	D Gregory	386.5	nodule	Rift Basin	5.09	465542.54	2.28	81.28	63.28	45.51
JL30A319	D Gregory	386.5	nodule	Rift Basin	4.02	465545.66	2.20	122.88	63.61	14.69
JL30A214	D Gregory	386.5	nodule	Rift Basin	11.21	465547.29	3.03	112.35	40.47	16.66
JL30A323	D Gregory	386.5	nodule	Rift Basin	3.48	465541.13	4.55	146.40	63.09	11.85
JL30A303	D Gregory	386.5	nodule	Rift Basin	2.31	465541.67	2.46	101.45	71.40	19.98
JL30A215	D Gregory	386.5	nodule	Rift Basin	3.47	465548.13	1.81	71.75	42.82	56.65
JL30A216	D Gregory	386.5	nodule	Rift Basin	16.67	465547.42	2.94	106.38	34.47	50.20
JL30A314	D Gregory	386.5	nodule	Rift Basin	3.58	465544.73	3.27	154.52	61.79	31.48
JL30A313	D Gregory	386.5	nodule	Rift Basin	8.43	465541.83	6.80	251.24	60.83	15.74
JL30A302	D Gregory	386.5	nodule	Rift Basin	4.81	465543.19	3.59	120.70	72.98	25.77
JL30A305	D Gregory	386.5	nodule	Rift Basin	3.01	465541.83	5.60	139.60	76.83	25.63
JL30A210	D Gregory	386.5	nodule	Rift Basin	4.23	465545.85	4.37	145.21	39.09	37.57
JL30A220	D Gregory	386.5	nodule	Rift Basin	10.39	465543.72	18.36	146.47	40.35	66.83
JL30A318	D Gregory	386.5	nodule	Rift Basin	2.76	465544.95	3.58	129.04	63.53	17.43
JL30A222	D Gregory	386.5	nodule	Rift Basin	5.83	465542.47	16.56	159.17	41.61	18.51
JL30A307	D Gregory	386.5	nodule	Rift Basin	3.80	465540.30	3.03	130.18	91.01	25.59

Table A6.1: LA-ICPMS Analyses of Pyrite from Chapter 4

File	As(ppm)	Se(ppm)	Mo(ppm)	Ag(ppm)	Cd(ppm)	Sb(ppm)	Te(ppm)	Au(ppm)	Pb(ppm)	Bi(ppm)
JL30A282	8	29.9	33.9	0.03	0.12	0.58	<0.13	<0.01	1.40	0.03
JL30A320	41	98.2	19.4	0.28	0.89	16.50	0.13	<0.01	19.72	0.07
JL30A211	20	52.7	19.1	0.19	0.35	3.82	0.18	<0.01	9.10	0.08
JL30A315	25	139.1	21.5	0.21	0.99	14.23	<0.13	0.01	18.70	0.09
JL30A213	18	52.2	21.2	0.16	0.32	4.76	0.17	<0.01	9.73	0.09
JL30A306	40	123.7	17.3	0.23	1.25	16.43	<0.13	<0.01	28.25	0.09
JL30A304	34	139.1	25.2	0.32	1.05	15.60	0.22	<0.01	26.55	0.10
JL30A312	40	86.9	31.0	0.42	1.48	19.46	0.21	<0.01	24.66	0.10
JL30A319	28	138.9	27.8	0.26	1.41	14.08	0.14	<0.01	23.36	0.11
JL30A214	22	57.6	29.1	0.18	0.47	5.37	0.12	<0.01	12.66	0.11
JL30A323	45	115.3	30.2	0.37	0.80	16.06	0.24	<0.01	24.29	0.11
JL30A303	43	127.2	21.5	0.25	1.14	18.66	0.23	<0.01	30.56	0.11
JL30A215	19	61.2	22.4	0.24	0.99	5.31	0.11	0.01	13.94	0.11
JL30A216	22	48.3	28.3	0.24	0.76	5.10	0.20	<0.01	11.90	0.11
JL30A314	32	176.8	29.2	0.34	1.24	16.46	0.24	<0.01	25.71	0.12
JL30A313	43	87.5	36.3	0.36	0.94	17.77	0.18	0.01	27.88	0.12
JL30A302	38	112.5	26.0	0.33	0.99	18.82	0.23	<0.01	31.37	0.12
JL30A305	43	129.0	27.2	0.34	1.24	18.52	0.25	0.01	32.64	0.12
JL30A210	28	48.4	32.5	0.27	0.82	6.92	0.17	<0.01	15.26	0.14
JL30A220	36	45.6	40.5	0.33	0.95	5.17	0.30	<0.01	14.36	0.14
JL30A318	31	122.7	28.6	0.36	0.98	18.51	0.28	<0.01	29.11	0.15
JL30A222	40	53.9	59.9	0.33	0.57	7.04	0.43	0.01	18.84	0.16
JL30A307	48	111.0	34.5	0.42	1.34	22.63	0.24	<0.01	37.26	0.17

Table A6.1: LA-ICPMS Analyses of Pyrite from Chapter 4										
File	Analyst	Age (Ma)	Pyrite type	Setting	Mn (ppm)	Fe (ppm)	Co (ppm)	Ni (ppm)	Cu (ppm)	Zn (ppm)
JL30A223	D Gregory	386.5	nodule	Rift Basin	7.09	465543.35	43.77	166.36	43.00	18.28
JL30A301	D Gregory	386.5	nodule	Rift Basin	8.83	465543.47	2.70	102.08	68.85	29.45
JL30A227	D Gregory	386.5	nodule	Rift Basin	40.54	465543.92	12.25	119.41	56.32	21.42
JL30A212	D Gregory	386.5	nodule	Rift Basin	16.75	465547.60	2.17	90.02	44.20	50.37
JL30A225	D Gregory	386.5	nodule	Rift Basin	15.41	465543.92	26.41	149.50	51.55	23.53
JL30A311	D Gregory	386.5	nodule	Rift Basin	151.41	465532.06	11.45	508.16	101.87	31.49
JL30A316	D Gregory	386.5	nodule	Rift Basin	6.74	465542.31	3.97	164.82	84.17	12.00
JL30A221	D Gregory	386.5	nodule	Rift Basin	45.24	465543.18	27.08	167.56	54.20	40.35
JL30A226	D Gregory	386.5	nodule	Rift Basin	15.05	465543.96	37.97	177.44	47.70	38.42
JL30A317	D Gregory	386.5	nodule	Rift Basin	76.64	465536.15	5.16	194.28	101.86	28.30
JL30A224	D Gregory	386.5	nodule	Rift Basin	20.46	465540.68	22.67	202.99	67.58	98.56
JL30A324	D Gregory	386.5	nodule	Rift Basin	475.15	465470.56	24.87	518.73	217.47	3.40
JL30A240	D Gregory	387.0	nodule	Rift Basin	7.40	465537.84	1.53	38.77	45.34	22.08
JL30A241	D Gregory	387.0	nodule	Rift Basin	14.29	465541.08	2.69	90.30	50.09	8.33
JL30A238	D Gregory	387.0	nodule	Rift Basin	1.74	465542.92	1.92	83.18	47.18	15.00
JL30A242	D Gregory	387.0	nodule	Rift Basin	1.44	465542.18	1.13	60.73	52.13	9.76
JL30A239	D Gregory	387.0	nodule	Rift Basin	14.52	465542.10	1.75	66.31	57.01	44.90
JL30A250	D Gregory	387.0	framboid	Rift Basin	23.42	465538.47	47.93	426.40	155.59	25.93
JL30A243	D Gregory	387.0	nodule	Rift Basin	3.90	465541.48	2.19	85.42	61.82	18.56
JL30A237	D Gregory	387.0	nodule	Rift Basin	3.70	465541.89	2.77	73.08	62.80	28.89
JL30A247	D Gregory	387.0	framboid	Rift Basin	214.07	465533.31	120.45	937.71	471.61	37.35
JL30A329	D Gregory	387.0	small euhedral	Rift Basin	3.12	465068.02	0.09	82.22	75.17	15.09
JL30A249	D Gregory	387.0	framboid	Rift Basin	22.23	465530.26	100.71	2939.01	190.24	8.11

Table A6.1: LA-ICPMS Analyses of Pyrite from Chapter 4

File	As(ppm)	Se(ppm)	Mo(ppm)	Ag(ppm)	Cd(ppm)	Sb(ppm)	Te(ppm)	Au(ppm)	Pb(ppm)	Bi(ppm)
JL30A223	37.0	48.7	56.37	0.29	0.79	6.40	0.21	<0.01	18.22	0.17
JL30A301	36.6	116.2	27.17	0.44	1.21	18.06	0.16	0.01	29.65	0.17
JL30A227	34.9	53.8	58.11	0.52	0.83	5.59	0.27	<0.01	15.07	0.18
JL30A212	21.1	57.8	29.57	0.38	0.80	3.90	0.12	<0.01	15.78	0.18
JL30A225	34.9	41.6	57.15	0.47	0.82	6.39	0.36	<0.01	18.97	0.19
JL30A311	79.3	100.6	84.33	1.01	1.38	28.08	0.30	0.01	40.70	0.20
JL30A316	40.9	140.2	39.18	0.48	0.97	18.50	0.39	<0.01	30.11	0.21
JL30A221	37.7	47.1	60.87	0.62	0.79	6.01	0.22	<0.01	19.89	0.23
JL30A226	34.7	50.9	48.12	0.45	0.93	5.97	0.31	<0.01	20.01	0.25
JL30A317	64.0	140.0	48.36	0.79	1.67	31.21	0.41	0.01	45.50	0.29
JL30A224	47.0	62.9	74.42	0.64	1.52	8.26	0.39	<0.01	27.65	0.32
JL30A324	309.7	36.1	116.29	5.32	12.16	34.25	<0.13	<0.01	81.80	0.46
JL30A240	57.7	143.7	16.77	0.18	2.64	36.01	0.24	<0.01	16.65	0.07
JL30A241	45.5	312.4	21.80	0.23	2.62	44.03	0.27	<0.01	21.51	0.08
JL30A238	38.7	172.5	23.52	0.23	2.36	43.78	0.27	<0.01	24.21	0.09
JL30A242	41.4	265.6	13.37	0.19	2.54	42.40	0.27	<0.01	24.46	0.10
JL30A239	41.7	314.0	22.10	0.27	3.47	43.01	0.14	0.01	26.74	0.12
JL30A250	55.3	507.3	50.42	0.34	1.65	52.33	0.26	<0.01	21.98	0.13
JL30A243	44.0	292.1	20.53	0.25	3.13	45.09	0.28	<0.01	28.44	0.13
JL30A237	42.5	241.8	25.82	0.24	3.13	44.32	0.17	0.01	25.70	0.14
JL30A247	74.7	565.2	91.19	0.86	1.58	51.49	0.55	<0.01	20.79	0.14
JL30A329	1817.8	448.9	1.05	136.34	26.47	2878.35	0.17	0.13	116.14	0.15
JL30A249	86.1	409.6	35.75	0.37	2.30	43.11	0.62	0.01	25.81	0.17

Table A6.1: LA-ICPMS Analyses of Pyrite from Chapter 4										
File	Analyst	Age (Ma)	Pyrite type	Setting	Mn (ppm)	Fe (ppm)	Co (ppm)	Ni (ppm)	Cu (ppm)	Zn (ppm)
JL30A253	D Gregory	387.0	framboid	Rift Basin	88.77	465388.50	35.50	519.44	197.54	466.58
AU03A112	D Gregory	387.0	large anhedral	Rift Basin	19.95	465507.83	0.66	458.37	71.95	5.83
AU03A102	D Gregory	387.0	large anhedral	Rift Basin	5.85	465455.46	0.09	43.23	100.79	7.55
AU03A098	D Gregory	387.0	large anhedral	Rift Basin	2.98	465425.19	0.17	560.99	106.72	5.49
AU03A111	D Gregory	387.0	large anhedral	Rift Basin	13.72	465346.26	0.32	349.82	140.56	12.01
JL30A326	D Gregory	387.0	small euhedral	Rift Basin	1.77	465361.34	0.07	346.77	328.87	4.88
JL30A325	D Gregory	387.0	small euhedral	Rift Basin	2.48	465273.30	1.18	911.68	486.23	8.03
AU03A114	D Gregory	387.0	large anhedral	Rift Basin	2.65	465472.52	0.22	214.58	324.62	70.02
AU03A120	D Gregory	387.0	large anhedral	Rift Basin	10.17	465147.17	0.42	466.56	243.90	27.20
JL30A236	D Gregory	387.0	nodule	Rift Basin	8.23	465541.83	2.48	88.99	64.70	24.73
AU03A104	D Gregory	387.0	large anhedral	Rift Basin	17.89	465152.28	0.73	264.48	206.29	24.81
AU03A117	D Gregory	387.0	large anhedral	Rift Basin	13.12	465126.37	1.28	666.44	341.54	31.89
AU03A118	D Gregory	387.0	large anhedral	Rift Basin	6.93	465106.62	0.38	238.52	258.87	34.74
AU03A099	D Gregory	387.0	large anhedral	Rift Basin	8.74	465131.73	0.25	427.00	337.25	19.28
AU03A121	D Gregory	387.0	large anhedral	Rift Basin	27.14	464943.23	0.59	260.30	312.07	77.02
AU03A103	D Gregory	387.0	large anhedral	Rift Basin	22.11	465114.40	0.55	250.45	299.13	32.74
AU03A113	D Gregory	387.0	large anhedral	Rift Basin	0.80	465361.65	1.36	672.11	2218.12	665.85
AU03A108	D Gregory	387.0	large anhedral	Rift Basin	32.74	465101.70	1.52	439.55	321.95	22.52
AU03A110	D Gregory	387.0	large anhedral	Rift Basin	12.36	464872.69	4.75	1420.04	466.01	53.10
AU03A115	D Gregory	387.0	large anhedral	Rift Basin	1.11	465269.67	1.36	471.01	683.44	200.50
AU03A119	D Gregory	387.0	large anhedral	Rift Basin	17.27	464784.63	2.10	430.33	477.87	118.39
JL30A330	D Gregory	387.0	small euhedral	Rift Basin	0.36	465349.45	1.85	2591.07	1652.75	2.61
JL30A327	D Gregory	387.0	small euhedral	Rift Basin	0.54	465356.08	2.35	2692.32	1079.08	4.51

Table A6.1: LA-ICPMS Analyses of Pyrite from Chapter 4

File	As(ppm)	Se(ppm)	Mo(ppm)	Ag(ppm)	Cd(ppm)	Sb(ppm)	Te(ppm)	Au(ppm)	Pb(ppm)	Bi(ppm)
JL30A253	617	62.4	76.1	0.50	1.00	46.75	0.35	<0.01	28.04	0.18
AU03A112	170	189.9	11.1	0.68	1.23	63.99	0.25	0.01	18.72	0.23
AU03A102	366	250.8	2.0	0.92	1.85	62.05	0.22	<0.01	26.64	0.24
AU03A098	480	192.1	5.0	0.81	2.05	69.53	0.33	0.01	32.36	0.25
AU03A111	775	149.3	8.5	0.95	3.01	105.29	0.40	<0.01	47.68	0.32
JL30A326	719	613.7	6.4	69.52	9.74	1324.94	0.46	0.08	106.30	0.39
JL30A325	1049	578.3	3.0	105.70	14.86	1970.33	0.60	0.10	125.47	0.47
AU03A114	302	375.2	8.2	1.16	3.13	282.90	0.46	0.01	31.91	0.49
AU03A120	1521	62.6	4.6	1.88	4.74	165.11	0.33	<0.01	77.15	0.52
JL30A236	43	301.9	84.5	1.52	0.84	29.70	0.76	0.02	35.40	0.59
AU03A104	1502	92.5	5.6	1.65	5.38	188.21	0.66	0.02	81.39	0.61
AU03A117	1599	113.2	5.5	1.83	4.83	192.96	0.61	0.01	90.84	0.62
AU03A118	1673	44.2	3.1	2.08	6.31	227.84	0.62	0.01	102.31	0.72
AU03A099	1579	84.6	3.1	2.73	7.23	208.39	0.63	0.00	92.57	0.78
AU03A121	2285	64.0	9.0	2.51	6.12	238.03	0.62	0.01	103.68	0.85
AU03A103	1644	72.5	7.0	2.23	6.62	245.96	0.73	0.01	104.24	0.86
AU03A113	718	278.2	16.9	2.53	19.85	2095.79	0.68	0.02	56.93	0.88
AU03A108	1692	175.5	16.4	2.52	7.64	327.14	0.83	0.02	125.09	1.04
AU03A110	2550	91.1	14.6	3.38	8.55	346.20	1.07	0.01	141.74	1.17
AU03A115	1062	92.6	15.4	2.50	6.25	773.22	1.26	0.01	120.19	1.20
AU03A119	2880	76.2	31.5	3.28	7.55	466.67	1.29	0.01	185.68	1.28
JL30A330	763	610.1	8.5	50.86	8.69	1197.23	1.32	0.03	137.71	1.36
JL30A327	739	679.0	8.4	74.93	13.77	1691.03	1.22	0.04	166.56	1.42

Table A6.1: LA-ICPMS Analyses of Pyrite from Chapter 4

File	Analyst	Age (Ma)	Pyrite type	Setting	Mn (ppm)	Fe (ppm)	Co (ppm)	Ni (ppm)	Cu (ppm)	Zn (ppm)
AU03A101	D Gregory	387.0	large anhedral	Rift Basin	22.91	465050.62	1.14	403.71	460.90	105.11
AU03A100	D Gregory	387.0	large anhedral	Rift Basin	10.95	464883.90	0.93	684.73	581.93	44.88
AU03A109	D Gregory	387.0	large anhedral	Rift Basin	1.02	465213.59	0.10	355.96	436.20	6.64
JL30A332	D Gregory	387.0	small euhedral	Rift Basin	0.34	465316.02	1.14	1361.27	1011.28	5.51
JL30A248	D Gregory	387.0	framboid	Rift Basin	2030.67	465406.08	8.19	450.49	303.22	349.00
JL30A328	D Gregory	387.0	small euhedral	Rift Basin	1.75	465385.46	7.11	2996.06	1573.40	3.72
AU03A116	D Gregory	387.0	large anhedral	Rift Basin	16.42	464886.67	1.86	778.18	691.43	145.75
AU03A138	D Gregory	388.0	nodule	Rift Basin	158.90	465520.35	1.16	54.83	78.96	3.36
AU03A139	D Gregory	388.0	nodule	Rift Basin	27.78	465506.01	2.70	262.48	198.54	8.39
AU03A133	D Gregory	388.0	nodule	Rift Basin	13.49	465483.85	0.79	62.32	117.18	2.25
AU03A132	D Gregory	388.0	nodule	Rift Basin	15.51	465502.34	6.90	830.29	165.94	10.32
AU03A134	D Gregory	388.0	nodule	Rift Basin	40.91	465503.98	1.93	160.17	183.74	3.14
AU03A136	D Gregory	388.0	nodule	Rift Basin	37.37	465493.97	1.07	172.47	122.05	3.16
AU03A131	D Gregory	388.0	nodule	Rift Basin	19.88	465456.47	1.29	198.59	177.40	3.77
AU03A165	D Gregory	388.0	small euhedral	Rift Basin	94.06	465512.70	5.41	83.11	243.76	89.51
AU03A143	D Gregory	388.0	nodule	Rift Basin	25.92	465445.37	1.88	250.25	80.91	3.61
AU03A158	D Gregory	388.0	small euhedral	Rift Basin	87.63	465511.26	7.48	115.25	256.45	10.52
AU03A135	D Gregory	388.0	nodule	Rift Basin	28.89	465497.03	1.81	203.48	201.54	2.74
AU03A140	D Gregory	388.0	nodule	Rift Basin	9.80	465481.07	1.68	320.05	88.52	1.94
AU03A163	D Gregory	388.0	small euhedral	Rift Basin	204.64	465515.38	10.75	120.90	233.90	17.82
AU03A159	D Gregory	388.0	small euhedral	Rift Basin	76.27	465509.17	5.97	93.72	268.07	11.62
AU03A160	D Gregory	388.0	small euhedral	Rift Basin	23.36	465505.06	5.75	90.72	270.59	8.71
AU03A137	D Gregory	388.0	nodule	Rift Basin	61.91	465503.03	3.05	338.83	330.82	9.39

Table A6.1: LA-ICPMS Analyses of Pyrite from Chapter 4

File	As(ppm)	Se(ppm)	Mo(ppm)	Ag(ppm)	Cd(ppm)	Sb(ppm)	Te(ppm)	Au(ppm)	Pb(ppm)	Bi(ppm)
AU03A101	1883.0	66.5	7.98	3.37	13.10	415.13	1.41	0.01	162.68	1.50
AU03A100	2507.7	73.0	8.56	4.35	13.45	439.18	1.43	0.01	177.29	1.57
AU03A109	1272.5	91.7	0.76	3.19	16.07	529.59	1.36	0.02	191.25	1.78
JL30A332	888.7	573.6	29.15	76.78	16.66	1914.37	1.56	0.04	208.21	1.80
JL30A248	551.3	162.7	672.15	11.34	2.16	220.76	2.36	0.07	123.54	1.84
JL30A328	628.6	686.7	14.26	64.80	12.62	1754.21	1.48	0.04	210.86	1.94
AU03A116	2497.3	100.8	17.56	5.34	13.95	579.06	2.40	0.02	194.88	2.68
AU03A138	123.2	126.7	7.78	0.87	2.40	21.33	1.12	0.01	37.72	0.39
AU03A139	176.9	148.3	10.85	0.99	4.89	46.98	1.96	0.01	81.26	0.43
AU03A133	259.9	208.7	7.35	0.87	4.15	28.87	2.47	<0.01	52.14	0.45
AU03A132	190.7	160.3	13.79	1.25	4.38	37.44	1.74	0.01	68.95	0.50
AU03A134	184.5	143.3	11.70	1.15	4.38	41.67	1.86	<0.01	70.80	0.54
AU03A136	222.0	167.4	8.24	1.00	3.99	30.62	2.24	<0.01	51.51	0.55
AU03A131	362.5	122.5	8.78	1.23	5.16	36.43	1.91	0.01	67.46	0.56
AU03A165	151.9	77.3	18.85	1.29	7.44	42.59	0.63	0.01	115.66	0.56
AU03A143	404.1	222.6	8.23	1.11	3.16	43.41	0.41	<0.01	64.11	0.59
AU03A158	157.3	77.1	25.07	1.20	5.65	43.97	0.56	0.01	124.21	0.61
AU03A135	210.6	162.1	9.02	1.32	5.48	48.36	2.09	<0.01	77.39	0.64
AU03A140	270.4	270.4	9.84	1.26	2.67	37.03	0.54	<0.01	57.23	0.67
AU03A163	141.8	72.2	28.83	1.53	6.25	38.09	0.64	<0.01	114.14	0.70
AU03A159	165.1	70.4	14.86	1.41	6.26	46.95	0.56	0.01	133.54	0.71
AU03A160	180.5	73.9	15.35	1.55	6.12	48.58	0.64	<0.01	142.58	0.71
AU03A137	188.1	116.1	12.67	1.57	7.52	68.45	1.64	0.01	125.47	0.72

Table A6.1: LA-ICPMS Analyses of Pyrite from Chapter 4

File	Analyst	Age (Ma)	Pyrite type	Setting	Mn (ppm)	Fe (ppm)	Co (ppm)	Ni (ppm)	Cu (ppm)	Zn (ppm)
AU03A145	D Gregory	388.0	nodule	Rift Basin	11.47	465466.87	1.39	75.04	112.67	3.77
AU03A162	D Gregory	388.0	small euhedral	Rift Basin	205.67	465502.48	7.63	116.67	274.32	9.61
AU03A146	D Gregory	388.0	nodule	Rift Basin	17.22	465501.08	1.96	115.92	78.73	1.28
AU03A167	D Gregory	388.0	small euhedral	Rift Basin	21.78	465521.54	3.13	202.54	200.76	23.63
AU03A166	D Gregory	388.0	small euhedral	Rift Basin	76.81	465502.89	8.34	159.84	279.73	21.98
AU03A157	D Gregory	388.0	small euhedral	Rift Basin	90.12	465516.31	4.95	84.49	240.14	46.45
AU03A161	D Gregory	388.0	small euhedral	Rift Basin	38.82	465508.91	4.05	92.77	251.08	66.66
AU03A164	D Gregory	388.0	small euhedral	Rift Basin	57.39	465497.98	10.44	177.19	230.83	11.13
AU03A144	D Gregory	388.0	nodule	Rift Basin	4.00	465493.85	6.11	210.28	90.74	0.07
AU03A142	D Gregory	388.0	nodule	Rift Basin	18.47	465462.75	2.82	226.31	112.30	2.32
AU03A141	D Gregory	388.0	nodule	Rift Basin	7.23	465446.48	2.99	456.87	130.17	6.25
FE23A088	JA Halpin	450.0	small euhedral	Rift Basin	79.70	465542.98	20.12	128.85	223.84	56.11
FE23A098	JA Halpin	450.0	small anhedral	Rift Basin	564.60	465502.25	43.81	440.42	159.27	174.57
FE23A091	JA Halpin	450.0	small anhedral	Rift Basin	70.78	465523.56	797.68	967.44	921.33	122.95
FE23A097	JA Halpin	450.0	small anhedral	Rift Basin	627.65	465531.56	54.93	406.51	206.88	237.18
FE23A108	JA Halpin	450.0	small anhedral	Rift Basin	1212.78	465501.56	43.91	481.24	248.89	386.92
FE23A082	JA Halpin	450.0	framboid	Rift Basin	778.37	465463.42	87.58	642.51	975.84	286.66
FE23A100	JA Halpin	450.0	small anhedral	Rift Basin	1522.20	465505.22	167.25	938.64	443.65	441.99
FE23A110	JA Halpin	450.0	small anhedral	Rift Basin	1563.35	465513.72	175.10	915.33	419.70	511.17
FE23A083	JA Halpin	450.0	framboid	Rift Basin	528.20	465519.76	217.40	899.89	571.62	256.53
FE23A095	JA Halpin	450.0	small anhedral	Rift Basin	1569.57	465511.06	151.90	919.77	491.49	511.76
FE23A099	JA Halpin	450.0	small anhedral	Rift Basin	1903.55	465506.03	186.18	1402.39	619.33	558.09
FE23A111	JA Halpin	450.0	small anhedral	Rift Basin	2017.15	465509.38	249.85	1375.92	629.05	598.89

Table A6.1: LA-ICPMS Analyses of Pyrite from Chapter 4

File	As(ppm)	Se(ppm)	Mo(ppm)	Ag(ppm)	Cd(ppm)	Sb(ppm)	Te(ppm)	Au(ppm)	Pb(ppm)	Bi(ppm)
AU03A145	324	207.1	8.7	1.22	2.83	32.92	0.69	0.01	63.81	0.73
AU03A162	190	65.5	27.9	1.88	5.80	48.64	0.83	0.02	137.20	0.76
AU03A146	195	253.1	9.8	1.32	2.45	33.29	0.48	0.01	57.96	0.76
AU03A167	119	83.7	11.5	1.58	4.43	37.28	0.47	0.01	109.89	0.77
AU03A166	189	59.6	23.1	1.68	6.34	50.68	0.59	<0.0065	145.27	0.80
AU03A157	138	70.9	16.6	1.47	5.69	40.94	0.55	0.01	116.10	0.81
AU03A161	166	75.3	13.1	1.60	6.57	46.59	0.72	<0.0065	132.65	0.81
AU03A164	207	118.4	20.2	1.88	6.20	40.19	0.57	0.01	120.20	0.82
AU03A144	222	247.6	17.4	1.28	2.99	41.93	0.71	<0.01	76.55	0.84
AU03A142	339	250.3	15.3	1.51	3.11	46.51	0.69	<0.01	79.93	0.92
AU03A141	400	237.1	14.4	2.11	3.48	61.85	0.84	<0.01	103.78	1.11
FE23A088	38	3.8	18.3	0.21	0.21	1.10	0.21	<0.01	67.76	0.58
FE23A098	191	1.6	139.9	2.76	1.06	9.51	0.46	0.03	157.18	1.56
FE23A091	111	4.8	73.4	0.72	0.28	2.42	0.18	0.04	136.36	2.22
FE23A097	81	<0.78	55.8	2.74	0.48	4.73	<0.13	0.03	245.78	3.32
FE23A108	194	4.6	101.7	3.46	1.62	11.77	0.50	0.03	193.92	3.36
FE23A082	336	2.5	101.5	1.84	2.11	7.99	0.75	<0.0065	182.72	4.80
FE23A100	180	4.8	38.6	6.46	2.30	13.98	0.86	0.04	811.17	9.68
FE23A110	148	4.6	30.4	3.56	2.44	11.31	0.66	0.03	751.55	9.84
FE23A083	125	8.6	86.3	0.95	0.97	5.14	0.56	<0.0065	198.48	10.01
FE23A095	158	3.4	28.1	3.67	2.43	12.42	0.69	0.03	953.72	10.70
FE23A099	177	2.6	45.2	7.87	3.33	13.08	0.97	0.05	1051.83	15.29
FE23A111	164	4.3	28.8	6.01	2.77	13.25	0.88	0.05	1065.26	16.33

Table A6.1: LA-ICPMS Analyses of Pyrite from Chapter 4

File	Analyst	Age (Ma)	Pyrite type	Setting	Mn (ppm)	Fe (ppm)	Co (ppm)	Ni (ppm)	Cu (ppm)	Zn (ppm)
FE23A109	JA Halpin	450.0	small anhedral	Rift Basin	2026.29	465516.33	246.75	1218.08	802.32	642.60
NO16A017	J Halpin	455.0	large anhedral		13.05	465549.13	14.71	385.00	545.22	18.74
NO16A022	J Halpin	455.0	large anhedral		19.33	465548.75	29.47	331.82	468.08	21.21
NO16A011	J Halpin	455.0	large anhedral		12.38	465530.95	44.22	573.61	313.53	19.97
NO16A013	J Halpin	455.0	large anhedral		37.85	465541.86	34.95	207.15	228.81	39.17
NO16A007	J Halpin	455.0	large anhedral		46.52	465542.87	22.26	190.54	204.29	45.65
NO16A014	J Halpin	455.0	large anhedral		25.32	465546.39	13.08	250.50	385.69	25.00
NO16A018	J Halpin	455.0	large anhedral		12.45	465550.14	20.64	364.09	586.67	19.15
NO16A010	J Halpin	455.0	large anhedral		60.74	465542.61	14.69	146.81	194.31	58.24
NO16A012	J Halpin	455.0	large anhedral		25.95	465548.62	23.11	245.48	335.78	21.57
NO16A008	J Halpin	455.0	large anhedral		36.84	465543.59	60.24	573.53	395.04	26.63
NO16A020	J Halpin	455.0	large anhedral		33.20	465546.17	28.77	348.43	552.38	26.16
NO16A009	J Halpin	455.0	large anhedral		10.05	465545.19	51.34	550.49	352.94	19.47
NO16A019	J Halpin	455.0	large anhedral		43.52	465539.08	54.48	448.27	448.89	35.82
NO16A021	J Halpin	455.0	large anhedral		29.79	465544.69	24.64	311.04	449.64	22.98
NO16A016	J Halpin	455.0	large anhedral		70.75	465542.22	58.21	442.63	352.37	35.40
NO16A102	J Halpin	456.0	large anhedral		3.45	465396.55	18.72	261.85	56.48	1.68
NO16A100	J Halpin	456.0	large anhedral		3.29	465094.64	12.50	189.26	42.78	2.55
NO16A090	J Halpin	456.0	large anhedral		6.47	465317.38	13.45	193.15	38.07	2.51
NO16A104	J Halpin	456.0	large anhedral		1.30	465368.15	8.24	140.67	29.08	2.21
NO16A096	J Halpin	456.0	large anhedral		4.98	465148.85	16.45	254.32	54.55	4.08
NO16A105	J Halpin	456.0	large anhedral		1.03	465408.80	12.96	122.19	26.75	2.34
NO16A099	J Halpin	456.0	large anhedral		18.03	465304.33	26.61	420.32	74.46	2.17

Table A6.1: LA-ICPMS Analyses of Pyrite from Chapter 4

File	As(ppm)	Se(ppm)	Mo(ppm)	Ag(ppm)	Cd(ppm)	Sb(ppm)	Te(ppm)	Au(ppm)	Pb(ppm)	Bi(ppm)
FE23A109	138.3	<0.78	28.01	4.74	3.21	11.47	1.07	<0.01	1125.45	16.39
NO16A017	15.4	1.5	6.51	1.06	0.28	0.28	0.29	<0.01	113.86	<0.01
NO16A022	16.8	1.6	6.46	0.83	0.35	0.47	<0.13	<0.01	136.81	<0.01
NO16A011	83.5	1.5	39.04	2.91	0.41	1.34	<0.13	<0.01	429.60	<0.01
NO16A013	42.6	2.1	14.21	0.58	0.57	0.77	0.21	<0.01	501.54	<0.01
NO16A007	38.8	1.7	7.10	0.58	0.50	0.71	<0.13	<0.01	512.73	<0.01
NO16A014	25.7	<0.78	7.44	0.99	0.26	0.54	<0.13	<0.01	164.27	0.01
NO16A018	11.6	1.3	5.58	0.77	0.18	0.42	<0.13	<0.01	89.25	0.01
NO16A010	39.8	2.3	7.25	0.51	0.82	0.71	<0.13	<0.01	572.84	0.02
NO16A012	17.3	<0.78	8.77	0.93	0.14	0.56	<0.13	<0.01	109.36	0.02
NO16A008	36.1	<0.78	13.88	1.34	0.41	0.98	<0.13	<0.01	260.95	0.02
NO16A020	26.5	1.6	8.60	1.00	0.42	0.70	<0.13	<0.01	178.56	0.02
NO16A009	30.1	<0.78	10.72	1.34	0.35	0.65	<0.13	<0.01	217.13	0.03
NO16A019	53.1	1.9	17.27	1.11	0.49	1.04	<0.13	<0.01	236.77	0.04
NO16A021	32.0	1.3	13.47	1.21	0.26	0.56	<0.13	<0.01	171.59	0.11
NO16A016	41.3	1.5	16.75	1.71	0.30	1.06	<0.13	<0.01	262.12	0.18
NO16A102	587.0	2.9	1.30	0.89	0.12	27.34	<0.13	<0.01	245.50	<0.01
NO16A100	1718.1	3.8	3.36	0.52	0.10	52.39	<0.13	<0.01	251.99	<0.01
NO16A090	883.6	2.0	4.89	0.53	<0.066	57.32	0.21	<0.01	293.38	<0.01
NO16A104	693.4	2.4	0.89	0.62	<0.066	52.87	<0.13	<0.01	270.09	0.01
NO16A096	1515.0	2.2	11.00	0.84	0.15	56.62	<0.13	<0.01	298.68	0.01
NO16A105	541.1	<0.78	0.48	0.75	<0.066	57.51	<0.13	<0.01	284.78	0.02
NO16A099	932.5	3.1	2.79	1.59	0.12	38.70	<0.13	<0.01	259.71	0.02

Table A6.1: LA-ICPMS Analyses of Pyrite from Chapter 4										
File	Analyst	Age (Ma)	Pyrite type	Setting	Mn (ppm)	Fe (ppm)	Co (ppm)	Ni (ppm)	Cu (ppm)	Zn (ppm)
NO16A092	J Halpin	456.0	large anhedral		0.08	465383.90	20.92	552.58	113.36	2.06
NO16A094	J Halpin	456.0	large anhedral		54.60	465341.44	26.75	427.38	96.60	5.57
NO16A098	J Halpin	456.0	large anhedral		5.87	465407.54	23.32	310.89	69.95	2.89
NO16A091	J Halpin	456.0	large anhedral		29.99	465334.67	28.52	305.08	53.61	3.71
NO16A097	J Halpin	456.0	large anhedral		4.61	465309.74	20.88	297.81	71.36	5.08
NO16A093	J Halpin	456.0	large anhedral		7.94	465357.15	34.90	544.80	101.38	3.72
NO16A103	J Halpin	456.0	large anhedral		4.18	465317.75	17.45	259.68	45.36	2.99
NO16A089	J Halpin	456.0	large anhedral		0.92	465254.27	10.74	167.14	45.88	2.59
NO16A036	J Halpin	457.0	large anhedral		0.07	465541.46	56.75	252.06	48.68	2.07
NO16A040	J Halpin	457.0	large anhedral		5.85	465541.21	69.19	256.26	45.02	4.09
NO16A039	J Halpin	457.0	large anhedral		4.26	465544.73	33.42	235.47	50.96	4.78
NO16A037	J Halpin	457.0	large anhedral		5.71	465541.08	48.51	348.03	71.14	5.38
NO16A035	J Halpin	457.0	large anhedral		2.88	465542.77	44.98	208.29	43.12	2.84
NO16A045	J Halpin	457.0	large anhedral		1.04	465522.44	239.66	1044.88	35.03	1.83
NO16A045	J Halpin	457.0	large anhedral		1.04	465522.44	239.66	1044.88	35.03	1.83
NO16A043	J Halpin	457.0	large anhedral		0.17	465536.24	194.89	727.41	17.67	1.17
NO16A044	J Halpin	457.0	large anhedral		4.80	465532.86	145.08	958.07	18.93	1.79
NO16A032	J Halpin	457.0	large anhedral		0.07	465543.03	96.41	521.91	11.24	3.84
NO16A046	J Halpin	457.0	large anhedral		0.99	465452.89	197.34	1171.86	46.24	1.26
NO16A046	J Halpin	457.0	large anhedral		0.99	465452.89	197.34	1171.86	46.24	1.26
NO16A047	J Halpin	457.0	large anhedral		6.99	465334.63	214.40	1418.61	57.14	1.62
NO16A047	J Halpin	457.0	large anhedral		6.99	465334.63	214.40	1418.61	57.14	1.62
NO16A031	J Halpin	457.0	large anhedral		12.50	465492.70	512.80	1372.56	13.53	1.30

Table A6.1: LA-ICPMS Analyses of Pyrite from Chapter 4

File	As(ppm)	Se(ppm)	Mo(ppm)	Ag(ppm)	Cd(ppm)	Sb(ppm)	Te(ppm)	Au(ppm)	Pb(ppm)	Bi(ppm)
NO16A092	634	2.0	2.5	3.84	0.19	24.50	<0.13	<0.01	244.93	0.02
NO16A094	793	<0.78	4.7	2.26	0.18	26.98	<0.13	<0.01	284.02	0.03
NO16A098	546	<0.78	1.1	1.21	0.10	32.69	<0.13	<0.01	287.36	0.04
NO16A091	819	2.1	4.3	1.29	0.15	58.35	0.33	<0.01	373.37	0.04
NO16A097	912	2.6	2.1	1.31	0.19	43.95	0.22	<0.01	299.29	0.05
NO16A093	735	<0.78	2.1	2.47	0.29	36.82	<0.13	<0.01	356.49	0.07
NO16A103	882	2.9	3.3	0.76	<0.066	37.21	0.21	<0.01	233.72	0.16
NO16A089	1120	3.4	4.2	0.50	0.18	49.49	<0.13	<0.01	274.31	0.17
NO16A036	44	2.2	2.1	1.04	0.13	3.41	<0.13	<0.01	102.40	<0.01
NO16A040	45	1.6	0.7	0.43	<0.066	3.56	<0.13	<0.01	171.68	0.01
NO16A039	32	1.7	1.0	0.25	<0.066	2.13	<0.13	<0.01	93.66	0.01
NO16A037	46	2.1	0.7	0.40	0.14	4.45	0.31	<0.01	176.13	0.02
NO16A035	39	2.0	1.0	0.35	<0.066	3.32	<0.13	<0.01	88.44	0.02
NO16A045	115	2.8	2.2	0.52	<0.066	7.08	<0.13	<0.01	217.13	0.02
NO16A045	115	2.8	2.2	0.52	<0.066	7.08	<0.13	<0.01	217.13	0.02
NO16A043	64	<0.78	1.1	0.18	<0.066	6.68	<0.13	<0.01	187.44	0.03
NO16A044	76	1.7	1.4	0.22	<0.066	7.23	<0.13	<0.01	358.78	0.03
NO16A032	38	<0.78	1.8	0.33	<0.066	3.14	<0.13	<0.01	123.26	0.03
NO16A046	376	<0.78	5.9	0.55	<0.066	13.34	<0.13	<0.01	211.59	0.04
NO16A046	376	<0.78	5.9	0.55	<0.066	13.34	<0.13	<0.01	211.59	0.04
NO16A047	819	1.7	11.7	1.02	<0.066	23.36	<0.13	<0.01	166.43	0.04
NO16A047	819	1.7	11.7	1.02	<0.066	23.36	<0.13	<0.01	166.43	0.04
NO16A031	227	3.2	4.2	0.58	<0.066	14.98	<0.13	<0.01	359.84	0.05

Table A6.1: LA-ICPMS Analyses of Pyrite from Chapter 4

File	Analyst	Age (Ma)	Pyrite type	Setting	Mn (ppm)	Fe (ppm)	Co (ppm)	Ni (ppm)	Cu (ppm)	Zn (ppm)
NO16A030	J Halpin	457.0	large anhedral		24.36	465443.84	516.22	2243.47	15.33	5.39
NO16A038	J Halpin	457.0	large anhedral		23.38	465540.13	56.51	305.04	49.08	6.53
NO16A034	J Halpin	457.0	large anhedral		27.39	465541.61	48.15	212.47	38.55	0.03
NO16A125	J Halpin	458.0	small euhedral		95.16	464588.29	94.98	531.07	184.42	71.85
NO16A124	J Halpin	458.0	small euhedral		122.56	465337.33	41.94	290.71	69.07	109.70
NO16A126	J Halpin	458.0	small euhedral		286.27	465351.15	38.12	233.26	61.20	124.65
NO16A127	J Halpin	458.0	small euhedral		202.23	465337.88	38.49	324.01	76.63	192.26
NO16A114	J Halpin	458.0	small euhedral		220.97	465298.20	61.98	498.46	69.40	188.58
NO16A123	J Halpin	458.0	small euhedral		147.63	465398.80	25.82	172.86	58.18	136.22
NO16A115	J Halpin	458.0	small euhedral		225.60	465301.92	61.32	671.94	93.25	194.03
NO16A117	J Halpin	458.0	small euhedral		201.73	465174.09	93.64	758.55	91.44	167.30
NO16A113	J Halpin	458.0	small euhedral		205.93	465200.79	70.90	426.76	81.42	174.62
NO16A128	J Halpin	458.0	small euhedral		83.48	465273.94	54.59	469.64	78.21	94.16
NO16A116	J Halpin	458.0	small euhedral		251.21	465051.09	109.81	618.31	96.61	163.92
NO16A119	J Halpin	458.0	small euhedral		195.14	465223.22	104.81	972.53	133.79	187.42
NO16A120	J Halpin	458.0	small euhedral		308.42	464899.13	95.41	678.16	128.01	279.41
NO16A118	J Halpin	458.0	small euhedral		258.86	465153.02	62.37	705.35	247.04	221.10
NO16A131	J Halpin	458.0	small euhedral		568.11	465391.36	99.42	677.78	119.44	198.61
NO16A132	J Halpin	458.0	small euhedral		491.30	465390.39	100.94	678.20	120.82	224.70
NO16A072	J Halpin	459.0	large anhedral		0.47	465522.25	11.89	138.97	214.42	9.19
NO16A067	J Halpin	459.0	large euhedral		1.01	465524.63	4.65	98.49	275.77	7.78
NO16A071	J Halpin	459.0	large anhedral		0.05	465501.79	10.02	105.87	87.08	7.84
NO16A062	J Halpin	459.0	large euhedral		1.25	465514.45	6.46	165.40	183.55	13.26

Table A6.1: LA-ICPMS Analyses of Pyrite from Chapter 4

File	As(ppm)	Se(ppm)	Mo(ppm)	Ag(ppm)	Cd(ppm)	Sb(ppm)	Te(ppm)	Au(ppm)	Pb(ppm)	Bi(ppm)
NO16A030	409.8	3.4	7.72	0.81	0.23	30.87	<0.13	<0.01	776.22	0.07
NO16A038	49.1	2.8	1.48	0.48	0.14	2.91	<0.13	<0.01	148.12	0.09
NO16A034	43.6	<0.78	1.84	0.43	0.14	2.61	<0.13	<0.01	115.14	0.13
NO16A125	3615.1	7.9	17.31	2.78	0.21	288.24	<0.13	<0.01	1069.23	0.49
NO16A124	808.9	15.8	23.52	2.54	0.26	392.19	<0.13	<0.01	1380.59	0.64
NO16A126	757.1	12.8	29.35	2.38	0.62	294.96	<0.13	<0.01	1250.43	0.69
NO16A127	806.8	16.4	38.82	2.92	0.36	394.73	<0.13	<0.01	1686.94	0.74
NO16A114	955.5	14.0	45.69	3.36	0.50	352.27	<0.13	<0.01	1514.82	0.82
NO16A123	578.6	16.9	30.24	2.61	0.28	288.55	<0.13	<0.01	1182.57	0.87
NO16A115	941.6	16.1	50.76	3.81	0.43	404.73	<0.13	<0.01	1788.01	0.96
NO16A117	1420.5	13.3	47.67	3.23	0.61	320.17	0.54	<0.01	1444.63	0.97
NO16A113	1320.4	15.2	43.24	3.09	0.40	349.86	<0.13	<0.01	1457.26	0.97
NO16A128	1046.4	11.6	15.18	4.01	0.26	878.48	<0.13	<0.01	1742.06	1.00
NO16A116	1881.3	13.6	49.83	3.39	0.41	366.44	<0.13	<0.01	1496.00	1.11
NO16A119	1236.4	15.1	60.68	3.71	0.29	421.07	<0.13	<0.01	1845.54	1.37
NO16A120	2450.6	25.3	48.49	4.52	1.48	664.41	0.39	<0.01	2437.28	1.53
NO16A118	1499.4	29.8	64.14	4.73	1.10	717.56	<0.13	0.02	2587.30	1.59
NO16A131	606.5	3.7	18.28	12.27	1.44	211.04	0.48	<0.01	598.75	3.70
NO16A132	610.1	2.7	15.15	13.47	1.37	207.91	<0.13	<0.01	605.03	4.07
NO16A072	116.1	<0.78	5.37	0.66	<0.066	2.48	<0.13	<0.01	33.40	<0.01
NO16A067	107.2	1.6	4.21	0.95	<0.066	0.82	0.26	<0.01	19.81	0.02
NO16A071	192.8	<0.78	16.97	1.23	<0.066	2.29	<0.13	<0.01	44.79	0.02
NO16A062	145.3	<0.78	8.03	1.58	<0.066	1.08	0.28	<0.01	28.11	0.04

Table A6.1: LA-ICPMS Analyses of Pyrite from Chapter 4										
File	Analyst	Age (Ma)	Pyrite type	Setting	Mn (ppm)	Fe (ppm)	Co (ppm)	Ni (ppm)	Cu (ppm)	Zn (ppm)
NO16A070	J Halpin	459.0	large anhedral		1.23	465487.58	17.00	163.30	235.11	10.86
NO16A073	J Halpin	459.0	large anhedral		7.36	465465.22	3.19	119.65	93.29	11.01
NO16A058	J Halpin	459.0	large euhedral		16.58	465492.37	56.70	197.50	98.51	17.79
NO16A065	J Halpin	459.0	large euhedral		23.19	465503.56	16.86	77.28	106.51	37.74
NO16A061	J Halpin	459.0	large euhedral		5.37	465512.75	14.37	191.98	219.84	12.76
NO16A066	J Halpin	459.0	large euhedral		0.19	465522.45	48.52	108.28	144.89	115.13
NO16A064	J Halpin	459.0	large euhedral		10.10	465497.89	28.40	215.60	147.54	17.10
NO16A074	J Halpin	459.0	large anhedral		5.56	465422.69	26.30	181.02	249.77	16.22
NO16A057	J Halpin	459.0	large euhedral		1.90	465439.12	36.12	145.36	78.05	15.05
NO16A063	J Halpin	459.0	large euhedral		20.86	465486.80	34.78	252.50	168.36	19.23
NO16A056	J Halpin	459.0	large euhedral		25.90	465456.62	54.44	243.47	135.49	28.83
MY03A096	K Orth	490.0	small euhedral		205.77	465429.22	43.05	3031.21	47.30	224.54
MY03A097	K Orth	490.0	small euhedral		902.28	465053.46	23.46	1208.14	356.84	27.48
MY03A095	K Orth	490.0	small euhedral		390.77	465305.66	146.51	2634.72	515.58	17.77
MY03A084	K Orth	490.0	nodule		2460.54	464073.36	11.41	564.26	81.55	48.27
MY03A108	K Orth	490.0	large anhedral		100.45	465382.96	101.51	3488.04	100.29	0.34
MY03A111	K Orth	490.0	large anhedral		17.42	465325.51	261.28	4571.91	54.39	12.55
MY03A109	K Orth	490.0	large anhedral		188.28	465312.61	166.92	4694.95	174.24	0.84
MY03A107	K Orth	490.0	large anhedral		21.79	465275.73	391.79	4701.85	259.55	15.50
MY03A086	K Orth	490.0	nodule		2893.97	463912.36	20.33	531.38	371.55	45.48
MY03A085	K Orth	490.0	nodule		1373.45	464245.90	188.73	4245.02	283.29	1564.14
MY03A110	K Orth	490.0	large anhedral		231.13	465343.82	204.13	3957.97	658.63	13.15
MY03A117	K Orth	490.0	large anhedral		223.13	465346.42	161.10	2684.22	986.58	55.37

Table A6.1: LA-ICPMS Analyses of Pyrite from Chapter 4

File	As(ppm)	Se(ppm)	Mo(ppm)	Ag(ppm)	Cd(ppm)	Sb(ppm)	Te(ppm)	Au(ppm)	Pb(ppm)	Bi(ppm)
NO16A070	246	1.6	9.8	1.26	<0.066	2.66	<0.13	<0.01	63.89	0.06
NO16A073	330	<0.78	33.9	1.28	<0.066	2.93	<0.13	<0.01	90.65	0.07
NO16A058	228	1.7	13.3	0.49	<0.066	2.00	<0.13	<0.01	126.78	0.08
NO16A065	186	32.8	8.4	0.63	0.27	2.63	<0.13	<0.01	131.02	0.10
NO16A061	152	2.0	13.2	1.17	<0.066	1.64	<0.13	<0.01	63.73	0.10
NO16A066	115	9.8	5.4	0.73	0.22	2.58	<0.13	<0.01	155.02	0.13
NO16A064	207	2.1	30.9	1.40	0.23	3.22	<0.13	<0.01	120.19	0.16
NO16A074	489	2.3	10.1	1.05	0.16	3.45	<0.13	0.01	127.89	0.18
NO16A057	428	1.9	48.2	0.77	0.38	4.35	<0.13	<0.01	162.11	0.20
NO16A063	249	3.3	24.9	1.37	0.29	4.62	<0.13	<0.01	182.89	0.22
NO16A056	362	3.1	75.4	0.99	0.61	7.62	0.46	<0.01	294.33	0.58
MY03A096	465	104.5	8.7	3.70	6.58	11.70	0.52	0.01	62.39	0.10
MY03A097	1872	264.8	47.9	23.14	4.84	45.22	0.43	0.04	99.31	0.21
MY03A095	928	207.5	36.3	8.58	2.55	36.39	2.14	0.01	77.35	0.25
MY03A084	5544	399.5	165.5	308.94	2.74	203.89	2.87	0.55	51.51	0.44
MY03A108	638	90.4	46.8	1.45	0.28	23.50	1.55	<0.01	43.32	0.45
MY03A111	853	96.3	89.0	2.44	0.57	23.78	3.13	<0.01	51.62	0.46
MY03A109	902	118.7	13.7	1.60	0.19	25.46	2.02	0.01	36.15	0.52
MY03A107	1040	113.3	88.4	3.35	0.70	30.34	2.10	<0.01	53.34	0.55
MY03A086	6147	450.6	182.6	418.15	3.53	257.29	6.22	0.41	88.84	0.69
MY03A085	4898	342.5	224.7	283.14	37.36	178.33	4.81	0.37	92.92	0.70
MY03A110	785	144.1	169.5	3.16	1.05	38.22	1.67	<0.01	88.41	0.77
MY03A117	775	152.0	57.7	3.78	1.68	47.40	1.79	0.01	86.75	0.86

Table A6.1: LA-ICPMS Analyses of Pyrite from Chapter 4

File	Analyst	Age (Ma)	Pyrite type	Setting	Mn (ppm)	Fe (ppm)	Co (ppm)	Ni (ppm)	Cu (ppm)	Zn (ppm)
MY03A087	K Orth	490.0	small euhedral		2049.96	463620.69	116.86	1841.38	183.36	55.33
MY03A116	K Orth	490.0	large anhedral		263.34	465334.32	171.76	2825.93	918.67	199.45
MY03A115	K Orth	490.0	large anhedral		648.40	465317.59	130.90	2356.10	1155.51	25.62
MY03A114	K Orth	490.0	large anhedral		629.49	465310.86	134.69	2099.51	957.38	21.53
MY03A113	K Orth	490.0	large anhedral		203.84	465320.94	267.65	3397.19	565.52	6.58
MY03A112	K Orth	490.0	large anhedral		309.30	465154.56	149.93	2841.54	907.31	6.46
MY03A094	K Orth	490.0	small euhedral		231.73	465155.42	119.52	2608.59	1221.93	76.42
MY03A082	K Orth	490.0	nodule		1386.70	464362.32	174.94	3275.92	2077.43	124.66
MY03A092	K Orth	490.0	small euhedral		279.55	465163.62	99.48	2618.59	888.72	43.30
MY03A083	K Orth	490.0	nodule		1752.25	463570.33	46.93	2234.35	522.90	112.82
MY03A093	K Orth	490.0	small euhedral		281.72	465149.48	129.51	2724.42	1066.55	59.33
MY03A091	K Orth	490.0	small euhedral		178.17	464952.78	223.37	4228.00	766.88	53.34
MY03A089	K Orth	490.0	small euhedral		204.24	464947.96	167.50	3137.87	1060.82	30.14
MY03A090	K Orth	490.0	small euhedral		176.45	464832.02	191.02	3256.87	893.55	84.97
MY03A088	K Orth	490.0	small euhedral		195.30	464991.07	206.04	3432.98	1172.00	24.13
MY03A098	K Orth	490.0	small euhedral		202.62	464979.05	181.05	3931.19	832.07	42.50
FE10A035.D	JA Halpin	500.0	nodule	Rift Basin	0.84	465485.71	104.45	273.14	242.43	37.76
FE10A034.D	JA Halpin	500.0	nodule	Rift Basin	1.87	465475.29	81.10	249.21	190.16	36.31
FE10A037.D	JA Halpin	500.0	nodule	Rift Basin	1.09	465466.34	83.51	279.75	194.56	39.34
FE10A036.D	JA Halpin	500.0	nodule	Rift Basin	1.45	465463.05	136.77	348.13	242.75	73.44
FE10A038.D	JA Halpin	500.0	nodule	Rift Basin	9.04	465469.92	93.19	285.79	236.70	41.00
FE10B016	JA Halpin	500.0	nodule	Rift Basin	2.12	465482.85	88.30	234.70	236.78	16.18
FE10B017	JA Halpin	500.0	nodule	Rift Basin	3.94	465476.85	93.12	248.55	200.34	14.37

Table A6.1: LA-ICPMS Analyses of Pyrite from Chapter 4										
File	As(ppm)	Se(ppm)	Mo(ppm)	Ag(ppm)	Cd(ppm)	Sb(ppm)	Te(ppm)	Au(ppm)	Pb(ppm)	Bi(ppm)
MY03A087	7240.2	498.2	193.13	423.46	4.25	265.14	4.55	0.66	96.19	0.88
MY03A116	820.2	179.9	151.78	4.24	4.79	50.77	1.84	0.01	112.65	0.95
MY03A115	882.9	250.4	245.31	3.49	1.52	67.31	1.37	<0.01	137.74	1.13
MY03A114	908.0	160.1	53.81	3.27	1.66	67.52	1.20	0.01	120.20	1.14
MY03A113	870.3	165.3	204.79	3.92	1.05	65.55	2.12	<0.01	148.56	1.28
MY03A112	1493.6	184.5	11.06	3.61	1.19	73.93	1.40	<0.01	124.35	1.31
MY03A094	1490.4	150.0	449.80	22.83	1.76	117.37	2.39	0.02	235.25	1.36
MY03A082	4461.7	302.5	145.08	219.95	5.19	197.84	8.23	0.12	191.27	1.37
MY03A092	1459.7	150.9	481.57	28.22	2.07	108.16	3.06	0.01	241.44	1.43
MY03A083	7428.9	531.2	283.47	382.25	5.38	304.42	6.65	0.70	176.84	1.47
MY03A093	1512.7	144.7	853.66	23.93	1.68	121.91	2.51	0.02	351.76	1.62
MY03A091	2249.6	165.8	696.41	22.44	1.46	150.02	3.61	0.03	285.12	1.73
MY03A089	2267.7	177.8	290.99	26.05	1.31	130.74	3.73	0.05	222.78	1.82
MY03A090	2702.0	218.2	119.67	26.96	2.56	149.93	4.49	0.02	187.10	1.85
MY03A088	2106.1	199.3	329.05	27.81	1.31	154.38	4.90	<0.01	269.62	2.29
MY03A098	2151.2	176.6	470.73	25.78	2.19	178.61	3.58	0.02	333.13	2.30
FE10A035.D	253.0	108.2	0.64	7.98	1.21	36.11	0.58	0.09	195.29	1.03
FE10A034.D	292.0	103.3	0.58	7.34	1.35	42.39	0.58	0.07	184.60	1.03
FE10A037.D	325.5	127.5	0.62	8.55	1.26	44.43	0.71	0.12	207.72	1.20
FE10A036.D	337.9	127.3	0.78	9.17	2.20	49.24	0.71	0.12	226.75	1.23
FE10A038.D	312.1	123.7	0.80	8.44	1.20	43.89	0.76	0.12	212.26	1.24
FE10B016	263.7	191.7	3.46	5.42	1.34	290.15	<0.13	0.07	326.96	3.18
FE10B017	286.2	194.2	3.43	5.49	1.49	294.66	<0.13	0.08	302.25	3.51

Table A6.1: LA-ICPMS Analyses of Pyrite from Chapter 4

File	Analyst	Age (Ma)	Pyrite type	Setting	Mn (ppm)	Fe (ppm)	Co (ppm)	Ni (ppm)	Cu (ppm)	Zn (ppm)
FE10B018	JA Halpin	500.0	nodule	Rift Basin	5.35	465481.19	98.82	250.79	213.33	126.94
FE10B019	JA Halpin	500.0	nodule	Rift Basin	3.27	465466.69	98.51	254.33	263.51	102.42
FE10B021	JA Halpin	500.0	framboid	Rift Basin	337.06	465458.32	230.30	316.04	228.69	124.86
FE10B020	JA Halpin	500.0	framboid	Rift Basin	285.08	465370.04	231.97	432.57	203.47	75.78
FE10B022	JA Halpin	500.0	framboid	Rift Basin	244.57	465474.21	204.34	406.81	128.93	77.96
FE10B010	JA Halpin	500.0	framboid	Rift Basin	219.57	465275.38	369.86	669.24	274.31	225.49
FE10B007	JA Halpin	500.0	framboid	Rift Basin	250.79	465168.58	449.23	731.77	426.71	138.36
MA26A046	JA Halpin	540.0	large euhedral	Deep Facies	<0.02	465224.59	4.02	580.93	82.62	0.73
MA26A044	JA Halpin	540.0	large euhedral	Deep Facies	<0.02	465426.74	0.03	53.65	96.06	1.42
MA26A041	JA Halpin	540.0	large euhedral	Deep Facies	1.33	465123.01	1.30	165.17	581.60	0.77
MA26A038	JA Halpin	540.0	large euhedral	Deep Facies	<0.02	465339.61	0.40	55.16	173.06	1.30
MA26A042	JA Halpin	540.0	large euhedral	Deep Facies	<0.02	465417.14	0.21	58.24	323.61	3.82
MA26A043	JA Halpin	540.0	large euhedral	Deep Facies	<0.02	465164.38	1.39	194.30	207.45	1.50
MA26A045	JA Halpin	540.0	large euhedral	Deep Facies	6.81	465287.49	2.40	195.62	235.30	20.65
MA26A033	JA Halpin	540.0	large euhedral	Deep Facies	<0.02	465180.55	3.56	340.65	1593.43	3.58
MA26A036	JA Halpin	540.0	large euhedral	Deep Facies	<0.02	465355.05	10.61	1107.23	315.57	1.69
MA26A035	JA Halpin	540.0	large euhedral	Deep Facies	<0.02	465301.37	2.04	320.60	2082.00	5.22
MA26A039	JA Halpin	540.0	large euhedral	Deep Facies	0.37	465245.95	1.25	420.51	232.76	1.89
MA26A040	JA Halpin	540.0	large euhedral	Deep Facies	3.47	465425.46	1.02	336.72	85.80	11.07
MA26A031	JA Halpin	540.0	large euhedral	Deep Facies	<0.02	465197.78	9.94	739.52	2703.27	9.85
MA26A034	JA Halpin	540.0	large euhedral	Deep Facies	<0.02	464975.64	26.30	1620.41	877.62	1.71
MA26A037	JA Halpin	540.0	large euhedral	Deep Facies	<0.02	465169.81	8.84	548.94	1013.54	3.27
MA26A032	JA Halpin	540.0	large euhedral	Deep Facies	0.81	465221.16	3.87	479.88	849.03	2.40

Table A6.1: LA-ICPMS Analyses of Pyrite from Chapter 4

File	As(ppm)	Se(ppm)	Mo(ppm)	Ag(ppm)	Cd(ppm)	Sb(ppm)	Te(ppm)	Au(ppm)	Pb(ppm)	Bi(ppm)
FE10B018	270	147.0	3.9	6.14	3.02	347.04	<0.13	0.08	427.03	3.87
FE10B019	324	158.0	4.7	7.44	3.28	399.28	<0.13	0.10	303.84	4.05
FE10B021	356	41.1	10.0	9.96	0.56	40.37	<0.128	0.12	240.80	5.23
FE10B020	686	71.4	8.1	13.06	0.35	134.34	<0.128	0.18	326.71	6.12
FE10B022	296	54.9	15.4	9.18	0.79	42.90	<0.128	0.16	316.66	6.95
FE10B010	1041	82.8	5.1	27.70	0.97	104.08	<0.128	0.25	521.52	10.05
FE10B007	1441	143.0	61.8	23.99	2.19	100.86	<0.128	0.30	693.92	15.68
MA26A046	1231	199.9	46.4	1.86	0.20	35.68	0.13	0.01	66.02	<0.01
MA26A044	474	170.1	42.1	1.46	0.15	24.76	<0.13	<0.01	81.18	<0.01
MA26A041	1612	236.2	74.2	1.84	0.21	86.78	<0.13	<0.01	73.46	0.02
MA26A038	800	112.9	13.2	0.80	0.25	21.52	<0.13	0.01	69.53	0.03
MA26A042	510	105.4	46.6	1.60	0.15	18.55	<0.13	<0.01	67.09	0.04
MA26A043	1457	224.8	27.5	2.33	0.41	43.45	<0.13	0.01	123.81	0.04
MA26A045	996	144.0	90.6	1.70	0.95	49.98	<0.13	0.01	55.25	0.05
MA26A033	1396	151.4	226.2	7.60	0.45	131.12	0.17	0.01	76.77	0.07
MA26A036	743	130.6	13.9	3.55	0.32	58.76	0.25	0.02	111.24	0.09
MA26A035	944	60.6	360.5	8.00	0.24	126.43	0.25	0.01	58.31	0.09
MA26A039	1151	128.9	56.6	4.55	0.31	54.13	0.29	0.01	68.26	0.11
MA26A040	479	196.6	11.4	1.15	0.33	13.10	<0.13	<0.01	80.18	0.12
MA26A031	1332	119.2	313.7	10.63	0.41	168.69	0.47	0.02	96.94	0.13
MA26A034	2164	290.1	60.1	10.92	0.65	229.37	0.43	0.03	249.05	0.14
MA26A037	1437	184.7	67.2	8.92	0.46	135.91	0.46	0.04	234.56	0.15
MA26A032	1244	164.4	82.9	10.62	0.40	131.25	0.46	0.03	236.57	0.22

Table A6.1: LA-ICPMS Analyses of Pyrite from Chapter 4

File	Analyst	Age (Ma)	Pyrite type	Setting	Mn (ppm)	Fe (ppm)	Co (ppm)	Ni (ppm)	Cu (ppm)	Zn (ppm)
MA21B083	D Gregory	550.0	small anhedral	Deep Facies	974.64	465321.91	7.64	88.70	78.33	43.04
MA21B098	D Gregory	550.0	small anhedral	Deep Facies	157.95	465515.28	23.68	322.63	140.33	2067.00
MA21B086	D Gregory	550.0	small anhedral	Deep Facies	448.88	465413.93	26.88	310.64	113.64	16.73
MA21B088	D Gregory	550.0	small anhedral	Deep Facies	215.77	465343.91	18.61	350.66	219.29	3.24
MA21B084	D Gregory	550.0	small anhedral	Deep Facies	621.00	465401.19	22.72	258.49	122.92	28.98
MA21B080	D Gregory	550.0	small anhedral	Deep Facies	698.83	465433.13	40.58	408.21	274.32	18.48
MA21B094	D Gregory	550.0	small anhedral	Deep Facies	733.10	465397.71	40.45	496.73	323.15	78.05
MA21B090	D Gregory	550.0	small anhedral	Deep Facies	837.41	465426.39	40.80	503.28	285.82	28.74
MA21B082	D Gregory	550.0	small anhedral	Deep Facies	48.73	465369.93	49.32	454.38	338.29	60.71
MA21B096	D Gregory	550.0	small anhedral	Deep Facies	909.79	465405.02	34.81	473.02	355.29	44.20
MA21B089	D Gregory	550.0	small anhedral	Deep Facies	481.32	465416.78	42.97	559.11	357.06	4.08
MA21B097	D Gregory	550.0	small anhedral	Deep Facies	715.70	465445.32	55.73	627.79	418.51	114.56
MA21B095	D Gregory	550.0	small anhedral	Deep Facies	6.47	465440.86	42.74	709.53	417.01	68.94
MA21B081	D Gregory	550.0	small anhedral	Deep Facies	1317.14	465427.69	72.55	571.41	239.42	30.46
MA21B085	D Gregory	550.0	small anhedral	Deep Facies	2280.92	465405.20	72.25	666.25	318.37	22.14
MA21B076	D Gregory	550.0	small anhedral	Deep Facies	1940.63	464883.75	51.22	1467.83	8268.30	76.37
JL24A032	JA Halpin	630.0	nodule	Deep Facies	331.10	465454.96	739.33	1065.60	352.39	53.47
JL24A033	JA Halpin	630.0	nodule	Deep Facies	158.92	465477.38	591.62	1379.73	194.24	33.59
JL24A034	JA Halpin	630.0	nodule	Deep Facies	532.46	465285.71	709.48	1014.16	621.48	87.22
JL24A038	JA Halpin	630.0	nodule	Deep Facies	186.70	465415.62	976.27	1231.02	838.97	36.07
JL24A031	JA Halpin	630.0	nodule	Deep Facies	293.60	465392.21	774.62	1135.71	507.35	229.49
JL24A046	JA Halpin	630.0	nodule	Deep Facies	490.99	465441.02	703.48	1091.96	356.49	213.14
JL24A043	JA Halpin	630.0	nodule	Deep Facies	123.69	465420.66	781.90	1419.34	288.02	21.14

Table A6.1: LA-ICPMS Analyses of Pyrite from Chapter 4

File	As(ppm)	Se(ppm)	Mo(ppm)	Ag(ppm)	Cd(ppm)	Sb(ppm)	Te(ppm)	Au(ppm)	Pb(ppm)	Bi(ppm)
MA21B083	866.6	436.6	275.57	250.61	4.94	172.67	<0.13	0.03	1248.99	0.69
MA21B098	142.2	149.7	39.97	14.62	149.63	39.29	0.44	<0.01	211.24	1.32
MA21B086	521.9	270.6	274.73	146.55	6.95	154.06	0.43	<0.01	905.24	1.48
MA21B088	784.2	183.6	67.87	39.72	3.66	67.35	<0.13	<0.01	462.97	1.55
MA21B084	569.6	290.2	248.59	164.58	6.92	183.81	0.29	<0.01	998.94	1.80
MA21B080	450.0	215.5	349.42	102.51	6.68	120.25	0.52	<0.01	679.89	2.77
MA21B094	582.7	270.5	213.01	133.98	20.18	170.48	0.98	<0.01	1475.52	3.02
MA21B090	475.2	258.2	186.86	112.27	12.83	132.11	0.75	0.05	1066.09	3.13
MA21B082	686.8	274.8	308.50	31.90	7.71	116.10	1.45	<0.01	317.07	3.46
MA21B096	555.3	306.2	81.97	62.28	12.29	117.99	1.05	<0.01	723.03	3.58
MA21B089	511.2	250.2	191.55	106.52	8.72	139.09	0.80	<0.01	1121.92	3.64
MA21B097	404.3	290.4	297.25	123.40	20.00	137.04	1.22	<0.01	1130.19	3.66
MA21B095	421.0	254.7	56.14	38.12	12.39	125.50	1.47	<0.01	609.80	4.70
MA21B081	470.4	270.1	538.12	124.83	10.74	139.22	1.03	<0.01	731.32	4.71
MA21B085	554.6	372.1	400.05	221.99	8.91	223.91	0.98	0.05	1153.87	8.20
MA21B076	2508.2	1321.0	4998.00	892.03	43.76	1212.13	14.68	0.87	5144.04	43.41
JL24A032	368.2	6.4	57.74	1.27	1.49	14.37	0.28	0.02	75.05	0.21
JL24A033	284.2	4.1	41.87	0.99	1.06	10.25	0.24	0.02	77.57	0.24
JL24A034	1002.3	22.2	171.20	1.51	1.30	33.35	0.68	0.07	111.99	0.28
JL24A038	515.6	8.7	59.49	1.40	1.65	16.28	0.39	0.03	126.50	0.34
JL24A031	603.3	14.1	94.74	1.48	2.65	18.34	0.51	0.05	118.35	0.35
JL24A046	420.4	7.9	55.62	1.25	4.71	15.23	0.47	0.03	112.27	0.43
JL24A043	496.7	6.2	53.95	1.34	1.71	18.14	0.55	0.03	119.86	0.46

Table A6.1: LA-ICPMS Analyses of Pyrite from Chapter 4										
File	Analyst	Age (Ma)	Pyrite type	Setting	Mn (ppm)	Fe (ppm)	Co (ppm)	Ni (ppm)	Cu (ppm)	Zn (ppm)
JL24A037	JA Halpin	630.0	nodule	Deep Facies	300.99	465371.61	907.78	1246.73	560.69	54.07
JL24A044	JA Halpin	630.0	nodule	Deep Facies	202.60	465412.77	838.68	1268.85	389.27	35.48
JL24A036	JA Halpin	630.0	nodule	Deep Facies	251.20	465350.56	806.70	1205.28	405.74	310.67
JL24A045	JA Halpin	630.0	nodule	Deep Facies	335.44	465423.87	794.48	1246.26	576.50	73.08
JL24A040	JA Halpin	630.0	nodule	Deep Facies	138.11	465452.29	687.27	1097.50	426.82	20.63
JL24A047	JA Halpin	630.0	nodule	Deep Facies	389.99	465290.77	849.23	1218.98	635.41	91.28
JL24A011	JA Halpin	630.0	small anhedral	Deep Facies	627.79	465243.53	421.65	675.82	3460.41	389.45
JL24A010	JA Halpin	630.0	small anhedral	Deep Facies	489.78	465299.21	286.55	818.34	6738.81	360.68
JL24A042	JA Halpin	630.0	nodule	Deep Facies	422.77	465271.13	979.37	1125.12	404.53	42.07
JL24A014	JA Halpin	630.0	small anhedral	Deep Facies	387.95	465388.72	451.97	1635.63	1524.81	198.48
JL24A013	JA Halpin	630.0	small anhedral	Deep Facies	834.90	465405.07	525.32	905.60	1180.50	246.38
JL24A035	JA Halpin	630.0	nodule	Deep Facies	1032.47	465236.06	850.38	807.84	9873.09	2554.68
JL24A041	JA Halpin	630.0	nodule	Deep Facies	851.67	465112.02	724.38	1050.93	704.15	119.10
JL24A020	JA Halpin	630.0	small anhedral	Deep Facies	711.16	465314.36	270.66	623.57	2346.83	376.39
JL24A012	JA Halpin	630.0	small anhedral	Deep Facies	617.33	465268.16	317.76	694.58	8742.46	638.07
JL24A007	JA Halpin	630.0	small anhedral	Deep Facies	375.06	465335.16	374.04	917.88	1930.92	499.19
JL24A023	JA Halpin	630.0	small anhedral	Deep Facies	981.22	465342.39	268.50	590.06	2291.35	414.47
JL24A021	JA Halpin	630.0	small anhedral	Deep Facies	560.26	465214.67	228.84	667.76	2184.42	487.82
JL24A019	JA Halpin	630.0	small anhedral	Deep Facies	986.02	465368.16	323.98	606.63	8567.25	2127.31
JL24A022	JA Halpin	630.0	small anhedral	Deep Facies	878.69	465394.49	285.48	717.48	2005.59	882.71
JL24A016	JA Halpin	630.0	small anhedral	Deep Facies	560.52	465116.13	215.90	754.30	2793.98	584.32
JL24A018	JA Halpin	630.0	small anhedral	Deep Facies	847.81	465330.19	245.14	763.44	2996.63	360.57
JL24A017	JA Halpin	630.0	small anhedral	Deep Facies	442.64	465000.62	191.79	823.04	1565.15	354.00

Table A6.1: LA-ICPMS Analyses of Pyrite from Chapter 4										
File	As(ppm)	Se(ppm)	Mo(ppm)	Ag(ppm)	Cd(ppm)	Sb(ppm)	Te(ppm)	Au(ppm)	Pb(ppm)	Bi(ppm)
JL24A037	680	13.8	102.7	1.72	1.66	22.18	0.41	0.05	156.41	0.49
JL24A044	526	7.7	52.9	1.81	1.70	20.04	0.55	0.03	154.09	0.61
JL24A036	759	13.6	112.1	1.96	4.43	24.87	0.57	0.06	207.84	0.63
JL24A045	485	7.6	58.1	1.57	1.85	18.80	0.65	0.03	176.84	0.65
JL24A040	378	5.1	39.6	2.03	1.29	23.87	0.27	0.03	196.96	0.70
JL24A047	983	20.6	161.7	2.05	1.63	29.98	0.81	0.09	207.94	0.73
JL24A011	1160	33.3	142.2	1.03	1.77	14.42	0.35	0.05	57.79	0.82
JL24A010	952	24.0	147.1	0.82	1.85	10.44	0.49	0.03	93.67	0.97
JL24A042	1057	15.8	137.4	2.23	1.82	33.75	1.10	0.08	242.16	1.00
JL24A014	616	17.4	87.5	1.24	0.71	13.65	0.49	0.04	81.37	1.00
JL24A013	555	14.6	114.8	0.89	1.03	8.73	0.39	0.04	72.21	1.00
JL24A035	1188	22.8	224.3	1.62	14.03	40.33	1.15	0.07	252.69	1.00
JL24A041	1653	34.4	299.1	2.17	1.32	47.56	1.46	0.14	243.95	1.02
JL24A020	895	67.4	100.1	0.94	1.43	22.05	0.59	0.13	92.62	1.18
JL24A012	1068	21.0	159.1	1.02	3.12	12.68	0.79	0.05	121.30	1.18
JL24A007	817	18.6	162.6	0.91	2.68	11.43	0.34	0.03	105.87	1.24
JL24A023	790	56.0	98.5	1.32	1.82	18.61	0.73	0.11	102.54	1.49
JL24A021	1268	94.5	115.2	1.61	2.39	34.80	0.94	0.19	123.85	1.63
JL24A019	693	60.2	98.6	1.09	9.03	19.44	0.78	0.10	119.18	1.74
JL24A022	595	38.5	90.9	1.87	4.01	17.75	0.66	0.11	122.47	1.74
JL24A016	1638	135.7	123.8	1.80	2.87	47.67	0.94	0.24	127.64	1.99
JL24A018	836	62.3	94.9	1.85	1.45	25.44	0.84	0.13	140.28	2.15
JL24A017	2070	167.7	135.8	2.25	1.93	61.22	1.14	0.30	165.01	2.44

Table A6.1: LA-ICPMS Analyses of Pyrite from Chapter 4										
File	Analyst	Age (Ma)	Pyrite type	Setting	Mn (ppm)	Fe (ppm)	Co (ppm)	Ni (ppm)	Cu (ppm)	Zn (ppm)
JL24A089	JA Halpin	630.0	small anhedral		68.68	465037.67	107.54	661.31	367.83	216.53
JL24A098	JA Halpin	630.0	small anhedral		81.43	465384.14	324.18	322.33	399.75	66.19
JL24A096	JA Halpin	630.0	small anhedral		2026.61	465417.47	993.18	889.09	526.17	78.33
JL24A088	JA Halpin	630.0	small anhedral		430.57	465117.02	398.54	801.59	577.04	221.67
JL24A103	JA Halpin	630.0	small anhedral		81.78	465298.76	215.92	268.81	302.04	32.59
JL24A095	JA Halpin	630.0	small anhedral		82.08	465462.04	231.27	232.19	330.90	56.70
JL24A091	JA Halpin	630.0	small anhedral		3493.51	465414.46	924.94	1371.98	442.70	59.20
JL24A092	JA Halpin	630.0	small anhedral		2315.23	465400.25	977.56	1449.03	416.82	70.54
JL24A101	JA Halpin	630.0	small anhedral		1105.86	465129.73	612.61	651.21	1011.91	256.10
JL24A075	JA Halpin	640.0	small anhedral	Deep Facies	222.27	465517.13	235.99	1008.56	120.88	132.78
JL24A055	JA Halpin	640.0	small anhedral	Deep Facies	2502.90	465448.72	60.98	284.07	452.70	114.28
JL24A069	JA Halpin	640.0	small anhedral	Deep Facies	1431.57	465283.54	49.05	1020.35	768.96	114.45
JL24A068	JA Halpin	640.0	small anhedral	Deep Facies	1550.72	465277.49	57.11	1093.10	809.79	115.05
JL24A070	JA Halpin	640.0	small anhedral	Deep Facies	1500.44	465267.16	59.01	1168.57	838.65	128.99
JL24A073	JA Halpin	640.0	small anhedral	Deep Facies	2825.87	465327.49	70.60	1124.63	749.65	196.89
JL24A074	JA Halpin	640.0	small anhedral	Deep Facies	1845.43	465285.24	77.12	1324.62	962.03	519.71
JL24A072	JA Halpin	640.0	small anhedral	Deep Facies	3078.88	465330.24	77.97	1267.63	842.91	193.92
JL24A067	JA Halpin	640.0	small anhedral	Deep Facies	1573.77	465258.94	53.56	1231.65	892.65	97.53
JL24A062	JA Halpin	640.0	small anhedral	Deep Facies	2292.99	465247.24	84.73	1446.78	947.62	218.22
JL24A061	JA Halpin	640.0	small anhedral	Deep Facies	2262.71	465240.43	62.74	1396.58	995.66	182.48
JL24A063	JA Halpin	640.0	small anhedral	Deep Facies	2100.14	465239.57	68.19	1406.79	1018.00	229.66
JL24A064	JA Halpin	640.0	small anhedral	Deep Facies	2096.04	465251.31	93.14	1404.31	971.16	158.36
JL24A065	JA Halpin	640.0	small anhedral	Deep Facies	2194.51	465237.91	77.45	1434.74	1020.66	154.98

Table A6.1: LA-ICPMS Analyses of Pyrite from Chapter 4

File	As(ppm)	Se(ppm)	Mo(ppm)	Ag(ppm)	Cd(ppm)	Sb(ppm)	Te(ppm)	Au(ppm)	Pb(ppm)	Bi(ppm)
JL24A089	1931.6	75.7	101.97	3.28	1.17	54.33	0.26	0.13	1108.82	2.64
JL24A098	633.5	5.5	34.41	1.12	0.26	11.95	1.25	0.08	505.68	13.21
JL24A096	508.7	40.0	14.16	2.35	4.27	125.83	0.92	<0.01	2260.68	16.50
JL24A088	1634.3	102.4	79.90	3.38	2.91	89.00	1.15	0.16	9045.16	17.26
JL24A103	953.4	13.6	53.48	2.68	<0.066	17.12	0.98	0.11	625.02	19.32
JL24A095	341.7	17.0	47.02	1.65	1.55	37.20	<0.13	0.07	886.31	23.30
JL24A091	519.9	20.0	18.80	2.98	5.15	99.23	1.31	0.06	1033.59	24.89
JL24A092	573.2	19.6	21.31	2.90	5.06	102.50	1.40	0.07	962.64	26.79
JL24A101	1586.7	133.9	81.06	4.40	3.10	53.38	6.19	0.12	1644.37	34.10
JL24A075	135.3	72.1	38.76	0.50	1.42	4.21	0.25	0.01	37.37	0.66
JL24A055	391.6	106.1	120.39	1.40	1.88	15.13	0.76	<0.01	91.46	1.95
JL24A069	1010.4	77.5	85.53	4.19	5.39	27.79	2.36	0.05	252.75	5.08
JL24A068	1033.1	79.0	72.84	4.49	6.04	31.17	2.42	0.06	267.87	5.30
JL24A070	1071.8	86.2	87.32	4.67	6.17	32.56	2.44	0.06	287.09	5.75
JL24A073	845.8	93.7	51.33	5.42	5.30	35.97	3.25	0.11	249.85	5.80
JL24A074	1004.0	122.2	72.63	5.23	7.76	30.17	3.01	0.10	290.48	5.99
JL24A072	835.4	95.7	52.61	5.89	5.87	37.63	3.77	0.10	267.29	6.19
JL24A067	1102.6	87.3	82.86	5.16	6.54	33.00	2.81	0.07	300.07	6.23
JL24A062	1146.4	131.6	111.48	6.45	6.59	42.24	4.20	0.09	325.39	8.09
JL24A061	1171.9	134.6	79.25	7.14	6.67	42.79	4.35	0.10	332.29	8.20
JL24A063	1175.1	131.3	81.62	6.97	6.69	42.93	4.24	0.10	333.65	8.29
JL24A064	1131.2	132.1	93.47	6.63	6.41	40.81	4.11	0.11	320.00	8.35
JL24A065	1181.4	126.2	100.54	6.85	6.20	42.00	4.10	0.08	332.58	9.08

Table A6.1: LA-ICPMS Analyses of Pyrite from Chapter 4

File	Analyst	Age (Ma)	Pyrite type	Setting	Mn (ppm)	Fe (ppm)	Co (ppm)	Ni (ppm)	Cu (ppm)	Zn (ppm)
JL24A056	JA Halpin	640.0	small anhedral	Deep Facies	1289.50	465234.53	122.15	1734.61	1263.27	124.77
JL24A057	JA Halpin	640.0	small anhedral	Deep Facies	1492.07	465159.35	102.71	1839.51	1384.98	175.83
JL24A058	JA Halpin	640.0	small anhedral	Deep Facies	1373.61	465177.36	107.59	1681.04	1333.06	224.78
JL24A059	JA Halpin	640.0	small anhedral	Deep Facies	1782.76	465158.90	124.43	1787.44	1501.05	205.09
JL24A136	JA Halpin	657.0	small anhedral		7069.71	465467.84	54.07	329.71	350.23	102.38
JL24A131	JA Halpin	657.0	small anhedral		4999.37	465290.08	100.25	493.55	698.96	221.15
JL24A132	JA Halpin	657.0	small anhedral		5218.30	465411.70	60.17	323.49	549.61	176.82
JL24A139	JA Halpin	657.0	small anhedral		7292.47	465347.27	66.60	442.00	643.72	187.53
JL24A121	JA Halpin	657.0	small anhedral		6885.46	465515.90	140.21	132.55	1139.00	157.05
JL24A120	JA Halpin	657.0	small anhedral		6636.67	465514.24	122.13	159.68	1314.08	156.81
JL24A133	JA Halpin	657.0	small anhedral		7532.23	465392.30	51.21	444.66	793.72	159.02
JL24A112	JA Halpin	657.0	small anhedral		7621.20	465520.33	113.09	147.50	1697.09	262.45
JL24A143	JA Halpin	657.0	small anhedral		7452.44	465390.67	56.65	470.31	644.88	196.81
JL24A140	JA Halpin	657.0	small anhedral		7575.10	465387.73	106.37	524.02	803.09	147.11
JL24A111	JA Halpin	657.0	small anhedral		6767.86	465510.31	120.68	162.15	1221.04	178.25
JL24A141	JA Halpin	657.0	small anhedral		6620.03	465420.52	99.79	568.16	879.40	176.50
JL24A118	JA Halpin	657.0	small anhedral		6069.42	465511.86	146.79	164.97	981.60	247.80
JL24A134	JA Halpin	657.0	small anhedral		9331.69	465492.97	104.98	401.35	592.93	144.46
JL24A115	JA Halpin	657.0	small anhedral		7235.90	465505.83	196.34	192.09	1114.04	232.10
JL24A122	JA Halpin	657.0	small anhedral		5806.77	465515.02	127.14	159.46	1181.11	150.20
JL24A142	JA Halpin	657.0	small anhedral		9979.27	465479.23	131.56	479.50	686.05	161.49
JL24A114	JA Halpin	657.0	small anhedral		7446.31	465508.44	166.65	183.55	1211.28	210.22
JL24A119	JA Halpin	657.0	small anhedral		6313.72	465510.31	118.75	177.23	936.79	160.71

Table A6.1: LA-ICPMS Analyses of Pyrite from Chapter 4										
File	As(ppm)	Se(ppm)	Mo(ppm)	Ag(ppm)	Cd(ppm)	Sb(ppm)	Te(ppm)	Au(ppm)	Pb(ppm)	Bi(ppm)
JL24A056	1194	158.5	151.1	6.51	10.06	50.33	4.81	0.09	452.91	10.56
JL24A057	1476	189.8	184.8	7.17	10.47	60.54	6.12	0.11	511.12	12.52
JL24A058	1408	193.2	291.8	7.36	9.78	59.61	5.78	0.12	515.81	12.65
JL24A059	1477	213.8	449.4	7.06	8.67	65.57	5.86	0.11	555.22	13.17
JL24A136	320	18.9	70.0	1.06	3.15	27.82	0.75	<0.01	912.68	5.30
JL24A131	986	31.4	69.0	1.14	2.29	48.41	1.84	<0.01	900.92	5.63
JL24A132	530	10.7	69.7	0.67	2.03	32.26	1.23	<0.01	859.76	5.63
JL24A139	772	28.4	68.9	1.16	2.44	45.73	1.76	0.04	1046.07	5.77
JL24A121	140	4.9	8.1	3.06	0.79	14.48	<0.13	<0.01	1982.13	6.20
JL24A120	146	5.1	5.8	2.13	0.37	12.47	<0.13	<0.01	1629.04	6.26
JL24A133	603	23.6	60.7	1.30	1.78	43.66	1.13	<0.01	1026.56	6.44
JL24A112	123	8.3	5.8	2.45	1.07	10.62	<0.13	<0.01	1492.28	6.62
JL24A143	609	23.0	62.5	0.97	1.78	39.14	1.51	<0.01	973.04	6.67
JL24A140	620	24.5	99.9	1.58	1.93	41.01	2.15	<0.01	1200.96	7.64
JL24A111	161	3.1	4.6	3.80	<0.066	14.30	<0.13	<0.01	1728.73	8.39
JL24A141	497	32.4	50.9	1.80	1.99	36.29	1.40	0.04	1386.14	8.73
JL24A118	155	9.7	7.0	2.56	0.64	11.68	<0.13	<0.01	1796.41	8.73
JL24A134	226	11.0	112.7	1.44	3.62	37.44	1.65	<0.01	1598.96	9.37
JL24A115	178	<0.78	8.1	4.33	<0.066	18.15	<0.13	<0.01	2182.21	9.48
JL24A122	143	25.2	5.5	3.79	1.89	17.08	<0.13	<0.01	2108.19	9.81
JL24A142	277	11.1	91.2	1.66	3.21	35.13	1.70	0.03	1739.20	10.38
JL24A114	168	7.0	7.5	4.14	1.15	15.99	<0.13	<0.01	2530.77	10.47
JL24A119	161	6.8	4.9	4.52	1.56	15.59	<0.13	<0.01	2419.14	13.66

Table A6.1: LA-ICPMS Analyses of Pyrite from Chapter 4

File	Analyst	Age (Ma)	Pyrite type	Setting	Mn (ppm)	Fe (ppm)	Co (ppm)	Ni (ppm)	Cu (ppm)	Zn (ppm)
JL24A135	JA Halpin	657.0	small anhedral		8668.93	465476.98	106.06	357.99	437.92	150.61
MY09A049	E Lounejeva	860.0	small euhedral	Deep Facies	0.06	465530.05	1306.71	125.66	2.77	0.66
MY09A053	E Lounejeva	860.0	small euhedral	Deep Facies	2.71	465549.39	14.28	11.03	14.29	5.17
MY09A048	E Lounejeva	860.0	small euhedral	Deep Facies	1.17	465523.20	1045.90	155.09	82.48	10.71
MY09A058	E Lounejeva	860.0	small euhedral	Deep Facies	422.90	465548.99	54.69	18.44	7.95	11.74
MY09A050	E Lounejeva	860.0	small euhedral	Deep Facies	0.13	465547.10	15.03	19.75	81.63	21.08
MY09A055	E Lounejeva	860.0	small euhedral	Deep Facies	16.23	465547.02	56.64	51.19	33.97	27.95
MY09A010	E Lounejeva	860.0	nodule	Deep Facies	188.99	465547.58	20.67	163.06	212.05	76.72
MY09A015	E Lounejeva	860.0	nodule	Deep Facies	15.10	465498.25	320.40	592.69	55.84	4.35
MY09A017	E Lounejeva	860.0	nodule	Deep Facies	9.47	465483.91	298.53	427.92	125.11	3.22
MY09A014	E Lounejeva	860.0	nodule	Deep Facies	679.93	465522.40	315.01	590.29	131.53	113.06
MY09A011	E Lounejeva	860.0	nodule	Deep Facies	142.10	465522.02	233.20	419.32	1005.10	125.22
MY09A012	E Lounejeva	860.0	nodule	Deep Facies	144.54	465496.14	451.56	343.52	270.92	53.34
MY09A016	E Lounejeva	860.0	nodule	Deep Facies	42.10	465464.05	312.13	566.97	485.03	12.85
MY09A013	E Lounejeva	860.0	nodule	Deep Facies	267.92	465523.57	278.90	329.53	155.91	81.93
MY09A009	E Lounejeva	860.0	nodule	Deep Facies	309.92	465444.72	357.79	478.18	87.35	49.74
MY09A008	E Lounejeva	860.0	nodule	Deep Facies	347.62	465416.85	411.49	585.74	109.80	55.88
MA08A027	E Lounejeva	980.0	large anhedral	Shelf Facies	112.10	465455.18	893.43	925.98	2186.16	1707.17
MA08A079	E Lounejeva	980.0	large anhedral	Shelf Facies	105.36	465050.03	731.03	1819.63	1542.17	27.79
MA08A081	E Lounejeva	980.0	large anhedral	Shelf Facies	109.79	464789.77	885.36	2398.33	1156.26	19.67
MA08A077	E Lounejeva	980.0	large anhedral	Shelf Facies	177.64	464838.47	829.97	2404.05	995.32	21.87
MA08A044	E Lounejeva	980.0	large anhedral	Shelf Facies	126.75	465184.17	635.44	1288.66	1466.04	37.02
MA08A062	E Lounejeva	980.0	large anhedral	Shelf Facies	122.99	465096.65	829.54	1717.71	2774.54	30.45

Table A6.1: LA-ICPMS Analyses of Pyrite from Chapter 4										
File	As(ppm)	Se(ppm)	Mo(ppm)	Ag(ppm)	Cd(ppm)	Sb(ppm)	Te(ppm)	Au(ppm)	Pb(ppm)	Bi(ppm)
JL24A135	285.7	15.9	103.13	1.48	2.39	32.91	0.70	0.03	1286.82	17.02
MY09A049	86.9	13.6	<0.01	0.05	<0.066	0.31	0.07	<0.01	5.18	0.10
MY09A053	14.4	26.7	0.05	0.13	0.04	0.57	0.16	<0.01	13.61	0.14
MY09A048	112.5	17.1	0.01	0.05	0.07	0.20	0.09	<0.01	11.27	0.15
MY09A058	15.9	26.1	0.15	0.08	<0.066	0.55	0.10	<0.0065	15.53	0.24
MY09A050	23.0	26.8	0.06	0.16	0.06	1.14	<0.13	<0.01	35.38	0.33
MY09A055	23.3	19.9	0.16	0.33	0.15	1.00	0.13	0.01	34.17	0.53
MY09A010	21.2	1.7	0.46	0.27	0.03	0.85	<0.13	0.01	30.64	0.57
MY09A015	206.0	19.9	5.62	0.20	0.26	4.67	0.29	<0.01	81.12	1.78
MY09A017	259.7	23.1	3.48	0.37	<0.066	7.64	0.17	0.01	103.25	2.64
MY09A014	115.5	4.3	7.35	0.83	0.04	12.69	0.65	0.06	205.57	3.33
MY09A011	117.0	8.0	1.18	1.39	0.46	10.54	0.36	0.02	196.19	3.77
MY09A012	213.9	13.5	0.31	0.81	0.32	19.73	0.34	0.02	223.15	4.74
MY09A016	334.1	23.6	11.27	0.42	0.15	20.10	0.41	0.01	231.54	4.78
MY09A013	111.1	3.7	0.81	0.75	0.05	17.98	0.47	0.03	291.21	5.66
MY09A009	406.6	6.9	11.90	1.51	0.10	36.86	0.90	0.12	317.65	9.33
MY09A008	511.0	8.1	14.08	1.95	0.07	46.21	1.19	0.15	404.87	11.03
MA08A027	367.3	50.8	8.40	5.49	9.34	40.16	6.03	0.21	204.83	20.19
MA08A079	1885.2	9.4	17.68	12.33	0.36	84.06	8.31	0.37	189.12	25.30
MA08A081	2860.3	11.5	21.08	15.33	0.29	121.61	10.38	0.45	211.41	30.28
MA08A077	2677.9	13.3	23.55	15.10	0.38	127.35	11.00	0.48	235.43	31.57
MA08A044	1382.7	8.0	11.41	13.15	0.53	94.73	10.37	0.40	261.88	33.01
MA08A062	1710.6	9.1	14.03	13.05	0.41	101.96	11.23	0.41	266.77	33.99

Table A6.1: LA-ICPMS Analyses of Pyrite from Chapter 4

File	Analyst	Age (Ma)	Pyrite type	Setting	Mn (ppm)	Fe (ppm)	Co (ppm)	Ni (ppm)	Cu (ppm)	Zn (ppm)
MA08A083	E Lounejeva	980.0	large anhedral	Shelf Facies	120.18	465207.25	777.75	1405.00	1380.15	26.77
MA08A084	E Lounejeva	980.0	large anhedral	Shelf Facies	113.16	465178.36	945.62	1420.26	1549.18	36.01
MA08A085	E Lounejeva	980.0	large anhedral	Shelf Facies	105.35	465167.10	703.28	1424.65	1477.90	22.23
MA08A080	E Lounejeva	980.0	large anhedral	Shelf Facies	84.95	465101.57	760.15	1716.69	1509.64	22.51
MA08A061	E Lounejeva	980.0	large anhedral	Shelf Facies	340.67	465004.53	858.02	2251.75	1198.95	33.94
MA08A078	E Lounejeva	980.0	large anhedral	Shelf Facies	49.55	464918.94	794.07	1843.40	1370.41	16.19
MA08A046	E Lounejeva	980.0	large anhedral	Shelf Facies	126.93	465280.50	935.91	1078.74	1672.62	29.67
MA08A086	E Lounejeva	980.0	large anhedral	Shelf Facies	54.07	464985.69	813.39	2142.42	1006.88	16.05
MA08A023	E Lounejeva	980.0	large anhedral	Shelf Facies	118.96	465409.83	870.70	1116.44	2906.00	32.40
MA08A068	E Lounejeva	980.0	large anhedral	Shelf Facies	91.64	465352.28	1255.78	962.65	691.43	14.16
MA08A082	E Lounejeva	980.0	large anhedral	Shelf Facies	68.63	464977.01	972.13	1904.20	1393.31	21.43
MA08A019	E Lounejeva	980.0	large anhedral	Shelf Facies	171.44	465280.92	837.38	2196.95	2366.96	32.68
MA08A021	E Lounejeva	980.0	large anhedral	Shelf Facies	72.48	465244.59	730.90	1555.04	669.43	13.79
MA08A018	E Lounejeva	980.0	large anhedral	Shelf Facies	170.58	465243.41	860.43	2207.32	3256.21	44.87
MA08A035	E Lounejeva	980.0	large anhedral	Shelf Facies	108.02	465204.86	768.60	1439.37	1718.72	24.13
MA08A026	E Lounejeva	980.0	large anhedral	Shelf Facies	130.74	465350.10	668.16	1469.54	1512.29	49.12
MA08A041	E Lounejeva	980.0	large anhedral	Shelf Facies	149.82	465318.53	792.37	1077.52	1831.80	34.98
MA08A016	E Lounejeva	980.0	large anhedral	Shelf Facies	143.07	465406.67	999.80	1009.08	2455.44	35.00
MA08A042	E Lounejeva	980.0	large anhedral	Shelf Facies	133.77	465146.66	852.63	1591.62	2857.81	26.27
MA08A020	E Lounejeva	980.0	large anhedral	Shelf Facies	121.94	465127.52	898.89	2581.55	1195.30	18.50
MA08A064	E Lounejeva	980.0	large anhedral	Shelf Facies	176.93	465083.89	867.69	1741.96	910.37	21.26
MA08A039	E Lounejeva	980.0	large anhedral	Shelf Facies	102.34	465030.27	852.36	1865.91	1428.65	23.19
MA08A058	E Lounejeva	980.0	large anhedral	Shelf Facies	96.90	465344.16	1216.16	1070.59	1442.75	23.94

Table A6.1: LA-ICPMS Analyses of Pyrite from Chapter 4

File	As(ppm)	Se(ppm)	Mo(ppm)	Ag(ppm)	Cd(ppm)	Sb(ppm)	Te(ppm)	Au(ppm)	Pb(ppm)	Bi(ppm)
MA08A083	1296	10.0	12.4	12.26	0.42	88.61	11.07	0.46	280.75	34.88
MA08A084	1404	10.3	12.5	12.27	0.48	90.43	11.20	0.46	295.93	35.09
MA08A085	1447	7.6	12.5	12.60	0.42	89.48	10.63	0.44	284.91	35.16
MA08A080	1692	7.8	15.5	13.32	0.43	93.77	10.81	0.47	275.63	35.22
MA08A061	2056	12.0	9.4	16.04	0.53	114.77	11.58	0.50	235.62	38.72
MA08A078	2376	7.7	17.9	16.09	0.48	95.85	12.12	0.50	298.98	40.74
MA08A046	1022	13.4	13.2	13.14	0.58	98.43	13.27	0.48	373.74	41.34
MA08A086	2126	8.0	14.9	16.68	0.39	102.88	12.90	0.51	296.65	42.03
MA08A023	537	13.6	8.6	13.62	0.55	96.09	13.02	0.53	332.80	42.07
MA08A068	753	26.4	15.5	11.27	0.39	86.61	13.42	0.46	396.58	42.73
MA08A082	2159	10.4	17.8	13.82	0.51	110.16	12.98	0.48	399.30	42.83
MA08A019	1020	16.7	13.1	15.80	0.70	143.48	14.13	0.66	362.45	44.01
MA08A021	1156	8.5	12.9	14.78	0.44	107.83	14.05	0.54	339.80	45.64
MA08A018	1161	16.5	13.5	17.26	0.91	151.79	15.21	0.68	373.39	45.68
MA08A035	1305	9.2	13.0	16.74	0.58	113.27	15.06	0.56	424.40	48.56
MA08A026	761	12.1	9.4	15.65	0.87	123.99	16.01	0.63	433.73	49.06
MA08A041	879	9.5	8.0	15.43	0.58	108.13	15.34	0.55	406.24	50.85
MA08A016	549	15.2	6.3	15.10	0.70	108.49	16.77	0.68	452.34	51.02
MA08A042	1523	9.6	14.1	17.91	0.61	126.47	15.73	0.61	461.54	51.18
MA08A020	1595	11.8	13.9	18.15	0.56	136.72	16.22	0.66	360.70	51.72
MA08A064	1758	13.1	13.8	15.77	0.42	150.63	16.99	0.61	477.64	51.94
MA08A039	1959	9.5	16.0	18.03	0.57	126.51	16.30	0.58	427.53	52.10
MA08A058	783	18.3	10.6	14.24	0.63	106.37	15.89	0.55	481.64	52.20

Table A6.1: LA-ICPMS Analyses of Pyrite from Chapter 4

File	Analyst	Age (Ma)	Pyrite type	Setting	Mn (ppm)	Fe (ppm)	Co (ppm)	Ni (ppm)	Cu (ppm)	Zn (ppm)
MA08A025	E Lounejeva	980.0	large anhedral	Shelf Facies	344.07	465009.76	1018.22	3812.50	1872.48	23.97
MA08A067	E Lounejeva	980.0	large anhedral	Shelf Facies	121.47	465352.50	1218.32	1033.43	2192.94	28.13
MA08A060	E Lounejeva	980.0	large anhedral	Shelf Facies	156.05	464700.76	1095.48	2684.81	1163.34	23.91
MA08A066	E Lounejeva	980.0	large anhedral	Shelf Facies	127.88	465059.08	825.27	2025.33	1356.17	19.82
MA08A045	E Lounejeva	980.0	large anhedral	Shelf Facies	117.09	465209.94	778.25	1460.04	2309.33	169.31
MA08A024	E Lounejeva	980.0	large anhedral	Shelf Facies	139.48	465122.75	1006.97	2708.98	2902.55	45.87
MA08A056	E Lounejeva	980.0	large anhedral	Shelf Facies	191.04	464774.30	1109.66	2672.07	1440.95	32.40
MA08A069	E Lounejeva	980.0	large anhedral	Shelf Facies	99.26	465384.86	1304.54	962.79	690.04	13.46
MA08A038	E Lounejeva	980.0	large anhedral	Shelf Facies	144.60	465300.91	1011.46	1096.46	1867.96	35.52
MA08A063	E Lounejeva	980.0	large anhedral	Shelf Facies	290.83	464475.03	1356.50	3534.79	1762.34	40.72
MA08A047	E Lounejeva	980.0	large anhedral	Shelf Facies	166.54	465381.10	1203.10	1228.98	2495.99	46.67
MA08A017	E Lounejeva	980.0	large anhedral	Shelf Facies	99.31	465371.69	771.21	1209.82	4510.37	45.49
MA08A059	E Lounejeva	980.0	large anhedral	Shelf Facies	94.91	465258.96	911.65	1331.83	1642.30	31.04
MA08A057	E Lounejeva	980.0	large anhedral	Shelf Facies	102.49	465125.50	1006.40	1670.66	1730.53	28.35
MA08A048	E Lounejeva	980.0	large anhedral	Shelf Facies	99.76	465268.45	841.54	1320.08	3048.59	41.46
MA08A014	E Lounejeva	980.0	large anhedral	Shelf Facies	111.89	465269.21	913.61	1996.75	3393.67	32.50
MA08A022	E Lounejeva	980.0	large anhedral	Shelf Facies	158.36	465322.66	930.94	1358.16	2711.15	48.76
MA08A040	E Lounejeva	980.0	large anhedral	Shelf Facies	280.03	465248.87	701.24	1497.35	1489.26	25.12
MA08A036	E Lounejeva	980.0	large anhedral	Shelf Facies	165.49	465026.03	1011.40	2219.43	2649.84	30.99
MA08A043	E Lounejeva	980.0	large anhedral	Shelf Facies	647.65	464954.28	1060.59	2769.63	2355.65	127.80
MA08A037	E Lounejeva	980.0	large anhedral	Shelf Facies	505.89	465021.21	1001.70	2540.21	1487.15	29.27
MA08A013	E Lounejeva	980.0	large anhedral	Shelf Facies	146.36	465305.90	953.81	2255.84	9114.10	63.03
MA08A015	E Lounejeva	980.0	large anhedral	Shelf Facies	74.63	465363.29	967.55	1347.44	5679.87	38.19

Table A6.1: LA-ICPMS Analyses of Pyrite from Chapter 4										
File	As(ppm)	Se(ppm)	Mo(ppm)	Ag(ppm)	Cd(ppm)	Sb(ppm)	Te(ppm)	Au(ppm)	Pb(ppm)	Bi(ppm)
MA08A025	2036.1	21.0	23.33	19.82	0.65	211.50	17.13	0.73	394.96	52.49
MA08A067	752.1	18.9	10.46	14.66	0.50	114.06	17.68	0.61	481.61	52.90
MA08A060	3193.8	11.0	19.30	18.24	0.53	153.08	16.59	0.58	392.92	53.15
MA08A066	1851.3	12.1	13.32	17.17	0.46	145.99	17.93	0.62	473.26	53.40
MA08A045	1286.2	10.4	11.22	16.80	2.47	141.14	17.09	0.60	490.20	53.43
MA08A024	1612.8	20.7	18.14	18.44	0.86	186.02	18.08	0.69	452.88	53.92
MA08A056	2918.3	12.9	18.72	17.71	0.66	179.47	17.56	0.57	400.47	54.01
MA08A069	630.8	24.8	10.03	15.13	0.42	108.18	18.46	0.64	531.28	55.87
MA08A038	945.3	12.9	8.79	16.07	0.44	119.07	17.08	0.61	498.38	56.86
MA08A063	4039.5	17.4	21.11	18.89	0.46	203.67	19.72	0.63	382.57	57.26
MA08A047	644.9	15.8	7.41	16.81	0.95	120.45	18.59	0.67	554.37	57.66
MA08A017	680.1	12.2	7.83	18.06	1.16	130.46	18.67	0.75	513.00	59.07
MA08A059	1102.5	9.9	10.39	16.65	0.54	131.37	18.45	0.60	489.29	59.48
MA08A057	1602.5	10.5	13.52	17.59	0.59	140.93	18.91	0.59	491.59	61.14
MA08A048	1066.9	11.0	10.37	19.14	1.01	146.05	19.70	0.67	598.98	61.54
MA08A014	1064.1	18.4	12.89	18.29	0.77	162.14	20.98	0.84	519.26	63.06
MA08A022	863.8	14.0	8.44	17.79	1.04	139.11	20.67	0.76	520.79	63.44
MA08A040	1140.3	9.9	4.00	18.03	0.59	152.57	16.33	0.64	455.85	64.75
MA08A036	1975.2	11.8	10.84	22.22	0.70	154.35	18.96	0.66	478.88	65.65
MA08A043	2244.0	17.1	8.89	24.59	2.14	203.46	18.38	0.77	457.97	67.82
MA08A037	1993.2	16.4	8.69	22.53	0.69	194.49	19.13	0.72	461.41	68.80
MA08A013	926.6	20.7	13.62	21.95	1.60	197.28	24.31	1.03	669.85	69.27
MA08A015	711.6	18.6	7.67	21.35	1.15	163.91	25.01	0.95	681.23	75.56

Table A6.1: LA-ICPMS Analyses of Pyrite from Chapter 4

File	Analyst	Age (Ma)	Pyrite type	Setting	Mn (ppm)	Fe (ppm)	Co (ppm)	Ni (ppm)	Cu (ppm)	Zn (ppm)
MA08A065	E Lounejeva	980.0	large anhedral	Shelf Facies	1110.22	464643.07	1316.38	3748.63	1394.77	24.31
MA26A061	JA Halpin	1290.0	framboid	Shelf Facies	19.01	465524.85	945.57	513.34	15.94	39.92
MA26A084	JA Halpin	1290.0	framboid	Shelf Facies	521.35	465482.10	53.49	110.68	614.85	36.24
MA26A056	JA Halpin	1290.0	framboid	Shelf Facies	2446.55	465515.30	44.60	199.25	226.09	573.03
MA26A077	JA Halpin	1290.0	framboid	Shelf Facies	920.75	465493.41	64.05	166.52	831.49	86.90
MA26A087	JA Halpin	1290.0	framboid	Shelf Facies	1312.31	465475.72	98.00	274.60	748.71	1388.06
MA26A057	JA Halpin	1290.0	framboid	Shelf Facies	97.79	465498.16	1212.17	686.26	112.50	51.77
MA26A078	JA Halpin	1290.0	framboid	Shelf Facies	845.17	465471.16	73.06	198.10	378.61	96.98
FE23A136	JA Halpin	1290.0	framboid	Shelf Facies	140.23	465435.83	117.65	269.25	858.48	40.44
FE23A135	JA Halpin	1290.0	framboid	Shelf Facies	642.25	465441.44	155.34	321.83	488.27	60.68
FE23A133	JA Halpin	1290.0	framboid	Shelf Facies	505.97	465391.23	214.31	389.10	534.10	90.74
FE23A142	JA Halpin	1290.0	framboid	Shelf Facies	153.67	465427.20	153.33	406.70	481.71	46.88
FE23A145	JA Halpin	1290.0	framboid	Shelf Facies	70.60	465319.53	344.56	518.61	84.99	47.13
FE23A149	JA Halpin	1290.0	framboid	Shelf Facies	137.02	465375.02	333.42	397.90	153.78	82.98
FE23A138	JA Halpin	1290.0	framboid	Shelf Facies	194.99	465284.14	457.92	608.75	121.59	146.55
MA26A076	JA Halpin	1290.0	framboid	Shelf Facies	431.49	465428.31	56.85	124.72	157.46	103.27
FE23A147	JA Halpin	1290.0	framboid	Shelf Facies	129.02	465412.49	294.22	467.87	112.41	89.48
FE23A139	JA Halpin	1290.0	framboid	Shelf Facies	14.37	465207.40	527.28	696.72	122.65	68.64
FE23A141	JA Halpin	1290.0	framboid	Shelf Facies	165.56	465233.49	495.85	604.39	94.82	135.15
FE23A146	JA Halpin	1290.0	framboid	Shelf Facies	86.91	465148.10	470.86	532.84	103.97	67.13
FE23A144	JA Halpin	1290.0	framboid	Shelf Facies	111.83	465223.38	452.28	543.64	114.18	96.44
FE23A143	JA Halpin	1290.0	framboid	Shelf Facies	157.25	465399.27	253.30	411.57	189.38	67.11
MA26A082	JA Halpin	1290.0	framboid	Shelf Facies	5.41	461160.18	1483.11	4084.57	153.63	4.62

Table A6.1: LA-ICPMS Analyses of Pyrite from Chapter 4

File	As(ppm)	Se(ppm)	Mo(ppm)	Ag(ppm)	Cd(ppm)	Sb(ppm)	Te(ppm)	Au(ppm)	Pb(ppm)	Bi(ppm)
MA08A065	3410	32.4	13.9	25.74	0.68	320.21	29.99	0.90	593.80	93.95
MA26A061	106	6.6	3.6	0.24	<0.066	2.97	<0.128	<0.0065	34.32	0.31
MA26A084	267	5.5	9.8	0.49	<0.066	2.62	<0.13	<0.01	23.08	0.31
MA26A056	142	14.8	22.6	<0.01	0.92	1.19	<0.13	<0.01	12.37	0.40
MA26A077	224	4.9	8.5	0.67	<0.066	4.28	0.35	<0.01	22.88	0.44
MA26A087	290	25.5	40.3	0.60	2.47	6.28	0.80	<0.01	105.19	0.66
MA26A057	206	10.9	16.7	<0.01	0.43	6.74	<0.13	<0.01	28.82	0.66
MA26A078	307	<0.78	108.6	0.58	0.33	4.53	<0.13	0.02	25.99	0.69
FE23A136	440	6.6	10.1	2.20	0.12	4.94	0.50	0.01	16.40	0.87
FE23A135	419	11.2	25.3	1.22	0.32	5.17	0.61	0.04	20.18	0.94
FE23A133	607	13.2	24.4	1.56	0.50	5.73	0.74	0.03	26.92	1.03
FE23A142	472	12.5	23.9	1.21	0.37	6.62	0.67	<0.0065	60.92	1.72
FE23A145	876	29.9	6.0	1.23	0.13	11.85	0.97	0.03	85.22	2.56
FE23A149	668	23.4	19.2	1.50	0.35	11.31	1.38	0.04	65.02	2.78
FE23A138	1008	26.7	9.4	1.48	0.09	13.10	1.34	0.03	96.40	2.84
MA26A076	468	34.0	389.9	<0.01	<0.066	12.87	<0.13	<0.01	80.61	3.27
FE23A147	527	24.7	20.0	1.36	0.41	11.75	1.29	0.04	153.66	3.34
FE23A139	1296	31.3	11.1	1.71	0.21	19.23	1.41	<0.0065	111.01	3.41
FE23A141	1198	30.7	7.5	1.57	0.16	14.24	1.26	0.04	127.59	3.42
FE23A146	1518	28.6	10.1	1.61	0.12	15.69	1.58	0.05	110.79	3.90
FE23A144	1236	30.9	11.6	1.90	0.31	16.07	1.52	0.06	257.19	4.17
FE23A143	577	25.3	244.5	1.82	0.22	14.87	1.29	0.05	202.60	4.29
MA26A082	16459	82.9	2.1	2.39	0.39	96.79	0.98	0.03	766.55	4.67

Table A6.1: LA-ICPMS Analyses of Pyrite from Chapter 4

File	Analyst	Age (Ma)	Pyrite type	Setting	Mn (ppm)	Fe (ppm)	Co (ppm)	Ni (ppm)	Cu (ppm)	Zn (ppm)
MA26A060	JA Halpin	1290.0	framboid	Shelf Facies	41.92	464410.68	1295.96	4364.19	115.25	31.79
MA26A063	JA Halpin	1290.0	framboid	Shelf Facies	10.72	462829.38	1468.78	5894.78	202.92	125.03
MA26A054	JA Halpin	1290.0	framboid	Shelf Facies	0.03	462347.58	2580.76	5272.83	111.31	0.57
MA07A032	JA Halpin	1290.0	nodule	Shelf Facies	40.03	464777.07	155.85	736.17	4429.19	1646.91
MA07A033	JA Halpin	1290.0	nodule	Shelf Facies	6.76	465012.67	132.24	856.18	2675.65	6.94
MA07A035	JA Halpin	1290.0	nodule	Shelf Facies	207.48	464232.27	264.30	573.88	9134.71	297.92
MA08A131	E Lounejeva	1360.0	nodule	Deep Facies	2.70	460309.91	13.88	183.93	112.16	33.80
MA08A132	E Lounejeva	1360.0	nodule	Deep Facies	5.00	460107.73	29.54	405.20	137.80	2.95
MA08A134	E Lounejeva	1360.0	nodule	Deep Facies	2.24	460286.48	23.14	277.83	136.37	122.72
MA08A139	E Lounejeva	1360.0	nodule	Deep Facies	3.82	460421.45	30.68	399.90	139.08	44.95
MA08A142	E Lounejeva	1360.0	nodule	Deep Facies	6.29	460310.18	26.80	409.69	129.15	450.99
MA08A135	E Lounejeva	1360.0	nodule	Deep Facies	2.51	459600.71	17.82	327.25	209.21	111.76
MA08A141	E Lounejeva	1360.0	nodule	Deep Facies	3.35	459906.00	22.73	358.13	143.56	331.86
MA08A136	E Lounejeva	1360.0	nodule	Deep Facies	4.34	461027.45	26.36	265.42	160.81	412.27
MA08A140	E Lounejeva	1360.0	nodule	Deep Facies	3.79	460798.87	28.24	330.25	153.83	140.72
MA08A144	E Lounejeva	1360.0	nodule	Deep Facies	4.75	460165.20	29.65	290.98	224.77	191.48
MA08A137	E Lounejeva	1360.0	nodule	Deep Facies	3.50	460169.34	28.66	380.10	185.45	183.75
MA08A143	E Lounejeva	1360.0	nodule	Deep Facies	4.28	460584.49	33.70	306.58	187.40	214.43
MA08A133	E Lounejeva	1360.0	nodule	Deep Facies	3.75	460268.59	33.83	361.10	197.58	254.83
MA08A138	E Lounejeva	1360.0	nodule	Deep Facies	3.75	460217.37	30.09	352.43	223.53	461.62
MA23A389	V Maslennikov	1550.0	nodule	Restricted Basin	39.69	465193.41	61.30	141.78	279.17	45.12
AP17A075	E Lounejeva	1550.0	nodule	Restricted Basin	115.98	465243.33	58.63	214.78	249.30	76.11
AP17A086	E Lounejeva	1550.0	nodule	Restricted Basin	192.98	465332.59	69.89	199.70	264.54	134.85

Table A6.1: LA-ICPMS Analyses of Pyrite from Chapter 4

File	As(ppm)	Se(ppm)	Mo(ppm)	Ag(ppm)	Cd(ppm)	Sb(ppm)	Te(ppm)	Au(ppm)	Pb(ppm)	Bi(ppm)
MA26A060	4280.6	53.1	395.95	1.68	<0.066	27.83	<0.128	0.11	170.74	5.55
MA26A063	10204.9	58.1	6.16	2.42	<0.066	39.46	1.47	<0.0065	261.19	5.69
MA26A054	12009.9	86.6	25.69	2.01	0.34	55.13	1.54	0.04	332.33	6.68
MA07A032	2907.9	26.3	20.70	2.73	1.51	41.61	0.75	0.05	4274.34	7.67
MA07A033	2025.2	26.8	17.52	2.57	0.07	40.23	0.76	0.06	4238.57	8.99
MA07A035	4949.0	36.0	23.69	4.75	0.29	73.97	0.90	0.10	6641.62	12.19
MA08A131	19644.0	44.2	10.92	5.38	4.07	2084.02	0.08	0.04	168.02	0.17
MA08A132	20401.5	47.8	11.71	9.29	6.03	1481.07	<0.13	0.06	339.64	0.21
MA08A134	19731.8	49.3	12.84	7.56	6.22	1774.88	0.06	0.06	291.32	0.23
MA08A139	19226.1	50.9	9.97	9.33	6.73	1334.44	<0.13	0.08	334.80	0.25
MA08A142	19643.0	51.2	11.50	9.00	13.49	1711.22	0.12	0.08	298.45	0.27
MA08A135	22301.0	43.3	11.67	6.64	5.90	1424.17	<0.13	0.07	260.42	0.28
MA08A141	21157.3	45.3	13.26	8.52	11.18	1560.84	<0.13	0.09	252.51	0.32
MA08A136	16955.8	39.6	17.02	8.10	13.90	1443.95	<0.13	0.06	229.66	0.33
MA08A140	17812.1	55.7	14.12	8.07	6.85	1350.31	0.12	0.07	279.89	0.35
MA08A144	20186.2	71.1	18.42	6.61	10.61	1305.40	<0.13	0.06	328.39	0.35
MA08A137	20170.6	66.9	20.15	8.83	9.11	1552.99	0.13	0.08	315.95	0.43
MA08A143	18615.3	51.3	24.29	8.55	14.34	1504.77	<0.13	0.08	321.07	0.48
MA08A133	19798.8	55.7	24.90	11.21	11.79	1518.16	0.13	0.09	361.99	0.52
MA08A138	19990.7	63.5	40.03	11.39	14.25	1570.20	0.26	0.10	331.60	0.79
MA23A389	1348.1	4.3	49.08	8.12	0.40	8.53	0.19	<0.01	324.50	1.48
AP17A075	1161.0	3.6	29.06	8.96	0.27	7.75	0.22	0.01	272.35	1.53
AP17A086	826.7	3.3	44.47	9.83	0.50	10.11	0.32	0.01	278.54	1.57

Table A6.1: LA-ICPMS Analyses of Pyrite from Chapter 4										
File	Analyst	Age (Ma)	Pyrite type	Setting	Mn (ppm)	Fe (ppm)	Co (ppm)	Ni (ppm)	Cu (ppm)	Zn (ppm)
AP17A088	E Lounejeva	1550.0	nodule	Restricted Basin	99.02	465245.86	47.00	231.43	259.08	82.33
AP17A076	E Lounejeva	1550.0	nodule	Restricted Basin	26.50	465091.64	33.75	188.15	213.87	23.97
AP17A085	E Lounejeva	1550.0	nodule	Restricted Basin	33.61	465223.00	44.57	222.61	142.96	51.57
AP17A079	E Lounejeva	1550.0	nodule	Restricted Basin	2.25	465242.01	49.53	195.04	194.42	11.08
AP17A083	E Lounejeva	1550.0	nodule	Restricted Basin	35.58	465186.27	71.72	248.67	339.42	46.95
AP17A067	E Lounejeva	1550.0	nodule	Restricted Basin	37.85	465183.47	88.58	216.97	3244.26	33.26
AP17A068	E Lounejeva	1550.0	nodule	Restricted Basin	31.39	465126.18	78.71	257.15	393.52	42.43
AP17A080	E Lounejeva	1550.0	nodule	Restricted Basin	20.73	465353.95	72.96	292.97	265.07	23.19
MA23A396	V Maslennikov	1550.0	nodule	Restricted Basin	128.81	465224.29	182.31	393.77	333.60	90.07
MA23A395	V Maslennikov	1550.0	nodule	Restricted Basin	83.19	465275.77	84.31	284.16	240.02	79.25
AP17A072	E Lounejeva	1550.0	nodule	Restricted Basin	82.15	465260.44	75.90	306.29	242.05	56.50
AP17A078	E Lounejeva	1550.0	nodule	Restricted Basin	95.79	465257.23	113.38	291.14	203.00	87.29
AP17A069	E Lounejeva	1550.0	nodule	Restricted Basin	82.62	465257.46	150.18	321.84	227.48	77.02
AP17A066	E Lounejeva	1550.0	nodule	Restricted Basin	141.88	465400.30	43.67	428.05	320.17	81.41
MA23A388	V Maslennikov	1550.0	nodule	Restricted Basin	63.50	465286.28	99.12	304.88	312.38	41.20
AP17A087	E Lounejeva	1550.0	nodule	Restricted Basin	100.12	465351.92	186.02	407.20	248.41	95.64
AP17A074	E Lounejeva	1550.0	nodule	Restricted Basin	24.34	465323.17	164.86	503.52	327.19	30.02
AP17A077	E Lounejeva	1550.0	nodule	Restricted Basin	41.40	465333.10	141.70	363.82	288.72	50.43
MA23A390	V Maslennikov	1550.0	nodule	Restricted Basin	29.02	465374.83	64.41	312.87	292.17	21.39
AP17A070	E Lounejeva	1550.0	nodule	Restricted Basin	28.84	465267.70	84.56	378.89	277.68	24.20
MA23A393	V Maslennikov	1550.0	nodule	Restricted Basin	12.17	465371.20	174.52	454.51	341.94	23.72
AP17A071	E Lounejeva	1550.0	nodule	Restricted Basin	12.34	465274.75	136.28	425.71	221.87	17.94
MA23A391	V Maslennikov	1550.0	nodule	Restricted Basin	17.73	465293.09	191.26	431.29	364.15	17.67

Table A6.1: LA-ICPMS Analyses of Pyrite from Chapter 4

File	As(ppm)	Se(ppm)	Mo(ppm)	Ag(ppm)	Cd(ppm)	Sb(ppm)	Te(ppm)	Au(ppm)	Pb(ppm)	Bi(ppm)
AP17A088	1152	3.4	46.7	9.67	0.41	9.52	0.24	0.01	297.17	1.60
AP17A076	1729	2.4	22.2	8.82	0.21	6.83	0.20	0.00	316.29	1.70
AP17A085	1237	4.3	122.5	15.91	0.45	11.06	0.46	0.02	201.54	1.75
AP17A079	1166	3.3	20.3	7.78	0.13	7.48	0.22	0.01	414.92	1.92
AP17A083	1375	4.2	45.6	9.39	0.32	8.72	0.23	0.01	270.42	1.96
AP17A067	1385	5.2	24.2	10.96	0.34	8.55	0.21	0.01	281.99	2.07
AP17A068	1600	4.3	28.5	10.38	0.25	9.00	0.22	0.01	354.03	2.20
AP17A080	747	2.6	16.5	9.85	0.34	8.26	0.30	0.01	228.98	2.29
MA23A396	1232	5.2	37.3	14.63	0.52	12.20	0.38	0.01	381.12	2.31
MA23A395	1040	7.5	69.6	12.73	0.43	14.13	0.38	0.01	511.42	2.37
AP17A072	1097	3.7	24.5	13.32	0.27	9.09	0.33	0.01	335.04	2.38
AP17A078	1109	5.0	56.8	10.64	0.51	11.18	0.35	0.01	304.16	2.45
AP17A069	1108	4.6	37.0	12.31	0.39	10.42	0.29	0.01	322.90	2.45
AP17A066	573	3.5	20.1	29.08	0.58	9.03	0.49	0.02	162.72	2.62
MA23A388	1000	5.4	27.6	11.95	0.32	10.18	0.36	0.01	353.31	2.66
AP17A087	754	5.2	51.9	15.91	0.41	14.11	0.46	0.01	378.97	2.86
AP17A074	862	3.5	17.7	14.94	0.41	10.96	0.39	0.02	300.82	3.02
AP17A077	825	4.2	17.5	15.64	0.33	10.63	0.51	0.02	352.48	3.15
MA23A390	668	4.0	19.0	13.23	0.33	11.45	0.41	0.01	399.75	3.17
AP17A070	1070	4.3	18.5	13.76	0.33	10.97	0.52	0.02	347.64	3.21
MA23A393	682	4.2	18.7	14.43	0.44	11.48	0.40	0.01	358.24	3.29
AP17A071	1043	3.8	17.8	14.83	0.26	10.92	0.62	0.02	386.95	3.59
MA23A391	975	4.8	16.8	16.24	0.30	13.24	0.52	0.02	422.45	3.88

Table A6.1: LA-ICPMS Analyses of Pyrite from Chapter 4

File	Analyst	Age (Ma)	Pyrite type	Setting	Mn (ppm)	Fe (ppm)	Co (ppm)	Ni (ppm)	Cu (ppm)	Zn (ppm)
AP17A084	E Lounejeva	1550.0	nodule	Restricted Basin	29.24	465320.80	142.62	518.54	268.02	25.96
MA23A392	V Maslennikov	1550.0	nodule	Restricted Basin	1.17	465222.33	150.18	508.11	353.89	16.82
AP17A081	E Lounejeva	1550.0	nodule	Restricted Basin	27.74	465388.43	131.59	549.33	265.13	22.00
MA26A107	JA Halpin	1640.0	framboid	Deep Facies	49.89	465501.09	8.42	19.47	36.53	8.97
MA26A098	JA Halpin	1640.0	framboid	Deep Facies	41.75	465479.91	16.79	48.91	30.24	1.62
MA26A108	JA Halpin	1640.0	framboid	Deep Facies	193.28	465515.38	14.29	35.96	33.40	2.79
MA26A109	JA Halpin	1640.0	framboid	Deep Facies	19.50	465450.33	12.23	31.38	47.64	1.05
MA26A110	JA Halpin	1640.0	framboid	Deep Facies	129.66	465473.16	7.84	59.49	70.31	2.45
MA26A104	JA Halpin	1640.0	framboid	Deep Facies	43.46	465415.94	11.56	54.43	61.01	0.09
MA26A099	JA Halpin	1640.0	framboid	Deep Facies	546.93	465479.78	16.45	42.18	61.51	3.61
MA26A112	JA Halpin	1640.0	framboid	Deep Facies	435.91	465445.79	32.27	115.38	63.40	9.29
MA26A111	JA Halpin	1640.0	framboid	Deep Facies	527.01	465474.97	31.22	57.12	52.45	15.55
MA26A106	JA Halpin	1640.0	framboid	Deep Facies	1326.24	465394.92	62.16	114.13	117.59	5.99
MA26A097	JA Halpin	1640.0	framboid	Deep Facies	82.81	465374.41	48.49	96.11	130.19	1.68
MA26A101	JA Halpin	1640.0	framboid	Deep Facies	0.80	465448.52	30.12	89.06	156.46	1.53
MA26A103	JA Halpin	1640.0	framboid	Deep Facies	525.35	465305.12	80.72	148.15	161.92	3.70
MA26A100	JA Halpin	1640.0	framboid	Deep Facies	162.31	465382.40	28.88	121.55	134.79	2.52
MA26A102	JA Halpin	1640.0	framboid	Deep Facies	10.50	465358.62	62.82	165.24	313.24	3.74
MY07A090	JA Halpin	1690.0	large anhedral	Shelf Facies	0.76	465419.67	12.79	170.33	25.14	1.88
MY07A089	JA Halpin	1690.0	large anhedral	Shelf Facies	7.96	465384.62	31.46	145.10	30.27	4.22
MY07A088	JA Halpin	1690.0	large anhedral	Shelf Facies	4.59	465410.32	80.81	313.40	28.76	0.56
MY07A087	JA Halpin	1690.0	large anhedral	Shelf Facies	19.48	465373.18	60.14	196.91	33.63	5.34
MY07A091	JA Halpin	1690.0	large anhedral	Shelf Facies	72.55	465425.47	39.92	49.07	91.27	8.25

Table A6.1: LA-ICPMS Analyses of Pyrite from Chapter 4

File	As(ppm)	Se(ppm)	Mo(ppm)	Ag(ppm)	Cd(ppm)	Sb(ppm)	Te(ppm)	Au(ppm)	Pb(ppm)	Bi(ppm)
AP17A084	870.8	3.5	12.32	19.75	0.39	12.85	0.82	0.04	363.03	4.93
MA23A392	1239.7	4.7	20.24	22.92	0.46	15.41	0.98	0.04	490.24	5.62
AP17A081	617.4	3.9	19.63	24.73	0.56	15.68	1.05	0.05	432.09	6.46
MA26A107	195.4	4.0	2.70	0.56	0.05	8.87	0.12	<0.01	201.75	0.33
MA26A098	274.7	10.4	2.00	0.12	<0.066	4.76	0.06	<0.01	127.69	0.41
MA26A108	141.8	6.4	4.18	0.17	<0.066	5.85	<0.13	<0.01	138.19	0.58
MA26A109	385.5	13.0	6.41	0.23	0.07	4.84	<0.13	0.01	126.69	0.62
MA26A110	300.0	19.8	1.23	0.51	0.05	4.94	0.10	0.01	109.46	0.66
MA26A104	514.4	15.1	2.11	0.17	0.07	5.16	<0.13	<0.01	116.93	0.88
MA26A099	275.2	6.6	9.13	0.42	<0.066	8.13	0.17	<0.01	203.14	1.09
MA26A112	402.6	13.0	6.62	0.35	0.03	8.06	0.16	<0.01	205.02	1.11
MA26A111	293.2	9.0	19.44	0.41	0.09	8.66	0.54	0.01	223.22	2.18
MA26A106	593.1	11.3	33.67	0.77	<0.066	15.48	0.33	0.02	362.31	2.56
MA26A097	670.0	15.3	26.75	0.54	0.08	16.15	0.21	<0.01	383.08	2.63
MA26A101	392.3	14.5	16.07	0.81	0.20	16.10	0.23	<0.01	412.78	2.64
MA26A103	929.6	13.1	46.11	0.72	0.29	17.30	0.26	<0.01	395.50	2.74
MA26A100	640.0	22.1	15.69	0.79	0.22	14.99	0.45	0.01	369.41	2.85
MA26A102	729.1	19.4	44.54	1.89	0.25	30.95	1.10	<0.01	728.04	6.17
MY07A090	500.4	18.0	9.88	0.79	<0.066	41.24	0.76	0.07	650.73	11.24
MY07A089	631.7	26.3	15.37	0.97	0.16	57.75	<0.13	0.12	1065.57	12.82
MY07A088	535.4	22.5	6.47	1.07	<0.066	52.96	0.73	<0.01	743.95	17.90
MY07A087	674.6	23.3	15.17	2.24	<0.066	63.75	<0.13	0.18	661.81	21.27
MY07A091	478.7	<0.78	46.96	2.61	<0.066	131.80	1.25	0.19	3590.91	23.13

Table A6.1: LA-ICPMS Analyses of Pyrite from Chapter 4

File	Analyst	Age (Ma)	Pyrite type	Setting	Mn (ppm)	Fe (ppm)	Co (ppm)	Ni (ppm)	Cu (ppm)	Zn (ppm)
MY07A093	JA Halpin	1690.0	large anhedral	Shelf Facies	6.41	465279.42	121.73	209.29	17.91	7.65
MY07A033	JA Halpin	1690.0	large anhedral	Shelf Facies	26.87	464964.24	346.14	295.85	20.80	25.99
MY07A062	JA Halpin	1690.0	large anhedral	Shelf Facies	34.26	465130.02	740.50	1310.60	26.59	7.06
MY07A036	JA Halpin	1690.0	large anhedral	Shelf Facies	22.66	464757.26	333.84	1443.18	27.67	1648.20
MY07A094	JA Halpin	1690.0	large anhedral	Shelf Facies	67.92	465393.46	508.79	619.61	22.85	77.11
MY07A040	JA Halpin	1690.0	large anhedral	Shelf Facies	19.92	464672.11	371.86	271.45	23.40	24.93
MY07A042	JA Halpin	1690.0	large anhedral	Shelf Facies	162.84	464491.20	1953.80	1495.14	35.25	95.11
MY07A034	JA Halpin	1690.0	large anhedral	Shelf Facies	59.06	464439.82	153.92	102.65	32.18	15.46
MY07A038	JA Halpin	1690.0	large anhedral	Shelf Facies	107.26	464624.16	571.56	357.99	36.90	29.56
MY07A044	JA Halpin	1690.0	large anhedral	Shelf Facies	91.70	464856.80	253.48	480.65	18.88	24.55
MY07A039	JA Halpin	1690.0	large anhedral	Shelf Facies	29.03	464823.16	563.05	313.16	29.77	39.87
MY07A043	JA Halpin	1690.0	large anhedral	Shelf Facies	112.27	464667.08	1339.41	809.75	21.41	59.37
MY07A081	JA Halpin	1690.0	nodule	Shelf Facies	70.72	463857.62	417.01	2067.64	843.27	5.49
MY07A035	JA Halpin	1690.0	large anhedral	Shelf Facies	124.62	464621.86	1066.25	780.59	23.71	34.53
MY07A029	JA Halpin	1690.0	large anhedral	Shelf Facies	0.50	464552.83	1812.11	249.82	15.80	0.38
MY07A095	JA Halpin	1690.0	large anhedral	Shelf Facies	30.47	465360.62	184.29	333.09	28.68	14.05
MY07A032	JA Halpin	1690.0	large anhedral	Shelf Facies	93.99	464360.41	1947.99	295.02	22.85	14.36
MY07A041	JA Halpin	1690.0	large anhedral	Shelf Facies	142.07	464054.51	1472.95	1044.75	49.05	29.45
MY07A031	JA Halpin	1690.0	large anhedral	Shelf Facies	55.90	464417.68	782.11	229.62	28.26	6.57
MY07A067	JA Halpin	1690.0	large anhedral	Shelf Facies	198.43	465010.14	1339.12	1367.55	42.57	28.58
MY07A084	JA Halpin	1690.0	nodule	Shelf Facies	4.62	465289.82	326.52	1943.88	794.56	4.00
MY07A030	JA Halpin	1690.0	large anhedral	Shelf Facies	62.70	464009.89	1335.08	262.73	33.33	11.35
MY07A096	JA Halpin	1690.0	large anhedral	Shelf Facies	2.29	465318.03	65.64	288.32	42.48	4.83

Table A6.1: LA-ICPMS Analyses of Pyrite from Chapter 4

File	As(ppm)	Se(ppm)	Mo(ppm)	Ag(ppm)	Cd(ppm)	Sb(ppm)	Te(ppm)	Au(ppm)	Pb(ppm)	Bi(ppm)
MY07A093	1026	25.0	3.1	0.68	<0.066	23.04	<0.13	0.13	349.74	23.36
MY07A033	2207	27.0	14.9	3.57	0.37	85.31	0.84	0.21	216.32	24.93
MY07A062	1586	48.6	2.3	4.26	<0.066	80.06	1.83	0.11	543.69	25.39
MY07A036	2982	30.5	18.6	4.78	5.29	84.18	1.36	0.17	237.04	29.98
MY07A094	599	36.0	4.6	1.10	0.08	33.12	<0.13	0.07	355.34	32.50
MY07A040	3301	26.2	18.9	6.63	0.09	120.46	1.61	0.33	307.43	33.55
MY07A042	3979	33.5	61.2	3.27	0.32	98.42	1.59	0.24	319.84	33.99
MY07A034	4171	79.6	37.2	5.60	0.38	139.56	1.38	0.70	514.66	41.38
MY07A038	3481	12.6	17.7	7.58	<0.066	193.70	2.37	0.34	471.76	41.64
MY07A044	2609	35.8	36.3	8.32	<0.066	98.06	<0.13	0.24	269.57	42.86
MY07A039	2735	14.8	116.3	8.11	0.42	125.83	1.76	0.28	350.46	43.75
MY07A043	3320	28.0	42.8	7.17	<0.066	115.38	2.54	0.16	298.57	46.39
MY07A081	6353	23.4	19.4	1.22	0.24	28.57	0.87	0.09	463.81	48.00
MY07A035	3489	28.4	26.0	9.81	0.27	133.57	2.72	0.21	319.88	52.90
MY07A029	3748	89.3	28.6	5.91	<0.066	95.97	1.28	0.60	293.99	57.70
MY07A095	722	16.9	3.2	0.85	0.07	31.28	<0.13	0.20	480.22	72.72
MY07A032	4469	104.1	26.7	9.63	<0.066	131.44	2.15	0.81	376.35	73.37
MY07A041	5615	72.6	27.1	9.87	0.07	255.27	4.49	1.24	704.15	75.21
MY07A031	4254	118.0	33.0	9.65	0.09	142.90	1.84	0.94	427.30	77.09
MY07A067	2035	20.8	7.8	13.99	<0.066	169.90	<0.13	0.15	1195.68	96.08
MY07A084	987	23.0	3.9	1.64	0.18	25.40	3.73	0.06	255.19	98.51
MY07A030	5782	107.8	36.0	8.75	0.16	177.59	2.54	1.87	657.99	102.61
MY07A096	881	23.2	1.9	1.13	0.07	36.92	1.32	0.42	1081.77	111.25

Table A6.1: LA-ICPMS Analyses of Pyrite from Chapter 4										
File	Analyst	Age (Ma)	Pyrite type	Setting	Mn (ppm)	Fe (ppm)	Co (ppm)	Ni (ppm)	Cu (ppm)	Zn (ppm)
MY07A097	JA Halpin	1690.0	large anhedral	Shelf Facies	4.49	465390.84	210.69	410.41	33.56	5.99
MY07A066	JA Halpin	1690.0	large anhedral	Shelf Facies	60.21	465016.85	1142.60	1684.92	64.62	12.98
MY07A061	JA Halpin	1690.0	large anhedral	Shelf Facies	0.70	464952.58	1055.03	1812.98	77.29	0.06
MY07A064	JA Halpin	1690.0	large anhedral	Shelf Facies	226.19	465049.91	842.89	1176.46	62.69	44.98
MY07A082	JA Halpin	1690.0	nodule	Shelf Facies	95.04	464473.09	300.81	1964.83	1011.35	6.38
MY07A063	JA Halpin	1690.0	large anhedral	Shelf Facies	32.73	464962.23	1804.18	2353.39	83.55	10.57
MY07A083	JA Halpin	1690.0	nodule	Shelf Facies	747.13	464748.65	268.32	1697.64	943.07	15.97
MY07A085	JA Halpin	1690.0	nodule	Shelf Facies	63.76	465042.10	248.69	1549.89	514.66	8.37
MY07A065	JA Halpin	1690.0	large anhedral	Shelf Facies	20.90	464776.10	1253.73	1655.21	179.37	0.19
MY28A109	JA Halpin	1840.0	microcrystaline clusters	Deep Facies	101.71	465534.63	0.32	1429.59	1789.20	78.08
MY28A110	JA Halpin	1840.0	microcrystaline clusters	Deep Facies	55.77	465544.66	0.25	1491.20	1302.85	26.41
MY28A115	JA Halpin	1840.0	microcrystaline clusters	Deep Facies	110.73	465544.78	0.22	1578.10	424.10	56.36
MY28A113	JA Halpin	1840.0	microcrystaline clusters	Deep Facies	183.77	465535.85	0.42	1465.57	1804.82	80.34
MY28A114	JA Halpin	1840.0	microcrystaline clusters	Deep Facies	92.68	465541.42	0.10	2277.08	564.97	70.22
MY28A131	JA Halpin	1840.0	microcrystaline clusters	Deep Facies	20.32	465550.79	11.02	670.19	146.58	19.68
MY28A124	JA Halpin	1840.0	microcrystaline clusters	Deep Facies	35.39	465551.84	10.27	675.67	124.56	24.83
MY28A130	JA Halpin	1840.0	microcrystaline clusters	Deep Facies	12.00	465548.83	10.08	663.71	255.65	37.08
MY28A127	JA Halpin	1840.0	microcrystaline clusters	Deep Facies	86.29	465549.74	11.03	692.83	146.38	48.91
MY28A125	JA Halpin	1840.0	microcrystaline clusters	Deep Facies	84.52	465550.43	10.15	654.78	159.99	44.01
MY28A129	JA Halpin	1840.0	microcrystaline clusters	Deep Facies	53.13	465548.55	10.48	664.32	255.64	47.61
MY28A126	JA Halpin	1840.0	microcrystaline clusters	Deep Facies	271.33	465548.51	9.71	623.50	149.15	48.22
MY28A128	JA Halpin	1840.0	microcrystaline clusters	Deep Facies	59.88	465548.74	12.19	711.74	182.18	21.66
MY28A138	JA Halpin	1840.0	microcrystaline clusters	Deep Facies	1.15	465549.51	11.92	712.28	227.64	51.86

Table A6.1: LA-ICPMS Analyses of Pyrite from Chapter 4

File	As(ppm)	Se(ppm)	Mo(ppm)	Ag(ppm)	Cd(ppm)	Sb(ppm)	Te(ppm)	Au(ppm)	Pb(ppm)	Bi(ppm)
MY07A097	608.4	32.2	20.14	1.38	<0.066	35.99	<0.13	0.42	1069.80	111.66
MY07A066	2009.6	40.1	10.73	15.98	<0.066	180.70	5.24	0.27	970.99	114.48
MY07A061	2250.3	31.0	4.60	18.77	0.10	237.92	4.55	0.43	1527.10	125.87
MY07A064	1885.7	20.3	9.61	24.75	0.11	250.48	10.69	0.42	1300.93	154.69
MY07A082	4046.7	21.7	19.80	1.75	1.06	30.68	6.21	0.09	418.50	181.24
MY07A063	2214.2	32.8	16.60	31.48	0.40	309.27	9.42	0.57	1531.61	198.24
MY07A083	3014.4	26.9	15.05	2.13	0.42	30.48	9.46	0.12	455.84	264.75
MY07A085	1915.0	27.3	5.51	1.64	<0.066	30.10	10.19	0.08	433.35	292.82
MY07A065	2911.5	16.1	15.78	76.56	<0.066	700.28	31.85	1.21	2292.96	444.80
MY28A109	69.7	66.0	5.60	17.68	0.20	36.25	<0.13	<0.01	1226.22	0.78
MY28A110	32.1	40.4	6.00	13.33	0.12	25.44	<0.13	<0.01	654.18	0.81
MY28A115	31.7	40.5	28.34	5.13	0.15	44.21	<0.13	<0.01	236.60	1.65
MY28A113	65.1	64.7	5.56	17.28	<0.066	53.14	<0.13	0.03	1051.35	1.92
MY28A114	44.3	49.9	15.33	8.87	<0.066	93.07	<0.13	0.03	378.35	2.35
MY28A131	9.2	53.5	2.72	19.49	0.16	20.10	1.15	0.01	161.27	7.62
MY28A124	5.2	72.4	2.48	18.55	0.18	14.94	1.76	0.00	253.88	12.76
MY28A130	16.5	59.4	4.15	35.39	0.15	26.25	2.97	0.00	317.87	13.68
MY28A127	13.1	42.1	2.73	23.08	0.19	18.73	2.20	0.00	219.25	14.00
MY28A125	10.5	30.9	2.63	24.35	0.27	17.60	2.55	0.01	183.10	14.69
MY28A129	17.6	45.9	2.99	34.85	0.24	23.39	2.95	0.01	251.94	15.39
MY28A126	17.7	62.0	2.87	24.68	0.18	18.30	3.34	0.01	290.60	15.76
MY28A128	16.8	59.8	4.34	31.81	0.16	15.55	3.23	0.01	325.81	16.22
MY28A138	14.0	48.5	7.11	25.68	0.08	32.44	2.58	0.00	242.46	19.41

Table A6.1: LA-ICPMS Analyses of Pyrite from Chapter 4

File	Analyst	Age (Ma)	Pyrite type	Setting	Mn (ppm)	Fe (ppm)	Co (ppm)	Ni (ppm)	Cu (ppm)	Zn (ppm)
MY28A133	JA Halpin	1840.0	microcrystaline clusters	Deep Facies	134.06	465549.51	13.25	640.94	216.49	91.20
MY28A135	JA Halpin	1840.0	microcrystaline clusters	Deep Facies	1.59	465545.99	12.57	576.84	180.57	73.36
MY28A137	JA Halpin	1840.0	microcrystaline clusters	Deep Facies	9.03	465548.69	11.83	651.78	368.61	41.79
MY28A134	JA Halpin	1840.0	microcrystaline clusters	Deep Facies	199.10	465548.70	13.08	721.59	197.66	61.36
MY28A136	JA Halpin	1840.0	microcrystaline clusters	Deep Facies	172.10	465547.14	15.60	777.19	239.62	82.65
MY28A132	JA Halpin	1840.0	microcrystaline clusters	Deep Facies	88.60	465549.00	12.23	598.54	292.42	134.78
MY28A177	JA Halpin	1840.0	microcrystaline clusters	Deep Facies	8.45	465526.55	13.80	714.56	262.00	73.27
MY28A184	JA Halpin	1840.0	microcrystaline clusters	Deep Facies	2.33	465545.18	13.80	696.74	279.42	55.15
MY28A180	JA Halpin	1840.0	microcrystaline clusters	Deep Facies	0.32	465546.04	11.16	775.52	309.00	52.53
MY28A179	JA Halpin	1840.0	microcrystaline clusters	Deep Facies	49.22	465523.30	23.89	1103.35	462.49	163.03
MY28A183	JA Halpin	1840.0	microcrystaline clusters	Deep Facies	11.80	465546.36	19.05	932.93	390.76	104.72
MA23A219	V Maslennikov	2000.0	nodule	Rift Basin	13.89	465392.06	35.89	1179.82	1111.97	71.59
AP27A020	JA Halpin	2000.0	nodule	Rift Basin	0.67	465518.23	15.39	105.38	78.40	31.52
MA23A231	V Maslennikov	2000.0	nodule	Rift Basin	0.64	465396.54	30.79	650.28	615.06	104.47
MA23A227	V Maslennikov	2000.0	nodule	Rift Basin	9.36	465283.36	38.43	2161.35	499.59	29.97
MA23A233	V Maslennikov	2000.0	nodule	Rift Basin	16.08	465298.57	26.61	1095.49	647.76	36.09
AP27A017	JA Halpin	2000.0	nodule	Rift Basin	19.94	465472.79	36.72	261.66	172.51	134.21
AP27A016	JA Halpin	2000.0	nodule	Rift Basin	43.70	465455.29	41.20	289.54	271.18	81.21
AP27A019	JA Halpin	2000.0	nodule	Rift Basin	8.86	465483.21	33.94	210.50	176.99	57.08
AP27A021	JA Halpin	2000.0	nodule	Rift Basin	24.37	465446.89	47.39	295.35	222.99	180.17
AP27A018	JA Halpin	2000.0	nodule	Rift Basin	18.43	465469.17	37.85	270.67	208.14	88.72
MA26A023	JA Halpin	2000.0	nodule	Rift Basin	27.93	465463.57	40.52	271.67	217.89	177.74
MA26A021	JA Halpin	2000.0	nodule	Rift Basin	5.97	465486.43	23.98	214.02	196.81	66.76

Table A6.1: LA-ICPMS Analyses of Pyrite from Chapter 4

File	As(ppm)	Se(ppm)	Mo(ppm)	Ag(ppm)	Cd(ppm)	Sb(ppm)	Te(ppm)	Au(ppm)	Pb(ppm)	Bi(ppm)
MY28A133	14	26.2	256.7	23.09	0.21	30.33	3.30	0.01	171.40	19.67
MY28A135	27	41.1	18.2	18.85	0.20	28.80	2.72	0.01	191.64	19.77
MY28A137	17	46.4	25.2	38.21	0.21	30.14	2.71	0.01	253.17	19.81
MY28A134	17	44.3	2.3	28.71	0.40	19.42	1.69	0.01	270.85	21.00
MY28A136	23	33.2	20.3	33.00	0.54	63.73	2.94	0.03	316.40	26.13
MY28A132	16	58.9	4.2	30.07	0.15	22.93	3.12	0.01	384.39	27.09
MY28A177	100	43.4	16.8	13.21	0.24	19.00	4.90	0.07	266.58	48.63
MY28A184	30	59.9	24.6	16.28	<0.066	20.29	4.32	0.14	298.90	50.76
MY28A180	27	45.8	66.0	14.92	<0.066	15.29	4.01	<0.01	290.09	57.05
MY28A179	112	59.2	75.0	14.65	<0.066	47.08	5.12	<0.01	344.04	57.87
MY28A183	26	67.9	90.3	18.83	<0.066	21.30	4.28	<0.01	339.57	69.92
MA23A219	604	43.2	13.7	4.53	0.40	32.98	1.34	0.08	46.90	0.39
AP27A020	131	17.4	1.8	1.44	0.35	33.45	0.91	0.09	19.13	0.51
MA23A231	587	34.4	14.1	3.58	0.52	40.04	1.73	0.09	59.98	0.53
MA23A227	1011	50.3	12.3	3.43	0.23	44.55	1.88	0.09	66.58	0.54
MA23A233	954	48.1	10.1	4.22	0.25	52.10	2.04	0.20	46.49	0.69
AP27A017	301	20.1	10.3	2.34	0.59	62.96	1.02	0.13	34.82	0.78
AP27A016	367	21.6	8.2	2.35	0.58	76.89	1.33	0.15	46.06	0.85
AP27A019	262	20.8	8.1	1.95	0.39	57.67	1.00	0.10	34.53	0.86
AP27A021	398	21.7	13.3	2.19	0.70	72.78	1.34	0.09	39.30	0.87
AP27A018	315	22.0	14.2	2.22	0.41	67.31	1.13	0.12	39.57	0.90
MA26A023	336	35.5	6.6	2.27	1.48	63.28	1.58	0.10	38.28	0.91
MA26A021	250	22.1	6.8	2.47	0.35	63.23	1.06	0.10	32.52	0.96

Table A6.1: LA-ICPMS Analyses of Pyrite from Chapter 4

File	Analyst	Age (Ma)	Pyrite type	Setting	Mn (ppm)	Fe (ppm)	Co (ppm)	Ni (ppm)	Cu (ppm)	Zn (ppm)
AP27A015	JA Halpin	2000.0	nodule	Rift Basin	10.25	465477.07	32.43	248.38	163.00	70.89
MA26A015	JA Halpin	2000.0	nodule	Rift Basin	30.12	465448.74	34.02	296.77	199.87	395.45
MA26A013	JA Halpin	2000.0	nodule	Rift Basin	0.84	465459.94	31.50	274.28	228.98	93.44
AU010013	E Lounejeva	2170.0	large euhedral	Deep Facies	1023.08	465502.38	503.30	1484.11	4010.33	17.07
AU010016	E Lounejeva	2170.0	large euhedral	Deep Facies	737.29	465508.47	640.72	1612.96	827.18	7.11
AU010011	E Lounejeva	2170.0	large euhedral	Deep Facies	473.26	465511.36	303.70	1017.30	1721.06	11.00
AU010010	E Lounejeva	2170.0	large euhedral	Deep Facies	679.49	465510.56	376.55	1506.81	1041.69	7.63
AU010015	E Lounejeva	2170.0	large euhedral	Deep Facies	580.97	465505.52	550.39	1511.82	566.85	1.91
AU010012	E Lounejeva	2170.0	large euhedral	Deep Facies	472.63	465505.47	480.42	1252.02	636.81	9.44
AU010014	E Lounejeva	2170.0	large euhedral	Deep Facies	6211.97	465480.85	195.86	881.10	1687.28	19.54
AU010027	E Lounejeva	2170.0	large euhedral	Deep Facies	2198.52	465492.48	537.54	1053.96	1767.31	68.73
AU010026	E Lounejeva	2170.0	large euhedral	Deep Facies	292.16	465058.59	472.40	1537.94	708.62	35.11
AU010024	E Lounejeva	2170.0	large euhedral	Deep Facies	377.85	465322.26	326.52	1575.44	536.20	37.79
AU010023	E Lounejeva	2170.0	large euhedral	Deep Facies	255.65	464979.80	528.90	1844.73	669.58	31.30
AU010021	E Lounejeva	2170.0	large euhedral	Deep Facies	312.40	464873.25	489.68	1492.19	673.01	118.48
AU010025	E Lounejeva	2170.0	large euhedral	Deep Facies	310.45	465003.52	399.44	1660.56	748.62	71.51
AU010022	E Lounejeva	2170.0	large euhedral	Deep Facies	306.26	465287.07	416.73	1544.55	572.11	116.78
AU010029	E Lounejeva	2170.0	large euhedral	Deep Facies	250.91	465195.28	461.80	1961.69	709.00	31.10
AU010020	E Lounejeva	2170.0	large euhedral	Deep Facies	322.75	465413.57	392.64	1923.06	600.68	27.40
MA26A087	D Gregory	2504.0	large euhedral	Deep Facies	241.26	464372.30	88.02	317.10	578.54	0.66
MA26A091	D Gregory	2504.0	large euhedral	Deep Facies	182.38	464962.78	52.41	196.07	249.28	0.86
MA26A085	D Gregory	2504.0	large euhedral	Deep Facies	33.64	464777.35	168.49	416.16	634.89	0.42
MA26A089	D Gregory	2504.0	large euhedral	Deep Facies	2678.63	465488.57	126.47	224.43	164.32	5.71

Table A6.1: LA-ICPMS Analyses of Pyrite from Chapter 4

File	As(ppm)	Se(ppm)	Mo(ppm)	Ag(ppm)	Cd(ppm)	Sb(ppm)	Te(ppm)	Au(ppm)	Pb(ppm)	Bi(ppm)
AP27A015	285.4	21.9	8.31	2.30	0.30	62.62	1.35	0.12	41.71	1.01
MA26A015	391.5	20.2	11.37	2.37	1.70	68.39	1.44	0.12	41.98	1.05
MA26A013	349.5	5.8	14.27	2.95	0.23	86.06	1.80	0.12	48.48	1.29
AU010013	190.5	43.8	5.33	1.38	0.70	24.09	0.60	0.01	373.94	0.81
AU010016	167.7	44.7	10.79	1.02	0.28	28.70	0.87	0.03	429.88	1.20
AU010011	156.9	41.8	3.87	0.93	0.18	16.95	0.99	0.04	291.17	1.43
AU010010	159.9	37.0	1.89	0.94	0.17	27.75	1.16	0.03	486.33	1.55
AU010015	178.8	45.7	7.65	0.90	0.13	25.79	1.01	0.02	390.72	1.61
AU010012	179.0	44.3	5.86	0.88	0.34	21.95	1.38	0.03	320.13	2.16
AU010014	271.2	35.9	4.37	2.19	0.29	46.42	2.62	0.07	592.48	4.00
AU010027	227.6	59.5	4.93	1.63	0.27	20.35	4.65	0.06	231.86	7.86
AU010026	1853.2	70.7	30.11	5.27	0.25	59.83	15.17	0.17	524.22	14.44
AU010024	865.4	54.5	19.21	5.52	0.51	68.86	16.99	0.26	542.45	14.50
AU010023	2148.4	108.7	30.35	6.10	0.63	105.31	14.38	0.19	562.69	14.58
AU010021	2547.5	64.4	34.49	4.99	0.89	61.75	15.03	0.16	503.81	14.70
AU010025	2059.5	69.5	34.07	6.00	0.42	77.20	17.23	0.18	543.14	15.94
AU010022	997.2	52.3	29.99	5.88	0.57	72.75	16.83	0.25	606.14	16.04
AU010029	1341.1	56.1	48.55	6.37	0.22	52.97	17.93	0.23	661.60	17.28
AU010020	523.3	84.6	12.95	7.39	0.38	66.77	25.31	0.33	760.75	19.36
MA26A087	4424.3	21.8	4.55	0.90	<0.066	31.74	<0.13	<0.01	317.34	0.04
MA26A091	2212.1	18.4	2.02	0.30	0.06	17.83	<0.13	0.01	192.28	0.06
MA26A085	2906.8	25.8	3.05	0.74	0.08	30.12	<0.13	0.02	204.28	0.16
MA26A089	242.3	11.4	8.50	1.05	<0.066	18.72	0.30	0.02	199.15	0.22

Table A6.1: LA-ICPMS Analyses of Pyrite from Chapter 4

File	Analyst	Age (Ma)	Pyrite type	Setting	Mn (ppm)	Fe (ppm)	Co (ppm)	Ni (ppm)	Cu (ppm)	Zn (ppm)
MA26A088	D Gregory	2504.0	large euhedral	Deep Facies	9472.57	465505.92	11.29	48.74	18.51	14.96
MA26A090	D Gregory	2504.0	large euhedral	Deep Facies	9025.34	465493.36	35.91	89.98	143.07	30.89
MA26A026	D Gregory	2504.0	nodule	Deep Facies	9.43	465497.63	1.16	15.11	108.03	2.94
MA26A027	D Gregory	2504.0	nodule	Deep Facies	1.69	465453.36	2.94	28.31	359.59	3.37
MA26A028	D Gregory	2504.0	nodule	Deep Facies	2.88	465476.80	2.03	18.76	183.99	3.90
MA26A007	D Gregory	2504.0	microcrystaline clusters	Deep Facies	486.47	465006.45	45.88	113.88	98.94	47.28
MA26A013	D Gregory	2504.0	microcrystaline clusters	Deep Facies	864.74	465256.15	50.69	119.94	51.71	43.88
MA26A032	D Gregory	2504.0	nodule	Deep Facies	4.44	465472.88	1.09	16.44	193.72	3.51
MA26A008	D Gregory	2504.0	microcrystaline clusters	Deep Facies	555.06	465270.93	52.41	124.82	48.09	38.16
MA26A014	D Gregory	2504.0	microcrystaline clusters	Deep Facies	979.22	465269.97	51.18	113.04	49.22	76.96
MA26A011	D Gregory	2504.0	microcrystaline clusters	Deep Facies	438.38	465234.55	55.52	125.25	52.97	29.69
MA26A029	D Gregory	2504.0	nodule	Deep Facies	0.68	465456.59	2.11	19.98	228.85	0.62
MA26A022	D Gregory	2504.0	microcrystaline clusters	Deep Facies	536.13	465257.00	58.54	130.58	50.39	21.85
MA26A020	D Gregory	2504.0	microcrystaline clusters	Deep Facies	942.64	465277.01	48.38	129.31	42.00	55.32
MA26A012	D Gregory	2504.0	microcrystaline clusters	Deep Facies	927.85	465229.95	56.17	121.17	51.98	73.53
MA26A009	D Gregory	2504.0	microcrystaline clusters	Deep Facies	793.75	465254.88	52.07	128.51	49.17	60.74
MA26A010	D Gregory	2504.0	microcrystaline clusters	Deep Facies	565.17	465255.18	54.08	115.50	50.63	47.19
MA26A021	D Gregory	2504.0	microcrystaline clusters	Deep Facies	542.32	465265.26	55.06	130.60	54.02	31.64
MA26A017	D Gregory	2504.0	microcrystaline clusters	Deep Facies	332.88	465212.00	54.89	130.62	55.75	13.58
MA26A015	D Gregory	2504.0	microcrystaline clusters	Deep Facies	664.42	465254.51	49.16	129.70	52.87	47.47
MA26A016	D Gregory	2504.0	microcrystaline clusters	Deep Facies	517.32	465241.20	56.11	130.94	51.32	29.40
MA26A115	D Gregory	2504.0	small euhedral	Deep Facies	2181.58	465383.14	178.72	266.84	137.25	1.00
MA26A031	D Gregory	2504.0	nodule	Deep Facies	4.41	465469.39	1.66	19.03	163.17	1.30

Table A6.1: LA-ICPMS Analyses of Pyrite from Chapter 4

File	As(ppm)	Se(ppm)	Mo(ppm)	Ag(ppm)	Cd(ppm)	Sb(ppm)	Te(ppm)	Au(ppm)	Pb(ppm)	Bi(ppm)
MA26A088	177	9.2	1.3	0.22	<0.066	3.32	<0.13	<0.01	22.35	0.48
MA26A090	224	26.9	2.0	1.91	0.12	9.56	0.56	0.04	75.49	0.50
MA26A026	208	1.3	0.7	0.68	<0.066	8.36	0.35	0.01	37.19	0.92
MA26A027	374	5.0	1.0	1.27	<0.066	11.13	0.50	0.03	46.05	1.15
MA26A028	286	2.8	1.0	0.88	0.14	13.02	0.56	0.02	68.42	1.46
MA26A007	2049	26.7	6.6	0.31	0.15	14.61	0.72	0.03	87.24	1.54
MA26A013	1113	19.8	10.9	0.36	<0.066	19.21	0.88	<0.01	97.16	1.63
MA26A032	301	2.0	0.6	1.26	0.10	21.58	0.71	0.04	100.96	1.64
MA26A008	1058	22.3	7.0	0.32	0.13	15.80	0.65	<0.01	81.65	1.67
MA26A014	1061	20.9	6.9	0.36	0.14	17.02	1.00	0.04	84.65	1.70
MA26A011	1194	21.0	6.7	0.31	0.18	19.89	0.90	0.04	93.65	1.71
MA26A029	362	3.6	0.7	1.46	0.14	26.94	0.78	0.05	115.47	1.72
MA26A022	1110	22.3	7.1	0.33	0.21	17.87	0.97	0.03	91.29	1.75
MA26A020	1035	16.5	17.4	0.31	<0.066	19.74	0.93	<0.01	92.13	1.78
MA26A012	1211	21.0	5.9	0.30	<0.066	19.72	0.93	0.02	88.58	1.78
MA26A009	1118	21.4	7.9	0.29	0.21	16.12	0.76	<0.01	87.96	1.78
MA26A010	1117	22.0	7.4	0.26	0.22	19.09	0.75	0.02	106.70	1.80
MA26A021	1079	20.8	9.6	0.34	<0.066	19.72	0.98	0.03	95.31	1.84
MA26A017	1278	22.1	7.0	0.33	0.11	20.52	0.89	0.03	98.91	1.87
MA26A015	1119	20.1	8.8	0.26	0.12	19.14	1.12	0.02	97.44	1.96
MA26A016	1169	19.9	7.0	0.31	0.17	19.77	1.10	0.05	94.27	2.09
MA26A115	637	11.7	0.7	1.17	<0.066	12.47	1.40	<0.01	102.02	2.24
MA26A031	314	4.9	0.6	1.72	0.13	29.59	1.04	0.05	136.86	2.38

Table A6.1: LA-ICPMS Analyses of Pyrite from Chapter 4

File	Analyst	Age (Ma)	Pyrite type	Setting	Mn (ppm)	Fe (ppm)	Co (ppm)	Ni (ppm)	Cu (ppm)	Zn (ppm)
MA26A030	D Gregory	2504.0	nodule	Deep Facies	10.93	465413.71	3.35	27.53	249.42	4.76
MA26A107	D Gregory	2504.0	small euhedral	Deep Facies	415.92	465296.89	430.67	293.50	215.38	1.05
MA26A106	D Gregory	2504.0	small euhedral	Deep Facies	1280.16	465275.72	719.62	274.56	207.11	6.64
MA26A083	D Gregory	2504.0	large euhedral	Deep Facies	3499.16	465477.29	242.66	425.75	255.14	40.19
MA26A075	D Gregory	2504.0	small anhedral	Deep Facies	4388.27	465342.17	199.07	485.80	321.55	43.11
MA26A082	D Gregory	2504.0	large euhedral	Deep Facies	5351.31	465493.89	133.99	346.50	210.59	75.37
MA26A077	D Gregory	2504.0	small anhedral	Deep Facies	3562.51	465435.09	168.03	415.70	244.14	30.41
MA26A070	D Gregory	2504.0	small anhedral	Deep Facies	3492.44	465456.28	196.77	463.74	282.30	38.45
MA26A071	D Gregory	2504.0	microcrystaline clusters	Deep Facies	4383.43	465500.25	165.28	399.85	234.27	47.72
MA26A081	D Gregory	2504.0	large euhedral	Deep Facies	4593.95	465485.34	157.09	366.44	207.82	55.93
MA26A119	D Gregory	2504.0	small euhedral	Deep Facies	2102.78	465259.57	556.99	609.79	331.96	13.05
MA26A073	D Gregory	2504.0	microcrystaline clusters	Deep Facies	2261.79	465478.47	153.50	395.23	228.48	29.22
MA26A076	D Gregory	2504.0	small anhedral	Deep Facies	2808.97	465509.50	156.74	409.72	245.71	41.68
MA26A072	D Gregory	2504.0	small anhedral	Deep Facies	1269.91	465481.06	189.34	553.17	380.64	49.05
MA26A118	D Gregory	2504.0	small euhedral	Deep Facies	1275.12	465165.50	588.94	772.66	466.85	28.02
MA26A112	D Gregory	2504.0	small euhedral	Deep Facies	1127.31	465352.95	974.99	635.29	337.52	8.63
MA26A110	D Gregory	2504.0	small euhedral	Deep Facies	2366.47	465291.37	692.70	850.33	413.27	23.20
MA26A117	D Gregory	2504.0	small euhedral	Deep Facies	47.10	465371.24	703.91	996.28	541.44	62.03
MA26A116	D Gregory	2504.0	small euhedral	Deep Facies	197.12	465257.24	663.65	943.46	541.45	128.57
MA26A121	D Gregory	2504.0	small euhedral	Deep Facies	2414.83	465358.13	689.63	822.67	471.65	375.38
MA26A109	D Gregory	2504.0	small euhedral	Deep Facies	2096.04	465258.40	872.33	925.07	490.18	20.85
MA26A111	D Gregory	2504.0	small euhedral	Deep Facies	1078.38	465409.05	771.17	945.34	472.50	257.60
MA26A108	D Gregory	2504.0	small euhedral	Deep Facies	3625.57	465393.90	830.56	1004.17	459.33	8.11

Table A6.1: LA-ICPMS Analyses of Pyrite from Chapter 4

File	As(ppm)	Se(ppm)	Mo(ppm)	Ag(ppm)	Cd(ppm)	Sb(ppm)	Te(ppm)	Au(ppm)	Pb(ppm)	Bi(ppm)
MA26A030	522.7	4.4	0.69	1.66	<0.066	40.34	1.15	0.07	187.02	2.41
MA26A107	960.4	11.9	1.20	2.12	0.28	20.62	3.04	0.05	138.93	3.78
MA26A106	1039.7	11.5	1.18	1.75	0.33	24.32	3.51	0.04	161.02	5.81
MA26A083	284.5	15.0	3.49	5.69	0.49	61.13	5.99	0.06	358.20	9.90
MA26A075	790.8	14.0	6.10	5.50	0.40	65.65	6.13	0.10	402.47	9.95
MA26A082	222.3	14.0	4.35	5.46	0.29	61.97	6.44	0.07	354.05	10.36
MA26A077	442.6	13.6	4.90	6.50	0.33	64.38	6.78	0.07	366.64	10.83
MA26A070	363.3	15.6	3.53	8.52	0.43	70.10	7.16	0.07	368.49	10.86
MA26A071	198.5	13.9	3.54	6.64	0.36	65.59	6.87	0.06	358.40	10.86
MA26A081	254.4	12.9	2.81	5.77	0.55	65.51	6.29	0.10	385.49	11.12
MA26A119	1100.2	19.5	1.45	5.02	0.86	47.02	8.37	0.08	295.70	11.49
MA26A073	280.1	12.6	3.40	6.78	0.46	68.79	7.79	0.07	374.66	11.65
MA26A076	163.8	12.7	3.76	7.20	0.32	71.34	7.48	0.08	379.18	11.69
MA26A072	270.4	14.6	3.68	11.52	0.65	86.22	9.73	0.12	431.40	13.08
MA26A118	1452.6	19.0	1.51	7.43	1.30	60.49	12.13	0.11	364.28	14.46
MA26A112	750.4	21.4	1.56	5.66	0.90	57.30	10.29	0.09	311.47	14.83
MA26A110	981.1	17.4	1.57	7.70	1.07	74.58	14.10	0.14	413.61	17.37
MA26A117	681.9	15.9	0.41	10.83	1.96	72.89	14.70	0.17	407.78	17.55
MA26A116	1108.9	15.0	0.76	9.94	2.22	83.91	17.36	0.17	454.98	18.62
MA26A121	731.0	24.4	1.95	7.93	4.44	73.54	14.53	0.10	440.88	19.52
MA26A109	1104.6	24.6	2.11	8.26	1.54	82.54	15.95	0.16	492.20	21.13
MA26A111	540.2	20.7	0.88	9.49	3.28	90.86	20.16	0.15	524.70	24.35
MA26A108	596.9	23.2	1.82	9.51	1.56	96.40	20.25	0.16	538.35	28.04

Table A6.1: LA-ICPMS Analyses of Pyrite from Chapter 4

File	Analyst	Age (Ma)	Pyrite type	Setting	Mn (ppm)	Fe (ppm)	Co (ppm)	Ni (ppm)	Cu (ppm)	Zn (ppm)
MA26A120	D Gregory	2504.0	small euhedral	Deep Facies	1173.64	465337.00	983.48	1127.79	496.91	25.71
MA21B134	D Gregory	2521.0	small euhedral	Deep Facies	346.58	465325.56	547.18	1107.90	415.98	1.05
MA21B132	D Gregory	2521.0	small euhedral	Deep Facies	715.91	465435.52	324.92	641.77	168.49	3.66
MA21B119	D Gregory	2521.0	small euhedral	Deep Facies	1052.45	465524.01	136.43	724.10	32.64	34.87
MA21B122	D Gregory	2521.0	small euhedral	Deep Facies	822.07	465512.27	341.46	1225.61	19.59	40.75
MA21B112	D Gregory	2521.0	small euhedral	Deep Facies	903.10	465214.92	1103.97	1663.11	544.04	7.92
MA21B133	D Gregory	2521.0	small euhedral	Deep Facies	1414.14	465323.04	1286.24	2303.88	564.66	3.82
MA21B124	D Gregory	2521.0	small euhedral	Deep Facies	823.96	465074.55	1575.79	2129.60	918.80	41.71
MA21B125	D Gregory	2521.0	small euhedral	Deep Facies	1368.00	465212.96	1438.99	1596.32	477.48	72.32
MA21B128	D Gregory	2521.0	small euhedral	Deep Facies	429.56	464779.50	1767.89	2224.68	1563.84	55.06
MA21B116	D Gregory	2521.0	small euhedral	Deep Facies	1491.89	465389.77	912.29	1817.23	199.78	0.91
MA21B120	D Gregory	2521.0	small euhedral	Deep Facies	14.98	465474.50	390.57	184.87	87.09	37.12
MA21B131	D Gregory	2521.0	small euhedral	Deep Facies	1160.21	464876.49	1970.40	2941.47	3760.98	12.59
MA21B130	D Gregory	2521.0	small euhedral	Deep Facies	136.83	465524.08	189.42	220.60	64.57	39.70
MA26A153	D Gregory	2530.0	large euhedral	Deep Facies	<0.02	465404.54	4.03	13.88	28.80	0.30
MA26A140	D Gregory	2530.0	large euhedral	Deep Facies	<0.02	465422.39	4.43	18.15	35.77	0.54
MA26A156	D Gregory	2530.0	large euhedral	Deep Facies	<0.02	465404.24	3.90	11.53	26.90	0.31
MA26A155	D Gregory	2530.0	large euhedral	Deep Facies	<0.02	465379.42	4.17	13.92	56.28	0.33
MA26A151	D Gregory	2530.0	large euhedral	Deep Facies	<0.02	465392.03	2.43	11.03	26.81	0.22
MA26A145	D Gregory	2530.0	large euhedral	Deep Facies	4.09	465426.47	4.58	25.55	49.87	0.67
MA26A157	D Gregory	2530.0	large euhedral	Deep Facies	<0.02	465425.29	3.11	8.73	25.03	0.53
MA26A138	D Gregory	2530.0	large euhedral	Deep Facies	0.20	465425.97	2.24	10.25	29.83	<0.02
MA26A158	D Gregory	2530.0	large euhedral	Deep Facies	<0.02	465437.92	4.87	32.55	25.41	0.36

Table A6.1: LA-ICPMS Analyses of Pyrite from Chapter 4

File	As(ppm)	Se(ppm)	Mo(ppm)	Ag(ppm)	Cd(ppm)	Sb(ppm)	Te(ppm)	Au(ppm)	Pb(ppm)	Bi(ppm)
MA26A120	810	32.0	4.1	11.20	1.30	107.36	22.00	0.20	630.73	29.46
MA21B134	853	112.1	0.7	0.58	0.27	17.24	1.73	0.04	178.55	2.59
MA21B132	441	121.6	0.4	0.61	0.24	11.19	2.13	0.04	102.62	2.64
MA21B119	109	90.0	0.6	0.63	0.56	13.07	2.32	0.02	149.85	3.37
MA21B122	153	121.6	0.9	0.74	0.89	10.75	3.23	0.04	139.92	4.91
MA21B112	1267	93.0	1.3	1.31	0.53	24.29	4.64	0.06	261.36	6.15
MA21B133	862	189.9	1.8	1.72	0.40	26.11	5.64	0.06	284.18	8.32
MA21B124	1793	179.9	3.3	2.61	1.08	57.24	6.56	0.10	617.45	9.24
MA21B125	1275	175.5	4.8	2.68	0.65	34.78	8.36	<0.01	405.21	9.25
MA21B128	2899	123.0	5.6	2.35	0.74	33.99	7.26	0.16	398.89	9.30
MA21B116	612	154.4	4.3	2.35	0.36	32.40	8.90	0.13	332.91	11.99
MA21B120	295	22.5	54.1	1.50	0.80	24.60	12.44	0.06	208.93	12.87
MA21B131	2535	174.8	29.0	12.68	0.43	86.11	9.00	0.13	1256.56	13.34
MA21B130	109	24.9	5.5	3.33	0.23	24.37	17.22	0.17	175.13	16.93
MA26A153	557	100.3	0.4	0.02	0.25	0.89	<0.13	<0.01	9.23	0.03
MA26A140	490	114.7	0.5	0.08	0.25	0.90	0.29	<0.01	8.91	0.08
MA26A156	558	100.5	0.4	0.02	0.38	0.96	0.54	<0.01	11.53	0.12
MA26A155	651	117.4	0.3	0.06	0.13	0.96	0.48	<0.01	11.49	0.18
MA26A151	604	112.9	0.3	0.07	0.19	1.08	0.34	<0.01	11.57	0.21
MA26A145	475	96.4	0.4	0.11	0.12	0.62	0.13	<0.01	9.22	0.27
MA26A157	479	94.2	0.5	0.06	0.22	1.23	<0.13	<0.01	14.23	0.27
MA26A138	477	93.2	0.4	0.04	0.23	1.00	<0.13	<0.01	11.05	0.31
MA26A158	432	75.6	0.1	0.10	0.21	1.47	<0.13	<0.01	16.31	0.82

Table A6.1: LA-ICPMS Analyses of Pyrite from Chapter 4

File	Analyst	Age (Ma)	Pyrite type	Setting	Mn (ppm)	Fe (ppm)	Co (ppm)	Ni (ppm)	Cu (ppm)	Zn (ppm)
MA26A154	D Gregory	2530.0	large euhedral	Deep Facies	2.94	465413.36	12.67	38.48	39.79	0.79
MA26A139	D Gregory	2530.0	large euhedral	Deep Facies	0.29	465454.12	4.32	16.46	29.62	0.27
MA26A144	D Gregory	2530.0	large euhedral	Deep Facies	<0.02	465499.70	16.32	41.31	0.73	1.13
MA26A137	D Gregory	2530.0	large euhedral	Deep Facies	1.78	465426.71	3.87	14.54	43.61	0.60
MA26A210	D Gregory	2561.0	large euhedral	Deep Facies	0.63	465348.43	1069.83	977.98	384.92	4.67
MA26A226	D Gregory	2561.0	large euhedral	Deep Facies	4.13	465330.08	716.50	735.16	504.20	2874.02
MA26A222	D Gregory	2561.0	large euhedral	Deep Facies	9.29	465326.22	777.74	793.74	565.01	20.10
MA26A225	D Gregory	2561.0	large euhedral	Deep Facies	23.14	465305.66	825.62	795.59	250.80	19.12
MA26A224	D Gregory	2561.0	large euhedral	Deep Facies	12.93	465267.80	984.53	972.97	329.74	7.04
FE27A007	D Gregory	2561.0	large anhedral	Deep Facies	29.72	465463.75	409.33	575.84	346.93	16.63
FE27A032	D Gregory	2561.0	large anhedral	Deep Facies	60.32	465463.81	634.44	951.03	414.93	23.99
MA26A223	D Gregory	2561.0	large euhedral	Deep Facies	6.56	465244.20	1000.82	974.10	698.94	8.39
FE27A017	D Gregory	2561.0	large anhedral	Deep Facies	251.49	465436.98	453.71	702.15	703.50	102.67
FE27A041	D Gregory	2561.0	large anhedral	Deep Facies	7.38	465446.86	607.41	963.74	586.73	377.85
FE27A019	D Gregory	2561.0	large anhedral	Deep Facies	94.36	465443.53	508.74	718.37	413.40	52.97
MA26A209	D Gregory	2561.0	large euhedral	Deep Facies	341.27	465049.14	1403.08	1243.05	624.18	7.40
FE27A132	D Gregory	2561.0	nodule	Deep Facies	3096.26	464907.61	1495.48	1627.84	267.94	1.01
FE27A018	D Gregory	2561.0	large anhedral	Deep Facies	17.26	465458.56	426.28	603.07	449.14	18.18
FE27A033	D Gregory	2561.0	large anhedral	Deep Facies	4.10	465455.37	645.15	992.21	585.81	43.38
FE27A011	D Gregory	2561.0	large anhedral	Deep Facies	98.13	465422.31	584.78	796.26	487.51	50.34
MA26A217	D Gregory	2561.0	microcrystalline clusters	Deep Facies	3.04	465147.61	1134.41	995.63	1965.83	375.55
FE27A010	D Gregory	2561.0	large anhedral	Deep Facies	81.22	465424.49	585.18	824.34	931.98	37.21
FE27A015	D Gregory	2561.0	large anhedral	Deep Facies	45.96	465422.36	578.34	828.64	416.56	59.36

Table A6.1: LA-ICPMS Analyses of Pyrite from Chapter 4

File	As(ppm)	Se(ppm)	Mo(ppm)	Ag(ppm)	Cd(ppm)	Sb(ppm)	Te(ppm)	Au(ppm)	Pb(ppm)	Bi(ppm)
MA26A154	524.1	103.7	0.25	0.30	0.16	1.44	0.60	<0.01	15.36	0.91
MA26A139	371.3	92.4	0.36	0.21	0.36	1.59	1.00	0.03	15.11	1.33
MA26A144	200.6	47.1	0.22	0.33	0.44	0.86	<0.13	<0.01	13.79	1.83
MA26A137	474.0	98.0	0.52	0.16	0.28	2.44	1.38	0.02	18.22	2.14
MA26A210	767.3	18.5	0.86	25.42	1.80	114.98	8.65	0.32	57.34	21.46
MA26A226	836.0	4.9	1.16	17.08	75.68	136.36	15.19	0.29	133.25	24.49
MA26A222	850.5	5.1	1.23	18.26	1.60	152.92	15.37	0.30	134.98	26.86
MA26A225	927.5	15.6	1.35	17.34	1.38	160.21	16.00	0.28	819.43	27.02
MA26A224	1069.4	12.4	1.63	21.53	2.09	184.73	18.42	0.32	318.27	32.37
FE27A007	335.3	36.8	1.71	8.39	3.34	112.77	52.91	0.45	513.90	34.05
FE27A032	335.0	25.4	0.93	9.31	3.60	123.95	42.08	0.42	423.52	34.67
MA26A223	1157.8	13.9	1.51	21.99	1.81	200.65	19.71	0.37	451.54	35.43
FE27A017	435.5	215.1	2.10	8.14	5.32	120.22	55.04	0.44	2557.32	37.00
FE27A041	398.5	23.6	0.96	11.98	13.08	147.73	58.30	0.50	358.53	38.45
FE27A019	411.0	43.0	1.59	8.60	4.21	135.74	63.76	0.46	367.25	39.50
MA26A209	1888.6	31.1	1.50	30.42	1.87	250.90	26.22	0.46	680.90	42.51
FE27A132	2418.8	18.5	3.68	9.16	<0.066	258.35	6.40	0.14	529.92	43.50
FE27A018	354.7	435.5	1.84	9.90	6.77	125.96	60.50	0.58	6665.83	44.09
FE27A033	366.6	23.7	0.98	12.60	4.16	159.70	58.87	0.56	446.13	44.40
FE27A011	490.5	98.4	2.19	10.29	5.41	164.29	75.52	0.55	1453.84	46.10
MA26A217	1519.7	110.5	1.50	27.18	6.08	234.44	27.99	0.43	4671.89	46.32
FE27A010	482.3	38.7	1.75	10.02	9.35	163.31	76.84	0.45	479.70	46.86
FE27A015	490.3	54.8	1.68	10.54	5.98	161.39	77.81	0.58	626.14	47.58

Table A6.1: LA-ICPMS Analyses of Pyrite from Chapter 4

File	Analyst	Age (Ma)	Pyrite type	Setting	Mn (ppm)	Fe (ppm)	Co (ppm)	Ni (ppm)	Cu (ppm)	Zn (ppm)
FE27A008	D Gregory	2561.0	large anhedral	Deep Facies	227.11	465423.64	562.35	826.54	432.51	97.02
FE27A036	D Gregory	2561.0	large anhedral	Deep Facies	56.55	465404.84	725.08	1051.65	618.47	1136.46
FE27A014	D Gregory	2561.0	large anhedral	Deep Facies	22.91	465422.76	545.18	764.88	646.28	18.08
FE27A012	D Gregory	2561.0	large anhedral	Deep Facies	195.21	465407.09	630.35	896.58	407.47	86.51
FE27A013	D Gregory	2561.0	large anhedral	Deep Facies	106.23	465394.15	714.28	1025.05	460.29	54.83
FE27A016	D Gregory	2561.0	large anhedral	Deep Facies	160.52	465403.34	658.39	964.66	416.23	92.36
FE27A039	D Gregory	2561.0	large anhedral	Deep Facies	23.63	465434.59	587.67	866.49	412.01	112.99
MA26A218	D Gregory	2561.0	microcrystalline clusters	Deep Facies	0.81	465101.14	1272.40	1164.20	1717.46	47.89
FE27A037	D Gregory	2561.0	large anhedral	Deep Facies	124.85	465433.20	539.96	803.36	518.97	54.09
MA26A219	D Gregory	2561.0	microcrystalline clusters	Deep Facies	5.43	465084.38	1248.79	922.23	334.90	11.40
FE27A048	D Gregory	2561.0	large anhedral	Deep Facies	228.93	465374.76	766.93	1106.65	403.74	66.83
FE27A128	D Gregory	2561.0	nodule	Deep Facies	5661.77	464503.08	1816.01	1957.90	278.93	104.55
FE27A043	D Gregory	2561.0	large anhedral	Deep Facies	11.49	465415.15	575.53	847.03	410.01	42.88
FE27A044	D Gregory	2561.0	large anhedral	Deep Facies	197.05	465442.87	839.02	1224.72	3434.93	175.93
FE27A049	D Gregory	2561.0	large anhedral	Deep Facies	183.96	465379.90	771.68	1110.30	419.18	56.74
FE27A009	D Gregory	2561.0	large anhedral	Deep Facies	222.44	465405.37	626.15	909.24	306.08	112.05
MA26A211	D Gregory	2561.0	large euhedral	Deep Facies	1.15	465037.65	1540.46	1411.39	1246.56	24.43
FE27A046	D Gregory	2561.0	large anhedral	Deep Facies	335.67	465327.58	813.55	1245.78	431.37	95.22
MA26A220	D Gregory	2561.0	microcrystalline clusters	Deep Facies	11.70	465083.75	1325.79	949.39	454.72	13.12
FE27A050	D Gregory	2561.0	large anhedral	Deep Facies	278.23	465356.78	829.25	1225.71	469.00	83.84
MA26A208	D Gregory	2561.0	microcrystalline clusters	Deep Facies	1.72	464936.87	1792.64	1601.45	563.39	9.78
MA26A221	D Gregory	2561.0	microcrystalline clusters	Deep Facies	4.97	465045.91	1359.38	1057.88	1310.97	52.65
FE27A038	D Gregory	2561.0	large anhedral	Deep Facies	84.88	465402.73	685.24	1006.25	282.30	402.92

Table A6.1: LA-ICPMS Analyses of Pyrite from Chapter 4

File	As(ppm)	Se(ppm)	Mo(ppm)	Ag(ppm)	Cd(ppm)	Sb(ppm)	Te(ppm)	Au(ppm)	Pb(ppm)	Bi(ppm)
FE27A008	486	53.7	2.0	9.42	4.16	167.75	80.80	0.42	504.04	48.07
FE27A036	556	37.9	0.8	13.47	90.41	195.41	86.82	0.63	462.73	48.51
FE27A014	489	316.3	2.0	11.00	6.25	157.54	76.46	0.62	5207.61	49.25
FE27A012	548	89.2	1.5	9.83	4.62	182.05	87.56	0.46	986.15	50.17
FE27A013	596	57.1	2.5	11.44	4.95	190.53	92.85	0.52	410.87	51.25
FE27A016	562	71.3	1.6	10.13	6.73	179.59	88.10	0.51	762.14	51.67
FE27A039	445	37.4	0.9	12.09	5.11	179.34	74.22	0.65	519.14	52.16
MA26A218	1694	14.3	0.9	32.04	2.70	290.32	33.90	0.51	344.23	52.22
FE27A037	450	130.8	1.1	12.31	5.64	190.69	88.34	0.70	1694.54	55.23
MA26A219	1757	51.0	5.0	26.67	1.20	301.12	39.39	0.46	2416.57	56.31
FE27A048	669	183.3	0.8	12.59	5.26	219.07	112.52	0.53	1340.37	56.39
FE27A128	3934	19.3	3.0	9.54	0.20	318.90	8.48	0.24	483.12	56.42
FE27A043	517	276.4	1.1	15.90	6.59	187.62	94.66	0.91	3223.69	56.82
FE27A044	413	132.7	1.7	13.18	22.47	181.10	73.37	0.44	3142.68	57.48
FE27A049	649	119.6	1.1	12.20	6.36	229.53	112.43	0.54	845.36	57.57
FE27A009	554	93.9	5.5	8.58	5.16	203.02	99.77	0.40	1197.39	58.51
MA26A211	1932	25.3	0.8	36.70	4.06	322.42	35.12	0.64	533.84	58.99
FE27A046	845	127.0	1.1	12.97	5.73	233.56	118.39	0.52	766.12	59.56
MA26A220	1759	59.8	4.1	25.39	1.24	330.94	38.68	0.41	2793.03	59.87
FE27A050	736	158.6	1.0	13.32	6.53	251.95	129.60	0.56	1048.99	65.70
MA26A208	2309	48.7	0.8	40.80	2.54	360.59	42.97	0.62	1455.83	65.71
MA26A221	1901	151.3	2.8	32.92	3.02	325.32	41.17	0.52	8478.17	66.15
FE27A038	564	139.1	6.3	10.26	46.92	234.22	113.24	0.55	1693.06	68.71

Table A6.1: LA-ICPMS Analyses of Pyrite from Chapter 4

File	Analyst	Age (Ma)	Pyrite type	Setting	Mn (ppm)	Fe (ppm)	Co (ppm)	Ni (ppm)	Cu (ppm)	Zn (ppm)
FE27A047	D Gregory	2561.0	microcrystaline clusters	Deep Facies	205.26	465364.30	793.67	1175.54	311.15	53.20
MA26A213	D Gregory	2561.0	large euhedral	Deep Facies	391.14	464923.72	1872.04	1430.09	457.23	4.41
MA26A204	D Gregory	2561.0	microcrystalline clusters	Deep Facies	0.50	464912.23	1784.15	1379.72	2524.54	175.98
FE27A034	D Gregory	2561.0	large anhedral	Deep Facies	173.84	465373.47	895.74	1203.19	704.66	76.13
FE27A035	D Gregory	2561.0	microcrystaline clusters	Deep Facies	321.87	465355.20	929.09	1401.73	635.93	515.58
MA26A212	D Gregory	2561.0	large euhedral	Deep Facies	9.62	464881.63	2057.96	1673.57	1702.01	61.88
FE27A040	D Gregory	2561.0	microcrystaline clusters	Deep Facies	265.85	465374.90	991.87	1445.42	464.52	81.19
MA26A205	D Gregory	2561.0	microcrystalline clusters	Deep Facies	692.30	465012.90	1474.15	949.21	1903.33	76.60
FE27A122	D Gregory	2561.0	nodule	Deep Facies	23.74	464870.85	1929.71	1520.58	313.41	18.70
FE27A126	D Gregory	2561.0	nodule	Deep Facies	0.59	464816.83	1605.21	1246.00	233.21	163.89
MA26A206	D Gregory	2561.0	microcrystalline clusters	Deep Facies	5.04	464856.74	1906.43	1534.20	4038.57	4140.47
FE27A127	D Gregory	2561.0	nodule	Deep Facies	12.90	464737.26	2266.88	1826.93	349.79	1404.10
FE27A135	D Gregory	2561.0	nodule	Deep Facies	157.91	464704.79	2098.01	1796.72	291.17	18.04
MA26A207	D Gregory	2561.0	microcrystalline clusters	Deep Facies	4.75	464870.54	1842.08	1378.49	2367.26	109.04
FE27A136	D Gregory	2561.0	nodule	Deep Facies	5.12	464681.40	2196.67	1807.72	315.09	16.07
FE27A133	D Gregory	2561.0	nodule	Deep Facies	9.54	464777.14	2150.94	2120.60	378.56	5.24
FE27A124	D Gregory	2561.0	nodule	Deep Facies	6.85	464818.35	1907.83	1951.01	335.69	4.93
FE27A123	D Gregory	2561.0	nodule	Deep Facies	11.79	464788.09	2095.03	1688.45	285.60	8.44
FE27A134	D Gregory	2561.0	nodule	Deep Facies	1562.17	464650.67	2391.37	1971.68	338.39	9.94
FE27A125	D Gregory	2561.0	nodule	Deep Facies	2.57	464751.85	2551.88	2347.86	478.47	13.40
FE27A045	D Gregory	2561.0	microcrystaline clusters	Deep Facies	197.90	465303.13	1064.91	1539.91	455.51	44.82
MA21B057	D Gregory	2563.0	small euhedral	Deep Facies	32.51	465515.73	632.78	1469.07	118.09	9.07
MA21B064	D Gregory	2563.0	small euhedral	Deep Facies	20.37	465525.06	422.48	946.30	141.02	7.05

Table A6.1: LA-ICPMS Analyses of Pyrite from Chapter 4

File	As(ppm)	Se(ppm)	Mo(ppm)	Ag(ppm)	Cd(ppm)	Sb(ppm)	Te(ppm)	Au(ppm)	Pb(ppm)	Bi(ppm)
FE27A047	707.9	135.8	1.86	11.59	4.91	261.74	132.28	0.64	1020.87	69.50
MA26A213	2358.5	29.4	2.32	38.19	3.03	386.01	43.04	0.60	538.11	69.57
MA26A204	2401.5	104.4	0.82	42.31	5.25	395.39	46.43	0.70	3692.20	73.79
FE27A034	673.5	146.8	66.55	12.83	6.39	271.55	126.32	0.67	2442.73	74.09
FE27A035	741.9	85.3	1.50	13.25	39.50	292.87	138.46	0.56	772.34	75.92
MA26A212	2516.1	37.7	1.04	43.44	4.89	438.63	46.56	0.68	1095.51	77.13
FE27A040	668.1	100.0	1.26	13.93	6.03	270.29	115.99	0.66	1343.38	77.98
MA26A205	2024.3	211.7	2.73	32.41	2.23	348.32	43.71	0.50	8637.30	78.67
FE27A122	2556.5	12.6	2.50	11.05	0.12	372.83	10.83	0.30	554.51	79.72
FE27A126	2758.9	10.0	6.45	7.55	0.64	350.54	8.99	0.15	559.17	80.05
MA26A206	2609.4	105.6	0.62	46.38	78.56	424.71	49.99	0.73	4448.86	80.10
FE27A127	3057.0	12.4	1.58	13.34	5.25	432.01	12.17	0.24	484.75	80.20
FE27A135	3178.7	12.8	3.47	12.77	0.25	443.75	12.74	0.23	576.81	83.16
MA26A207	2557.7	44.3	1.39	39.33	4.41	438.63	50.24	0.63	1307.91	83.44
FE27A136	3266.3	13.7	3.57	13.14	0.17	456.53	12.23	0.23	580.43	83.55
FE27A133	2907.6	12.5	1.10	16.18	0.27	440.95	14.43	0.33	579.30	88.27
FE27A124	2753.2	12.0	1.91	13.97	0.19	425.89	13.86	0.33	584.52	88.90
FE27A123	2866.6	12.5	3.07	13.69	0.34	423.30	13.14	0.32	604.30	90.77
FE27A134	3381.4	15.2	5.75	14.62	0.13	468.56	14.35	0.27	655.50	90.95
FE27A125	3002.4	15.1	0.95	18.29	0.31	468.57	13.56	0.35	582.13	92.71
FE27A045	937.0	279.6	2.38	16.21	8.09	363.53	193.59	0.80	1995.93	97.95
MA21B057	140.5	22.5	0.30	1.68	0.18	25.77	2.84	0.07	588.73	14.52
MA21B064	105.6	13.1	0.40	1.87	0.31	28.18	2.35	0.06	557.31	17.00

Table A6.1: LA-ICPMS Analyses of Pyrite from Chapter 4

File	Analyst	Age (Ma)	Pyrite type	Setting	Mn (ppm)	Fe (ppm)	Co (ppm)	Ni (ppm)	Cu (ppm)	Zn (ppm)
MA21B056	D Gregory	2563.0	small euhedral	Deep Facies	29.33	465355.88	3674.63	10817.51	5204.59	7.47
MA21B063	D Gregory	2563.0	small euhedral	Deep Facies	75.40	465515.43	457.40	1554.30	62.05	15.32
MA21B061	D Gregory	2563.0	small euhedral	Deep Facies	65.07	465526.07	494.69	1584.92	64.86	8.91
MA21B066	D Gregory	2563.0	small euhedral	Deep Facies	45.46	465521.81	496.92	1493.04	70.67	26.04
MA21B062	D Gregory	2563.0	small euhedral	Deep Facies	40.81	465521.18	600.84	2481.80	94.65	8.79
MA21B058	D Gregory	2563.0	small euhedral	Deep Facies	48.59	465516.75	665.52	2298.51	91.03	13.52
MA21B047	D Gregory	2563.0	small euhedral	Deep Facies	60.89	465516.10	593.74	2615.53	65.60	14.03
MA21B049	D Gregory	2563.0	small euhedral	Deep Facies	49.20	465504.02	701.11	2658.91	108.06	8.20
MA21B044	D Gregory	2563.0	small euhedral	Deep Facies	30.96	465502.97	981.36	3668.36	110.52	5.99
MA21B067	D Gregory	2563.0	small euhedral	Deep Facies	61.47	465371.47	3690.64	8318.42	4109.54	17.59
FE27A176	D Gregory	2575.0	large euhedral	Deep Facies	27.87	462233.84	196.74	637.25	256.41	2.93
FE27A175	D Gregory	2575.0	large euhedral	Deep Facies	10.41	464489.51	234.29	2672.65	94.18	134.48
FE27A071	D Gregory	2575.0	nodule	Deep Facies	2237.24	465269.99	138.42	517.17	182.58	4.72
FE27A160	D Gregory	2575.0	large euhedral	Deep Facies	24.29	462070.06	323.42	1309.98	265.03	5.55
FE27A067	D Gregory	2575.0	large euhedral	Deep Facies	1289.14	465262.72	375.16	1040.61	167.16	5.43
FE27A185	D Gregory	2575.0	large euhedral	Deep Facies	59.18	462842.59	286.29	1477.89	130.20	6.07
FE27A174	D Gregory	2575.0	large euhedral	Deep Facies	51.44	463474.84	460.39	2294.59	145.74	4.04
FE27A073	D Gregory	2575.0	nodule	Deep Facies	3.50	465507.57	180.97	769.42	262.28	6.67
FE27A072	D Gregory	2575.0	nodule	Deep Facies	0.63	465512.00	231.17	711.47	185.00	5.47
FE27A075	D Gregory	2575.0	nodule	Deep Facies	6.53	465512.23	146.26	661.04	213.17	6.09
FE27A184	D Gregory	2575.0	large euhedral	Deep Facies	102.73	463311.72	1995.52	1881.71	130.94	148.77
FE27A068	D Gregory	2575.0	large euhedral	Deep Facies	349.74	465450.08	257.24	842.24	177.45	12.19
FE27A065	D Gregory	2575.0	large euhedral	Deep Facies	487.89	465476.62	257.36	771.52	177.37	8.67

Table A6.1: LA-ICPMS Analyses of Pyrite from Chapter 4

File	As(ppm)	Se(ppm)	Mo(ppm)	Ag(ppm)	Cd(ppm)	Sb(ppm)	Te(ppm)	Au(ppm)	Pb(ppm)	Bi(ppm)
MA21B056	739	61.9	9.9	10.82	<0.066	68.52	3.02	0.09	1361.80	18.17
MA21B063	142	18.8	1.1	1.59	<0.066	32.76	2.55	<0.01	563.85	19.92
MA21B061	102	14.0	0.4	1.58	<0.066	30.04	2.40	0.06	547.31	20.05
MA21B066	118	22.5	0.9	1.50	0.45	33.98	2.08	0.12	585.86	20.05
MA21B062	120	18.6	0.4	2.14	<0.066	34.83	2.98	0.08	578.06	21.79
MA21B058	137	19.9	0.6	2.08	<0.066	38.46	3.07	0.08	609.37	24.55
MA21B047	139	27.7	0.8	2.53	<0.066	40.45	5.62	<0.01	594.21	24.87
MA21B049	184	23.4	0.5	2.49	<0.066	43.65	4.33	0.11	701.95	25.78
MA21B044	188	24.0	4.2	3.90	<0.066	44.35	5.28	0.10	647.71	28.46
MA21B067	681	85.1	37.7	7.92	<0.066	94.82	6.52	0.12	1580.60	43.08
FE27A176	12436	25.6	1.6	0.48	0.11	193.96	<0.13	0.12	454.02	0.18
FE27A175	3985	31.2	1.0	0.31	0.40	97.13	<0.13	<0.01	176.23	0.56
FE27A071	1061	27.4	1.1	1.96	0.13	33.29	0.55	0.04	99.67	0.86
FE27A160	13050	23.9	1.7	1.24	0.13	298.00	0.31	0.07	556.47	1.31
FE27A067	1088	28.1	0.8	3.63	0.14	74.75	1.58	0.09	184.79	1.80
FE27A185	10155	20.4	1.5	1.62	0.07	331.90	0.35	0.07	588.04	1.97
FE27A174	7787	30.5	1.3	1.72	<0.066	200.54	0.47	0.06	395.26	2.21
FE27A073	171	7.5	0.6	4.76	0.12	84.30	1.57	0.12	189.27	2.29
FE27A072	154	8.4	0.6	3.67	<0.066	80.74	1.50	0.08	192.37	2.35
FE27A075	154	9.3	0.5	4.22	0.10	79.52	1.52	0.11	168.95	2.45
FE27A184	8398	29.1	2.5	1.89	1.05	252.68	0.51	0.07	520.68	2.51
FE27A068	386	15.4	0.7	4.45	0.19	103.81	1.92	0.11	230.45	2.65
FE27A065	287	13.5	1.1	4.08	0.28	125.71	2.36	0.08	280.51	3.17

Table A6.1: LA-ICPMS Analyses of Pyrite from Chapter 4

File	Analyst	Age (Ma)	Pyrite type	Setting	Mn (ppm)	Fe (ppm)	Co (ppm)	Ni (ppm)	Cu (ppm)	Zn (ppm)
FE27A076	D Gregory	2575.0	nodule	Deep Facies	1.32	465506.39	247.30	817.41	188.24	6.07
FE27A066	D Gregory	2575.0	large euhedral	Deep Facies	1192.29	465448.86	397.99	777.92	155.27	0.38
FE27A159	D Gregory	2575.0	large euhedral	Deep Facies	800.49	464394.60	267.51	1144.99	108.57	0.98
FE27A074	D Gregory	2575.0	nodule	Deep Facies	3.59	465503.84	236.69	897.86	170.21	14.65
FE27A069	D Gregory	2575.0	large euhedral	Deep Facies	694.33	465467.49	284.61	911.87	137.99	4.89
FE27A161	D Gregory	2575.0	large euhedral	Deep Facies	32.88	463630.49	558.57	1692.27	112.83	102.09
FE27A164	D Gregory	2575.0	small anhedral	Deep Facies	174.86	463279.53	977.82	3325.99	207.92	10.95
FE27A064	D Gregory	2575.0	large euhedral	Deep Facies	1045.69	465429.49	517.87	1128.37	152.02	26.00
FE27A190	D Gregory	2575.0	small anhedral	Deep Facies	2792.21	464632.68	1193.28	3139.76	119.81	1266.67
FE27A178	D Gregory	2575.0	small anhedral	Deep Facies	133.58	465296.79	460.53	2311.47	96.05	1003.13
FE27A179	D Gregory	2575.0	small anhedral	Deep Facies	502.90	465240.96	526.22	2553.21	89.80	116.03
FE27A182	D Gregory	2575.0	small anhedral	Deep Facies	243.77	465238.90	580.82	2563.47	103.14	25.07
FE27A166	D Gregory	2575.0	small anhedral	Deep Facies	734.60	464598.42	877.01	2921.62	107.02	15.53
FE27A177	D Gregory	2575.0	small anhedral	Deep Facies	105.72	465284.76	546.16	2617.76	100.32	31.64
FE27A180	D Gregory	2575.0	small anhedral	Deep Facies	422.34	465253.00	471.94	2668.43	109.15	2354.51
FE27A186	D Gregory	2575.0	small anhedral	Deep Facies	411.76	465249.34	672.05	3011.12	101.85	38.38
FE27A163	D Gregory	2575.0	small anhedral	Deep Facies	2762.68	464961.44	837.46	3212.21	118.20	9.94
FE27A189	D Gregory	2575.0	small anhedral	Deep Facies	619.47	464747.49	986.48	4167.48	167.18	15.66
FE27A181	D Gregory	2575.0	small anhedral	Deep Facies	2770.51	464773.81	807.83	3605.73	147.01	19.31
FE27A187	D Gregory	2575.0	small anhedral	Deep Facies	2261.79	465243.87	618.29	3489.96	129.57	28.88
FE27A162	D Gregory	2575.0	small anhedral	Deep Facies	4.98	465276.46	622.25	2824.44	98.58	58.82
FE27A165	D Gregory	2575.0	small anhedral	Deep Facies	633.46	465243.25	562.47	2985.29	122.47	280.05
FE27A188	D Gregory	2575.0	small anhedral	Deep Facies	260.45	465240.77	727.59	5132.03	147.10	59.48

Table A6.1: LA-ICPMS Analyses of Pyrite from Chapter 4

File	As(ppm)	Se(ppm)	Mo(ppm)	Ag(ppm)	Cd(ppm)	Sb(ppm)	Te(ppm)	Au(ppm)	Pb(ppm)	Bi(ppm)
FE27A076	175.5	9.9	0.54	5.02	0.13	103.37	2.15	0.13	261.91	3.36
FE27A066	391.0	16.3	1.21	4.05	0.21	137.94	2.36	0.10	315.25	3.45
FE27A159	4340.8	26.8	1.81	2.65	<0.066	95.17	1.14	0.11	295.63	3.51
FE27A074	185.1	10.6	0.52	6.07	0.11	108.67	2.24	0.16	293.40	3.73
FE27A069	321.2	16.6	1.56	5.62	0.14	174.25	3.30	0.17	430.34	5.08
FE27A161	7203.5	31.7	1.97	4.02	0.27	284.79	1.41	0.13	779.32	5.64
FE27A164	8518.4	43.1	2.85	3.94	0.08	292.25	1.68	0.17	699.47	6.23
FE27A064	463.6	22.9	2.93	5.52	0.38	249.53	4.49	0.18	632.89	7.26
FE27A190	3448.8	36.6	5.46	9.81	4.86	280.99	3.07	0.27	625.90	12.27
FE27A178	960.8	27.0	0.73	13.52	3.75	265.67	4.15	0.31	568.47	14.66
FE27A179	1169.9	25.4	0.86	12.81	0.67	310.16	4.47	0.35	612.71	15.14
FE27A182	1177.7	25.6	1.28	12.54	0.25	305.72	4.58	0.30	580.75	15.36
FE27A166	3577.2	39.9	2.20	11.30	0.09	306.44	4.10	0.26	640.18	15.68
FE27A177	1005.8	23.8	0.65	14.26	0.24	281.06	4.15	0.33	595.96	16.10
FE27A180	1124.8	27.2	1.43	13.88	8.01	329.46	4.92	0.34	677.58	17.02
FE27A186	1138.5	39.0	1.13	15.45	0.31	324.42	4.62	0.37	758.64	17.29
FE27A163	2217.1	42.9	3.01	12.47	0.17	338.42	5.02	0.34	725.53	19.20
FE27A189	3018.7	47.7	2.15	15.98	0.27	377.97	4.99	0.42	866.14	19.76
FE27A181	2920.1	45.0	3.43	16.25	<0.066	388.52	5.93	0.43	866.31	20.60
FE27A187	1159.0	35.7	3.33	17.12	0.27	390.64	5.87	0.49	841.57	20.60
FE27A162	1036.9	32.3	1.22	16.10	0.60	367.34	5.80	0.42	696.02	20.94
FE27A165	1161.3	37.8	2.68	15.46	1.52	383.03	5.60	0.36	758.89	21.31
FE27A188	1170.6	32.9	6.12	18.93	0.28	404.91	6.11	0.49	960.43	22.34

Table A6.1: LA-ICPMS Analyses of Pyrite from Chapter 4

File	Analyst	Age (Ma)	Pyrite type	Setting	Mn (ppm)	Fe (ppm)	Co (ppm)	Ni (ppm)	Cu (ppm)	Zn (ppm)
AP27A081	JA Halpin	2680.0	nodule	Rift Basin	7.14	465393.33	376.28	364.65	76.76	24.28
AP27A084	JA Halpin	2680.0	nodule	Rift Basin	10.58	465365.89	470.06	434.12	90.97	14.03
AP27A082	JA Halpin	2680.0	nodule	Rift Basin	11.02	465386.82	393.09	366.57	98.35	50.03
AP27A079	JA Halpin	2680.0	nodule	Rift Basin	8.61	465383.96	438.12	378.51	94.42	18.05
AP27A080	JA Halpin	2680.0	nodule	Rift Basin	8.38	465377.22	479.60	403.43	96.51	26.65
AP27A083	JA Halpin	2680.0	nodule	Rift Basin	16.28	465301.67	680.32	637.57	152.14	105.50
AP27A086	JA Halpin	2680.0	nodule	Rift Basin	9.85	465316.75	561.82	547.01	133.43	94.20
AP27A085	JA Halpin	2680.0	nodule	Rift Basin	12.79	465313.13	669.92	580.28	125.52	7.64
AP27A062	JA Halpin	2680.0	nodule	Rift Basin	70.02	465344.81	218.68	570.00	266.89	43.54
AP27A049	JA Halpin	2680.0	nodule	Rift Basin	52.09	465322.86	246.42	628.69	105.28	192.48
AP27A058	JA Halpin	2680.0	nodule	Rift Basin	37.53	465337.47	236.00	614.70	662.79	194.83
AP27A068	JA Halpin	2680.0	nodule	Rift Basin	41.63	465301.98	256.84	628.98	485.14	1842.89
AP27A037	JA Halpin	2680.0	nodule	Rift Basin	39.93	465321.88	244.88	709.87	170.81	41.43
AP27A036	JA Halpin	2680.0	nodule	Rift Basin	39.62	465336.05	234.88	686.06	114.59	24.44
AP27A059	JA Halpin	2680.0	nodule	Rift Basin	40.29	465342.32	272.53	557.71	244.72	74.82
AP27A039	JA Halpin	2680.0	nodule	Rift Basin	36.18	465332.03	228.97	702.93	218.37	50.51
AP27A040	JA Halpin	2680.0	nodule	Rift Basin	27.55	465299.76	292.69	765.23	550.11	44.70
AP27A045	JA Halpin	2680.0	nodule	Rift Basin	37.71	465312.01	300.28	707.09	107.65	37.16
AP27A066	JA Halpin	2680.0	nodule	Rift Basin	49.31	465326.89	285.71	574.28	135.80	40.23
AP27A041	JA Halpin	2680.0	nodule	Rift Basin	29.06	465321.05	224.14	761.45	188.18	92.65
AP27A044	JA Halpin	2680.0	nodule	Rift Basin	37.84	465287.59	303.08	752.14	136.27	191.44
AP27A046	JA Halpin	2680.0	nodule	Rift Basin	55.49	465279.57	288.96	838.25	228.99	71.52
AP27A038	JA Halpin	2680.0	nodule	Rift Basin	47.51	465313.97	254.04	757.74	170.80	70.82

Table A6.1: LA-ICPMS Analyses of Pyrite from Chapter 4

File	As(ppm)	Se(ppm)	Mo(ppm)	Ag(ppm)	Cd(ppm)	Sb(ppm)	Te(ppm)	Au(ppm)	Pb(ppm)	Bi(ppm)
AP27A081	599	<0.78	0.7	5.77	0.21	31.64	10.06	0.09	242.26	9.74
AP27A084	702	3.8	0.9	6.03	0.11	36.52	11.33	0.10	260.28	10.54
AP27A082	623	3.0	0.7	6.35	0.20	33.15	11.17	0.10	249.86	10.57
AP27A079	634	3.1	0.9	7.31	0.16	32.99	10.41	0.08	261.80	10.83
AP27A080	659	2.8	1.0	7.37	<0.066	37.25	12.65	0.11	271.38	11.41
AP27A083	942	9.8	1.1	8.48	0.13	51.85	18.64	0.12	380.07	14.79
AP27A086	886	8.5	0.5	8.35	0.28	51.23	16.95	0.12	364.24	15.06
AP27A085	900	11.6	1.0	8.90	0.09	51.53	16.77	0.13	408.44	16.51
AP27A062	781	8.1	0.5	8.35	0.21	70.24	14.36	0.34	443.12	22.71
AP27A049	863	13.2	0.4	7.96	0.49	69.73	13.26	0.42	426.85	23.25
AP27A058	808	14.1	0.2	9.68	0.50	72.68	14.72	0.34	528.83	24.02
AP27A068	941	18.7	0.3	8.94	5.69	69.27	14.14	0.33	480.22	24.12
AP27A037	867	13.4	0.3	8.57	0.06	73.70	15.01	0.46	440.23	24.16
AP27A036	814	8.8	0.4	8.68	0.17	75.34	16.77	0.40	428.64	24.40
AP27A059	790	9.6	0.3	9.61	0.22	71.15	14.78	0.35	477.30	24.68
AP27A039	829	8.9	0.4	8.08	0.29	74.26	15.13	0.38	443.88	24.71
AP27A040	950	10.0	0.7	9.47	0.24	76.82	16.65	0.44	501.44	24.96
AP27A045	904	9.4	0.3	8.59	0.24	78.10	15.35	0.46	484.34	25.57
AP27A066	848	15.8	0.5	9.95	<0.066	73.98	15.20	0.43	522.62	25.67
AP27A041	870	9.2	0.3	7.42	0.35	78.93	15.51	0.43	459.12	25.74
AP27A044	995	7.8	0.3	8.44	0.54	81.65	16.88	0.42	478.21	25.86
AP27A046	1025	8.6	0.2	8.34	0.16	81.14	17.02	0.41	492.24	26.12
AP27A038	896	18.1	0.4	8.59	0.25	83.87	16.08	0.47	491.63	26.24

Table A6.1: LA-ICPMS Analyses of Pyrite from Chapter 4

File	Analyst	Age (Ma)	Pyrite type	Setting	Mn (ppm)	Fe (ppm)	Co (ppm)	Ni (ppm)	Cu (ppm)	Zn (ppm)
AP27A035	JA Halpin	2680.0	nodule	Rift Basin	42.71	465296.19	266.21	821.33	116.88	55.95
AP27A067	JA Halpin	2680.0	nodule	Rift Basin	44.84	465328.16	271.75	597.68	399.59	57.81
AP27A060	JA Halpin	2680.0	nodule	Rift Basin	31.58	465309.22	259.13	692.81	773.67	452.12
AP27A071	JA Halpin	2680.0	nodule	Rift Basin	44.19	465322.52	244.50	599.97	841.74	132.71
AP27A070	JA Halpin	2680.0	nodule	Rift Basin	49.94	465276.45	394.80	662.47	586.61	28.57
AP27A042	JA Halpin	2680.0	nodule	Rift Basin	33.55	465334.06	225.98	666.65	86.38	21.83
AP27A065	JA Halpin	2680.0	nodule	Rift Basin	42.66	465332.77	234.79	599.30	632.21	108.45
AP27A048	JA Halpin	2680.0	nodule	Rift Basin	33.01	465270.76	330.44	808.23	186.92	78.65
AP27A057	JA Halpin	2680.0	nodule	Rift Basin	70.95	465319.12	242.17	629.05	900.41	86.47
AP27A064	JA Halpin	2680.0	nodule	Rift Basin	36.24	465310.90	260.32	622.22	728.99	157.45
AP27A047	JA Halpin	2680.0	nodule	Rift Basin	36.64	465269.67	328.69	800.76	216.95	39.92
AP27A069	JA Halpin	2680.0	nodule	Rift Basin	49.96	465275.11	326.29	765.67	919.47	278.26
AP27A063	JA Halpin	2680.0	nodule	Rift Basin	27.37	465269.23	308.70	692.15	227.75	57.11
AP27A043	JA Halpin	2680.0	nodule	Rift Basin	27.91	465282.20	313.35	779.59	428.51	774.67
AP27A061	JA Halpin	2680.0	nodule	Rift Basin	53.15	465236.13	426.65	773.67	338.05	551.67
JL23A077	E Lounejeva	3470.0	nodule		6.28	465397.42	170.89	2051.97	24.70	18.39
JL23A079	E Lounejeva	3470.0	nodule		43.00	465416.83	432.37	3108.03	40.00	8.33
JL23A075	E Lounejeva	3470.0	nodule		40.59	465416.63	535.56	3555.74	47.92	83.69
JL23A078	E Lounejeva	3470.0	nodule		12.53	465412.74	406.52	3130.60	62.23	17.09
JL23A076	E Lounejeva	3470.0	nodule		11.98	465423.79	368.13	2849.21	49.43	11.19
JL23A072	E Lounejeva	3470.0	nodule		28.69	465413.42	793.10	4659.85	20.64	25.86
JL23A073	E Lounejeva	3470.0	nodule		93.91	465415.86	423.33	3325.26	60.77	20.29
JL23A071	E Lounejeva	3470.0	nodule		8.26	465363.22	224.02	2958.50	51.73	9.56

Table A6.1: LA-ICPMS Analyses of Pyrite from Chapter 4

File	As(ppm)	Se(ppm)	Mo(ppm)	Ag(ppm)	Cd(ppm)	Sb(ppm)	Te(ppm)	Au(ppm)	Pb(ppm)	Bi(ppm)
AP27A035	963.0	11.9	0.58	8.92	0.15	83.80	16.13	0.46	536.84	26.25
AP27A067	843.2	12.9	0.36	9.47	0.17	77.66	15.44	0.35	523.98	26.27
AP27A060	914.2	6.8	0.22	10.07	1.82	79.44	15.87	0.37	484.43	26.30
AP27A071	864.4	12.1	0.37	10.48	0.42	77.92	16.02	0.36	540.10	26.33
AP27A070	1037.0	12.3	0.58	11.15	0.14	81.91	16.25	0.45	555.64	26.68
AP27A042	821.2	10.2	0.20	8.78	0.10	77.93	15.62	0.50	448.61	26.71
AP27A065	826.0	9.6	0.37	10.07	0.33	79.86	15.21	0.43	521.57	27.10
AP27A048	1058.3	9.2	0.76	9.09	0.38	86.24	18.11	0.45	524.82	27.27
AP27A057	877.1	6.5	0.34	10.40	0.45	83.08	16.56	0.39	530.25	27.44
AP27A064	907.9	13.4	0.46	10.06	0.61	78.96	15.51	0.36	545.51	27.64
AP27A047	1062.4	10.5	0.50	9.12	0.21	84.43	17.95	0.47	530.59	28.36
AP27A069	1042.0	9.7	0.29	10.50	0.78	90.81	16.95	0.40	613.26	29.62
AP27A063	1064.0	9.8	0.49	9.91	0.31	90.66	18.73	0.47	587.79	29.92
AP27A043	1015.4	10.9	0.35	8.90	2.44	86.50	18.13	0.46	536.14	30.35
AP27A061	1188.0	12.5	0.45	11.10	1.62	93.73	20.38	0.46	631.76	31.71
JL23A077	583.8	4.8	8.10	4.99	0.17	31.96	0.89	0.02	100.59	0.13
JL23A079	511.0	7.4	5.59	7.50	0.08	50.07	1.52	0.05	149.35	0.18
JL23A075	511.8	8.4	4.88	7.58	0.38	50.90	1.59	0.04	146.57	0.19
JL23A078	526.4	7.2	4.65	7.63	0.13	52.17	1.40	0.05	164.76	0.20
JL23A076	485.0	7.0	6.62	7.57	<0.066	46.12	1.58	0.05	139.91	0.20
JL23A072	523.8	8.5	16.50	7.69	0.29	46.58	1.48	0.05	154.89	0.21
JL23A073	514.7	6.8	4.93	7.81	0.14	63.00	1.67	0.05	210.00	0.22
JL23A071	711.9	5.3	17.42	7.93	0.26	47.13	1.51	0.05	181.40	0.23

Table A6.1: LA-ICPMS Analyses of Pyrite from Chapter 4

File	Analyst	Age (Ma)	Pyrite type	Setting	Mn (ppm)	Fe (ppm)	Co (ppm)	Ni (ppm)	Cu (ppm)	Zn (ppm)
JL23A053	E Lounejeva	3470.0	nodule		0.69	465286.89	125.58	1657.06	55.80	2.75
JL23A056	E Lounejeva	3470.0	nodule		0.67	465299.77	166.11	2094.46	59.94	358.48
JL23A062	E Lounejeva	3470.0	nodule		1.72	465370.38	480.36	3491.20	46.21	2442.30
JL23A074	E Lounejeva	3470.0	nodule		51.86	465397.77	723.83	4415.60	61.44	71.68
JL23A068	E Lounejeva	3470.0	nodule		1.91	465341.39	231.00	2702.63	62.81	19.21
JL23A067	E Lounejeva	3470.0	nodule		1.24	465334.24	191.71	2606.49	60.26	8.02
JL23A063	E Lounejeva	3470.0	nodule		14.66	465385.85	701.04	3850.59	88.09	8.20
JL23A054	E Lounejeva	3470.0	nodule		12.21	465261.82	362.20	3405.70	67.07	6531.92
JL23A061	E Lounejeva	3470.0	nodule		2.71	465254.12	417.97	3778.12	79.71	887.52
JL23A069	E Lounejeva	3470.0	nodule		1.53	465308.84	219.26	2766.38	85.13	16.42
JL23A070	E Lounejeva	3470.0	nodule		1.89	465262.05	198.98	2635.25	71.62	27.65
JL23A080	E Lounejeva	3470.0	nodule		4.87	465420.72	1632.50	6076.75	130.66	1.90
JL23A055	E Lounejeva	3470.0	nodule		0.65	465199.98	366.04	4065.94	54.72	3382.06
MY02A097	K Orth	3515.0	large anhedral		228.13	465356.92	1088.95	4132.04	2372.82	21.36
MY02A093	K Orth	3515.0	large anhedral		219.07	464793.55	1415.29	1925.38	1985.89	26.72
MY02A096	K Orth	3515.0	large anhedral		124.81	465466.80	1038.63	4567.73	1289.47	17.60
MY02A094	K Orth	3515.0	large anhedral		147.24	464968.93	1785.28	1897.08	2131.56	12.91
MY02A091	K Orth	3515.0	large anhedral		246.37	465133.64	1755.88	2654.66	2385.82	54.78
MY02A095	K Orth	3515.0	large anhedral		147.14	464915.03	1632.96	2098.86	1908.68	23.63
MY02A090	K Orth	3515.0	large anhedral		178.29	465152.35	1919.71	2841.32	2712.28	32.33
MY02A092	K Orth	3515.0	large anhedral		115.55	465325.33	1293.79	3506.68	2728.64	4.93

Table A6.1: LA-ICPMS Analyses of Pyrite from Chapter 4

File	As(ppm)	Se(ppm)	Mo(ppm)	Ag(ppm)	Cd(ppm)	Sb(ppm)	Te(ppm)	Au(ppm)	Pb(ppm)	Bi(ppm)
JL23A053	998	6.7	37.9	5.93	<0.066	52.49	1.15	0.03	160.91	0.23
JL23A056	950	6.7	35.6	6.00	0.86	44.68	1.18	0.04	181.43	0.24
JL23A062	685	8.8	65.3	7.66	6.07	47.76	1.31	0.04	175.95	0.26
JL23A074	582	9.8	5.3	9.65	0.48	77.45	2.04	0.06	240.33	0.26
JL23A068	794	7.5	16.4	9.00	0.18	59.20	1.49	0.05	213.67	0.27
JL23A067	820	7.9	21.4	9.42	0.12	62.30	1.58	0.05	511.74	0.29
JL23A063	627	10.2	7.1	7.07	0.25	56.11	1.25	0.04	253.64	0.29
JL23A054	1092	8.0	70.0	11.07	15.88	73.28	1.75	0.06	253.71	0.36
JL23A061	1121	7.9	63.0	10.59	2.23	75.67	1.90	0.07	241.11	0.36
JL23A069	916	8.0	28.6	11.20	0.20	82.57	2.03	0.07	278.55	0.36
JL23A070	1091	8.2	29.2	11.51	0.22	83.82	2.05	0.08	380.62	0.38
JL23A080	496	10.8	2.5	10.61	0.30	126.04	2.55	0.07	540.20	0.43
JL23A055	1323	10.8	123.5	13.92	8.32	103.85	2.50	0.06	322.30	0.44
MY02A097	736	2.6	0.2	2.96	0.08	8.51	0.48	0.04	35.82	2.15
MY02A093	2846	4.3	0.6	4.88	0.08	32.26	0.76	0.03	80.53	2.51
MY02A096	324	2.4	0.6	3.23	0.14	8.99	0.94	0.05	31.76	2.97
MY02A094	2189	3.0	0.4	4.45	0.19	22.19	0.89	0.02	59.80	2.98
MY02A091	1572	3.4	0.2	4.45	0.15	25.15	0.97	0.03	77.29	3.22
MY02A095	2391	3.5	0.5	5.10	0.19	29.01	1.16	0.03	81.12	3.59
MY02A090	1502	4.3	0.2	5.22	0.13	26.39	1.27	0.03	72.15	4.39
MY02A092	854	2.8	0.4	5.04	0.20	20.11	1.06	0.03	89.32	4.47

Appendix 7:

Geology of the Mount Bruce Supergroup

The geology of the Mount Bruce Supergroup and problems with nomenclature across the basin are discussed in detail in Trendall (1990a) and references therein. Age dates for the different units in the Hamersley Basin are presented in (Trendall, 1990a; Trendall et al., 2004, Thorne and Trendall, 2001) and references therein. The following is a summary of lithological units and dating analyses based on these studies.

The Mount Bruce Supergroup is made up of the Fortescue Group, Hamersley Group and Turree Creek Group, which unconformably overlie granite-greenstone belt rocks of the Pilbura Craton. At a regional scale the lithologies on either side of the unconformity are readily distinguished and the contact is easily mapped (Trendall, 1990c), though occasionally the lithology on either side of the contact is very similar. Detailed mapping often reveals that there is not a single contact but rather a series of several unconformable surfaces (Trendall, 1990b). The paleo-topography at the time of deposition of the Fortescue Group rocks on the unconformity is interpreted to be of relatively low relief with a series of low ridges rarely over 100 m high (Trendall, 1990b). Evidence of this is particularly well exposed in the Lionel area where well defined, steep sided ridges that are parallel to strike are well defined. The existence of these ridges is supported by the presence of large boulders in conglomerates in the paleo valleys (Williams, 1989) and the filling of paleo valleys by basal lavas (Blight, 1985).

A7.1 The Fortescue Group

The oldest unit of the Hamersley Basin is the Fortescue Group. It is made up of a series of six volcanic and sedimentary units: the Mt Roe Basalt (Lower Volcanic Unit); Hardey Formation (Lower Sedimentary Unit); Kylena Formation (Middle Volcanic Unit); Tumbiana Formation (Middle Sedimentary Unit); Maddina Formation (Upper Volcanic Unit) and the Jeerinah Formation (Upper Sedimentary Unit) (Trendall, 1990b; Hickman and Van Kranendonk, 2012). These units are interpreted to have been deposited in four different stages. Crustal extension between 2.78 and 2.77 Ga resulted in local rifting and the emplacement of north northeast trending dolorite dykes and the extrusion of the Mt Roe

Basalt (Hickman and Van Kranendonk, 2012). Between 2.77 and 2.75 Ga folding and faulting predominated. This tectonic activity was accompanied by the deposition of the Hardey Formation. The Hardey formation is made up of lacustrine shale deposited in shallow rift basins and thick sequences of fluvial conglomerate and sandstone (Hickman and Van Kranendonk, 2012). Plume related ultramafic, mafic and felsic volcanism between 2.75 and 2.71 Ga resulted in the deposition of the volcanic rocks of the Kylena Formation (Arndt et al., 2001). These extrusive flows are separated by the Tumbiana Formation (2.73-2.72 Ga), which is made up of stromatolitic limestones and volcaniclastic successions (Hickman and Van Kranendonk, 2012). This is followed by the deposition of the Jeerinah formation (2.71-2.63 Ma). It is composed of basal shore facies (sandstone and stromatolitic limestone) followed by deeper facies rocks (mudstone; carbonate rocks; carbonaceous, pyritic shale and chert) indicating a northerly marine transgression (Hickman and Van Kranendonk, 2012).

The Mt Roe Basalt (Lower Volcanic Unit) is predominantly composed of well-jointed basaltic flows that commonly contain vesicles and/or amygdaloids. The basalts appear to have been deposited both sub-aqueously and sub-aerially (Trendall, 1990b). Evidence for this includes the presence of individual flows in some locations (suggesting sub-aerial deposition) (Kriewaldt, 1964a; Blake, 1984) and the presence of pillows and hyaloclastites in other locations (Hickman, 1983 and Blake, 1984). The basalt flows are variable intercalated with a variety of minor sedimentary layers, including conglomerate, arkose sandstone and siltstone. Age dates for the unit include 2775±10 Ma; 2763±13 Ma (Arndt et al., 1991) and 2772±2 Ma (Wingate, 1999).

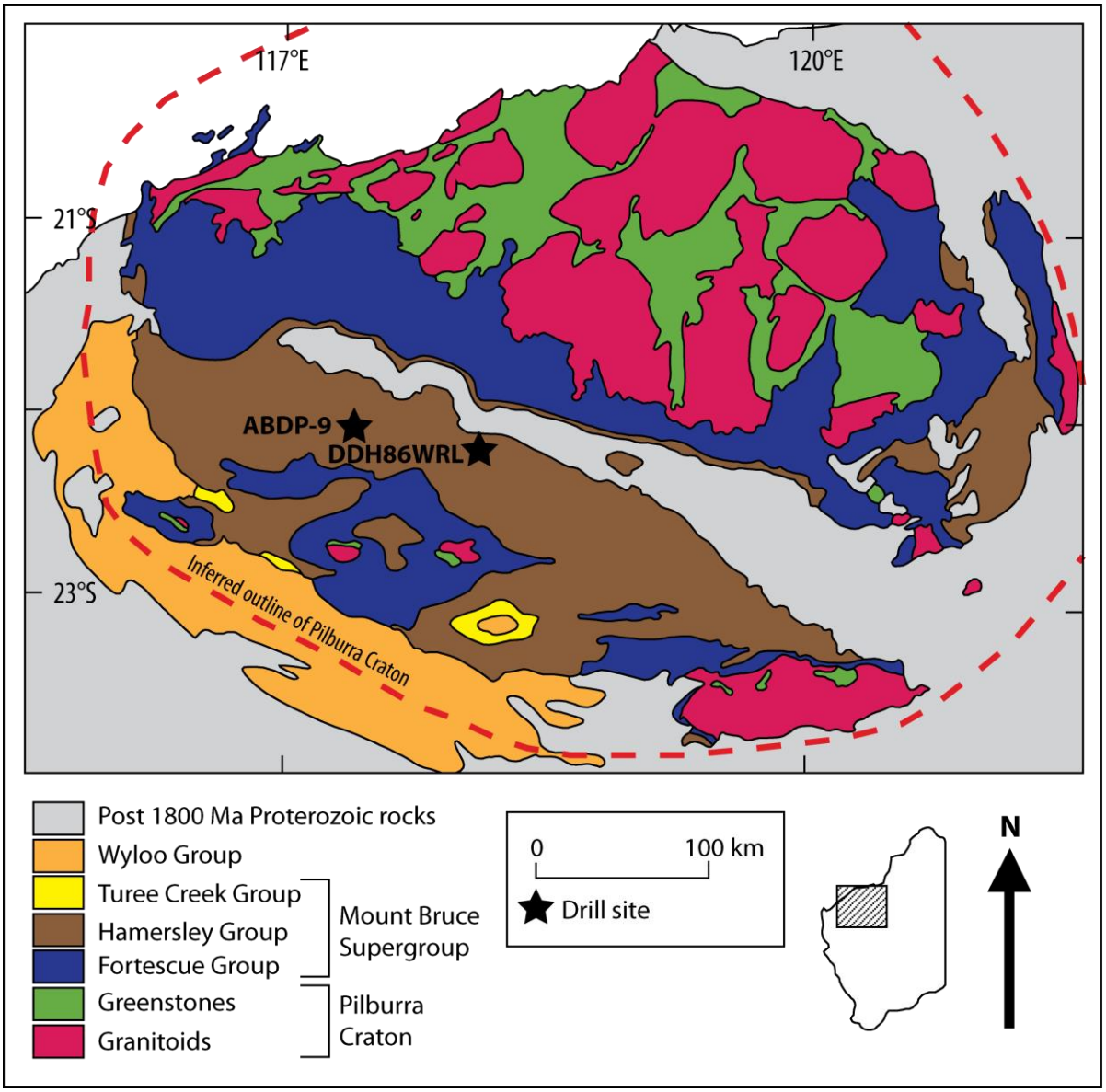

Figure A7.1: Regional Geology of the Pilbara Craton and location of ABDP9 and DDH86WRL1. Modified after Hickman and Van Kranendonk (2012).

The Mt Roe Basalt (Lower Volcanic Unit) is overlain by the Hardey Formation (Lower Sedimentary Unit). There is some erosion of the underlying basalts either prior to of during the deposition of the Hardey Formation (Lower Sedimentary Unit) locally. The evidence includes the presence of angular basaltic blocks (Blight, 1985) in some of the lower sedimentary units and the presence of erosional surface in some of the basalts (Blake, 1984). However; in most places the Hardey Formation (Lower Sedimentary Unit) forms a conformable contact with the underlying basalts (Trendall, 1990b). Where basalts are not present, the basal contact is formed with the underlying granite greenstone units. The Hardey Formation is composed of a minor conglomerate at the base conglomerate overlain by a

series of coarse-grained arkose, fine-grained arenite and shale with sub-arkose grit (Blight, 1985). More detailed mapping has shown that this unit forms a coarsening upward sequence up to a thickness of 80 m and has been interpreted to represent a transition from a lacustrine depositional setting to a braided river system (Trendall, 1990b). Several age dates for the deposition of this unit have been collected in recent years, these include: 2764±8 Ma (Arndt et al., 1991), 2763±8 Ma (Nelson, 1996), 2760±4 Ma (Nelson, 2002), 2766±7 Ma (Nelson, 2002), 2750±4 Ma (Hall, 2002).

Table A7.1: Summary of different stratigraphic subdivision of the Fortescue Group (modified after Thorne and Trendall, 2001)

Entire Basin (Trendall, 1990b)	Northern Hamersley (Hickman, 1983)	Roebourne (Ryan, 1966)	Yarraloola (Williams, 1968)	Pyramid (Krietwaldt and Ryan, 1967)	Mount Bruce (de la Hunty, 1965)	Roy Hill (MacLeod and de la Hunty, 1965)	Balfour Downs (de la Hunty, 1964)	Nullagine and Marble Bar (Noldar and Wyatt, 1962)
Upper Sedimentary Unit	Jeerinah Formation		Jeerinah Formation Roy Hill Shale; Nallanaring Volc Mbr; Warrie Mbr; Woodiana sst. Mbr.	Jeerinah Formation Roy Hill Shale; Warrie Mbr.; Woodiana sst. Mbr.	Jeerinah Formation	Jeerinah Formation Roy Hill Shale; Warrie Mbr.; Woodiana sst. Mbr.	Lewin Shale	Carawine Dolomite and Tumbiana Pisolite
Upper Volcanic Unit	Maddina Basalt		Maddina Volcanics	Maddina Basalt	Mount Jope Volcanics Bunjinah Pillow Lava Mbr	Mount Jope Volcanics Maddina Basalt Mbr.	Little Deg Grey Lava	Upper Little de Grey Lava
Middle Sedimentary Unit	Kuruna sst.; Nymerina basalt; Tubiana Frm.		Pillingini Tuff	Pillingini Tuff	Pyradie Pyroclastic Member	Kuruna sst. Mbr. Nymerina Basalt Mbr. Tumbiana Pisolite Mbr.	Tumbiana Pisolite	Tumbiana Pisolite
Middle Volcanic Unit	Kylena Basalt		Kylena Volcanics	Kylena Basalt	Boongal Pillow Lava Member	Kylena Basalt Mbr.	Little De Grey Lava	Little De Grey Lava Coongan Volcanics
Lower Sedimentary Unit	Hardey Sandstone	Sandstone south of Mount Ada	Cliff Springs Frm. Lyre Creek Agglomerate Mbr.	Cliff Springs Frm. Lyre Creek Agglomerate Mbr.	Hardey Sandstone		Beatons Creek Congl.	Green Hole Congl.; lwr Coongan volc.; Glen Herring Shale; Beatons Creek Congl.
Lower Volcanic Unit	Mount Roe Basalt	Mount Roe Basalt	Mount Roe Basalt	Mount Roe Basalt				

*Frm. = formation; Mbr. = member, Congl. = Conglomerate

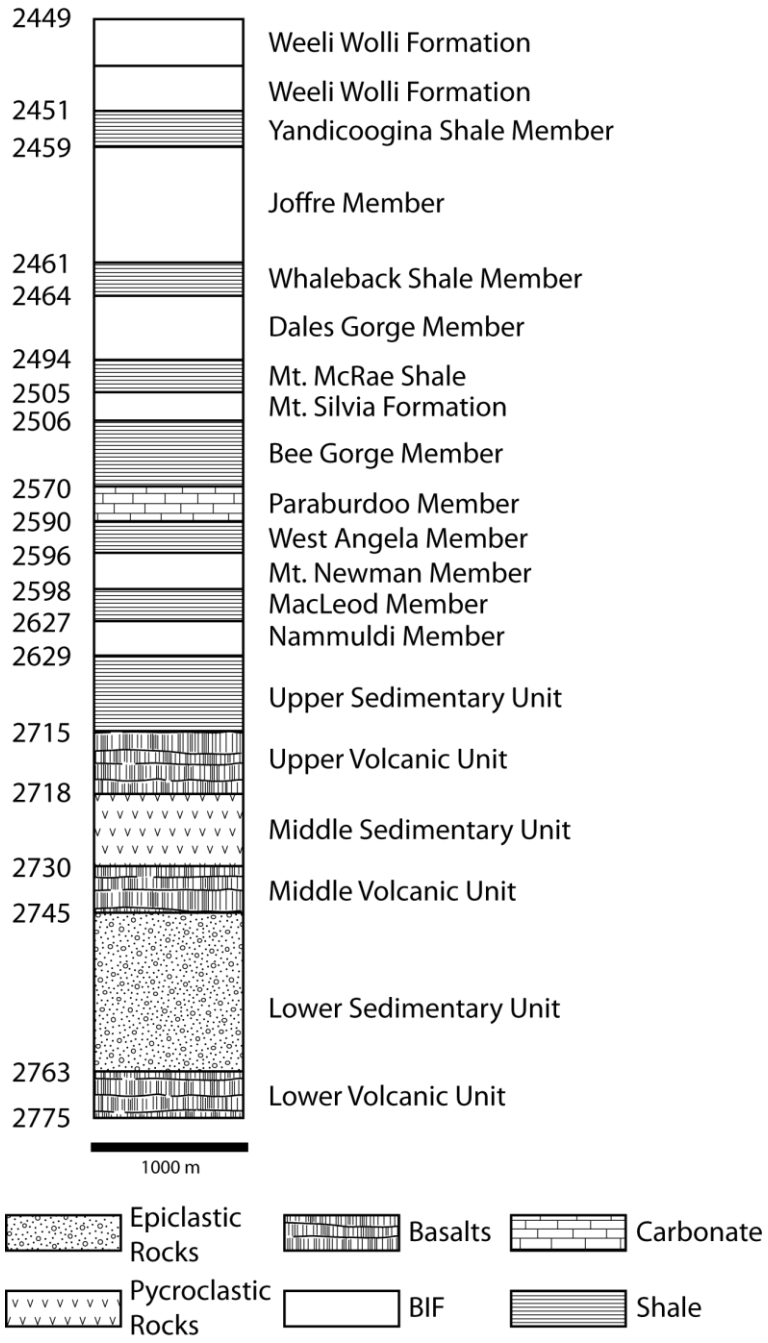

Figure A7.2: Stratigraphic column for the Fortescue and Hamersley Groups after Trendall et al. (2004).

The Hardey Formation (Lower Sedimentary Unit) is then overlain by the Kylena Formation (Middle Volcanic unit), which is composed predominantly of massive dark green to dark grey amygdaloidal and vesicular basalt without distinctive features (Trendall, 1990b). The presence of pillows and columnar joints can be observed locally while pisolitic tuff, agglomerate and sediments occur between the individual flows (Trendall, 1990b). Usually the different flows are less than 4 m thick and the tops can be identified by the presence of vesicles while the bases are much coarser grained (Hickman, 1983). The thickest the Kylena Formation (Middle Volcanic unit) reaches is 2400 m (Kriewaldt, 1964b), though it is more commonly 200 m thick. In most areas the unit directly overlies the Hardey Formation (Lower Sedimentary Unit); however at Roy Hill and Balfour Downs it directly overlies the granite-greenstone terranes of the Pilbura Craton (Trendall, 1990b). The Kylena Formation (Middle Volcanic unit) has been dated to approximately 2741 Ma (Blake et al., 2000) and is capped by the predominantly pyroclastic dominated rocks of the Tumbiana Formation (Middle Sedimentary Unit).

The Tumbiana Formation (Middle Sedimentary Unit) contains distinctive accretionary lapilli tuff (Trendall, 1965). The lapilli are ellipsoidal and tend to be flattened sub-parallel to bedding. Usually the lapilli are 2 to 10 mm in diameter, but they can be as large as 40 mm or as small as 0.5 mm (Trendall, 1965). The unit was probably composed predominantly of fine grained pyroclastic material; however this has been subsequently altered to a largely chlorite cryptocrystalline aggregate (Trendall, 1990b). It has been dated to 2715±6 Ma (Arndt et al., 1991) and 2710±6 Ma (Nelson, 2001). The most distinctive characteristics of this unit are the up to 10 cm thick beds of closely packed, clast-supported lapilli which often have secondary carbonate rich matrix (Trendall, 1990b). However the abundance of these layers varies significantly and in some places lapilli are only found rarely scattered within a largely tuffaceous rock. The Tumbiana Formation (Middle Sedimentary Unit) also contains minor agglomerate, thin basaltic flows, sandstone, siltstone and carbonate rocks that are sometimes stromatolitic (Trendall, 1990b).

The Maddina Formation (Upper Volcanic Unit) directly overlies the Tumbiana Formation (Middle Sedimentary Unit). It is composed predominantly of dark green, massive basalt flows which have flow tops that contain significant amygdaloids (Trendall, 1990b). Unlike the flows from the lower and middle volcanic units, the flows from the Maddina Formation (Upper Volcanic Unit) are relatively thick, varying between 30 and 50 m. Lesser amounts of felsic rocks, tuff and lava are intercalated with the basalt flows (Trendall, 1990b). Maddina Formation (Upper Volcanic Unit) is dated to 2717±2 Ma (Nelson, 1998) and in most areas the is 500-600 m thick. However, it has been described as being as thick as 4100 m in some places (Tyler, 1986).

The top unit of the Fortescue Group is the Jeerinah Formation (Upper Sedimentary Unit). The Jeerinah Formation has been dated from 2629±5 Ma (Trendall et al., 2004) to 2684±6 Ma and 2690±16 Ma (Arndt, 1991). Subsequently it has been subdivided into the Woodiana Sandstone, the Warrie Member and the Roy Hill Shale Member (MacLeod and de la Hunty, 1966). The Woodiana Sandstone is composed of well sorted quartz sandstone with minor siltstone and arkose. It is the only sedimentary unit interpreted to be of terrigenous origin from the Jeerinah Formation (Upper Sedimentary Unit) to the top of the overlying Hamersley group. It is up to 60 m thick on Roy Hill and continues to outcrop to the west. It is patchy to the north and east but absent south of the South Hamersley Inlier (Trendall, 1990b). The Warrie Member overlies the Woodiana Sandstone and is often difficult to distinguish from

the overlying Roy Hill Member. It is made up of thinly bedded shale, chert and dolomite, with the dolomite typically defining the upper part of the sequence. The thickness of the unit is variable, ranging between 80 m and 300 m. The Roy Hill Member forms the top of the Jeerinah Formation (Upper Sedimentary Unit) and is composed of black shale with high organic carbon content, up to 17% in some samples (Trendall, 1990b). The presence of 1-3 cm wide pyrite concretions is common. White weathering is common in the black shale dominanted Roy Hill Member. In some areas basalts are found to be intercalated with the sedimentary rocks of the Jeerinah Formation (Upper Sedimentary Unit) (Trendall, 1990b).

Several igneous bodies are known to intrude the volcanic and sedimentary units of the Fortescue Group. The dark green to dark purple to black Gidley Granophyre intrudes the unconformable contact between the underlying granite greenstone terrane and the Fortescue Group near the Dampier Archipelago (Trendall, 1990b). This unit is predominantly composed of finely intergrown quartz and alkali feldspar (Trendall, 1990b). Near Pyramid, Roebourne and Yarraloola the extensive Cooya Dolerite intrudes the contact between the Lower Sedimentary Unit and the Middle Volcanic Unit (Kriewaldt and Ryan, 1967). In the eastern part of the basin the Middle Sedimentary Unit is commonly intruded by a series of dacite porphyries. However the mode of emplacement is still a matter of debate as some evidence of extrusion has been documented in some localities (Trendall, 1990b). Zircon dating of the porphyries has yielded emplacement ages of 2768±10 Ma (Pidgeon, 1984). A series of small hornblende and adamellite stocks and related horneblende porphyry dykes cut the Fortescue Group from the Bamboo Creek area to a location approximately 150 km to the south. Finally the Upper Sedimentary Unit is commonly intruded by a series of dolerite sills.

A7.2 Hamersley Group

The Hamersley Group overlies the Fortescue Group and is made up of a series of banded iron formations (BIFs) that are periodically interrupted by shale or carbonate units (Trendall, 1990b). In the south and west parts of the basin, the shales and BIFs represent a continuation of the transgression that was apparent during the deposition of the Jeerinah Formation (Hickman and Van Kranendonk, 2012). However this is not present in the east where the Hamersley Group appears to have been deposited in shallow water (Hickman and Van Kranendonk, 2012). The dark grey to black shale units are typically finely laminated and interbedded with chert and/or carbonate (Trendall, 1990b). Generally the BIFs are hard, fine

grained and obviously banded, with bands generally between 5-15 mm thick but occasionally ranging up to 100 mm. They are made up of 80% interbands of chert and chert with a matrix of fine grained iron rich minerals. The remaining 20% is generally composed of monomineralic bands of magnetite, carbonate, stilpnomelane or riebeckite (Trendall, 1990b).

The basal sequence is the Marra Mamba Iron Formation. It is made up of the Nammuldi Member BIF at the base and Mt. Newman Member BIF at the top, with the two BIFs separated by the shales of the MacLeod Member. The BIFs occur in two different types: shaly BIF and massive BIF with macrobands of shale and carbonate (Trendall, 1983; Blockley, 1979; Ewers and Morris, 1980). Chert bands are generally thick and widely spaced while development of chert pods is common and particularly abundant in the lower part of the sequence. The outcrop expression of the Marra Mamba Iron Formation is as dark grey/brown low sinuous ridges covered with debris composed of chert pods (Trendall, 1983; Blockley, 1979; Ewers and Morris, 1980). The Mt. Newman Member has been dated by Trendall et al. (1998) to 2597±5 Ma. The Carawine Dolomite overlies Marra Mamba Iron Formation. It is composed of a series of dolomite and limestone layers with minor interbeds of chert, argillite and tuff (Trendall, 1990b).

The Carawine Dolomite is overlain by the mixed minor BIFs and shale units of the Mount Silvia Formation. The top of the Mount Silvia Formation is particularly shale rich and in places has been subdivided into the Bee Gorge Member (dated to 2561±8 Ma (Trendall et al., 1998) and 2565±9 Ma (Trendall et al., 2004)) and the upper most Mt McRae Shale. These upper shale intervals are carbonaceous and locally the Mt McRae Shale contains abundant pyrite nodules. The Mt McRae shale is overlain by the Brockman Iron Formation, which is subdivided into the Dales Gorge Member BIF, the Whaleback Shale Member, the Joffre Member BIF and the Yandicoogina Shale Member (Trendall, 1990b). The Dales Gorge member contains abundant, regularly spaced, chert interbeds that make up 25% of the thickness of the unit. The chert layers are thin and closely spaced compared to other BIFs in the Hamersley Group and podding is common in white chert intervals (Trendall, 1983; Trendall and Pepper, 1977; Compston et al., 1981; Ewers and Morris, 1981). The Dales Gorge Member has dates that range from 2495±16 Ma towards its base to 2461±6 Ma at the top of the interval (Trendall et al., 2004). Upon cessation of BIF deposition the shales of the Whaleback Shale Member (2463 +/-5 Ma (Trendall et al., 2004)) were deposited. After resumption of BIF deposition the Joffre Member was deposited. The Joffre Member contains

thin closely spaced shale interbeds while chert layers are relatively thick and widely spaced. Development of chert pods is common in both red and white chert layers (Trendall and de Laeter, 1972; Trendall, 1983). The Joffre Member has been dated between 2454±3 Ma and 2465±6 Ma; however the majority of the dates are from 2459±3 to 2461±5 Ma (Trendall et al., 2004; Nelson, 2001). Shale is again deposited after the cessation of BIF deposition forming the Yandicoogina Shale Member (Trendall, 1990b).

The Brockman Iron Formation is overlain by the BIFs and thickly intercalated shales of the Weeli Wolli Formation. It is dated from 2449±3 Ma to 2445±5 Ma (Trendall et al., 2004; Barley et al., 1997). Chert mesobands are present in some areas of the Weeli Wolli Formation as relatively thin and widely spaced bands but absent in other parts of the section and the occurrence of cross-pods is common at some levels (Trendall, 1990b; Trendell, 1983). The BIFs of the Boolgeeda Iron Formation overlie the Weeli Wolli Formation. They are identified by the general lack of chert mesobands and uncommon presence of pods. It is expressed in outcrop as black, dark grey or greenish dark grey scree covered ridges (Trendall, 1990b; Trendal, 1983).

Intrusive rocks form up to 40% of the thickness of the Hamersley Group. These are predominantly dolerite sills and sheets of dacite and/or rhyolite that for the Woongarra Volcanics (Trendall, 1990b). The dolorite sills are most common in the Weeli Wolli Formation. The Woongarra Volcanics occur between the Boolgeeda Iron Formation and the Weeli Wolli Formation (Trendall, 1990b) and have been dated to 2470±30 Ma by Compston et al. (1981) using zircon geochronology.

A7.3 Turee Creek Group

The Turree Creek Group conformably overlies the Boolgeeda Iron Formation of the Hamersley Group. The basal sequence is made up of thinly bedded greyish green siltstone that is interbedded with fine grained greywacke and fine grained sandstone higher in the sequence (Trendall, 1990b). Thin carbonate beds occur near the top of the group. The Turree Creek Group is overlain by a series of well sorted white to grey quartzites with minor carbonate and shale units (Trendall, 1990b). The group is commonly intruded by dolerite sills that can form a significant percentage of the total thickness of the group in some areas (Trendall, 1990b).

A7.4 References

Arndt N. T., Nelson D.R., Compston W., Trendall A.F., and Thorne A.M. (1991) The age of the Fortescue Group, Hamersley Basin, Western Australia, from ion microprobe results. Australian Journal of Earth Sciences, 38, 261-281.

Blake T. S. (1984) The lower Fortescue Group of the northern Pilbara Craton – stratigraphy and paleogeography, in Archean and Proterozoic Basins of the Pilbara, Western Australia – Evolution and Mineralization Potential edited by J.R.Muhling, D.I Groves and T.S. Blake: University of Western Australia, Geology Department and University Extension, Publication, no. 9, 123-143.

Blight, D.F. (1985) Economic potential of the lower Fortescue Group and adjacent units in the southern Hamersley Basin: Western Australia Geological Survey, Report 13.

Blockley J.G. (1979) A contribution to the stratigraphy of the Marra Mamba Iron Formation: Western Australia Geological Survey, Annual Report 1978, 71-73.

Compston, W., Williams, I.S., McCulloch, M.T., Foster, J.J., Arriens, P.A., and Trendall, A.F. (1981) A revised age for the Hamersley Group, in Sediments through the ages edited by D.I. Groves and others: Geological Society of Australia, Annual Convention, 5th , Perth W.A., 1981, Abstracts; Abstracts Series, no. 3, 40.

De la Hunty, L.E. (1965) Mount Bruce, W.A.: Western Australia Geological Survey, 1:250,000 Geological Series Explanatory Notes.

Ewers, W.E. and Morris, R.C. (1980) Chemical and mineralogical data from the uppermost section of the upper BIF member of the Marra Mamba Iron Formation. CSIRO Report FP23

Ewers, W.E. and Morris, R.C. (1981) Studies of the Dales Gorge Member of the Brockman Iron Formation, Western Australia. Economic Geology 76, 1929-1953.

Hall, C.E. (2002) Sedimentary, geochemistry and paleogeography of the lower Fortescue Group, Hamersley Province, Western Australia. PhD thesis, University of Western Australia, Perth (unpublished).

Hickman, A.H. (1983) Geology of the Pilbara Block and its environs: Western Australia Geological Survey, Bulletin 127, 268.

Hickman, A. H., and Van Kranendonk, M. J. (2012) Early Earth evolution: evidence from the 3.5-1.8 Ga geological history of the Pilbara region of Western Australia: Episodes, 35(1), 283.

Kriewaldt, M. (1964a) The Fortescue Group of the Roebourne region, North-West Division: Western Australia Geological Survey, Annual Report 1963, 30-34.

Kriewaldt, M. (1964b) Dampier and Barrow Island W.A.: Western Australia Geological Survey, 1:250,000 Geological Series Explanatory Notes.

Kriewaldt, M. and Ryan G.R. (1967) Pyramid W.A.: Western Australia Geological Survey, 1:250,000 Geological Series Explanatory Notes.

MacLeod, W.N. and de la Hunty, L.E. (1966) Roy Hill, W.A.: Western Australia Geological Survey, 1:250,000 Geological Series Explanatory Notes.

Nelson, D.R. (1996) Compilation of SHRIMP U-Pb zircon geochronology data 1995. Geological Survey of Western Australia Record 1996/5.

Nelson, D.R. (1998) Compilation of SHRIMP U-Pb zircon geochronology data 1997. Geological Survey of Western Australia Record 1998/2.

Nelson, D.R. (2001) Compilation of geochronology data 2000. Geological Survey of Western Australia Record 2001/2.

Nelson, D.R. (2002) Compilation of geochronology data 2001. Geological Survey of Western Australia Record 2002/2.

Pidgeon, R.T. (1984) Geochronological constraints on early volcanic evolution of the Pilbara Block, Western Australia. Australian Journal of Earth Science, 15, 971-974.

Thorne, A.M. and Trendall, A.F. (2001) Geology of the Fortescue Group, Pilbara Craton, Western Australia. Geological Survey of Western Australia Bulletin 144.

Trendall, A. (1990a) Geology and mineral resources of Western Australia. State Print. Division.

Trendall, A. (1990b) Hamersley Basin. in Geology and mineral resources of Western Australia: Western Australia Geological Survey, Memoir 3, p. 77-119.

Trendall, A. (1990c) Pilbura Craton Introduction. in Geology and mineral resources of Western Australia: Western Australia Geological Survey, Memoir 3, p. 77-119.

Trendall, A.F. and De Laeter, J.R. (1972) Apparent age, and origin, of black porcelanite of the Joffre Member, Geological Survey of Western Australia Annual Report for 1971, 68-74.

Trendall, A.F. and Pepper,R.S. (1977) Chemical composition of the Brockman Iron Formation: Western Australia Geological Survey, Record 1976/25.

Trendall A.F. (1965) Pisolithic tuffs in Western Australia: Geological Survey of Western Australia Annual Report for 1964, 51-55.

Trendall, A., Compston, W., Nelson, D., De Laeter, J., and Bennett, V. (2004) SHRIMP zircon ages constraining the depositional chronology of the Hamersley Group, Western Australia*. Australian Journal of Earth Sciences, 51(5), 621-644.

Trendall, A., Nelson, D., De Laeter, J., and Hassler, S. (1998) Precise zircon U-Pb ages from the Marra Mamba Iron Formation and Wittenoom Formation, Hamersley Group, Western Australia. Australian Journal of Earth Sciences, 45(1), 137-142.

Trendall A.F. (1983) The Hamersley Basin, in Iron-Formation – Facts and Problems edited by A.F. Trendall and R.C. Morris: Amsterdam, Elsevier, 69-129.

Tyler, I.M. (1986) Age and Stratigraphy of a sequence of metavolcanic and metasedimentary rocks in the Praire Downs – Deadman Hill area, southwestern margin of the Sylvania Dome: Western Australia Geological Survey, Report 19, Professional Papers for 1984, 83-87.

Williams I.R. (1989) Balfour Downs, W.A. (2nd edition): Western Australia Geological Survey, 1:250,000 Geological Series Explanatory Notes.

Appendix 8:

Simplified drill logs for Core analysed in Chapter 5

A8.1: Drill Log for DD86WRL1

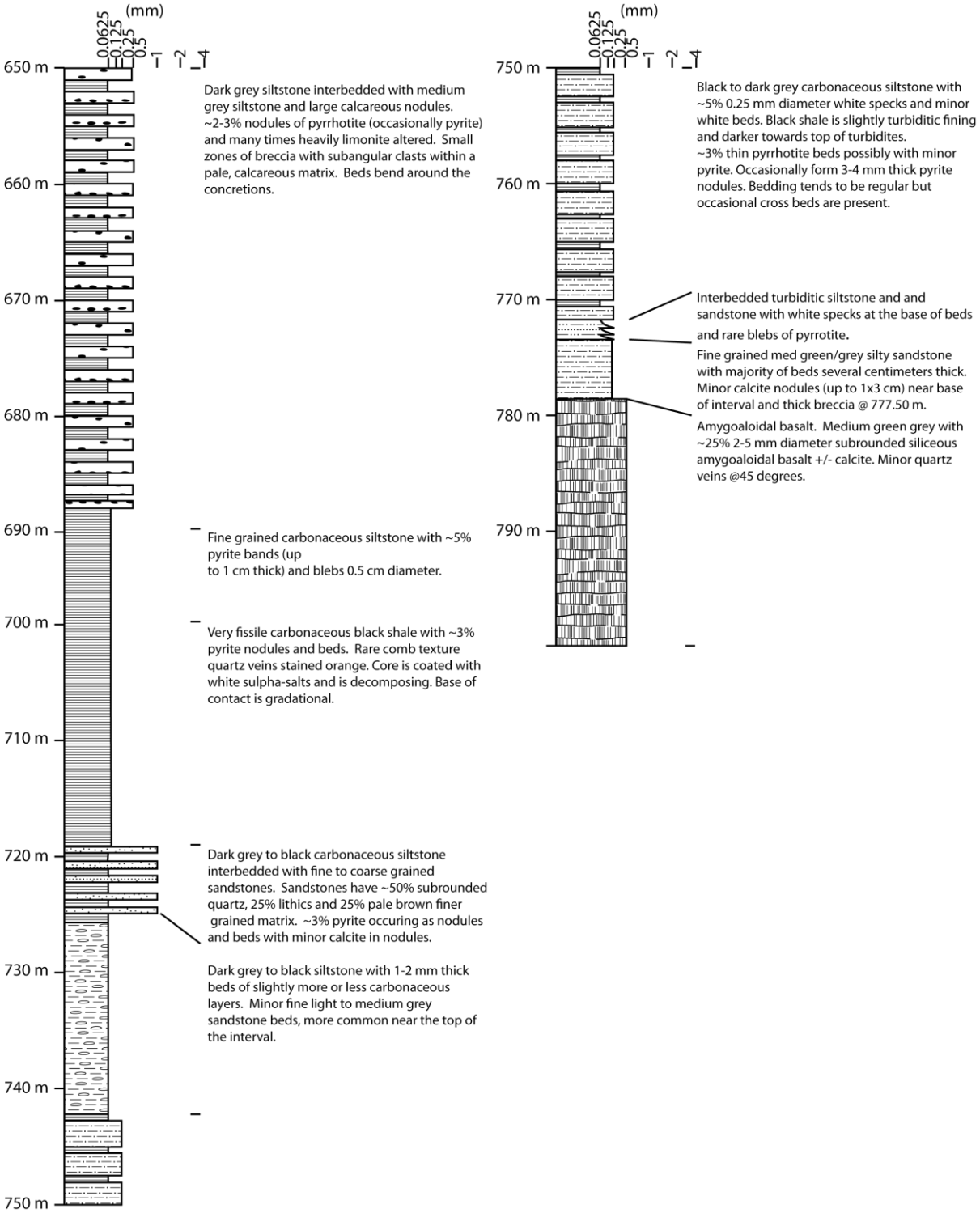

A8.2: Drill Log for ABDP9-1

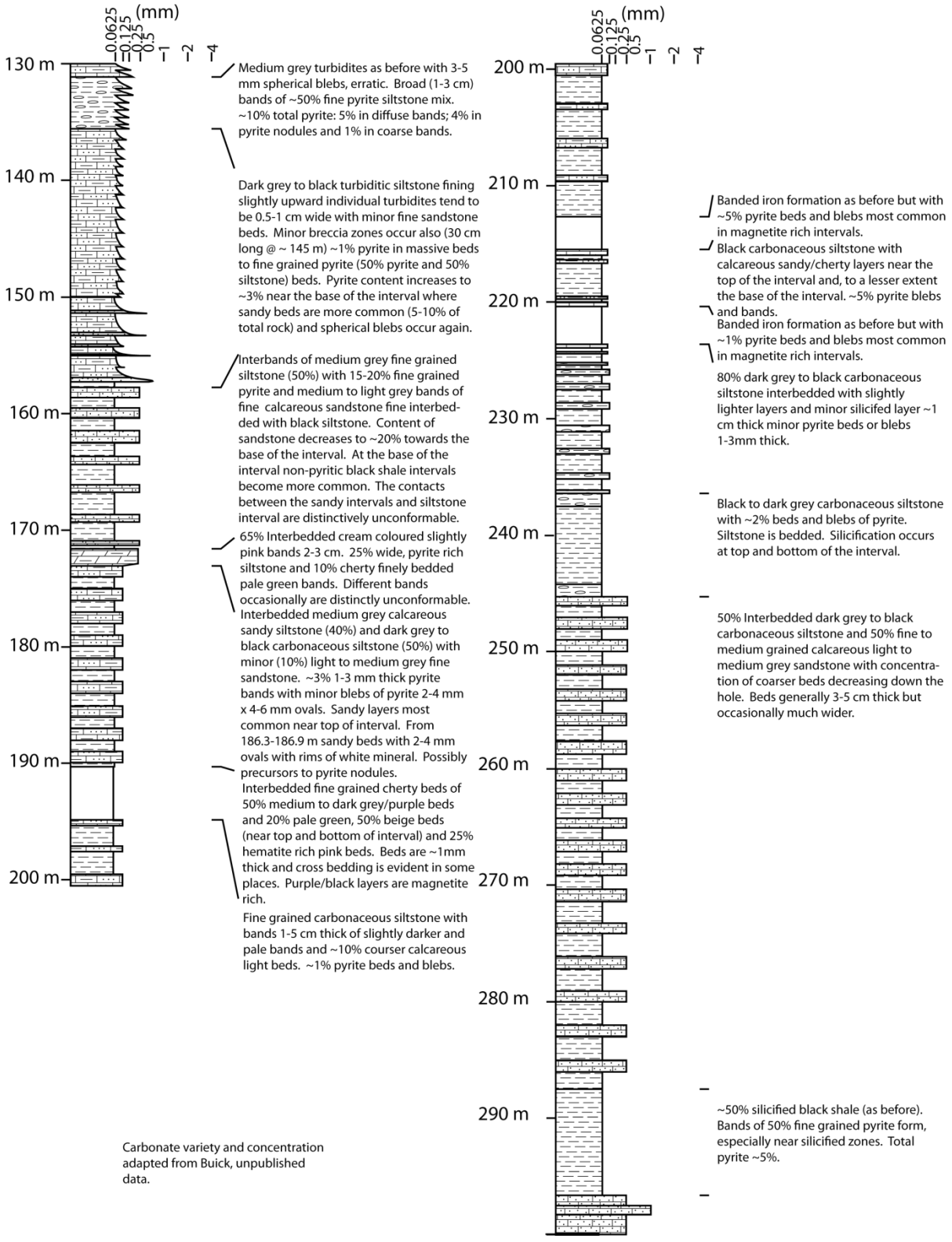

A8.2: Drill Log for ABDP9-2

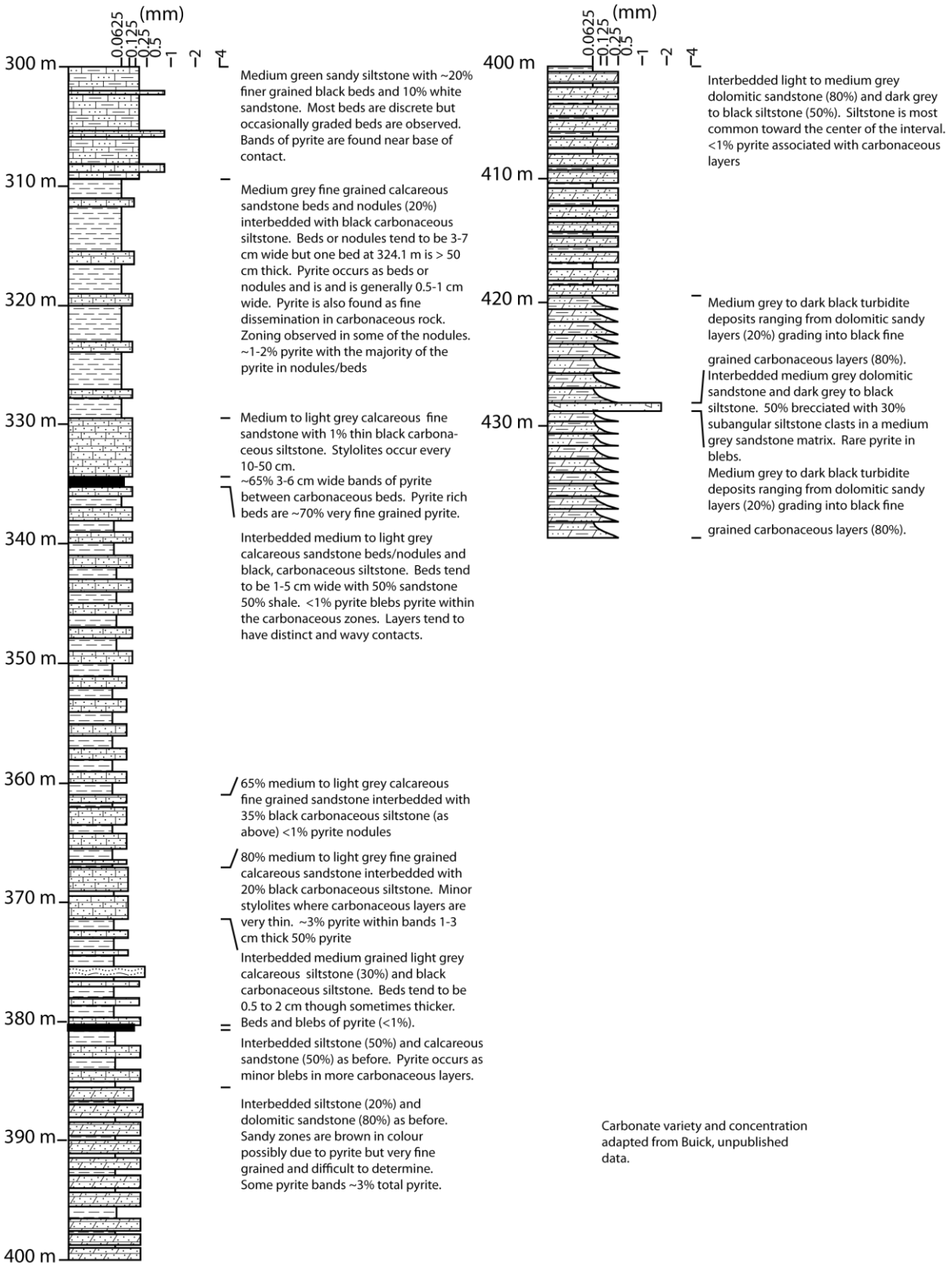

Appendix 9:

Methodology of Whole Rock Sampling

A9.1 Reasons for the size of whole rock samples

Samples for whole rock analysis were taken from 10-26 cm long sections of core near where pyrite was sampled for LA-ICPMS and SHRIMP-SI analysis. Most other studies (Anbar et al., 2007; Kaufman et al., 2007; Raiswell et al., 2011; Reinhard et al., 2009) of these units have utilized small (1-5 cm) sample intervals to more closely examine stratigraphic changes in the core. However, such a close examination of stratigraphic changes was not possible in this study for several reasons. First, authors, such as Anbar et al. (2007), were able to avoid pyritic band and nodules in their study, which also avoided anomalously high amounts of several elements that are found in pyrite. In this study the trace elements in pyrite were the focus so it was inappropriate to avoid the pyrite when sampling for whole rock analysis. Second, studies by Kakegawa et al. (1998) have shown that sulphides can be remobilised up to several centimetres to form pyrite nodules. This may also remobilise trace elements that are held in the original pyrite, organic matter and/or other minerals and incorporate them into the nodule. Therefore, to get an accurate trace element composition for the shale at the time of deposition the nodule and the sediment above and below it that has had sulphur and trace elements remobilised must be analysed. Without doing high resolution sulphur isotope studies such as those done by Kakegawa et al. (1998) it is difficult to determine the extent of the remobilisation of S and trace elements. Unfortunately due to the large number of samples these sorts of analyses were cost prohibitive. Similarly, a series of 1-2 cm long samples over the interval thought to contain the pyrite that was remobilised to form the nodules/bands would have been preferable but again due to the number of samples and number of techniques implemented it would have been cost prohibitive. Instead we selected a section of core (10-26 cm long) that was representative of the lithology observed in the core and analysed a large enough section to get and average trace element content over a period of deposition proximal to nodule formation. Examples of the core analysed are given below.

ABDP9 292.74-292.90 m

7 cm

Figure A9.1: Core sample ABDP9 taken from 292.74-292.90 m.

Core sample ABDP9 (292.74-292.90 m) shows the interlayering of finer grained, carbonaceous layers and coarser grained, less carbon rich layers (Figure A9.1). Pyrite is concentrated near the contacts of the sandy layers and the carbonaceous layers in varying abundance. Because of the alternating thicknesses of the layers in the interval a slightly longer interval was used to achieve an average sediment content representative of the interval.

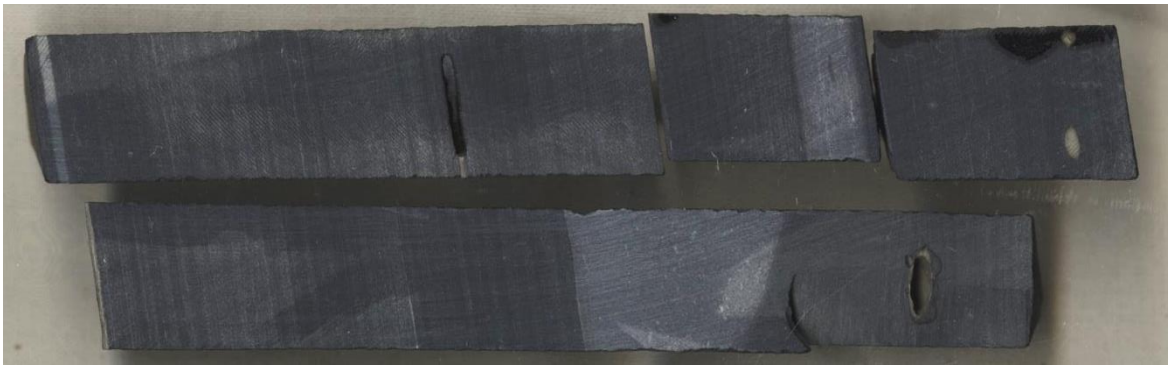

ABDP9 366.61-366.87 m

7 cm

Figure A9.2: Core sample from ABDP9 taken from 366.61-366.87 m.

Core sample ABDP9 (366.61-366.87 m) contains very fine interbeds of darker, more carbonaceous and lighter, less carbonaceous shale (Figure A9.3). This interval also contains pyrite nodules and bands (this scan shows some of these, though most are drilled out for S isotope analysis). Carbonate nodules are also present across these intervals (thick, lighter coloured bands). To achieve a section that has proportions of all these components representative of the stratigraphic section the relatively long section pictured here was taken.

Figure A9.3: Core sample from ABDP9 taken from 427.48-427.64 m.

Core sample ABDP9 (427.48-427.64 m) is 16 cm long because this interval is dominated by the lighter grey, coarser, organic poor successions, with only minor fine grained, black, carbonaceous layers associated with pyrite (Figure A9.3). Shorter intervals would have contained a higher proportion of the carbonaceous layers that is not representative of the entire unit.

Figure A9.4: Core sample from DD86WRL1 taken from 681.20-681.38 m.

Core sample DD86WRL1 (681.20-681.38 m) contains predominantly organic rich black shale with pyrite nodules and blebs. The difficulty in sampling arises in which low pyrite layers are representative of sections depleted during the formation of the nodules. To avoid this problem we sampled a large enough interval so that an average composition of a number of these nodules/bands and depleted layers is obtained.

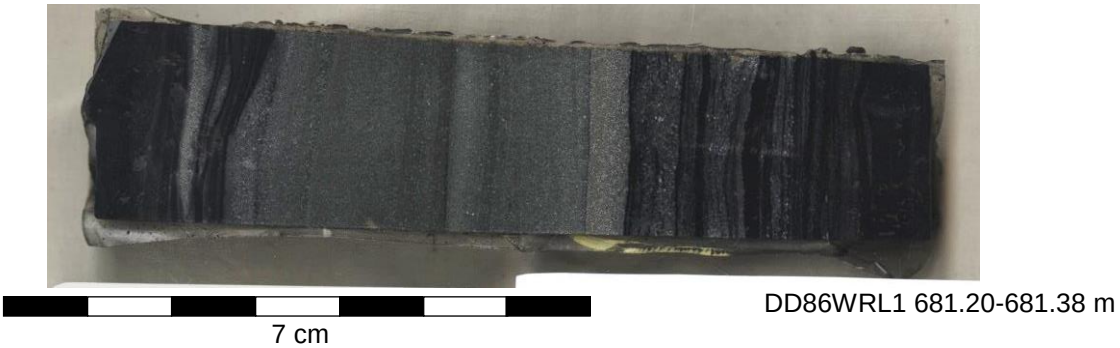

Figure A9.5: Core sample from DD86WRL1 681.20-681.38 m.

Core sample DD86WRL1 (681.20-681.38 m) shows a wide difference in composition with variable amounts of very fine grained carbonaceous beds and coarse grained light grey beds. Again, pyrite is associated with the carbonaceous beds and a long sample interval was needed to obtain a sample representative of the stratigraphy.

A9.2 References

Anbar, A. D., Duan, Y., Lyons, T. W., Arnold, G. L., Kendall, B., Creaser, R. A., Kaufman, A. J., Gordon, G. W., Scott, C., and Garvin, J., 2007, A whiff of oxygen before the great oxidation event?: Science, v. 317, no. 5846, p. 1903-1906.

Kakegawa, T., Kawai, H., and Ohmoto, H., 1998, Origins of pyrites in the~ 2.5 Ga Mt. McRae Shale, the Hamersley District, Western Australia: Geochimica et Cosmochimica Acta, v. 62, no. 19, p. 3205-3220.

Kaufman, A. J., Johnston, D. T., Farquhar, J., Masterson, A. L., Lyons, T. W., Bates, S., Anbar, A. D., Arnold, G. L., Garvin, J., and Buick, R., 2007, Late Archean biospheric oxygenation and atmospheric evolution: Science, v. 317, no. 5846, p. 1900-1903.

Raiswell, R., Reinhard, C. T., Derkowski, A., Owens, J., Bottrell, S. H., Anbar, A. D., and Lyons, T. W., 2011, Formation of syngenetic and early diagenetic iron minerals in the late Archean Mt. McRae Shale, Hamersley Basin, Australia: New insights on the patterns, controls and paleoenvironmental implications of authigenic mineral formation: Geochimica et Cosmochimica Acta, v. 75, no. 4, p. 1072-1087.

Reinhard, C. T., Raiswell, R., Scott, C., Anbar, A. D., and Lyons, T. W., 2009, A late Archean sulfidic sea stimulated by early oxidative weathering of the continents: Science, v. 326, no. 5953, p. 713-716.

Appendix 10:

Geochemical data presented in Chapter 5

Table A10.1: Bulk Sample ICPMS analyses of samples from DDH86WRL1											
SAMPLE#	Top sample interval (m)	Bottom sample interval (m)	**Li ppm**	**Be ppm**	**Sc ppm**	**V ppm**	**Co ppm**	**Ni ppm**	**Cu ppm**	**Cu ppm**	**Zn ppm**
DL			**0.040**	**0.026**	**0.009**	**0.037**	**0.003**	**0.011**	**0.013**	**0.014**	**0.334**
DG37	746.66	746.81	28.04	2.71	27.64	187.11	69.66	329.34	157.37	158.55	87.48
DG38	729.72	729.91	27.81	2.00	24.09	177.03	36.57	184.03	100.03	101.53	236.22
DG38b	729.72	729.91	26.92	1.85	23.10	170.92	36.71	192.47	98.94	101.16	226.12
DG39	719.87	720.09	15.24	1.66	23.26	176.26	27.03	146.89	55.23	54.89	149.25
DG40	707.37	707.55	16.61	1.58	16.24	93.49	68.41	507.33	196.10	202.57	531.78
DG41	688.00	688.18	18.28	0.19	6.37	54.02	17.21	37.39	123.48	125.66	1337.95
DG42	681.20	681.38	27.19	1.75	20.71	135.50	52.81	500.18	304.00	312.18	1251.55
DG43	651.80	651.95	22.41	2.15	12.45	100.90	29.38	105.68	44.71	44.85	110.39
DG43b	651.80	651.95	22.79	2.09	13.28	89.68	40.19	123.62	78.90	78.30	117.71
DG44	602.78	603.03	19.78	1.37	11.59	66.95	12.04	539.25	122.66	124.23	123.70
DG45	572.26	572.50	5.29	0.41	0.58	2.28	1.19	258.23	3.17	3.28	5.84
DG46	524.68	524.95	5.08	0.28	0.42	3.19	1.22	422.06	2.04	2.31	4.54
DG47	742.92	743.18	20.51	2.56	20.67	143.49	6.13	170.45	13.66	13.97	45.16
DG48	576.65	576.79	3.81	0.43	0.56	2.90	1.46	387.40	5.29	5.45	6.01
DG49	545.18	545.32	74.31	0.30	1.49	11.77	2.86	125.89	0.98	1.45	18.99

Table A10.1: Bulk Sample ICPMS analyses of samples from DDH86WRL1											
SAMPLE#	**Ga ppm**	**Rb ppm**	**Sr ppm**	**Y ppm**	**Cs ppm**	**La ppm**	**Ce ppm**	**Pr ppm**	**Nd ppm**	**Sm ppm**	**Eu ppm**
DL	**0.003**	**0.016**	**0.008**	**0.003**	**0.002**	**0.003**	**0.004**	**0.002**	**0.004**	**0.003**	**0.002**
DG37	22.62	262.53	8.96	41.88	9.98	59.77	119.67	14.18	53.16	10.79	1.56
DG38	19.13	143.93	34.23	18.30	9.23	16.44	32.33	3.90	15.02	3.25	0.86
DG38b	18.80	139.39	33.46	17.97	9.08	16.37	32.15	3.86	14.94	3.20	0.84
DG39	18.40	166.24	133.90	27.60	7.88	13.14	28.34	3.70	15.72	4.07	1.18
DG40	20.30	171.99	101.43	20.88	12.06	25.35	52.62	6.17	22.61	4.67	1.67
DG41	9.44	1.33	139.92	7.20	3.40	1.63	3.42	0.46	2.16	0.68	0.63
DG42	21.49	160.65	27.87	43.66	6.77	46.13	87.15	10.46	40.29	8.24	1.96
DG43	15.30	18.40	34.55	15.78	30.60	21.35	40.00	4.67	17.49	3.37	0.86
DG43b	13.38	24.97	33.03	13.96	40.58	18.40	34.78	4.06	15.20	2.92	0.75
DG44	11.90	0.44	48.43	19.20	0.26	17.48	35.42	4.26	16.36	3.46	0.77
DG45	0.40	9.01	15.96	2.73	0.98	0.93	1.81	0.21	0.84	0.18	0.06
DG46	0.41	14.51	14.17	2.94	3.09	1.07	1.67	0.19	0.79	0.16	0.06
DG47	22.41	265.93	4.57	21.12	8.48	3.58	7.65	1.00	4.51	1.44	0.48
DG48	0.38	5.77	10.02	3.27	0.51	0.74	1.25	0.16	0.65	0.15	0.07
DG49	1.56	106.35	55.22	9.75	12.95	6.33	10.17	1.20	5.02	1.02	0.41

Table A10.1: Bulk Sample ICPMS analyses of samples from DDH86WRL1

SAMPLE#	Gd ppm	Tb ppm	Dy ppm	Ho ppm	Er ppm	Tm ppm	Yb ppm	Lu ppm	W ppm	Tl ppm	Pb ppm
DL	**0.002**	**0.002**	**0.002**	**0.002**	**0.002**	**0.002**	**0.002**	**0.002**	**0.014**	**0.005**	**0.015**
DG37	9.05	1.47	8.43	1.58	4.32	0.59	3.42	0.46	1.08	1.65	22.49
DG38	3.12	0.53	3.19	0.66	2.07	0.32	2.10	0.32	2.49	3.23	47.32
DG38b	3.04	0.51	3.11	0.64	2.01	0.31	2.05	0.32	2.48	3.17	48.40
DG39	4.45	0.80	4.90	0.99	3.05	0.46	2.93	0.45	0.72	2.10	16.48
DG40	4.27	0.66	3.78	0.75	2.32	0.35	2.32	0.37	1.41	4.30	95.16
DG41	0.89	0.15	0.98	0.22	0.76	0.12	0.87	0.15	1.18	0.10	15.85
DG42	7.24	1.15	6.86	1.39	4.15	0.59	3.60	0.54	2.44	3.69	73.12
DG43	2.86	0.45	2.71	0.57	1.80	0.28	1.91	0.31	1.43	0.65	35.80
DG43b	2.48	0.39	2.38	0.49	1.59	0.25	1.71	0.28	1.22	0.69	59.07
DG44	3.23	0.56	3.50	0.72	2.23	0.34	2.32	0.36	1.87	0.13	37.55
DG45	0.20	0.03	0.24	0.06	0.21	0.04	0.27	0.05	0.33	0.05	1.60
DG46	0.19	0.03	0.21	0.05	0.18	0.03	0.18	0.03	0.48	0.05	0.52
DG47	2.22	0.47	3.36	0.78	2.66	0.42	2.85	0.45	1.81	1.50	12.40
DG48	0.21	0.04	0.25	0.07	0.23	0.04	0.24	0.05	0.39	0.03	0.84
DG49	1.10	0.17	0.98	0.21	0.62	0.09	0.52	0.09	0.16	0.42	1.24

Table A10.1: Bulk Sample ICPMS analyses of samples from DDH86WRL1

SAMPLE#	Th ppm	U ppm	Ti ppm	Cr ppm	Mn ppm	As ppm	Zr ppm	Nb ppm	Mo ppm	Ag ppm	Cd ppm
DL	**0.002**	**0.001**									
DG37	10.71	2.65	5340.74	257.07	412.27	22.62	171.20	11.99	2.19	0.17	0.51
DG38	5.27	1.95	6230.40	219.89	1327.87	13.75	123.16	8.79	4.02	0.18	0.84
DG38b	5.23	1.88	5910.45	217.17	1297.00	13.26	124.99	8.50	4.05	0.18	0.85
DG39	6.30	1.69	4784.72	137.20	2840.33	4.23	132.60	6.86	1.71	0.12	0.42
DG40	9.41	2.52	3478.86	195.62	1630.01	62.24	171.10	10.05	3.91	0.63	1.61
DG41	5.01	1.29	1690.10	172.79	3330.12	<DL	69.98	4.86	3.26	0.20	4.49
DG42	9.08	3.11	6724.28	296.92	363.74	17.24	192.13	16.92	5.39	0.55	3.69
DG43	8.50	2.37	3036.74	131.36	450.27	9.79	103.10	7.40	2.12	0.14	0.39
DG43b	6.12	1.99	2635.84	115.24	490.49	9.62	93.54	6.79	1.85	0.17	0.64
DG44	9.24	2.67	1802.32	213.39	1081.08	12.28	108.49	6.14	2.26	0.15	0.35
DG45	0.47	0.12	75.47	71.96	709.27	<DL	4.56	0.39	0.37	<DL	<DL
DG46	0.22	0.07	71.03	117.22	1363.81	<DL	1.99	0.27	0.50	<DL	<DL
DG47	11.54	2.98	3665.80	190.23	198.56	<DL	195.10	16.13	1.42	0.10	0.30
DG48	0.17	0.04	63.96	97.65	421.92	<DL	2.22	0.23	0.36	<DL	<DL
DG49	0.95	0.49	346.26	38.63	6773.18	2.47	9.52	0.87	0.35	<DL	<DL

Table A10.1: Bulk Sample ICPMS analyses of samples from DDH86WRL1

SAMPLE#	Sn ppm	Sb ppm	Te ppm	Ba ppm	Hf ppm	Ta ppm	Bi ppm
DL							
DG37	6.84	1.70	0.18	323.60	4.68	0.94	0.92
DG38	3.82	6.89	0.25	370.86	3.39	0.57	0.42
DG38b	3.73	6.95	0.24	363.49	3.36	0.59	0.43
DG39	3.24	0.72	0.13	339.50	3.69	0.43	0.09
DG40	6.46	5.52	1.01	229.14	4.52	0.73	0.92
DG41	2.17	0.24	0.60	3.50	1.86	0.31	1.23
DG42	7.23	7.93	1.75	348.34	4.86	1.02	0.95
DG43	1.78	0.77	0.21	27.16	2.63	0.70	0.34
DG43b	1.78	0.79	0.25	35.64	2.32	0.62	0.40
DG44	1.84	1.25	0.26	2.21	2.90	0.45	0.31
DG45	0.19	0.30	N/A	5.26	0.12	0.03	0.02
DG46	0.25	0.29	N/A	8.55	0.05	0.02	0.01
DG47	13.92	0.39	0.07	257.81	5.35	1.15	0.16
DG48	0.15	0.34	N/A	3.22	0.05	0.02	0.01
DG49	0.41	0.31	<DL	52.61	0.26	0.08	0.02

Table A10.2: Bulk sample XRF analyses of samples from DDH86WRL1 for major elements

Sample	Top sample interval (m)	Bottom sample interval (m)	SiO2 (%)	TiO2 (%)	Al2O3 (%)	Fe2O3 (%)	MnO (%)	MgO (%)	CaO (%)	Na2O (%)	K2O (%)
DG 37	746.66	746.81	59.69	0.94	17.48	7.93	0.05	2.27	0.89	0.05	5.85
DG 38	729.72	729.91	46.97	1.12	13.46	15.94	0.17	3.08	2.54	0.03	5.1
DG 38B	729.72	729.91	47.2	1.06	13.25	15.85	0.17	3.01	2.49	0.04	4.87
DG 39	719.87	720.09	34.35	0.80	11.65	10.09	0.36	4.81	11.51	0.06	6.22
DG 40	707.37	707.55	42.89	0.59	12.36	13.19	0.22	2.4	2.24	0.06	6.09
DG 41	688	688.18	45.32	0.32	5.9	20.27	0.44	6.23	5.5	0.03	0.03
DG 42	681.2	681.38	50.59	1.15	14.07	11.44	0.05	2.9	0.69	0.09	8.43
DG 43	651.8	651.95	37.97	0.59	10.16	28.11	0.06	10.02	1.32	0.18	0.23
DG 43B	651.8	651.95	37.82	0.57	9.94	28.5	0.06	9.92	1.38	0.2	0.25
DG 44	602.78	603.03	49.66	0.36	8.07	18.19	0.15	7.76	4.18	0.02	0.01
DG 45	572.26	572.5	53.44	0.02	0.35	31.07	0.09	4.02	4.24	0.1	0.14
DG 46	524.68	524.95	40.98	0.02	0.24	40.09	0.18	1.99	8.63	0.11	0.14
DG 47	742.92	743.18	68.81	0.66	16.09	3.25	0.03	1.66	0.5	0.05	5.57
DG 48	576.65	576.79	51.13	0.02	0.21	38.8	0.06	3.07	2.61	0.06	0.11
DG 49	545.18	545.32	9.9	0.07	1.34	13.56	0.90	13.88	23.20	0.21	0.71

Table A10.2: Bulk sample XRF analyses of samples from DDH86WRL1 for major elements

Sample	P2O5 (%)	Loss (%)	Total (%)	S %
DG 37	0.08	4.50	99.73	1.27
DG 38	0.06	11.07	99.54	6.44
DG 38B	0.07	11.05	99.05	6.26
DG 39	0.05	19.22	99.12	1.86
DG 40	0.10	18.93	99.06	9.92
DG 41	0.05	13.75	97.85	3.60
DG 42	0.14	9.85	99.40	6.46
DG 43	0.07	11.38	100.09	1.76
DG 43B	0.07	11.44	100.15	1.94
DG 44	0.06	10.54	98.99	1.08
DG 45	0.04	6.47	99.98	0.20
DG 46	0.07	7.42	99.86	0.06
DG 47	0.05	3.32	99.99	0.23
DG 48	0.08	3.62	99.76	0.33
DG 49	0.03	35.50	99.28	0.03

Table A10.3: Bulk sample XRF analyses of samples from DDH86WRL1 for trace elements													
SAMPLE#	Top sample interval (m)	Bottom sample interval (m)	**Sc (ppm)**	**Ba (ppm)**	**V (ppm)**	**Cr (ppm)**	**Ni (ppm)**	**Cu (ppm)**	**Zn (ppm)**	**Ga (ppm)**	**As (ppm)**	**Rb (ppm)**	**Sr (ppm)**
DG37	746.66	746.81	31.5	329.6	236	305	293	132	86.9	22.9	47.3	256	11.2
DG38	729.72	729.91	26.0	361.0	217	260	187	65.1	233	20.1	31.9	139	35.7
DG38b	729.72	729.91	24.5	347	210	256	180	62.5	227	19.6	31.0	135	34.4
DG39	719.87	720.09	33.5	348.7	230	169	149	43.6	150	19.4	3.8	163	139
DG40	707.37	707.55	16.8	235	112	224	629	167	611	21.9	119	170	123
DG41	688	688.18	7.7	<4	75.3	226	30.9	109	1438	10.8	<3	1.8	141
DG42	681.2	681.38	21.9	340	160	340	534	278	1169	21.5	31.6	150	28.4
DG43	651.8	651.95	13.7	18.0	133	169	95.2	27.0	129	15.8	13.5	14.9	35.8
DG43b	651.8	651.95	12.9	23.6	129	164	99.2	36.5	126	15.1	11.4	17.1	34.7
DG44	602.78	603.03	14.6	<4	86.8	242	510	104	138	11.7	18.9	<0.5	48.4
DG45	572.26	572.5	3.3	<4	<3	81.9	311	4.7	12.3	<2	3.6	8.7	16.2
DG46	524.68	524.95	2.4	6.7	<3	113	495	7.5	10.8	<2	<3	14.4	15.0
DG47	742.92	743.18	23.6	268	177	219	180	12.6	45.4	22.4	<3	259	7.6
DG48	576.65	576.79	<1.5	<4	<3	102	486	6.1	12.9	<2	<3	5.5	11.0
DG49	545.18	545.32	4.3	64.4	16.0	55.5	160	1.9	27.1	<2	<3	99.7	59.4

Table A10.3: Bulk sample XRF analyses of samples from DDH86WRL1 for trace elements												
SAMPLE#	**Y (ppm)**	**Zr (ppm)**	**Nb (ppm)**	**Mo (ppm)**	**Sn (ppm)**	**Pb (ppm)**	**Bi (ppm)**	**U (ppm)**	**Th (ppm)**	**La (ppm)**	**Ce (ppm)**	**Nd (ppm)**
DG37	42.3	179	12.9	1.8	5.7	20.7	<2	3.6	11.4	46.9	95.4	45.2
DG38	18.7	128	9.2	5	4.5	38.5	<2	2.1	6.6	12.6	25.4	11.7
DG38b	25.9	124	8.8	4.4	2.5	35.6	<2	<2	3.1	12.5	29.0	12.5
DG39	28.7	134	7.0	0.9	3.4	14.0	<2	2.3	4.1	11.1	32.6	14.2
DG40	20.7	172	10.2	4.7	5.5	81.4	2.2	3.5	8.5	17.8	33.2	14.9
DG41	7.7	70.1	5.1	4.4	<1	12.7	<2	<2	6.9	<4	<6	<4
DG42	45.2	185	17.0	5	5.3	67.1	<2	2.6	11.1	32.4	60.1	30.1
DG43	17	105	7.8	3.7	<1	22.2	<2	<2	11.9	22.9	39.6	20.4
DG43b	16	102	7.7	4.5	2.4	29.4	<2	<2	10.5	21.4	37.7	17.4
DG44	20.8	111	6.1	3.4	<1	30.4	<2	<2	13.0	15.6	34.5	17.3
DG45	3.5	4.8	0.7	2.1	<1	<1	<2	<2	<2	<4	<6	<4
DG46	3.7	2.0	0.8	1.8	<1	<1	<2	<2	<2	<4	<6	<4
DG47	21.4	204	16.0	1.3	14	11.3	<2	4.6	12.2	<4	10.8	<4
DG48	2.9	2.8	<0.5	1.7	2	<1	<2	<2	<2	<4	<6	<4
DG49	10.7	9.4	0.8	0.8	<1	2	<2	<2	<2	8.8	12.9	<4

Table A10.4: Bulk sample ICPMS analyses of samples from ABDP9 for trace elements

Sample	Upper limit (m)	Lower limit (m)	Li (ppm)	Be (ppm)	Sc (ppm)	V (ppm)	Co (ppm)	Ni (ppm)	Cu (ppm)	Cu (ppm)	Zn (ppm)	Ga (ppm)	Rb (ppm)
ABDP9-132.77	132.77	132.97	17.52	0.81	9.87	38.22	27.63	482.71	91.79	90.14	261.00	9.52	78.44
ABDP9-164.24	164.24	164.4	6.84	0.46	1.88	7.94	4.62	53.31	21.54	21.32	8.06	1.64	23.46
ABDP9-169.07	169.07	169.25	29.68	1.77	6.06	37.18	10.14	25.99	32.46	32.06	58.45	8.18	78.22
ABDP9-186.42	186.42	186.69	26.86	1.26	2.89	20.11	3.61	14.72	12.11	12.05	42.85	5.64	18.16
ABDP9-214.87	214.87	215.04	12.30	0.66	0.58	2.75	1.47	4.02	6.11	6.21	13.21	0.50	8.33
ABDP9-234.16	234.16	234.31	80.16	2.53	13.04	84.36	30.35	105.74	105.96	104.08	294.09	18.21	192.31
ABDP9-253.24	247.48	427.64	13.03	0.82	11.32	76.45	43.19	103.52	56.10	55.44	95.50	10.01	71.99
ABDP9-268.93	253.24	253.39	63.91	1.75	14.97	86.95	20.13	590.48	55.31	54.52	338.65	17.96	114.98
ABDP9-292.74	268.93	269.08	89.68	2.37	15.42	100.38	26.85	86.45	77.20	75.56	167.31	16.05	113.14
ABDP9-313.82	292.74	292.9	38.83	2.63	10.95	66.90	14.16	54.31	35.15	34.94	98.74	13.31	38.76
ABDP9-366.61A	313.82	314.02	43.93	1.74	14.70	91.41	28.78	117.89	55.83	54.70	180.10	17.25	101.63
ABDP9-366.61B	366.61	366.87	41.42	1.64	10.57	64.70	38.00	73.45	35.83	35.50	80.21	13.58	90.40
ABDP9-398.30	366.61	366.87	33.02	1.40	9.12	52.62	15.40	43.76	27.41	27.11	62.60	10.71	73.89
ABDP9-427.48	398.3	398.47	18.67	1.09	8.43	51.96	7.09	31.75	20.18	20.07	28.72	8.25	61.15
ABDP9-438.51	438.51	438.73	7.73	0.54	4.41	29.22	8.58	36.95	12.68	12.72	77.29	5.38	34.66

Table A10.4: Bulk sample ICPMS analyses of samples from ABDP9 for trace elements													
Sample	Sr (ppm)	Y (ppm)	Cs (ppm)	La (ppm)	Ce (ppm)	Pr (ppm)	Nd (ppm)	Sm (ppm)	Eu (ppm)	Gd (ppm)	Tb (ppm)	Dy (ppm)	Ho (ppm)
ABDP9-132.77	20.99	16.19	7.70	17.41	39.67	4.60	16.88	3.36	0.75	2.97	0.47	2.77	0.54
ABDP9-164.24	5.27	8.44	0.68	5.59	12.03	1.76	6.98	1.48	0.59	1.44	0.23	1.29	0.25
ABDP9-169.07	10.24	12.39	5.79	15.13	33.00	3.61	12.55	2.25	0.65	1.82	0.30	1.82	0.38
ABDP9-186.42	22.21	6.44	1.25	6.00	11.08	1.43	5.35	1.08	0.32	1.00	0.16	0.91	0.18
ABDP9-214.87	9.21	5.87	4.92	1.84	2.88	0.38	1.52	0.30	0.16	0.40	0.07	0.45	0.12
ABDP9-234.16	28.91	20.63	16.23	38.83	75.42	8.58	30.31	5.40	1.16	4.12	0.63	3.54	0.71
ABDP9-253.24	20.81	16.13	4.57	15.76	32.12	3.97	14.96	3.09	0.83	2.75	0.45	2.57	0.51
ABDP9-268.93	66.93	24.19	14.97	30.93	68.05	8.00	29.65	5.80	1.33	4.84	0.78	4.53	0.86
ABDP9-292.74	35.14	18.87	13.61	27.82	55.69	5.92	20.14	3.39	0.78	2.93	0.51	2.94	0.60
ABDP9-313.82	15.89	18.15	5.01	19.78	45.36	5.36	20.20	4.11	1.08	3.70	0.57	3.22	0.61
ABDP9-366.61A	50.79	23.97	3.44	30.90	67.88	7.89	28.73	5.56	1.20	4.72	0.76	4.27	0.84
ABDP9-366.61B	38.50	22.62	4.95	21.18	46.49	5.42	19.89	3.86	0.85	3.43	0.56	3.26	0.66
ABDP9-398.30	55.30	27.26	4.09	20.74	44.40	5.21	19.50	3.97	0.93	3.84	0.64	3.78	0.78
ABDP9-427.48	17.88	10.41	3.23	10.46	19.04	2.38	8.48	1.68	0.40	1.49	0.27	1.57	0.33
ABDP9-438.51	19.53	14.25	2.11	9.79	17.35	2.23	8.58	1.71	0.49	1.64	0.26	1.59	0.33

Table A10.4: Bulk sample ICPMS analyses of samples from ABDP9 for trace elements													
Sample	Er (ppm)	Tm (ppm)	Yb (ppm)	Lu (ppm)	W (ppm)	Tl (ppm)	Pb (ppm)	Th (ppm)	U (ppm)	Ti (ppm)	Cr (ppm)	Cr (ppm)	Mn (ppm)
ABDP9-132.77	1.70	0.25	1.67	0.28	2.23	2.88	64.00	7.63	2.28	1153.53	179.41	179.42	0.01
ABDP9-164.24	0.71	0.09	0.51	0.08	0.38	0.19	40.26	0.90	0.34	199.28	9.09	7.70	0.00
ABDP9-169.07	1.26	0.20	1.35	0.22	1.04	0.89	14.43	4.72	1.60	889.14	25.87	27.75	0.00
ABDP9-186.42	0.55	0.08	0.52	0.09	0.34	0.23	4.19	2.34	0.78	508.79	20.68	21.86	0.00
ABDP9-214.87	0.43	0.06	0.37	0.07	0.32	0.14	1.58	0.31	0.08	64.59	8.54	7.12	0.00
ABDP9-234.16	2.10	0.31	1.96	0.30	1.75	2.11	61.18	11.70	3.03	2417.57	140.80	148.60	0.00
ABDP9-253.24	1.52	0.23	1.42	0.23	1.23	0.73	20.30	5.29	1.75	1592.98	118.26	125.97	0.00
ABDP9-268.93	2.62	0.39	2.61	0.41	1.95	2.09	32.62	14.55	4.09	2543.66	0.02	236.55	0.00
ABDP9-292.74	1.82	0.28	1.76	0.28	2.42	1.21	35.11	11.14	3.11	2644.22	161.04	172.30	0.00
ABDP9-313.82	1.84	0.27	1.74	0.28	0.90	0.43	22.98	8.77	2.65	1809.78	98.11	102.64	0.00
ABDP9-366.61A	2.47	0.37	2.31	0.36	2.11	0.83	34.42	12.89	4.13	3139.22	146.12	154.92	0.00
ABDP9-366.61B	2.00	0.29	1.88	0.30	1.44	0.73	22.82	8.69	2.82	1945.95	93.36	99.60	0.00
ABDP9-398.30	2.35	0.36	2.21	0.36	0.78	0.58	15.55	7.45	2.62	1770.38	77.46	82.62	0.00
ABDP9-427.48	1.04	0.16	1.02	0.17	1.05	0.33	6.37	4.42	1.30	1467.92	83.42	88.22	0.00
ABDP9-438.51	1.06	0.15	0.96	0.16	1.07	0.24	7.67	2.76	0.92	808.95	43.71	46.40	0.00

Table A10.4: Bulk sample ICPMS analyses of samples from ABDP9 for trace elements													
Sample	As (ppm)	Zr (ppm)	Nb (ppm)	Mo (ppm)	Ag (ppm)	Cd (ppm)	Sn (ppm)	Sb (ppm)	Te (ppm)	Ba (ppm)	Hf (ppm)	Ta (ppm)	Bi (ppm)
ABDP9-132.77	212.43	67.54	5.56	8.31	0.34	0.83	2.78	15.18	0.50	140.27	2.14	0.51	1.67
ABDP9-164.24	275.47	7.53	0.71	1.32	0.12	0.04	0.52	4.92	0.02	32.50	0.23	0.08	0.06
ABDP9-169.07	14.08	48.33	3.73	1.55	0.12	0.12	1.30	2.02	0.14	97.70	1.42	0.24	0.40
ABDP9-186.42	6.79	16.71	1.49	0.42	0.04	0.04	0.50	0.47	0.03	40.94	0.52	0.14	0.07
ABDP9-214.87	2.40	2.13	0.20	0.42	0.04	0.14	0.60	0.20	0.13	11.99	0.06	0.03	0.10
ABDP9-234.16	35.33	119.22	8.89	5.01	0.27	1.08	3.47	8.41	0.77	272.55	3.03	0.70	0.81
ABDP9-253.24	26.95	42.12	3.91	3.38	0.17	0.24	1.31	9.56	0.10	150.18	1.25	0.40	0.30
ABDP9-268.93	11.45	98.55	8.65	2.89	0.14	0.93	4.32	5.59	0.32	256.37	3.20	1.00	0.81
ABDP9-292.74	14.45	72.34	7.73	2.44	0.29	6.73	8.26	6.37	2.70	200.00	2.22	0.73	1.78
ABDP9-313.82	9.11	56.92	6.12	2.89	0.13	0.30	1.96	2.72	0.20	158.37	1.79	0.45	0.38
ABDP9-366.61A	91.46	95.55	8.77	3.77	0.26	0.44	2.66	7.78	0.19	291.68	2.90	0.77	0.64
ABDP9-366.61B	29.54	65.63	5.71	2.40	0.18	0.15	1.91	7.18	0.14	247.34	1.96	0.56	0.93
ABDP9-398.30	11.76	56.28	4.90	1.90	0.08	0.12	1.57	3.12	0.05	208.17	1.73	0.50	0.30
ABDP9-427.48	4.53	37.47	3.66	1.56	0.04	0.04	1.17	2.08	0.03	122.92	1.15	0.34	0.12
ABDP9-438.51	20.52	22.06	2.23	1.09	0.04	0.26	0.70	2.59	0.02	68.08	0.68	0.23	0.13

Table A10.5: Bulk sample XRF analyses of samples from ABDP9 for trace elements

Sample	Top of Interval (m)	Bottom of Interval (m)	**Sc (ppm)**	**Ba (ppm)**	**V (ppm)**	**Cr (ppm)**	**Ni (ppm)**	**Cu (ppm)**	**Zn (ppm)**	**Ga (ppm)**	**As (ppm)**	**Rb (ppm)**	**Sr (ppm)**
ABDP9-132.77	132.77	132.97	6.2	115	38.3	141	468	71	208	8.0	669	63.5	14.6
ABDP9-164.24	164.24	164.4	<1.5	36.3	10.8	11.5	41.2	15.8	11	1.7	316	24.2	7.1
ABDP9-169.07	169.07	169.25	5.0	116	47.0	34.7	24.0	28.3	70	9.3	21.0	85.4	14.2
ABDP9-186.42	186.42	186.69	2.2	47.1	28.0	29.1	17.0	11.9	52	4.9	7.3	20.3	24.3
ABDP9-214.87	214.87	215.04	<1.5	10.5	<3	6.0	2.8	7.3	24	<1	<3	9.3	11.8
ABDP9-234.16	234.16	234.31	13.0	301	95.2	153	106	94.8	305	18.4	39.7	198	34.5
ABDP9-253.24	247.48	427.64	21.6	287	107	225	394	53.9	311	18.2	13.1	123	88.0
ABDP9-268.93	253.24	253.39	21.2	252	125	181	88.4	73.9	187	16.2	18.2	117	41.1
ABDP9-292.74	268.93	269.08	11.0	176	83.7	125	62.0	33.5	113	14.2	12.2	40.7	18.5
ABDP9-313.82	292.74	292.9	19.3	310	108	169	96.4	53.4	157	17.7	79.8	108	61.1
ABDP9-366.61A	313.82	314.02	14.5	280	82.3	120	79.8	33.7	90	14.1	48.3	97.3	46.0
ABDP9-366.61B	366.61	366.87	15.2	247	71.1	101	52.7	28.2	76	11.0	18.6	83.9	69.1
ABDP9-398.30	366.61	366.87	15.6	153	64.4	106	37.4	22.3	36	8.6	<3	68.4	22.4
ABDP9-427.48	398.3	398.47	18.0	166	93.3	140	106	56.2	110	10.1	44.2	76.3	24.6
ABDP9-438.51	438.51	438.73	10.0	81.1	36.0	54.3	38.6	12.8	88	6.0	31.7	39.1	24.7

Table A10.5: Bulk sample XRF analyses of samples from ABDP9 for trace elements													
Sample	Nd (ppm)	Y (ppm)	Zr (ppm)	Nb (ppm)	Mo (ppm)	Sn (ppm)	Pb (ppm)	Bi (ppm)	U (ppm)	Th (ppm)	La (ppm)	Ce (ppm)	Nd (ppm)
ABDP9-132.77	17.3	11.7	62.1	5.1	11.2	4.7	70.7	2.5	<2	5.5	17.5	As interference	17.3
ABDP9-164.24	5.9	8.0	8.7	0.8	3.3	<1	36.2	<2	<2	<2	4.8	As interference	5.9
ABDP9-169.07	15.4	13.5	59.4	4.3	3.5	2.7	15.3	<2	<2	8.2	16.8	32.1	15.4
ABDP9-186.42	5.6	8.8	21.0	2.1	2.1	<1	4.4	<2	<2	5.3	7.3	10	5.6
ABDP9-214.87	6.0	7.1	3.1	0.5	2.8	<1	1.1	<2	<2	3.3	<4	<6	6.0
ABDP9-234.16	30.1	20.6	123	9.7	5.6	3.0	60.8	<2	4.3	13.5	37.4	65.6	30.1
ABDP9-253.24	24.7	25.4	117	10.2	3.9	4.0	43.6	<2	5.6	16.9	35.9	62.1	24.7
ABDP9-268.93	13.6	19.3	87.1	8.8	2.4	9.3	38.6	<2	4.1	13.3	24.3	42.3	13.6
ABDP9-292.74	23.8	18.2	68.3	6.9	4.5	2.2	24.2	<2	<2	12.7	22.8	43.3	23.8
ABDP9-313.82	28.4	24.6	112	10.3	4.1	2.0	33.6	<2	5.1	14.6	35.3	61.8	28.4
ABDP9-366.61A	18.6	23.6	80.5	7.2	3.4	<1	27.2	<2	3.6	12.6	23.1	43.6	18.6
ABDP9-366.61B	19.5	27.9	70.2	6.1	3.4	1.7	20.0	<2	3.6	9.7	21.8	41.1	19.5
ABDP9-398.30	7.1	11.1	48.1	4.5	1.9	1.4	8.5	<2	2.1	6	13.5	22.6	7.1
ABDP9-427.48	13.2	16.6	51.0	4.7	3.9	<1	23.8	<2	2.6	6.9	19.0	31.9	13.2
ABDP9-438.51	5.3	16.3	29.2	2.6	1.9	<1	10.2	<2	<2	5.6	13.0	17.5	5.3

Table A10.6: Bulk sample XRF analyses of samples from ABDP9 for major elements

Sample	Top sample interval (m)	Bottom sample interval (m)	SiO2 (%)	TiO2 (%)	Al2O3 (%)	Fe2O3 (%)	MnO (%)	MgO (%)	CaO (%)	Na2O (%)	K2O (%)
ABDP9-132.77	132.77	132.97	32.15	0.24	7.00	32.65	0.17	1.51	1.84	0.23	2.47
ABDP9-164.24	164.24	164.4	42.48	0.04	1.24	29.24	0.22	4.50	1.37	0.03	0.74
ABDP9-169.07	169.07	169.25	34.13	0.18	5.14	26.72	0.64	5.81	3.91	0.05	2.33
ABDP9-186.42	186.42	186.69	41.45	0.10	3.19	22.50	1.20	5.18	6.07	0.04	0.45
ABDP9-214.87	214.87	215.04	44.27	0.02	0.32	40.84	0.07	3.11	2.88	0.05	0.12
ABDP9-234.16	234.16	234.31	52.64	0.46	13.36	11.96	0.13	3.23	2.32	0.77	3.94
ABDP9-253.24	247.48	427.64	45.93	0.49	12.67	6.83	0.51	2.70	11.69	1.28	2.32
ABDP9-268.93	253.24	253.39	38.20	0.50	12.13	11.32	0.24	3.12	14.72	0.44	2.03
ABDP9-292.74	268.93	269.08	34.42	0.37	9.51	30.28	0.33	5.67	2.96	0.20	1.46
ABDP9-313.82	292.74	292.9	48.11	0.58	13.35	6.21	0.25	3.13	10.31	2.99	3.38
ABDP9-366.61A	313.82	314.02	44.18	0.39	9.48	8.91	0.53	5.82	9.95	0.32	3.40
ABDP9-366.61B	366.61	366.87	34.66	0.34	7.81	6.06	0.56	4.22	20.67	0.27	2.87
ABDP9-398.30	366.61	366.87	23.15	0.28	6.18	7.80	0.61	11.02	18.98	0.08	3.08
ABDP9-427.48	398.3	398.47	26.45	0.29	6.64	5.25	0.42	11.98	17.67	0.07	3.49
ABDP9-438.51	438.51	438.73	15.05	0.15	3.32	2.78	0.53	15.93	23.74	0.06	1.66

Table A10.6: Bulk sample XRF analyses of samples from DDH86WRL1 for major elements

Sample	P2O5 (%)	Loss (%)	Total (%)	S %
DG 37	0.08	21.45	99.79	23.52
DG 38	0.13	19.55	99.54	6.10
DG 38B	0.04	20.48	99.43	2.73
DG 39	0.04	19.40	99.62	0.46
DG 40	0.16	7.81	99.64	0.69
DG 41	0.06	10.90	99.77	4.92
DG 42	0.05	16.10	100.56	1.65
DG 43	0.05	17.04	99.79	1.52
DG 43B	0.14	14.15	99.49	0.36
DG 44	0.07	11.14	99.52	1.58
DG 45	0.06	16.78	99.82	1.46
DG 46	0.05	22.03	99.54	0.49
DG 47	0.04	28.62	99.83	0.31
DG 48	0.05	27.03	99.32	2.27
DG 49	0.02	36.16	99.40	0.54

Table A10.6: Bulk sample XRF analyses of samples from ABDP9 for trace elements													
Sample	**Nd (ppm)**	**Y (ppm)**	**Zr (ppm)**	**Nb (ppm)**	**Mo (ppm)**	**Sn (ppm)**	**Pb (ppm)**	**Bi (ppm)**	**U (ppm)**	**Th (ppm)**	**La (ppm)**	**Ce (ppm)**	**Nd (ppm)**
ABDP9-132.77	17.3	11.7	62.1	5.1	11.2	4.7	70.7	2.5	<2	5.5	17.5	As interference	17.3
ABDP9-164.24	5.9	8.0	8.7	0.8	3.3	<1	36.2	<2	<2	<2	4.8	As interference	5.9
ABDP9-169.07	15.4	13.5	59.4	4.3	3.5	2.7	15.3	<2	<2	8.2	16.8	32.1	15.4
ABDP9-186.42	5.6	8.8	21.0	2.1	2.1	<1	4.4	<2	<2	5.3	7.3	10	5.6
ABDP9-214.87	6.0	7.1	3.1	0.5	2.8	<1	1.1	<2	<2	3.3	<4	<6	6.0
ABDP9-234.16	30.1	20.6	123	9.7	5.6	3.0	60.8	<2	4.3	13.5	37.4	65.6	30.1
ABDP9-253.24	24.7	25.4	117	10.2	3.9	4.0	43.6	<2	5.6	16.9	35.9	62.1	24.7
ABDP9-268.93	13.6	19.3	87.1	8.8	2.4	9.3	38.6	<2	4.1	13.3	24.3	42.3	13.6
ABDP9-292.74	23.8	18.2	68.3	6.9	4.5	2.2	24.2	<2	<2	12.7	22.8	43.3	23.8
ABDP9-313.82	28.4	24.6	112	10.3	4.1	2.0	33.6	<2	5.1	14.6	35.3	61.8	28.4
ABDP9-366.61A	18.6	23.6	80.5	7.2	3.4	<1	27.2	<2	3.6	12.6	23.1	43.6	18.6
ABDP9-366.61B	19.5	27.9	70.2	6.1	3.4	1.7	20.0	<2	3.6	9.7	21.8	41.1	19.5
ABDP9-398.30	7.1	11.1	48.1	4.5	1.9	1.4	8.5	<2	2.1	6	13.5	22.6	7.1
ABDP9-427.48	13.2	16.6	51.0	4.7	3.9	<1	23.8	<2	2.6	6.9	19.0	31.9	13.2
ABDP9-438.51	5.3	16.3	29.2	2.6	1.9	<1	10.2	<2	<2	5.6	13.0	17.5	5.3

Table A10.7: LA-ICPMS of pyrite from DDH86WRL1

Sample	**Bottom of interval (m)**	**Top of interval (m)**	Major geologic unit	Mn55 (ppm)	Fe57 (ppm)	Co59 (ppm)	Ni60 (ppm)	Cu65 (ppm)	Zn66 (ppm)	As75 (ppm)	Se77 (ppm)	Mo95 (ppm)
DG46	524.95	524.68	Jeerinah	402.66	465553	98.65	77.33	0.95	4.28	1.31	15.91	<0.01
DG46	524.95	524.68	Jeerinah	177.20	465547	117.98	75.26	1.66	0.53	23.25	15.95	0.17
DG46	524.95	524.68	Jeerinah	15.86	465538	74.98	11.33	39.21	2.22	57.91	25.75	0.10
DG46	524.95	524.68	Jeerinah	410.96	465546	12.62	3.56	3.56	1.57	27.60	7.34	0.07
DG46	524.95	524.68	Jeerinah	21.11	465541	15.07	7.03	17.24	0.00	46.38	12.57	0.05
DG46	524.95	524.68	Jeerinah	58.11	465542	18.77	2.16	10.08	0.18	40.47	9.05	0.06
DG46	524.95	524.68	Jeerinah	0.45	465219	6.05	1.13	81.62	1.17	1250.70	13.94	<0.01
DG46	524.95	524.68	Jeerinah	1.07	464872	33.61	1.60	45.91	0.43	2550.59	22.61	0.01
DG46	524.95	524.68	Jeerinah	33.60	465527	0.53	1.47	18.47	0.95	99.02	6.81	<0.01
DG46	524.95	524.68	Jeerinah	29.97	465538	3.97	2.35	13.79	1.60	58.61	9.67	<0.01
DG46	524.95	524.68	Jeerinah	112.58	465553	120.37	125.58	0.52	0.00	1.04	16.55	0.03
DG46	524.95	524.68	Jeerinah	1368.17	465553	116.53	125.52	1.71	1.25	0.86	13.65	0.09
DG45	572.5	572.26	Jeerinah	<0.01	465094	0.92	20.20	0.49	0.13	1722.04	15.19	<0.01
DG45	572.5	572.26	Jeerinah	1.22	464424	1.45	856.48	3.51	0.24	4228.98	12.08	<0.01
DG45	572.5	572.26	Jeerinah	29.85	464496	6.33	16.27	6.12	<0.02	3961.28	12.28	<0.01

Table A10.7: LA-ICPMS of pyrite from DDH86WRL1

Sample	Ag107 (ppm)	Cd111 (ppm)	Sb121 (ppm)	Te125 (ppm)	Au197 (ppm)	Tl205 (ppm)	Pb206 (ppm)	Pb207 (ppm)	Pb208 (ppm)	Bi209 (ppm)
DG46	0.76	0.03	1.05	0.80	0.02	0.31	16.69	11.64	13.87	2.91
DG46	1.07	0.07	2.10	1.10	0.02	0.47	28.21	21.85	25.10	4.15
DG46	0.93	<0.01	90.13	0.26	0.03	1.89	128.60	114.26	113.30	1.69
DG46	0.06	<0.01	7.87	<0.10	<0.01	0.06	15.06	12.98	13.30	0.12
DG46	0.48	<0.01	40.61	<0.10	0.01	0.31	53.35	53.99	53.30	0.43
DG46	0.24	<0.01	21.04	<0.10	<0.01	1.17	46.60	39.63	40.39	0.18
DG46	2.22	0.09	255.99	0.21	0.07	1.57	856.20	891.22	843.63	0.71
DG46	1.20	0.07	138.76	<0.10	0.07	0.15	616.57	650.37	620.41	3.93
DG46	0.41	0.11	60.35	<0.10	0.02	1.14	178.12	177.30	168.47	0.16
DG46	0.26	0.07	32.35	<0.10	0.01	1.90	65.33	58.50	57.28	0.22
DG46	1.05	<0.01	1.48	1.07	0.03	0.22	36.73	29.56	29.08	5.87
DG46	1.28	<0.01	2.14	1.65	0.03	0.51	35.55	29.50	26.63	5.81
DG45	0.08	<0.01	<0.09	1.20	<0.01	<0.01	2.10	2.27	2.19	0.30
DG45	0.31	0.05	0.67	1.48	0.02	<0.01	7.11	8.29	7.73	2.09
DG45	1.58	0.05	3.93	2.56	0.09	0.01	89.68	100.61	98.30	8.28

Table A10.7: LA-ICPMS of pyrite from DDH86WRL1

Sample	**Bottom of interval (m)**	**Top of interval (m)**	Major geologic unit	Mn55 (ppm)	Fe57 (ppm)	Co59 (ppm)	Ni60 (ppm)	Cu65 (ppm)	Zn66 (ppm)	As75 (ppm)	Se77 (ppm)	Mo95 (ppm)
DG45	572.5	572.26	Jeerinah	127.18	464297	28.33	1157.67	1.96	0.85	4705.69	14.38	<0.01
DG45	572.5	572.26	Jeerinah	60.19	464694	122.71	825.60	49.53	0.28	3217.78	11.61	0.02
DG45	572.5	572.26	Jeerinah	27.87	464595	23.75	606.84	26.51	0.11	3588.61	9.82	<0.01
DG45	572.5	572.26	Jeerinah	214.35	464739	6.84	20.49	4.98	0.26	3052.01	9.23	<0.01
DG45	572.5	572.26	Jeerinah	0.99	465398	7.67	118.18	0.50	<0.02	582.43	15.37	<0.01
DG45	572.5	572.26	Jeerinah	5.25	464314	111.67	1664.81	148.76	0.48	4644.28	10.72	<0.01
DG45	572.5	572.26	Jeerinah	146.83	464967	2.04	25.21	2.31	0.06	2196.37	14.18	0.04
DG45	572.5	572.26	Jeerinah	504.44	465201	21.92	46.30	4.37	0.24	1320.58	11.07	<0.01
DG45	572.5	572.26	Jeerinah	228.24	464860	58.52	145.50	9.18	0.08	2597.92	12.71	0.05
DG45	572.5	572.26	Jeerinah	0.01	465499	1.59	4.56	0.61	0.04	201.89	15.73	0.04
DG45	572.5	572.26	Jeerinah	0.62	465492	13.13	14.70	5.18	0.07	228.78	16.36	<0.01
DG45	572.5	572.26	Jeerinah	<0.01	465503	0.16	3.99	<0.25	0.12	186.63	14.34	0.02
DG45	572.5	572.26	Jeerinah	<0.01	465534	1.57	13.27	0.61	0.23	71.72	13.44	<0.01
DG45	572.5	572.26	Jeerinah	<0.01	465513	0.23	2.95	5.55	0.15	151.26	20.72	0.06
DG45	572.5	572.26	Jeerinah	<0.01	465486	1.67	2.81	1.59	0.13	251.29	14.68	0.01

Table A10.7: LA-ICPMS of pyrite from DDH86WRL1

Sample	Ag107 (ppm)	Cd111 (ppm)	Sb121 (ppm)	Te125 (ppm)	Au197 (ppm)	Tl205 (ppm)	Pb206 (ppm)	Pb207 (ppm)	Pb208 (ppm)	Bi209 (ppm)
DG45	1.43	0.10	2.15	2.92	0.04	0.02	373.77	418.92	397.53	4.21
DG45	3.66	0.13	9.72	8.01	0.11	0.47	140.56	136.05	128.68	24.83
DG45	2.25	0.08	5.47	3.75	0.09	0.04	78.83	89.72	97.56	12.02
DG45	2.03	0.14	3.97	2.76	0.07	0.01	389.60	558.48	402.63	9.92
DG45	0.15	<0.01	0.45	4.11	0.01	<0.01	4.15	5.17	5.04	0.84
DG45	1.93	0.05	1.10	4.44	0.04	0.08	358.04	593.56	635.17	5.93
DG45	0.29	0.03	0.81	2.68	0.03	0.01	9.20	10.27	10.15	1.86
DG45	0.72	0.04	2.27	2.42	0.01	0.02	20.43	21.17	21.04	5.12
DG45	2.04	0.08	7.58	3.43	0.07	0.05	58.32	59.10	62.09	19.04
DG45	0.08	0.01	0.47	6.13	<0.01	<0.01	7.70	9.06	7.85	2.05
DG45	0.62	0.03	1.72	5.56	0.02	0.16	21.43	25.26	22.97	6.70
DG45	0.05	<0.01	0.20	2.45	0.01	<0.01	3.01	4.80	3.97	0.70
DG45	0.07	0.01	0.25	1.08	<0.01	<0.01	3.64	4.78	3.73	0.74
DG45	0.38	<0.01	6.47	6.82	<0.01	<0.01	97.01	109.17	108.35	22.52
DG45	0.24	0.02	0.68	3.76	0.01	0.02	11.17	12.09	12.11	2.68

Table A10.7: LA-ICPMS of pyrite from DDH86WRL1												
Sample	**Bottom of interval (m)**	**Top of interval (m)**	Major geologic unit	Mn55 (ppm)	Fe57 (ppm)	Co59 (ppm)	Ni60 (ppm)	Cu65 (ppm)	Zn66 (ppm)	As75 (ppm)	Se77 (ppm)	Mo95 (ppm)
DG45	572.5	572.26	Jeerinah	<0.01	465502	0.14	0.80	<0.25	0.36	191.70	15.82	0.00
DG48	576.79	576.65	Jeerinah	<0.01	465496	71.94	69.04	<0.19	0.30	212.75	18.21	0.02
DG48	576.79	576.65	Jeerinah	<0.01	465506	6.01	55.08	<0.19	0.25	175.70	14.20	<0.01
DG48	576.79	576.65	Jeerinah	<0.01	465500	51.96	62.71	<0.19	<0.08	199.24	20.79	0.01
DG48	576.79	576.65	Jeerinah	<0.01	465505	70.03	75.03	<0.19	<0.08	181.79	19.48	0.01
DG48	576.79	576.65	Jeerinah	<0.01	465494	11.87	66.49	<0.19	0.27	223.03	18.25	<0.01
DG48	576.79	576.65	Jeerinah	<0.01	465511	1.79	12.40	<0.19	0.46	156.93	15.07	<0.01
DG48	576.79	576.65	Jeerinah	<0.01	465511	60.76	28.27	0.38	0.17	159.68	16.39	0.01
DG48	576.79	576.65	Jeerinah	<0.01	465514	25.81	92.42	<0.19	0.18	148.66	17.21	0.01
DG48	576.79	576.65	Jeerinah	<0.01	465504	59.78	85.97	0.39	0.18	183.66	11.44	<0.01
DG48	576.79	576.65	Jeerinah	<0.01	465504	6.52	31.73	0.53	0.37	184.21	15.36	0.01
DG48	576.79	576.65	Jeerinah	<0.01	465501	35.38	66.25	0.93	0.27	194.18	15.21	<0.01
DG48	576.79	576.65	Jeerinah	<0.01	465512	43.33	85.38	<0.19	0.42	153.20	18.56	0.01
DG48	576.79	576.65	Jeerinah	<0.01	465512	4.41	18.50	1.46	0.32	154.71	14.63	0.08
DG48	576.79	576.65	Jeerinah	<0.01	465553	0.33	0.04	0.87	0.21	2.25	52.68	<0.01

Table A10.7: LA-ICPMS of pyrite from DDH86WRL1

Sample	Ag107 (ppm)	Cd111 (ppm)	Sb121 (ppm)	Te125 (ppm)	Au197 (ppm)	Tl205 (ppm)	Pb206 (ppm)	Pb207 (ppm)	Pb208 (ppm)	Bi209 (ppm)
DG45	0.03	<0.01	0.18	3.95	0.01	<0.01	4.01	3.60	3.51	0.85
DG48	<0.01	<0.01	0.07	0.19	<0.01	<0.01	0.41	0.43	0.39	0.08
DG48	<0.01	0.03	<0.04	0.20	<0.01	<0.01	1.12	1.22	1.11	0.21
DG48	<0.01	0.01	<0.04	0.97	<0.01	<0.01	0.22	0.19	0.18	0.04
DG48	<0.01	0.01	<0.04	<0.06	<0.01	<0.01	0.23	0.06	0.08	0.03
DG48	<0.01	0.01	0.23	0.16	0.00	<0.01	3.41	4.73	3.62	0.85
DG48	0.01	<0.01	0.10	0.14	<0.01	<0.01	1.52	1.61	1.57	0.20
DG48	0.04	0.01	0.16	0.12	0.00	<0.01	2.45	2.68	2.53	0.56
DG48	0.01	0.02	<0.04	0.16	<0.01	<0.01	0.13	0.14	0.13	0.03
DG48	0.02	0.03	0.19	0.27	<0.01	<0.01	2.74	3.36	3.53	0.76
DG48	0.03	<0.01	0.23	0.30	<0.01	<0.01	3.85	4.27	4.04	0.72
DG48	0.09	0.01	0.52	0.33	<0.01	<0.01	7.44	8.16	7.68	1.61
DG48	0.01	0.02	<0.04	0.40	<0.01	<0.01	0.75	0.87	0.84	0.21
DG48	0.10	<0.01	0.72	0.17	<0.01	0.03	8.00	7.85	8.86	1.67
DG48	0.00	<0.01	<0.04	46.66	<0.01	<0.01	0.04	<0.03	0.07	<0.01

Table A10.7: LA-ICPMS of pyrite from DDH86WRL1

Sample	**Bottom of interval (m)**	**Top of interval (m)**	Major geologic unit	Mn55 (ppm)	Fe57 (ppm)	Co59 (ppm)	Ni60 (ppm)	Cu65 (ppm)	Zn66 (ppm)	As75 (ppm)	Se77 (ppm)	Mo95 (ppm)
DG44	603.03	602.78	Jeerinah	<0.01	465553	144.78	244.40	2.98	0.92	1.18	46.58	<0.01
DG44	603.03	602.78	Jeerinah	23.08	465553	152.03	249.29	0.48	1.30	1.18	50.76	0.02
DG44	603.03	602.78	Jeerinah	217.24	465553	155.04	230.46	<0.22	2.08	1.24	38.25	0.03
DG44	603.03	602.78	Jeerinah	0.92	465553	149.78	249.93	<0.22	0.68	1.01	42.19	0.01
DG44	603.03	602.78	Jeerinah	<0.46	465553	150.04	258.31	<0.22	<0.17	1.33	50.27	0.01
DG44	603.03	602.78	Jeerinah	3.17	465553	146.31	245.89	5.97	0.35	1.26	46.31	<0.01
DG44	603.03	602.78	Jeerinah	2250.32	465553	146.55	248.66	<0.22	19.43	1.18	49.72	<0.01
DG44	603.03	602.78	Jeerinah	1.16	465553	149.00	245.27	0.49	1.03	1.00	44.26	<0.01
DG44	603.03	602.78	Jeerinah	680.60	465553	144.34	222.31	<0.22	4.15	0.96	41.20	0.10
DG44	603.03	602.78	Jeerinah	<0.46	465553	142.33	236.25	<0.22	0.96	0.78	28.49	<0.01
DG44	603.03	602.78	Jeerinah	<0.46	465553	151.84	234.00	<0.22	0.70	1.08	50.94	<0.01
DG44	603.03	602.78	Jeerinah	<0.46	465553	146.37	208.25	<0.22	<0.17	0.96	44.86	<0.01
DG44	603.03	602.78	Jeerinah	1.95	465553	144.05	239.02	<0.22	<0.17	1.71	46.33	0.02
DG44	603.03	602.78	Jeerinah	<0.46	465553	138.75	230.42	<0.22	0.49	0.94	49.91	0.02
DG44	603.03	602.78	Jeerinah	<0.46	465553	155.89	240.56	0.63	0.35	1.26	54.78	<0.01

Table A10.7: LA-ICPMS of pyrite from DDH86WRL1

Sample	Ag107 (ppm)	Cd111 (ppm)	Sb121 (ppm)	Te125 (ppm)	Au197 (ppm)	Tl205 (ppm)	Pb206 (ppm)	Pb207 (ppm)	Pb208 (ppm)	Bi209 (ppm)
DG44	0.94	0.03	0.12	0.22	<0.01	<0.01	13.42	14.23	13.82	2.44
DG44	3.55	0.09	0.48	1.18	<0.01	0.14	372.05	407.67	390.95	12.58
DG44	1.95	0.08	0.84	0.75	0.00	0.24	232.46	248.75	238.44	5.59
DG44	0.94	<0.01	<0.05	0.26	0.00	<0.01	4.07	3.83	3.12	1.32
DG44	1.09	0.01	0.31	0.44	<0.01	0.02	9.95	10.86	10.92	4.91
DG44	2.93	<0.01	0.47	0.60	<0.01	0.04	15.66	15.93	15.35	6.85
DG44	2.84	0.15	0.41	0.58	<0.01	0.04	81.71	87.55	86.89	5.61
DG44	1.76	0.10	0.30	0.30	<0.01	0.02	14.46	14.63	15.33	5.63
DG44	1.10	0.17	0.95	0.23	<0.01	0.37	415.21	453.62	432.38	1.70
DG44	0.25	<0.01	<0.05	0.23	<0.01	<0.01	10.84	11.82	10.87	0.65
DG44	0.10	<0.01	<0.05	0.24	<0.01	<0.01	0.19	0.18	0.17	0.05
DG44	0.09	0.02	<0.05	<0.11	<0.01	<0.01	0.43	0.42	0.43	0.08
DG44	0.39	<0.01	<0.05	<0.11	<0.01	0.01	2.73	3.17	2.46	1.25
DG44	0.37	<0.01	0.10	<0.11	<0.01	0.04	10.30	12.54	10.68	1.66
DG44	0.68	<0.01	<0.05	<0.11	0.00	0.02	9.12	9.29	10.19	1.79

Table A10.7: LA-ICPMS of pyrite from DDH86WRL1

Sample	**Bottom of interval (m)**	**Top of interval (m)**	Major geologic unit	Mn55 (ppm)	Fe57 (ppm)	Co59 (ppm)	Ni60 (ppm)	Cu65 (ppm)	Zn66 (ppm)	As75 (ppm)	Se77 (ppm)	Mo95 (ppm)
DG44	603.03	602.78	Jeerinah	15.64	465553	154.87	242.62	<0.22	0.57	1.09	45.93	0.01
DG44	603.03	602.78	Jeerinah	<0.46	465553	154.67	218.57	<0.22	0.86	1.20	40.75	0.01
DG44	603.03	602.78	Jeerinah	5.08	465553	181.61	291.60	<0.22	0.86	1.31	60.61	0.01
DG44	603.03	602.78	Jeerinah	8.41	465553	158.94	228.78	0.43	0.74	0.98	61.80	<0.01
DG43	651.95	651.8	Jeerinah	3.04	465553	140.84	1162.79	0.87	0.29	1.23	12.89	<0.04
DG43	651.95	651.8	Jeerinah	<1.52	465553	150.77	1248.43	0.83	0.32	1.16	14.51	2.14
DG43	651.95	651.8	Jeerinah	<1.52	465553	133.50	1146.03	<0.38	0.28	1.16	11.25	0.11
DG43	651.95	651.8	Jeerinah	43.75	465553	126.48	1063.78	4.02	83.26	1.50	13.44	1.49
DG43	651.95	651.8	Jeerinah	129.35	465553	131.91	1121.77	3.30	0.79	1.57	11.04	0.40
DG43	651.95	651.8	Jeerinah	23.42	465553	128.35	1118.04	4.96	116.74	1.59	11.44	0.61
DG43	651.95	651.8	Jeerinah	13.19	465553	141.52	1152.32	1.00	0.68	1.09	12.40	0.07
DG43	651.95	651.8	Jeerinah	53.71	465553	130.41	1051.54	2.96	119.03	1.48	11.98	0.68
DG43	651.95	651.8	Jeerinah	45.42	465553	119.79	1061.79	4.46	99.18	1.70	10.20	1.17
DG43	651.95	651.8	Jeerinah	3.44	465553	136.35	1115.08	0.76	1.49	1.39	10.68	<0.04
DG43	651.95	651.8	Jeerinah	11.27	465552	124.68	1063.66	4.56	77.07	3.12	9.55	1.45

Table A10.7: LA-ICPMS of pyrite from DDH86WRL1

Sample	Ag107 (ppm)	Cd111 (ppm)	Sb121 (ppm)	Te125 (ppm)	Au197 (ppm)	Tl205 (ppm)	Pb206 (ppm)	Pb207 (ppm)	Pb208 (ppm)	Bi209 (ppm)
DG44	1.75	<0.01	<0.05	0.40	<0.01	0.03	18.88	21.30	27.52	3.85
DG44	1.00	<0.01	<0.05	<0.11	<0.01	0.01	6.00	6.23	6.10	2.66
DG44	1.38	0.09	0.22	0.42	<0.01	0.16	159.88	169.95	169.13	2.74
DG44	1.52	0.05	<0.05	0.23	<0.01	0.35	17.35	14.25	13.49	0.10
DG43	0.94	<0.02	0.42	0.23	0.01	0.96	18.75	14.21	15.02	1.20
DG43	1.24	0.08	0.51	<0.09	0.01	1.33	24.40	21.53	21.48	1.81
DG43	0.51	<0.02	<0.21	0.22	<0.01	0.23	9.53	7.52	7.47	0.98
DG43	2.74	<0.02	11.66	2.79	0.03	19.85	133.02	127.58	127.40	4.73
DG43	3.45	0.05	2.53	<0.09	0.02	37.08	40.17	35.89	33.85	2.42
DG43	3.55	0.09	14.10	3.89	0.03	26.33	161.82	154.36	151.05	5.34
DG43	1.41	0.12	1.04	0.23	<0.01	10.88	17.85	14.83	14.20	1.19
DG43	2.73	<0.02	8.13	2.35	0.02	17.94	99.12	89.72	89.83	3.69
DG43	3.03	<0.02	12.44	3.34	0.04	16.78	126.30	120.50	120.45	3.86
DG43	0.42	<0.02	0.46	0.18	<0.01	3.40	4.85	4.21	4.27	0.25
DG43	2.89	0.04	11.37	2.73	0.06	14.25	128.92	122.21	123.43	4.62

Table A10.7: LA-ICPMS of pyrite from DDH86WRL1												
Sample	**Bottom of interval (m)**	**Top of interval (m)**	Major geologic unit	Mn55 (ppm)	Fe57 (ppm)	Co59 (ppm)	Ni60 (ppm)	Cu65 (ppm)	Zn66 (ppm)	As75 (ppm)	Se77 (ppm)	Mo95 (ppm)
DG43	651.95	651.8	Jeerinah	46.65	465553	146.59	1229.19	5.17	138.72	2.13	12.31	1.22
DG43	651.95	651.8	Jeerinah	12.20	465553	140.01	1206.72	4.31	50.32	1.17	11.92	0.55
DG43	651.95	651.8	Jeerinah	284.65	465553	113.87	962.98	4.35	170.31	1.86	8.81	1.25
DG43	651.95	651.8	Jeerinah	23.15	465553	137.79	1212.66	2.79	24.08	0.76	11.07	0.20
DG43	651.95	651.8	Jeerinah	10.30	465553	137.27	1333.21	2.63	14.62	1.14	9.66	0.24
DG43	651.95	651.8	Jeerinah	75.74	465553	132.15	1150.07	3.81	30.73	1.54	9.77	0.74
DG43	651.95	651.8	Jeerinah	23.85	465553	133.48	1300.06	3.07	12.45	1.11	12.51	0.29
DG43	651.95	651.8	Jeerinah	27.40	465553	153.52	1216.25	1.50	25.29	1.10	10.45	0.10
DG42	681.38	681.2	Jeerinah	6.30	465467	242.00	821.60	233.24	19.28	323.24	8.28	2.39
DG42	681.38	681.2	Jeerinah	8.21	465482	192.19	638.80	204.43	59.71	268.51	6.58	2.69
DG42	681.38	681.2	Jeerinah	3.42	465470	243.40	787.92	201.76	23.29	312.39	7.73	2.71
DG42	681.38	681.2	Jeerinah	2.04	465491	158.43	443.70	482.94	122.09	233.14	6.41	4.21
DG42	681.38	681.2	Jeerinah	1.10	465468	229.05	708.39	219.07	76.55	319.98	8.86	3.53
DG42	681.38	681.2	Jeerinah	7.58	465434	331.83	1132.15	319.03	3.11	444.91	9.57	2.20
DG42	681.38	681.2	Jeerinah	4.89	465467	236.85	846.11	259.46	5.53	321.39	8.20	2.53

Table A10.7: LA-ICPMS of pyrite from DDH86WRL1

Sample	Ag107 (ppm)	Cd111 (ppm)	Sb121 (ppm)	Te125 (ppm)	Au197 (ppm)	Tl205 (ppm)	Pb206 (ppm)	Pb207 (ppm)	Pb208 (ppm)	Bi209 (ppm)
DG43	3.62	<0.02	12.86	3.40	0.03	17.33	161.36	146.15	145.53	5.75
DG43	3.40	<0.02	11.08	2.64	0.02	19.96	136.02	129.03	122.27	5.30
DG43	3.16	0.92	10.65	2.12	0.03	17.36	120.78	112.01	111.01	4.52
DG43	1.60	0.12	1.40	0.32	0.01	9.30	24.11	15.74	17.02	0.86
DG43	1.86	<0.02	2.19	0.49	0.01	10.24	39.05	24.72	27.06	0.96
DG43	2.34	<0.02	1.56	0.44	<0.01	11.86	23.87	15.39	15.95	0.68
DG43	1.72	0.04	1.23	<0.09	0.01	11.65	18.27	11.66	12.21	0.53
DG43	1.33	<0.02	0.46	<0.09	<0.01	9.03	7.97	4.68	5.12	0.25
DG42	7.90	0.26	56.44	14.91	0.08	12.13	254.73	287.99	279.11	7.20
DG42	6.57	0.43	42.83	11.07	0.05	11.47	190.14	217.88	210.38	5.53
DG42	7.26	0.24	52.34	13.30	0.07	15.12	221.86	258.84	247.48	6.57
DG42	5.56	0.56	38.25	10.88	0.05	9.48	224.01	255.01	250.22	5.67
DG42	7.05	0.43	51.54	12.76	0.07	13.86	235.54	264.16	255.97	6.61
DG42	9.77	0.20	86.17	21.85	0.11	11.03	431.36	484.24	472.99	10.76
DG42	7.48	0.19	52.07	13.63	0.07	13.24	224.98	256.19	249.08	6.43

Table A10.7: LA-ICPMS of pyrite from DDH86WRL1												
Sample	**Bottom of interval (m)**	**Top of interval (m)**	Major geologic unit	Mn55 (ppm)	Fe57 (ppm)	Co59 (ppm)	Ni60 (ppm)	Cu65 (ppm)	Zn66 (ppm)	As75 (ppm)	Se77 (ppm)	Mo95 (ppm)
DG42	681.38	681.2	Jeerinah	31.28	465444	334.40	990.49	246.73	1.18	407.53	9.01	3.59
DG42	681.38	681.2	Jeerinah	17.76	465456	321.94	907.85	279.81	32.38	362.51	8.73	3.20
DG42	681.38	681.2	Jeerinah	9.06	465508	171.62	447.48	125.65	16.52	169.28	8.97	1.89
DG42	681.38	681.2	Jeerinah	153.28	465497	235.16	488.47	119.47	53.50	210.57	11.26	1.99
DG42	681.38	681.2	Jeerinah	5.54	465492	197.46	544.24	182.84	67.93	230.02	7.63	2.28
DG42	681.38	681.2	Jeerinah	9.05	465512	145.68	367.32	122.32	34.77	152.79	4.79	1.41
DG42	681.38	681.2	Jeerinah	3.87	465478	242.93	657.78	180.14	36.81	283.30	11.11	3.40
DG42	681.38	681.2	Jeerinah	4487.83	465478	181.71	372.42	88.45	9.20	283.06	14.17	1.75
DG42	681.38	681.2	Jeerinah	108.95	465493	229.70	607.44	171.55	96.80	226.27	10.22	1.22
DG42	681.38	681.2	Jeerinah	1535.96	465486	205.68	521.02	222.52	38.05	250.93	10.61	0.89
DG42	681.38	681.2	Jeerinah	52.36	465511	184.84	353.53	176.49	372.26	159.35	5.38	1.48
DG41	688.18	688	Jeerinah	39.57	465553	174.87	419.81	2.41	173.51	0.80	17.52	35.41
DG41	688.18	688	Jeerinah	10.35	465553	180.64	448.79	2.45	50.04	0.76	16.80	62.44
DG41	688.18	688	Jeerinah	412.71	465553	227.39	437.26	1.16	305.87	1.71	16.46	60.88
DG41	688.18	688	Jeerinah	53.83	465553	177.53	372.97	2.33	314.74	1.12	17.31	130.39

Table A10.7: LA-ICPMS of pyrite from DDH86WRL1

Sample	Ag107 (ppm)	Cd111 (ppm)	Sb121 (ppm)	Te125 (ppm)	Au197 (ppm)	Tl205 (ppm)	Pb206 (ppm)	Pb207 (ppm)	Pb208 (ppm)	Bi209 (ppm)
DG42	8.33	0.35	72.88	18.22	0.08	19.02	317.14	366.12	355.70	9.36
DG42	7.87	0.21	58.78	14.22	0.06	16.00	244.81	285.84	273.90	7.05
DG42	3.69	0.22	26.85	6.23	0.04	3.89	124.93	144.39	146.32	3.64
DG42	4.37	0.37	37.02	8.58	0.06	3.07	210.86	249.85	231.19	5.24
DG42	5.81	0.44	37.88	8.81	0.06	7.18	171.89	193.10	183.54	5.00
DG42	3.91	0.21	26.54	6.41	0.05	3.10	134.68	154.45	146.07	3.80
DG42	5.95	0.32	37.25	8.70	0.05	13.71	152.24	176.98	171.23	4.62
DG42	2.92	0.11	28.05	5.75	0.03	1.94	186.32	218.03	214.37	3.48
DG42	5.33	0.33	48.56	11.79	0.05	2.91	257.56	293.90	283.53	6.63
DG42	3.80	0.19	37.65	8.23	0.05	2.65	216.05	245.10	239.32	5.17
DG42	4.14	1.50	28.86	6.95	0.06	2.68	159.86	175.10	171.57	3.98
DG41	1.52	0.67	0.40	5.00	0.07	1.05	84.90	88.85	85.55	12.23
DG41	1.39	0.21	0.32	3.78	0.01	1.10	64.71	68.17	70.80	11.99
DG41	0.58	0.58	<0.07	1.85	<0.01	0.55	28.56	27.25	27.66	5.40
DG41	1.75	1.44	0.41	4.71	0.04	1.03	70.34	70.20	72.10	11.93

Table A10.7: LA-ICPMS of pyrite from DDH86WRL1												
Sample	**Bottom of interval (m)**	**Top of interval (m)**	Major geologic unit	Mn55 (ppm)	Fe57 (ppm)	Co59 (ppm)	Ni60 (ppm)	Cu65 (ppm)	Zn66 (ppm)	As75 (ppm)	Se77 (ppm)	Mo95 (ppm)
DG41	688.18	688	Jeerinah	528.19	465553	182.73	384.73	2.30	1.08	1.13	17.28	3.52
DG41	688.18	688	Jeerinah	3.29	465553	183.23	431.59	2.47	0.64	0.99	19.49	2.43
DG41	688.18	688	Jeerinah	1.78	465553	201.09	445.92	1.67	0.09	1.07	20.77	1.54
DG41	688.18	688	Jeerinah	1.42	465553	175.52	434.37	2.41	0.36	1.37	18.53	1.68
DG41	688.18	688	Jeerinah	108.08	465553	193.47	404.75	0.75	83.60	1.05	15.16	2.39
DG41	688.18	688	Jeerinah	6.11	465553	191.65	404.93	<0.37	21.22	0.97	16.69	0.06
DG41	688.18	688	Jeerinah	4.84	465553	184.79	427.17	3.56	447.18	0.96	17.74	2.64
DG41	688.18	688	Jeerinah	42.00	465553	185.43	379.13	1.39	82.78	1.21	16.37	0.61
DG41	688.18	688	Jeerinah	15.52	465553	177.82	447.60	3.52	551.42	0.93	17.67	1.30
DG41	688.18	688	Jeerinah	2.94	465553	195.74	452.50	<0.37	1.86	1.27	17.64	0.06
DG41	688.18	688	Jeerinah	26.05	465553	183.11	435.21	1.52	364.47	0.79	16.53	0.30
DG41	688.18	688	Jeerinah	24.23	465553	201.42	421.31	0.84	74.21	0.84	16.27	0.04
DG41	688.18	688	Jeerinah	5.95	465553	195.21	408.50	0.92	8.88	0.87	13.62	0.05
DG41	688.18	688	Jeerinah	20.67	465553	184.96	416.86	0.91	41.27	1.17	14.74	0.06
DG41	688.18	688	Jeerinah	67.26	465553	194.36	426.41	1.08	147.60	1.08	17.33	0.29

Table A10.7: LA-ICPMS of pyrite from DDH86WRL1

Sample	Ag107 (ppm)	Cd111 (ppm)	Sb121 (ppm)	Te125 (ppm)	Au197 (ppm)	Tl205 (ppm)	Pb206 (ppm)	Pb207 (ppm)	Pb208 (ppm)	Bi209 (ppm)
DG41	1.97	0.02	0.39	6.29	0.04	0.61	111.37	125.44	120.96	14.50
DG41	1.81	0.04	0.47	6.20	0.04	0.69	104.90	125.89	107.43	14.12
DG41	1.09	0.04	0.24	4.27	0.03	0.39	68.71	74.69	70.94	8.27
DG41	1.73	0.01	0.41	5.44	0.03	0.57	99.96	112.71	108.55	13.00
DG41	0.58	0.27	0.17	1.43	0.01	0.35	25.58	28.99	26.88	4.52
DG41	0.22	0.49	<0.07	0.86	<0.01	0.16	14.14	15.57	15.88	2.77
DG41	1.20	1.53	0.30	3.64	0.02	1.05	68.57	68.58	70.05	11.29
DG41	0.62	0.33	<0.07	1.81	0.02	0.41	28.88	29.43	30.98	4.94
DG41	1.32	2.52	0.85	4.04	0.02	1.37	75.55	71.50	74.16	12.10
DG41	0.22	<0.01	<0.07	0.84	0.02	0.15	14.49	14.28	15.30	1.82
DG41	0.59	1.67	0.14	1.55	0.02	0.42	32.49	32.90	32.11	5.55
DG41	0.55	0.36	0.17	1.95	0.01	0.43	32.13	31.98	29.53	4.50
DG41	0.47	0.20	<0.07	1.22	<0.01	0.21	25.11	28.05	27.41	3.94
DG41	0.23	0.22	<0.07	0.75	<0.01	0.17	16.88	15.65	18.02	2.57
DG41	0.55	0.87	0.20	1.43	0.01	0.47	36.36	36.08	36.05	5.28

Table A10.7: LA-ICPMS of pyrite from DDH86WRL1

Sample	**Bottom of interval (m)**	**Top of interval (m)**	Major geologic unit	Mn55 (ppm)	Fe57 (ppm)	Co59 (ppm)	Ni60 (ppm)	Cu65 (ppm)	Zn66 (ppm)	As75 (ppm)	Se77 (ppm)	Mo95 (ppm)
DG41	688.18	688	Jeerinah	27.71	465553	214.78	467.07	1.74	88.95	1.18	19.44	2.39
DG40	707.55	707.37	Jeerinah	20.04	465309	294.78	488.82	393.26	13.51	913.44	23.20	9.77
DG40	707.55	707.37	Jeerinah	17.66	465139	342.73	901.24	578.61	18.92	1551.39	29.27	14.81
DG40	707.55	707.37	Jeerinah	51.46	465391	229.76	426.48	371.83	9.13	606.85	16.75	10.36
DG40	707.55	707.37	Jeerinah	26.03	465277	328.53	734.25	5958.49	22.34	1033.23	24.94	61.33
DG40	707.55	707.37	Jeerinah	8.46	465372	193.83	534.78	360.14	2.45	678.02	18.97	9.65
DG40	707.55	707.37	Jeerinah	8.21	465507	229.20	416.90	295.15	3.37	171.85	32.31	5.19
DG40	707.55	707.37	Jeerinah	9.64	465498	302.17	566.00	409.09	3.14	208.18	35.50	4.34
DG40	707.55	707.37	Jeerinah	4.61	465184	435.11	783.10	506.84	1.82	1381.90	28.58	8.56
DG40	707.55	707.37	Jeerinah	6.88	465162	307.84	679.89	537.47	1.00	1464.87	28.27	15.16
DG40	707.55	707.37	Jeerinah	6.33	465320	210.96	451.70	391.60	0.04	872.25	18.44	8.42
DG40	707.55	707.37	Jeerinah	10.72	465523	356.59	340.51	849.55	407.15	113.95	17.25	1.06
DG40	707.55	707.37	Jeerinah	13.26	465334	166.21	362.25	507.38	50.88	820.16	14.10	1.88
DG40	707.55	707.37	Jeerinah	20.35	465492	162.29	244.68	655.62	476.40	229.06	10.79	0.58
DG40	707.55	707.37	Jeerinah	13.00	465501	405.12	694.78	743.95	85.05	196.19	18.09	0.80

Table A10.7: LA-ICPMS of pyrite from DDH86WRL1

Sample	Ag107 (ppm)	Cd111 (ppm)	Sb121 (ppm)	Te125 (ppm)	Au197 (ppm)	Tl205 (ppm)	Pb206 (ppm)	Pb207 (ppm)	Pb208 (ppm)	Bi209 (ppm)
DG41	0.94	1.42	0.32	2.32	0.03	0.73	71.96	68.37	67.48	7.74
DG40	1.73	0.18	19.32	4.29	0.02	2.25	283.53	319.90	298.66	4.98
DG40	2.74	0.31	26.08	6.65	0.03	2.89	393.54	432.92	418.28	7.13
DG40	1.67	0.43	20.99	4.03	0.01	2.49	293.27	327.09	311.08	5.41
DG40	2.36	0.53	26.03	5.94	0.03	3.39	336.00	377.56	360.82	6.04
DG40	1.76	0.37	20.47	4.24	0.03	2.81	285.51	318.36	306.35	4.68
DG40	2.88	0.20	13.01	5.62	0.03	51.89	172.17	206.83	190.58	3.22
DG40	4.17	0.25	20.10	8.38	0.06	61.82	272.93	315.41	300.05	5.13
DG40	3.81	0.31	29.24	7.72	0.03	3.42	417.89	463.39	444.91	7.50
DG40	2.88	0.28	26.67	7.01	0.03	3.14	370.66	422.83	399.03	7.49
DG40	2.09	0.28	23.93	5.65	0.03	3.43	305.10	343.33	335.62	5.99
DG40	2.72	0.87	10.28	3.65	0.03	9.64	106.49	121.54	118.04	2.17
DG40	2.00	0.16	9.10	2.96	0.02	11.16	112.83	128.52	129.25	2.19
DG40	3.05	1.16	11.90	3.81	0.04	7.37	151.40	170.96	163.58	2.81
DG40	5.24	0.35	29.62	10.76	0.05	6.34	291.39	334.72	312.74	6.38

Table A10.7: LA-ICPMS of pyrite from DDH86WRL1

Sample	**Bottom of interval (m)**	**Top of interval (m)**	Major geologic unit	Mn55 (ppm)	Fe57 (ppm)	Co59 (ppm)	Ni60 (ppm)	Cu65 (ppm)	Zn66 (ppm)	As75 (ppm)	Se77 (ppm)	Mo95 (ppm)
DG40	707.55	707.37	Jeerinah	21.28	465500	393.57	771.51	752.06	70.80	198.33	20.75	0.82
DG40	707.55	707.37	Jeerinah	7.84	464798	559.08	1201.48	754.16	19.95	2828.31	48.62	24.16
DG40	707.55	707.37	Jeerinah	1.19	464851	528.22	1007.50	872.29	8.43	2630.62	47.71	21.01
DG40	707.55	707.37	Jeerinah	0.97	464655	723.53	1234.40	890.56	11.96	3365.53	52.85	38.86
DG40	707.55	707.37	Jeerinah	0.54	464669	637.10	1278.68	852.60	9.19	3312.42	52.75	32.03
DG40	707.55	707.37	Jeerinah	2.90	464765	611.27	1291.65	789.97	32.41	2951.29	45.95	22.81
DG39	720.09	719.87	Jeerinah	4.36	465443	738.78	2418.31	410.27	3.05	412.83	11.71	0.34
DG39	720.09	719.87	Jeerinah	8.80	465452	641.11	2505.64	383.70	3.11	378.67	12.25	0.48
DG39	720.09	719.87	Jeerinah	5.46	465448	763.72	1969.30	344.18	392.65	395.46	13.79	0.61
DG39	720.09	719.87	Jeerinah	2.98	465492	548.87	895.31	179.38	3.89	228.31	7.29	0.65
DG39	720.09	719.87	Jeerinah	15.57	465456	674.29	2157.79	352.18	6.36	364.06	9.56	0.35
DG39	720.09	719.87	Jeerinah	753.75	465443	166.34	229.43	102.38	4.97	411.51	7.56	0.58
DG39	720.09	719.87	Jeerinah	15.64	465533	109.87	224.59	56.19	89.71	74.46	10.52	0.20
DG39	720.09	719.87	Jeerinah	4.84	465475	1191.87	1193.78	137.27	20.56	293.81	10.04	0.75
DG39	720.09	719.87	Jeerinah	4.82	465472	1302.71	1082.37	121.79	256.45	304.33	11.72	0.86

Table A10.7: LA-ICPMS of pyrite from DDH86WRL1

Sample	Ag107 (ppm)	Cd111 (ppm)	Sb121 (ppm)	Te125 (ppm)	Au197 (ppm)	Tl205 (ppm)	Pb206 (ppm)	Pb207 (ppm)	Pb208 (ppm)	Bi209 (ppm)
DG40	5.53	0.47	37.11	13.11	0.07	3.00	386.87	454.95	414.13	8.21
DG40	5.28	0.38	36.34	10.77	0.08	3.54	551.23	621.97	599.39	10.21
DG40	5.55	0.38	36.82	11.67	0.08	3.12	540.38	599.92	573.64	10.17
DG40	8.82	0.41	43.41	15.17	0.11	3.66	693.16	774.30	740.25	12.24
DG40	6.96	0.61	42.52	14.18	0.10	3.95	646.77	719.60	698.70	11.87
DG40	6.83	0.57	44.82	12.60	0.09	4.58	654.23	730.80	699.14	12.30
DG39	7.56	0.19	49.81	13.37	0.13	14.44	871.85	977.84	953.29	6.79
DG39	8.83	0.25	53.28	16.19	0.15	12.58	982.18	1111.25	1061.34	7.48
DG39	7.20	2.00	43.45	11.48	0.13	14.47	736.82	835.47	805.80	6.12
DG39	3.26	0.15	18.36	1.77	0.07	12.58	281.71	317.04	300.48	2.53
DG39	8.14	0.18	52.60	15.25	0.17	10.43	937.15	1058.38	1020.56	7.65
DG39	0.86	0.11	12.59	0.70	0.01	2.13	269.64	301.10	285.78	0.72
DG39	1.46	0.35	6.93	1.26	0.02	12.55	117.22	126.60	123.77	1.26
DG39	4.20	0.14	25.01	5.58	0.06	8.69	353.55	391.81	378.34	3.28
DG39	4.02	0.52	22.88	5.12	0.05	8.04	321.91	370.21	349.33	3.05

Table A10.7: LA-ICPMS of pyrite from DDH86WRL1

Sample	**Bottom of interval (m)**	**Top of interval (m)**	Major geologic unit	Mn55 (ppm)	Fe57 (ppm)	Co59 (ppm)	Ni60 (ppm)	Cu65 (ppm)	Zn66 (ppm)	As75 (ppm)	Se77 (ppm)	Mo95 (ppm)
DG39	720.09	719.87	Jeerinah	6.37	465471	975.41	1257.69	162.02	600.77	308.14	10.31	0.85
DG39	720.09	719.87	Jeerinah	4.75	465462	1321.24	1251.06	128.05	52.99	340.94	19.93	1.27
DG39	720.09	719.87	Jeerinah	1393.36	465507	410.73	1956.77	164.24	103.05	172.15	17.46	0.47
DG39	720.09	719.87	Jeerinah	6.99	465521	778.40	1090.76	61.96	447.67	120.30	21.04	0.17
DG39	720.09	719.87	Jeerinah	4.76	465526	377.31	2899.73	86.37	215.80	102.76	24.65	0.24
DG39	720.09	719.87	Jeerinah	35.53	465517	602.33	1155.39	68.48	13.79	137.01	20.15	0.38
DG38	729.91	729.72	Jeerinah	239.08	465473	271.61	261.28	74.98	48.88	301.14	3.77	1.87
DG38	729.91	729.72	Jeerinah	15.26	465469	303.20	293.83	82.27	16.40	316.37	3.28	1.82
DG38	729.91	729.72	Jeerinah	36.97	465476	313.59	274.68	79.55	4.73	290.66	2.88	1.70
DG38	729.91	729.72	Jeerinah	35.80	465466	308.48	295.32	90.73	47.78	326.47	2.67	1.12
DG38	729.91	729.72	Jeerinah	14.40	465432	216.93	489.57	144.76	2.22	455.91	2.47	3.22
DG38	729.91	729.72	Jeerinah	11.15	465435	157.63	408.77	116.86	2.51	442.76	2.07	3.60
DG38	729.91	729.72	Jeerinah	16.70	465376	254.27	597.44	159.75	2.14	664.23	3.09	3.28
DG38	729.91	729.72	Jeerinah	281.50	465390	421.44	627.21	180.96	33.70	613.05	9.98	2.54
DG38	729.91	729.72	Jeerinah	2089.35	465400	396.50	582.16	164.49	18.28	574.06	6.68	2.51

Table A10.7: LA-ICPMS of pyrite from DDH86WRL1

Sample	Ag107 (ppm)	Cd111 (ppm)	Sb121 (ppm)	Te125 (ppm)	Au197 (ppm)	Tl205 (ppm)	Pb206 (ppm)	Pb207 (ppm)	Pb208 (ppm)	Bi209 (ppm)
DG39	4.93	1.38	26.66	5.80	0.07	9.85	339.12	381.10	358.04	3.35
DG39	4.02	0.14	24.40	4.67	0.06	7.35	361.13	395.81	380.93	3.18
DG39	3.83	0.40	27.62	5.19	0.05	6.58	471.95	522.81	496.93	2.78
DG39	2.68	1.04	17.12	2.20	0.05	2.86	332.33	374.81	349.00	1.59
DG39	2.30	0.45	17.56	2.82	0.03	2.47	332.05	364.07	347.75	1.90
DG39	2.93	<0.05	15.96	1.78	0.06	3.01	349.27	378.66	369.96	1.31
DG38	1.82	0.32	45.25	1.78	0.02	5.21	280.53	307.42	302.34	3.48
DG38	2.11	0.26	50.83	2.27	0.02	5.59	325.04	360.38	347.54	3.83
DG38	2.21	0.20	50.36	2.15	0.03	4.53	320.02	356.60	341.30	3.93
DG38	2.24	0.44	51.76	1.90	0.03	3.79	323.43	360.43	359.81	3.83
DG38	1.58	0.30	52.39	2.00	0.04	9.01	314.16	368.10	351.03	4.53
DG38	1.32	0.20	51.47	2.10	0.04	11.31	259.90	298.51	291.98	3.75
DG38	1.73	0.34	80.94	4.06	0.06	13.31	451.66	507.47	493.83	5.86
DG38	2.11	0.34	84.34	3.28	0.03	11.52	356.89	395.57	385.85	5.08
DG38	2.09	0.30	74.46	2.69	0.02	11.33	333.15	371.21	359.74	4.46

Table A10.7: LA-ICPMS of pyrite from DDH86WRL1												
Sample	**Bottom of interval (m)**	**Top of interval (m)**	Major geologic unit	Mn55 (ppm)	Fe57 (ppm)	Co59 (ppm)	Ni60 (ppm)	Cu65 (ppm)	Zn66 (ppm)	As75 (ppm)	Se77 (ppm)	Mo95 (ppm)
DG38	729.91	729.72	Jeerinah	30.89	465460	319.25	469.77	827.14	289.30	349.29	6.78	1.54
DG38	729.91	729.72	Jeerinah	2.11	465463	198.73	258.27	155.30	8.42	337.49	2.47	1.21
DG38	729.91	729.72	Jeerinah	12.23	465390	268.87	936.48	266.13	205.60	610.74	8.65	1.63
DG38	729.91	729.72	Jeerinah	14.43	465425	471.60	542.19	410.77	52.38	481.57	5.23	2.04
DG38	729.91	729.72	Jeerinah	288.23	465399	402.88	589.40	194.26	33.94	578.48	5.24	2.21
DG38	729.91	729.72	Jeerinah	6.16	465451	363.83	510.91	435.71	351.39	382.51	7.27	1.63
DG38	729.91	729.72	Jeerinah	63.00	465480	302.87	443.76	527.50	204.63	273.11	7.15	1.37
DG38	729.91	729.72	Jeerinah	50.04	465477	227.66	248.31	83.92	7.38	285.73	2.57	1.23
DG38	729.91	729.72	Jeerinah	25.91	465473	280.73	264.04	80.26	9.10	301.12	2.60	1.51
DG38	729.91	729.72	Jeerinah	20.00	465459	252.76	220.47	105.23	22.16	354.72	2.67	1.14
DG47	743.18	742.92	Jeerinah	11.11	465553	380.31	4114.34	0.90	<0.01	0.72	36.85	0.14
DG47	743.18	742.92	Jeerinah	1.37	465553	324.94	3746.73	1.12	0.00	0.94	32.17	1.95
DG47	743.18	742.92	Jeerinah	8.73	465553	344.00	3958.52	<0.41	<0.01	0.71	30.66	0.76
DG47	743.18	742.92	Jeerinah	10.24	465553	241.49	3735.05	<0.41	0.68	0.89	31.10	0.55
DG47	743.18	742.92	Jeerinah	17.35	465553	312.72	3883.84	1.05	0.73	0.96	31.79	0.13

Table A10.7: LA-ICPMS of pyrite from DDH86WRL1

Sample	Ag107 (ppm)	Cd111 (ppm)	Sb121 (ppm)	Te125 (ppm)	Au197 (ppm)	Tl205 (ppm)	Pb206 (ppm)	Pb207 (ppm)	Pb208 (ppm)	Bi209 (ppm)
DG38	1.71	10.01	55.17	2.26	0.03	6.67	276.80	311.16	301.74	3.30
DG38	1.17	0.24	31.07	0.85	0.01	9.84	172.36	189.98	185.16	1.90
DG38	2.46	1.49	89.55	3.79	0.04	15.08	402.06	460.49	441.93	5.38
DG38	1.98	0.45	67.33	2.75	0.03	9.33	294.95	343.19	325.40	4.12
DG38	2.05	0.23	80.23	3.17	0.03	9.64	358.96	399.58	385.41	4.95
DG38	1.71	1.92	59.91	2.11	0.02	6.25	271.82	305.09	291.98	3.49
DG38	1.54	1.21	50.03	1.44	0.02	5.05	272.20	308.47	298.74	2.99
DG38	2.12	0.10	47.62	2.00	0.03	3.67	322.67	350.00	344.35	3.70
DG38	1.99	0.14	50.45	1.87	0.02	4.11	308.98	345.98	336.89	3.70
DG38	1.43	0.23	39.15	1.14	0.02	3.73	268.32	289.48	284.47	2.84
DG47	0.58	<0.01	10.40	1.57	<0.01	0.37	20.40	20.87	21.15	3.24
DG47	0.70	0.05	14.35	1.93	<0.01	0.81	29.25	29.78	33.44	4.63
DG47	0.77	<0.01	8.04	1.39	<0.01	0.31	20.30	15.57	16.23	2.73
DG47	0.39	0.03	47.34	13.69	<0.01	0.42	8.94	8.68	8.70	2.23
DG47	0.29	<0.01	4.80	0.95	<0.01	0.13	10.17	10.02	10.34	1.83

Table A10.7: LA-ICPMS of pyrite from DDH86WRL1												
Sample	**Bottom of interval (m)**	**Top of interval (m)**	Major geologic unit	Mn55 (ppm)	Fe57 (ppm)	Co59 (ppm)	Ni60 (ppm)	Cu65 (ppm)	Zn66 (ppm)	As75 (ppm)	Se77 (ppm)	Mo95 (ppm)
DG47	743.18	742.92	Jeerinah	13.97	465553	617.50	4110.14	0.99	1.17	0.84	25.37	0.09
DG47	743.18	742.92	Jeerinah	9.21	465553	320.64	3863.52	<0.41	0.78	0.99	26.74	<0.05
DG47	743.18	742.92	Jeerinah	9.49	465553	583.73	4361.61	1.03	<0.01	0.70	27.00	0.20
DG47	743.18	742.92	Jeerinah	3.11	465553	390.12	3997.06	0.88	0.20	1.01	29.41	0.62
DG47	743.18	742.92	Jeerinah	14.35	465553	243.01	3581.16	1.23	0.85	1.02	26.37	1.02
DG47	743.18	742.92	Jeerinah	13.43	465553	462.86	4100.00	0.93	1.15	0.76	35.21	0.09
DG47	743.18	742.92	Jeerinah	10.61	465553	279.59	3602.57	1.26	<0.01	0.69	27.45	0.28
DG47	743.18	742.92	Jeerinah	32.27	465553	341.47	3781.44	0.83	2.09	0.79	33.87	<0.05
DG47	743.18	742.92	Jeerinah	90.02	465553	462.41	4110.76	1.01	7.07	0.82	35.58	1.80
DG47	743.18	742.92	Jeerinah	53.12	465553	456.72	3939.51	1.01	4.29	0.65	43.10	0.10
DG47	743.18	742.92	Jeerinah	21.83	465553	388.18	3740.33	1.02	1.17	0.79	31.82	0.50
DG47	743.18	742.92	Jeerinah	37.29	465553	398.99	3791.43	1.28	2.53	1.00	34.89	0.12
DG47	743.18	742.92	Jeerinah	11.42	465553	512.23	3887.22	0.83	1.25	0.78	35.36	3.79
DG47	743.18	742.92	Jeerinah	292.93	465497	16.40	329.12	155.16	50.49	209.67	32.62	80.08
DG37	746.81	746.66	Jeerinah	52.35	446722	35439.78	8632.76	50.42	381.46	70550.62	778.55	<10.11

Table A10.7: LA-ICPMS of pyrite from DDH86WRL1

Sample	Ag107 (ppm)	Cd111 (ppm)	Sb121 (ppm)	Te125 (ppm)	Au197 (ppm)	Tl205 (ppm)	Pb206 (ppm)	Pb207 (ppm)	Pb208 (ppm)	Bi209 (ppm)
DG47	1.13	0.04	10.53	1.06	<0.01	0.35	20.38	19.51	20.45	2.45
DG47	0.51	0.10	5.98	1.28	<0.01	0.29	12.84	13.48	13.61	2.69
DG47	0.73	<0.01	7.41	1.11	<0.01	0.30	12.85	11.85	13.73	2.37
DG47	0.89	0.03	13.17	13.78	<0.01	0.62	26.20	25.15	27.38	5.04
DG47	0.65	<0.01	8.97	1.38	<0.01	0.30	17.22	17.38	20.49	3.01
DG47	0.34	<0.01	6.28	1.51	<0.01	0.23	11.06	11.54	12.19	1.88
DG47	0.42	0.08	6.49	1.10	0.02	0.21	12.06	13.55	12.11	2.36
DG47	0.33	<0.01	3.84	0.76	0.01	0.09	7.73	7.60	7.95	1.26
DG47	0.88	0.08	11.91	1.63	<0.01	0.49	24.31	25.48	26.75	4.02
DG47	0.77	0.07	12.01	1.93	0.01	0.49	26.49	27.05	30.52	4.32
DG47	0.87	<0.01	15.46	3.05	0.02	1.06	45.45	33.14	37.82	6.67
DG47	0.71	0.05	10.04	2.17	0.02	0.41	30.10	28.85	32.58	7.21
DG47	1.02	<0.01	18.21	2.75	0.02	1.29	47.43	38.19	42.50	8.36
DG47	3.59	8.34	22.92	<0.38	<0.01	29.34	49.29	43.39	43.90	0.30
DG37	406.85	12.30	1227.33	422.27	262.56	0.95	5457.87	5058.48	4435.25	129.03

Table A10.7: LA-ICPMS of pyrite from DDH86WRL1

Sample	**Bottom of interval (m)**	**Top of interval (m)**	Major geologic unit	Mn55 (ppm)	Fe57 (ppm)	Co59 (ppm)	Ni60 (ppm)	Cu65 (ppm)	Zn66 (ppm)	As75 (ppm)	Se77 (ppm)	Mo95 (ppm)
DG37	746.81	746.66	Jeerinah	1236.53	426550	65834.05	14957.15	257.37	860.00	146126.49	1148.29	20.21
DG37	746.81	746.66	Jeerinah	1102.30	463706	1981.69	2101.21	294.21	2638.33	6919.05	612.38	70.62
DG37	746.81	746.66	Jeerinah	180.26	465388	247.35	1218.85	77.02	6922.71	620.17	725.78	543.17
DG37	746.81	746.66	Jeerinah	23.21	462755	4604.43	3759.70	23.60	866.82	10483.40	369.95	182.75
DG37	746.81	746.66	Jeerinah	88.49	452727	20187.82	7073.24	91.40	260.94	48053.38	423.34	217.56

Table A10.7: LA-ICPMS of pyrite from DDH86WRL1

Sample	Ag107 (ppm)	Cd111 (ppm)	Sb121 (ppm)	Te125 (ppm)	Au197 (ppm)	Tl205 (ppm)	Pb206 (ppm)	Pb207 (ppm)	Pb208 (ppm)	Bi209 (ppm)
DG37	218.23	42.51	4529.45	1175.97	89.85	8.11	18863.00	17693.83	16762.52	249.88
DG37	215.52	<6.15	477.68	240.33	12.34	12.22	16388.34	17384.35	13758.00	79.94
DG37	153.91	<6.15	116.81	70.12	4.78	6.10	4820.71	5042.99	4483.49	31.46
DG37	88.98	17.37	244.60	156.01	4.42	1.77	3061.78	3322.70	3021.75	53.35
DG37	278.47	16.46	713.56	367.55	32.01	4.54	9200.85	8919.02	7843.94	109.15

Table A10.8: LA-ICPMS of pyrite from ABDP9

Sample name	Upper limit (m)	Lower limit (m)	S34 (ppm)	Mn55 (ppm)	Fe57 (ppm)	Co59 (ppm)	Ni60 (ppm)	Cu65 (ppm)	Zn66 (ppm)	As75 (ppm)	Se77 (ppm)
DG23	132.77	132.97	565703	486.47	465006	45.88	113.88	98.94	47.28	2048.54	26.74
DG23	132.77	132.97	561701	555.06	465271	52.41	124.82	48.09	38.16	1057.66	22.29
DG23	132.77	132.97	548329	793.75	465255	52.07	128.51	49.17	60.74	1117.79	21.38
DG23	132.77	132.97	542996	565.17	465255	54.08	115.50	50.63	47.19	1116.68	22.01
DG23	132.77	132.97	557886	438.38	465235	55.52	125.25	52.97	29.69	1193.93	21.02
DG23	132.77	132.97	546032	927.85	465230	56.17	121.17	51.98	73.53	1211.19	21.00
DG23	132.77	132.97	563537	864.74	465256	50.69	119.94	51.71	43.88	1113.01	19.85
DG23	132.77	132.97	543426	979.22	465270	51.18	113.04	49.22	76.96	1061.24	20.93
DG23	132.77	132.97	552286	664.42	465255	49.16	129.70	52.87	47.47	1119.17	20.12
DG23	132.77	132.97	577363	517.32	465241	56.11	130.94	51.32	29.40	1169.04	19.88
DG23	132.77	132.97	576963	332.88	465212	54.89	130.62	55.75	13.58	1278.43	22.09
DG23	132.77	132.97	583524	942.64	465277	48.38	129.31	42.00	55.32	1034.89	16.52
DG23	132.77	132.97	571818	542.32	465265	55.06	130.60	54.02	31.64	1078.88	20.81
DG23	132.77	132.97	550762	536.13	465257	58.54	130.58	50.39	21.85	1109.85	22.27
DG23	132.77	132.97	538506	9.43	465498	1.16	15.11	108.03	2.94	208.32	1.29

Table A10.8: LA-ICPMS of pyrite from ABDP9

Sample	Mo95 (ppm)	Ag107 (ppm)	Cd111 (ppm)	Sb121 (ppm)	Te125 (ppm)	Au197 (ppm)	Tl205 (ppm)	Pb206 (ppm)	Pb207 (ppm)	Pb208 (ppm)	Bi209 (ppm)
DG23	6.62	0.31	0.15	14.61	0.72	0.03	2.52	87.24	92.77	86.41	1.54
DG23	7.02	0.32	0.13	15.80	0.65	<0.01	1.78	81.65	84.87	79.91	1.67
DG23	7.91	0.29	0.21	16.12	0.76	<0.01	2.46	87.96	94.60	88.34	1.78
DG23	7.42	0.26	0.22	19.09	0.75	0.02	4.68	106.70	114.00	109.27	1.80
DG23	6.68	0.31	0.18	19.89	0.90	0.04	3.85	93.65	105.07	97.32	1.71
DG23	5.87	0.30	<0.04	19.72	0.93	0.02	3.58	88.58	98.26	95.05	1.78
DG23	10.95	0.36	<0.04	19.21	0.88	<0.01	3.87	97.16	104.85	99.67	1.63
DG23	6.94	0.36	0.14	17.02	1.00	0.04	3.11	84.65	90.18	85.44	1.70
DG23	8.84	0.26	0.12	19.14	1.12	0.02	3.85	97.44	106.76	98.96	1.96
DG23	6.99	0.31	0.17	19.77	1.10	0.05	4.82	94.27	100.96	95.92	2.09
DG23	7.01	0.33	0.11	20.52	0.89	0.03	5.29	98.91	110.71	103.30	1.87
DG23	17.43	0.31	<0.04	19.74	0.93	<0.01	4.30	92.13	102.19	97.46	1.78
DG23	9.60	0.34	<0.04	19.72	0.98	0.03	3.63	95.31	102.97	97.40	1.84
DG23	7.08	0.33	0.21	17.87	0.97	0.03	3.57	91.29	99.70	94.60	1.75
DG23	0.72	0.68	<0.04	8.36	0.35	0.01	0.35	37.19	42.75	41.61	0.92

Table A10.8: LA-ICPMS of pyrite from ABDP9

Sample name	Upper limit (m)	Lower limit (m)	S34 (ppm)	Mn55 (ppm)	Fe57 (ppm)	Co59 (ppm)	Ni60 (ppm)	Cu65 (ppm)	Zn66 (ppm)	As75 (ppm)	Se77 (ppm)
DG23	132.77	132.97	543714	1.69	465453	2.94	28.31	359.59	3.37	374.20	5.01
DG23	132.77	132.97	547674	2.88	465477	2.03	18.76	183.99	3.90	286.37	2.84
DG23	132.77	132.97	558738	0.68	465457	2.11	19.98	228.85	0.62	362.07	3.56
DG23	132.77	132.97	541612	10.93	465414	3.35	27.53	249.42	4.76	522.71	4.43
DG23	132.77	132.97	558987	4.41	465469	1.66	19.03	163.17	1.30	314.14	4.88
DG23	132.77	132.97	549286	4.44	465473	1.09	16.44	193.72	3.51	301.04	1.99
DG23	132.77	132.97	434645	1948.16	464420	93.62	447.85	418.74	15.42	4244.29	20.74
DG23	132.77	132.97	614200	6.75	464895	207.85	606.18	282.57	5.94	2466.32	27.05
DG23	132.77	132.97	655540	790.50	464807	241.82	1141.27	303.36	67.42	2796.75	36.85
DG25	169.07	169.25	514834	3492.44	465456	196.77	463.74	282.30	38.45	363.26	15.57
DG25	169.07	169.25	512958	4383.43	465500	165.28	399.85	234.27	47.72	198.51	13.93
DG25	169.07	169.25	548743	1269.91	465481	189.34	553.17	380.64	49.05	270.40	14.64
DG25	169.07	169.25	548766	2261.79	465478	153.50	395.23	228.48	29.22	280.09	12.59
DG25	169.07	169.25	554142	4388.27	465342	199.07	485.80	321.55	43.11	790.77	14.03
DG25	169.07	169.25	535355	2808.97	465510	156.74	409.72	245.71	41.68	163.84	12.66

Table A10.8: LA-ICPMS of pyrite from ABDP9

Sample	Mo95 (ppm)	Ag107 (ppm)	Cd111 (ppm)	Sb121 (ppm)	Te125 (ppm)	Au197 (ppm)	Tl205 (ppm)	Pb206 (ppm)	Pb207 (ppm)	Pb208 (ppm)	Bi209 (ppm)
DG23	1.00	1.27	<0.04	11.13	0.50	0.03	1.21	46.05	52.38	51.12	1.15
DG23	0.97	0.88	0.14	13.02	0.56	0.02	0.96	68.42	76.21	69.45	1.46
DG23	0.67	1.46	0.14	26.94	0.78	0.05	1.09	115.47	128.91	128.42	1.72
DG23	0.69	1.66	<0.04	40.34	1.15	0.07	2.25	187.02	194.59	187.17	2.41
DG23	0.59	1.72	0.13	29.59	1.04	0.05	1.09	136.86	152.23	152.75	2.38
DG23	0.64	1.26	0.10	21.58	0.71	0.04	1.03	100.96	112.14	106.81	1.64
DG23	4.65	0.68	<0.04	26.78	1.03	<0.01	1.17	181.74	201.55	186.58	2.70
DG23	11.85	1.81	0.08	51.71	4.63	0.04	16.00	320.80	327.98	311.54	10.07
DG23	104.98	2.62	<0.04	47.95	3.03	0.05	6.30	506.28	453.60	434.61	8.42
DG25	3.53	8.52	0.43	70.10	7.16	0.07	6.51	368.49	388.55	356.09	10.86
DG25	3.54	6.64	0.36	65.59	6.87	0.06	5.35	358.40	379.30	353.07	10.86
DG25	3.68	11.52	0.65	86.22	9.73	0.12	7.85	431.40	460.77	424.30	13.08
DG25	3.40	6.78	0.46	68.79	7.79	0.07	5.06	374.66	391.41	364.62	11.65
DG25	6.10	5.50	0.40	65.65	6.13	0.10	4.92	402.47	414.28	387.55	9.95
DG25	3.76	7.20	0.32	71.34	7.48	0.08	5.58	379.18	399.59	370.98	11.69

Table A10.8: LA-ICPMS of pyrite from ABDP9											
Sample name	**Upper limit (m)**	**Lower limit (m)**	**S34 (ppm)**	**Mn55 (ppm)**	**Fe57 (ppm)**	**Co59 (ppm)**	**Ni60 (ppm)**	**Cu65 (ppm)**	**Zn66 (ppm)**	**As75 (ppm)**	**Se77 (ppm)**
DG25	169.07	169.25	517174	3562.51	465435	168.03	415.70	244.14	30.41	442.65	13.63
DG25	169.07	169.25	512763	4593.95	465485	157.09	366.44	207.82	55.93	254.36	12.92
DG25	169.07	169.25	505361	5351.31	465494	133.99	346.50	210.59	75.37	222.32	14.00
DG25	169.07	169.25	518263	3499.16	465477	242.66	425.75	255.14	40.19	284.53	15.03
DG25	169.07	169.25	414275	10499.26	465511	143.66	290.95	179.34	51.47	157.38	14.52
DG25	169.07	169.25	599854	33.64	464777	168.49	416.16	634.89	0.42	2906.85	25.76
DG25	169.07	169.25	538994	241.26	464372	88.02	317.10	578.54	0.66	4424.34	21.78
DG25	169.07	169.25	472025	2678.63	465489	126.47	224.43	164.32	5.71	242.26	11.36
DG25	169.07	169.25	434388	9025.34	465493	35.91	89.98	143.07	30.89	224.33	26.90
DG25	169.07	169.25	514299	182.38	464963	52.41	196.07	249.28	0.86	2212.14	18.43
DG26	186.42	186.69	599451	1280.16	465276	719.62	274.56	207.11	6.64	1039.70	11.52
DG26	186.42	186.69	548122	415.92	465297	430.67	293.50	215.38	1.05	960.38	11.90
DG26	186.42	186.69	547057	2366.47	465291	692.70	850.33	413.27	23.20	981.08	17.41
DG26	186.42	186.69	586475	1078.38	465409	771.17	945.34	472.50	257.60	540.18	20.66
DG26	186.42	186.69	539440	2181.58	465383	178.72	266.84	137.25	1.00	637.26	11.71

Table A10.8: LA-ICPMS of pyrite from ABDP9

Sample	Mo95 (ppm)	Ag107 (ppm)	Cd111 (ppm)	Sb121 (ppm)	Te125 (ppm)	Au197 (ppm)	Tl205 (ppm)	Pb206 (ppm)	Pb207 (ppm)	Pb208 (ppm)	Bi209 (ppm)
DG25	4.90	6.50	0.33	64.38	6.78	0.07	4.48	366.64	386.63	359.76	10.83
DG25	2.81	5.77	0.55	65.51	6.29	0.10	4.00	385.49	400.48	378.60	11.12
DG25	4.35	5.46	0.29	61.97	6.44	0.07	3.97	354.05	367.98	341.10	10.36
DG25	3.49	5.69	0.49	61.13	5.99	0.06	4.57	358.20	369.06	347.69	9.90
DG25	3.93	4.46	0.38	57.58	5.98	0.06	3.38	322.51	334.64	313.48	10.75
DG25	3.05	0.74	0.08	30.12	<0.15	0.02	1.57	204.28	227.23	217.64	0.16
DG25	4.55	0.90	<0.03	31.74	<0.15	<0.01	2.58	317.34	383.28	340.64	0.04
DG25	8.50	1.05	<0.03	18.72	0.30	0.02	6.95	199.15	223.44	198.83	0.22
DG25	2.00	1.91	0.12	9.56	0.56	0.04	3.91	75.49	79.85	74.34	0.50
DG25	2.02	0.30	0.06	17.83	<0.15	0.01	0.30	192.28	221.97	203.04	0.06
DG26	1.18	1.75	0.33	24.32	3.51	0.04	7.89	161.02	169.78	163.25	5.81
DG26	1.20	2.12	0.28	20.62	3.04	0.05	9.66	138.93	154.26	146.77	3.78
DG26	1.57	7.70	1.07	74.58	14.10	0.14	39.38	413.61	462.17	414.01	17.37
DG26	0.88	9.49	3.28	90.86	20.16	0.15	46.90	524.70	548.15	525.06	24.35
DG26	0.67	1.17	<0.14	12.47	1.40	<0.02	3.60	102.02	105.29	100.11	2.24

Table A10.8: LA-ICPMS of pyrite from ABDP9											
Sample name	**Upper limit (m)**	**Lower limit (m)**	**S34 (ppm)**	**Mn55 (ppm)**	**Fe57 (ppm)**	**Co59 (ppm)**	**Ni60 (ppm)**	**Cu65 (ppm)**	**Zn66 (ppm)**	**As75 (ppm)**	**Se77 (ppm)**
DG26	186.42	186.69	547110	197.12	465257	663.65	943.46	541.45	128.57	1108.94	15.03
DG26	186.42	186.69	540343	47.10	465371	703.91	996.28	541.44	62.03	681.86	15.87
DG26	186.42	186.69	551773	1275.12	465166	588.94	772.66	466.85	28.02	1452.63	19.02
DG26	186.42	186.69	584903	2102.78	465260	556.99	609.79	331.96	13.05	1100.21	19.50
DG26	186.42	186.69	591433	2414.83	465358	689.63	822.67	471.65	375.38	730.96	24.38
DG27	214.87	215.04	574399	1.78	465427	3.87	14.54	43.61	0.60	474.01	98.03
DG27	214.87	215.04	539908	0.20	465426	2.24	10.25	29.83	<0.11	476.81	93.19
DG27	214.87	215.04	555540	0.29	465454	4.32	16.46	29.62	0.27	371.33	92.41
DG27	214.87	215.04	544848	<0.10	465422	4.43	18.15	35.77	0.54	490.21	114.68
DG27	214.87	215.04	553690	4.09	465426	4.58	25.55	49.87	0.67	474.91	96.45
DG27	214.87	215.04	537334	<0.10	465392	2.43	11.03	26.81	0.22	603.94	112.87
DG27	214.87	215.04	570460	<0.10	465405	4.03	13.88	28.80	0.30	557.08	100.33
DG27	214.87	215.04	549859	2.94	465413	12.67	38.48	39.79	0.79	524.05	103.67
DG27	214.87	215.04	539070	<0.10	465379	4.17	13.92	56.28	0.33	651.19	117.37
DG27	214.87	215.04	540311	<0.10	465404	3.90	11.53	26.90	0.31	558.23	100.47

Table A10.8: LA-ICPMS of pyrite from ABDP9

Sample	**Mo95 (ppm)**	**Ag107 (ppm)**	**Cd111 (ppm)**	**Sb121 (ppm)**	**Te125 (ppm)**	**Au197 (ppm)**	**Tl205 (ppm)**	**Pb206 (ppm)**	**Pb207 (ppm)**	**Pb208 (ppm)**	**Bi209 (ppm)**
DG26	0.76	9.94	2.22	83.91	17.36	0.17	52.22	454.98	495.40	461.10	18.62
DG26	0.41	10.83	1.96	72.89	14.70	0.17	68.30	407.78	432.83	404.69	17.55
DG26	1.51	7.43	1.30	60.49	12.13	0.11	49.02	364.28	387.94	364.93	14.46
DG26	1.45	5.02	0.86	47.02	8.37	0.08	34.05	295.70	312.73	289.93	11.49
DG26	1.95	7.93	4.44	73.54	14.53	0.10	57.62	440.88	476.33	438.13	19.52
DG27	0.52	0.16	0.28	2.44	1.38	0.02	1.28	18.22	21.30	20.77	2.14
DG27	0.43	0.04	0.23	1.00	<0.07	<0.01	1.23	11.05	13.02	11.82	0.31
DG27	0.36	0.21	0.36	1.59	1.00	0.03	1.48	15.11	18.41	15.75	1.33
DG27	0.48	0.08	0.25	0.90	0.29	<0.01	2.00	8.91	10.01	9.85	0.08
DG27	0.38	0.11	0.12	0.62	0.13	<0.01	0.88	9.22	10.90	10.02	0.27
DG27	0.28	0.07	0.19	1.08	0.34	<0.01	2.13	11.57	13.85	12.36	0.21
DG27	0.37	0.02	0.25	0.89	<0.07	<0.01	1.64	9.23	10.88	10.00	0.03
DG27	0.25	0.30	0.16	1.44	0.60	<0.01	0.91	15.36	18.00	16.52	0.91
DG27	0.33	0.06	0.13	0.96	0.48	<0.01	1.97	11.49	12.87	12.38	0.18
DG27	0.36	0.02	0.38	0.96	0.54	<0.01	2.21	11.53	13.08	11.84	0.12

Table A10.8: LA-ICPMS of pyrite from ABDP9											
Sample name	**Upper limit (m)**	**Lower limit (m)**	**S34 (ppm)**	**Mn55 (ppm)**	**Fe57 (ppm)**	**Co59 (ppm)**	**Ni60 (ppm)**	**Cu65 (ppm)**	**Zn66 (ppm)**	**As75 (ppm)**	**Se77 (ppm)**
DG27	214.87	215.04	555130	<0.10	465425	3.11	8.73	25.03	0.53	479.35	94.24
DG27	214.87	215.04	550389	<0.10	465438	4.87	32.55	25.41	0.36	432.04	75.59
DG28	234.16	234.31	591666	198.37	465348	313.01	1324.41	294.91	8.97	767.28	36.63
DG28	234.16	234.31	532822	4.21	465414	341.29	2334.70	658.20	51.49	521.90	64.11
DG28	234.16	234.31	559601	100.44	465367	459.56	2205.02	628.99	107.52	697.31	30.57
DG28	234.16	234.31	555820	209.08	465204	435.04	2034.06	530.40	175.42	1307.04	33.82
DG28	234.16	234.31	548853	1.01	465428	386.94	1798.66	599.85	233.68	467.91	22.25
DG28	234.16	234.31	567496	449.02	465367	470.93	1912.74	512.13	241.97	698.15	37.60
DG28	234.16	234.31	551049	153.94	465428	250.53	673.10	370.64	295.23	467.36	14.71
DG28	234.16	234.31	602807	363.73	465322	477.43	1457.22	378.98	352.07	867.82	36.14
DG28	234.16	234.31	573238	326.10	465376	491.27	1907.89	474.54	805.52	662.46	33.06
DG29	253.24	253.39	531233	3.09	465415	511.65	1624.87	440.91	2.53	516.65	33.25
DG29	253.24	253.39	539420	0.75	465483	292.45	1333.67	362.86	3.92	263.09	28.37
DG29	253.24	253.39	531094	2.27	465480	297.41	1417.57	380.00	4.93	273.14	29.13
DG29	253.24	253.39	536286	2.09	465460	342.67	1586.48	425.15	5.03	350.16	33.89

Table A10.8: LA-ICPMS of pyrite from ABDP9

Sample	Mo95 (ppm)	Ag107 (ppm)	Cd111 (ppm)	Sb121 (ppm)	Te125 (ppm)	Au197 (ppm)	Tl205 (ppm)	Pb206 (ppm)	Pb207 (ppm)	Pb208 (ppm)	Bi209 (ppm)
DG26	0.53	0.06	0.22	1.23	<0.07	<0.01	1.69	14.23	14.61	14.19	0.27
DG26	0.11	0.10	0.21	1.47	<0.07	<0.01	0.47	16.31	17.58	16.43	0.82
DG26	1.98	8.06	<0.34	77.25	9.07	0.09	11.73	285.86	333.29	312.38	6.71
DG26	1.04	20.07	0.68	287.58	39.98	0.26	16.44	735.43	795.71	773.87	26.96
DG26	0.67	18.97	0.78	256.35	40.45	0.26	14.26	702.81	750.26	751.09	23.63
DG27	2.50	15.32	0.89	232.34	33.57	0.24	9.10	695.66	775.18	757.63	20.99
DG27	0.69	15.64	1.16	229.08	37.13	0.27	23.87	977.58	1047.55	1000.88	23.34
DG27	1.41	14.39	1.33	205.44	29.10	0.24	12.22	653.58	691.62	672.20	18.88
DG27	0.97	4.83	1.14	46.64	5.12	0.09	32.42	169.57	181.44	181.02	4.56
DG27	2.60	9.66	1.95	133.56	18.25	0.13	11.52	507.15	552.65	537.55	11.21
DG27	1.35	14.07	3.20	255.42	44.22	0.22	10.20	760.37	839.74	801.82	25.62
DG27	1.11	13.12	0.71	269.40	20.80	0.57	49.80	649.94	722.34	653.75	40.30
DG27	0.51	12.61	0.45	263.16	18.27	0.61	3.11	798.49	893.26	812.19	38.15
DG27	0.44	12.67	0.46	277.54	19.37	0.62	2.05	794.34	876.63	801.55	39.18
DG27	0.99	13.32	0.58	306.22	19.74	0.65	21.12	801.32	886.56	812.69	44.59

Table A10.8: LA-ICPMS of pyrite from ABDP9

Sample name	Upper limit (m)	Lower limit (m)	S34 (ppm)	Mn55 (ppm)	Fe57 (ppm)	Co59 (ppm)	Ni60 (ppm)	Cu65 (ppm)	Zn66 (ppm)	As75 (ppm)	Se77 (ppm)
DG29	253.24	253.39	549660	1.67	465451	453.12	1602.55	458.16	5.29	383.71	33.74
DG29	253.24	253.39	532312	14.11	465416	588.01	902.41	317.84	6.29	512.93	27.44
DG29	253.24	253.39	540468	6.83	465439	580.59	1710.00	590.05	8.25	427.65	50.19
DG29	253.24	253.39	535839	2.58	465467	377.99	1402.16	383.66	10.45	323.60	29.51
DG29	253.24	253.39	532148	2.33	465452	440.05	1594.00	443.25	13.01	379.90	33.12
DG29	253.24	253.39	540780	3.62	465469	310.49	1394.51	363.24	13.71	316.90	31.44
DG29	253.24	253.39	545085	0.14	465429	366.05	1534.01	401.06	13.76	466.92	29.13
DG29	253.24	253.39	546335	10.82	465418	557.01	1520.11	376.60	18.09	507.54	31.06
DG29	253.24	253.39	542043	8.57	465431	578.50	1473.90	434.85	82.79	458.05	55.62
DG30	268.93	269.08	523693	29.72	465464	409.33	575.84	346.93	16.63	335.27	36.79
DG30	268.93	269.08	520558	227.11	465424	562.35	826.54	432.51	97.02	485.52	53.65
DG30	268.93	269.08	530124	222.44	465405	626.15	909.24	306.08	112.05	553.98	93.93
DG30	268.93	269.08	520042	81.22	465424	585.18	824.34	931.98	37.21	482.33	38.65
DG30	268.93	269.08	524036	98.13	465422	584.78	796.26	487.51	50.34	490.52	98.38
DG30	268.93	269.08	530027	195.21	465407	630.35	896.58	407.47	86.51	547.53	89.20

Table A10.8: LA-ICPMS of pyrite from ABDP9

Sample	Mo95 (ppm)	Ag107 (ppm)	Cd111 (ppm)	Sb121 (ppm)	Te125 (ppm)	Au197 (ppm)	Tl205 (ppm)	Pb206 (ppm)	Pb207 (ppm)	Pb208 (ppm)	Bi209 (ppm)
DG29	0.98	14.24	0.77	279.07	21.34	0.62	37.21	713.28	791.67	722.87	42.52
DG29	3.59	8.99	0.61	101.39	11.02	0.29	103.87	224.77	245.72	222.27	17.06
DG29	0.89	18.07	0.97	361.19	26.95	0.95	8.83	1109.73	1255.02	1139.70	56.12
DG29	0.70	11.96	0.57	264.92	19.52	0.60	8.10	736.35	828.16	761.46	37.10
DG29	0.63	14.26	0.62	307.30	23.06	0.66	8.74	813.45	909.03	835.02	43.51
DG29	0.93	12.99	0.54	271.64	17.77	0.63	15.20	776.43	846.18	776.23	40.86
DG29	0.77	12.51	0.66	291.76	20.17	0.64	7.43	803.22	880.31	842.09	40.42
DG29	1.13	11.43	0.57	279.55	22.90	0.56	14.57	793.61	873.30	813.40	37.91
DG29	1.15	15.29	1.71	299.89	27.33	0.75	18.45	894.11	1000.02	914.11	46.18
DG30	1.71	8.39	3.34	112.77	52.91	0.45	0.72	513.90	557.56	550.28	34.05
DG30	2.05	9.42	4.16	167.75	80.80	0.42	1.01	504.04	543.30	538.42	48.07
DG30	5.53	8.58	5.16	203.02	99.77	0.40	1.34	1197.39	1295.65	1275.11	58.51
DG30	1.75	10.02	9.35	163.31	76.84	0.45	0.76	479.70	520.94	515.85	46.86
DG30	2.19	10.29	5.41	164.29	75.52	0.55	0.66	1453.84	1763.77	1713.51	46.10
DG30	1.47	9.83	4.62	182.05	87.56	0.46	0.88	986.15	1078.96	1077.08	50.17

Table A10.8: LA-ICPMS of pyrite from ABDP9

Sample name	Upper limit (m)	Lower limit (m)	S34 (ppm)	Mn55 (ppm)	Fe57 (ppm)	Co59 (ppm)	Ni60 (ppm)	Cu65 (ppm)	Zn66 (ppm)	As75 (ppm)	Se77 (ppm)
DG30	268.93	269.08	523899	106.23	465394	714.28	1025.05	460.29	54.83	596.02	57.13
DG30	268.93	269.08	523077	22.91	465423	545.18	764.88	646.28	18.08	488.81	316.29
DG30	268.93	269.08	517082	45.96	465422	578.34	828.64	416.56	59.36	490.32	54.77
DG30	268.93	269.08	533492	160.52	465403	658.39	964.66	416.23	92.36	561.57	71.26
DG30	268.93	269.08	517485	251.49	465437	453.71	702.15	703.50	102.67	435.53	215.12
DG30	268.93	269.08	514411	17.26	465459	426.28	603.07	449.14	18.18	354.71	435.50
DG30	268.93	269.08	530856	94.36	465444	508.74	718.37	413.40	52.97	411.01	42.98
DG30	268.93	269.08	545392	60.32	465464	634.44	951.03	414.93	23.99	335.05	25.40
DG30	268.93	269.08	476708	4.10	465455	645.15	992.21	585.81	43.38	366.64	23.72
DG30	268.93	269.08	534534	173.84	465373	895.74	1203.19	704.66	76.13	673.48	146.82
DG30	268.93	269.08	536599	321.87	465355	929.09	1401.73	635.93	515.58	741.93	85.27
DG30	268.93	269.08	524173	56.55	465405	725.08	1051.65	618.47	1136.46	555.96	37.87
DG30	268.93	269.08	533192	124.85	465433	539.96	803.36	518.97	54.09	449.73	130.78
DG30	268.93	269.08	509680	84.88	465403	685.24	1006.25	282.30	402.92	563.87	139.11
DG30	268.93	269.08	500569	23.63	465435	587.67	866.49	412.01	112.99	444.52	37.45

Table A10.8: LA-ICPMS of pyrite from ABDP9

Sample	Mo95 (ppm)	Ag107 (ppm)	Cd111 (ppm)	Sb121 (ppm)	Te125 (ppm)	Au197 (ppm)	Tl205 (ppm)	Pb206 (ppm)	Pb207 (ppm)	Pb208 (ppm)	Bi209 (ppm)
DG30	2.46	11.44	4.95	190.53	92.85	0.52	1.11	410.87	441.97	443.91	51.25
DG30	1.97	11.00	6.25	157.54	76.46	0.62	1.06	5207.61	5591.44	5457.14	49.25
DG30	1.68	10.54	5.98	161.39	77.81	0.58	0.80	626.14	659.49	657.21	47.58
DG30	1.63	10.13	6.73	179.59	88.10	0.51	1.02	762.14	831.71	799.84	51.67
DG30	2.10	8.14	5.32	120.22	55.04	0.44	0.93	2557.32	2842.31	2900.88	37.00
DG30	1.84	9.90	6.77	125.96	60.50	0.58	0.85	6665.83	7459.68	7228.50	44.09
DG30	1.59	8.60	4.21	135.74	63.76	0.46	0.75	367.25	403.91	395.17	39.50
DG30	0.93	9.31	3.60	123.95	42.08	0.42	2.21	423.52	447.81	447.25	34.67
DG30	0.98	12.60	4.16	159.70	58.87	0.56	3.46	446.13	484.42	462.68	44.40
DG30	66.55	12.83	6.39	271.55	126.32	0.67	2.64	2442.73	2607.26	2547.90	74.09
DG30	1.50	13.25	39.50	292.87	138.46	0.56	2.17	772.34	830.68	815.48	75.92
DG30	0.81	13.47	90.41	195.41	86.82	0.63	3.11	462.73	484.16	471.09	48.51
DG30	1.09	12.31	5.64	190.69	88.34	0.70	1.31	1694.54	1798.80	1756.22	55.23
DG30	6.31	10.26	46.92	234.22	113.24	0.55	2.44	1693.06	1841.93	1810.66	68.71
DG30	0.89	12.09	5.11	179.34	74.22	0.65	6.00	519.14	558.20	549.79	52.16

Table A10.8: LA-ICPMS of pyrite from ABDP9

Sample name	Upper limit (m)	Lower limit (m)	S34 (ppm)	Mn55 (ppm)	Fe57 (ppm)	Co59 (ppm)	Ni60 (ppm)	Cu65 (ppm)	Zn66 (ppm)	As75 (ppm)	Se77 (ppm)
DG30	268.93	269.08	486141	265.85	465375	991.87	1445.42	464.52	81.19	668.14	100.04
DG30	268.93	269.08	498463	7.38	465447	607.41	963.74	586.73	377.85	398.52	23.60
DG30	268.93	269.08	525532	11.49	465415	575.53	847.03	410.01	42.88	517.33	276.37
DG30	268.93	269.08	482227	197.05	465443	839.02	1224.72	3434.93	175.93	413.47	132.74
DG30	268.93	269.08	550131	197.90	465303	1064.91	1539.91	455.51	44.82	937.02	279.62
DG30	268.93	269.08	558481	335.67	465328	813.55	1245.78	431.37	95.22	845.41	127.00
DG30	268.93	269.08	562556	205.26	465364	793.67	1175.54	311.15	53.20	707.85	135.76
DG30	268.93	269.08	558685	228.93	465375	766.93	1106.65	403.74	66.83	668.65	183.33
DG30	268.93	269.08	550098	183.96	465380	771.68	1110.30	419.18	56.74	649.39	119.58
DG30	268.93	269.08	552250	278.23	465357	829.25	1225.71	469.00	83.84	736.02	158.60
DG31	292.74	292.90	552536	0.50	464912	1784.15	1379.72	2524.54	175.98	2401.52	104.37
DG31	292.74	292.90	550890	692.30	465013	1474.15	949.21	1903.33	76.60	2024.35	211.70
DG31	292.74	292.90	534483	5.04	464857	1906.43	1534.20	4038.57	4140.47	2609.41	105.62
DG31	292.74	292.90	555914	4.75	464871	1842.08	1378.49	2367.26	109.04	2557.69	44.29
DG31	292.74	292.90	543160	1.72	464937	1792.64	1601.45	563.39	9.78	2309.22	48.74

Table A10.8: LA-ICPMS of pyrite from ABDP9

Sample	Mo95 (ppm)	Ag107 (ppm)	Cd111 (ppm)	Sb121 (ppm)	Te125 (ppm)	Au197 (ppm)	Tl205 (ppm)	Pb206 (ppm)	Pb207 (ppm)	Pb208 (ppm)	Bi209 (ppm)
DG30	1.26	13.93	6.03	270.29	115.99	0.66	2.20	1343.38	1440.47	1419.45	77.98
DG30	0.96	11.98	13.08	147.73	58.30	0.50	2.10	358.53	389.97	386.67	38.45
DG30	1.15	15.90	6.59	187.62	94.66	0.91	1.27	3223.69	3490.08	3413.21	56.82
DG30	1.74	13.18	22.47	181.10	73.37	0.44	1.30	3142.68	3411.46	3291.09	57.48
DG30	2.38	16.21	8.09	363.53	193.59	0.80	3.00	1995.93	2152.10	2114.65	97.95
DG30	1.14	12.97	5.73	233.56	118.39	0.52	2.71	766.12	824.42	806.91	59.56
DG30	1.86	11.59	4.91	261.74	132.28	0.64	3.37	1020.87	1084.50	1066.13	69.50
DG30	0.85	12.59	5.26	219.07	112.52	0.53	1.54	1340.37	1449.70	1437.82	56.39
DG30	1.07	12.20	6.36	229.53	112.43	0.54	1.74	845.36	928.62	880.53	57.57
DG30	1.03	13.32	6.53	251.95	129.60	0.56	2.42	1048.99	1166.81	1112.08	65.70
DG31	0.82	42.31	5.25	395.39	46.43	0.70	6.61	3692.20	3752.36	3692.74	73.79
DG31	2.73	32.41	2.23	348.32	43.71	0.50	5.57	8637.30	8723.21	8414.92	78.67
DG31	0.62	46.38	78.56	424.71	49.99	0.73	12.79	4448.86	3694.88	3578.62	80.10
DG31	1.39	39.33	4.41	438.63	50.24	0.63	11.44	1307.91	1297.29	1216.57	83.44
DG31	0.81	40.80	2.54	360.59	42.97	0.62	5.78	1455.83	1494.48	1368.70	65.71

Table A10.8: LA-ICPMS of pyrite from ABDP9

Sample name	Upper limit (m)	Lower limit (m)	S34 (ppm)	Mn55 (ppm)	Fe57 (ppm)	Co59 (ppm)	Ni60 (ppm)	Cu65 (ppm)	Zn66 (ppm)	As75 (ppm)	Se77 (ppm)
DG31	292.74	292.90	527529	341.27	465049	1403.08	1243.05	624.18	7.40	1888.58	31.10
DG31	292.74	292.90	525932	0.63	465348	1069.83	977.98	384.92	4.67	767.31	18.50
DG31	292.74	292.90	526770	1.15	465038	1540.46	1411.39	1246.56	24.43	1931.62	25.26
DG31	292.74	292.90	548029	9.62	464882	2057.96	1673.57	1702.01	61.88	2516.14	37.69
DG31	292.74	292.90	529438	391.14	464924	1872.04	1430.09	457.23	4.41	2358.47	29.35
DG31	292.74	292.90	553064	3.04	465148	1134.41	995.63	1965.83	375.55	1519.68	110.49
DG31	292.74	292.90	547603	0.81	465101	1272.40	1164.20	1717.46	47.89	1693.77	14.31
DG31	292.74	292.90	538951	5.43	465084	1248.79	922.23	334.90	11.40	1756.57	51.01
DG31	292.74	292.90	548028	11.70	465084	1325.79	949.39	454.72	13.12	1758.90	59.81
DG31	292.74	292.90	531221	4.97	465046	1359.38	1057.88	1310.97	52.65	1900.67	151.31
DG31	292.74	292.90	551850	9.29	465326	777.74	793.74	565.01	20.10	850.52	5.09
DG31	292.74	292.90	550028	6.56	465244	1000.82	974.10	698.94	8.39	1157.79	13.92
DG31	292.74	292.90	540136	12.93	465268	984.53	972.97	329.74	7.04	1069.40	12.44
DG31	292.74	292.90	557849	23.14	465306	825.62	795.59	250.80	19.12	927.55	15.59
DG31	292.74	292.90	538376	4.13	465330	716.50	735.16	504.20	2874.02	836.05	4.94

Table A10.8: LA-ICPMS of pyrite from ABDP9

Sample	Mo95 (ppm)	Ag107 (ppm)	Cd111 (ppm)	Sb121 (ppm)	Te125 (ppm)	Au197 (ppm)	Tl205 (ppm)	Pb206 (ppm)	Pb207 (ppm)	Pb208 (ppm)	Bi209 (ppm)
DG31	1.50	30.42	1.87	250.90	26.22	0.46	10.43	680.90	715.27	677.57	42.51
DG31	0.86	25.42	1.80	114.98	8.65	0.32	20.13	57.34	59.76	54.88	21.46
DG31	0.84	36.70	4.06	322.42	35.12	0.64	12.94	533.84	783.01	527.05	58.99
DG31	1.04	43.44	4.89	438.63	46.56	0.68	23.30	1095.51	768.77	960.43	77.13
DG31	2.32	38.19	3.03	386.01	43.04	0.60	18.88	538.11	616.94	532.21	69.57
DG31	1.50	27.18	6.08	234.44	27.99	0.43	2.98	4671.89	4744.44	4709.47	46.32
DG31	0.94	32.04	2.70	290.32	33.90	0.51	3.53	344.23	362.99	329.40	52.22
DG31	4.97	26.67	1.20	301.12	39.39	0.46	4.84	2416.57	2452.09	2459.49	56.31
DG31	4.12	25.39	1.24	330.94	38.68	0.41	5.39	2793.03	2513.11	2439.34	59.87
DG31	2.75	32.92	3.02	325.32	41.17	0.52	3.33	8478.17	8569.64	8036.37	66.15
DG31	1.23	18.26	1.60	152.92	15.37	0.30	1.50	134.98	145.37	134.44	26.86
DG31	1.51	21.99	1.81	200.65	19.71	0.37	5.26	451.54	470.88	438.52	35.43
DG31	1.63	21.53	2.09	184.73	18.42	0.32	5.63	318.27	325.49	310.74	32.37
DG31	1.35	17.34	1.38	160.21	16.00	0.28	3.25	819.43	837.26	786.66	27.02
DG31	1.16	17.08	75.68	136.36	15.19	0.29	1.16	133.25	127.69	120.16	24.49

Table A10.8: LA-ICPMS of pyrite from ABDP9

Sample name	Upper limit (m)	Lower limit (m)	S34 (ppm)	Mn55 (ppm)	Fe57 (ppm)	Co59 (ppm)	Ni60 (ppm)	Cu65 (ppm)	Zn66 (ppm)	As75 (ppm)	Se77 (ppm)
DG32	313.82	314.02	532290	0.92	463670	775.15	4166.32	58.59	0.69	7056.24	75.55
DG32	313.82	314.02	513854	3.26	463609	530.60	3145.32	57.56	0.88	7284.82	59.53
DG32	313.82	314.02	540276	7.45	463869	174.18	2787.61	48.58	1.32	6310.94	42.34
DG32	313.82	314.02	523504	13.35	464015	262.19	1696.05	79.14	2.05	5763.47	36.48
DG32	313.82	314.02	546722	10.78	463712	371.04	2237.62	94.72	2.19	6896.54	37.72
DG32	313.82	314.02	501834	19.02	464829	246.89	606.39	140.20	2.49	2712.58	10.87
DG32	313.82	314.02	548969	15.14	463450	166.44	3553.43	72.82	2.68	7880.03	47.75
DG32	313.82	314.02	525725	16.60	465251	216.43	508.48	101.60	2.79	1132.95	8.25
DG32	313.82	314.02	539201	15.61	463297	296.68	1935.47	139.18	3.18	8452.49	33.84
DG32	313.82	314.02	522861	20.64	464007	229.04	2209.48	45.36	3.22	5791.88	43.51
DG32	313.82	314.02	546467	15.64	464722	291.30	1714.68	35.12	3.23	3114.91	43.30
DG32	313.82	314.02	520061	23.54	465162	228.11	496.00	128.89	3.30	1466.79	8.99
DG32	313.82	314.02	568163	25.71	463998	222.49	2383.56	54.84	3.94	5825.25	40.12
DG32	313.82	314.02	521946	14.88	464926	427.19	1114.55	155.00	4.23	2348.50	13.49
DG32	313.82	314.02	533040	2.00	463289	408.32	4680.91	45.07	4.28	8481.65	89.37

Table A10.8: LA-ICPMS of pyrite from ABDP9

Sample	Mo95 (ppm)	Ag107 (ppm)	Cd111 (ppm)	Sb121 (ppm)	Te125 (ppm)	Au197 (ppm)	Tl205 (ppm)	Pb206 (ppm)	Pb207 (ppm)	Pb208 (ppm)	Bi209 (ppm)
DG32	4.05	2.47	<0.03	47.28	1.55	0.11	0.46	182.03	192.27	187.47	4.16
DG32	5.63	5.79	0.07	117.75	3.22	0.23	1.10	239.35	244.51	241.82	7.46
DG32	2.47	5.51	0.08	133.45	3.01	0.21	0.95	281.02	305.34	272.96	7.77
DG32	1.28	5.00	<0.03	145.09	2.67	0.20	2.14	248.98	269.16	249.49	6.78
DG32	1.93	5.42	<0.03	139.02	2.87	0.20	1.78	231.09	257.04	241.50	7.08
DG32	34.56	4.90	0.44	585.02	2.17	0.15	29.30	351.80	397.07	363.83	6.81
DG32	5.11	8.13	0.14	248.57	5.23	0.33	2.57	487.86	519.24	492.86	14.69
DG32	36.26	5.86	0.25	612.44	3.23	0.18	36.39	268.09	278.51	267.35	7.95
DG32	1.14	4.98	<0.03	174.45	2.97	0.19	2.93	241.92	273.19	246.25	7.43
DG32	1.60	4.31	<0.03	158.60	2.68	0.15	1.85	298.88	322.64	308.58	7.61
DG32	1.81	3.68	<0.03	129.13	3.00	0.14	0.90	247.37	273.32	252.40	8.00
DG32	38.58	5.89	0.42	661.42	3.08	0.16	33.04	328.06	341.57	315.96	7.94
DG32	1.53	5.34	<0.03	178.40	3.36	0.19	1.77	318.67	344.41	325.67	8.82
DG32	53.16	6.54	0.26	526.06	3.12	0.21	26.08	346.33	349.30	337.96	9.36
DG32	2.88	4.27	0.08	74.29	2.38	0.21	1.38	1059.03	1177.37	1246.98	6.02

Table A10.8: LA-ICPMS of pyrite from ABDP9

Sample name	Upper limit (m)	Lower limit (m)	S34 (ppm)	Mn55 (ppm)	Fe57 (ppm)	Co59 (ppm)	Ni60 (ppm)	Cu65 (ppm)	Zn66 (ppm)	As75 (ppm)	Se77 (ppm)
DG32	313.82	314.02	536596	12.77	464767	344.83	1551.83	30.93	6.27	2945.95	39.48
DG32	313.82	314.02	516373	18.51	464913	482.27	901.60	140.50	6.87	2399.61	13.77
DG32	313.82	314.02	528538	13.86	464242	746.84	976.13	153.38	15.17	4910.67	15.88
DG32	313.82	314.02	549148	10.36	459522	817.38	1080.06	240.82	228.58	22596.95	59.94
DG32	313.82	314.02	490383	16.53	465376	205.97	577.83	90.49	<0.35	663.33	5.69
DG33	366.61	366.87	547789	23.74	464871	1929.71	1520.58	313.41	18.70	2556.55	12.55
DG33	366.61	366.87	544571	11.79	464788	2095.03	1688.45	285.60	8.44	2866.62	12.48
DG33	366.61	366.87	526769	6.85	464818	1907.83	1951.01	335.69	4.93	2753.24	12.02
DG33	366.61	366.87	533480	2.57	464752	2551.88	2347.86	478.47	13.40	3002.37	15.13
DG33	366.61	366.87	573729	0.59	464817	1605.21	1246.00	233.21	163.89	2758.94	10.00
DG33	366.61	366.87	566084	12.90	464737	2266.88	1826.93	349.79	1404.10	3057.02	12.42
DG33	366.61	366.87	491024	5661.77	464503	1816.01	1957.90	278.93	104.55	3934.40	19.33
DG33	366.61	366.87	547329	4.72	464782	2178.08	1949.92	382.88	4011.21	2889.04	12.61
DG33	366.61	366.87	477913	3096.26	464908	1495.48	1627.84	267.94	1.01	2418.82	18.47
DG33	366.61	366.87	537099	9.54	464777	2150.94	2120.60	378.56	5.24	2907.62	12.46

Table A10.8: LA-ICPMS of pyrite from ABDP9

Sample	Mo95 (ppm)	Ag107 (ppm)	Cd111 (ppm)	Sb121 (ppm)	Te125 (ppm)	Au197 (ppm)	Tl205 (ppm)	Pb206 (ppm)	Pb207 (ppm)	Pb208 (ppm)	Bi209 (ppm)
DG32	3.28	4.09	<0.03	91.46	2.45	0.16	0.53	172.93	187.79	177.47	6.22
DG32	27.79	9.23	0.32	494.15	5.07	0.24	17.41	458.54	498.12	463.10	12.97
DG32	28.56	9.68	0.24	447.64	6.41	0.32	16.55	445.72	486.43	442.11	14.40
DG32	1.51	5.07	0.85	220.70	1.95	0.19	4.71	2341.53	2687.20	2623.05	6.88
DG32	27.51	5.30	0.22	627.25	2.51	0.17	44.50	187.18	174.17	187.32	6.59
DG33	2.50	11.05	0.12	372.83	10.83	0.30	7.47	554.51	586.82	551.56	79.72
DG33	3.07	13.69	0.34	423.30	13.14	0.32	4.38	604.30	639.84	610.12	90.77
DG33	1.91	13.97	0.19	425.89	13.86	0.33	2.93	584.52	621.36	601.66	88.90
DG33	0.95	18.29	0.31	468.57	13.56	0.35	3.60	582.13	594.10	565.15	92.71
DG33	6.45	7.55	0.64	350.54	8.99	0.15	10.71	559.17	578.20	558.73	80.05
DG33	1.58	13.34	5.25	432.01	12.17	0.24	6.58	484.75	510.54	492.92	80.20
DG33	3.01	9.54	0.20	318.90	8.48	0.24	6.17	483.12	515.14	504.04	56.42
DG33	0.62	15.30	13.54	448.04	13.96	0.28	6.80	575.34	623.32	599.09	90.13
DG33	3.68	9.16	<0.06	258.35	6.40	0.14	3.18	529.92	547.70	529.89	43.50
DG33	1.10	16.18	0.27	440.95	14.43	0.33	6.20	579.30	601.97	587.07	88.27

Table A10.8: LA-ICPMS of pyrite from ABDP9

Sample name	Upper limit (m)	Lower limit (m)	S34 (ppm)	Mn55 (ppm)	Fe57 (ppm)	Co59 (ppm)	Ni60 (ppm)	Cu65 (ppm)	Zn66 (ppm)	As75 (ppm)	Se77 (ppm)
DG33	366.61	366.87	526047	1562.17	464651	2391.37	1971.68	338.39	9.94	3381.45	15.20
DG33	366.61	366.87	557476	157.91	464705	2098.01	1796.72	291.17	18.04	3178.69	12.76
DG33	366.61	366.87	546908	5.12	464681	2196.67	1807.72	315.09	16.07	3266.33	13.73
DG34	398.30	398.47	639778	1045.69	465429	517.87	1128.37	152.02	26.00	463.61	22.87
DG34	398.30	398.47	603608	487.89	465477	257.36	771.52	177.37	8.67	287.05	13.52
DG34	398.30	398.47	611311	1192.29	465449	397.99	777.92	155.27	0.38	391.05	16.28
DG34	398.30	398.47	593040	1289.14	465263	375.16	1040.61	167.16	5.43	1088.39	28.14
DG34	398.30	398.47	551125	349.74	465450	257.24	842.24	177.45	12.19	386.48	15.40
DG34	398.30	398.47	594410	694.33	465467	284.61	911.87	137.99	4.89	321.24	16.63
DG34	398.30	398.47	513984	2237.24	465270	138.42	517.17	182.58	4.72	1061.16	27.38
DG34	398.30	398.47	550827	0.63	465512	231.17	711.47	185.00	5.47	154.50	8.40
DG34	398.30	398.47	547889	3.50	465508	180.97	769.42	262.28	6.67	171.07	7.47
DG34	398.30	398.47	532415	3.59	465504	236.69	897.86	170.21	14.65	185.06	10.63
DG34	398.30	398.47	539716	6.53	465512	146.26	661.04	213.17	6.09	153.63	9.26
DG34	398.30	398.47	535010	1.32	465506	247.30	817.41	188.24	6.07	175.51	9.95

Table A10.8: LA-ICPMS of pyrite from ABDP9

Sample	Mo95 (ppm)	Ag107 (ppm)	Cd111 (ppm)	Sb121 (ppm)	Te125 (ppm)	Au197 (ppm)	Tl205 (ppm)	Pb206 (ppm)	Pb207 (ppm)	Pb208 (ppm)	Bi209 (ppm)
DG33	5.75	14.62	0.13	468.56	14.35	0.27	7.85	655.50	688.14	646.39	90.95
DG33	3.47	12.77	0.25	443.75	12.74	0.23	9.99	576.81	604.66	594.52	83.16
DG33	3.57	13.14	0.17	456.53	12.23	0.23	9.61	580.43	592.57	580.76	83.55
DG34	2.93	5.52	0.38	249.53	4.49	0.18	2.75	632.89	666.38	632.10	7.26
DG34	1.15	4.08	0.28	125.71	2.36	0.08	1.49	280.51	292.56	283.00	3.17
DG34	1.21	4.05	0.21	137.94	2.36	0.10	1.15	315.25	336.80	312.68	3.45
DG34	0.75	3.63	0.14	74.75	1.58	0.09	0.92	184.79	196.39	189.95	1.80
DG34	0.71	4.45	0.19	103.81	1.92	0.11	0.93	230.45	249.86	239.88	2.65
DG34	1.56	5.62	0.14	174.25	3.30	0.17	0.98	430.34	451.60	440.66	5.08
DG34	1.07	1.96	0.13	33.29	0.55	0.04	2.77	99.67	106.65	103.96	0.86
DG34	0.56	3.67	<0.05	80.74	1.50	0.08	0.61	192.37	197.32	188.05	2.35
DG34	0.56	4.76	0.12	84.30	1.57	0.12	0.67	189.27	204.03	197.70	2.29
DG34	0.52	6.07	0.11	108.67	2.24	0.16	0.70	293.40	309.34	292.82	3.73
DG34	0.53	4.22	0.10	79.52	1.52	0.11	0.71	168.95	177.32	167.42	2.45
DG34	0.54	5.02	0.13	103.37	2.15	0.13	0.63	261.91	263.83	257.05	3.36

Table A10.8: LA-ICPMS of pyrite from ABDP9

Sample name	Upper limit (m)	Lower limit (m)	S34 (ppm)	Mn55 (ppm)	Fe57 (ppm)	Co59 (ppm)	Ni60 (ppm)	Cu65 (ppm)	Zn66 (ppm)	As75 (ppm)	Se77 (ppm)
DG35	427.48	427.64	564661	<53.37	465475	444.57	598.47	198.42	5.41	292.55	8.88
DG35	427.48	427.64	579149	<53.37	465459	503.03	566.23	126.47	11.02	351.72	8.20
DG35	427.48	427.64	566174	<53.37	465470	442.54	608.81	208.92	115.60	312.40	6.61
DG35	427.48	427.64	584825	<53.37	465461	401.30	600.33	38.35	200.79	345.98	8.14
DG35	427.48	427.64	576540	<53.37	465441	693.73	648.90	683.41	500.32	421.39	10.34
DG35	427.48	427.64	554356	<53.37	465429	483.25	610.53	62.33	831.54	463.70	10.23
DG35	427.48	427.64	619049	<53.37	465450	468.26	530.35	37.46	1433.66	385.58	6.70
DG35	427.48	427.64	593258	380.27	465475	493.62	721.64	736.52	1566.14	291.39	5.84
DG35	427.48	427.64	605603	<53.37	465438	641.99	693.19	785.38	2920.14	433.18	8.67
DG35	427.48	427.64	614990	106.74	465425	822.55	783.80	266.40	<2.70	481.16	12.30
DG35	427.48	427.64	576146	<53.37	465462	483.39	600.77	183.65	<2.70	340.73	7.49
DG35	427.48	427.64	620903	<53.37	465421	549.41	554.48	38.98	<2.70	496.74	8.47
DG36	438.50	438.73	550400	800.49	464395	267.51	1144.99	108.57	0.98	4340.81	26.84
DG36	438.50	438.73	539049	32.88	463630	558.57	1692.27	112.83	102.09	7203.52	31.65
DG36	438.50	438.73	604130	4.98	465276	622.25	2824.44	98.58	58.82	1036.92	32.29

Table A10.8: LA-ICPMS of pyrite from ABDP9

Sample	**Mo95 (ppm)**	**Ag107 (ppm)**	**Cd111 (ppm)**	**Sb121 (ppm)**	**Te125 (ppm)**	**Au197 (ppm)**	**Tl205 (ppm)**	**Pb206 (ppm)**	**Pb207 (ppm)**	**Pb208 (ppm)**	**Bi209 (ppm)**
DG35	20.47	1.27	0.42	100.57	1.02	0.05	4.33	191.20	192.66	187.83	2.81
DG35	28.99	1.15	0.45	109.00	0.97	0.04	6.42	177.93	184.93	176.51	3.13
DG35	38.94	1.32	1.07	116.77	0.74	<0.01	6.84	191.99	196.69	191.63	3.07
DG35	25.30	1.27	1.12	103.33	0.90	0.04	8.94	229.01	231.78	226.07	2.17
DG35	27.05	1.21	2.23	101.26	0.81	0.03	11.17	205.82	212.85	204.16	2.58
DG35	45.69	1.31	4.68	101.00	1.03	0.06	6.90	242.93	251.85	245.05	2.39
DG35	45.69	1.25	4.77	95.76	0.72	0.04	11.22	216.32	220.27	212.76	2.01
DG35	38.40	1.57	5.89	128.12	1.64	0.10	9.63	195.08	199.95	191.70	3.75
DG35	28.55	1.71	8.49	119.15	0.96	0.05	10.87	211.15	215.45	211.67	2.99
DG35	43.61	1.57	0.18	106.52	0.86	0.08	4.64	212.08	211.07	202.87	3.14
DG35	59.64	1.37	0.56	127.54	0.93	0.07	9.32	206.07	209.45	203.00	3.65
DG35	17.21	0.99	0.73	90.16	1.09	<0.01	6.75	234.80	242.34	235.13	1.84
DG36	1.81	2.65	<0.05	95.17	1.14	0.11	1.00	295.63	316.49	309.05	3.51
DG36	1.97	4.02	0.27	284.79	1.41	0.13	11.22	779.32	852.86	827.31	5.64
DG36	1.22	16.10	0.60	367.34	5.80	0.42	1.71	696.02	755.72	716.21	20.94

Table A10.8: LA-ICPMS of pyrite from ABDP9											
Sample name	**Upper limit (m)**	**Lower limit (m)**	**S34 (ppm)**	**Mn55 (ppm)**	**Fe57 (ppm)**	**Co59 (ppm)**	**Ni60 (ppm)**	**Cu65 (ppm)**	**Zn66 (ppm)**	**As75 (ppm)**	**Se77 (ppm)**
DG36	438.50	438.73	571974	2762.68	464961	837.46	3212.21	118.20	9.94	2217.14	42.88
DG36	438.50	438.73	557666	174.86	463280	977.82	3325.99	207.92	10.95	8518.41	43.05
DG36	438.50	438.73	576668	633.46	465243	562.47	2985.29	122.47	280.05	1161.35	37.85
DG36	438.50	438.73	569886	734.60	464598	877.01	2921.62	107.02	15.53	3577.21	39.88
DG36	438.50	438.73	531072	51.44	463475	460.39	2294.59	145.74	4.04	7786.69	30.52
DG36	438.50	438.73	516229	10.41	464490	234.29	2672.65	94.18	134.48	3985.22	31.19
DG36	438.50	438.73	545813	105.72	465285	546.16	2617.76	100.32	31.64	1005.83	23.81
DG36	438.50	438.73	554996	133.58	465297	460.53	2311.47	96.05	1003.13	960.78	27.02
DG36	438.50	438.73	561232	502.90	465241	526.22	2553.21	89.80	116.03	1169.95	25.44
DG36	438.50	438.73	562253	422.34	465253	471.94	2668.43	109.15	2354.51	1124.84	27.16
DG36	438.50	438.73	523366	2770.51	464774	807.83	3605.73	147.01	19.31	2920.09	44.95
DG36	438.50	438.73	558052	243.77	465239	580.82	2563.47	103.14	25.07	1177.65	25.61
DG36	438.50	438.73	562527	411.76	465249	672.05	3011.12	101.85	38.38	1138.53	39.01
DG36	438.50	438.73	558052	2261.79	465244	618.29	3489.96	129.57	28.88	1159.04	35.66
DG36	438.50	438.73	542779	260.45	465241	727.59	5132.03	147.10	59.48	1170.63	32.88

Table A10.8: LA-ICPMS of pyrite from ABDP9

Sample	Mo95 (ppm)	Ag107 (ppm)	Cd111 (ppm)	Sb121 (ppm)	Te125 (ppm)	Au197 (ppm)	Tl205 (ppm)	Pb206 (ppm)	Pb207 (ppm)	Pb208 (ppm)	Bi209 (ppm)
DG36	3.01	12.47	0.17	338.42	5.02	0.34	2.05	725.53	766.75	741.95	19.20
DG36	2.85	3.94	0.08	292.25	1.68	0.17	11.12	699.47	757.17	790.98	6.23
DG36	2.68	15.46	1.52	383.03	5.60	0.36	1.93	758.89	809.20	766.89	21.31
DG36	2.20	11.30	0.09	306.44	4.10	0.26	1.31	640.18	699.67	670.27	15.68
DG36	1.30	1.72	<0.05	200.54	0.47	0.06	1.02	395.26	444.15	413.88	2.21
DG36	1.01	0.31	0.40	97.13		<0.01	0.91	176.23	204.89	196.69	0.56
DG36	0.65	14.26	0.24	281.06	4.15	0.33	1.20	595.96	640.10	620.04	16.10
DG36	0.73	13.52	3.75	265.67	4.15	0.31	1.64	568.47	619.26	581.24	14.66
DG36	0.86	12.81	0.67	310.16	4.47	0.35	1.50	612.71	633.82	608.24	15.14
DG36	1.43	13.88	8.01	329.46	4.92	0.34	2.53	677.58	689.62	681.44	17.02
DG36	3.43	16.25	<0.05	388.52	5.93	0.43	1.80	866.31	918.30	868.25	20.60
DG36	1.28	12.54	0.25	305.72	4.58	0.30	1.74	580.75	630.72	606.71	15.36
DG36	1.13	15.45	0.31	324.42	4.62	0.37	2.11	758.64	805.12	764.42	17.29
DG36	3.33	17.12	0.27	390.64	5.87	0.49	1.87	841.57	886.65	868.48	20.60
DG36	6.12	18.93	0.28	404.91	6.11	0.49	2.15	960.43	1004.62	971.89	22.34

Table A10.8: LA-ICPMS of pyrite from ABDP9

Sample name	Upper limit (m)	Lower limit (m)	S34 (ppm)	Mn55 (ppm)	Fe57 (ppm)	Co59 (ppm)	Ni60 (ppm)	Cu65 (ppm)	Zn66 (ppm)	As75 (ppm)	Se77 (ppm)
DG36	438.50	438.73	547718	619.47	464747	986.48	4167.48	167.18	15.66	3018.71	47.71
DG36	438.50	438.73	532467	2792.21	464633	1193.28	3139.76	119.81	1266.67	3448.83	36.58

Table A10.8: LA-ICPMS of pyrite from ABDP9

Sample	**Mo95 (ppm)**	**Ag107 (ppm)**	**Cd111 (ppm)**	**Sb121 (ppm)**	**Te125 (ppm)**	**Au197 (ppm)**	**Tl205 (ppm)**	**Pb206 (ppm)**	**Pb207 (ppm)**	**Pb208 (ppm)**	**Bi209 (ppm)**
DG36	2.15	15.98	0.27	377.97	4.99	0.42	1.54	866.14	930.76	883.34	19.76
DG36	5.46	9.81	4.86	280.99	3.07	0.27	2.97	625.90	672.23	644.26	12.27

Appendix 11:

Geology of the St Ives Gold District

A11.1 History of Mining and Exploration in the St Ives District

Gold was first mined in the late 1800s and early 1900s in the St Ives area at Cooee, Delta Island, Orchin, Red Hill and Victory Deposits. The most significant production was at Red Hill, which produced 31,000 oz before closing in 1907 (Roberts and Elias 1990). Upon the closure of the Red Hill mine explanation for addition gold mineralisation decreased significantly until the discovery of the Ives Reward Deposit approximately 10 km south-southwest of the Victory Deposit. Ives Reward produced 10,000 oz prior to the closure of the mine in the late 1930s (Roberts and Elias, 1990). An over twenty year period of inactivity in the region followed the closure of Ives Reward until 1966 when komatiite-hosted nickel sulfide ore was discovered by Western Mining Corporation Limited (WMC) at Red Hill (Woodall and Travis, 1969). Though free gold was occasionally encountered during the nickel mining, it was not until the value of gold increased in 1974 that the area was again assessed for gold potential. This exploration suggested that the gold was associated with only near surface oxidized rocks and were not appropriate for modern bulk mining techniques (Roberts and Elias 1990). A further increase in the price of gold in 1979-1980 resulted in renewed exploration and a gold ore body amenable to modern bulk mining methods was discovered below the Hunt shoot nickel ore body. The renewed exploration also targeted historic deposits and as a result of this exploration the Victory-Defiance complex was discovered in June 1980 in the vicinity of the old Victory and Ives Reward workings. Since then exploration has been constant with several discoveries being made, the most recent of which is the Athena-Hamlet complex in 2009. As of June 2009, a total of 9.2 Moz have been produced in the St. Ives district from 40 open pits and 16 underground operations (Gold Fields Limited, 2009). There is a remaining 5.6 Moz in resource and 2.3 Moz in reserve, with a mine life that extends to 2014 as of June 2009 (Gold Fields Limited, 2009).

A11.2 Stratigraphic Units

The St. Ives district lies within the volcano-stratigraphic sequences that make up the Eastern Goldfields Superterrane in the Yilgarn craton, Western Australia. These rocks were

deposited during a period of regional extension between 2700 and 2660 Ma (Barley and Groves, 1987). The stratigraphy, from oldest to youngest, consists of the Lunnon Basalt, the Kambalda Komatiite, the Devon Consuls Basalt, the Kapai Slate, the Paringa Basalt, the Black Flag Group and the Merougill Formation (Figure A11.1).

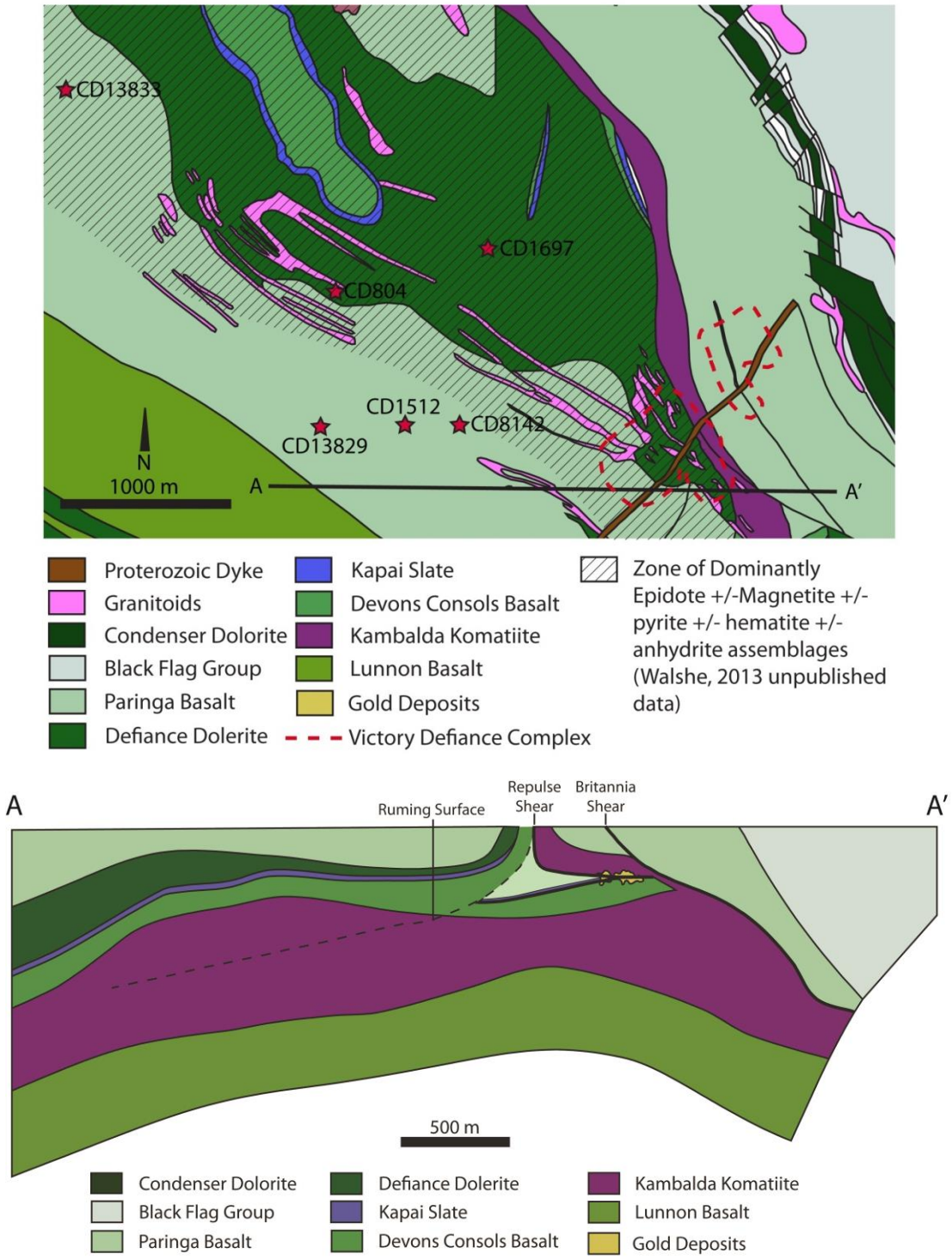

Figure A11.1: Local geology of the St. Ives gold district and location of drill holes used in this study. Both map and section are constructed using the models built by CSIRO.

A11.2.1 Lunnon Basalt

The Lunnon Basalt is the oldest identified unit in the St. Ives area. However the presence of an older basement is suggested by >3.5 Ga age dates from the cores of xenocrystic zircons taken from samples from the Lunnon Basalt, Devon Consuls Basalt and Paringa Basalt by Compston et al. (1986). These zircons have later overgrowths that occur at 3.2 to 3.1 Ga and a final overgrowth at 2.7 Ga, when the Lunnon Basalt was extruded.

The Lunnon Basalt is at least 2000 m thick with a lateral extent of at least 500 km^2 and it immediately underlies the Kambalda Komatiite Formation (Squire et al., 1998). Throughout the Eastern Goldfields Super Terrane, stratigraphically equivalent units have been observed, potentially representing 1.5 million km^3 of erupted basalt (Lesher and Arndt, 1995). The unit is tholeiitic in composition and is characterised by moderately high MgO concentrations, high Ni and Cr contents, low concentration of incompatible elements and minor depletion in light rare earth elements (LREE) (La/Smn = 0.76 to 0.85; Redman and Keays, 1985). The Lunnon Basalt is made up of 2-30 m thick flows that consist of four different lithofacies: basalt breccia, massive basalt, pillowed basalt and sulphidic metasediments (Squire et al., 1998). The pillowed flows make up approximately 45% of the stratigraphy (Squire et al., 1998) and are identified by well developed rims with radial and sub-concentric perlitic fractures and periodic flow top breccias (Gresham and Loftus-Hills, 1981; Squire et al., 1998). The massive basalt comprises a similar percentage of the stratigraphy (45%) as the pillowed flows (Squire et al., 1998). It is fine to medium grained and occurs in flows that range in thickness from 10 to 140 m (Squire et al., 1998). These basalts are believed to have been deposited in deep water (minimum 700 m depth) on the sea floor (Squire et al., 1998). The eruptions were generally passive and lava was transported in lava tubes with a very low slope and a paleo-flow towards the west. Basalt breccias forming at the tops of flows and interflow sediments make up the rest of the stratigraphy found in the Lunnon Basalt (Fiorentini, 2010).

The flows of the Lunnon Basalt have been divided into an upper and lower sequence, with the two sequences being separated by interflow sediments. The lower sequence can be distinguished from the upper by the presence of olivine phenocrysts (Redman and Keays, 1985), vesicles and amygdales (Squire et al., 1998). Geochemically the lower sequence can be distinguished from the upper sequence in that the lower sequence is slightly less evolved (0.69% TiO_2 and 8.3% MgO) than the upper sequence (0.97% TiO_2 and 7.8% MgO).

A11.2.2 Kambalda Komatiite

The Kambalda Komatiite is split into two different formations, the lower Silver Lake Member and the upper Tripod Hill Member (Fiorentini, 2010). The Silver Lake Member comprises approximately one third of the komatiitic sequence and varies in thickness from 50 to 200 m. It is characterised by a series of thick channels flanked by thinner flows on the edges (Beresford et al., 2002; Hill et al., 1995; Lesher and Arndt, 1995). The channels are identified by thick layered olivine adcumulates and mesocumulates that may be capped by spinifex textured komatiites. These layered olivine adcumulates and mesocumulates are colloquially referred to as dunite lenses. The flanking areas consist of thinner composite sheets of olivine othocumulates with spinifex texture (Hill et al., 1995). The channel and flank environments can be mineralogically distinguished in that pyroxene is absent from the main channel deposits but can be observed in the flanking areas. The basal flow channels are believed to reside in a pre-existing linear topographical lows (5-30 m deep) that were subsequently deepened by thermo-mechanical erosion and/or deformation during emplacement of the flows (Gemuts and Theron, 1975; Groves et al., 1986; Lesher, 1983; Lesher, 1989; Lesher et al., 1984; Stone et al., 2004; Stone et al., 2005; Williams et al., 1998). The adcumulates are considered to have developed in the floor of komatiitic magma chambers during a period of turbulent lava flow slightly below the liquidus temperature of the crystals (Hill et al., 1995). This is because, for cumulates of large, non-zoned crystals to form, two conditions need to be met. First, the level of supercooling must be low, such that the growth of crystals is favoured over the nucleation of new crystals. Second, the nutrient depleted boundary layer that surrounds growing crystals must be physically removed. The orthocumulates form in less turbid conditions at a cooler temperature, which allows nucleation of polyhedral crystals and trapping of the chemically depleted material around the crystals, giving rise to a homogeneous orthocumulate body (Hill et al., 1995).

The initial liquid composition of the Silver Lake Member was up to 30 wt% MgO, while the olivine in equilibrium with it would have been approximately Fo_{94}. This is similar to the Fo_{90-94} compositions inferred for the olivine cumulate zones (Lesher, 1989; Ross and Hopkins, 1979). The channel facies contain greater than 40 wt% MgO, while the channel facies spinifex textured zone contains 16-31 wt% MgO. However, the flanking facies is characterised by lower MgO and Fo compositions (35-40 wt% MgO and Fo_{89-91}) and the spinifex textures on the flank are also relatively low with 12-21% MgO (Lesher and Arndt, 1995). The trace element compositions of spinifex textured samples from the channel facies

(0.31-0.53 wt% TiO_2, 385-1610 ppm Cr and 1280-3670 ppm Ni) and that of the flanking facies (0.41-0.55 wt% TiO_2, 424-1810 ppm Cr and 71-410 ppm Ni) exhibit significant variation (Lesher and Arndt, 1995). The channel facies exhibits a slight depletion in LREE over HREE; while the flanking facies exhibits a LREE enrichment over the channel facies (Lesher and Arndt, 1995). The preceding evidence suggests that the flanking facies is more contaminated by crustal rocks than the channel facies. This may be because the channel facies received a much higher degree of recharge that transported and diluted the crustal contamination obtained by thermo-mechanical erosion of the base of the channel (Lesher and Arndt, 1995; Lesher et al., 2001).

The Silver Lake Member contains significant nickel sulfide deposits that have been mined since the 1960's. Three types of nickel ore mineralisation settings have been observed in the St. Ives area: basal contact mineralisation, hanging-wall mineralisation and structurally (re)mobilised ore (Fiorentini, 2010).

The basal mineralisation is by far the most significant mineralisation in terms of quantity and grade. It occurs in channels that have thermo-mechanically erroded into the top of the underlying Lunnon Basalt. The mineralisation is generally 1-3 m thick but can be as thick as 10 m in some areas (Fiorentini, 2010). It consists of massive sulfide (>80% sulfide) at the base with matrix-style mineralisation (40-80% sulfide with serpentine or talc pseudomorphs after olivine) above. Massive ore consists of pentlandite, pyrrhotite, pyrite and chalcopyrite. Recrystallisation of the ore under direct stress resulted in alternating bands of pyrrhotite and pentlandite-rich layers that are generally parallel to the nearest wall rocks (Ewers and Hudson, 1972). The matrix-style mineralisation ranges from 1-3 m thick and grades from 60-80% sulfide at the base of the unit to 40-60% at the top of the unit (Gresham and Loftus-Hills, 1981; Keays et al., 1981).

The hanging wall ore occurs with spinifex-textured komatiite at the contact between the basal ultramafic flow unit and the second flow unit (Groves et al., 1986). Structurally mobilized ore is found within fold hinges, fault dilation zones and shear zones and have been mechanically transported away from the primary accumulation site (Lesher and Keays, 2002).

The Tripod Hill Member comprises approximately two thirds of the Kambalda Komatiite and ranges in thickness from 100-1000 m. The Tripod Hill Member consists of a series of thin

(1-10 m) komatiitic flows that are well differentiated, ranging from flow top breccias at the top to thick spinifex zones below the flow breccias to well-developed orthocumulates that form the base of the flow (Gresham and Loftus-Hills, 1981). The MgO content in the Tripod Hill Member is generally lower than the Silver Lake Member due to a lower proportion of olivine cumulate. A trend of lowering MgO content is observed up section through the Tripod Hill Member. The Tripod Hill Member displays higher LREE contents than the underlying Silver Lake Member presumably due to a higher degree of crustal contamination; estimated at 5% by Lesher et al. (2001). The unit displays normal background values of chalcophile element and contains no interflow sediments. It is interpreted that no sulfide liquid equilibrated with these komatiites during crystallisation and fractionation and as such the komatiites are not prospective for nickel sulfide mineralisation (Fiorentini, 2010).

A11.2.3 Devon Consuls Basalt

The Kambalda Komatiite is overlain by a sequence of siliceous, high magnesium series basalts which are split into two units separated by a thin, continuous 1-10 m thick shale unit called the Kapai Slate. The lower basalt unit is known as the Devon Consuls Basalt (DCB) and the upper basalt unit is known as the Paringa Basalt (Redman and Keays, 1985). The contact between the DCB and the underlying Kambalda Komatiite is generally sharp except at St. Ives and Tramways; however interfingering relationships have been observed (Gresham and Loftus-Hills, 1981). Both of the basalt units contain up to 30% phenocrysts of olivine, pyroxene and feldspar (Redman and Keays, 1985).

There are two types of basalt observed within the 60-100 m thick DCB. These are variolitic pillowed flows and massive lava flows with minor thin, differentiated dolerite sills (Neumayr et al., 2004). The varioles in the variolitic flows are felsic and up to 2 cm in diameter. They are generally concentrated near the pillow margin and the inter-pillow material is dominated by aphyric halyoclastite (Neumayr et al., 2004). The unit can be separated into two distinct zones, a lower coarse grained gabbroic zone and an upper fine grained aphyric zone (Neumayr et al., 2004).

The DCB can also be separated into two geochemical groups. The first is a high-Si and low-Mg basalt containing 52-60 wt% SiO_2, 4-6 wt% MgO, 6.7-7.4 wt% FeO_{tot}, 0.71-0.83 wt%TiO_2, 742-896 ppm Cr and 231-278 ppm Ni. The second is a low-Si and high-Mg basalt containing 47-52 wt% SiO_2, 9-16 wt% MgO, 9.8-12 wt% FeO_{tot}, 0.64-0.77 wt% TiO_2, 576-1173 ppm Cr, and 152-393 ppm Ni (Arndt and Jenner, 1986; Redman and Keays, 1985).

There is no depletion in the abundances in chalcophile elements which suggests that the basalts were sulfide undersaturated when they were emplaced. The basalts exhibit a flat HREE pattern, slight LREE enrichment and no Nb depletion when normalized to primitive mantle (Arndt and Jenner, 1986; Bateman et al., 2001). U-Pb and SHRIMP dating of xenocrystic zircons yielded a date of emplacement of the DCB of 2693 ± 50 (Compston et al., 1986).

A11.2.4 Kapai Slate

The Kapai Slate is a persistent, 1-10 m thick, shale unit that is found between the DCB and Paringa Basalt throughout the St. Ives district. It has been divided into five subunits: laminated siliceous magnetite-bearing slate to phyllite, siliceous pyrrhotite-bearing slate to phyllite, magnetite-bearing chert to phyllite and carbonaceous pyrite-bearing slate to phyllite and sulfide-bearing chert (Conners et al., 2005).

The unit has four different generations of pyrite. The oldest is comprised of fine (~10 µm diameter) euhedral pyrite crystals accumulated into bands with a black shale matrix, which may be diagenetic pyrite. The second generation is in the form of nodules which appear to be an agglomeration of several smaller grained pyrite crystals with minor recrystallisation. The third generation is pyrite bands/veins which are coarse grained and near massive with up to 5% sphalerite and trace chalcopyrite. The youngest generation is very coarse grained and massive and occurs as thick bands cutting bedding and older sulfides.

The second and third generations contain variable pyrrhotite alteration ranging from 20% to 90%. The youngest pyrite generation appears to overprint the pyrrhotite, but overprinting relationships are difficult to determine. The other sulfides present tend to be associated more with pyrrhotite than pyrite. In some areas the Kapai slate contains 0.5-1 cm magnetite bands.

A11.2.5 Paringa Basalt

Conformably overlying the Kapai Slate is the Paringa Basalt, which is greater than 500 m thick sequence of pillowed basalt and massive mafic flows. The pillowed flows contain chlorite-albite rich varioles, but the varioles are less common than in the underlying DCB. The massive units are characterised by radiating needles of chlorite and amphiboles after

acicular pyroxene in a fine grained matrix (Nguyen et al., 1998). The massive sequences commonly have medium to coarse grained intervals within the central section and have been described both as massive sheet flows and intrusive units (Gresham and Loftus-Hills, 1981; Said and Kerrich, 2009; Fiorentini, 2010). Near the base of the Paringa Basalt, broad zones of hyaloclastic breccia are observed with thin, cherty interflow sediments (Neumayr et al., 2004).

The Paringa Basalt is geochemically characterised by ~10.6 wt% MgO, 10.7 wt% FeO, 13.0 wt% Al_2O_3 1070-2020 ppm Cr, 280-470 ppm Ni and strong LREE enrichment (Arndt and Jenner, 1986; Lesher and Arndt, 1995).

A11.2.6 Black Flag Group

The Paringa Basalt is conformably overlain by the greater than 1 km thick Black Flag Group. The Back Flag Group is made up of felsic volcanic and sedimentary successions (Watchorn, 1998) that have been dated at 2676 ± 4 Ma (J.C Claoue-Long, I.H. Campbell and R. Hill, unpublished data, 1991). Five different lithofacies have been described at St. Ives. These include: felsic cobble conglomerate, mafic cobble breccia, plagioclase-rich granule breccia, volcanic sandstone and siltstone, and mudstone (Squire et al., 2007).

At the Junction and Argo Deposits the base of the Black Flag Group is made up of the felsic cobble conglomerate; however Junction and Argo are the only locations that this unit has been observed. The conglomerate is poorly sorted and made up of subrounded weakly plagioclase ± quartz-phyric dacite clasts up to 25 cm in diameter that are supported by a sand matrix (Squire et al., 2007).

The mafic volcanic breccia directly overlies the Paringa Basalt in some places (e.g., Nelsons Fleet) and overlies the felsic cobble breccia at the Junction and Argo Deposits. It is poorly sorted and composed of angular clasts of aphyric basalt up to 20.5 cm wide and plagioclase ± quartz-phyric dacite clasts up to 15 cm in diameter supported in a sand matrix (Squire et al., 2007).

The mudstone beds are most common on the western side of the St Ives camp (especially near Lut). They are moderately well sorted and generally less than 10 cm thick (Squire et al.,

2007). These beds are most commonly found interbedded with the sandstone but are found with the other lithologies within the Black Flag Group.

The volcanic sandstone and siltstone beds dominate the western side of the Black Flag Group. They form in beds of moderately well sorted, massive to diffusely stratified volcanic material that are generally in excess of 3 m thick. The beds are dominated by immature volcanic plagioclase and grain size rarely exceeds 2 mm in diameter (Squire et al., 2007).

The Black Flag Group is dominated by plagioclase-rich granule breccia on the eastern limb of the Kambalda Dome. The beds are massive to diffusely stratified and tend to be greater than 5 m thick. The breccia is matrix supported with less than 4 mm diameter plagioclase crystals and minor felsic lithic fragments and trace quartz crystals (Squire et al., 2007).

A11.2.7 Merrugal Formation

Unconformably overlying the Black Flag Group is the approximately 2000 m thick Merrugal Formation (Watchorn, 1998). It is made up of six primary lithologies: stratified tabular-bedded clast-supported conglomerate, diffuse conglomerate layers and single clast lags, tabular bedded massive and planar bedded sandstone, parallel-stratified channel-fill sandstone, trough cross-bedded sandstone and rare cross-stratified sandstone (Krapez et al., 2008b). The beds appear to have been deposited syn- to post-deformation as they lack a penetrative fabric and have discordant, shallow dips (Watchorn, 1998). Detrital zircons from the Merrugal Formation yield an unimodal age population of 2665 Ma (Kositcin et al., 2008). This closely matches the age of the Kambalda Granodiorite, which correlates with the peak in high-Ca granitic magmatism in the Eastern Goldfields Super Terrane (Kositcin et al., 2008). The Merrugal Formation likely formed from the remnants of pyroclastic eruptions associated with the granitic magmatism (Squire et al., under review).

The Black Flag Group and the Merrugal beds have recently been defined as part of the same sequence (Krapez et al., 2008a); however they have been separated here to be consistent with the majority of the literature on the subject.

A11.3 Intrusive units

A11.3.1 Dolerites

Several sill like mafic intrusions occur within the St. Ives stratigraphy with varying degrees of differentiation and highly variable thickness (Conners et al., 2005). Of these the most important are the Defiance Dolerite, the Junction Dolerite and the Condenser Dolerite.

The contact between the Kapai slate and the Paringa basalt was intruded by the Defiance Dolerite. The Defiance Dolerite is composed of medium to coarse grained differentiated mafic units (Nguyen et al., 1998) and has the geochemical composition of high Mg basalt (Timmermans, 2010). It is up to 300 m thick on the eastern side of the St. Ives district and significantly thinner and less differentiated on the western side (Nguyen et al., 1998). The lateral extent of the Defiance Dolerite is unknown. It is main host of gold mineralisation at the Revenge Deposit and is an important host in the Victory-Defiance-Orchin area (Clark, 1987; Roberts and Elias, 1990b). The geochemical composition of the Defiance Dolerite is similar to that of the basalts that it intrudes and thus it is interpreted to be a synvolcanic sill (Neumayr et al., 2004). Several of the smaller dolerites have the same kind of relationship to their host rocks and are considered to be synvolcanic sills as well (Neumayr et al., 2004).

The Condenser and Junction Dolerites are up to 500 m thick and are the only dolerites that intrude the Black Flag Group. They have the composition of an iron tholeiite, which is distinctly different from the Defiance Dolerite and the Black Flag Group host rocks (Neumayr et al., 2004). These Dolerites are believed to have been differentiated from a tholeiitic parent magma in situ (Neumayr et al., 2004). They have been dated to 2680±8 Ma using SHRIMP analyses of magmatic zircons (Carey, 1994) and are considered to be equivalent to the extremely well mineralized Golden Mile Dolerite at Kalgoorlie (Neumayr et al., 2004).

A11.3.2 Granitoids

The majority of granitic intrusions in the Eastern Goldfields Super Terrane are very similar in mineralogy; therefore, distinctions have been made using geochemical and geochronological parameters (Champion and Cassidy, 2007). The granitoids are separated into the following types: high-Ca (>60%), low-Ca (>20%), high-high field strength elements (5-10%), mafic (5-10%) and syenitic (<5%). Of these only the high-Ca and syenitic granitoids have been observed in the St. Ives area (Champion and Cassidy, 2007).

The high-Ca granitoids are granodioritic, granitic to trondhjemitic and are found both within and outside the greenstone belts. They form both ovoid plutons and small dykes or sills and some have been deformed to gneiss. The granitoids contain 68-77% SiO_2, are sodic and are characteristically Sr-undepleted and Y-depleted (Champion and Cassidy, 2007). This suggests they are derived from a basaltic precursor at high pressure (Champion and Cassidy, 2007). This may have resulted from partial melting of a subducted oceanic slab or partial melting of thickened mafic crust (Timmerman, 2010).

The only syenitic rocks found in the St. Ives region are from the Little Sandy Syenite. They have a distinctive red colour and contain phenocrysts of orthoclase, green pyroxene and no modal quartz (Champion and Cassidy, 2007). The syenites are elevated in total alkalis (10-12% $Na_2O + K_2O$) and have been dated between 2655 and 2645 Ma (Champion and Cassidy, 2007).

A11.4 Metamorphism and Alteration

The metamorphic history and alteration of the St. Ives district have been summarised by Roberts and Elias (1990b) and a brief summary of this work is presented here. The St. Ives area has been regionally metamorphosed between upper greenschist and lower amphibolite facies. The metamorphic assemblage contains hornblende/actinolite-plagioclase-chlorite-epidote-quartz-sphene/ilmenite and the original igneous textures are preserved by the metamorphism.

The gold deposits have distinct alteration zoning within the mafic host rocks. The innermost alteration, closest to mineralisation, is the albite alteration zone. It is surrounded by a biotite alteration zone and an outer chlorite alteration zone. The albite alteration zone is generally bleached and quartz veined. It contains the highest gold grades and the gold is found within well formed euhedral pyrite. The mineral assemblage that defines the albite zone is albite-ankerite/dolomite-quartz-pyrite with minor chlorite, biotite, muscovite and calcite (Roberts and Elias, 1990a). Geochemically the alteration zone is depleted in SiO_2, CaO, K_2O and Al_2O_3 and enriched in Na_2O relative to the outer alteration zones. The biotite alteration zone marks a change in the bulk rock composition with an increase in K_2O and a decrease in MgO, CaO and FeO (Roberts and Elias, 1990a). The mineral assemblage for this zone is albite-biotite-quartz-calcite/dolomite-magnetite-muscovite. The chlorite zone contains an alteration

assemblage of chlorite-albite-quartz-calcite-magnetite +/- biotite/muscovite/epidote (Roberts and Elias, 1990a). The igneous textures are progressively more obliterated within the chlorite alteration zone and relict ilmenite boxworks are preserved in some places.

A11.5 Structural Geology

The structural history of the St. Ives District has been discussed in detailed by Blewett et al. (2010) and Miller et al. (2010). A brief summary of this work is presented here. There are six major phases of deformation recognised in the St. Ives area: D_1 (thrusting), D_{1e} (extension), D_2 (NE-SW compression), D_3 (NE-SW extension), D_4 (NE-SW extension) and D_5 (NE-SW shortening) (Miller, 2010).

An early thrusting event that imbricates the Lunnon Basalt has been termed D_1 by Swager (1997). This faulting has been subsequently folded by D_2 deformation events. The Foster Fault is considered to be an example of D_1 faulting. However, there is some controversy over the presence of this early faulting due to a lack of meso-scale evidence of north-south thrusting from drill core and field mapping in the St. Ives area. Alternatively, the Foster Thrust may have formed during early D_2 thrusting, which imbricated the Lunnon Basalt before being folded during the late northeast-southwest D_2 contraction.

The main structural trend of the early fault structures is west-northwest. They are interpreted from gravity data, dolerite trends and the orientation of porphyry dyke swarms. Nd model age maps produced by Champion and Cassidy (2007) have defined an older regional boundary trending north-northwest. This boundary defines the map patterns of the constituent terranes of the Eastern Goldfields Super Terrane (EGST), including its western margin (Champion and Cassidy, 2007). The regional Boulder-Lefroy Fault originated during the early development of the EGST and is parallel to the same trend. The D_{1e} architecture formed where pre-existing north-northwest boundaries were obliquely extended with an inferred extension direction of northeast-southwest. The Boulder-Lefroy Fault likely marks the axis of this earlier boundary. The west-northwest trending faults are extensional faults while breached relay faults are oblique to the earlier rift axis and have accommodated large-scale oblique extension (Miller, 2010). These faults formed small grabens that were infilled with syn-rifting sediments and volcanic rocks (i.e., the Black Flag Group). This early rift architecture is inferred to have controlled the distribution of the dolerite. It is unknown to

what degree the faults acted as feeders for the dolerites and to what degree they acted as barriers to the magma's horizontal flow.

The northeast-southwest D_2 compression marks the first major inversion of the earlier rift architecture. This resulted in the reactivation of the older normal faults as well as the formation of new neoformed faults, such as the Delta Fault.

In the onset of the D_2 compression the majority of the movement was along the pre-existing west-northwest D_{1e} faults. As the D_{1e} faults were not optimally oriented for slip during the D_2 compression, north trending thrust faults were developed and linked up the earlier D_{1e} faults (Miller, 2010). These linking faults became important contractional jogs for subsequent gold mineralisation. The geometries of the faults developed during D_2 are lens-like and they control the development of compressional and transtensional zones during reactivation in D_4 (Miller, 2010).

After the D_2 compression there was a renewed extensional regime referred to as D_3. The folding of intrusive dykes, which crosscut the D_2 folds is what distinguishes the D_3 events from earlier structures. Movement during D_3 is interpreted to be northeast-southwest extension is inferred based on the trend of the main dykes and early steep vein arrays on the Repulse Shear (Miller, 2010). The majority of the porphyritic intrusive rocks are interpreted to have been emplaced during the D_3 phase. Gravity lows associated with some west-northwest trending faults are interpreted to reflect large intrusive bodies at depth that were emplaced preferentially into the faults (Miller, 2010).

The D_3 extension was followed by a period of east-west to west northwest-east southeast compression, termed D_4. The stress field caused by the D_4 compression resulted in sinistral movement along northwest- and north-northwest trending faults from the pre-existing D_{1e}, D_2 and D_3 architecture (Miller, 2010). The faults that exhibited sinistral movement include: the Boulder-Lefroy Fault, the Playa Fault, the Bellisle Fault and the Delta Fault. Local areas of extension were found within left-stepping transtensional jogs while local areas of compression where found within right stepping compressional jogs. During the D_4 event new north to north-northeast trending faults that cross cut older structures were formed (Miller, 2010).

The majority of the gold mineralisation in the St. Ives District is considered by Blewett et al. (2010) to have formed during the D_4 event. Movement along the Playa Fault is believed to

have created permeability in the footwall and hanging wall units that acted as an important fluid conduit. The flanks of the Kambalda antiform and the boundaries of some of the major intrusive bodies (Neumayr et al., 2008) are also important conduits for the mineralising fluids. The areas associated with left- and right-stepping jogs in the north-northwest trending faults are also important areas where ore fluids have focussed. However, only segments of these faults are interpreted as being active during mineralisation. The mineralisation along these faults is interpreted to be due to fluid flow allowed by failure during periodic seismicity (Cox and Ruming, 2004).

The final major phase of deformation is D_5 dextral faulting and reactivation due to northeast-southwest shortening. This shortening resulted in north to northeast trending dextral faulting and the generation of extensive northeast-southwest trending vein arrays. In most areas these vein arrays are associated with low-grade mineralisation.

A11.6 References

Arndt, N.T., and Jenner, G.A. (1986) Crustally contaminated komatiites and basalts from Kambalda, Western Australia. Chemical Geology, 56(3-4), 229-255.

Barley, M.E., and Groves, D.I. (1987) Hydrothermal alteration of Archaean supracrustal sequences in the central Norse-Wiluna belt, Western Australia. In S.E. Ho, and D.I. Groves, Eds. Recent advances in understanding Precambrian gold deposits, p. 51-66. University of Western Australia, Geology Department and University Extention, Publication 11.

Bateman, R., Costa, S., Swe, T., and Lambert, D. (2001) Archaean mafic magmatism in the Kalgoorlie area of the Yilgarn Craton, Western Australia; a geochemical and Nd isotopic study of the petrogenetic and tectonic evolution of a greenstone belt. Precambrian Research, 108(1-2), 75-112.

Beresford, S., Cas, R., Lahaye, Y., and Jane, M. (2002) Facies architecture of an Archean komatiite-hosted Ni-sulphide ore deposit, Victor, Kambalda, Western Australia; implications for komatiite lava emplacement. Journal of Volcanology and Geothermal Research, 118(1-2), 57-75.

Blewett, R.S., Czarnota, K., Henson, P.A., and Champion, D.C. (2010) Structural-event framework for the eastern Yilgarn Craton, Western Australia, and its implications for orogenic gold Precambrian Research, 183(2), 203-229.

Carey, M. (1994) Petrography and geochemistry of selected sills from the Kambalda-Kalgoorlie region, WA. unpublished BSc (Honours) thesis, Australian National University, Canberra.

Champion, D.C., and Cassidy, K.F. (2007) An overview of the Yilgarn Craton and its crustal evolution. Record - Geoscience Australia, 8-13.

Clark, M.E. (1987) The geology and of the Victory gold mine, Kambalda, Western Australia. unpublished PhD thesis, Queen's University, Kingston, Ontario.

Compston, W., Williams, I.S., Campbell, I.H., and Gresham, J.J. (1986) Zircon xenocrysts from the Kambalda volcanics; age constraints and direct evidence for older continental crust below the Kambalda-Norseman greenstones. Earth and Planetary Science Letters, 76(3-4), 299-311.

Conners, K., Donaldson, J.S., Morrison, R.S., Davy's, C., and Neumayr, P. (2005) The Stratigraphy of the Kambalda-St Ives District: Workshop Notes.

Cox, S.F., and Ruming, K. (2004) The St Ives mesothermal gold system, Western Australia - a case of golden aftershocks? Journal of Structural Geology, 26(6-7), 1109-1125.

Fiorentini, M.L. (2010) The Kambalda Nickel Camp. In T.C. McCuaig, J.M. Miller, and S. Beresford, Eds. Controls on Giant Mineral Systems in Yilgarn Craton Field Guide, p. 37.

Gemuts, I., and Theron, A. (1975) The Archean between Coolgardie and Norseman-stratigraphy and mineralization. In C.L. Knight, Ed. Economoic Geology of Australia and Papua New Guinea, Volume 1 - Metals, The Australasian Institute of Mining and Metallurgy Mongraphy 5, p. 66-74.

Gresham, J.J., and Loftus-Hills, G.D. (1981) The geology of the Kambalda nickel field, Western Australia. Economic Geology and the Bulletin of the Society of Economic Geologists, 76(6), 1373-1416.

Groves, D.I., Korkiakoski, E.A., McNaughton, N.J., Lesher, C.M., and Cowden, A. (1986) Thermal erosion by komatiites at Kambalda, Western Australia and the genesis of nickel ores. Nature (London), 319(6049), 136-139.

Hill, R.E.T., Barnes, S.J., Gole, M.J., and Dowling, S.E. (1995) The volcanology of komatiites as deduced from field relationships in the Norseman-Wiluna greenstone belt, Western Australia. Lithos, 34(1-3), 159-188.

Keays, R.R., Ross, J.R., and Woolrich, P. (1981) Precious metals in volcanic peridotite-associated nickel sulfide deposits in Western Australia; II, Distribution within the ores and host rocks at Kambalda. Economic Geology and the Bulletin of the Society of Economic Geologists, 76(6), 1645-1674.

Kositcin, N., Brown, S.J.A., Barley, M.E., Krapez, B., Cassidy, K.F., Champion, D.C., Gee, M.A.M., and Swager, C. (2008) SHRIMP U/Pb zircon age constraints on the late Archaean tectonostratigraphic architecture of the Eastern Goldfields Superterrane, Yilgarn Craton, Western Australia. Precambrian Research, 161(1-2), 5-33.

Krapez, B., Barley, M.E., and Brown, S.J.A. (2008a) Late Archean synorogenic basins of the Eastern Goldfields Superterrane, Yilgarn Craton, Western Australia; Part 1, Kalgoorlie and Gindalbie terranes. Precambrian Research, 161, 135-153.

Krapez, B., Barley, M.E., Gee, M.A.M., and Swager, C. (2008b) Late Archaean synorogenic basins of the Eastern Goldfields Superterrane, Yilgarn Craton, Western Australia; Part III, Signatures of tectonic escape in arc-continent collision zone. Precambrian Research, 161(1-2), 183-199.

Lesher, C.M. (1983) Localization and genesis of komatiite-associated Fe-Ni-Cu sulphide mineralization at Kambalda, Western Australia, p. 199. unpublished PhD thesis, University of Western Australia.

-. (1989) Komatiite-associated nickel sulfide deposits. Reviews in Economic Geology, 4, 45-101.

Lesher, C.M., and Arndt, N.T. (1995) REE and Nd isotope geochemistry, petrogenesis and volcanic evolution of contaminated komatiites at Kambalda, Western Australia. Lithos, 34(1-3), 127-157.

Lesher, C.M., Arndt, N.T., and Groves, D.I. (1984) Genesis of komatiite-associated nickel sulphide deposits at Kambalda, West-Australia: A distal volcanic model. In D.L. Buchan, and M.L. Jones, Eds. Sulphide deposits in mafic and ultramafic rocks, Proceedings of International Geological Correlation Program Projects 161 and 91, Third Nickel Sulphide Field Conference, p. 70-80. Institution of Mining and Metallurgy, London, Perth, Western Australia.

Lesher, C.M., Burnham, O.M., Keays, R.R., Barnes, S.J., and Hulbert, L. (2001) Trace-element geochemistry and petrogenesis of barren and ore-associated komatiites. The Canadian Mineralogist, 39, 673-696.

Lesher, C.M., and Keays, R.R. (2002) Komatiite-associated Ni-Cu-(PGE) deposits; geology, mineralogy, geochemistry, and genesis. Special Volume - Canadian Institute of Mining and Metallurgy (1982), 54, 579-617.

Miller, J.M. (2010) The St Ives Goldfields, Yilgarn, Western Australia. In T.C. McCuaig, J.M. Miller, and S. Beresford, Eds. Controls on Giant Mineral Systems in Yilgarn Craton Field Guide, p. 42.

Miller, J.M., Blewett, R.S., Tunjic, S., and Conners, K. (2010) The role of early formed structures on the development of the world class St Ives Goldfield, Yilgarn. Precambrian Research, 183(2), 292-315.

Neumayr, P., Walshe, J., Connors, K., Cox, S., Morrison, R.S., Stolz, E., Harris, M., and Beresford, S.W. (2004) Gold mineralization in the St Ives camp near Kambalda. Record - Geological Survey of Western Australia, 23-45.

Neumayr, P., Walshe, J., Hagemann, S., Petersen, K., Roache, A., Frikken, P., Horn, L., and Halley, S. (2008) Oxidized and reduced mineral assemblages in greenstone belt rocks

of the St. Ives gold camp, Western Australia: vectors to high-grade ore bodies in Archaean gold deposits? Mineralium Deposita, 43(3), 363-371.

Nguyen, P.T., Cox, S.F., Harris, L.B., and Powell, C.M. (1998) Fault-valve behaviour in optimally oriented shear zones; an example at the Revenge gold mine, Kambalda, Western Australia. Journal of Structural Geology, 20(12), 1625-1640.

Redman, B.A., and Keays, R.R. (1985) Archean basic volcanism in the Eastern Goldfields Province, Yilgarn Block, Western Australia. Precambrian Research, 30(2), 113-152.

Roberts, D., and Elias, M. (1990a) Gold deposits of the Kambalda-St Ives region. Geology of the mineral deposits of Australia and Papua New Guinea. Australasian Institute of Mining and Metallurgy Monograph, 14, 479-491.

Roberts, D.E., and Elias, M. (1990b) Gold deposits of the Kambalda-St Ives region. Monograph Series - Australasian Institute of Mining and Metallurgy, 14, 479-491.

Ross, J.R., and Hopkins, G.M.F. (1979) Kambalda nickel sulfide deposits. In C.L. Knight, Ed. Economoic Geology of Australia and Papua New Guinea, Volume 1 - Metals, The Australasian Institute of Mining and Metallurgy Mongraphy 5, p. 100-121.

Squire, R.J., Allen, M.A., Cas, R.A.F., Cambell, I.H., Blewett, R.S., and Nemchin, A.A. (under review) Transition from greenstone volcanism to cratonisation in the eastern Yilgarn Craton, Western Australia, revealed by provenance characteristics of late Archean sedimentary successions

Squire, R.J., Cas, R.A.F., and Champion, D.C. (2007) The Black Flags Group: A vector to ore at St Ives. Geoconferences (WA) Inc. Kalgoorlie '07 Conference, Kalgoorlie, Western Australia.

Squire, R.J., Cas, R.A.F., Clout, J.M.F., and Behets, R. (1998) Volcanology of the Archaean Lunnon Basalt and its relevance to nickel sulfide-bearing trough structures at Kambalda, Western Australia. Australian Journal of Earth Sciences, 45(5), 695-715.

Stone, W.E., Archibald, N.J., Blenkinsop, T.G., Vearncombe, J.R., and Reddy, S.M. (2004) Structural controls on nickel sulphide ore shoots in Archaean komatiite, Kambalda, WA; the volcanic trough controversy revisited. Journal of Structural Geology, 26(6-7), 1173-1194.

Stone, W.E., Beresford, S.W., and Archibald, N.J. (2005) Structural setting and shape analysis of nickel sulfide shoots at the Kambalda Dome, Western Australia; implications for deformation and remobilization. Economic Geology and the Bulletin of the Society of Economic Geologists, 100(7), 1441-1455.

Swager, C.P. (1997) Tectono-stratigraphy of late Archaean greenstone terranes in the southern Eastern Goldfields, Western Australia. Precambrian Research, 83(1-3), 11-42.

Timmermans, L.J. (2010) Architecture and evolution of possible intrusion-related Late Archean Au deposits in the Bellerophon - Little Sandy region, St Ives, Western Australia, p. 36. unpublished BSc (Honours) thesis, Monash University.

Watchorn, R.B. (1998) Kambalda-St. Ives gold deposits. Monograph Series - Australasian Institute of Mining and Metallurgy, 22, 243-254.

Williams, D.A., Kerr, R.C., and Lesher, C.M. (1998) Emplacement and erosion by Archean komatiite lava flows at Kambalda; revisited. Journal of Geophysical Research, 103(B11), 27.

Appendix 12:

Drill logs from St Ives gold district

A12.1 CD804

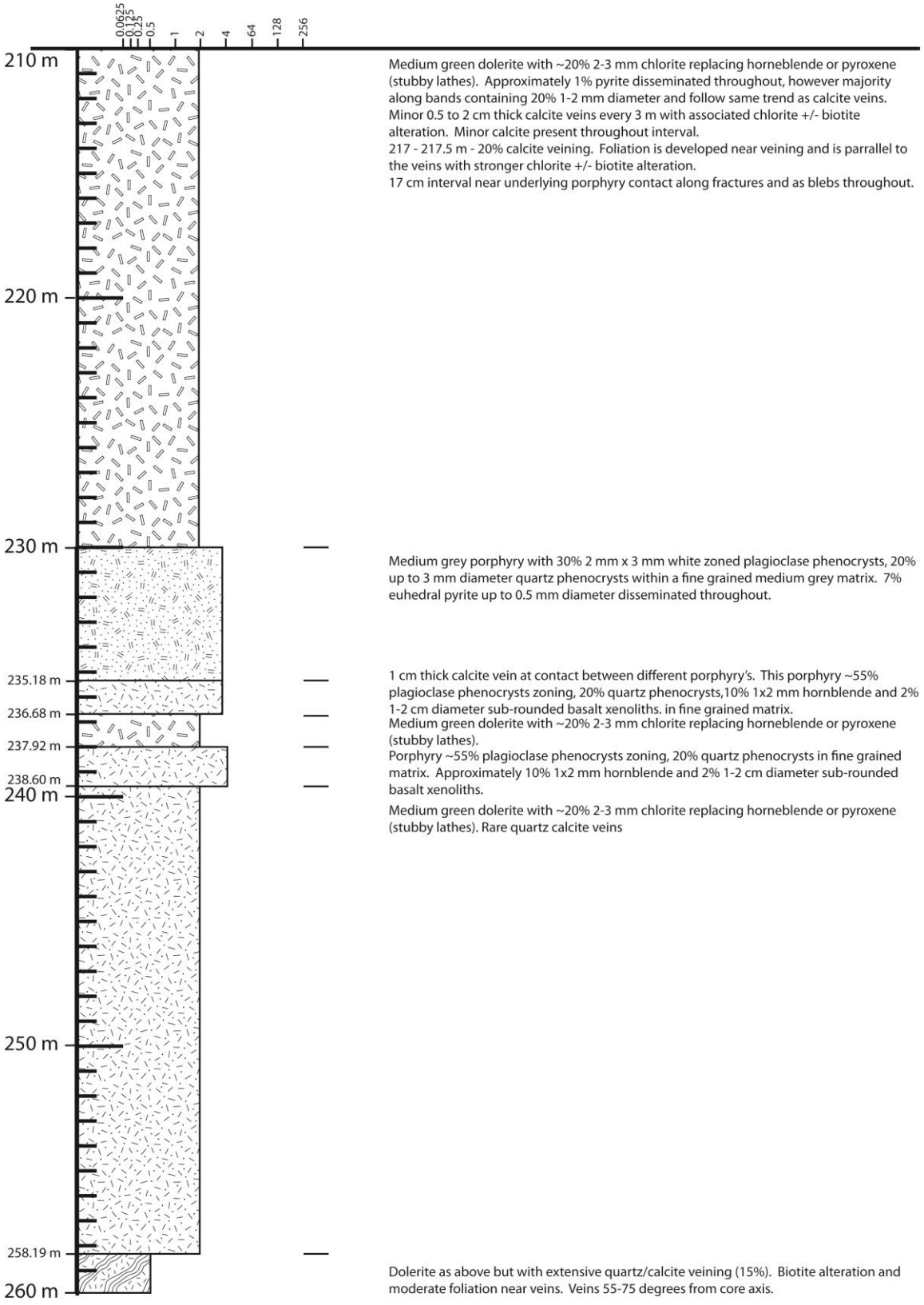
CD804 page 1 of 3
0.0625
0.125
0.25
0.5
1
2
4
64
128
256
210 m
220 m
230 m
235.18 m
236.68 m
237.92 m
238.60 m
240 m
250 m
258.19 m
260 m
Medium green dolerite with ~20% 2-3 mm chlorite replacing horneblende or pyroxene (stubby lathes). Approximately 1% pyrite disseminated throughout, however majority along bands containing 20% 1-2 mm diameter and follow same trend as calcite veins. Minor 0.5 to 2 cm thick calcite veins every 3 m with associated chlorite +/- biotite alteration. Minor calcite present throughout interval.
217 - 217.5 m - 20% calcite veining. Foliation is developed near veining and is parrallel to the veins with stronger chlorite +/- biotite alteration.
17 cm interval near underlying porphyry contact along fractures and as blebs throughout.
Medium grey porphyry with 30% 2 mm x 3 mm white zoned plagioclase phenocrysts, 20% up to 3 mm diameter quartz phenocrysts within a fine grained medium grey matrix. 7% euhedral pyrite up to 0.5 mm diameter disseminated throughout.
1 cm thick calcite vein at contact between different porphyry's. This porphyry ~55% plagioclase phenocrysts zoning, 20% quartz phenocrysts,10% 1x2 mm hornblende and 2% 1-2 cm diameter sub-rounded basalt xenoliths. in fine grained matrix.
Medium green dolerite with ~20% 2-3 mm chlorite replacing horneblende or pyroxene (stubby lathes).
Porphyry ~55% plagioclase phenocrysts zoning, 20% quartz phenocrysts in fine grained matrix. Approximately 10% 1x2 mm hornblende and 2% 1-2 cm diameter sub-rounded basalt xenoliths.
Medium green dolerite with ~20% 2-3 mm chlorite replacing horneblende or pyroxene (stubby lathes). Rare quartz calcite veins
Dolerite as above but with extensive quartz/calcite veining (15%). Biotite alteration and moderate foliation near veins. Veins 55-75 degrees from core axis.

CD804 page 2 of 3

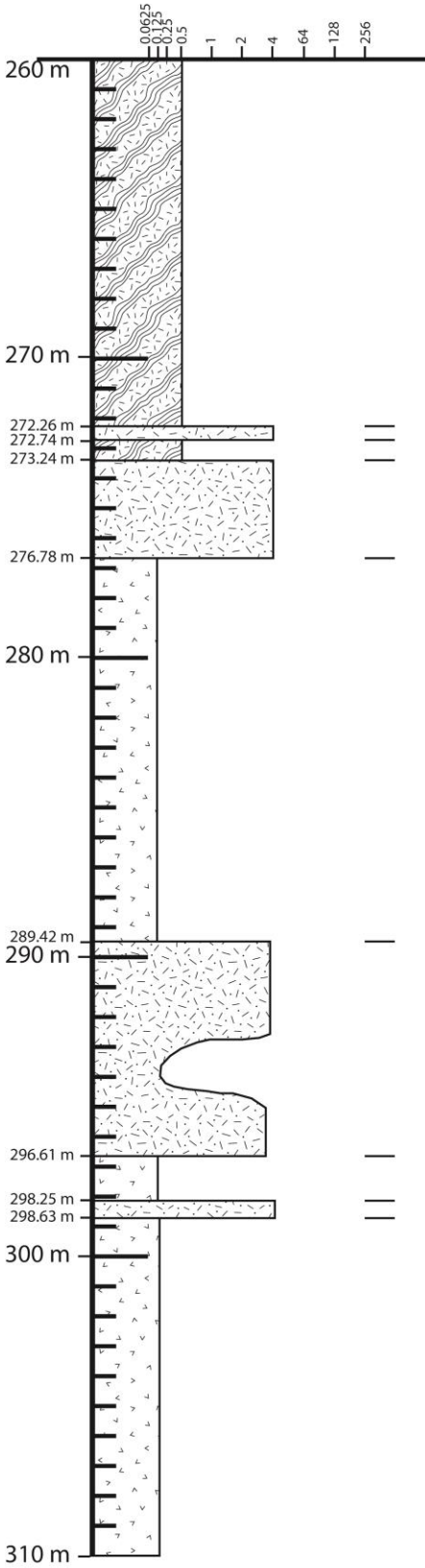

Dolerite as above but with extensive quartz/calcite veining (15%). Biotite alteration and moderate foliation near veins. Veins 55-75 degrees from core axis.

Porphyry ~55% plagioclase phenocrysts zoning, 20% quartz phenocrysts,10% 1x2 mm hornblende and 2% 1-2 cm diameter sub-rounded basalt xenoliths in fine grained matrix. Trace disseminated pyrite and 4% quartz +/- calcite veining 3-7 mm wide.

Dolerite as above but with extensive quartz/calcite veining (15%). Biotite alteration and moderate foliation near veins. Veins 55-75 degrees from core axis.

Porphyry ~55% plagioclase phenocrysts zoning, 20% quartz phenocrysts,10% 1x2 mm hornblende and 2% 1-2 cm diameter sub-rounded basalt xenoliths in fine grained matrix. Trace disseminated pyrite and 4% quartz +/- calcite

Fine to medium grained, medium green basalt with weak to moderate calcite. Trace disseminatedpyrite, rare 1-3 mm quartz veins. Veins more common near the top. Bottom contact 20-30 cm of moderate biotite alteration.

Porphyry ~55% plagioclase phenocrysts zoning, 20% quartz phenocrysts,10% 1x2 mm hornblende and 2% up to 30 cm diameter rounded basalt xenoliths in fine grained matrix. Trace disseminated pyrite and 4% quartz +/- calcite veining 3-7 mm wide. Irregular partial melt contact at bottom of interval. Center of interval is much finer grained.

Fine grained medium green basalt ~3% cut by 1-2 mm calcite veins with minor magnetite.

Porphyry ~55% plagioclase phenocrysts zoning, 20% quartz phenocrysts,10% 1x2 mm hornblende and 2% 1-2 cm diameter sub-rounded basalt xenoliths in fine grained matrix.

Fine grained medium green basalt ~3% cut by 1-4 mm calcite veins. When several veins occur in clumps, foliation develops and moderate biotite alteration presence.

CD804 page 3 of 3

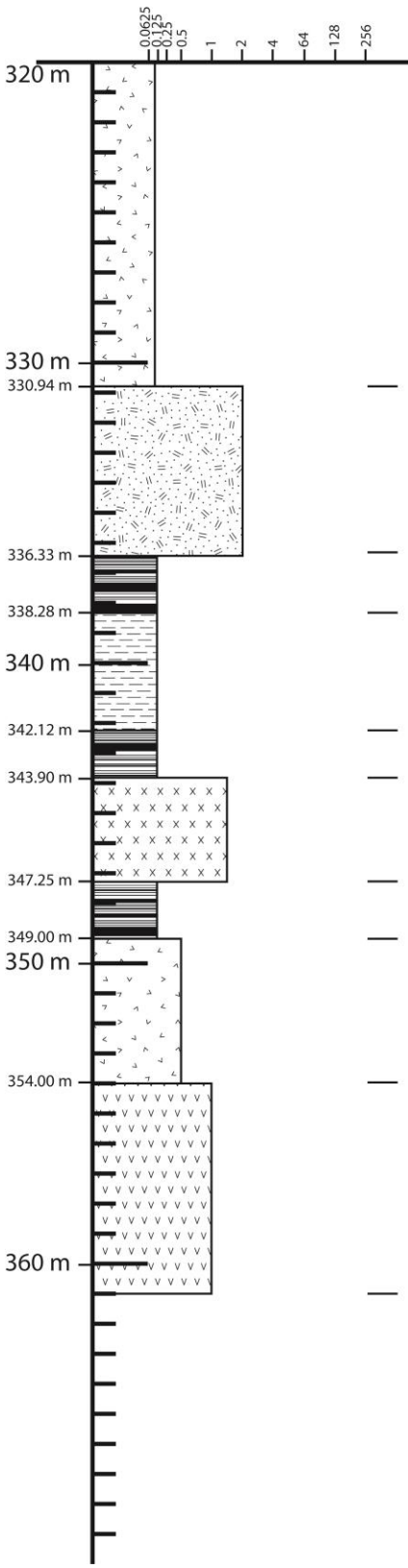

Fine grained medium green basalt ~3% cut by 1-4 mm calcite veins. When several veins occur in clumps, foliation develops and moderate biotite alteration presence.

Dark grey weakly to moderately foliated porphyry. Moderate to strong biotite alteration. ~5% quartz/calcite veining with orientations approximately parrallel to foliation. Near verticle veins at the bottom of the interval has more biotite alteration and stronger foliation with erratic contact with underlying shale.

Interbedded dark grey to black mudstone light to medium grey mudstone (75:25) many of the darker beds have been strongly magnetite altered. Pyrite is most prevalent in darker layers and occurs as blebs.

Interbedded dark grey to black mudstone light to medium grey mudstone (75:25) many of the darker beds have been strongly magnetite altered. 10-20 cm thick quartz veins with 5% yrite/pyrrhotite and 3% magnetite. Minor magnetite, 10% pyrite and 10% pyrrhotite, occurring as net texture between veins and blebs else where.

Interbedded dark grey to black mudstone light to medium grey mudstone (75:25) many of the darker beds have been strongly magnetite altered. Pyrite is most prevalent in darker layers and occurs as blebs.

Medium grey fine to medium grained intrusion ~20% 2x3 mm hornblende phenocrysts in a fine to medium grained plagioclase rich light grey matrix.

Interbedded dark grey to black mudstone light to medium grey mudstone (50:50) many of the darker beds have been strongly magnetite altered. Pyrite and pyrrhotite (13%) are prevalent in darker layers and occurs as blebs.

Medium grained dark green basalt, some halioclastic texture and minor calcite veins.

Medium green pillow basalt with up to 1 cm diameter varioles in 5-20 cm intervals every 1 m.

A12.2 CD1512

CD1512 page 1 of 3

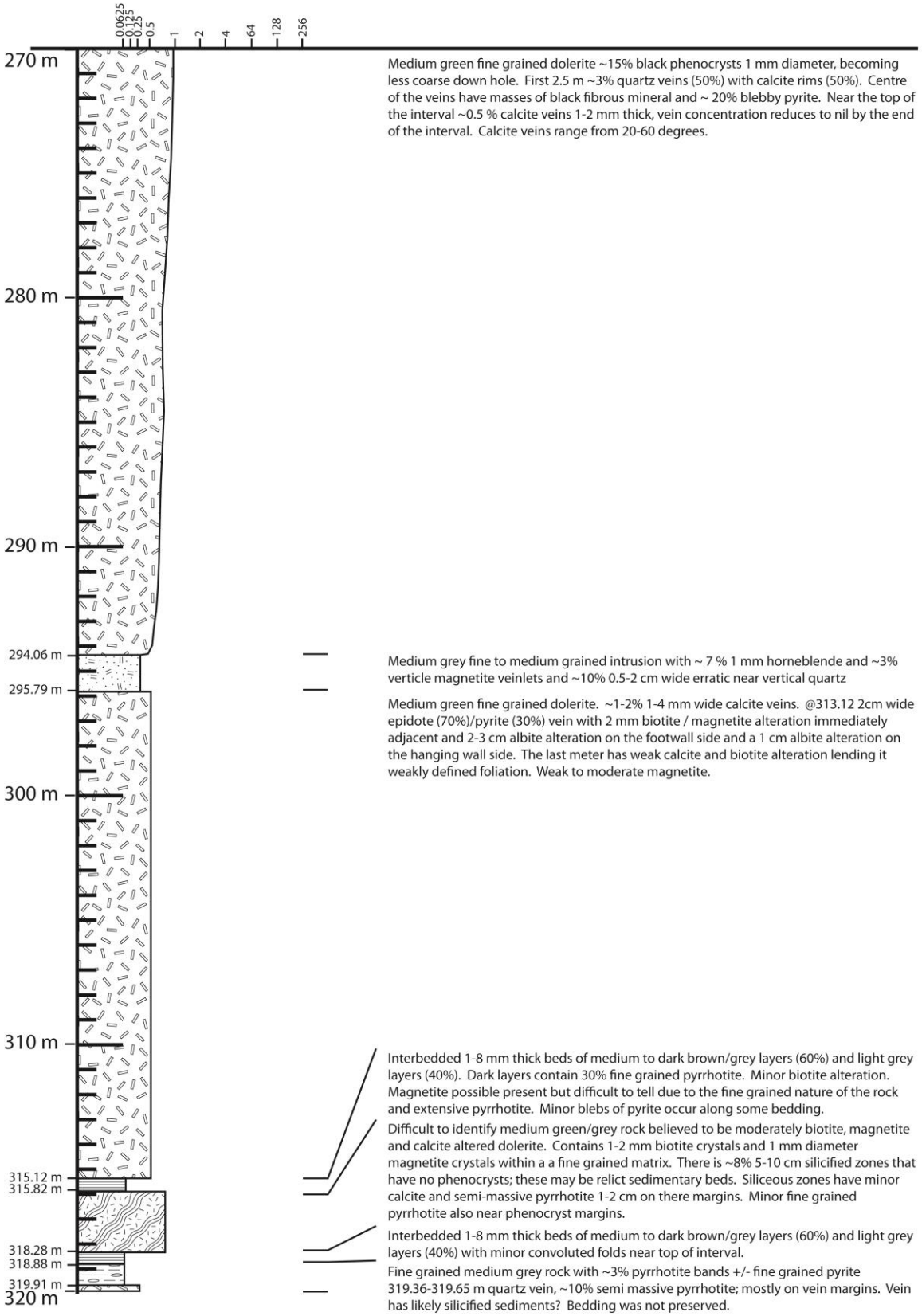

CD1512 page 2 of 3

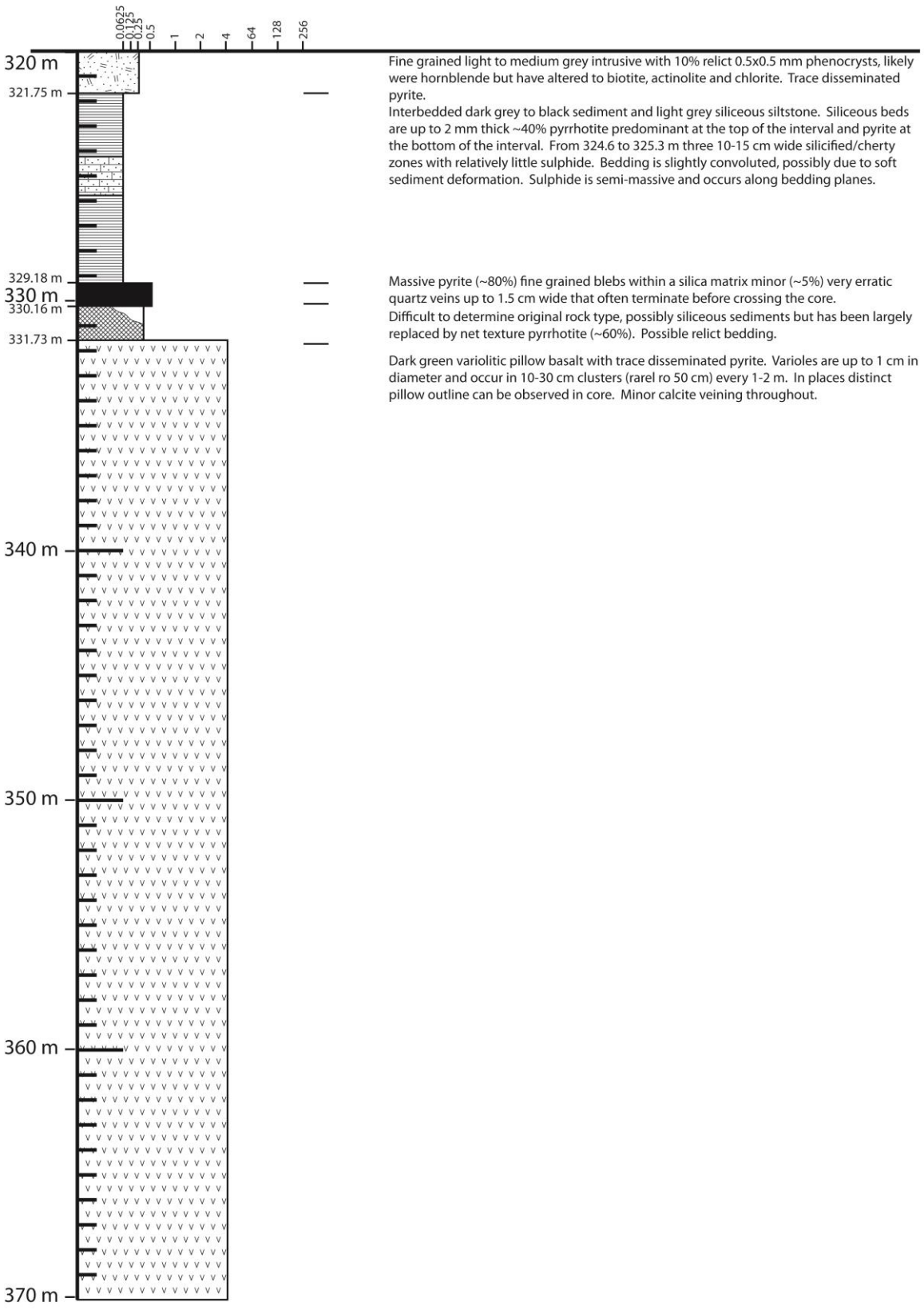

Fine grained light to medium grey intrusive with 10% relict 0.5x0.5 mm phenocrysts, likely were hornblende but have altered to biotite, actinolite and chlorite. Trace disseminated pyrite.
Interbedded dark grey to black sediment and light grey siliceous siltstone. Siliceous beds are up to 2 mm thick ~40% pyrrhotite predominant at the top of the interval and pyrite at the bottom of the interval. From 324.6 to 325.3 m three 10-15 cm wide silicified/cherty zones with relatively little sulphide. Bedding is slightly convoluted, possibly due to soft sediment deformation. Sulphide is semi-massive and occurs along bedding planes.

Massive pyrite (~80%) fine grained blebs within a silica matrix minor (~5%) very erratic quartz veins up to 1.5 cm wide that often terminate before crossing the core.
Difficult to determine original rock type, possibly siliceous sediments but has been largely replaced by net texture pyrrhotite (~60%). Possible relict bedding.

Dark green variolitic pillow basalt with trace disseminated pyrite. Varioles are up to 1 cm in diameter and occur in 10-30 cm clusters (rarel ro 50 cm) every 1-2 m. In places distinct pillow outline can be observed in core. Minor calcite veining throughout.

CD1512 page 3 of 3

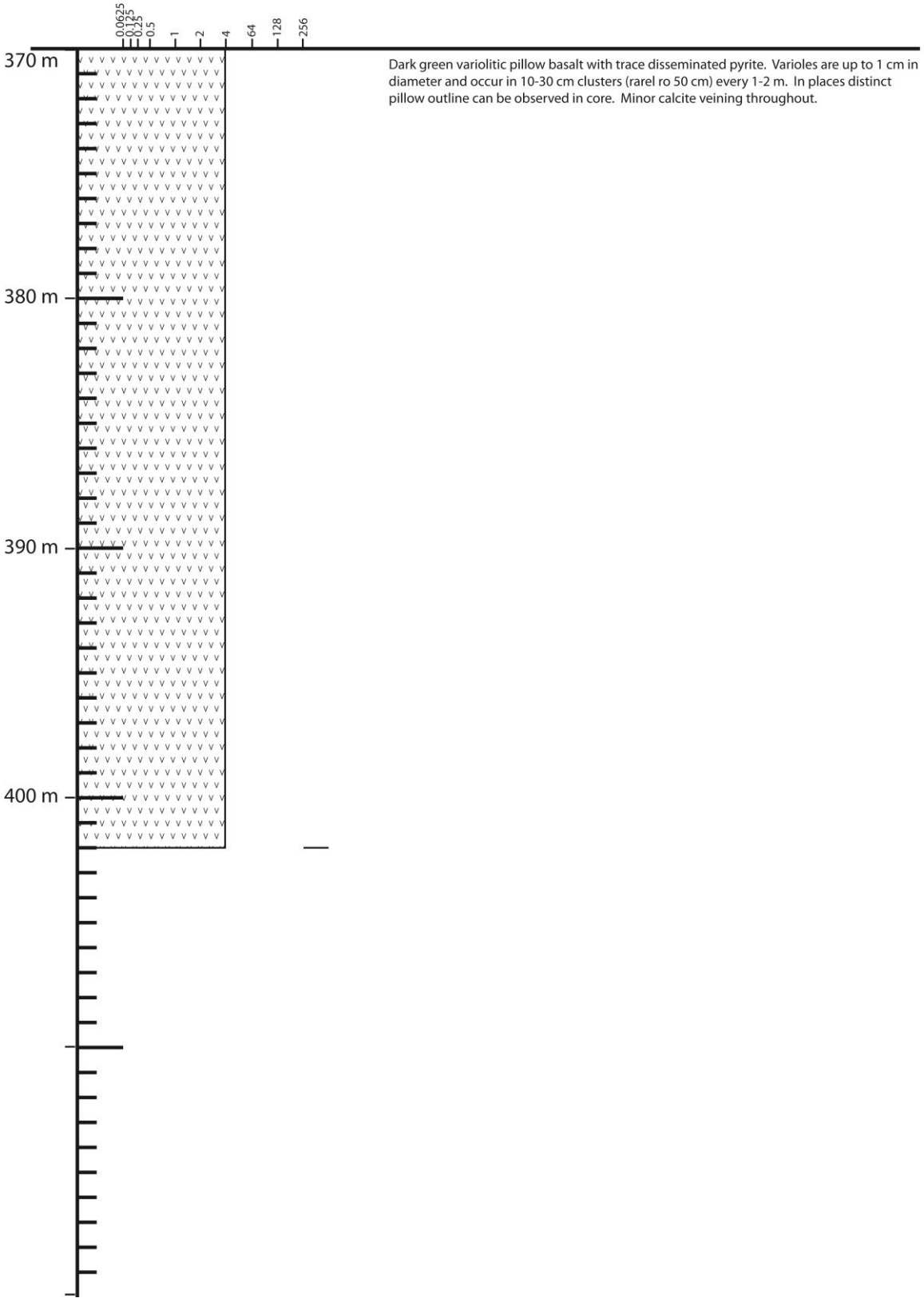

A12.3 CD1697

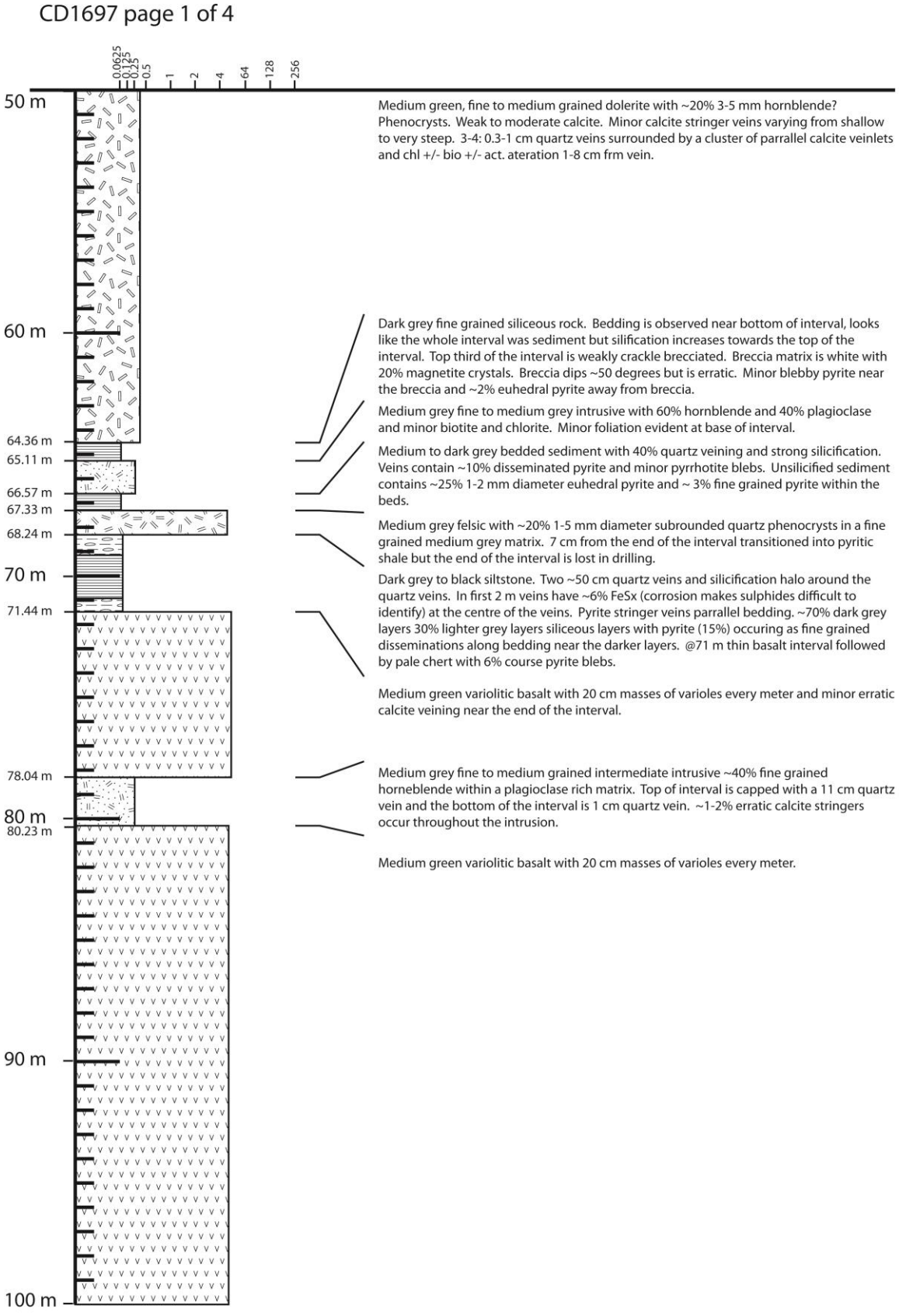
CD1697 page 1 of 4
0.0625
0.125
0.25
0.5
1
2
4
64
128
256
50 m
60 m
64.36 m
65.11 m
66.57 m
67.33 m
68.24 m
70 m
71.44 m
78.04 m
80 m
80.23 m
90 m
100 m
Medium green, fine to medium grained dolerite with ~20% 3-5 mm hornblende? Phenocrysts. Weak to moderate calcite. Minor calcite stringer veins varying from shallow to very steep. 3-4: 0.3-1 cm quartz veins surrounded by a cluster of parrallel calcite veinlets and chl +/- bio +/- act. ateration 1-8 cm frm vein.
Dark grey fine grained siliceous rock. Bedding is observed near bottom of interval, looks like the whole interval was sediment but silification increases towards the top of the interval. Top third of the interval is weakly crackle brecciated. Breccia matrix is white with 20% magnetite crystals. Breccia dips ~50 degrees but is erratic. Minor blebby pyrite near the breccia and ~2% euhedral pyrite away from breccia.
Medium grey fine to medium grey intrusive with 60% hornblende and 40% plagioclase and minor biotite and chlorite. Minor foliation evident at base of interval.
Medium to dark grey bedded sediment with 40% quartz veining and strong silicification. Veins contain ~10% disseminated pyrite and minor pyrrhotite blebs. Unsilicified sediment contains ~25% 1-2 mm diameter euhedral pyrite and ~ 3% fine grained pyrite within the beds.
Medium grey felsic with ~20% 1-5 mm diameter subrounded quartz phenocrysts in a fine grained medium grey matrix. 7 cm from the end of the interval transitioned into pyritic shale but the end of the interval is lost in drilling.
Dark grey to black siltstone. Two ~50 cm quartz veins and silicification halo around the quartz veins. In first 2 m veins have ~6% FeSx (corrosion makes sulphides difficult to identify) at the centre of the veins. Pyrite stringer veins parrallel bedding. ~70% dark grey layers 30% lighter grey layers siliceous layers with pyrite (15%) occuring as fine grained disseminations along bedding near the darker layers. @71 m thin basalt interval followed by pale chert with 6% course pyrite blebs.
Medium green variolitic basalt with 20 cm masses of varioles every meter and minor erratic calcite veining near the end of the interval.
Medium grey fine to medium grained intermediate intrusive ~40% fine grained horneblende within a plagioclase rich matrix. Top of interval is capped with a 11 cm quartz vein and the bottom of the interval is 1 cm quartz vein. ~1-2% erratic calcite stringers occur throughout the intrusion.
Medium green variolitic basalt with 20 cm masses of varioles every meter.

CD1697 page 2 of 4

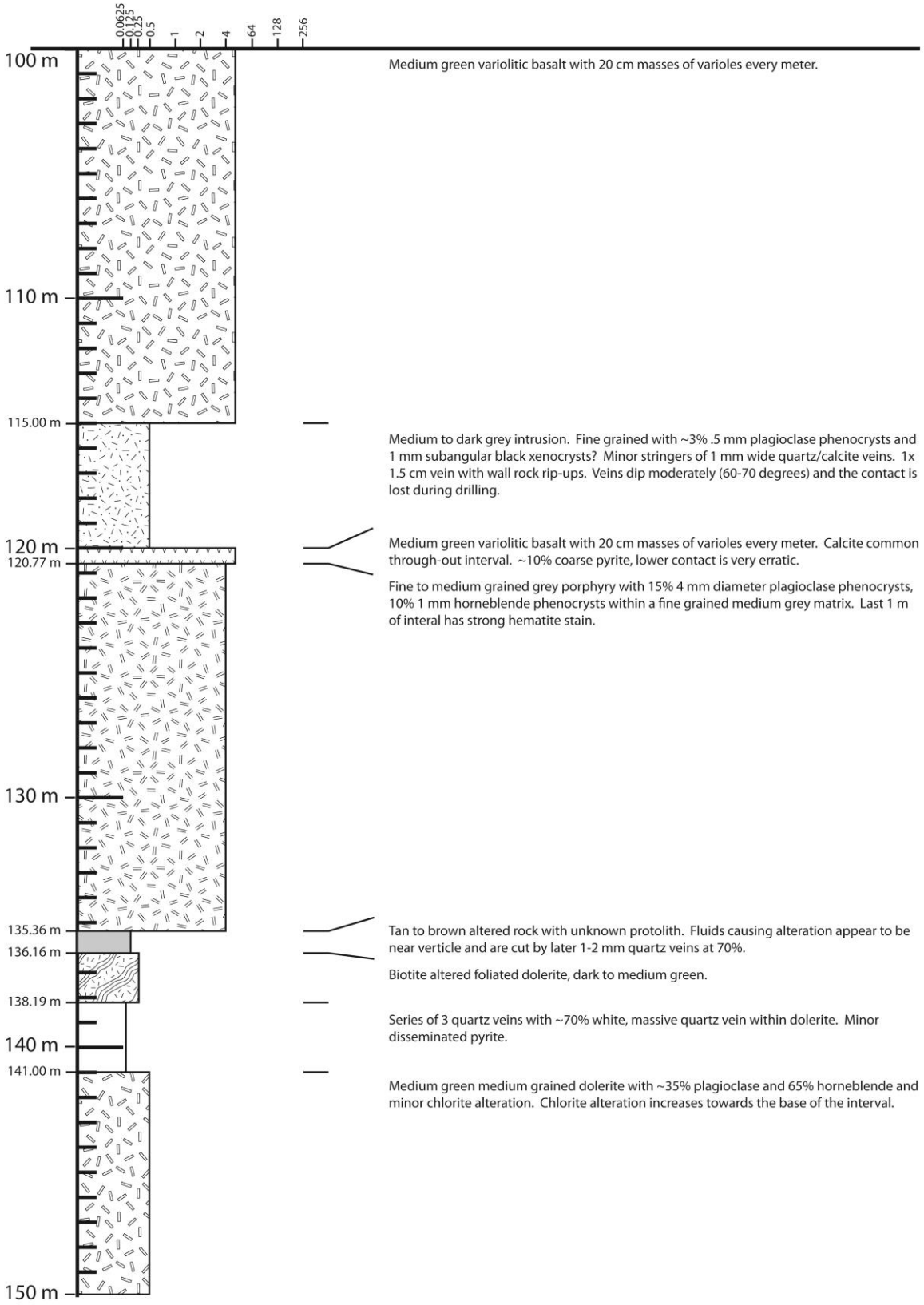

CD1697 page 3 of 4

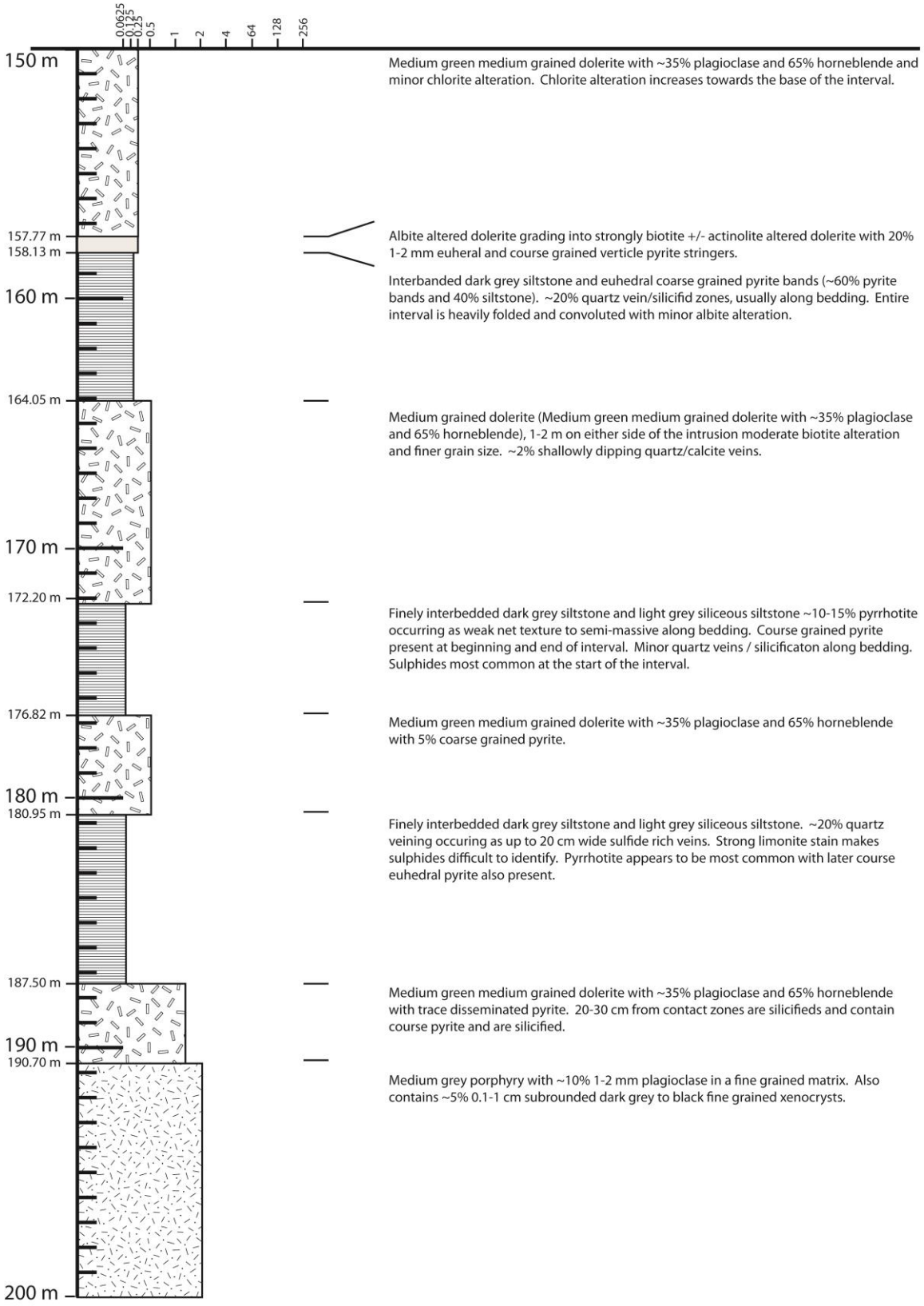

CD1697 page 4 of 4

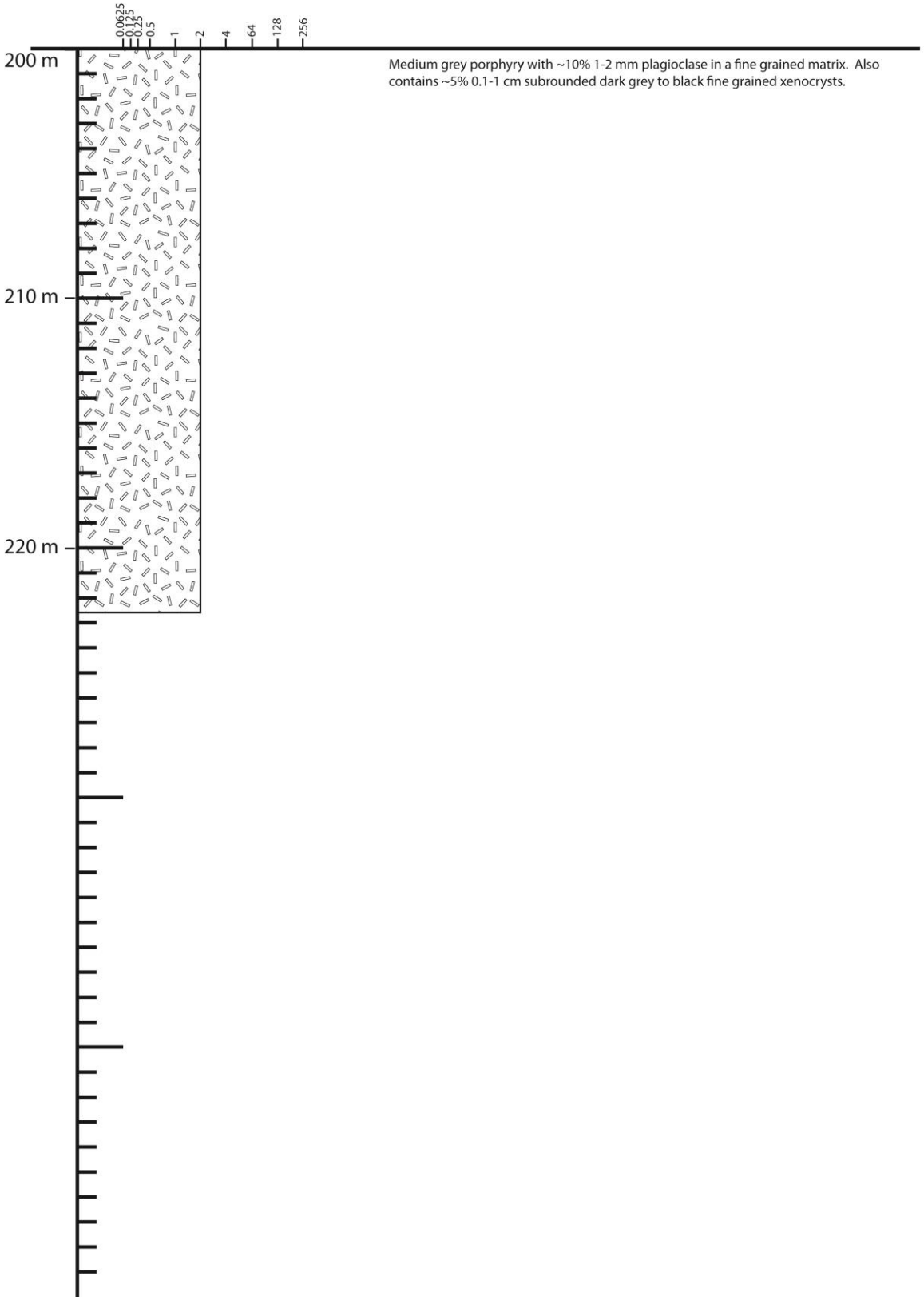

A12.4 CD8142

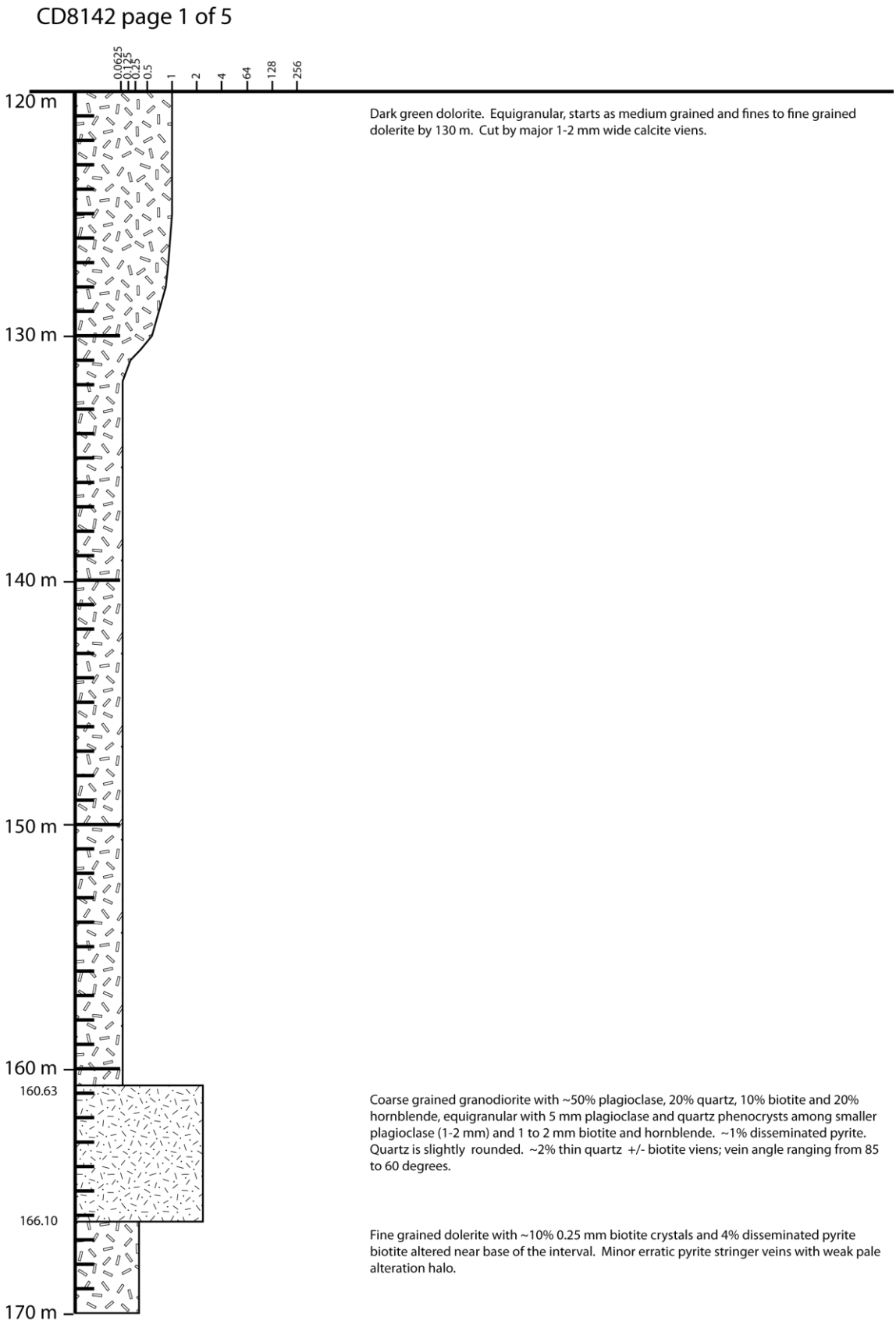
CD8142 page 1 of 5
0.0625
0.125
0.25
0.5
1
2
4
64
128
256
120 m
130 m
140 m
150 m
160 m
160.63
166.10
170 m
Dark green dolorite. Equigranular, starts as medium grained and fines to fine grained dolerite by 130 m. Cut by major 1-2 mm wide calcite viens.
Coarse grained granodiorite with ~50% plagioclase, 20% quartz, 10% biotite and 20% hornblende, equigranular with 5 mm plagioclase and quartz phenocrysts among smaller plagioclase (1-2 mm) and 1 to 2 mm biotite and hornblende. ~1% disseminated pyrite. Quartz is slightly rounded. ~2% thin quartz +/- biotite viens; vein angle ranging from 85 to 60 degrees.
Fine grained dolerite with ~10% 0.25 mm biotite crystals and 4% disseminated pyrite biotite altered near base of the interval. Minor erratic pyrite stringer veins with weak pale alteration halo.

CD8142 page 2 of 5

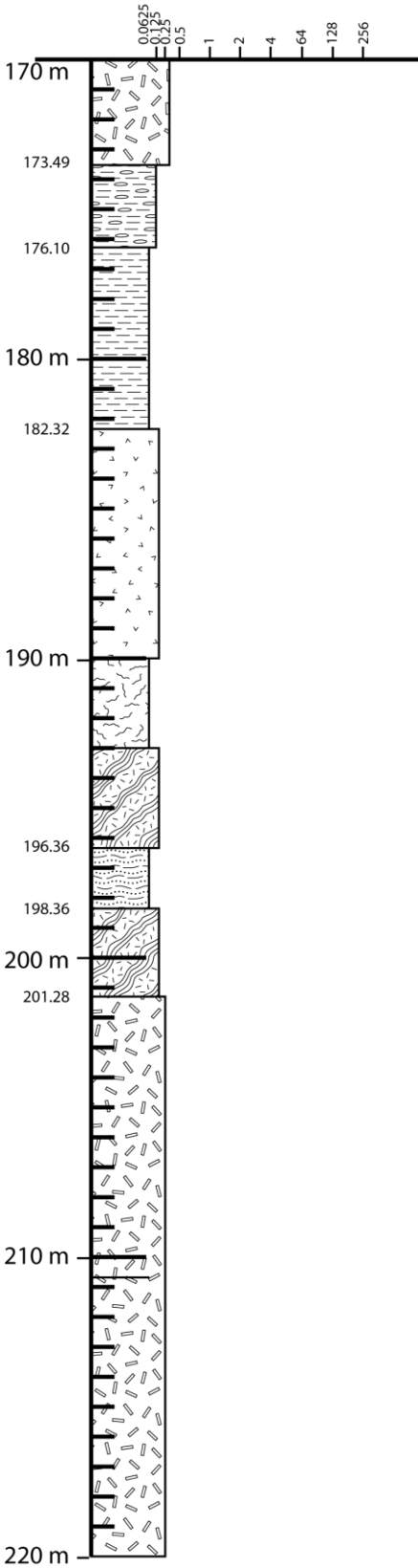

Difficult to tell as much of this interval has had it's sulfides weathered out into brown/yellow slightly green sulpha-salts. This has strongly stained the rock and in some cases made it fall apart (until ~182 m). Some sections are a bright green colour and silicified, believed to be veining/silicification of shale. The more weathered sections may represent areas where had high sulphide concentration due to remobilisation of sulphides from silicified, sulfide poor sections.

Finely bedded siltstone, likely dark and finely interbedded though stain makes difficult to tell.

Dark green basalt with ~7% very erratic quartz +/- calcite veins ~3% disseminated pyrite.

Quartz rich section, may contain up to 30% basalt protolith @ center of interval but to tell whether its very silicified basalt or chlorite stained quartz. Top contact contains several very small amphibole needles, bottom contact lost is drilling. ~4% erratic pyrrhotite stringers, also contain chlorite +/- amphibole. Stingers most common at bottom of interval.

Strongly foliated basalt with minor separation of felsic mafics and minor crenulations. 194.4 - 194.84 m milky quartz veining, contains ~10% encorporated wall rock, a second similar veins occurs at 195.70 m and is 16 cm wide.

Interbedded dark grey siltstone and blebby to semimassive bands of pyrrhotite (after pyrite) ~30% pyrrhotite across inteval. Very heavily folded across entire interval except first 50 cm. Folds are generally quite open.

Foliated basalts as before with ~50% milky quartz veining; veins thickest near center of the interval (up to 40 cm) and most common at centre as well.

Medium green doleritewith ~10% 0.5 to 0.125 mm hornblende +/- biotite phenocrysts surrounding ~3-4 spheres of green matrix. Minor pyrite as present. Grain size fines down hole.

CD8142 page 3 of 5

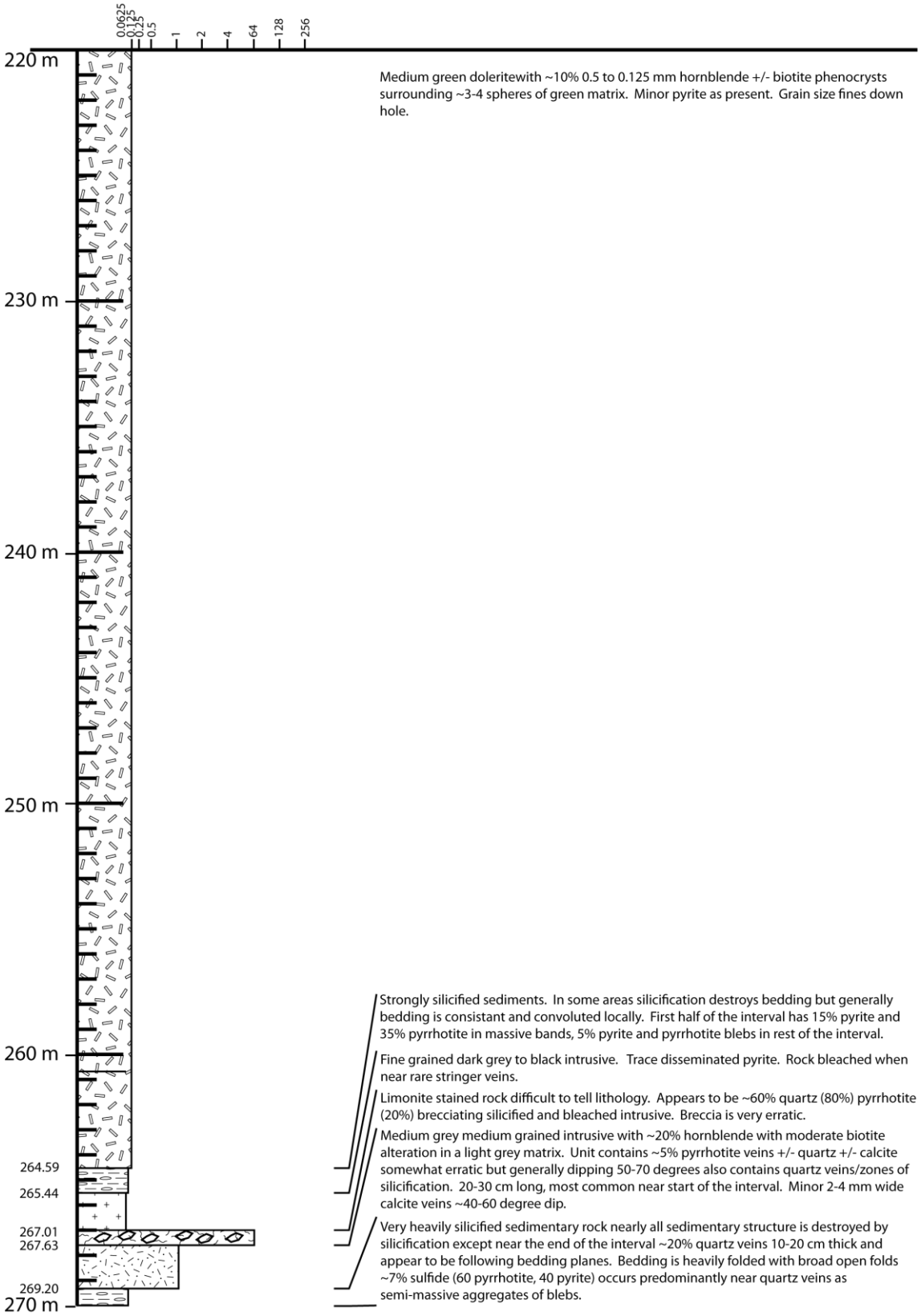

CD8142 page 4 of 5

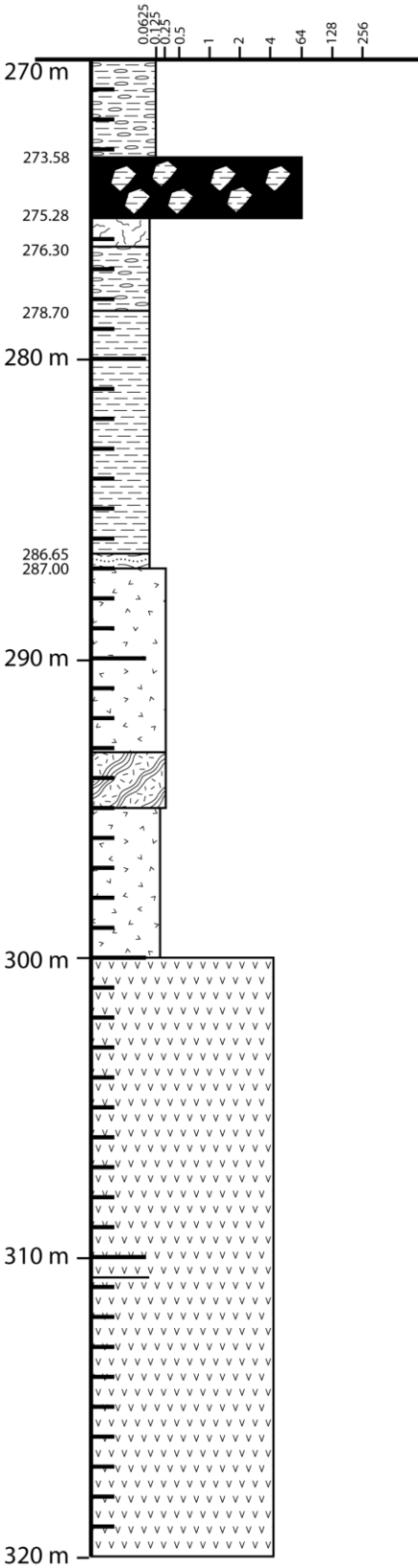

Very heavily silicified sedimentary rock nearly all sedimentary structure is destroyed by silicification except near the end of the interval ~20% quartz veins 10-20 cm thick and appear to be following bedding planes. Bedding is heavily folded with broad open folds ~7% sulfide (60 pyrrhotite, 40 pyrite) occurs predominantly near quartz veins as semi-massive aggregates of blebs.

~60% subangular silica altered siltstone (pale grey) within a fine grained black matrix. ~15% pyrite +/- pyrrhotite blebby to semi-massive in the matrix.

Very silicified sedimentary rock with 2 x 10-20 cm thick medium grey intrusions with 20% 1-2 mm diameter hornblende crystals with ~80% plagioclase. Also contains 5-10 cm masses of nearly massive pyrrhotite.

Well laminated light and dark grey siltstone. Some areas bedding is destroyed by alteration but generally consitent across the interval. ~35% dark beds and 65% light beds. ~25% sulfide, predominantly pyrrhotite, some pyrite.

Very convoluted interval of same siltstone as above.

Medium green basalt with minor erratic calcite veining. 2 m in middle of the interval are moderately foliated.

Medium green variolitic basalt with 20-30 cm clusters of 0.5 cm diameters of varioles ever 1 m.

CD8142 page 5 of 5

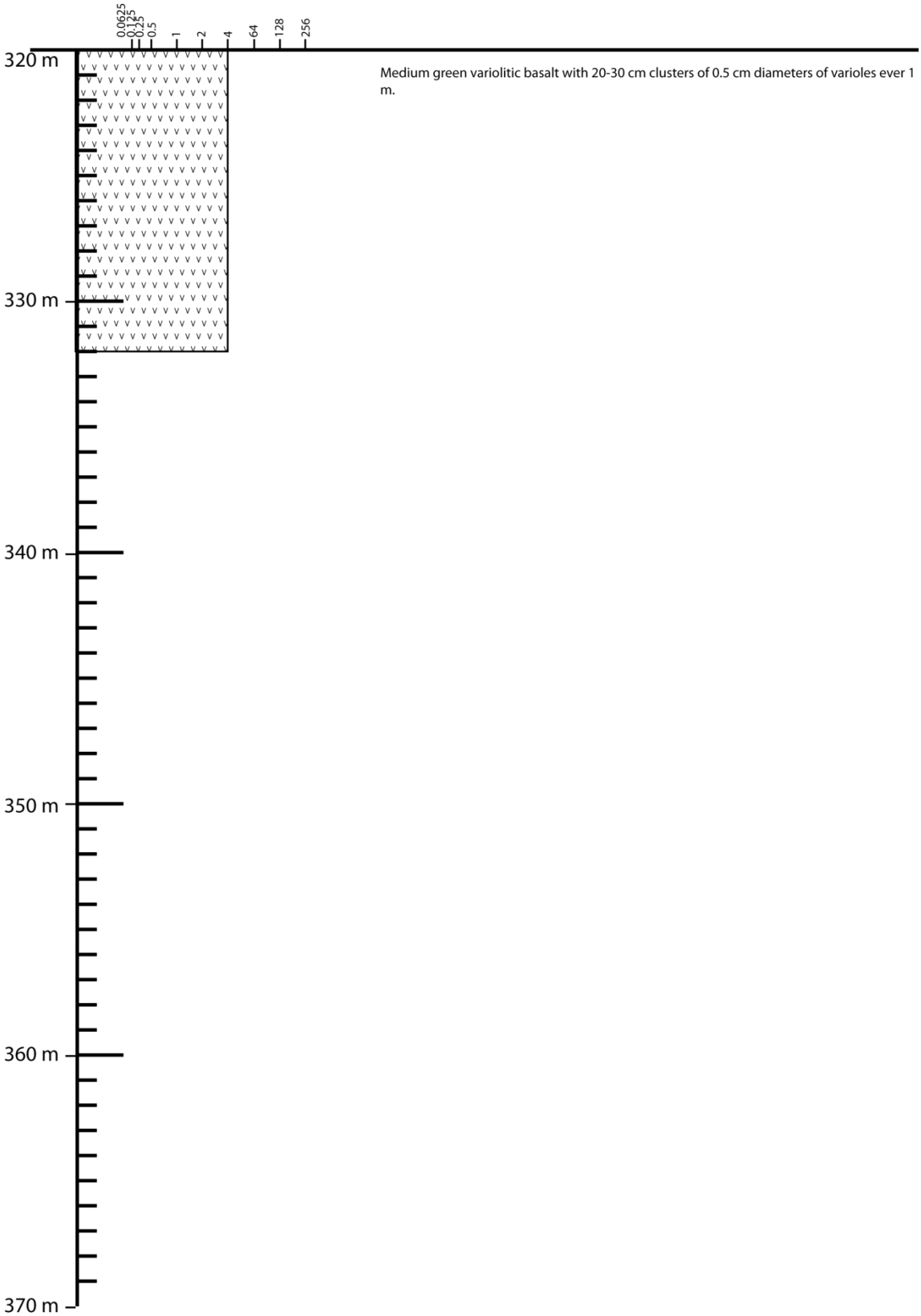

A12.5 CD13829

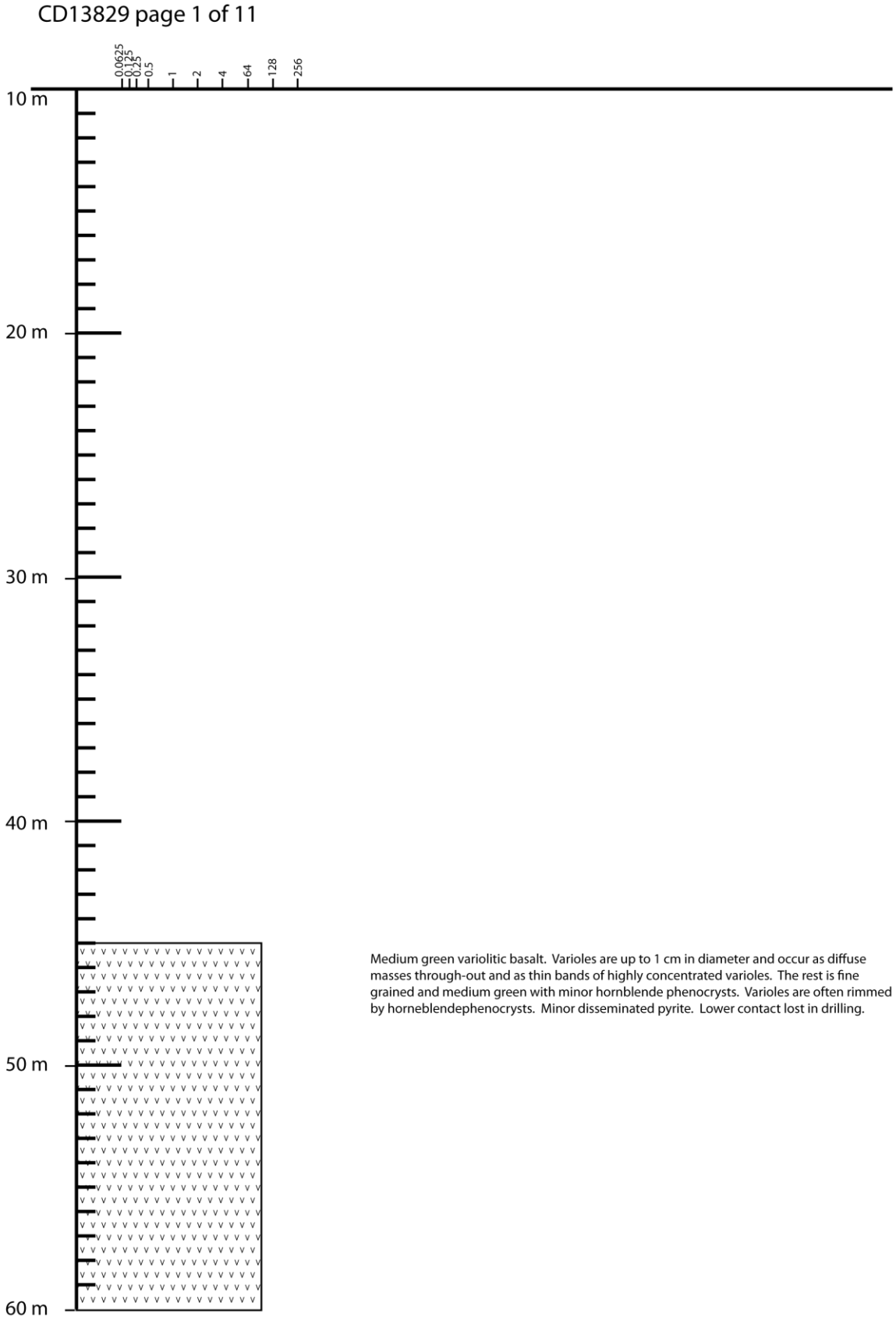

CD13829 page 2 of 11

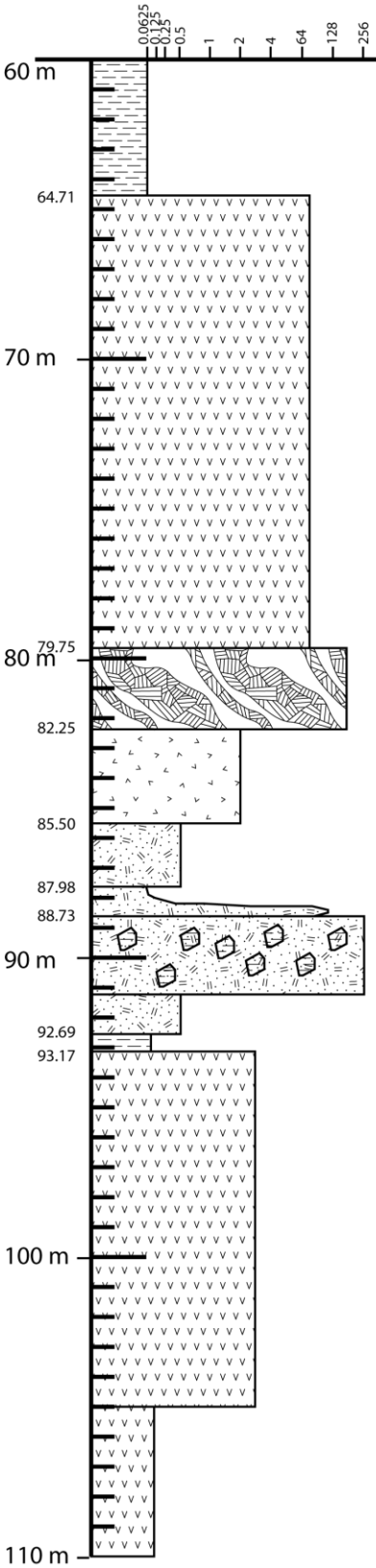

Interbedded light grey (65%) and medium brown (35%) bands ~1-6 mm thick beds. ~10% bedded pyrrhotite +/- pyrite. Bedding is slightly convoluted and often exhibits short offsets.

Medium green basalt as before however here very few varioles until ~71 m. Near top of interval 1-2% disseminated pyrite and minor quartz calcite stringers throughout interval.

Coarse grained white quartz vein with ~15% large subangular basalt rip-ups with minor limonite stain. Clasts most common at interval margins.

Medium green basalt with no varioles. Hornblende 1-2 mm, phenocrysts rim pale spheres, possibly relict varioles but difficult to tell.

Medium grey intrusion with 10% 0.5 mm hornblende needles within a fine grained matrix.

Top of interval is bedded interflow sediment, light grey (65%) and medium brown (35%) bands ~1-6 mm thick beds. Grades into a breccia with 20% angular chert clasts within a fine grained dark grey matrix.

Medium to coarse grained medium grey intrusive with ~20% 1-2 mm hornblende phenocrysts within 15% very large (>5 cm) subangular siltstone xenoliths. @ 91 m no more Xenoliths and intrusion is fine grained.

Interflow sediment, light grey (65%) and medium brown (35%) bands ~1-6 mm thick beds.

Medium green variolitic basalt. Varioles are white and rare, occurring most commonly at the base of the interval.

Fine grained green basalt with weak magnetite alteration ~5% very erratic chlorite/serpentine veins in top 3 m (possible halyoclastite texture). Rimmed by 3 mm fine grained pyrrhotite and magnetite in erratic veins.

CD13829 page 3 of 11

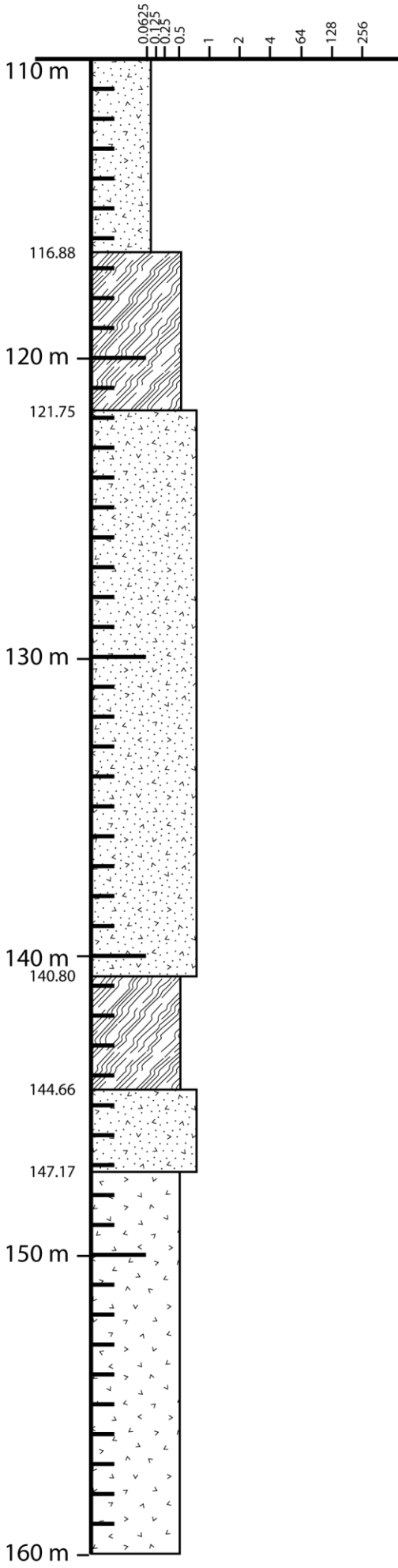

Fine grained green basalt with weak magnetite alteration ~5% very erratic chlorite/serpentine veins in top 3 m (possible halyoclastite texture). Rimme grained pyrrhotite and magnetite in erratic veins.

Fine grained green basalt with weak magnetite, strongly sheered with mod biotite +/- chlorite alteration defining shear planes. ~2% 1-3 mm calcite vei mm (up to 23 cm) quartz veins both parrallel to shear plane.

Medium grained green basalt with 1 mm long hornblende (10%). ~5% 2 m carbonate veins (possibly halyoclastite texture?). ~20% fine grained pyrrho

Medium grained green basalt, strongly foliated and moderate biotite +/- ch ~2% 1 mm to 1 cm wide calcite veins parrallel to foliation. Wider veins cont quartz; most often near the center of the veins.

150 to 155 m rock heavily fractured, possible vein.

CD13829 page 4 of 11

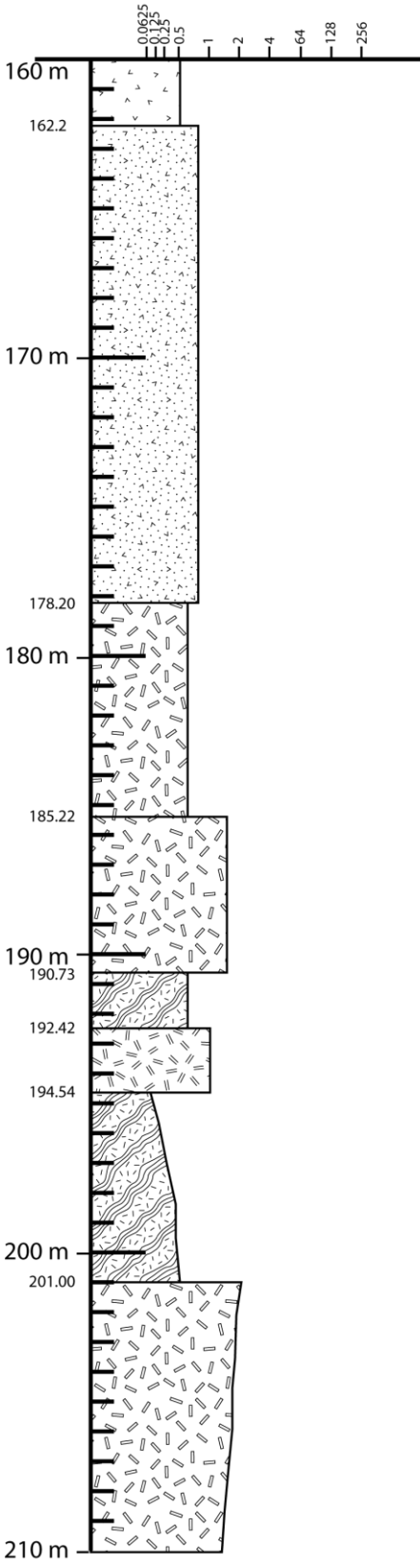

Medium green fine grained basalt with 2% erratic calcite stringer veins and 1% 4 mm wide chlorite alteration halos around quartz stringer veins.

Medium to fine grained dolerite with 35% 0.5 mm plagioclase crystals 15% 1-5 mm long hornblende needles in fine grained medium green matrix. Cut by erratic chlorite and calcite veins. Near the end of the interval a 1.5 and a 4 cm wide quartz calcite vein with chlorite laminae cut unit steeply (85 and 80 degrees). Upper contact not well defined.

Medium grained medium green/grey dolerite with 25% stubby hornblende crystals within a medium green fine grained matrix. Moderate calcite altered unit has ~4% 1-2 mm wide calcite veins, these are more frequent with depth. 3% disseminated pyrite and 3% disseminated pyrrhotite. Between 190.73 and 192.42 the unit is strongly foliated.

Dark grey porphyry with ~10% 1 mm diameter plagioclase phenocrysts and 10% 2 mm hornblende +/- shale xenoliths and minor calcite. ~3% disseminated pyrite.

Fine grained medium green dolerite progressively coarsening and more foliation down hole. Where foliated foliation is defined by biotite alteration. 2% 1 mm pyrite blebs at beginning of the interval decreasing to no pyrite by the end. 3% quartz (70%)/ calcite (30%) veins.

~40% plagioclase 10% hornblende (2 mm diameter and 1 mm diameter respectively) in a fine grained medium green matrix. First 5 m of the interval contains 20% plagioclase, 40% hornblende +/- biotite with ~8% disseminated pyrite, grain size decreases across interval..

CD13829 page 5 of 11

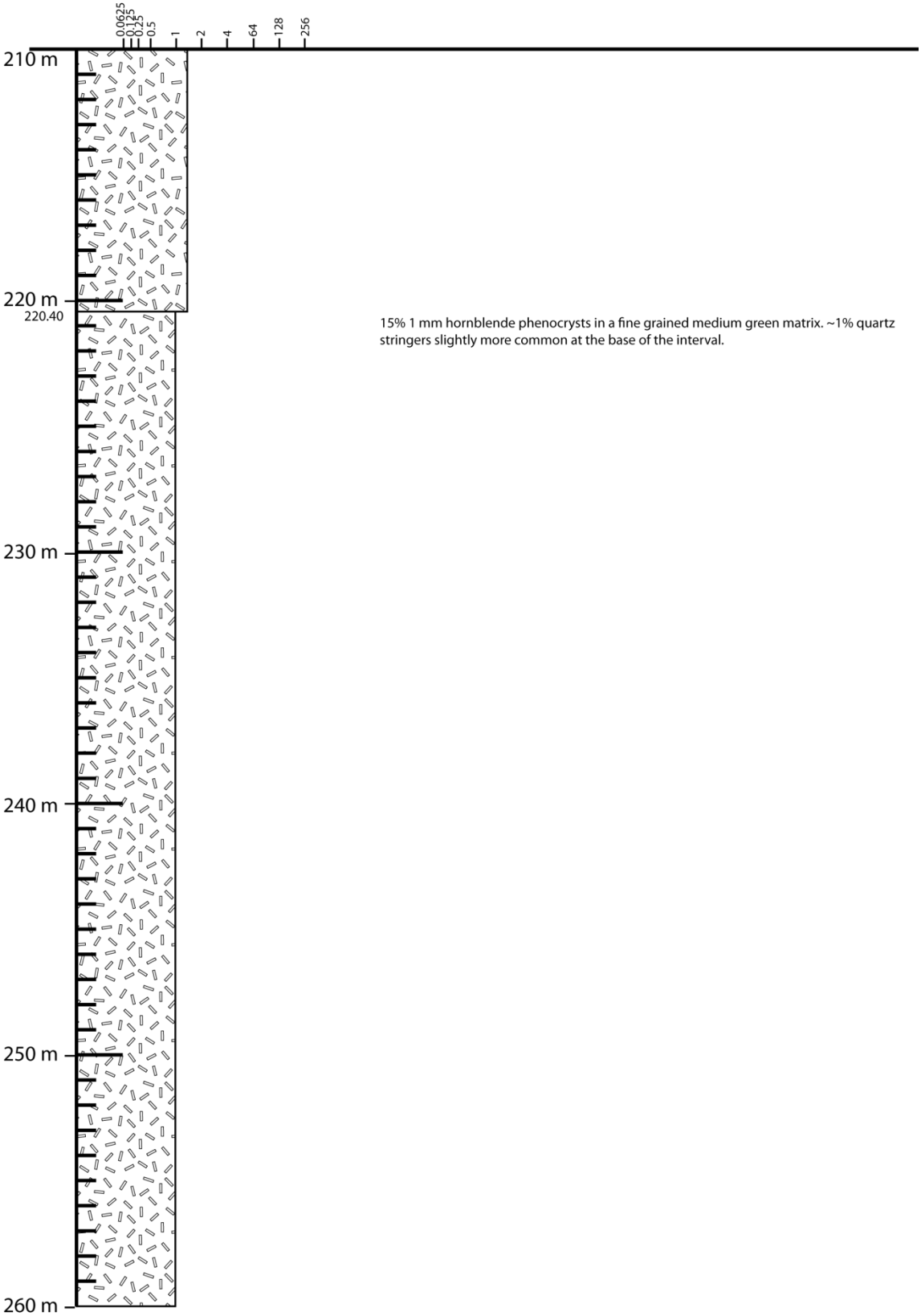

15% 1 mm hornblende phenocrysts in a fine grained medium green matrix. ~1% quartz stringers slightly more common at the base of the interval.

CD13829 page 6 of 11

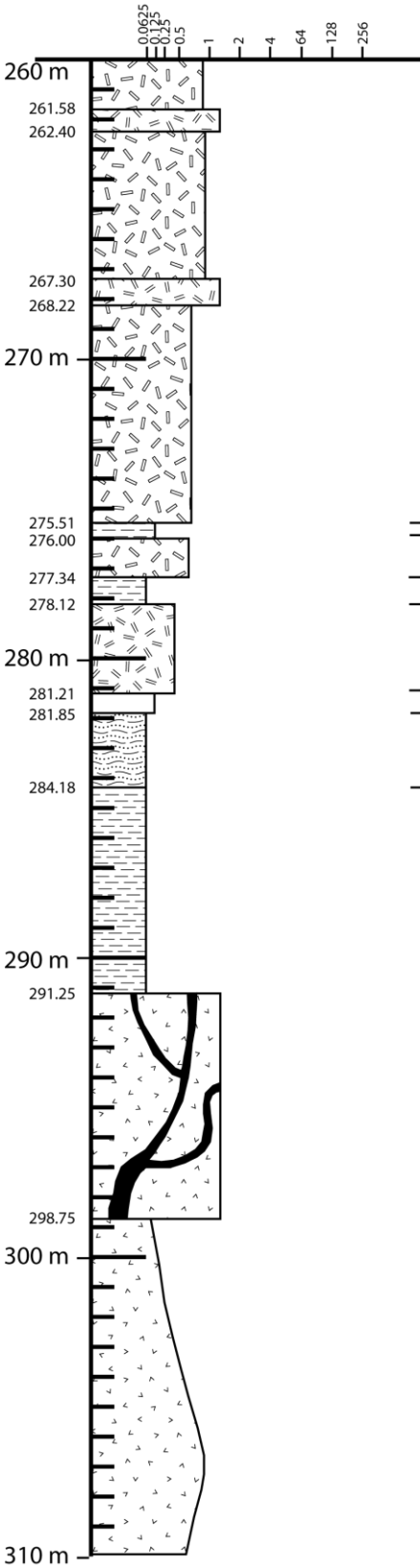

Dark grey porphyry with ~ 15% hornblende phenocrysts within a fine grained dark grey groundmass. Contains ~5% blebby pyrrhotite.

15% 1 mm hornblende phenocrysts in a fine grained medium green matrix. ~5% pinkish 1-3 mm carbonate veins. 265.75-260 m erratic near verticle chlorite alteration with 20% net texture pyrrhotite.

Dark grey porphyry with ~ 15% hornblende phenocrysts within a fine grained dark grey groundmass.

Fine grained medium green dolorite with zones of up to 25% magnetite. 272.61-272.86 m strong calcite veining (~30%) with foliation parrallel to the vein.

Brecciated sediment +/- dolerite. ~20% distinct siliceous beds are brecciated (little rotation of clasts)by pyrrhotite/calcite veins nearly verticle and erratic. (~20% pyrrhotite). Other beds have strong chlorite alteration and may be dolerite or sediments or both.

Fine grained medium green dolorite here ~40% strongly calcite alteration in a steep, curving zone, rest has weak calcite. Margins of strong calcite have 2 mm biotite crystals. Less altered parts of rock have ~20% pyrrhotite.

Interbedded medium green fine grained and pale cherty layers (85/15). Cherty layers appear to coarsen upwards. ~30% sulphide with 90& pyrrhotite and 10% pyrite. Possible minor magnetite but difficult to tell due to small amount and amount of pyrrhotite.

Fine grained medium grey porphyry with 15-20% 0.5 mm hornblende phenocrysts.

Silicified light to medium grey zone with ~8% 5 cm thick quartz veins, likely silicified intrusion though difficult to tell. Veins dip ~85 degrees. ~3% later pyrrhotite/calcite veins (60/40) dipping @75 degrees.

Dark grey shale with interbedded pyrite rich and pyrite poor horizons (~30% pyritic horizons, 65% shale horizons 5% calcite rich horizons). Bedding is evident but highly contorted in this interval.

Dark grey shale with interbedded pyrite rich and pyrite poor horizons mostly fine grained pyrite but some rare blebs. ~10% pyrite at the start of the interval increasing to 40% at 290.25 m before decreasing to 20% pyrite by the end.

Mixture of fine grained medium green basalt and coarse grained with 60% 1.5 mm diameter plagioclase phenocrysts with a fine grained chlorite rich matrix (65%, 35%). Interval is brecciated by 1-8 mm wide erratic chlorite +/- pyrrhotite veins +/- calcite (10% of interval). The veins are most commonly associated with the coarse grained material.

Interval starts as massive fine grained medium green basalt, down hole increases in amount of hornblende phenocrysts, at mid point of interval more 1mm plagioclase crystals are also present. Phenocryts decrease to nil by the end of the interval.

CD13829 page 7 of 11

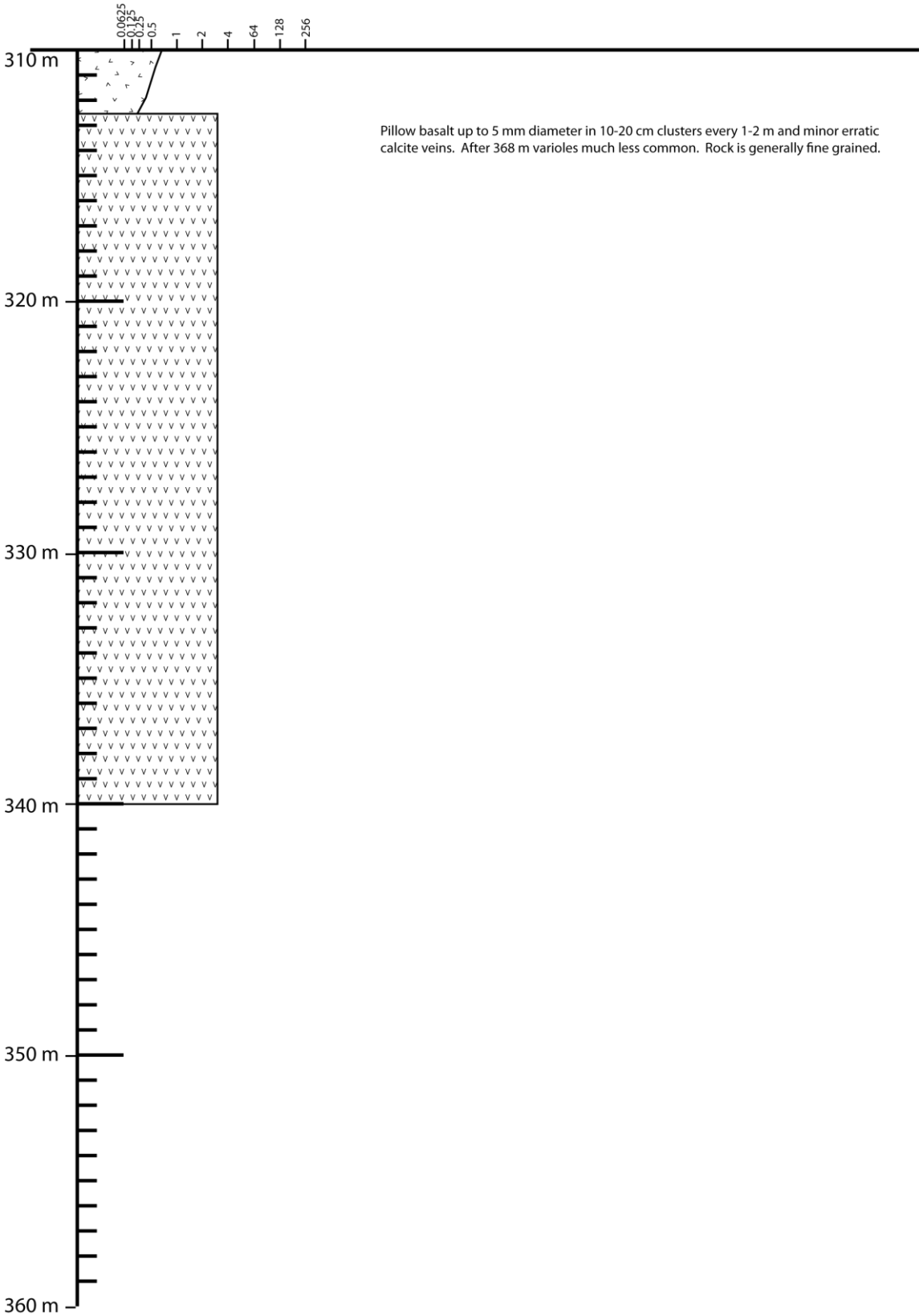

CD13829 page 8 of 11

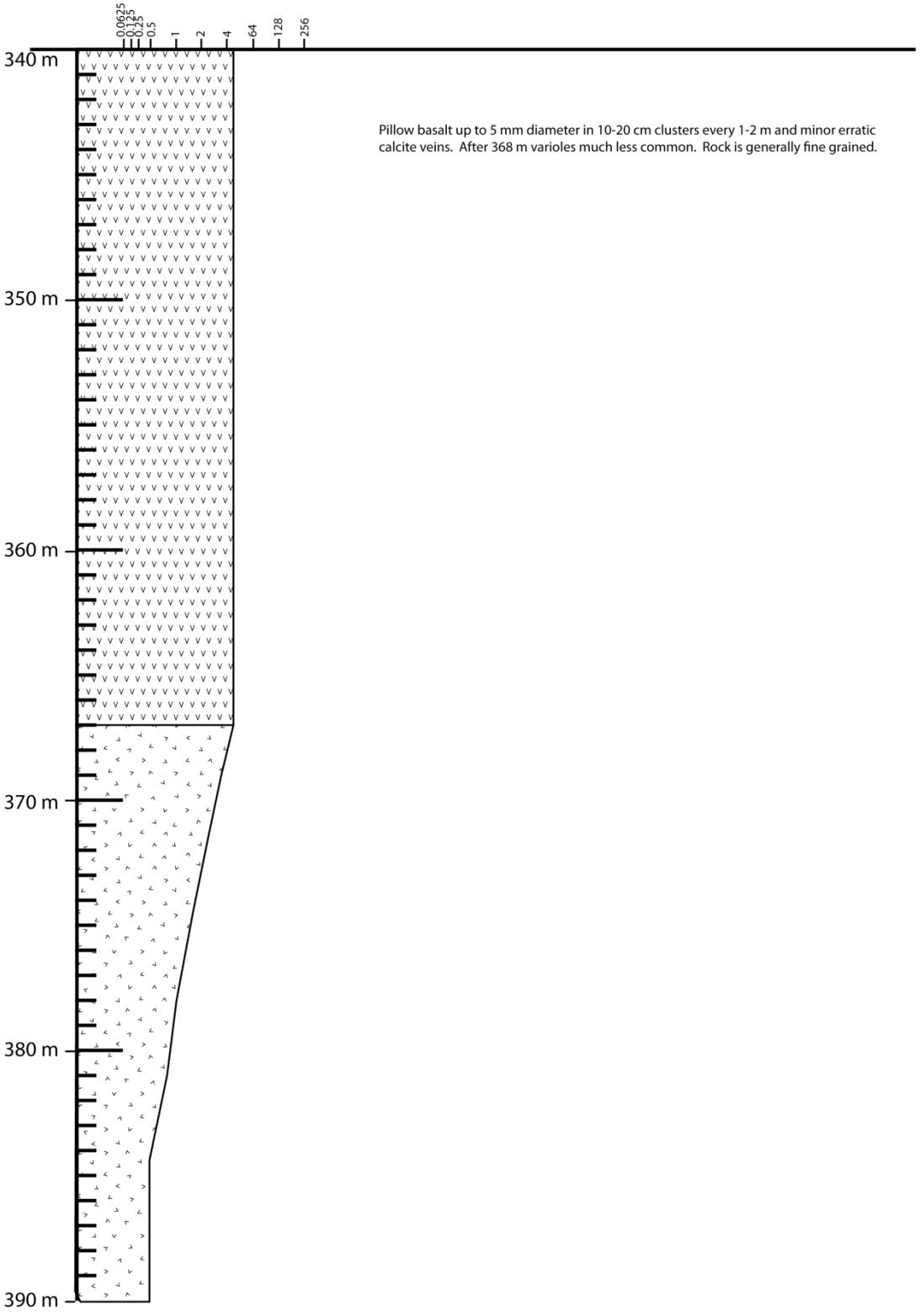

CD13829 page 9 of 11

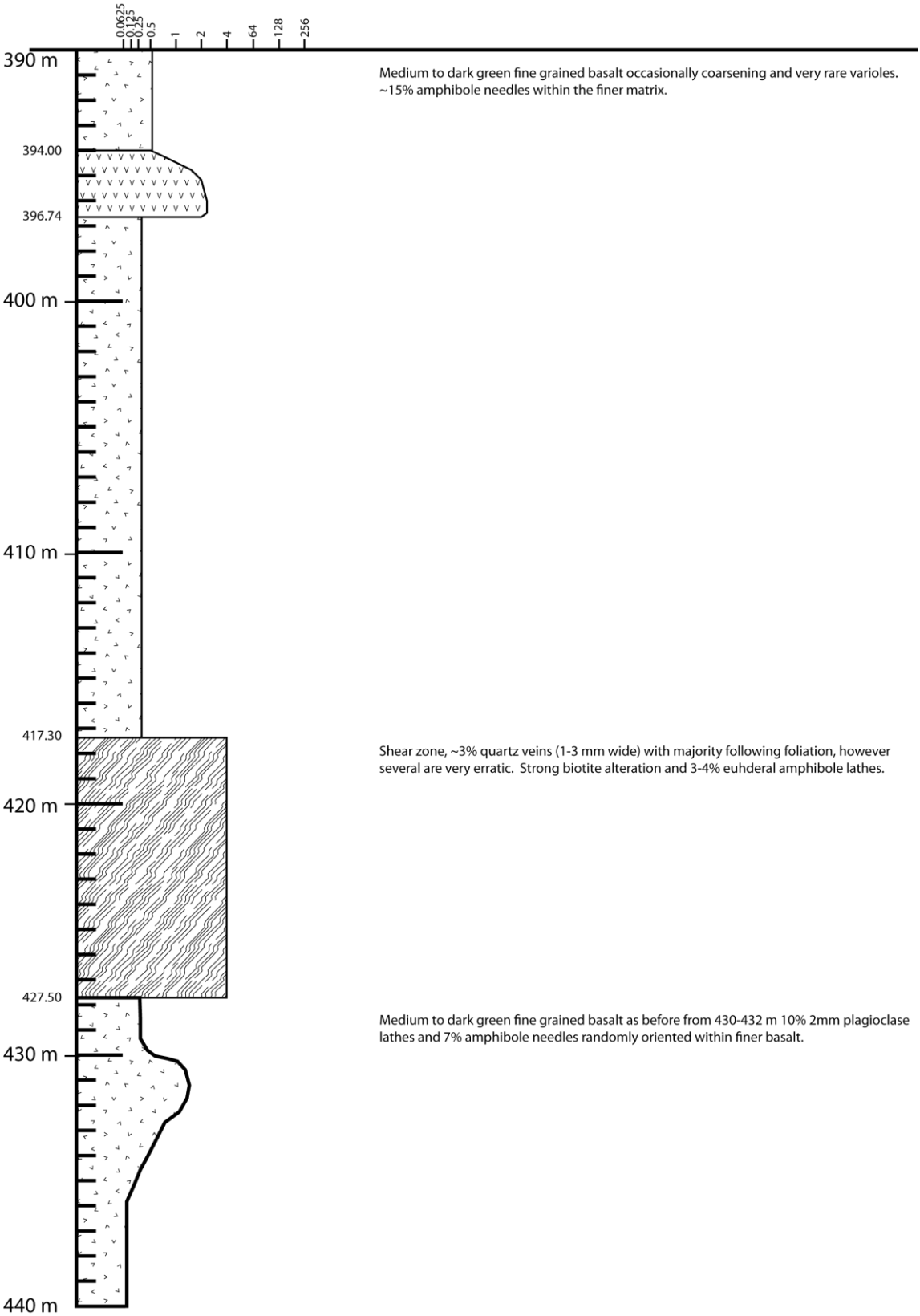

CD13829 page 10 of 11

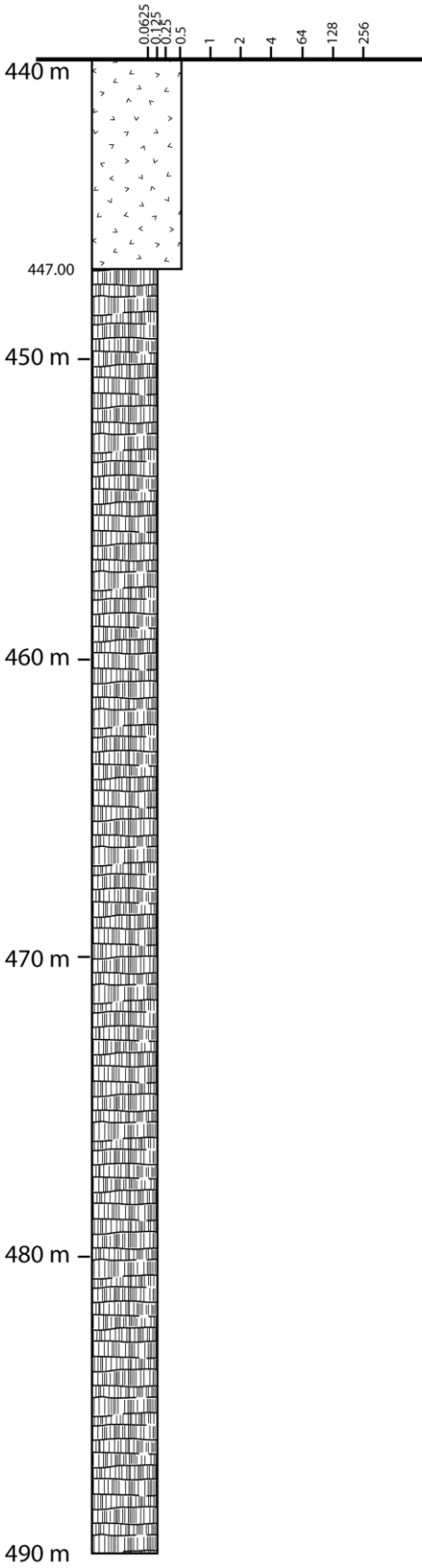

Medium to dark green fine grained basalt occasionally coarsening and very rare varioles. ~15% amphibole needles within the finer matrix.

Dark to very dark green komatiite with ~ 2% pyrite blebs +/- weak pyrrhotite. Generally fine grained with relict spinifex texture in some places. Most of the texture destroyed by alteration. Base of section convoluted with strong chlorite alteration.

CD13829 page 11 of 11

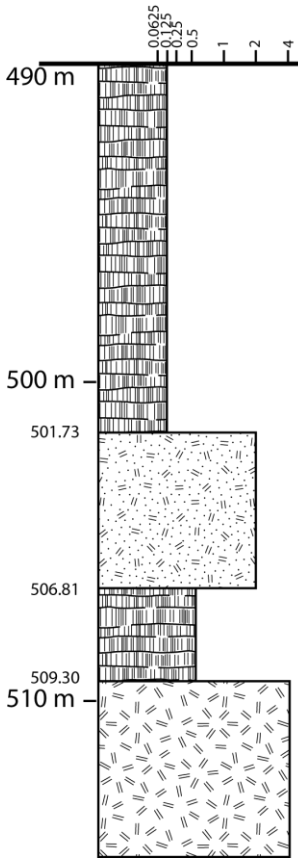

Dark to very dark green komatiite with ~ 2% pyrite blebs +/- weak pyrrhotite. Generally fine grained with relict spinifex texture in some places. Most of the texture destroyed by alteration. Base of section convoluted with strong chlorite alteration.

Medium grey porphyry with 5% 2 mm plagioclase phenocrysts and 15% 0.5 mm hornblende phenocrysts within a fine grained matrix. Hornblende altered to chlorite and actinolite. Minor blebby pyrite. Trace 1 cm subrounded komatiite? Xenoliths.

Dark to very dark green komatiite with ~ 2% pyrite blebs +/- weak pyrrhotite. Generally fine grained with relict spinifex texture in some places. Most of the texture destroyed by alteration. Base of section convoluted with strong chlorite alteration.

Coarse grained granodiorite. 60% plagioclase, 10% quartz and 30% mafics. Mafics altered to chlorite +/- biotite +/- actinolite.

A12.6 CD13833

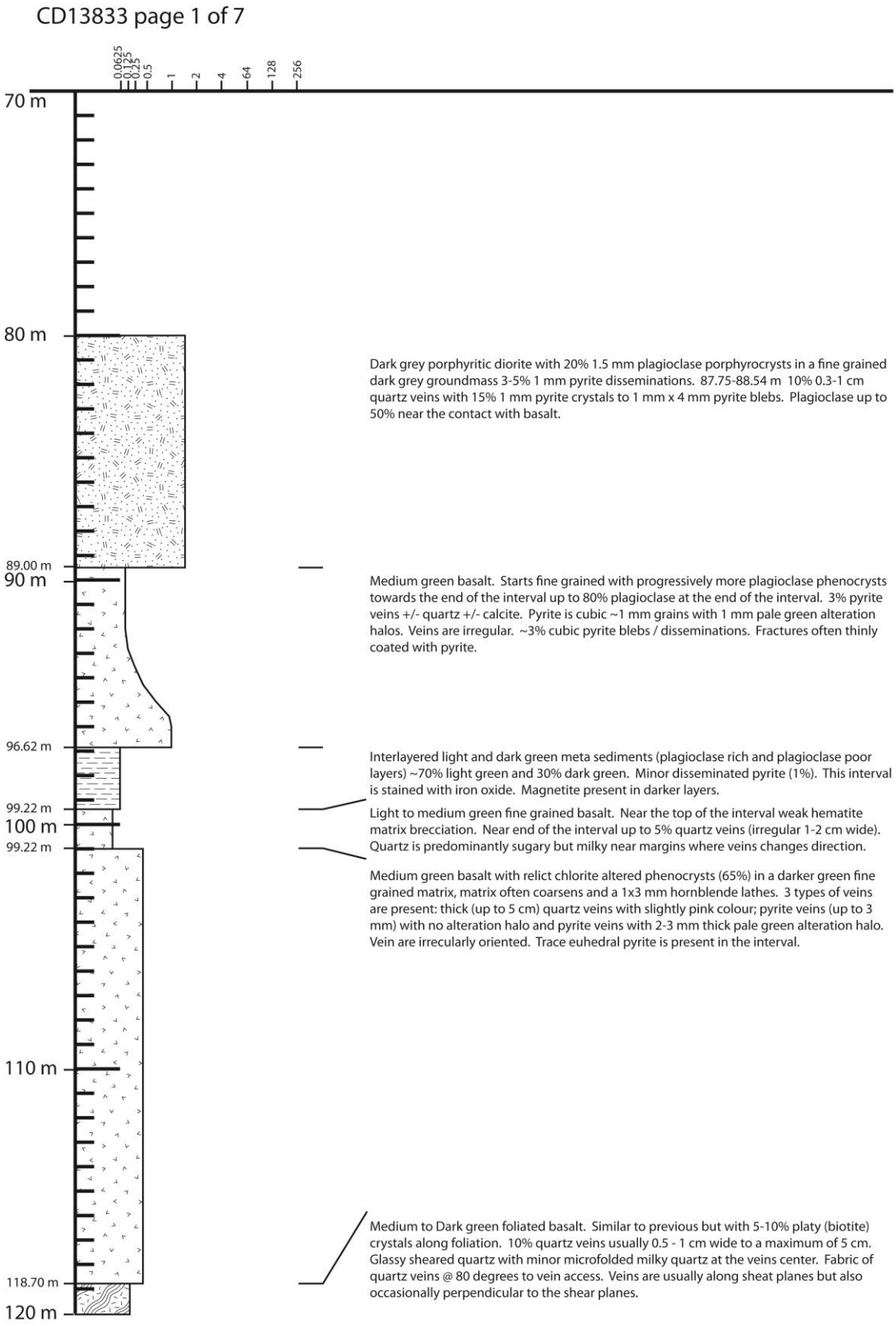

CD13833 page 2 of 7

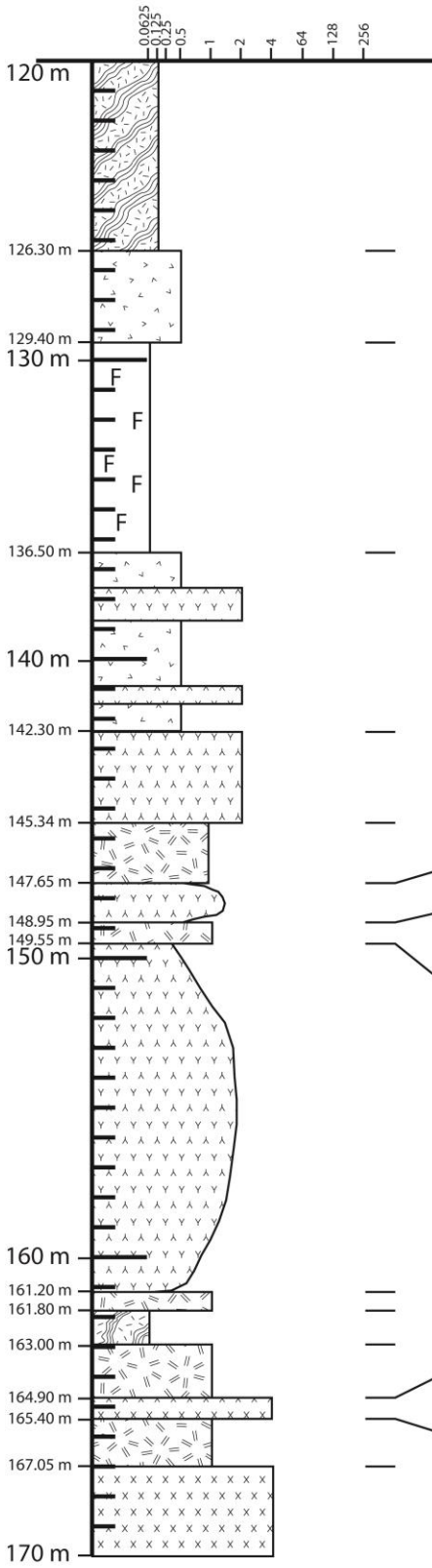

Medium to Dark green foliated basalt. Similar to previous but with 5-10% platy (biotite) crystals along foliation. 10% quartz veins usually 0.5 - 1 cm wide to a maximum of 5 cm. Glassy sheared quartz with minor microfolded milky quartz at the veins center. Fabric of quartz veins @ 80 degrees to vein access. Veins are usually along sheat planes but also occasionally perpendicular to the shear planes.

Medium green basalt with 15% 1.5 mm thin hornblende lathes and 15% 1 mm stubby plagioclase lathes within a fine grained matrix. Slightly layered texture of darker to lighter green layers ~1-5 cm thick.

Fault rubble with minor pink intrusion / alteration.

80% medium green basalt with 35% 1.5 mm hornblende lathes 35% 1 mm stubby plagioclase lathes within a fine grained and green matrix. 20% lenses of medium green granophyre. Contains 50% 2 cm long horneblende blades with spaces between hornblende filled with plagioclase.

Medium grey granophyre with 50% 2 cm long hornblende blades with interstitial space filled with plagioclase.

Medium grey porpyry 70% sub angular clasts within a fine grained dark grey / black matrix. Minor up to 2 cm dark grey xenoliths 1 % fine grained disseminated pyrite.

Medium grey granophyre with 50% 2 cm long hornblende blades with interstitial space filled with plagioclase. Margins of the interval are fine grained.

Medium grey porpyry 70% sub angular clasts within a fine grained dark grey / black matrix. Minor up to 2 cm dark grey xenoliths 1 % fine grained disseminated pyrite. Minor hematite staining present.

Medium green granophyre contains 40% hornblende blades and 60% chlorite alteration stained plagioclase. Tends to be coarsest near the center of the interval and ~0.5 cm hornblende blades at the ends of the interval. 2% 5-10 cm wide quartz breccias with 25% partially dissolved black clasts and 2x1 cm fine grained pyrite blebs. 3% ~2 cm wide light pink porphyry dykes. 1% thin pyrite veins with 3 mm light green alteration halo.

Medium grey porpyry 70% sub angular clasts within a fine grained dark grey / black matrix.

Medium grey fine grained basalt with a weak fabric ~3% pyrite in veins/line along foliation.

Medium grey porphyry with minor very erratic 0.5 cm quartz veins.

Coarse grained felsic porphyry beige with 10% rounded 5 mm quartz phenocrysts 15% 3 mm plagioclase lathes; 5% fine mafic phenocrysts. Remainder is beige and plagioclase rich matrix and minor disseminated pyrite.

Medium grey porpyry 70% sub angular clasts within a fine grained dark grey / black matrix.

Coarse grained felsic porphyry, lighter in colour towards base of interval.

CD13833 page 3 of 7

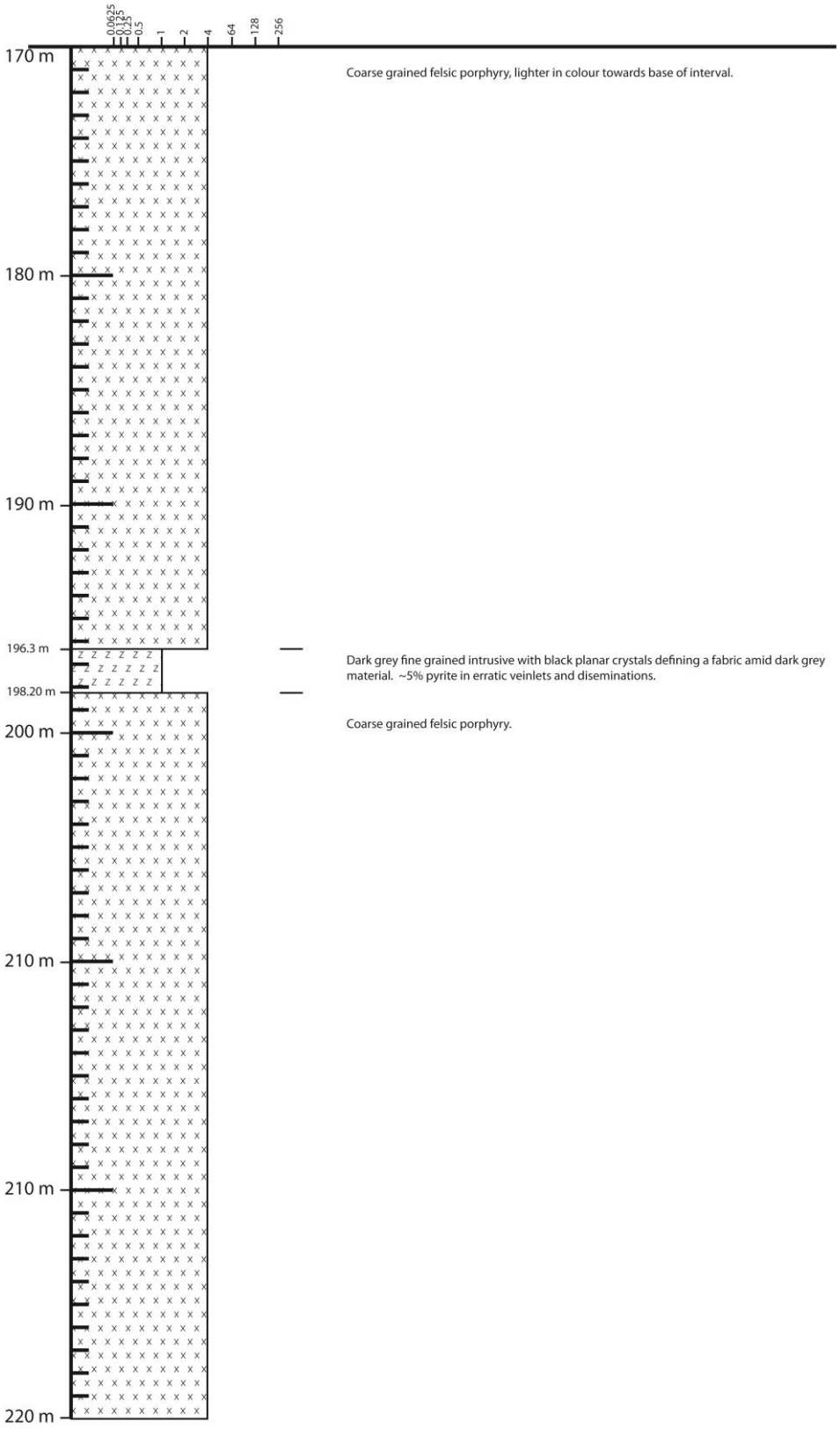

CD13833 page 4 of 7

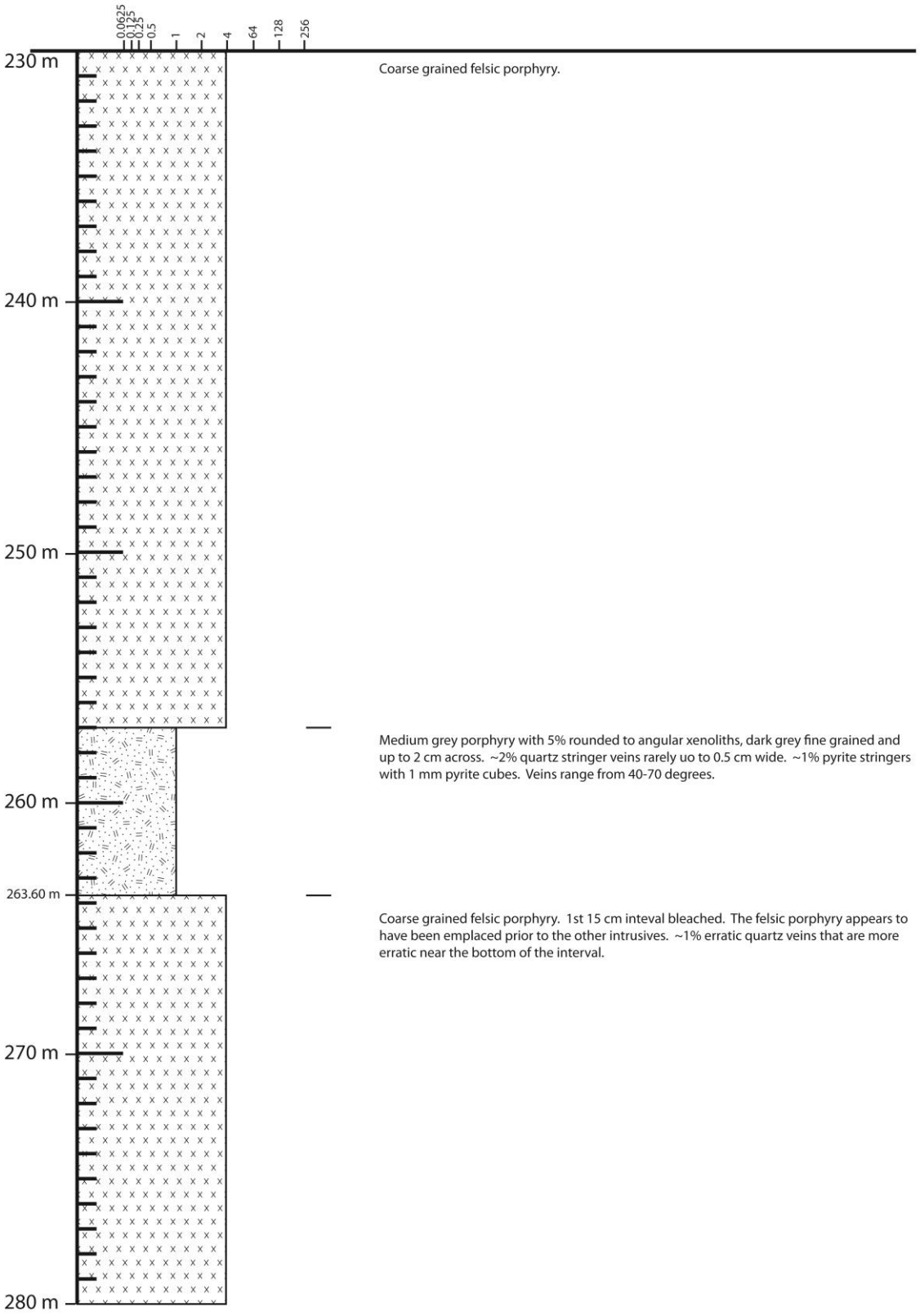

CD13833 page 5 of 7

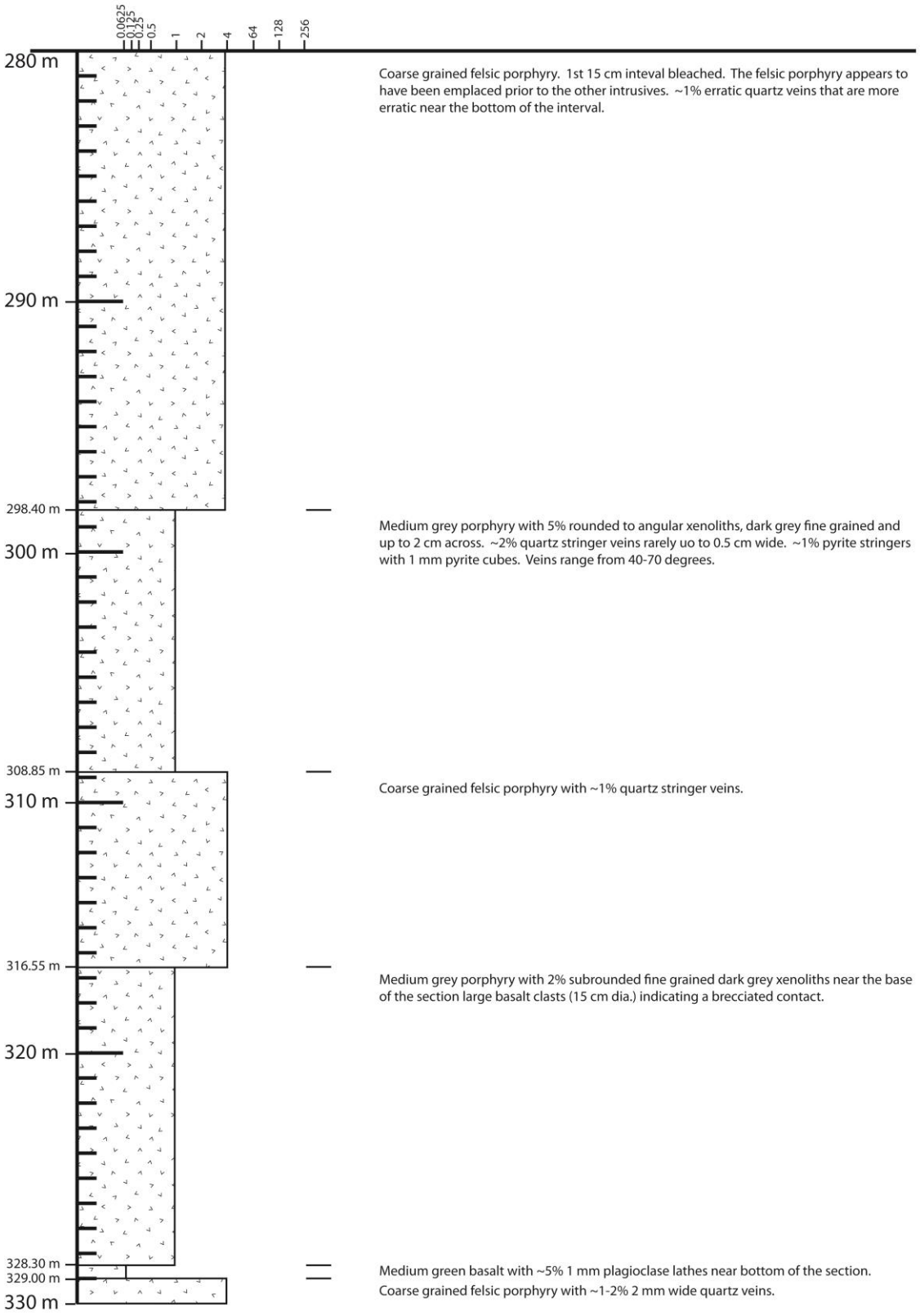

CD13833 page 6 of 7

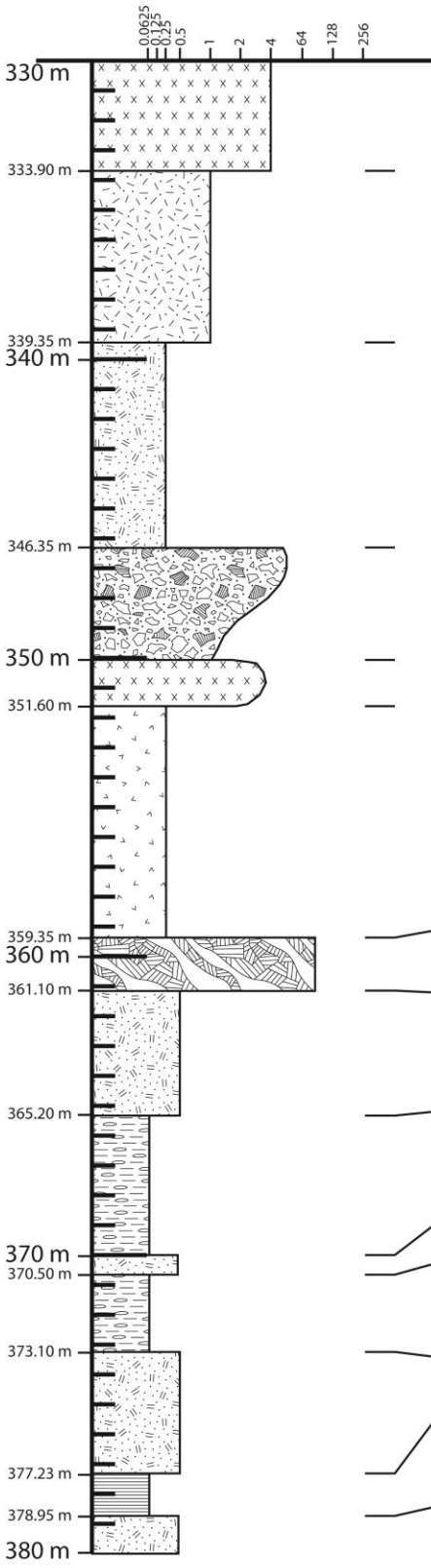

Coarse grained felsic porphyry with ~1-2% 2 mm wide quartz veins.

Medium grey porphyry with 2% subangular basalt clasts. Minor quartz veins (maximum 2 mm wide).

Fine grained medium to dark green basalt with weakly defined pillows by 0.5 cm thick serpentice rich intervals. From 341.6-342.2 m brecciated by medium grey porphyry. Large angular clasts.

~25% 2-4 cm diameter sub rounded basalt clasts within a medium grey porphyry matrix contains progressively less basalt.

Coarse grained porphyry but lacks quartz phenocrysts.

Dark green basalt with 15% 0.25 mm hornblende? Phenocrysts within a fine grained matrix. Top 15 cm much lighter green.

Quartz veins varying from 3 cm to 3 mm clasts are large, up to 8 cm across and made up largely of meta sediments. ~3% pyrite associated near the quartz veins in large clots or clumps; some minor pyrite along bedding.

Dark grey diorite? Intrusive with ~15%. 0.5% hornblende? Phenocrysts within a fine grained matrix. ~5% serpentine rich (light green) veins cut the unit giving a planar appearance. Minor erratic quartz veins. As progresses down the interval more silicification is presented. Last 20 cm is predominantly quartz.

Interbedded light grey chert and dark grey mudstone ~40% chart and 60% mudstone, darker beds contain magnetite. The unit is cut by ~2% thin quartz veins. These veins offset the beds up to 5 cm. ~1% pyrite occuring in clumps ~ parrellel to bedding. Crystals are both cubic and amorphous. Minor pyrite occurs along veins (the former is more common near the top of the interval and the later near the bottom).

Dark grey diorite? Intrusive with ~15%. 0.5% hornblende? Phenocrysts within a fine grained matrix.

Interbedded light grey chert and dark grey mudstone ~40% chart and 60% mudstone, darker beds contain magnetite. The unit is cut by ~2% thin quartz veins. These veins offset the beds up to 5 cm. ~1% pyrite occuring in clumps ~ parrellel to bedding. Crystals are both cubic and amorphous. Minor pyrite occurs along veins (the former is more common near the top of the interval and the later near the bottom).

Dark grey diorite? Intrusive with ~15%. 0.5% hornblende? Phenocrysts within a fine grained matrix and ~10% 0.5 cm diameter plagioclase phenocrysts.

Interbedded dark grey to black and light grey siltstone (~60% light and 40% dark) folding is observed in core with fold axis @378.5 m. ~8% pyrite with majority occuring as blebs and cubic 0.3 cm crystals along bedding planes with minor steep veins. ~5% pyrrhotite occurs along bedding planes, concentrated near fold hinges. Pyrrhotite is finer grained than pyrite.

Dark grey diorite? Intrusive with ~15%. 0.5% hornblende? Phenocrysts within a fine grained matrix and ~10% 0.5 cm diameter plagioclase phenocrysts. Contains 3% disseminated pyrite.

CD13833 page 7 of 7

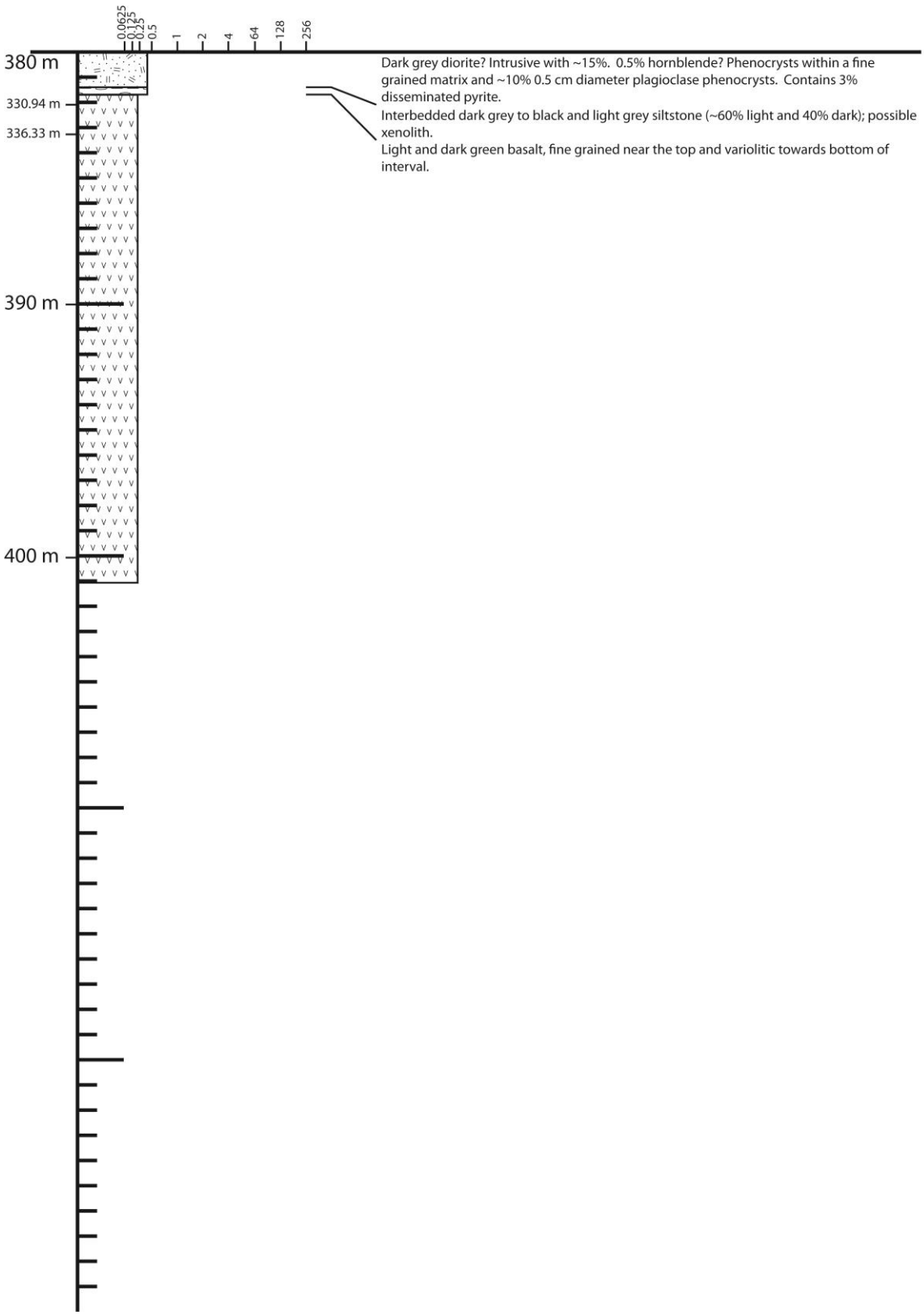

Appendix 13:

Geochemical analyses presented in Chapter 6

Table A13.1: LA-ICPMS of pyrite St Ives Gold District

Depth (m)	Drill Hole	Group	Mg (ppm)	Al (ppm)	Ca (ppm)	Ti (ppm)	V (ppm)	Cr (ppm)	Mn (ppm)	Cu (ppm)	Zn (ppm)
260.5-260.8	C7177	Ore (altered porphyry)	0.60	2.17	<67.45	3517.55	98.28	21.80	<0.2	5081.92	6.52
260.5-260.8	C7177	Ore (altered porphyry)	<0.19	<0.68	<61.91	3.49	<0.03	1.36	<0.27	1.53	0.71
260.5-260.8	C7177	Ore (altered porphyry)	0.98	377.95	<67.69	732.67	13.59	5.59	<0.24	16.38	3.04
260.5-260.8	C7177	Ore (altered porphyry)	3.55	973.77	<69.62	1156.68	20.35	15.76	<0.19	4.06	13.05
260.5-260.8	C7177	Ore (altered porphyry)	<0.23	<0.55	<45.55	1.04	<0.02	<0.56	<0.16	<0.08	<0.17
260.5-260.8	C7177	Ore (altered porphyry)	<0.29	<0.93	<61.24	11.40	0.12	<1.22	<0.25	0.52	0.54
260.5-260.8	C7177	Ore (altered porphyry)	0.35	<0.53	<76.81	1.42	<0.05	<0.95	<0.22	<0.12	<0.2
260.5-260.8	C7177	Ore (altered porphyry)	<0.27	<0.56	<70.06	<0.60	<0.03	<0.74	<0.24	0.96	<0.13
260.5-260.8	C7177	Ore (altered porphyry)	<0.21	<0.38	<65.21	<0.59	<0.04	<0.77	<0.24	<0.1	<0.15
260.5-260.8	C7177	Ore (altered porphyry)	<0.22	<0.49	<63.90	2.63	<0.04	<0.92	<0.23	<0.11	<0.16
260.5-260.8	C7177	Ore (altered porphyry)	42.73	14.38	<55.70	1.94	0.24	<1.08	<0.19	0.70	<0.18
260.5-260.8	C7177	Ore (altered porphyry)	<0.29	<0.48	<41.47	1.55	0.03	1.09	<0.18	0.17	<0.16
260.5-260.8	C7177	Ore (altered porphyry)	2.34	206.50	<67.47	9702.10	90.96	102.41	2.68	14.76	2.43
260.5-260.8	C7177	Ore (altered porphyry)	<0.23	<0.52	<42.53	<0.93	<0.03	<0.66	<0.21	1.98	<0.17
288.79-289	CD13829	sedimentary pyrite	38.55	232.35	<46.65	3.87	0.47	1.29	13.22	115.33	119.22

Table A13.1: LA-ICPMS of pyrite St Ives Gold District												
Analysis	As (ppm)	Se (ppm)	Sr (ppm)	Zr (ppm)	Mo (ppm)	Ag (ppm)	Cd (ppm)	Sb (ppm)	Te (ppm)	Ba (ppm)	Gd (ppm)	Hf (ppm)
Ap15a007.csv	27.01	28.81	0.61	0.13	0.31	9.41	0.23	1.87	39.60	0.18	0.10	0.04
Ap15a016.csv	3.36	21.52	<0.01	<0.01	<0.02	0.10	<0.02	0.07	3.40	<0.03	<0.05	<0.02
Ap15a017.csv	2.93	10.61	1.12	0.09	<0.05	0.33	<0.04	0.59	5.77	0.52	<0.04	0.02
Ap15a018.csv	<0.57	11.78	0.65	0.06	0.32	0.25	<0.06	0.57	6.47	0.09	<0.04	<0.01
Ap15a019.csv	1.57	10.39	<0.01	<0.01	0.03	0.02	<0.09	<0.02	<0.08	<0.03	<0.01	<0.01
Ap15a020.csv	<0.95	18.17	0.02	0.02	<0.03	<0.02	<0.1	<0.02	1.86	<0.03	<0.03	<0.02
Ap15a008.csv	6.32	27.07	<0.01	<0.01	0.03	2.13	<0.07	0.04	3.38	<0.04	0.06	<0.01
Ap15a009.csv	2.82	19.68	<0.01	<0.02	<0.02	0.28	<0.1	<0.03	2.32	<0.06	0.03	<0.01
Ap15a010.csv	3.72	19.44	<0.01	<0.01	<0.01	<0.01	<0.14	<0.02	<0.1	<0.04	<0.03	<0.01
Ap15a011.csv	2.84	18.22	<0.01	<0.01	<0.04	<0.01	<0.09	<0.02	<0.16	<0.03	<0.03	<0.01
Ap15a012.csv	8.64	21.43	<0.01	0.01	<0.03	0.06	<0.06	<0.04	1.25	<0.03	<0.03	<0.01
Ap15a013.csv	2.96	19.14	<0.01	<0.01	<0.03	<0.01	<0.08	<0.02	<0.13	<0.02	<0.03	<0.01
Ap15a014.csv	18.82	26.04	8.61	0.34	174.34	3.02	<0.09	5.15	73.13	14.57	0.45	0.05
Ap15a015.csv	4.91	20.87	<0.01	<0.02	<0.04	0.17	<0.13	<0.03	2.56	<0.02	<0.01	<0.01
Ap15b007.csv	833.35	5.38	0.43	0.06	1.03	5.95	0.55	40.13	15.71	5.18	<0.03	<0.01

Table A13.1: LA-ICPMS of pyrite St Ives Gold District

Analysis	Ta	W	Au	Tl	Pb206 **	Pb207 **	Pb208 **	Bi	Th	U
Ap15a007.csv	0.22	125.33	0.62	<0.01	29.99	33.82	34.10	14.99	0.50	
Ap15a016.csv	<0.01	0.06	0.48	<0.01	3.00	3.41	3.04	4.74	<0.01	<0.01
Ap15a017.csv	0.04	22.32	0.34	<0.01	9.69	11.13	11.15	6.48	0.11	0.02
Ap15a018.csv	0.05	49.68	0.40	<0.01	11.74	13.85	13.19	7.39	0.12	0.01
Ap15a019.csv	<0.01	<0.02	0.02	<0.01	0.03	0.04	0.06	0.04	<0.01	<0.01
Ap15a020.csv	<0.01	0.39	0.06	<0.01	0.41	0.49	0.54	1.93	<0.01	<0.01
Ap15a008.csv	<0.01	<0.02	0.31	<0.01	92.26	106.93	103.76	8.92	<0.01	<0.01
Ap15a009.csv	<0.01	<0.01	0.54	<0.01	3.97	4.57	4.22	4.28	<0.01	<0.01
Ap15a010.csv	<0.01	<0.02	<0.01	<0.01	0.05	0.05	0.04	0.07	<0.01	<0.01
Ap15a011.csv	<0.01	0.06	<0.01	<0.01	<0.01	<0.01	0.05	0.07	<0.01	<0.01
Ap15a012.csv	<0.01	<0.01	<0.01	<0.01	3.89	4.71	4.93	4.27	<0.01	<0.01
Ap15a013.csv	<0.01	<0.01	<0.01	<0.01	0.02	<0.01	0.01	0.01	<0.01	<0.01
Ap15a014.csv	0.53	224.88	6.37	<0.01	86.68	103.52	96.63	38.49	2.59	0.46
Ap15a015.csv	<0.01	<0.01	0.96	<0.01	0.56	0.58	0.59	1.84	<0.01	<0.01
Ap15b007.csv	<0.01	0.06	0.55	3.86	265.58	312.84	295.91	9.69	<0.01	<0.01

** The number after the Pb refers to isotope used to calculate the total Pb in the sample

Table A13.1: LA-ICPMS of pyrite St Ives Gold District											
Depth (m)	Drill Hole	Group	Mg (ppm)	Al (ppm)	Ca (ppm)	Ti (ppm)	V (ppm)	Cr (ppm)	Mn (ppm)	Cu (ppm)	Zn (ppm)
288.79-289	CD13829	sedimentary pyrite	35.46	262.57	<49.94	4.66	0.47	1.62	16.27	137.17	54.21
288.79-289	CD13829	sedimentary pyrite	947.82	17003.23	203.56	139.62	23.65	43.44	32.44	75.82	96.96
288.79-289	CD13829	sedimentary pyrite	1064.29	16845.06	616.05	134.62	19.03	41.68	59.12	95.54	664.30
288.79-289	CD13829	sedimentary pyrite	2240.77	40729.64	1264.97	304.46	45.22	88.21	80.97	125.15	495.28
288.79-289	CD13829	sedimentary pyrite	555.62	8656.14	744.01	80.45	10.01	22.64	29.74	86.00	257.40
288.79-289	CD13829	sedimentary pyrite	565.63	8095.09	236.25	245.43	11.18	31.91	26.90	73.68	318.50
288.79-289	CD13829	sedimentary pyrite	44.58	299.11	<58.91	3.98	0.65	2.50	18.77	125.34	75.54
288.79-289	CD13829	sedimentary pyrite	36.33	155.97	<47.34	4.00	0.28	2.17	19.88	5663.20	126.76
288.79-289	CD13829	sedimentary pyrite	22.86	87.67	<52.34	4.00	0.16	<0.72	14.42	124.56	80.19
288.79-289	CD13829	sedimentary pyrite	14.80	43.36	<42.02	2.64	0.09	<1.00	20.04	147.80	138.69
288.79-289	CD13829	sedimentary pyrite	39.40	95.82	2328.33	1.68	0.06	<0.54	160.30	1437.57	91.72
288.79-289	CD13829	sedimentary pyrite	18.50	118.51	<72.68	1.38	0.04	1.35	12.12	110.53	105.49
288.79-289	CD13829	sedimentary pyrite	22.69	106.86	<41.36	3.30	0.24	<0.62	28.20	245.40	48.04
288.79-289	CD13829	sedimentary pyrite	14.98	64.54	<60.80	3.60	0.12	<1.09	19.67	3414.03	65.20
288.79-289	CD13829	sedimentary pyrite	1110.96	27580.56	2272.69	97.37	11.32	18.07	92.86	206.76	433.08

Table A13.1: LA-ICPMS of pyrite St Ives Gold District

Analysis	As (ppm)	Se (ppm)	Sr (ppm)	Zr (ppm)	Mo (ppm)	Ag (ppm)	Cd (ppm)	Sb (ppm)	Te (ppm)	Ba (ppm)	Gd (ppm)	Hf (ppm)
Ap15b016.csv	1109.16	10.44	0.76	0.12	1.22	7.73	0.27	58.71	22.95	8.53	<0.04	<0.01
Ap15b018.csv	698.64	9.70	9.81	7.59	1.31	2.86	<0.13	24.34	9.18	98.41	0.10	0.19
Ap15b019.csv	604.44	18.70	16.62	5.87	1.21	2.56	1.53	24.45	11.00	98.33	0.17	0.18
Ap15b020.csv	636.34	16.12	46.10	23.11	1.91	3.16	1.12	26.75	12.69	223.74	0.10	0.59
Ap15b021.csv	756.60	20.85	8.06	2.59	4.23	3.12	0.55	24.81	11.31	52.63	0.09	0.09
Ap15b022.csv	745.12	20.07	3.62	50.91	0.83	3.27	0.75	20.93	8.34	56.50	0.28	1.12
Ap15b008.csv	996.03	10.44	0.47	0.15	0.56	7.49	0.34	50.82	20.08	7.04	0.02	<0.01
Ap15b009.csv	846.31	11.12	0.51	0.12	0.80	7.60	0.49	43.23	16.09	4.94	<0.03	<0.01
Ap15b010.csv	946.72	8.83	0.46	0.05	0.95	6.99	0.22	47.73	18.38	4.92	<0.02	<0.01
Ap15b011.csv	972.69	7.20	0.36	0.03	1.17	6.73	0.36	51.81	20.09	3.66	<0.02	<0.01
Ap15b012.csv	583.00	24.66	57.22	0.09	0.26	5.24	0.30	38.45	11.20	2.85	0.17	<0.01
Ap15b013.csv	1259.81	12.26	1.11	0.06	0.28	5.33	0.39	37.36	13.95	2.28	<0.04	<0.01
Ap15b014.csv	991.89	10.01	0.39	0.19	0.70	7.49	0.19	46.36	19.03	4.15	0.05	0.01
Ap15b015.csv	975.22	14.96	0.50	0.05	0.57	7.32	<0.15	51.39	18.01	3.38	<0.05	<0.01
Ap15b034.csv	501.05	5.40	82.36	4.88	2.31	8.06	0.98	37.87	14.00	102.37	0.02	0.15

Table A13.1: LA-ICPMS of pyrite St Ives Gold District										
Analysis	Ta (ppm)	W (ppm)	Au (ppm)	Tl (ppm)	Pb206 (ppm)	Pb207 (ppm)	Pb208 (ppm)	Bi (ppm)	Th (ppm)	U (ppm)
Ap15b016.csv	<0.01	0.08	0.56	5.68	425.70	498.98	484.02	14.11	<0.01	<0.01
Ap15b018.csv	0.01	0.30	0.25	9.56	171.01	196.10	195.53	5.27	0.87	0.09
Ap15b019.csv	<0.01	0.27	0.15	15.23	173.94	202.15	194.42	5.86	0.06	0.08
Ap15b020.csv	<0.01	0.56	0.18	17.82	214.61	247.64	238.25	7.05	0.41	0.26
Ap15b021.csv	<0.01	1.07	0.22	13.56	198.77	229.63	222.02	6.91	0.22	0.05
Ap15b022.csv	0.04	0.28	0.22	8.10	168.35	193.37	193.67	4.88	1.90	0.48
Ap15b008.csv	<0.01	0.09	0.60	4.56	392.62	445.18	437.02	12.00	<0.01	0.01
Ap15b009.csv	<0.01	0.05	0.47	4.27	356.13	408.25	404.37	10.21	<0.01	<0.01
Ap15b010.csv	<0.01	0.07	0.56	2.12	368.86	426.26	400.16	11.26	<0.01	0.01
Ap15b011.csv	<0.01	0.06	0.53	1.63	361.05	415.41	410.13	13.04	<0.01	<0.01
Ap15b012.csv	<0.01	0.04	0.26	1.19	425.29	488.72	480.32	8.49	0.01	<0.01
Ap15b013.csv	<0.01	0.03	0.41	2.78	311.55	338.87	335.62	8.72	0.01	<0.01
Ap15b014.csv	<0.01	0.08	0.62	4.31	330.60	383.23	368.07	11.11	0.01	<0.01
Ap15b015.csv	<0.01	<0.02	0.44	4.13	450.16	527.74	496.83	11.85	<0.01	<0.01
Ap15b034.csv	<0.01	0.36	0.32	12.39	376.92	433.62	417.51	13.42	0.03	0.07

Table A13.1: LA-ICPMS of pyrite St Ives Gold District											
Depth (m)	Drill Hole	Group	Mg (ppm)	Al (ppm)	Ca (ppm)	Ti (ppm)	V (ppm)	Cr (ppm)	Mn (ppm)	Cu (ppm)	Zn (ppm)
288.79-289	CD13829	sedimentary pyrite	676.20	11095.73	356.44	90.65	10.05	16.74	35.13	166.91	725.84
288.79-289	CD13829	sedimentary pyrite	1165.21	25590.06	4336.21	116.05	14.70	27.38	116.44	233.59	449.88
288.79-289	CD13829	sedimentary pyrite	2577.41	58926.13	3788.15	242.36	31.87	50.36	138.20	241.91	1836.64
288.79-289	CD13829	sedimentary pyrite	472.90	20003.50	6571.06	14.65	1.59	2.76	164.43	156.76	269.01
288.79-289	CD13829	sedimentary pyrite	386.04	6634.59	<97.43	46.23	6.44	10.56	25.73	193.69	1135.69
288.79-289	CD13829	sedimentary pyrite	1247.88	24053.47	1126.80	119.00	18.15	27.73	65.06	207.58	569.51
288.79-289	CD13829	sedimentary pyrite	245.09	6742.54	871.55	18.84	2.01	3.70	33.18	137.97	382.61
288.79-289	CD13829	sedimentary pyrite	185.08	3238.24	243.55	20.35	2.31	5.15	19.30	181.22	866.93
288.79-289	CD13829	sedimentary pyrite	1705.35	31743.00	2025.21	229.59	22.87	45.18	97.48	193.96	390.14
288.79-289	CD13829	sedimentary pyrite	1563.71	36434.97	3342.95	146.40	16.78	30.42	112.78	205.66	977.54
288.79-289	CD13829	sedimentary pyrite		<5.23		<5.45	<0.28	<6.50	<2.37	<1.46	<1.61
288.79-289	CD13829	sedimentary pyrite		<1.12		3.14	<0.06	<1.74	<0.49	<0.28	<0.41
288.79-289	CD13829	sedimentary pyrite		<0.98		3.09	<0.08	<1.05	<0.48	<0.3	0.83
288.79-289	CD13829	sedimentary pyrite		<1.07		<1.23	<0.11	<1.52	<0.38	<0.32	<0.59
288.79-289	CD13829	sedimentary pyrite		5.32		2.95	<0.08	<1.29	0.89	<0.29	64.56

Table A13.1: LA-ICPMS of pyrite St Ives Gold District

Analysis	As (ppm)	Se (ppm)	Sr (ppm)	Zr (ppm)	Mo (ppm)	Ag (ppm)	Cd (ppm)	Sb (ppm)	Te (ppm)	Ba (ppm)	Gd (ppm)	Hf (ppm)
Ap15b043.csv	563.86	8.36	5.88	1.55	1.73	8.89	1.18	31.50	12.06	73.02	<0.04	0.07
Ap15b044.csv	526.91	12.26	50.98	5.53	1.99	7.58	0.85	37.94	14.18	116.56	<0.07	0.13
Ap15b045.csv	517.18	10.35	133.77	23.84	2.59	8.79	3.45	40.97	14.98	219.22	<0.12	0.65
Ap15b046.csv	594.94	8.36	95.96	2.33	1.85	8.39	0.52	40.24	13.74	23.99	0.17	0.06
Ap15b047.csv	485.54	9.19	5.39	6.66	1.97	9.37	2.14	36.56	13.46	46.60	0.07	0.21
Ap15b036.csv	477.73	7.77	23.66	11.68	2.68	8.02	1.27	36.10	14.54	123.60	0.18	0.27
Ap15b037.csv	547.06	11.44	19.94	0.39	1.43	6.96	1.05	28.16	9.63	20.58	<0.05	<0.01
Ap15b039.csv	512.20	5.89	4.13	0.16	1.47	8.95	1.64	31.65	10.96	23.99	<0.03	<0.01
Ap15b041.csv	524.72	5.93	38.95	5.12	1.91	7.94	0.90	36.40	12.68	167.08	<0.01	0.14
Ap15b042.csv	538.84	8.31	82.96	56.91	2.07	7.38	2.63	37.98	13.57	134.63	0.54	1.60
SE09A086.csv	691.83	19.15	<0.01	<0.08	<0.21	0.14	<0.49	<0.14	<0.66	<0.01	<0.01	<0.08
SE09A087.csv	250.97	11.50	<0.01	<0.03	<0.04	<0.02	<0.03	<0.04	<0.31	<0.01	<0.01	<0.01
SE09A088.csv	91.83	23.82	<0.01	<0.02	<0.02	<0.01	<0.09	<0.03	<0.42	<0.01	<0.01	<0.01
SE09A089.csv	87.47	26.02	<0.01	0.04	<0.04	<0.01	<0.1	<0.04	<0.3	<0.01	<0.01	<0.01
SE09A090.csv	481.56	12.93	<0.01	0.04	<0.04	0.03	<0.3	0.08	<0.28	<0.01	<0.01	<0.01

Table A13.1: LA-ICPMS of pyrite St Ives Gold District

Analysis	Ta (ppm)	W (ppm)	Au (ppm)	Tl (ppm)	Pb206 (ppm)	Pb207 (ppm)	Pb208 (ppm)	Bi (ppm)	Th (ppm)	U (ppm)
Ap15b043.csv	<0.01	0.34	0.43	6.99	322.52	367.58	354.88	9.42	0.01	0.02
Ap15b044.csv	0.01	0.28	0.36	12.10	362.91	423.38	403.19	12.08	0.04	0.08
Ap15b045.csv	<0.01	0.66	0.37	20.17	403.46	461.45	441.85	14.71	0.10	0.35
Ap15b046.csv	<0.01	0.18	0.43	4.44	374.14	425.37	411.63	11.04	0.02	0.04
Ap15b047.csv	<0.01	0.20	0.46	6.17	333.74	382.26	373.47	11.23	0.06	0.12
Ap15b036.csv	0.01	0.52	0.42	12.81	331.76	380.69	370.41	13.44	0.14	0.17
Ap15b037.csv	<0.01	0.15	0.38	4.26	306.73	349.34	347.24	8.74	0.01	0.01
Ap15b039.csv	<0.01	0.15	0.47	4.98	306.84	355.36	342.56	9.80	<0.01	0.01
Ap15b041.csv	<0.01	0.49	0.38	13.15	365.42	421.84	411.96	12.09	0.05	0.12
Ap15b042.csv	<0.01	0.48	0.36	14.75	361.42	421.38	397.71	12.77	0.13	0.70
SE09A086.csv	0.03	0.10	<0.04	<0.08			0.32	<0.05	<0.01	<0.07
SE09A087.csv	<0.01	<0.01	<0.01	<0.01			<0.02	<0.01	<0.01	<0.01
SE09A088.csv	0.01	<0.02	<0.01	<0.01			<0.02	<0.01	<0.01	<0.01
SE09A089.csv	<0.01	<0.03	<0.01	<0.01			<0.02	<0.01	<0.01	<0.01
SE09A090.csv	<0.01	0.03	<0.01	<0.01			1.20	<0.01	<0.01	<0.01

Table A13.1: LA-ICPMS of pyrite St Ives Gold District											
Depth (m)	Drill Hole	Group	Mg (ppm)	Al (ppm)	Ca (ppm)	Ti (ppm)	V (ppm)	Cr (ppm)	Mn (ppm)	Cu (ppm)	Zn (ppm)
288.79-289	CD13829	sedimentary pyrite		4915.05		<35.98	10.76	<53.51	<15.62	<8.93	57.49
288.79-289	CD13829	sedimentary pyrite		326.30		5.97	0.82	<1.61	8.63	19.07	57.65
288.79-289	CD13829	sedimentary pyrite		878.14		3.63	<0.12	<2.01	123.61	85.15	1.93
288.79-289	CD13829	sedimentary pyrite		4806.46		<68.70	8.83	<55.21	<24.64	66.15	<19.38
288.79-289	CD13829	sedimentary pyrite		<1.05		<1.67	<0.06	<1.44	39.71	1104.78	325.73
288.79-289	CD13829	sedimentary pyrite		<1.04		<1.02	<0.08	<1.05	<0.51	<0.23	0.99
288.79-289	CD13829	sedimentary pyrite		<1.78		<1.93	<0.10	<1.80	<0.73	<0.38	<0.61
288.79-289	CD13829	sedimentary pyrite		1989.76		<36.42	<2.46	<51.12	76.96	24.15	970.20
288.79-289	CD13829	sedimentary pyrite		382.93		<36.04	<1.82	<47.71	29.11	67.95	113.73
288.79-289	CD13829	sedimentary pyrite		121.50		<18.29	<1.53	<19.75	56.97	93.73	3336.41
377.96-378.3	CD13833	Magnetite altered Kapai		220.91		57.61	0.88	<3.76	<1.23	14.78	<0.83
377.96-378.3	CD13833	Magnetite altered Kapai		10375.41		82.75	7.28	10.62	65.54	15.00	10.50
377.96-378.3	CD13833	Magnetite altered Kapai		214.95		<7.63	<0.47	<14.07	<3.98	4.40	<3.17
377.96-378.3	CD13833	Magnetite altered Kapai		<9.13		<9.19	<0.57	<17.22	<3.99	11.23	<3.7
377.96-378.3	CD13833	Magnetite altered Kapai		87.47		<3.02	<0.27	<5.86	<1.81	11.63	<1.9

Table A13.1: LA-ICPMS of pyrite St Ives Gold District

Analysis	As (ppm)	Se (ppm)	Sr (ppm)	Zr (ppm)	Mo (ppm)	Ag (ppm)	Cd (ppm)	Sb (ppm)	Te (ppm)	Ba (ppm)	Gd (ppm)	Hf (ppm)
SE09A096.csv	959.05	<39.21	<0.01	<0.81	<0.7	2.42	3.78	11.11	<6.78	<0.01	<0.01	<0.44
SE09A091.csv	984.77	10.15	<0.01	0.73	<0.04	1.09	<0.03	5.72	1.59	<0.01	<0.01	<0.01
SE09A092.csv	1061.56	7.88	<0.01	<0.03	<0.05	0.50	0.10	3.27	0.67	<0.01	<0.01	<0.01
SE09A094.csv	590.39	<58.15	<0.01	<1.11	<1.62	2.25	<12.54	15.10	<14.76	<0.01	<0.01	<0.52
SE09A097.csv	24.50	33.77	<0.01	<0.03	<0.03	3.70	0.96	6.58	0.86	<0.01	<0.01	<0.01
SE09A098.csv	689.54	13.30	<0.01	<0.02	<0.03	0.03	<0.03	<0.04	<0.23	<0.01	<0.01	<0.01
SE09A099.csv	613.83	20.98	<0.01	<0.03	<0.06	<0.02	<0.14	<0.05	0.42	<0.01	<0.01	<0.02
SE09A100.csv	1432.74	<25.89	<0.01	48.08	<0.85	2.39	4.52	11.62	<6.18	<0.01	<0.01	1.34
SE09A101.csv	618.94	<27.53	<0.01	2.02	<0.84	2.10	<5.18	13.86	18.12	<0.01	<0.01	<0.12
SE09A102.csv	774.77	<22.36	<0.01	10.69	<0.78	2.07	<4.88	11.12	<7.17	<0.01	<0.01	<0.24
SE09A005.csv	<1.61	75.17	<0.01	<0.05	<0.1	1.68	<1.17	12.15	1.86	<0.01	<0.01	<0.02
SE09A006.csv	<2	51.75	<0.01	15.56	<0.05	3.77	0.18	7.29	3.25	<0.01	<0.01	0.34
SE09A007.csv	<6.01	37.49	<0.01	0.25	<0.29	0.57	<0.17	2.33	<1.72	<0.01	<0.01	0.09
SE09A008.csv	<6.55	57.26	<0.01	0.08	<0.28	1.83	1.81	2.04	<2.28	<0.01	<0.01	<0.07
SE09A009.csv	<3.26	58.78	<0.01	<0.11	<0.09	0.98	0.44	1.64	<0.37	<0.01	<0.01	<0.04

Table A13.1: LA-ICPMS of pyrite St Ives Gold District

Analysis	Ta (ppm)	W (ppm)	Au (ppm)	Tl (ppm)	Pb206 (ppm)	Pb207 (ppm)	Pb208 (ppm)	Bi (ppm)	Th (ppm)	U (ppm)
SE09A096.csv	<0.09	<0.83	<0.45	1.62			91.74	1.54	<0.01	<0.05
SE09A091.csv	<0.01	<0.01	0.05	1.39			46.42	1.36	<0.01	<0.01
SE09A092.csv	<0.01	<0.04	0.04	0.10			59.88	0.56	<0.01	<0.01
SE09A094.csv	<0.3	<1.29	1.04	8.20			121.83	2.44	<0.01	<0.83
SE09A097.csv	<0.01	<0.01	0.06	0.11			177.93	0.49	<0.01	0.01
SE09A098.csv	<0.01	<0.02	<0.01	<0.01			0.21	<0.01	<0.01	<0.01
SE09A099.csv	<0.01	<0.02	<0.02	<0.02			0.10	<0.02	<0.01	<0.01
SE09A100.csv	<0.11	<0.49	<0.27	5.33			105.76	2.36	<0.01	<0.32
SE09A101.csv	<0.09	<0.68	<0.21	12.04			123.73	2.62	<0.01	<0.26
SE09A102.csv	<0.1	<0.56	<0.16	3.50			104.80	1.87	<0.01	0.08
SE09A005.csv	0.11	0.32	<0.03	0.55			377.02	32.63	<0.01	0.01
SE09A006.csv	0.04	0.30	0.07	1.12			189.74	39.29	<0.01	4.26
SE09A007.csv	<0.01	<0.2	<0.1	0.51			94.76	7.19	<0.01	<0.07
SE09A008.csv	<0.02	<0.12	<0.13	0.31			165.68	9.98	<0.01	<0.08
SE09A009.csv	<0.02	<0.13	0.08	0.58			245.76	5.58	<0.01	<0.03

Table A13.1: LA-ICPMS of pyrite St Ives Gold District											
Depth (m)	Drill Hole	Group	Mg (ppm)	Al (ppm)	Ca (ppm)	Ti (ppm)	V (ppm)	Cr (ppm)	Mn (ppm)	Cu (ppm)	Zn (ppm)
377.96-378.3	CD13833	Magnetite altered Kapai		<0.75		1.79	<0.06	<2.10	0.93	<0.25	<0.33
377.96-378.3	CD13833	Magnetite altered Kapai		205.34		14.04	0.87	<7.71	<2.67	14.54	<1.48
377.96-378.3	CD13833	Magnetite altered Kapai		17.87		37.99	<0.22	<4.18	<2.4	33.61	<1.55
377.96-378.3	CD13833	Magnetite altered Kapai		66.72		14.17	<0.25	<7.30	<2.08	6.87	<1.55
377.96-378.3	CD13833	Magnetite altered Kapai		9.53		3.54	<0.08	<1.38	<0.48	0.39	<0.31
377.96-378.3	CD13833	Magnetite altered Kapai		<0.76		2.36	<0.05	<1.51	<0.4	<0.22	<0.27
377.96-378.3	CD13833	Magnetite altered Kapai		276.39		3.22	1.00	8.15	1.21	<0.23	<0.34
377.96-378.3	CD13833	Magnetite altered Kapai		23.73		<1.06	<0.06	<1.41	<0.54	<0.21	<0.43
377.96-378.3	CD13833	Magnetite altered Kapai		600.70		16.22	3.93	<12.48	<4.23	25.99	<3.5
377.96-378.3	CD13833	Magnetite altered Kapai		46.52		16.15	<0.40	<7.32	<3	13.15	<2.4
377.96-378.3	CD13833	Magnetite altered Kapai		456.05		<8.75	<0.67	<11.39	<4.83	14.77	<4.17
377.96-378.3	CD13833	Magnetite altered Kapai		13.45		<3.50	<0.27	<6.58	<1.94	<0.91	<1.47
377.96-378.3	CD13833	Magnetite altered Kapai		293.14		86.17	1.55	<9.35	<3.13	12.25	<1.92
377.96-378.3	CD13833	Magnetite altered Kapai		38.19		5.29	<0.06	<1.22	<0.36	<0.23	<0.4
377.96-378.3	CD13833	Magnetite altered Kapai		1603.29		7.26	0.30	<0.85	<0.44	6.52	1.05

Table A13.1: LA-ICPMS of pyrite St Ives Gold District

Analysis	As (ppm)	Se (ppm)	Sr (ppm)	Zr (ppm)	Mo (ppm)	Ag (ppm)	Cd (ppm)	Sb (ppm)	Te (ppm)	Ba (ppm)	Gd (ppm)	Hf (ppm)
SE09A012.csv	<0.82	44.33	<0.01	<0.01	<0.03	<0.02	<0.08	<0.03	8.29	<0.01	<0.01	<0.01
SE09A018.csv	<3.57	62.26	<0.01	<0.06	<0.14	12.43	<0.42	3.76	13.96	<0.01	<0.01	<0.03
SE09A019.csv	<4.01	59.37	<0.01	1.33	<0.13	5.09	<0.42	35.24	10.40	<0.01	<0.01	<0.02
SE09A020.csv	<3.73	69.99	<0.01	0.45	<0.15	2.67	<0.55	2.46	2.92	<0.01	<0.01	0.03
SE09A022.csv	13.95	47.28	<0.01	<0.02	<0.02	<0.01	<0.03	<0.03	7.30	<0.01	<0.01	<0.01
SE09A011.csv	150.97	11.73	<0.01	0.11	<0.04	<0.01	<0.03	<0.03	0.35	<0.01	<0.01	<0.01
SE09A024.csv	<0.75	50.59	<0.01	0.17	<0.03	0.04	0.15	0.06	4.15	<0.01	<0.01	<0.01
SE09A025.csv	<0.8	28.51	<0.01	<0.01	0.06	0.02	<0.03	<0.03	<0.31	<0.01	<0.01	<0.01
SE09A028.csv	<6.98	<9.08	<0.01	0.98	<0.19	17.94	<0.66	25.66	27.48	<0.01	<0.01	<0.09
SE09A029.csv	<5.59	14.94	<0.01	0.98	<0.22	8.06	<0.13	5.74	15.30	<0.01	<0.01	<0.03
SE09A030.csv	<8.65	<13.91	<0.01	13.61	<0.18	96.56	<0.25	9.75	76.94	<0.01	<0.01	0.56
SE09A031.csv	<3.42	57.47	<0.01	2.55	<0.14	3.92	<0.1	0.36	10.65	<0.01	<0.01	<0.05
SE09A032.csv	<4.14	34.47	<0.01	<0.06	<0.22	4.45	<0.14	6.80	13.33	<0.01	<0.01	<0.09
SE09A033.csv	2.07	63.95	<0.01	0.56	<0.02	0.03	<0.14	<0.03	58.62	<0.01	<0.01	<0.01
SE09A034.csv	29.62	30.34	<0.01	43.33	<0.03	0.13	<0.07	<0.04	10.42	<0.01	<0.01	1.26

Table A13.1: LA-ICPMS of pyrite St Ives Gold District

Analysis	Ta (ppm)	W (ppm)	Au (ppm)	Tl (ppm)	Pb206 (ppm)	Pb207 (ppm)	Pb208 (ppm)	Bi (ppm)	Th (ppm)	U (ppm)
SE09A012.csv	<0.01	<0.02	0.04	<0.01			1.51	1.09	<0.01	<0.01
SE09A018.csv	<0.02	<0.18	0.27	0.91			270.03	51.87	<0.01	<0.01
SE09A019.csv	0.04	<0.1	0.19	1.61			698.10	56.24	<0.01	<0.06
SE09A020.csv	<0.01	<0.11	0.09	0.52			263.72	32.99	<0.01	0.04
SE09A022.csv	<0.01	<0.03	0.02	<0.01			0.24	0.48	<0.01	<0.01
SE09A011.csv	<0.01	<0.01	<0.01	<0.01			0.02	<0.01	<0.01	<0.01
SE09A024.csv	<0.01	<0.03	<0.01	0.03			3.59	1.21	<0.01	<0.01
SE09A025.csv	<0.01	<0.01	<0.01	<0.01			0.27	0.17	<0.01	<0.01
SE09A028.csv	<0.03	0.21	0.36	0.96			586.88	138.85	<0.01	<0.09
SE09A029.csv	<0.02	0.08	<0.08	0.53			291.25	92.87	<0.01	<0.03
SE09A030.csv	<0.05	<0.17	0.24	0.54			387.90	168.11	<0.01	<0.08
SE09A031.csv	<0.01	<0.07	<0.05	<0.02			4.25	12.85	<0.01	0.31
SE09A032.csv	<0.03	<0.14	<0.05	0.53			378.20	50.79	<0.01	0.07
SE09A033.csv	<0.01	0.02	<0.01	<0.01			4.18	1.50	<0.01	0.02
SE09A034.csv	<0.01	<0.01	0.16	0.02			2.48	3.91	<0.01	0.46

Table A13.1: LA-ICPMS of pyrite St Ives Gold District

Depth (m)	Drill Hole	Group	Mg (ppm)	Al (ppm)	Ca (ppm)	Ti (ppm)	V (ppm)	Cr (ppm)	Mn (ppm)	Cu (ppm)	Zn (ppm)
377.96-378.3	CD13833	Magnetite altered Kapai		618.64		71.42	3.97	<7.69	<2.76	28.31	6.73
377.96-378.3	CD13833	Magnetite altered Kapai		20.77		40.44	<0.46	<9.49	<3.03	12.53	<2.21
377.96-378.3	CD13833	Magnetite altered Kapai		83453.54		8192.10	300.72	455.31	808.14	19.36	162.77
377.96-378.3	CD13833	Magnetite altered Kapai		5487.22		115.29	11.84	<7.21	6.31	4.97	6.17
377.96-378.3	CD13833	Magnetite altered Kapai		1291.76		<4.24	0.68	<6.49	<2.13	5.74	59.35
327.33-327.55	CD1512	sedimentary pyrite		3270.47		18.86	3.80	6.17	15.93	114.93	370.67
327.33-327.55	CD1512	sedimentary pyrite		2188.58		8.32	2.46	3.69	15.15	111.91	394.78
327.33-327.55	CD1512	sedimentary pyrite		609.12		6.33	1.17	<1.28	10.55	83.81	217.91
327.33-327.55	CD1512	sedimentary pyrite		1901.72		49.26	2.51	6.12	19.22	1200.24	346.35
327.33-327.55	CD1512	sedimentary pyrite		839.57		19.86	1.24	<1.29	16.01	80.66	88.43
327.33-327.55	CD1512	sedimentary pyrite		520.21		15.20	0.74	<1.46	17.45	91.01	1207.69
327.33-327.55	CD1512	sedimentary pyrite		1855.32		20.29	1.82	2.85	18.79	82.17	222.15
327.33-327.55	CD1512	sedimentary pyrite		384.60		7.48	0.59	<0.82	18.35	92.91	171.87
327.33-327.55	CD1512	sedimentary pyrite		1783.98		10779.58	8.56	<7.63	142.38	107.71	7194.86
327.33-327.55	CD1512	sedimentary pyrite		15438.35		142.02	18.24	35.42	81.82	168.55	2109.58

Table A13.1: LA-ICPMS of pyrite St Ives Gold District

Analysis	As (ppm)	Se (ppm)	Sr (ppm)	Zr (ppm)	Mo (ppm)	Ag (ppm)	Cd (ppm)	Sb (ppm)	Te (ppm)	Ba (ppm)	Gd (ppm)	Hf (ppm)
SE09A035.csv	<3.85	30.60	<0.01	45.98	<0.1	23.75	0.33	11.26	28.72	<0.01	<0.01	1.25
SE09A036.csv	<5.28	45.21	<0.01	0.29	<0.12	11.64	<0.88	5.79	11.18	<0.01	<0.01	0.04
SE09A037.csv	<7.44	<11.5	<0.01	<0.11	<0.19	12.02	<2.02	6.57	6.56	<0.01	<0.01	<0.06
SE09A038.csv	<5.08	15.03	<0.01	72.76	<0.19	1.00	<0.91	2.32	<1.66	<0.01	<0.01	2.14
SE09A039.csv	<2.72	31.22	<0.01	1.38	<0.15	1.32	<0.35	5.14	<0.37	<0.01	<0.01	0.07
AU19A024.csv	439.44	4.11	<0.01	0.38	1.25	5.37	1.00	34.88	3.86	<0.01	<0.01	0.01
AU19A025.csv	509.20	4.35	<0.01	0.23	1.26	5.46	1.21	39.06	4.23	<0.01	<0.01	<0.01
AU19A026.csv	570.79	<1.64	<0.01	0.34	1.33	5.46	0.64	33.38	4.31	<0.01	<0.01	0.01
AU19A027.csv	638.03	<2.06	<0.01	0.95	1.65	6.11	1.54	48.78	6.04	<0.01	<0.01	0.04
AU19A028.csv	1250.14	9.04	<0.01	0.09	1.02	5.25	0.47	46.10	5.91	<0.01	<0.01	<0.01
AU19A029.csv	1160.13	8.54	<0.01	0.77	1.64	7.36	3.67	68.89	9.25	<0.01	<0.01	0.01
AU19A030.csv	1377.10	8.57	<0.01	0.13	1.42	4.79	0.60	50.22	5.49	<0.01	<0.01	<0.01
AU19A031.csv	1014.85	<2.58	<0.01	0.18	0.86	6.11	0.96	69.09	10.56	<0.01	<0.01	<0.01
AU19A032.csv	1111.03	72.80	<0.01	4.45	4.13	8.31	29.56	54.84	7.56	<0.01	<0.01	0.18
AU19A033.csv	1134.78	31.05	<0.01	1.54	3.74	5.84	3.52	54.35	10.03	<0.01	<0.01	0.05

Table A13.1: LA-ICPMS of pyrite St Ives Gold District

Analysis	Ta (ppm)	W (ppm)	Au (ppm)	Tl (ppm)	Pb206 (ppm)	Pb207 (ppm)	Pb208 (ppm)	Bi (ppm)	Th (ppm)	U (ppm)
SE09A035.csv	0.04	0.31	0.13	1.73			653.64	95.66	<0.01	0.36
SE09A036.csv	<0.01	<0.12	0.15	0.88			342.70	86.13	<0.01	<0.06
SE09A037.csv	2.41	13.38	<0.11	4.22			486.62	45.67	<0.01	1.37
SE09A038.csv	0.03	0.30	<0.04	0.57			57.01	49.64	<0.01	0.89
SE09A039.csv	<0.01	<0.1	<0.07	0.45			123.83	14.11	<0.01	0.10
AU19A024.csv	0.01	0.25	0.44	2.96			331.03	3.24	<0.01	0.02
AU19A025.csv	<0.01	0.15	0.58	3.20			243.57	4.03	<0.01	<0.01
AU19A026.csv	<0.01	0.13	0.48	2.85			214.45	3.34	<0.01	0.01
AU19A027.csv	0.03	0.25	0.56	1.80			340.61	4.76	<0.01	0.02
AU19A028.csv	<0.01	0.21	0.41	4.96			293.85	4.53	<0.01	<0.01
AU19A029.csv	<0.01	0.16	0.56	4.27			407.05	6.38	<0.01	0.02
AU19A030.csv	<0.01	0.63	0.34	3.93			308.44	4.44	<0.01	<0.01
AU19A031.csv	<0.01	0.20	0.45	2.86			419.38	6.22	<0.01	0.01
AU19A032.csv	2.88	0.28	0.50	51.69			283.29	4.10	<0.01	1.87
AU19A033.csv	0.02	0.32	0.42	32.10			381.39	4.45	<0.01	0.09

Table A13.1: LA-ICPMS of pyrite St Ives Gold District											
Depth (m)	Drill Hole	Group	Mg (ppm)	Al (ppm)	Ca (ppm)	Ti (ppm)	V (ppm)	Cr (ppm)	Mn (ppm)	Cu (ppm)	Zn (ppm)
327.33-327.55	CD1512	sedimentary pyrite		22707.49		254.89	26.07	28.05	69.83	60.56	65.25
327.33-327.55	CD1512	sedimentary pyrite		11112.14		146.42	13.95	<18.53	33.63	72.74	21.15
327.33-327.55	CD1512	sedimentary pyrite		7613.75		172.35	6.89	<20.48	81.52	49.04	53.78
327.33-327.55	CD1512	sedimentary pyrite		20110.43		252.39	18.22	48.13	87.44	50.32	34.76
327.33-327.55	CD1512	sedimentary pyrite		226.96		<1.79	<0.04	<1.44	7.01	142.89	31.09
327.33-327.55	CD1512	sedimentary pyrite		7.12		9.29	<0.04	<1.96	21.83	77.59	81.32
327.33-327.55	CD1512	sedimentary pyrite		259.51		3.58	0.24	<1.37	18.42	63.99	105.83
327.33-327.55	CD1512	sedimentary pyrite		66.10		3.71	<0.05	1.69	21.69	72.07	57.70
327.33-327.55	CD1512	sedimentary pyrite		<0.62		<1.62	<0.07	<1.34	28.45	78.44	345.47
327.33-327.55	CD1512	sedimentary pyrite		48.54		3.61	<0.04	<2.31	18.86	72.34	143.01
327.33-327.55	CD1512	sedimentary pyrite		414.84		40.69	0.84	<1.31	28.40	72.76	58.68
327.33-327.55	CD1512	sedimentary pyrite		192.09		7.46	0.14	2.01	46.99	51.71	1622.64
327.33-327.55	CD1512	sedimentary pyrite		416.72		7.92	0.63	<1.55	658.65	343.25	27312.79
327.33-327.55	CD1512	sedimentary pyrite		249.80		7.56	0.35	<2.00	171.34	71.93	3199.62
327.33-327.55	CD1512	sedimentary pyrite		978.51		136.62	1.78	7.11	175.53	100.51	7545.66

Table A13.1: LA-ICPMS of pyrite St Ives Gold District

Analysis	As (ppm)	Se (ppm)	Sr (ppm)	Zr (ppm)	Mo (ppm)	Ag (ppm)	Cd (ppm)	Sb (ppm)	Te (ppm)	Ba (ppm)	Gd (ppm)	Hf (ppm)
AU19A034.csv	710.98	22.10	<0.01	2.27	2.54	2.82	0.34	37.18	7.36	<0.01	<0.01	0.08
AU19A035.csv	655.61	<19	<0.01	20.14	4.15	2.79	<0.26	33.61	5.65	<0.01	<0.01	0.65
AU19A036.csv	557.11	<51.45	<0.01	1.85	2.80	2.45	<0.45	26.86	4.79	<0.01	<0.01	<0.05
AU19A037.csv	722.34	<36.68	<0.01	4.47	1.97	1.32	2.52	20.05	<3.18	<0.01	<0.01	0.19
AU19A038.csv	307.20	31.80	<0.01	0.07	<0.01	1.57	0.24	1.41	<0.20	<0.01	<0.01	<0.01
AU19A041.csv	894.35	4.83	<0.01	0.03	0.99	5.94	<0.12	74.95	10.20	<0.01	<0.01	<0.01
AU19A042.csv	826.13	6.57	<0.01	0.20	0.65	5.93	0.33	66.65	9.97	<0.01	<0.01	0.01
AU19A043.csv	910.29	4.57	<0.01	0.78	0.83	6.95	0.19	76.01	10.47	<0.01	<0.01	0.03
AU19A044.csv	1039.57	5.21	<0.01	<0.01	1.64	7.70	0.83	87.91	14.70	<0.01	<0.01	<0.01
AU19A045.csv	1000.33	7.42	<0.01	0.03	1.56	7.15	0.55	85.17	13.37	<0.01	<0.01	<0.01
AU19A046.csv	726.49	12.86	<0.01	4.02	9.86	6.91	0.36	63.46	10.46	<0.01	<0.01	0.04
AU19A047.csv	856.03	5.38	<0.01	0.36	2.65	8.61	3.19	76.34	10.95	<0.01	<0.01	0.02
AU19A048.csv	846.84	13.25	<0.01	<0.01	1.73	9.91	62.46	67.52	9.12	<0.01	<0.01	<0.01
AU19A049.csv	1072.89	10.97	<0.01	0.31	5.88	10.17	8.92	98.40	17.42	<0.01	<0.01	0.01
AU19A050.csv	1232.40	8.25	<0.01	2.75	3.09	10.63	18.20	103.80	17.10	<0.01	<0.01	0.05

Table A13.1: LA-ICPMS of pyrite St Ives Gold District

Analysis	Ta (ppm)	W (ppm)	Au (ppm)	Tl (ppm)	Pb206 (ppm)	Pb207 (ppm)	Pb208 (ppm)	Bi (ppm)	Th (ppm)	U (ppm)
AU19A034.csv	<0.01	0.80	0.30	13.78			184.74	3.78	<0.01	0.03
AU19A035.csv	<0.01	0.28	0.26	25.31			154.08	3.17	<0.01	0.52
AU19A036.csv	<0.02	<0.1	0.29	21.12			130.44	1.98	<0.01	<0.02
AU19A037.csv	<0.04	0.44	<0.14	15.65			94.52	1.89	<0.01	0.10
AU19A038.csv	<0.01	<0.01	<0.01	<0.01			9.01	0.17	<0.01	<0.01
AU19A041.csv	<0.01	0.16	0.57	1.39			465.01	7.61	<0.01	<0.01
AU19A042.csv	<0.01	0.14	0.65	1.01			384.18	7.00	<0.01	0.01
AU19A043.csv	<0.01	0.10	0.70	1.05			443.53	7.63	<0.01	0.01
AU19A044.csv	<0.01	0.14	0.94	1.13			580.44	9.40	<0.01	<0.01
AU19A045.csv	<0.01	0.30	0.85	1.05			501.98	8.89	<0.01	0.01
AU19A046.csv	<0.01	1.10	0.80	1.64			443.23	6.73	<0.01	0.15
AU19A047.csv	<0.01	0.30	0.98	4.04			437.84	7.69	<0.01	0.01
AU19A048.csv	<0.01	0.28	0.61	1.43			449.02	6.77	<0.01	<0.01
AU19A049.csv	<0.01	0.31	1.10	2.43			547.04	10.03	<0.01	0.01
AU19A050.csv	<0.01	0.60	0.96	1.96			598.19	10.44	<0.01	0.07

Table A13.1: LA-ICPMS of pyrite St Ives Gold District

Depth (m)	Drill Hole	Group	Mg (ppm)	Al (ppm)	Ca (ppm)	Ti (ppm)	V (ppm)	Cr (ppm)	Mn (ppm)	Cu (ppm)	Zn (ppm)
327.33-327.55	CD1512	sedimentary pyrite		2.55			<0.04	<1.72	5.91	24.10	56.20
327.33-327.55	CD1512	sedimentary pyrite		103.21		<1.32	<0.03	<1.64	11.49	28.26	137.01
327.33-327.55	CD1512	sedimentary pyrite		<1.18		<2.22	<0.08	<1.97	9.58	22.09	463.08
327.33-327.55	CD1512	sedimentary pyrite		1018.16		<1.61	0.42	<1.44	43.25	18.30	15.83
327.33-327.55	CD1512	sedimentary pyrite		1811.94		<2.02	0.14	<2.28	54.02	41.53	17.31
327.33-327.55	CD1512	sedimentary pyrite		353.21		<2.04	<0.11	<1.79	108.80	2451.06	7106.40
327.33-327.55	CD1512	sedimentary pyrite		1224.87		18.19	1.93	<2.08	14.29	92.97	87.16
327.33-327.55	CD1512	sedimentary pyrite		332.35		6.50	0.39	<1.73	18.39	80.82	55.08
327.33-327.55	CD1512	sedimentary pyrite		122.38		<1.79	0.27	<2.18	10.65	71.50	85.40
327.33-327.55	CD1512	sedimentary pyrite		116.30		10.81	0.27	<1.54	12.99	100.75	104.37
327.33-327.55	CD1512	sedimentary pyrite		292.11		13.66	0.40	<1.63	12.11	99.64	78.02
327.33-327.55	CD1512	sedimentary pyrite		8.39		<7.55	<0.09	<3.64	27.98	158.44	132.23
327.33-327.55	CD1512	sedimentary pyrite		142.84		<4.54	<0.11	<3.98	9.12	<0.68	21.28
327.33-327.55	CD1512	sedimentary pyrite		12.04		<2.82	<0.11	<2.87	60.53	216.14	4.65
327.33-327.55	CD1512	sedimentary pyrite		158.18		<4.20	<0.17	<4.82	12.88	34.57	169.60

Table A13.1: LA-ICPMS of pyrite St Ives Gold District

Analysis	As (ppm)	Se (ppm)	Sr (ppm)	Zr (ppm)	Mo (ppm)	Ag (ppm)	Cd (ppm)	Sb (ppm)	Te (ppm)	Ba (ppm)	Gd (ppm)	Hf (ppm)
AU19A051.csv	509.54	16.17	<0.01	0.01	1.77	4.50	0.18	41.63	7.38	<0.01	<0.01	<0.01
AU19A052.csv	526.06	19.00	<0.01	0.02	0.55	6.30	0.20	43.05	5.83	<0.01	<0.01	<0.01
AU19A053.csv	532.70	11.56	<0.01	<0.01	0.13	3.69	1.23	42.43	3.29	<0.01	<0.01	<0.01
AU19A054.csv	271.20	17.03	<0.01	0.15	0.60	6.54	<0.04	25.13	3.21	<0.01	<0.01	<0.01
AU19A055.csv	419.18	18.00	<0.01	0.24	0.53	7.36	0.12	41.42	4.95	<0.01	<0.01	0.01
AU19A056.csv	324.17	15.24	<0.01	0.09	0.13	11.20	19.04	37.41	3.97	<0.01	<0.01	<0.01
AU19A057.csv	889.46	6.76	<0.01	2.33	3.15	6.52	0.31	66.05	8.18	<0.01	<0.01	0.06
AU19A058.csv	884.77	3.76	<0.01	0.21	1.39	5.17	0.17	68.50	9.03	<0.01	<0.01	<0.01
AU19A059.csv	752.12	<2.64	<0.01	0.13	3.48	7.12	0.20	52.54	7.88	<0.01	<0.01	<0.01
AU19A060.csv	859.05	3.98	<0.01	0.32	3.45	6.13	0.47	63.06	8.44	<0.01	<0.01	0.01
AU19A061.csv	919.75	<2.29	<0.01	0.25	1.94	7.48	0.32	66.84	9.09	<0.01	<0.01	0.01
AU19A062.csv	988.02	20.73	<0.01	<0.01	<0.07	3.17	0.70	4.03	<0.3	<0.01	<0.01	<0.01
AU19A063.csv	688.55	<9.03	<0.01	<0.01	0.07	<0.05	<0.06	0.82	<0.49	<0.01	<0.01	<0.01
AU19A064.csv	13.40	26.62	<0.01	<0.07	<0.03	1.57	<0.07	6.28	<0.13	<0.01	<0.01	<0.01
AU19A065.csv	553.28	31.68	<0.01	0.26	<0.03	2.00	0.61	7.06	<0.36	<0.01	<0.01	<0.01

Table A13.1: LA-ICPMS of pyrite St Ives Gold District

Analysis	Ta (ppm)	W (ppm)	Au (ppm)	Tl (ppm)	Pb206 (ppm)	Pb207 (ppm)	Pb208 (ppm)	Bi (ppm)	Th (ppm)	U (ppm)
AU19A051.csv	<0.01	0.21	0.49	1.01			378.49	4.50	<0.01	<0.01
AU19A052.csv	<0.01	0.11	0.70	0.63			769.02	4.89	<0.01	0.01
AU19A053.csv	<0.01	0.04	0.42	0.55			220.86	4.34	<0.01	<0.01
AU19A054.csv	<0.01	0.10	0.17	4.41			352.02	2.31	<0.01	0.07
AU19A055.csv	0.02	<0.02	0.17	3.60			327.70	3.73	<0.01	0.02
AU19A056.csv	<0.01	<0.01	0.25	3.67			449.79	2.91	<0.01	0.03
AU19A057.csv	<0.01	0.31	0.68	4.01			369.66	5.83	<0.01	0.04
AU19A058.csv	<0.01	0.21	0.47	1.40			383.24	6.45	<0.01	0.03
AU19A059.csv	<0.01	0.45	0.72	7.29			291.00	4.96	<0.01	0.01
AU19A060.csv	<0.01	0.22	0.48	4.31			340.11	5.34	<0.01	0.01
AU19A061.csv	<0.01	0.15	0.58	2.84			377.33	5.80	<0.01	0.01
AU19A062.csv	<0.01	<0.01	0.18	<0.03			69.24	0.53	<0.01	<0.01
AU19A063.csv	<0.01	<0.01	<0.01	<0.03			3.57	0.06	<0.01	<0.01
AU19A064.csv	<0.01	<0.02	<0.02	0.21			235.92	0.11	<0.01	<0.01
AU19A065.csv	<0.01	<0.01	0.16	0.09			37.56	0.64	<0.01	<0.01

Table A13.1: LA-ICPMS of pyrite St Ives Gold District											
Depth (m)	Drill Hole	Group	Mg (ppm)	Al (ppm)	Ca (ppm)	Ti (ppm)	V (ppm)	Cr (ppm)	Mn (ppm)	Cu (ppm)	Zn (ppm)
327.33-327.55	CD1512	sedimentary pyrite		57.22		<2.81	<0.11	<3.37	20.08	523.78	133.58
376-376.24	CD1512	Basalt pyrite	910.92	566.60	300.95	3.12	1.12	19.29	29.60	<0.13	8.55
376-376.24	CD1512	Basalt pyrite	414.64	527.20	552.17	5.36	1.38	21.82	19.35	<0.12	22.68
376-376.24	CD1512	Basalt pyrite	443.97	262.45	217.37	3.27	0.63	17.97	23.49	0.51	77.16
376-376.24	CD1512	Basalt pyrite	400.67	6301.96	4591.61	12.86	4.99	83.02	55.12	0.31	19.04
376-376.24	CD1512	Basalt pyrite	850.54	497.73	503.39	18.40	1.34	61.05	27.63	0.33	3.02
376-376.24	CD1512	Basalt pyrite	622.25	1153.44	1182.02	11.12	2.40	71.61	25.80	<0.12	18.99
376-376.24	CD1512	Basalt pyrite	79.84	23.79	<75.47	<0.65	0.13	4.49	2.04	<0.12	1.42
376-376.24	CD1512	Basalt pyrite	8574.30	6733.96	8062.10	94.82	23.82	539.76	276.72	10.69	72.48
376-376.24	CD1512	Basalt pyrite	162.74	201.52	252.44	2.32	0.20	2.02	10.73	4.37	20.46
376-376.24	CD1512	Basalt pyrite	72.81	264.12	178.37	<0.89	0.22	8.01	5.09	<0.12	12.02
265-265.24	CD8142	non ore mineralized Kapai	777.09	464.91	<61.22	27.18	1.12	109.38	4.72	2.86	1.39
265-265.24	CD8142	non ore mineralized Kapai	2368.24	402.95	1011.22	15.47	2.47	60.29	27.40	4.61	2.08
265-265.24	CD8142	non ore mineralized Kapai	260.65	40.49	132.32	89.46	0.63	11.59	2.84	1.93	0.35
265-265.24	CD8142	non ore mineralized Kapai	671.75	213.67	215.47	6.05	0.68	24.35	6.08	2.34	1.15

Table A13.1: LA-ICPMS of pyrite St Ives Gold District

Analysis	As (ppm)	Se (ppm)	Sr (ppm)	Zr (ppm)	Mo (ppm)	Ag (ppm)	Cd (ppm)	Sb (ppm)	Te (ppm)	Ba (ppm)	Gd (ppm)	Hf (ppm)
AU19A066.csv	1432.64	22.45	<0.01	<0.01	<0.07	2.73	0.28	3.84	0.85	<0.01	<0.01	<0.01
Ap15c021.csv	<0.58	39.81	0.07	0.07	<0.05	1.15	<0.14	<0.03	<0.17	<0.07	<0.03	<0.01
Ap15c022.csv	<0.52	38.14	1.67	42.35	<0.05	0.40	<0.12	0.08	<0.12	0.23	<0.06	1.08
Ap15c024.csv	<0.71	37.57	0.21	2.99	<0.03	0.55	<0.18	0.04	<0.11	0.52	0.06	0.04
Ap15c030.csv	<0.62	42.33	24.98	0.20	<0.03	1.18	<0.15	<0.02	0.77	<0.04	0.24	<0.02
Ap15c032.csv	<0.66	43.80	1.10	0.60	<0.03	0.38	<0.11	0.08	<0.20	6.63	<0.03	0.03
Ap15c033.csv	<0.59	43.88	5.25	0.15	<0.03	0.42	<0.1	0.06	<0.11	0.11	0.13	<0.01
Ap15c034.csv	<0.63	44.89	0.11	0.06	<0.04	0.07	<0.1	<0.03	0.25	<0.04	0.03	<0.01
Ap15c026.csv	<0.93	43.07	20.21	4.91	<0.05	0.36	<0.06	0.20	<0.25	0.65	<0.06	0.11
Ap15c027.csv	<0.68	44.73	1.80	0.05	<0.04	0.15	<0.09	<0.02	0.70	0.27	<0.04	<0.01
Ap15c029.csv	<0.74	40.00	0.57	<0.01	<0.05	0.12	<0.14	<0.02	0.50	0.19	0.04	<0.01
Ap15F012.csv	70.89	49.30	0.06	0.46	<0.03	0.05	<0.11	0.20	1.20	2.02	<0.03	<0.01
Ap15F013.csv	23.02	39.33	0.24	0.26	<0.03	0.04	<0.09	0.20	1.62	1.00	<0.02	<0.01
Ap15F014.csv	27.42	16.41	0.03	0.12	<0.02	0.11	<0.05	0.09	1.27	0.09	0.01	<0.01
Ap15F015.csv	39.02	18.89	0.07	0.11	<0.02	0.27	<0.04	0.09	1.37	0.22	<0.04	0.01

Table A13.1: LA-ICPMS of pyrite St Ives Gold District

Analysis	Ta (ppm)	W (ppm)	Au (ppm)	Tl (ppm)	Pb206 (ppm)	Pb207 (ppm)	Pb208 (ppm)	Bi (ppm)	Th (ppm)	U (ppm)
AU19A066.csv	<0.01	<0.01	0.18	0.10			41.49	0.37	<0.01	<0.01
Ap15c021.csv	<0.01	<0.02	<0.01	0.04	2.40	2.70	2.89	2.75	<0.01	<0.01
Ap15c022.csv	<0.01	<0.01	<0.01	0.03	0.66	0.71	0.67	1.29	0.02	<0.01
Ap15c024.csv	<0.01	<0.02	<0.01	0.04	1.14	1.71	1.33	1.37	<0.01	<0.01
Ap15c030.csv	<0.01	<0.02	<0.01	0.16	1.55	1.71	1.84	1.21	<0.01	0.02
Ap15c032.csv	<0.01	<0.02	<0.01	0.07	0.86	1.12	0.96	0.83	<0.01	<0.01
Ap15c033.csv	<0.01	<0.02	<0.01	0.07	0.66	0.71	0.68	0.51	<0.01	0.01
Ap15c034.csv	<0.01	<0.02	<0.01	<0.01	0.14	0.11	0.19	0.16	<0.01	<0.01
Ap15c026.csv	<0.01	0.05	<0.01	0.14	1.93	1.67	1.82	1.31	0.01	<0.01
Ap15c027.csv	<0.01	<0.01	<0.01	0.03	0.84	0.91	1.50	0.91	<0.01	<0.01
Ap15c029.csv	<0.01	<0.02	<0.01	<0.01	0.19	0.17	0.22	0.20	<0.01	<0.01
Ap15F012.csv	<0.01	<0.02	0.03	0.04	3.90	4.31	4.16	6.15	<0.01	0.01
Ap15F013.csv	<0.01	<0.02	0.05	0.02	2.80	2.94	2.97	6.98	<0.01	<0.01
Ap15F014.csv	<0.01	0.11	0.03	<0.01	2.25	2.50	2.39	4.47	<0.01	<0.01
Ap15F015.csv	<0.01	<0.02	0.03	0.01	3.99	4.88	4.53	5.61	<0.01	<0.01

Table A13.1: LA-ICPMS of pyrite St Ives Gold District											
Depth (m)	Drill Hole	Group	Mg (ppm)	Al (ppm)	Ca (ppm)	Ti (ppm)	V (ppm)	Cr (ppm)	Mn (ppm)	Cu (ppm)	Zn (ppm)
265-265.24	CD8142	non ore mineralized Kapai	9857.94	1665.12	3120.87	42.76	6.30	152.55	90.07	17.84	8.56
265-265.24	CD8142	non ore mineralized Kapai	1449.81	868.12	<64.18	5.72	0.99	45.69	9.56	0.87	3.49
265-265.24	CD8142	non ore mineralized Kapai	38927.16	25786.66	876.15	169.89	38.90	883.51	281.12	20.93	105.14
265-265.24	CD8142	non ore mineralized Kapai	25315.47	14354.15	1476.52	109.53	23.66	483.24	180.62	13.50	54.32
265-265.24	CD8142	non ore mineralized Kapai	8.62	5.96	<51.89	<1.05	<0.04	1.59	<0.17	0.32	0.76
265-265.24	CD8142	non ore mineralized Kapai	1.13	0.36	<61.54	0.92	<0.02	<0.47	<0.19	0.26	<0.16
265-265.24	CD8142	non ore mineralized Kapai	831.53	900.11	1000.21	24.52	4.12	48.35	35.15	3709.71	21.35
342.69-343	CD804	Magnetite altered Kapai	<0.22	<0.57	<72.02	0.98	<0.04	<1.32	<0.25	0.43	<0.2
342.69-343	CD804	Magnetite altered Kapai	0.32	23.48	<71.19	<0.71	<0.03	<0.87	<0.26	0.51	<0.22
342.69-343	CD804	Magnetite altered Kapai	<0.24	6.59	<61.92	<1.06	<0.04	<1.32	<0.33	2.28	<0.21
342.69-343	CD804	Magnetite altered Kapai	<0.36	2.53	<84.28	1.27	<0.03	<0.92	<0.22	0.38	<0.21
342.69-343	CD804	Magnetite altered Kapai	3.25	<0.75	<72.99	1.19	<0.05	<1.14	0.44	63.01	1.68
342.69-343	CD804	Magnetite altered Kapai	4.26	105.75	<77.68	<0.78	0.07	<1.11	<0.27	0.58	0.41
342.69-343	CD804	Magnetite altered Kapai	<0.25	111.33	<68.07	1.16	<0.05	<1.10	<0.27	<0.11	<0.17
342.69-343	CD804	Magnetite altered Kapai	1.55	6.78	<62.19	<1.42	0.05	<0.85	<0.26	17.82	7.92

Table A13.1: LA-ICPMS of pyrite St Ives Gold District

Analysis	As (ppm)	Se (ppm)	Sr (ppm)	Zr (ppm)	Mo (ppm)	Ag (ppm)	Cd (ppm)	Sb (ppm)	Te (ppm)	Ba (ppm)	Gd (ppm)	Hf (ppm)
Ap15F016.csv	19.62	9.78	0.45	2.26	0.53	1.31	<0.08	1.24	11.70	0.71	<0.04	0.06
Ap15F007.csv	34.11	27.24	0.04	12.07	0.30	0.07	<0.07	0.13	0.55	0.60	<0.04	0.18
Ap15F008.csv	167.43	17.32	3.38	80.46	92.28	1.53	<0.14	6.86	22.63	21.54	0.33	1.33
Ap15F009.csv	66.25	17.75	0.77	30.75	38.36	1.22	<0.09	1.67	7.78	4.28	0.16	0.46
Ap15F023.csv	66.48	119.17	0.07	<0.01	<0.02	<0.02	<0.04	<0.02	0.22	0.15	<0.04	<0.01
Ap15F024.csv	70.96	101.32	0.01	<0.01	<0.02	<0.02	<0.1	<0.02	<0.12	<0.03	<0.02	<0.01
Ap15F025.csv	67.58	71.99	6.06	0.09	<0.02	4.82	0.62	0.12	6.80	0.52	0.06	<0.01
Ap15a042.csv	<0.6	24.02	<0.01	<0.01	<0.03	0.35	<0.09	<0.02	<0.17	<0.05	<0.04	<0.01
Ap15a043.csv	<0.48	18.14	0.09	<0.01	<0.03	4.91	<0.16	1.22	1.59	<0.06	<0.03	<0.01
Ap15a044.csv	<0.93	21.40	0.02	0.46	<0.03	1.52	<0.14	0.32	<0.14	<0.03	<0.04	<0.01
Ap15a045.csv	<0.61	21.26	<0.01	<0.02	<0.03	2.60	<0.07	0.91	0.92	<0.08	<0.03	<0.01
Ap15a046.csv	<0.58	25.14	0.53	<0.01	0.06	1.46	<0.08	0.70	<0.14	<0.04	<0.03	<0.01
Ap15a052.csv	<0.62	20.96	0.30	3.55	<0.03	2.25	0.16	1.47	1.08	0.31	<0.04	0.17
Ap15a040.csv	<0.69	21.24	0.44	4.08	0.06	1.00	<0.1	0.39	0.52	<0.03	<0.03	0.10
Ap15a041.csv	<0.68	26.39	0.67	0.31	<0.04	2.60	<0.09	1.13	0.38	0.08	0.01	<0.01

Table A13.1: LA-ICPMS of pyrite St Ives Gold District

Analysis	Ta (ppm)	W (ppm)	Au (ppm)	Tl (ppm)	Pb206 (ppm)	Pb207 (ppm)	Pb208 (ppm)	Bi (ppm)	Th (ppm)	U (ppm)
Ap15F016.csv	0.01	0.25	0.15	0.04	45.04	51.62	50.27	36.68	<0.01	<0.01
Ap15F007.csv	<0.01	0.15	<0.01	<0.01	1.78	1.65	1.69	2.41	0.35	0.28
Ap15F008.csv	0.01	1.97	0.18	0.12	66.22	37.03	43.27	29.26	2.52	2.84
Ap15F009.csv	<0.01	0.69	0.14	0.08	34.67	25.90	27.23	26.96	0.80	1.06
Ap15F023.csv	<0.01	<0.01	<0.01	<0.01	0.11	0.12	0.05	0.09	<0.01	<0.01
Ap15F024.csv	<0.01	<0.01	<0.01	0.01	<0.01	0.03	0.03	<0.01	<0.01	<0.01
Ap15F025.csv	<0.01	0.05	0.33	<0.01	1.03	1.17	1.09	5.00	0.05	0.01
Ap15a042.csv	<0.01	<0.02	<0.01	<0.01	0.89	1.03	0.98	0.38	<0.01	<0.01
Ap15a043.csv	<0.01	<0.01	<0.01	0.12	14.09	16.07	15.84	3.01	<0.01	<0.01
Ap15a044.csv	0.01	<0.01	<0.01	<0.01	6.06	6.70	6.76	2.24	<0.01	<0.01
Ap15a045.csv	<0.01	<0.02	<0.01	0.05	14.45	16.33	16.26	2.87	<0.01	<0.01
Ap15a046.csv	<0.01	<0.01	0.03	0.09	11.26	12.68	12.64	1.66	<0.01	<0.01
Ap15a052.csv	<0.01	<0.01	0.02	0.30	13.28	15.47	14.61	2.77	0.01	0.05
Ap15a040.csv	<0.01	<0.02	<0.01	0.02	2.45	2.82	2.79	0.38	<0.01	0.05
Ap15a041.csv	<0.01	<0.01	<0.01	0.14	16.06	18.77	17.86	2.82	<0.01	<0.01

Table A13.1: LA-ICPMS of pyrite St Ives Gold District											
Depth (m)	Drill Hole	Group	Mg (ppm)	Al (ppm)	Ca (ppm)	Ti (ppm)	V (ppm)	Cr (ppm)	Mn (ppm)	Cu (ppm)	Zn (ppm)
342.69-343	CD804	Magnetite altered Kapai	<0.25	<0.58	<78.53	<0.43	<0.03	<1.01	<0.26	<0.11	<0.22
342.69-343	CD804	Magnetite altered Kapai	<0.23	<0.69	<68.59	<0.97	<0.05	<0.72	<0.26	<0.1	<0.19
342.69-343	CD804	Magnetite altered Kapai	<0.27	<0.74	<68.36	<0.89	<0.04	<1.05	<0.24	<0.12	<0.2
342.69-343	CD804	Magnetite altered Kapai	<0.42	<0.87	<80.14	<0.93	<0.04	<0.81	<0.25	0.27	<0.21
342.69-343	CD804	Magnetite altered Kapai	<0.20	<0.70	<67.41	<0.64	<0.06	<0.65	<0.33	<0.12	<0.17
342.69-343	CD804	Magnetite altered Kapai	<0.34	<0.61	<67.79	1.56	<0.04	<1.11	<0.26	<0.23	<0.23
342.69-343	CD804	Magnetite altered Kapai	<0.47	<0.87	<58.90	2.14	<0.03	1.87	0.45	0.55	<0.18
342.69-343	CD804	Magnetite altered Kapai	26.10	2225.69	1665.89	137.48	0.74	<1.16	1.73	0.50	0.78
342.69-343	CD804	Magnetite altered Kapai	38.43	6501.35	1448.70	9.35	1.49	5.26	1.50	1.02	2.99
342.69-343	CD804	Magnetite altered Kapai	18.00	1154.54	260.62	5.12	0.44	<0.75	0.59	0.94	0.49
342.69-343	CD804	Magnetite altered Kapai	15.58	1193.26	185.12	2.94	0.40	<0.75	0.56	0.61	19.41
342.69-343	CD804	Magnetite altered Kapai	51.64	1684.20	274.49	195.43	0.61	2.08	3.37	1.00	8.71
342.69-343	CD804	Magnetite altered Kapai	194.68	4271.92	450.25	22.83	4.38	7.44	3.52	<0.14	3.43
342.69-343	CD804	Magnetite altered Kapai	9.03	667.17	199.24	1.54	0.12	<1.07	<0.23	<0.11	<0.19
342.69-343	CD804	Magnetite altered Kapai	24.41	1114.97	366.94	<0.61	0.18	<0.99	1.15	<0.14	1.71

Table A13.1: LA-ICPMS of pyrite St Ives Gold District

Analysis	As (ppm)	Se (ppm)	Sr (ppm)	Zr (ppm)	Mo (ppm)	Ag (ppm)	Cd (ppm)	Sb (ppm)	Te (ppm)	Ba (ppm)	Gd (ppm)	Hf (ppm)
Ap15a033.csv	<0.56	20.56	<0.01	<0.02	<0.05	0.34	<0.17	<0.02	<0.12	<0.02	<0.07	0.01
Ap15a034.csv	<0.54	21.15	<0.01	<0.01	<0.02	0.32	0.07	<0.03	<0.16	<0.04	<0.03	<0.01
Ap15a035.csv	<0.52	19.96	<0.01	<0.01	<0.03	0.42	<0.16	<0.02	<0.16	<0.04	0.02	<0.01
Ap15a036.csv	<0.79	23.54	<0.01	<0.02	<0.03	1.12	<0.08	<0.03	<0.15	0.04	0.01	<0.01
Ap15a037.csv	<0.63	21.77	<0.01	0.01	<0.02	1.06	<0.11	<0.03	<0.15	<0.08	<0.03	<0.02
Ap15a038.csv	<0.51	20.16	<0.01	<0.01	<0.06	1.16	<0.1	0.15	<0.17	<0.04	<0.04	0.01
Ap15a039.csv	<0.64	22.13	<0.01	<0.01	1.39	1.77	<0.11	0.42	0.57	<0.05	<0.03	<0.01
Ap15a053.csv	<0.54	22.78	11.11	19.31	0.66	8.23	<0.13	4.62	5.99	1.78	0.59	0.51
Ap15a054.csv	<0.76	19.87	22.25	11.07	<0.02	4.44	<0.12	4.00	2.14	2.81	<0.03	0.28
Ap15a055.csv	<0.59	21.59	4.41	0.40	<0.02	2.51	0.11	1.43	1.45	1.34	<0.03	0.01
Ap15a056.csv	<0.65	21.52	4.02	0.49	0.03	12.23	<0.12	5.64	7.35	0.69	0.24	<0.01
Ap15a057.csv	<0.65	24.10	4.89	0.18	0.04	9.85	<0.08	3.56	5.86	1.10	<0.03	<0.02
Ap15a058.csv	<0.76	23.70	7.00	3.06	0.05	24.75	<0.07	3.58	14.52	24.21	0.03	0.10
Ap15a059.csv	<0.44	21.71	1.96	0.01	<0.05	0.82	<0.05	0.74	0.36	0.32	<0.05	<0.01
Ap15a060.csv	<0.48	22.32	3.68	0.14	<0.04	2.26	<0.07	2.06	0.90	0.15	0.01	<0.01

Table A13.1: LA-ICPMS of pyrite St Ives Gold District

Analysis	Ta (ppm)	W (ppm)	Au (ppm)	Tl (ppm)	Pb206 (ppm)	Pb207 (ppm)	Pb208 (ppm)	Bi (ppm)	Th (ppm)	U (ppm)
Ap15a033.csv	<0.01	<0.01	<0.01	<0.01	0.68	0.76	0.76	0.26	<0.01	<0.01
Ap15a034.csv	<0.01	<0.01	<0.01	<0.01	0.18	0.20	0.17	0.07	<0.01	<0.01
Ap15a035.csv	<0.01	<0.01	<0.01	<0.01	0.75	0.77	0.74	0.32	<0.01	<0.01
Ap15a036.csv	<0.01	<0.02	<0.01	<0.01	2.69	3.13	3.10	1.18	<0.01	<0.01
Ap15a037.csv	<0.01	<0.01	<0.01	<0.01	2.55	2.96	2.88	0.99	<0.01	<0.01
Ap15a038.csv	<0.01	<0.01	<0.01	<0.01	4.08	4.55	4.52	1.62	<0.01	<0.01
Ap15a039.csv	<0.01	<0.01	<0.01	0.02	6.79	7.80	7.56	1.26	<0.01	<0.01
Ap15a053.csv	0.03	0.23	<0.01	0.46	29.30	32.08	30.78	3.36	0.23	0.28
Ap15a054.csv	<0.01	<0.02	<0.01	0.82	28.32	30.42	29.69	4.85	0.06	0.10
Ap15a055.csv	<0.01	<0.01	<0.01	0.25	10.07	11.58	11.10	1.86	0.01	<0.01
Ap15a056.csv	<0.01	<0.01	<0.01	0.98	39.64	45.13	44.10	5.68	0.57	0.03
Ap15a057.csv	0.02	0.36	0.03	0.68	29.00	32.91	32.84	5.26	0.03	<0.01
Ap15a058.csv	<0.01	0.16	<0.01	0.95	50.08	54.83	53.83	6.21	0.01	0.04
Ap15a059.csv	0.01	<0.01	<0.01	0.12	3.57	4.01	3.96	0.52	<0.01	<0.01
Ap15a060.csv	<0.01	<0.01	<0.01	0.34	14.82	16.76	16.21	3.33	0.02	<0.01

Table A13.1: LA-ICPMS of pyrite St Ives Gold District											
Depth (m)	Drill Hole	Group	Mg (ppm)	Al (ppm)	Ca (ppm)	Ti (ppm)	V (ppm)	Cr (ppm)	Mn (ppm)	Cu (ppm)	Zn (ppm)
342.69-343	CD804	Magnetite altered Kapai	20.91	776.22	165.87	5.34	0.36	<1.25	<0.24	<0.13	<0.2
342.69-343	CD804	Magnetite altered Kapai	2.11	208.77	<67.54	1.23	<0.04	<1.27	<0.25	0.30	<0.18
265-265.24	CD8142	non ore mineralized Kapai	176.74	566.87	<56.11	68.02	0.12	<0.99	8.80	2.93	1453.62
265-265.24	CD8142	non ore mineralized Kapai	248.94	3288.99	<84.20	783.24	0.88	<2.19	3.44	24.78	25.70
265-265.24	CD8142	non ore mineralized Kapai	160.76	5859.46	384.17	349.44	1.04	<1.47	4.15	19.52	12.38
265-265.24	CD8142	non ore mineralized Kapai	514.67	4892.71	129.38	446.53	2.29	6.22	9.24	12.20	536.02
265-265.24	CD8142	non ore mineralized Kapai	22.06	227.09	<90.36	624.21	0.16	<3.76	<0.67	7.77	2.03
265-265.24	CD8142	non ore mineralized Kapai	9.79	88.56	<25.80	0.98	0.01	<0.73	0.36	2168.72	9984.51
265-265.24	CD8142	non ore mineralized Kapai	19.80	266.15	<28.58	7.22	0.12	1.42	1.69	778.39	508.55
265-265.24	CD8142	non ore mineralized Kapai	330.16	1593.09	744.74	10.19	0.27	3.90	24.00	2774.87	2329.63
265-265.24	CD8142	non ore mineralized Kapai	17.56	81.55	<68.19	<0.87	<0.02	<2.27	6.34	3.70	2.18
265-265.24	CD8142	non ore mineralized Kapai	205.51	49.52	12760.56	1.56	<0.01	<0.79	695.31	342.54	208.35
265-265.24	CD8142	non ore mineralized Kapai	2.87	36.18	<26.36	1.14	<0.01	<0.67	1.25	552.77	533.60
265-265.24	CD8142	non ore mineralized Kapai	20.64	479.86	<24.13	41.24	0.26	4.01	1.26	56.98	35.62
265-265.24	CD8142	non ore mineralized Kapai	7.63	95.35	<28.37	2.95	0.09	<1.06	<0.12	213.25	12.03

Table A13.1: LA-ICPMS of pyrite St Ives Gold District

Analysis	As (ppm)	Se (ppm)	Sr (ppm)	Zr (ppm)	Mo (ppm)	Ag (ppm)	Cd (ppm)	Sb (ppm)	Te (ppm)	Ba (ppm)	Gd (ppm)	Hf (ppm)
Ap15a061.csv	<0.5	22.50	1.74	<0.01	<0.03	0.85	<0.11	0.85	0.51	1.61	<0.03	<0.01
Ap15a062.csv	<0.58	21.73	0.65	0.34	<0.02	0.90	<0.09	1.15	0.62	0.10	<0.04	<0.01
JA14B03.csv	3248.27	49.15	<0.01	10.73	<0.02	1.13	2.38	5.65	4.11	0.16	<0.01	0.31
JA14B04.csv	652.35	46.10	<0.01	12.47	0.10	1.30	<0.14	7.38	5.60	21.56	<0.01	0.26
JA14B05.csv	1199.78	37.52	<0.01	105.82	0.49	1.00	<0.16	25.60	24.42	21.74	<0.01	2.79
JA14B08.csv	1394.36	47.71	<0.01	66.44	0.29	1.17	0.57	11.71	25.21	21.28	<0.01	1.67
JA14B09.csv	1669.59	39.70	<0.01	57.85	<0.04	0.37	<0.32	3.40	8.30	1.62	<0.01	1.49
JA14B10.csv	344.01	70.43	<0.01	0.05	0.04	16.42	26.94	9.11	34.20	0.03	<0.01	<0.01
JA14B11.csv	981.26	66.07	<0.01	7.37	0.06	7.30	1.13	9.99	17.82	0.70	<0.01	0.08
JA14B13.csv	413.22	70.61	<0.01	0.02	0.02	31.41	6.67	13.42	15.37	2.44	<0.01	<0.01
JA14B14.csv	609.05	33.17	<0.01	0.09	<0.02	1.71	<0.18	2.38	9.48	0.24	<0.01	<0.01
JA14B16.csv	1229.53	34.12	<0.01	<0.01	0.13	4.90	1.03	2.76	16.18	0.42	<0.01	<0.01
JA14B18.csv	930.16	64.67	<0.01	<0.01	0.15	3.91	1.09	60.77	5.30	0.10	<0.01	<0.01
JA14B19.csv	1693.21	59.75	<0.01	0.61	<0.02	5.74	0.15	2.93	9.84	6.19	<0.01	0.02
JA14B20.csv	666.52	74.00	<0.01	0.18	1.08	1.59	<0.05	3.59	3.96	0.55	<0.01	<0.01

Table A13.1: LA-ICPMS of pyrite St Ives Gold District

Analysis	Ta (ppm)	W (ppm)	Au (ppm)	Tl (ppm)	Pb206 (ppm)	Pb207 (ppm)	Pb208 (ppm)	Bi (ppm)	Th (ppm)	U (ppm)
Ap15a061.csv	<0.01	0.03	<0.01	0.12	4.88	5.39	5.92	0.89	<0.01	<0.01
Ap15a062.csv	<0.01	<0.01	<0.01	0.14	5.83	6.95	6.53	1.07	0.01	0.01
JA14B03.csv	0.03	0.44	0.10	<0.01			8.35	9.20	<0.01	0.56
JA14B04.csv	0.28	1.67	0.28	2.01			37.51	10.20	<0.01	0.58
JA14B05.csv	0.09	1.42	0.85	0.67			104.12	42.58	<0.01	4.95
JA14B08.csv	0.22	2.42	0.92	0.73			59.27	36.03	<0.01	2.62
JA14B09.csv	0.21	2.81	0.48	<0.01			13.74	10.24	<0.01	2.02
JA14B10.csv	<0.01	0.02	2.12	0.02			64.39	37.04	<0.01	<0.01
JA14B11.csv	<0.01	0.04	1.14	0.03			74.09	31.43	<0.01	0.20
JA14B13.csv	<0.01	0.05	3.81	0.09			81.97	34.15	<0.01	<0.01
JA14B14.csv	0.01	<0.06	0.03	0.47			22.61	8.97	<0.01	0.11
JA14B16.csv	<0.01	<0.01	0.42	0.01			57.34	20.34	<0.01	<0.01
JA14B18.csv	<0.01	<0.01	0.55	0.12			249.08	24.29	<0.01	<0.01
JA14B19.csv	<0.01	0.28	1.14	0.04			209.23	20.77	<0.01	0.03
JA14B20.csv	<0.01	<0.01	0.30	0.02			23.34	6.84	<0.01	0.01

Table A13.1: LA-ICPMS of pyrite St Ives Gold District											
Depth (m)	Drill Hole	Group	Mg (ppm)	Al (ppm)	Ca (ppm)	Ti (ppm)	V (ppm)	Cr (ppm)	Mn (ppm)	Cu (ppm)	Zn (ppm)
265-265.24	CD8142	non ore mineralized Kapai	0.03	<0.28	<24.22	0.87	<0.01	<0.90	<0.17	15.96	0.92
265-265.24	CD8142	non ore mineralized Kapai	48.26	472.36	405.21	2.03	0.04	3.26	6.25	638.21	183.36
265-265.24	CD8142	non ore mineralized Kapai	1.62	2.72	<30.86	1.12	<0.01	<0.92	1.61	0.37	<0.23
265-265.24	CD8142	non ore mineralized Kapai	418.09	225.45	<27.24	3.55	0.05	1.86	1.71	3149.43	210.55
265-265.24	CD8142	non ore mineralized Kapai	16.37	187.62	250.28	2.63	0.09	<0.67	5.88	270.22	52.76
265-265.24	CD8142	non ore mineralized Kapai	2.68	73.45	<72.49	<0.44	0.02	<1.92	2.10	0.92	<0.42
265-265.24	CD8142	non ore mineralized Kapai	190.81	745.21	434.48	18.41	0.36	2.83	14.55	96.09	243.79
265-265.24	CD8142	non ore mineralized Kapai	484.05	6193.88	657.93	542.01	1.23	3.76	14.04	54.06	553.03
265-265.24	CD8142	non ore mineralized Kapai	30.38	224.69	<56.34	14.31	0.09	<1.5	1.15	7.07	2.09
265-265.24	CD8142	non ore mineralized Kapai	160.89	2446.22	<65.52	68.14	0.51	<2.89	2.97	7.94	7.04
265-265.24	CD8142	non ore mineralized Kapai	385.95	6785.23	330.38	480.04	1.44	8.36	6.83	21.66	628.61
265-265.24	CD8142	non ore mineralized Kapai	199.08	2138.29	<59.96	1255.83	0.81	6.88	12.19	7.76	1.73
265-265.24	CD8142	non ore mineralized Kapai	714.79	11536.25	949.10	960.40	2.46	7.08	24.79	30.39	4285.34
285.1-285.34	CD13829	sedimentary pyrite	38.56	818.63	<20.01	14.75	0.67	2.54	51.32	98.04	824.99
285.1-285.34	CD13829	sedimentary pyrite	22.82	165.40	<33.59	9.44	0.17	<0.83	51.50	1343.87	279.97

Table A13.1: LA-ICPMS of pyrite St Ives Gold District

Analysis	As (ppm)	Se (ppm)	Sr (ppm)	Zr (ppm)	Mo (ppm)	Ag (ppm)	Cd (ppm)	Sb (ppm)	Te (ppm)	Ba (ppm)	Gd (ppm)	Hf (ppm)
JA14B21.csv	530.72	58.38	<0.01	<0.01	0.12	0.12	<0.04	0.26	0.84	<0.02	<0.01	<0.01
JA14B27.csv	963.69	71.85	<0.01	0.06	0.09	28.21	0.83	8.42	22.37	1.68	<0.01	<0.01
JA14B28.csv	1184.90	14.29	<0.01	<0.01	<0.01	0.48	<0.11	0.55	1.00	<0.04	<0.01	<0.01
JA14B29.csv	355.58	73.04	<0.01	0.01	<0.01	6.76	0.84	1.60	4.88	2.35	<0.01	<0.01
JA14B30.csv	324.00	33.16	<0.01	0.99	0.14	1.81	<0.1	2.50	12.64	0.68	<0.01	<0.01
JA14B31.csv	837.25	31.00	<0.01	0.39	0.04	1.21	<0.1	1.91	3.72	0.22	<0.01	<0.01
JA14B35.csv	564.36	64.12	<0.01	0.22	0.44	11.87	0.59	5.71	17.88	6.73	<0.01	<0.01
JA14B36.csv	766.79	44.48	<0.01	33.24	1.45	2.28	1.09	34.89	44.48	27.20	<0.01	0.79
JA14B37.csv	2610.55	42.76	<0.01	4.32	<0.02	1.72	<0.21	1.52	3.87	1.23	<0.01	0.04
JA14B38.csv	1349.11	53.09	<0.01	0.82	<0.02	0.40	<0.23	6.58	14.11	18.20	<0.01	0.04
JA14B39.csv	1064.39	41.97	<0.01	78.18	0.28	2.28	1.71	35.46	49.36	30.22	<0.01	1.54
JA14B40.csv	3144.07	48.14	<0.01	65.01	<0.03	1.37	0.10	13.78	20.76	11.19	<0.01	1.58
JA14B41.csv	1027.77	56.21	<0.01	98.15	0.44	3.39	10.08	74.08	75.59	52.94	<0.01	2.39
JA14B44.csv	1011.62	10.42	<0.01	0.74	4.14	9.97	1.76	105.47	16.95	11.76	<0.01	0.01
JA14B45.csv	1365.42	32.17	<0.01	0.24	4.32	12.00	0.84	138.89	22.96	5.41	<0.01	<0.01

Table A13.1: LA-ICPMS of pyrite St Ives Gold District

Analysis	Ta (ppm)	W (ppm)	Au (ppm)	Tl (ppm)	Pb206 (ppm)	Pb207 (ppm)	Pb208 (ppm)	Bi (ppm)	Th (ppm)	U (ppm)
JA14B21.csv	<0.01	0.02	0.20	<0.01			1.92	1.06	<0.01	<0.01
JA14B27.csv	<0.01	0.04	1.51	0.07			339.81	56.18	<0.01	<0.01
JA14B28.csv	<0.01	<0.01	0.01	0.02			2.39	4.58	<0.01	<0.01
JA14B29.csv	<0.01	<0.01	1.21	0.16			17.00	4.54	<0.01	<0.01
JA14B30.csv	<0.01	<0.02	0.72	0.01			29.29	18.29	<0.01	0.02
JA14B31.csv	<0.01	<0.03	0.02	0.81			11.05	9.14	<0.01	<0.01
JA14B35.csv	<0.01	0.09	1.26	0.08			470.53	45.57	<0.01	<0.01
JA14B36.csv	0.22	1.43	0.65	1.02			154.64	62.58	<0.01	1.78
JA14B37.csv	<0.01	0.09	0.15	0.11			12.24	9.53	<0.01	0.11
JA14B38.csv	0.02	0.57	0.56	0.53			33.48	20.39	<0.01	0.04
JA14B39.csv	0.12	1.86	0.93	0.76			144.58	73.50	<0.01	2.84
JA14B40.csv	0.53	4.94	0.52	0.35			49.26	28.55	<0.01	2.23
JA14B41.csv	0.21	1.19	1.16	1.36			269.61	129.95	<0.01	4.27
JA14B44.csv	<0.01	0.39	0.82	1.49			503.45	12.72	<0.01	0.01
JA14B45.csv	<0.01	0.23	0.99	3.71			2863.53	17.63	<0.01	<0.01

Table A13.1: LA-ICPMS of pyrite St Ives Gold District											
Depth (m)	Drill Hole	Group	Mg (ppm)	Al (ppm)	Ca (ppm)	Ti (ppm)	V (ppm)	Cr (ppm)	Mn (ppm)	Cu (ppm)	Zn (ppm)
285.1-285.34	CD13829	sedimentary pyrite	53.98	272.49	<28.58	4.15	0.41	<0.72	39.06	51.09	528.53
285.1-285.34	CD13829	sedimentary pyrite	2234.80	50514.86	4778.52	432.20	27.79	79.39	138.58	197.79	359.23
285.1-285.34	CD13829	sedimentary pyrite	1252.08	23462.60	763.10	326.30	18.86	87.84	55.87	77.73	13.65
285.1-285.34	CD13829	sedimentary pyrite	1029.48	22799.96	1696.98	243.47	13.68	63.14	54.71	100.86	71.81
285.1-285.34	CD13829	sedimentary pyrite	829.30	17804.06	1778.10	149.48	9.66	40.14	54.22	101.55	101.77
285.1-285.34	CD13829	sedimentary pyrite	2095.37	38030.41	4157.25	371.40	21.30	73.19	150.95	89.49	1138.02
285.1-285.34	CD13829	sedimentary pyrite	1212.97	21189.37	<208.26	226.96	17.29	73.82	56.27	82.63	16.96
285.1-285.34	CD13829	sedimentary pyrite	37.24	275.76	99.65	3.07	0.12	3.36	36.22	91.56	54.73
285.1-285.34	CD13829	sedimentary pyrite	23.57	163.91	<22.81	6.85	0.13	2.07	27.95	99.22	52.47
285.1-285.34	CD13829	sedimentary pyrite	123.29	353.70	<31.01	6.54	0.41	<0.91	23.40	84.96	51.01
285.1-285.34	CD13829	sedimentary pyrite	58.22	511.09	48.82	3.56	0.18	<0.88	53.45	101.25	131.09
285.1-285.34	CD13829	sedimentary pyrite	17.08	99.88	153.54	8.97	0.16	<1.54	29.16	123.24	12.74
285.1-285.34	CD13829	sedimentary pyrite	2678.28	44574.80	<336.29	616.00	33.99	125.78	133.34	67.90	131.97
285.1-285.34	CD13829	sedimentary pyrite	2419.67	37023.98	<281.18	519.56	27.36	115.27	115.56	65.07	173.71
285.1-285.34	CD13829	sedimentary pyrite	1321.70	20942.00	<212.47	266.90	14.39	58.89	72.70	59.46	97.01

Table A13.1: LA-ICPMS of pyrite St Ives Gold District

Analysis	As (ppm)	Se (ppm)	Sr (ppm)	Zr (ppm)	Mo (ppm)	Ag (ppm)	Cd (ppm)	Sb (ppm)	Te (ppm)	Ba (ppm)	Gd (ppm)	Hf (ppm)
JA14B48.csv	855.08	14.78	<0.01	0.04	6.90	7.37	1.34	81.00	12.08	4.09	<0.01	<0.01
JA14B49.csv	949.87	98.41	<0.01	39.70	2.10	3.74	<0.71	76.62	9.45	292.59	<0.01	1.07
JA14B50.csv	804.19	11.27	<0.01	6.26	2.52	3.45	<0.32	51.13	8.52	185.43	<0.01	0.32
JA14B51.csv	1044.83	17.01	<0.01	12.80	2.80	3.39	0.94	64.24	8.38	160.80	<0.01	0.33
JA14B52.csv	817.93	11.81	<0.01	11.26	2.30	3.16	<0.4	40.58	8.22	120.96	<0.01	0.21
JA14B53.csv	836.63	9.24	<0.01	39.29	2.94	3.54	2.81	72.02	8.44	258.94	<0.01	0.99
JA14B54.csv	796.04	6.13	<0.01	21.92	2.05	3.47	<0.76	53.51	7.53	171.64	<0.01	0.48
JA14B57.csv	1029.92	5.92	<0.01	0.05	2.22	8.70	<0.14	107.33	15.39	5.44	<0.01	<0.01
JA14B58.csv	987.28	3.76	<0.01	0.10	2.44	9.66	0.22	113.35	16.14	5.90	<0.01	<0.01
JA14B59.csv	896.23	3.96	<0.01	0.32	3.41	8.59	0.22	92.88	13.48	7.62	<0.01	0.02
JA14B60.csv	1028.91	7.53	<0.01	0.61	1.28	10.68	0.33	116.26	16.55	5.99	<0.01	0.01
JA14B64.csv	1272.71	7.89	<0.01	0.49	3.17	10.77	<0.11	140.89	20.74	6.92	<0.01	0.02
JA14B65.csv	804.23	17.81	<0.01	16.75	99.04	3.13	<0.94	62.73	8.39	507.16	<0.01	0.50
JA14B66.csv	817.26	9.44	<0.01	38.53	1.75	3.40	<0.41	62.26	9.70	399.84	<0.01	0.90
JA14B67.csv	768.53	13.56	<0.01	7.07	1.89	3.34	<0.73	57.14	8.03	181.57	<0.01	0.17

Table A13.1: LA-ICPMS of pyrite St Ives Gold District

Analysis	Ta (ppm)	W (ppm)	Au (ppm)	Tl (ppm)	Pb206 (ppm)	Pb207 (ppm)	Pb208 (ppm)	Bi (ppm)	Th (ppm)	U (ppm)
JA14B48.csv	<0.01	0.55	0.67	0.60			758.96	10.12	<0.01	<0.01
JA14B49.csv	<0.02	1.40	0.23	50.38			184.86	10.85	<0.01	0.58
JA14B50.csv	<0.01	0.59	0.29	18.17			153.93	8.55	<0.01	<0.05
JA14B51.csv	<0.02	0.55	0.27	19.71			192.39	10.94	<0.01	0.20
JA14B52.csv	<0.01	0.69	0.38	16.56			143.99	7.58	<0.01	0.12
JA14B53.csv	<0.05	0.80	0.28	14.16			183.71	8.79	<0.01	0.32
JA14B54.csv	<0.02	0.47	0.31	16.94			154.01	8.59	<0.01	0.22
JA14B57.csv	<0.01	0.19	0.69	2.95			386.35	10.71	<0.01	<0.01
JA14B58.csv	<0.01	0.20	0.78	3.65			395.63	11.40	<0.01	<0.01
JA14B59.csv	<0.01	0.26	0.77	4.03			335.53	10.02	<0.01	0.01
JA14B60.csv	<0.01	0.38	0.76	3.09			497.43	12.50	<0.01	0.02
JA14B64.csv	<0.01	0.26	0.93	6.49			515.63	14.20	<0.01	0.02
JA14B65.csv	<0.02	51.47	0.22	32.79			195.63	6.77	<0.01	0.26
JA14B66.csv	<0.02	1.73	0.19	19.58			185.24	7.09	<0.01	0.60
JA14B67.csv	<0.01	0.66	0.26	17.05			162.71	6.89	<0.01	0.10

Table A13.1: LA-ICPMS of pyrite St Ives Gold District

Depth (m)	Drill Hole	Group	Mg (ppm)	Al (ppm)	Ca (ppm)	Ti (ppm)	V (ppm)	Cr (ppm)	Mn (ppm)	Cu (ppm)	Zn (ppm)
285.1-285.34	CD13829	sedimentary pyrite	673.74	12257.78	637.03	127.11	7.24	36.67	54.52	105.82	51.41
285.1-285.34	CD13829	sedimentary pyrite	1230.98	27976.63	2736.18	239.10	13.76	36.46	86.60	112.09	690.51
285.1-285.34	CD13829	sedimentary pyrite	2660.22	41658.76	1396.74	502.46	25.57	111.14	124.77	107.19	256.74
285.1-285.34	CD13829	sedimentary pyrite	630.26	11304.36	<138.54	122.31	7.88	20.68	33.56	91.66	48.51
285.1-285.34	CD13829	sedimentary pyrite	195.90	7395.10	2436.49	51.40	0.51	<6.68	514.77	760.61	10034.65
285.1-285.34	CD13829	sedimentary pyrite	1835.19	46546.83	6388.09	372.22	21.19	67.69	138.12	126.76	2827.08
285.1-285.34	CD13829	sedimentary pyrite	1070.45	21526.02	1846.70	209.85	10.60	35.28	79.42	74.63	44.66
285.1-285.34	CD13829	sedimentary pyrite	1815.70	36523.61	4774.34	282.14	14.62	36.00	155.02	86.42	3176.65
285.1-285.34	CD13829	sedimentary pyrite	2086.82	29390.17	859.88	375.86	22.97	47.69	132.20	74.53	451.76
285.1-285.34	CD13829	sedimentary pyrite	1816.02	32353.08	<461.69	1241.89	20.60	65.08	140.80	107.11	1445.08
285.1-285.34	CD13829	sedimentary pyrite	1228.57	20399.00	2058.04	221.83	10.74	64.01	69.57	66.59	771.67
285.1-285.34	CD13829	sedimentary pyrite	886.26	14858.72	<533.85	211.12	10.49	62.37	70.04	95.63	248.69
285.1-285.34	CD13829	sedimentary pyrite	495.28	10332.02	<388.67	115.56	6.52	<14.07	33.52	81.11	18.25
285.1-285.34	CD13829	sedimentary pyrite	411.42	8030.21	<382.28	86.08	5.26	<11.89	22.15	67.21	11.05
285.1-285.34	CD13829	sedimentary pyrite	390.56	9261.69	1634.17	72.09	4.12	<17.37	34.25	121.37	17.38

Table A13.1: LA-ICPMS of pyrite St Ives Gold District

Analysis	As (ppm)	Se (ppm)	Sr (ppm)	Zr (ppm)	Mo (ppm)	Ag (ppm)	Cd (ppm)	Sb (ppm)	Te (ppm)	Ba (ppm)	Gd (ppm)	Hf (ppm)
JA14B68.csv	675.71	6.98	<0.01	1.32	1.92	2.80	<0.4	59.55	8.07	104.93	<0.01	<0.03
JA14B69.csv	793.23	14.58	<0.01	44.02	2.94	3.52	1.74	58.38	9.31	180.95	<0.01	1.07
JA14B70.csv	950.11	18.46	<0.01	179.20	3.47	3.68	<1.05	66.15	10.92	349.82	<0.01	3.75
JA14B71.csv	867.55	38.73	<0.01	16.03	2.45	3.46	<0.34	51.70	7.02	100.62	<0.01	0.20
JA14B74.csv	2047.32	290.73	<0.01	1.78	9.64	23.90	27.21	104.90	20.91	9.23	<0.01	0.05
JA14B75.csv	780.03	22.04	<0.01	70.48	2.46	4.63	5.94	74.28	8.26	283.09	<0.01	2.08
JA14B76.csv	738.23	24.21	<0.01	6.23	2.07	3.24	0.95	62.65	7.72	147.60	<0.01	0.15
JA14B77.csv	652.80	10.91	<0.01	17.29	1.19	3.82	7.57	67.00	8.09	190.74	<0.01	0.41
JA14B78.csv	711.26	13.04	<0.01	15.42	1.83	3.45	<0.74	61.91	8.46	268.61	<0.01	0.30
JA14B79.csv	629.90	13.52	<0.01	22.17	2.01	3.27	<1.15	54.39	7.07	249.00	<0.01	0.38
JA14B80.csv	603.22	<6.32	<0.01	7.39	1.82	1.73	<0.98	46.83	5.97	149.76	<0.01	<0.1
JA14B81.csv	661.36	<6	<0.01	5.01	1.62	2.49	<1.11	52.87	7.18	147.96	<0.01	0.25
JA14B82.csv	790.42	28.81	<0.01	1.00	1.75	3.85	1.69	57.74	7.40	94.49	<0.01	<0.09
JA14B83.csv	631.66	<3.89	<0.01	0.74	1.85	3.56	<0.57	48.05	6.41	71.74	<0.01	<0.08
JA14B84.csv	697.36	12.35	<0.01	2.06	1.22	3.94	<0.81	42.49	7.55	57.67	<0.01	<0.07

Table A13.1: LA-ICPMS of pyrite St Ives Gold District										
Analysis	Ta (ppm)	W (ppm)	Au (ppm)	Tl (ppm)	Pb206 (ppm)	Pb207 (ppm)	Pb208 (ppm)	Bi (ppm)	Th (ppm)	U (ppm)
JA14B68.csv	<0.02	0.49	0.19	18.02			198.26	5.55	<0.01	0.04
JA14B69.csv	<0.02	0.60	0.26	14.83			162.87	6.91	<0.01	0.60
JA14B70.csv	<0.03	1.52	0.21	18.99			201.07	7.12	<0.01	1.95
JA14B71.csv	<0.01	0.33	0.25	30.18			164.35	6.34	<0.01	0.13
JA14B74.csv	<0.01	0.32	1.26	69.57			3915.36	17.56	<0.01	0.37
JA14B75.csv	0.05	1.43	0.21	24.81			222.49	10.14	<0.01	0.90
JA14B76.csv	<0.02	0.71	0.31	23.21			213.09	5.83	<0.01	0.05
JA14B77.csv	<0.04	0.62	0.18	21.63			173.08	5.76	<0.01	0.31
JA14B78.csv	<0.02	1.02	0.28	21.10			190.17	7.12	<0.01	0.38
JA14B79.csv	0.36	1.10	0.10	15.78			184.28	6.84	<0.01	0.22
JA14B80.csv	<0.03	0.74	0.12	22.32			159.54	4.54	<0.01	0.32
JA14B81.csv	<0.03	0.39	0.14	20.71			215.43	6.56	<0.01	<0.07
JA14B82.csv	<0.03	<0.21	0.72	25.29			177.81	6.64	<0.01	<0.04
JA14B83.csv	<0.02	<0.19	0.41	18.91			219.92	5.69	<0.01	0.05
JA14B84.csv	<0.04	0.36	0.35	12.62			168.37	5.09	<0.01	0.09

Table A13.1: LA-ICPMS of pyrite St Ives Gold District											
Depth (m)	Drill Hole	Group	Mg (ppm)	Al (ppm)	Ca (ppm)	Ti (ppm)	V (ppm)	Cr (ppm)	Mn (ppm)	Cu (ppm)	Zn (ppm)
285.1-285.34	CD13829	sedimentary pyrite	483.91	8173.39	<414.23	96.26	4.76	26.64	31.86	75.47	321.18
285.1-285.34	CD13829	sedimentary pyrite	2148.24	39926.34	8576.28	359.85	38.04	80.64	155.89	27.49	497.15
285.1-285.34	CD13829	sedimentary pyrite	2931.75	56068.01	2236.65	566.97	57.90	116.18	132.89	76.17	142.76
285.1-285.34	CD13829	sedimentary pyrite	3787.98	51843.44	1504.43	512.94	62.19	120.88	118.35	69.18	638.34
285.1-285.34	CD13829	sedimentary pyrite	5607.11	75688.61	2317.74	834.04	87.60	167.34	340.19	100.31	1674.02
285.1-285.34	CD13829	sedimentary pyrite	3260.02	62467.64	2456.50	641.29	70.32	135.51	128.76	87.52	797.12
285.1-285.34	CD13829	sedimentary pyrite	2521.70	42921.12	1259.99	438.34	50.02	98.48	128.27	214.51	2028.20
285.1-285.34	CD13829	sedimentary pyrite	2320.03	42490.54	1006.62	419.62	50.42	109.80	85.47	76.05	474.54
285.1-285.34	CD13829	sedimentary pyrite	3209.63	65184.80	3483.18	613.25	63.39	124.30	148.73	84.24	485.57
285.1-285.34	CD13829	sedimentary pyrite	1281.57	27056.99	1778.84	213.78	22.45	42.44	76.71	85.75	363.87
285.1-285.34	CD13829	sedimentary pyrite	1784.97	29578.01	<107.15	330.62	37.67	72.15	77.39	86.94	2866.66
285.1-285.34	CD13829	sedimentary pyrite	1936.65	32598.88	370.97	373.35	41.72	81.38	86.94	69.97	637.62
285.1-285.34	CD13829	sedimentary pyrite	2729.02	44795.89	<821.11	566.09	40.27	114.91	163.31	71.30	118.21
285.1-285.34	CD13829	sedimentary pyrite	851.75	10402.70	<582.85	171.12	16.76	36.14	123.01	67.00	19.74
285.1-285.34	CD13829	sedimentary pyrite	1723.35	31432.75	<600.73	425.11	29.42	59.37	135.31	63.44	34.56

Table A13.1: LA-ICPMS of pyrite St Ives Gold District

Analysis	As (ppm)	Se (ppm)	Sr (ppm)	Zr (ppm)	Mo (ppm)	Ag (ppm)	Cd (ppm)	Sb (ppm)	Te (ppm)	Ba (ppm)	Gd (ppm)	Hf (ppm)
JA14B85.csv	634.79	7.82	<0.01	1.91	1.18	3.55	<0.85	50.97	7.26	59.13	<0.01	<0.1
Ap15d007.csv	184.64	13.10	95.37	106.59	0.31	3.41	0.89	52.35	2.23	284.54	2.52	2.73
Ap15d016.csv	900.24	13.10	96.41	27.51	1.50	3.02	<0.14	66.41	6.91	391.10	0.22	0.59
Ap15d018.csv	765.90	17.48	58.75	45.52	1.73	3.26	1.33	63.58	7.39	365.50	0.28	1.01
Ap15d020.csv	726.86	26.88	85.99	446.21	7.33	3.29	3.37	75.09	6.70	577.33	1.60	12.17
Ap15d008.csv	720.15	15.37	90.54	36.58	2.06	3.15	1.16	65.03	6.64	478.62	0.36	1.10
Ap15d010.csv	1048.56	29.76	48.65	30.91	42.11	3.79	3.61	65.16	8.46	325.28	0.33	0.68
Ap15d011.csv	725.05	13.98	46.15	5.18	2.33	2.97	0.95	57.15	6.87	348.49	<0.05	0.14
Ap15d012.csv	728.10	13.30	133.99	20.26	2.48	2.74	0.71	61.42	7.22	430.02	0.31	0.62
Ap15d013.csv	658.29	7.34	73.30	10.70	1.89	3.61	0.82	61.78	6.90	152.52	0.13	0.23
Ap15d014.csv	678.98	15.43	17.35	5.13	1.74	3.79	6.12	65.16	7.90	240.01	0.07	0.13
Ap15d015.csv	676.27	8.02	27.70	18.66	1.91	2.84	1.21	59.50	5.59	268.50	0.15	0.50
JA14B100.csv	756.91	<9.15	<0.01	33.04	1.30	2.89	<1.41	49.63	8.10	424.39	<0.01	0.75
JA14B101.csv	705.81	54.82	<0.01	3.06	1.37	2.73	2.41	42.00	6.73	114.03	<0.01	<0.1
JA14B102.csv	640.68	<5.57	<0.01	11.48	3.43	2.97	<0.77	41.29	6.78	358.80	<0.01	0.44

Table A13.1: LA-ICPMS of pyrite St Ives Gold District

Analysis	Ta (ppm)	W (ppm)	Au (ppm)	Tl (ppm)	Pb206 (ppm)	Pb207 (ppm)	Pb208 (ppm)	Bi (ppm)	Th (ppm)	U (ppm)
JA14B85.csv	<0.04	<0.14	0.39	13.22			158.46	5.80	<0.01	<0.07
Ap15d007.csv	<0.01	1.15	0.06	15.39	286.37	321.75	322.54	1.42	1.60	2.30
Ap15d016.csv	<0.01	1.14	0.24	33.57	162.18	181.54	174.63	6.92	0.13	0.52
Ap15d018.csv	<0.01	1.18	0.29	39.66	178.69	207.93	199.72	6.62	0.24	0.53
Ap15d020.csv	0.03	3.62	0.60	33.40	203.02	226.84	229.14	5.60	2.07	7.65
Ap15d008.csv	<0.02	1.64	0.47	29.55	180.66	211.05	203.65	7.11	0.25	0.51
Ap15d010.csv	<0.01	12.17	0.30	53.01	177.54	205.34	199.37	6.87	0.25	0.44
Ap15d011.csv	<0.01	1.25	0.23	25.75	167.18	194.44	188.27	6.29	0.05	0.12
Ap15d012.csv	0.03	1.63	0.23	28.85	175.36	201.69	196.60	6.66	0.16	0.41
Ap15d013.csv	<0.01	0.51	0.61	17.40	238.64	270.71	267.35	6.10	0.09	0.16
Ap15d014.csv	<0.01	0.82	0.27	25.26	187.45	214.12	208.01	7.11	0.06	0.11
Ap15d015.csv	0.01	0.95	0.23	26.32	156.79	178.12	177.14	5.97	0.14	0.35
JA14B100.csv	<0.07	1.77	0.16	20.45			246.52	5.18	<0.01	0.76
JA14B101.csv	<0.05	<0.33	0.17	17.39			218.80	4.49	<0.01	0.26
JA14B102.csv	<0.03	3.54	0.10	14.69			237.05	3.99	<0.01	0.45

Table A13.1: LA-ICPMS of pyrite St Ives Gold District											
Depth (m)	Drill Hole	Group	Mg (ppm)	Al (ppm)	Ca (ppm)	Ti (ppm)	V (ppm)	Cr (ppm)	Mn (ppm)	Cu (ppm)	Zn (ppm)
285.1-285.34	CD13829	sedimentary pyrite	1779.81	29102.75	<678.94	491.77	31.04	96.48	176.42	61.75	1485.00
285.1-285.34	CD13829	sedimentary pyrite	648.88	9786.73	811.65	107.87	8.42	<11.38	194.45	50.43	18.49
285.1-285.34	CD13829	sedimentary pyrite	299.81	787.23	127.73	4.36	0.23	<1.01	18.02	348.67	1265.05
285.1-285.34	CD13829	sedimentary pyrite	246.90	1228.17	<63.01	1.64	0.09	<1.59	89.97	174.99	1710.94
285.1-285.34	CD13829	sedimentary pyrite	161.13	1691.21	4258.09	5156.91	2.01	<3.15	69.69	2361.44	7.98
285.1-285.34	CD13829	sedimentary pyrite	169.32	734.11	647.06	9.26	0.50	<2.63	683.72	550.47	1053.39
285.1-285.34	CD13829	sedimentary pyrite	362.77	1450.50	385.34	2.47	0.09	<2.05	137.23	1335.22	110.68
285.1-285.34	CD13829	sedimentary pyrite	602.16	7849.89	<386.58	157.14	6.93	26.10	61.41	54.00	17.95
285.1-285.34	CD13829	sedimentary pyrite	957.67	13221.49	<434.03	171.92	13.82	34.05	80.95	54.16	15.13
285.1-285.34	CD13829	sedimentary pyrite	719.28	8308.19	<534.47	117.19	8.76	<14.43	97.21	59.70	19.08
285.1-285.34	CD13829	sedimentary pyrite	187.06	2307.45	<219.28	<1.83	0.05	<5.07	221.28	4172.84	4.69
285.1-285.34	CD13829	sedimentary pyrite	118.22	756.10	407.55	22.94	0.71	<3.65	199.24	287.04	14159.53
285.1-285.34	CD13829	sedimentary pyrite	850.64	13461.89	2229.56	69.73	4.92	<7.89	174.69	52.76	11.15
285.1-285.34	CD13829	sedimentary pyrite	810.69	17859.56	3673.69	59.53	5.81	13.53	144.88	50.86	11.04
285.1-285.34	CD13829	sedimentary pyrite	880.01	17099.91	2354.26	118.80	9.72	14.66	146.34	64.91	16.95

Table A13.1: LA-ICPMS of pyrite St Ives Gold District

Analysis	As (ppm)	Se (ppm)	Sr (ppm)	Zr (ppm)	Mo (ppm)	Ag (ppm)	Cd (ppm)	Sb (ppm)	Te (ppm)	Ba (ppm)	Gd (ppm)	Hf (ppm)
JA14B103.csv	722.66	<5.36	<0.01	390.20	1.80	3.84	<1.86	43.53	5.99	364.71	<0.01	12.66
JA14B104.csv	687.95	9.49	<0.01	2.45	2.15	2.20	<0.8	40.35	5.50	107.63	<0.01	<0.08
JA14B105.csv	25.85	33.40	<0.01	0.07	<0.01	2.03	4.18	4.45	0.16	0.70	<0.01	0.01
JA14B106.csv	129.85	31.41	<0.01	0.03	<0.02	2.17	4.35	6.83	0.33	0.64	<0.01	<0.01
JA14B107.csv	95.45	29.69	<0.01	1.81	<0.03	4.97	<0.27	4.92	0.19	3.53	<0.01	0.15
JA14B108.csv	298.33	54.48	<0.01	0.40	0.08	1.61	4.04	12.21	1.34	5.77	<0.01	0.03
JA14B109.csv	98.04	30.83	<0.01	0.37	<0.02	3.62	<0.19	9.86	0.44	1.47	<0.01	<0.01
JA14B110.csv	698.52	<4.46	<0.01	1.55	1.67	2.94	<0.99	43.72	8.08	75.65	<0.01	<0.06
JA14B111.csv	618.62	11.96	<0.01	60.57	1.67	2.68	<1.26	38.36	4.94	155.09	<0.01	2.03
JA14B112.csv	726.97	14.72	<0.01	1.94	1.66	3.09	<0.88	47.23	8.10	85.17	<0.01	<0.04
JA14B115.csv	59.78	66.16	<0.01	107.85	<0.07	8.29	<0.26	16.55	10.25	4.67	<0.01	1.76
JA14B117.csv	2411.30	152.63	<0.01	0.57	4.38	7.84	36.66	67.52	12.82	6.44	<0.01	<0.02
JA14B118.csv	913.59	14.68	<0.01	3.01	1.29	3.29	<0.38	45.29	6.72	55.70	<0.01	0.10
JA14B119.csv	799.71	9.27	<0.01	3.50	1.12	2.89	<0.67	46.90	6.00	57.91	<0.01	0.10
JA14B120.csv	890.46	15.33	<0.01	28.43	0.99	3.08	<0.25	56.82	7.61	103.86	<0.01	0.86

Table A13.1: LA-ICPMS of pyrite St Ives Gold District

Analysis	Ta (ppm)	W (ppm)	Au (ppm)	Tl (ppm)	Pb206 (ppm)	Pb207 (ppm)	Pb208 (ppm)	Bi (ppm)	Th (ppm)	U (ppm)
JA14B103.csv	<0.03	1.14	0.18	17.79			236.74	4.09	<0.01	13.24
JA14B104.csv	<0.03	0.32	0.23	15.74			183.64	4.89	<0.01	0.20
JA14B105.csv	<0.01	<0.01	0.02	0.25			1088.83	0.28	<0.01	<0.01
JA14B106.csv	<0.01	<0.03	0.03	0.32			3317.20	0.54	<0.01	0.02
JA14B107.csv	1.52	0.44	0.14	0.47			59.76	0.26	<0.01	0.79
JA14B108.csv	<0.01	0.06	0.02	1.44			64.49	0.45	<0.01	<0.01
JA14B109.csv	<0.01	<0.02	0.04	0.53			118.76	0.37	<0.01	<0.01
JA14B110.csv	<0.02	0.37	0.21	12.42			200.90	4.71	<0.01	<0.07
JA14B111.csv	<0.04	0.46	0.18	17.99			211.64	3.26	<0.01	1.30
JA14B112.csv	<0.03	0.41	0.22	15.33			227.18	5.17	<0.01	0.09
JA14B115.csv	<0.02	0.13	0.07	1.71			96.83	4.58	<0.01	1.68
JA14B117.csv	<0.01	<0.07	0.84	52.52			311.93	5.23	<0.01	<0.01
JA14B118.csv	<0.02	<0.09	0.24	20.50			207.51	3.60	<0.01	0.09
JA14B119.csv	<0.01	0.16	0.19	12.72			211.20	4.80	<0.01	0.15
JA14B120.csv	<0.01	0.56	0.20	19.57			246.64	4.83	<0.01	1.17

Table A13.1: LA-ICPMS of pyrite St Ives Gold District

Depth (m)	Drill Hole	Group	Mg (ppm)	Al (ppm)	Ca (ppm)	Ti (ppm)	V (ppm)	Cr (ppm)	Mn (ppm)	Cu (ppm)	Zn (ppm)
285.1-285.34	CD13829	sedimentary pyrite	580.66	18590.83	4052.28	51.52	5.74	13.56	141.45	61.63	13.36
285.1-285.34	CD13829	sedimentary pyrite	3.25	4.83	<35.84	0.91	0.02	<2.13	3.73	43.29	11.19
285.1-285.34	CD13829	sedimentary pyrite	6.59	9.03	109.70	1.52	<0.02	<2.39	3.03	16.05	1.89
285.1-285.34	CD13829	sedimentary pyrite	256.66	810.96	<55.29	7.60	0.41	<1.97	9.54	43.87	17.91
285.1-285.34	CD13829	sedimentary pyrite	4781.19	65897.91	<897.98	769.29	61.97	280.00	220.65	76.94	63.26
285.1-285.34	CD13829	sedimentary pyrite	434.65	6447.21	<521.61	64.28	5.41	<17.85	71.28	72.96	107.92
285.1-285.34	CD13829	sedimentary pyrite	11.27	42.75	<60.89	<0.65	<0.01	<2.18	20.11	285.90	400.42
285.1-285.34	CD13829	sedimentary pyrite	2.93	15.22	<68.59	1.27	<0.01	<2.91	2.44	19.45	1.48
285.1-285.34	CD13829	sedimentary pyrite	181.52	116.05	<61.22	<0.63	<0.01	<1.96	47.33	28.25	100.37
285.1-285.34	CD13829	sedimentary pyrite	53.18	174.44	<60.81	4.37	<0.01	<2.26	21.16	42.12	171.37
285.1-285.34	CD13829	sedimentary pyrite	1514.97	21421.43	3412.59	168.72	21.54	33.18	380.88	189.17	4431.04
285.1-285.34	CD13829	sedimentary pyrite	573.43	8862.61	1963.21	36.69	3.59	5.97	327.60	159.31	27352.60
285.1-285.34	CD13829	sedimentary pyrite	2264.60	37780.50	4698.98	261.43	34.79	44.02	473.81	55.72	68.83
285.1-285.34	CD13829	sedimentary pyrite	3787.74	57141.13	1947.64	458.43	68.32	91.02	735.01	81.87	86.43
285.1-285.34	CD13829	sedimentary pyrite	1075.86	24798.00	9464.23	72.90	10.63	11.15	401.41	57.71	66.26

Table A13.1: LA-ICPMS of pyrite St Ives Gold District

Analysis	As (ppm)	Se (ppm)	Sr (ppm)	Zr (ppm)	Mo (ppm)	Ag (ppm)	Cd (ppm)	Sb (ppm)	Te (ppm)	Ba (ppm)	Gd (ppm)	Hf (ppm)
JA14B121.csv	1037.05	8.74	<0.01	2.54	1.17	3.36	<0.31	46.61	6.06	43.77	<0.01	0.13
JA14B86.csv	440.96	76.51	<0.01	0.08	8.81	1.43	<0.11	17.74	2.19	2.06	<0.01	<0.01
JA14B87.csv	1000.83	32.32	<0.01	0.04	4.28	0.86	0.13	13.31	2.10	1.21	<0.01	<0.01
JA14B88.csv	681.12	46.27	<0.01	0.01	6.50	3.51	0.20	39.33	7.31	1.90	<0.01	<0.01
JA14B89.csv	800.94	<8.81	<0.01	154.21	3.50	3.66	<1.98	62.47	10.19	741.60	<0.01	4.44
JA14B90.csv	847.61	12.08	<0.01	3.72	2.36	4.38	0.74	42.76	7.43	61.09	<0.01	<0.1
JA14B93.csv	851.30	12.93	<0.01	<0.01	0.63	6.16	0.96	50.02	7.79	0.84	<0.01	<0.02
JA14B94.csv	663.58	14.68	<0.01	<0.01	1.20	2.17	<0.11	12.50	2.19	0.16	<0.01	<0.01
JA14B95.csv	749.55	15.05	<0.01	0.02	0.44	5.22	0.51	39.79	5.06	0.54	<0.01	<0.02
JA14B96.csv	809.97	10.06	<0.01	0.07	0.90	7.43	<0.22	57.01	8.13	4.07	<0.01	<0.01
Ap15d031.csv	1672.18	118.28	57.80	23.14	7.76	6.65	8.50	65.47	9.85	117.74	0.22	0.71
Ap15d032.csv	1923.47	117.54	40.18	2.41	6.62	9.48	62.68	69.61	12.05	20.27	<0.04	0.04
Ap15d033.csv	738.73	7.77	121.41	22.86	2.52	2.77	<0.1	43.49	6.46	187.51	0.47	0.62
Ap15d034.csv	743.69	16.30	120.10	40.63	1.83	2.57	0.35	51.94	7.10	362.72	0.19	1.05
Ap15d035.csv	707.54	11.01	135.75	10.20	3.01	2.64	<0.1	44.87	5.62	68.98	0.20	0.25

Table A13.1: LA-ICPMS of pyrite St Ives Gold District

Analysis	Ta (ppm)	W (ppm)	Au (ppm)	Tl (ppm)	Pb206 (ppm)	Pb207 (ppm)	Pb208 (ppm)	Bi (ppm)	Th (ppm)	U (ppm)
JA14B121.csv	<0.02	<0.07	0.24	9.98			243.72	4.03	<0.01	0.06
JA14B86.csv	<0.01	0.09	0.09	35.30			177.25	1.18	<0.01	<0.01
JA14B87.csv	<0.01	1.17	0.05	17.15			90.71	1.02	<0.01	<0.01
JA14B88.csv	<0.01	<0.03	0.34	25.00			266.72	4.10	<0.01	<0.01
JA14B89.csv	<0.09	3.02	<0.05	22.65			254.52	5.99	<0.01	2.00
JA14B90.csv	<0.03	0.37	0.15	10.74			209.77	4.06	<0.01	<0.07
JA14B93.csv	<0.01	<0.03	0.45	1.26			249.64	4.48	<0.01	<0.01
JA14B94.csv	<0.01	0.07	0.21	0.19			64.76	1.42	<0.01	<0.01
JA14B95.csv	<0.01	<0.04	0.44	0.61			225.87	3.70	<0.01	<0.01
JA14B96.csv	<0.01	0.07	0.58	3.58			270.63	5.26	<0.01	<0.01
Ap15d031.csv	<0.01	3.05	0.52	46.32	347.43	396.55	387.57	4.90	0.46	0.56
Ap15d032.csv	0.01	0.20	0.89	56.64	355.63	411.34	398.34	5.18	0.04	0.09
Ap15d033.csv	0.01	1.50	0.20	16.11	200.19	227.55	223.10	3.58	0.84	0.67
Ap15d034.csv	0.01	1.44	0.15	26.63	221.05	246.57	241.14	4.36	0.37	0.89
Ap15d035.csv	<0.01	1.26	0.12	13.71	207.51	241.19	233.78	3.58	0.66	0.48

Table A13.1: LA-ICPMS of pyrite St Ives Gold District											
Depth (m) or UTM (MGA94-51)	Drill Hole	Group	Mg (ppm)	Al (ppm)	Ca (ppm)	Ti (ppm)	V (ppm)	Cr (ppm)	Mn (ppm)	Cu (ppm)	Zn (ppm)
285.1-285.34	CD13829	sedimentary pyrite	1449.61	18708.37	9795.57	11777.67	19.35	23.91	492.60	57.41	68.00
285.1-285.34	CD13829	sedimentary pyrite	4753.77	63825.53	1662.86	1739.29	96.39	129.34	721.97	72.67	141.33
285.1-285.34	CD13829	sedimentary pyrite	1989.40	35951.34	1319.95	318.88	46.43	60.25	187.41	62.50	41.50
285.1-285.34	CD13829	sedimentary pyrite	3022.94	40432.23	760.66	402.83	55.71	72.42	293.37	73.23	37.82
285.1-285.34	CD13829	sedimentary pyrite	973.86	31650.37	18080.35	69.51	8.27	8.37	423.45	59.83	71.80
6533680/383020	LP AB11	Ore (leviathan pit)	<0.16	<0.45	<54.91	<0.57	<0.02	<0.68	<0.18	0.20	0.38
533680/383020	LP AB11	Ore (leviathan pit)	<0.18	<0.35	<47.87	<0.58	<0.03	<0.55	<0.17	0.21	<0.15
533680/383020	LP AB11	Ore (leviathan pit)	<0.18	<0.50	<55.64	1.04	<0.02	<0.54	<0.15	<0.08	<0.12
533680/383020	LP AB11	Ore (leviathan pit)	8.77	6.72	<40.86	1.49	0.04	<0.49	<0.17	0.19	0.30
533680/383020	LP AB11	Ore (leviathan pit)	7.50	6.13	<54.29	1.26	<0.02	<0.62	<0.11	<0.09	<0.15
533680/383020	LP AB11	Ore (leviathan pit)	<0.24	<0.38	<38.16	0.93	<0.02	<0.64	<0.15	<0.08	<0.11
533680/383020	LP AB11	Ore (leviathan pit)	<0.18	<0.32	<50.37	1.05	<0.02	<0.46	<0.16	<0.09	<0.1
533680/383020	LP AB11	Ore (leviathan pit)	<0.16	<0.33	<40.08	1.16	<0.04	<0.57	<0.13	<0.08	<0.13
533680/383020	LP AB11	Ore (leviathan pit)	<0.13	<0.40	<43.65	<0.39	<0.01	<0.62	<0.16	<0.1	0.37
533680/383020	LP AB11	Ore (leviathan pit)	<0.12	<0.36	<53.45	0.82	<0.01	<0.70	<0.13	<0.06	0.29

Table A13.1: LA-ICPMS of pyrite St Ives Gold District

Analysis	As (ppm)	Se (ppm)	Sr (ppm)	Zr (ppm)	Mo (ppm)	Ag (ppm)	Cd (ppm)	Sb (ppm)	Te (ppm)	Ba (ppm)	Gd (ppm)	Hf (ppm)
Ap15d036.csv	681.11	13.48	47.27	9.21	1.46	2.69	0.33	42.90	5.49	61.59	5.40	0.31
Ap15d027.csv	608.35	11.42	43.74	31.87	2.99	2.49	<0.15	47.96	6.47	495.90	0.81	1.02
Ap15d028.csv	755.45	11.49	49.11	11.17	2.17	2.85	0.33	46.75	6.70	244.66	<0.04	0.37
Ap15d029.csv	1110.94	23.46	50.01	22.98	6.28	2.83	<0.11	46.87	6.65	284.96	0.14	0.59
Ap15d030.csv	845.30	12.81	172.00	11.63	1.49	2.39	<0.14	47.28	6.71	69.93	0.26	0.31
Ap15c016.csv	1.32	15.79	<0.01	0.01	<0.04	<0.01	<0.05	<0.02	<0.13	<0.02	<0.02	<0.01
Ap15c015.csv	1.96	15.83	<0.01	<0.01	<0.02	<0.01	<0.05	<0.02	<0.13	<0.02	<0.02	<0.01
Ap15c007.csv	2.47	11.41	<0.01	0.66	<0.05	<0.01	<0.1	<0.01	<0.1	<0.03	<0.02	<0.01
Ap15c008.csv	2.75	15.86	<0.01	<0.01	<0.01	0.04	<0.05	<0.01	0.53	<0.02	<0.04	<0.01
Ap15c009.csv	3.76	13.10	<0.01	0.40	<0.01	<0.01	<0.04	<0.02	<0.1	0.06	<0.03	0.01
Ap15c010.csv	2.52	12.28	<0.01	0.02	<0.01	<0.02	<0.07	<0.01	<0.11	<0.02	<0.03	<0.01
Ap15c011.csv	1.46	12.73	<0.01	<0.01	<0.01	<0.01	<0.03	<0.02	0.16	0.04	0.01	<0.01
Ap15c012.csv	1.42	8.58	<0.01	<0.01	<0.01	<0.01	<0.06	<0.02	<0.08	<0.03	0.01	<0.01
Ap15c013.csv	0.93	16.47	<0.01	<0.01	<0.02	<0.01	0.05	<0.02	0.26	<0.02	<0.02	<0.01
Ap15c014.csv	5.04	8.28	<0.01	<0.01	<0.02	<0.01	<0.07	<0.02	0.39	<0.02	0.01	<0.01

Table A13.1: LA-ICPMS of pyrite St Ives Gold District

Analysis	Ta (ppm)	W (ppm)	Au (ppm)	Tl (ppm)	Pb206 (ppm)	Pb207 (ppm)	Pb208 (ppm)	Bi (ppm)	Th (ppm)	U (ppm)
Ap15d036.csv	2.94	2.59	0.15	13.22	196.52	218.20	213.50	3.39	0.70	5.34
Ap15d027.csv	0.28	2.48	0.15	23.04	217.55	245.96	241.40	3.94	0.56	1.41
Ap15d028.csv	0.01	1.48	0.17	22.56	203.02	231.15	224.36	4.17	0.12	0.31
Ap15d029.csv	0.01	7.36	0.21	21.88	214.35	243.94	239.64	4.12	0.19	0.54
Ap15d030.csv	<0.01	0.33	0.39	20.97	218.97	248.47	243.08	3.65	1.40	0.37
Ap15c016.csv	<0.01	<0.02	<0.01	<0.01	0.04	0.03	0.04	0.01	<0.01	<0.01
Ap15c015.csv	<0.01	<0.01	0.01	<0.01	<0.02	<0.01	0.03	0.03	<0.01	<0.01
Ap15c007.csv	<0.01	<0.01	<0.01	<0.01	0.02	<0.01	0.02	0.02	<0.01	<0.01
Ap15c008.csv	<0.01	<0.01	0.21	<0.01	0.25	0.32	0.31	0.30	<0.01	<0.01
Ap15c009.csv	<0.01	0.01	0.04	<0.01	0.09	0.08	0.09	0.10	<0.01	<0.01
Ap15c010.csv	<0.01	<0.01	<0.01	<0.01	<0.01	<0.01	0.01	<0.01	<0.01	<0.01
Ap15c011.csv	<0.01	<0.01	<0.01	<0.01	0.02	<0.01	0.02	0.01	<0.01	<0.01
Ap15c012.csv	<0.01	<0.01	<0.01	<0.01	0.03	<0.01	<0.01	<0.01	<0.01	<0.01
Ap15c013.csv	<0.01	<0.01	0.03	<0.01	0.04	0.04	0.04	0.10	<0.01	<0.01
Ap15c014.csv	<0.01	<0.01	<0.01	<0.01	0.02	<0.01	0.01	0.04	<0.01	<0.01

Table A13.2: SHRIMP-SI analyses from St Ives Gold District

Sample	Pyrite Types	$\delta^{34}S$	$\Delta^{33}S$
CD8142	Recrystallized Kapai Slate	3.39	1.06
CD8142	Recrystallized Kapai Slate	5.16	1.30
CD8142	Recrystallized Kapai Slate	4.57	1.05
CD8142	Recrystallized Kapai Slate	2.30	1.01
CD8142	Recrystallized Kapai Slate	1.10	1.05
CD7176	Ore stage pyrite	-8.45	-0.13
CD7176	Ore stage pyrite	-7.71	0.04
CD7176	Ore stage pyrite	-8.23	0.21
CD7176	Ore stage pyrite	-8.09	0.24
CD13833	Magnetite Series Kapai Slate Pyrite	5.07	-0.05
CD13833	Magnetite Series Kapai Slate Pyrite	7.11	0.03
CD13833	Magnetite Series Kapai Slate Pyrite	1.91	0.18
CD13833	Magnetite Series Kapai Slate Pyrite	1.61	0.23
CD13829	Kapai Slate sedimentary pyrite	3.85	2.44
CD13829	Kapai Slate sedimentary pyrite	3.71	2.32
CD13829	Kapai Slate sedimentary pyrite	4.27	1.00
CD13829	Kapai Slate sedimentary pyrite	3.74	1.18
CD13829	Kapai Slate sedimentary pyrite	2.73	1.44
CD13829	Kapai Slate sedimentary pyrite	2.39	1.08
CD13829	Kapai Slate sedimentary pyrite	4.13	0.70
CD13829	Kapai Slate sedimentary pyrite	2.38	1.16
CD13829	Kapai Slate sedimentary pyrite	2.53	1.31
CD13829	Kapai Slate sedimentary pyrite	2.89	0.82
CD13829	Kapai Slate sedimentary pyrite	4.50	1.34
CD13829	Kapai Slate sedimentary pyrite	2.52	1.08
CD13829	Kapai Slate sedimentary pyrite	2.52	1.00
CD13829	Kapai Slate sedimentary pyrite	5.99	0.13
CD13829	Kapai Slate sedimentary pyrite	4.05	0.73
CD1512	Kapai Slate sedimentary pyrite	2.32	-0.86
CD1512	Kapai Slate sedimentary pyrite	2.39	-0.22
CD1512	Kapai Slate sedimentary pyrite	3.77	-0.34
CD1512	Kapai Slate sedimentary pyrite	4.48	-0.74
CD1512	Kapai Slate sedimentary pyrite	-0.21	-0.60
CD1512	Kapai Slate sedimentary pyrite	7.41	0.01
CD1512	Kapai Slate sedimentary pyrite	3.45	-0.14
CD1512	Kapai Slate sedimentary pyrite	4.18	0.83
CD1512	Kapai Slate sedimentary pyrite	2.80	-0.42
CD1512	Kapai Slate sedimentary pyrite	2.69	-0.44